Crystallography Reports, Vol. 45, No. 6, 2000, pp. 1001–1006. Translated from Kristallografiya, Vol. 45, No. 6, 2000, pp. 1085–1090.

THIN FILMS

Assembly and Structural Study of the Films of Immunoglobulin M on Solid Substrates

R. L. Kayushina*, A. L. Tolstikhina*, N. D. Stepina*, V. V. Belyaev*, V. A. Lapuk, and E. Yu. Varlamova*****

** Shubnikov Institute of Crystallography, Russian Academy of Sciences, Leninskiĭ pr. 59, Moscow, 117333 Russia*

*** Zelinskiĭ Institute of Organic Chemistry, Russian Academy of Sciences, Leninskiĭ pr. 47, Moscow, 117334 Russia*

**** Hematology Research Center, Russian Academy of Medical Sciences, Moscow, 125167 Russia*

Received February 15, 1999

Abstract—Immunoglobulin M (IgM) was immobilized from a solution by the method of charge self-assembly on solid substrates (ordered polyelectrolytes and as-cleaved mica). The process of film formation and the structural organization was controlled and studied by the methods of atomic-force microscopy and X-ray reflectometry. It was shown that adsorption from rather concentrated (0.680–0.068 mg/ml) IgM solutions gave rise to formation of 100- to 150-Å-thick continuous protein layers. At lower concentrations (0.006 mg/ml), no continuous protein films were formed. The substrates of mica-type atomically smooth surfaces provide a higher image resolution, which, in turn, allows the observation of isolated IgM molecules and their aggregates. In the image plane, the molecules have rounded contours 300–500 Å in diameter and 40–60 Å in height. © *2000 MAIK "Nauka/Interperiodica".*

INTRODUCTION

In recent years, the efforts of numerous researchers have been aimed at studying and employing the principles which underlay the functioning of biological systems. This approach is applicable to the design of sensitive elements of immunosensors based on antigen–antibody interactions [1]. The design of highly efficient immunosensors requires the preparation of ordered films of functionally active proteins, i.e., the obtaining of immobilized monolayers of immunoglobulins or protein assemblies on solid substrates. It should be taken into account that changes in strength of interactions between the protein molecules and the substrate surface and between macromolecules upon protein immobilization can give rise to aggregation on the substrate surface and structural changes in macromolecules, resulting in the loss of the protein activity. Hence, one has to develop appropriate procedures for assembling mono- and multilayer highly organized assemblies and comprehensive study of their structures.

In recent years, atomic-force microscopy (AFM) has been widely used for gaining information on the structures of biological samples and interactions between biomacromolecules. However, the application of this method to biological samples is limited by numerous factors such as sample "softness" and the mode of macromolecule immobilization on a substrate in order to attain a higher molecular resolution and image reproducibility. Thus, the data on the biomolecules dimensions determined by atomic-force microscopy method are sometimes inconsistent [2, 3].

Earlier, we demonstrated that protein films can be assembled on a polyelectrolyte substrate by the method of charge adsorption with the use of X-ray reflectometry and atomic-force microscopy to control the process of formation of such multilayer assemblies [4].

Below, we describe our study of the structural organization of the films of immunoglobulin M adsorbed on solid substrates as a function of the conditions of their assemblage by the AFM and X-ray reflectometry methods.

EXPERIMENTAL

Materials and methods. Polyelectrolyte (PE) films were prepared from solutions of various polymers—poly(sodium styrenesulfonate) (PSS, M = 100000, Serva), poly(allylamine hydrochloride) (PAA, M = 50000–65000, Aldrich), and poly(ethylenimine) (PEI, M = 50000, Aldrich) as well as the salts $MgSO_4 \cdot 7H_2O$, NaBr, and NaCl (reagent grade, Reakhim). The solutions were prepared with the use of tridistilled water (pH 6.4). We also used tris-HCl (Merck), Sepharose CL-4B (Pharmacia), and the Coomassie Brilliant Blue R-250 dye (Bio-Rad).

Monoclone immunoglobulin M (IgM) was isolated using a procedure developed earlier [5]. At the final

1063-7745/00/4506-1001$20.00 © 2000 MAIK "Nauka/Interperiodica"

stage of protein purification by gel-filtration through Sepharose CL-4B, we used only the fractions corresponding to the region of the maximum and to the subsequent elution-peak decrease, because, according to the data of ultracentrifugation, only these fractions were virtually free of associates. The protein solutions were concentrated in an ultrafiltration cell (model 8050, Amicon) with a Diaflo PM-30 membrane. Before the experiments, the solutions were filtered (an ME-25 membrane filter with a mesh diameter of 0.45 μm produced by Schleicher and Schuell). Protein concentrations were measured by spectrophotometry at λ = 280 nm. The protein solutions were prepared in a 0.01 M tris-HCl buffer (pH 8.3) containing 0.1 M NaCl. The homogeneity and purity of the initial protein samples were checked by the immunoelectrophoresis (the micro version) and analytical ultracentrifugation methods [6].

The protein on the immunoelectrophoregrams and the solid substrates was detected by coloring with a 0.5% aqueous solution of Coomassie Brilliant Blue R-250 containing 35% ethanol and 10% acetic acid (Reakhim). The removal of the excessive dye was performed in the same medium [7].

Preparations of samples. An adsorbed protein layer was formed on a glass substrate ($40 \times 10 \times 2$ mm) preliminarily coated with a thin polyelectrolyte (PE) film of the composition PEI + $(PSS/PAA)_n$, where n is the number of the PSS/PAA bilayers. Polyelectrolyte films on glass substrates were obtained by charge self-assembly method [8]. The second type of the substrate for preparing an IgM layer was the surface of as-cleaved mica.

Immunoglobulin M molecules were immobilized by immersing the substrates into the protein solutions at room temperature. The time necessary for the formation of the adsorbed protein layer on the substrates varied from two minutes to three hours. After protein adsorption, the samples were washed with distilled water or first with tris-HCl and then with water (two minutes). The concentrations of IgM solutions varied from 0.680 to 0.006 mg/ml.

Atomic-force microscopy. Topographic images of the protein and PE film surfaces were obtained using the contact and taping AFM modes [9]. In the contact mode, the 85-μm Si_3N_4 cantilevers were used (Park Scientific Instruments; resonance frequency 120 kHz, curvature radius of the tip was 500 Å). In the taping mode, 90-μm conducting Si cantilevers were used (Nanotekhnologiya-MDT; resonance frequency 165 kHz; curvature radius of the tip was 200 Å). The studies were made on P4-SPM-MDT and P47-SPM-MDT scanning probe microscopes (Nanotekhnologiya-MDT). To obtain precise metric data along the horizontal and vertical directions, the microscope was calibrated against the atomic images of highly oriented pyrolytic-graphite surface (the accuracy of the measurements along the *X*- and *Y*-axes was 1%) and against calibration test lattices (the accuracy of measurements along the *Z*-axis was 10%).

X-ray reflectometry. The formation of the films on the substrates was checked by small-angle X-ray reflectometry data [4]. The measurements were made on an automated AMUR-K small-angle X-ray diffractometer (designed and constructed at the Shubnikov Institute of Crystallography of the Russian Academy of Sciences) equipped with a proportional position-sensitive OD-2 detector used as a recorder. The reflectivity curve $I(2\theta)$ was measured using the θ–2θ method. The scattering angle 2θ varied from 0.5° to 3.0° (λ = 1.54 Å). The angular resolution of the detector in this angular range was 0.02°. The change in the film thickness with an increase of the number of adsorbed layers was determined from the changes in the period of the Kissig oscillations in the reflectivity curve.

RESULTS AND DISCUSSION

Earlier [10], we demonstrated that the surface morphology of PE films practically did not change in the range of n = 5–10. With this number of PE bilayers (the thickness of the film is 200–500 Å), the error in the determination of dimensions of the PE/protein films by the method of X-ray reflectometry is minimal, and the film thickness can be determined within an accuracy of 5% [4]. Since most of the surface of an IgM molecule is negatively charged at pH > 5.5, we used PAA polycations as the upper PE layer of the film in IgM adsorption. The X-ray reflection curves for the pure polyelectrolyte PEI + $(PSS/PAA)_8$ film (curve *1*) and the film obtained after immobilization of IgM from the solution containing 0.068 mg/ml of the protein at room temperature (curve *2*) are shown in Fig. 1. The thickness of the immobilized protein layer was estimated from the change in the angular distance between the maxima (minima) of the Kissig oscillations. Under the experimental conditions used, the thicknesses of the protein layers attained up to 100 Å.

The effect of the time of substrate exposure in the IgM solution on the protein-film thickness was estimated from the X-ray reflectometry data. A stable protein film was obtained from the solution containing 0.068 mg/ml of IgM within 30 minutes. The existence of a protein layer on the PE film was confirmed by coloring of the substrate with a Coomassie solution.

The atomic-force microscopy data demonstrated that the change in the protein concentration in the solutions affected the morphology of the surface of an adsorbed IgM layer. The concentrations of the protein in the solutions of about 0.6 mg/ml provided the formation of continuous protein layers on the surface of PE films. With a decrease of the concentration to 0.006 mg/ml (at the same adsorption time), isolated protein islands of approximately equal thicknesses were observed. The topographs of the film surface of the composition PEI + $(PSS/PAA)_5$ before and after the

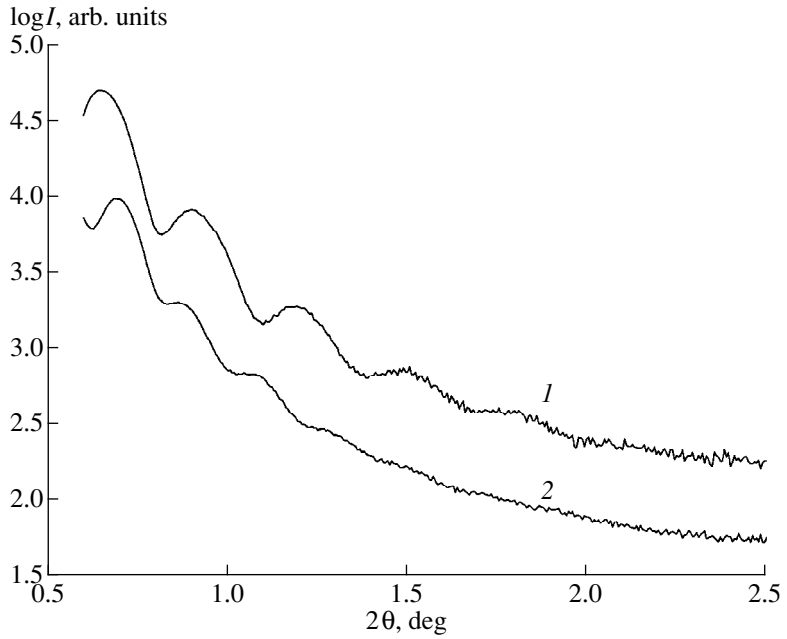

Fig. 1. X-ray reflection patterns from the polyelectrolyte film of composition PEI + $(PSS/PAA)_8$ applied onto a glass substrate by the method of charge self-assembly (*1*) before and (*2*) after immobilization of IgM on this substrate from a protein solution (at the concentration of 0.068 mg/ml).

application of a IgM layer from the protein solution of the concentration equal to 0.698 mg/ml are shown in Figs. 2a and 3a. The topographs were obtained in the taping mode at a scan rate of 1.6×10^4 Å/s. One can see the globules of various dimensions 250–300 Å in the horizontal direction and 30–40 Å in height (the major component of the PE layer) and rare individual agglomerates (attaining up to 900–1100 Å in length and 100–127 Å in height) on the surface of the pure PE film (Fig. 2a). The analysis of the surface profiles (one of them is shown in Fig. 2b) and the histograms of height distribution show that most of the heights (about 57.7%) range within ~30–40 Å. Morphologically, the protein film firmly attached to the PE substrate (Fig. 3a) seems to be smoother and more homogeneous than the pure PE film. The topographs yield the following characteristic dimensions of the globules on the surface: 270–400 Å (in the horizontal direction) and 60–70 Å (along the height). The histogram of the height distribution shows that the dominant height (for about 60.5% globules) is 50–60 Å.

Digital processing of the atomic-force microscopy data provided the analysis of the surface roughness. The algorithms for calculating the roughness parameters as a function of correlation roughness were described in [9]. Comparing two-dimensional functions of the correlation roughness, we came to a conclusion that the correlation between the globule dimensions is more pronounced for protein than for PE films. Morphologically, the protein films were more homogeneous. The correlation lengths L_c were determined as 238 and 441 Å for the protein and PE films, respectively. Hence, the protein surface of the PE film is coated with an almost continuous homogeneous layer, thus levelling the surface roughness.

The use of a PE film as a substrate providing a strong immobilization of biomolecules makes it possible to achieve a good image reproducibility. However, analysis of the images showed that the surfaces of these films are pronouncedly rough, thus reducing the image resolution. We believe that it is more expedient to immobilize biomolecules in the studies of intermolecular interactions, using fine-grain salt-free films studied in [10].

It should be emphasized that in [11], adsorption of immunoglobulin IgG and anti-IgG was performed on PE films. It was also shown that in this case, IgG molecules retained their activity in the antigen–antibody interactions on the surface.

To improve the resolution, IgM was adsorbed on a smooth surface of as-cleaved mica [12]. A protein is adsorbed on the mica surface due to electrostatic and hydrophobic interactions. The negative charge density on as-cleaved mica is about 2 e/nm^2 [13]. Positively charged regions of the protein molecule can interact with negatively charged centers on the mica surface. In this case, the neighboring protein molecules can interact via their hydrophobic regions. Adsorption of a protein from the solutions with the concentrations of about 0.680–0.068 mg/ml results in the formation of a continuous IgM film. The use of the AFM method in the taping mode provided imaging without breaking the layer structure.

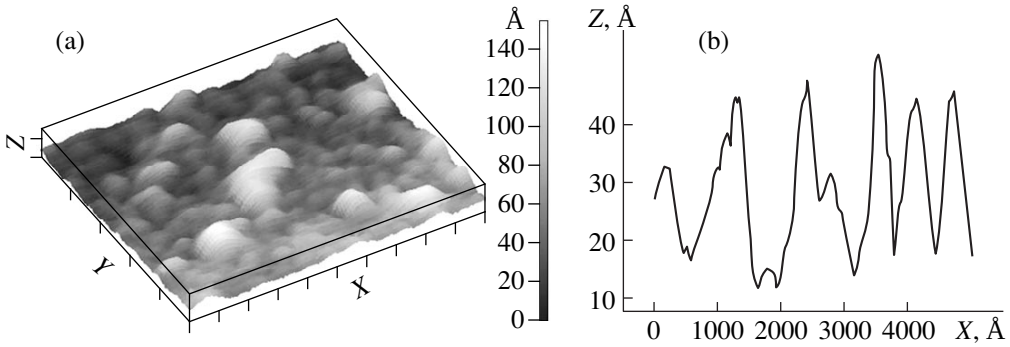

Fig. 2. (a) AFM image of the surface of the polyelectrolyte PEI + $(PSS/PAA)_5$ film applied onto a glass substrate by the method of charge self-assembly and (b) the profile of the surface parallel to the *X*-axis. The scanning range 5000 × 5000 Å. The experiment was made in the taping mode; the loading force applied to the cantilever was ~10^{-8} N (Figs. 2–5).

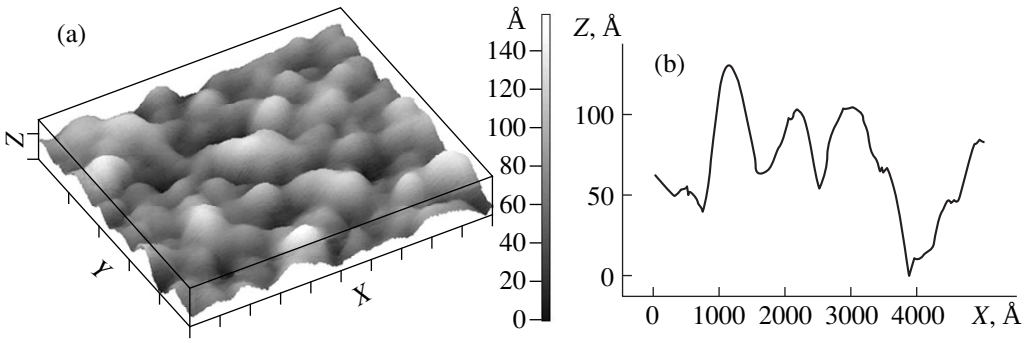

Fig. 3. (a) AFM image of the surface of the IgM film formed on the PE film (Fig. 2) by deposition from a protein solution with a concentration of 0.680 mg/ml and (b) the profile of the surface parallel to the *X*-axis. The scanning region was 5000 × 5000 Å.

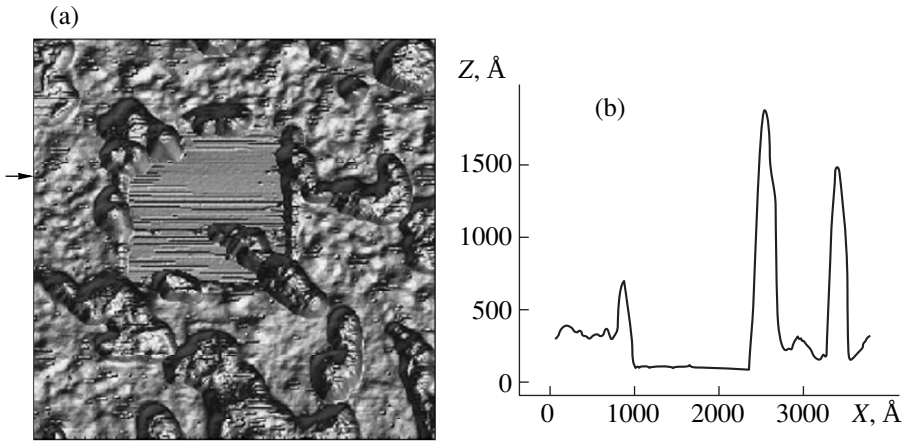

Fig. 4. (a) AFM image of the surface of the IgM film adsorbed on as-cleaved mica after the removal of the protein layer by repeated scanning of the corresponding film region (a square with a side of 15000 Å in the central region of the image) in the contact mode (~10^{-7} N). (b) The scanning range was 38470 × 43000 Å. The profile of the surface along the direction indicated by an arrow in Fig. 4a is parallel to the *X*-axis.

Under the scanning conditions in the contact mode with the application of the additional loading force (pressure ~10^{-7} N), the protein film was partially striped off the surface with the aid of an AFM cantilever. In turn, this allowed us to evaluate the thickness of the IgM film on the mica surface. The topograph of the surface of the protein film on mica obtained upon scanning a small area of this surface in the contact mode is shown in Fig. 4a. A square region completely free of immunoglobulin M can be seen in the topograph center.

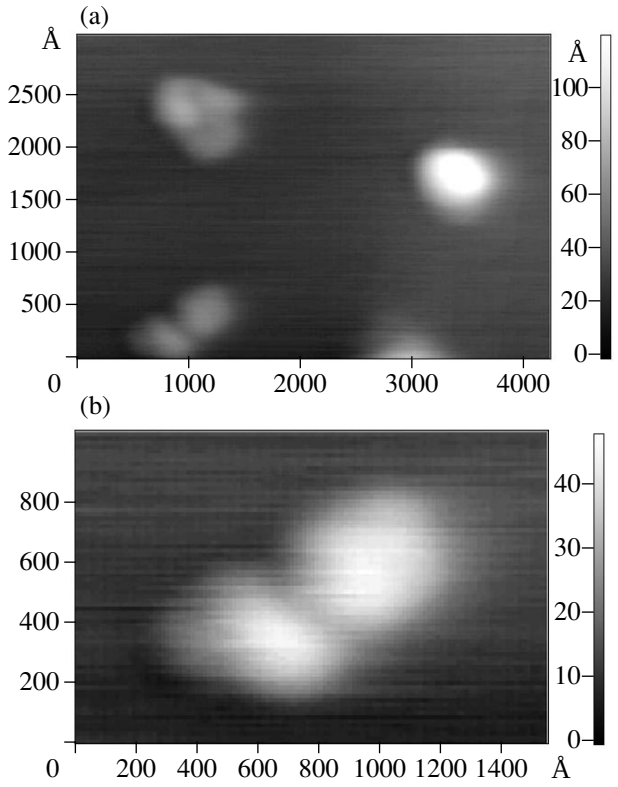

Fig. 5. AFM images of individual IgM molecules and their aggregates adsorbed on mica from the protein solutions with low concentrations ($c \cong 0.006$ mg/ml). The scanning regions were (a) 4200×3000 and (b) 1500×1000 Å.

The protein stripped from the substrate is seen at the periphery of the scanning region. The surface profile obtained along the direction indicated by an arrow in Fig. 4a is shown in Fig. 4b. On average, the thickness of the IgM film evaluated from the difference between the levels of the mica surface (within the square) and the IgM surface layer was 120–150 Å. This result agrees well with thickness of the protein film applied to the PE substrate obtained from the X-ray data.

We failed to determine the thickness of the protein layer on the PE film by removing the protein in the manner described above. Probably, our attempt was unsuccessful because the PE film (stronger than the IgM film) shows good adhesion to a glass substrate. In this case, the visual inspection of a cleaned square (with a depth of ~70 Å) does not allow an unambiguous answer to the question as to whether it is only the protein layer that is stripped, because the morphologies of the PE and the protein films are similar.

Experiments on protein adsorption from solutions on mica at lower concentrations indicated that isolated IgM molecules can be characterized using the AFM data. At low IgM concentrations in the solutions (of the order of 0.006 mg/ml), both isolated IgM molecules and characteristic protein aggregates are observed on the mica surface. Usually, the particles have rounded shapes, and their average dimension along the horizontal ranges within 400–500 and the height within 40–60 Å (Fig. 5). There are also smaller particles with a horizontal dimension of about 300 Å. Upon aggregation, molecules often form ellipsoidal particles with dimensions of about $600 \times 300 \times 50$ Å and more complicated aggregations.

As mentioned above, the known atomic-force microscopy data on the dimensions of individual IgM molecules are somewhat inconsistent. In [2], the dimensions of individual IgM molecules adsorbed on mica are indicated as 35 ± 5 nm. In [3], the diameter and the height of the molecules were determined to be 75.4 ± 7.9 and 1.2 ± 0.2 nm, respectively, whereas the use of another cantilever resulted in different values—36.3 ± 6.5 and 2.8 ± 0.5 nm, respectively.

The horizontal dimension of the macromolecules indicated in our study may be erroneous. The AFM image is, in essence, a convolution of the surface and probe images, which results in overestimation horizontal dimensions of the imaged objects due to the finite dimension of the probe tip and the effect of the lateral forces acting on the tip in the course of scanning.

CONCLUSIONS

Morphologically homogeneous IgM layers were obtained on solid PE substrates and on as-cleaved mica. It was shown that deposition from rather concentrated protein solutions (0.680–0.068 mg/ml) provides the formation of 100- to 150-Å-thick continuous protein layers. Adsorption from solutions of lower protein concentrations (up to 0.006 mg/ml), no continuous protein films are formed. The use of mica-like atomically smooth surfaces allows imaging of individual IgM molecules and their agglomerations and determination of their dimensions. The molecules in the image plane have rounded contours 300–500 Å in diameter and are 40–60 Å in height. The protein-layer thickness evaluated from X-ray reflectometry data agrees with the thickness determined from the atomic-force microscopy data.

ACKNOWLEDGMENTS

This study was supported by the Russian Foundation for Basic Research, project no. 96-04-50330.

REFERENCES

1. *Structure and Functions of Antibodies*, Ed. by L. Glynn and M. Steward (Wiley, Chichester, 1981; Mir, Moscow, 1983).
2. J. Yang, J. Mou, and Z. Shao, Biochim. Biophys. Acta **1199**, 105 (1994).
3. J. Thimonier, J. P. Chauvin, J. Barbet, and J. Rocca-Serra, J. Trace Microprobe Tech. **13** (3), 359 (1995).

4. R. L. Kayushina, N. D. Stepina, V.V. Belyaev, and Yu. I. Khurgin, Kristallografiya **41** (1), 156 (1996) [Crystallogr. Rep. **41**, 146 (1996)].
5. V. A. Lapuk, N. M. Khatiashvili, A. I. Chukhrova, and E. D. Kaverzneva, Biokhimiya **50**, 237 (1985).
6. V. A. Lapuk, V. Ya. Chernyak, and N. N. Magretova, Biokhimiya **61**, 85 (1996).
7. E. Harlow and D. Lane, *Antibodies: A Laboratory Manual* (Cold Spring Harbor Laboratory, 1988).
8. G. Decher, J. D. Hong, and J. Schmitt, Thin Solid Films **210/211**, 831 (1992).
9. P. A. Arutyunov, A. L. Tolstikhina, and V. N. Demidov, Mikroélektronika **27** (6), 431 (1998).
10. V. V. Belyaev, A. L. Tolstikhina, N. D. Stepina, and R. L. Kayushina, Kristallografiya **43** (1), 134 (1998) [Crystallogr. Rep. **43**, 124 (1998)].
11. F. Caruso, K. Niikura, D. N. Furlong, and Y. Okahata, Langmuir **13**, 3427 (1997).
12. A. L. Tolstikhina, R. L. Kayushina, N. D. Stepina, and V. A. Lapuk, in *Proceedings of the All-Russia Conference on Microprobing, Nizhniĭ Novgorod, 1999*, p. 243.
13. Yu. M. L'vov and G. Decher, Kristallografiya **39** (4), 69 (1994) [Crystallogr. Rep. **39**, 628 (1994)].

Translated by T. Safonova

Crystallography Reports, Vol. 45, No. 6, 2000, pp. 1007–1012. Translated from Kristallografiya, Vol. 45, No. 6, 2000, pp. 1091–1096.

SURFACE

Space–Time Self-Organization of the Vacancy–Impurity System of MBE-Grown Epitaxial (110)Si Layers

A. S. Perov*, A. A. Perov, and V. I. Perova****

** Institute of Education Development, Nizhniĭ Novgorod, Russia*

*** Nizhni Novgorod State University, Nizhniĭ Novgorod, Russia*

Received March 17, 1997; in final form, May 12, 1999

Abstract—The formation of nonuniform distributions of doping impurities (gallium or boron) in MBE-grown epitaxial (110)Si layers has been predicted. The effect is caused by vacancy self-organization and is associated with the formation of vacancy complexes consisting of one surface and two volume vacancies. The model suggested takes into account the impurity capture by kinks and surface vacancies and also the transitions of atoms between the surface and the bulk of crystal layers with due regard for the effect of an electric field induced by impurity ions. The spatial vacancy-impurity structures are calculated numerically. © *2000 MAIK "Nauka/Interperiodica".*

INTRODUCTION

The effect of the self-organization of epitaxial silicon layers grown from molecular beams in vacuum opens new vistas for constructing superlattices with unique quantum properties. Synergistic phenomena occurring during doping of epitaxial silicon layers [1–4] are of great importance for studying growth and the doping processes in semiconductor crystals.

Concentration self-oscillations of doping impurities in molecular-beam epitaxy (MBE) of silicon single crystals were first observed for (110)Si layers [1]. The self-oscillations can be caused by self-organization of either the system of impurities [1] or the system of surface (*S*) and volume (*V*) vacancies in a growing crystal [2]. Below, we consider a formal synergistic model [2] and then use it to predict the space–time self-organization of the vacancy–impurity system. We also use the concept stating that growth of (110)Si layers proceeds via growth of isolated chains of Si atoms [5].

A crystal surface is a powerful source of nonequilibrium *S*-vacancies formed because the growing atomic chains are close to a distance of one atomic diameter. The penetration of *S*-vacancies into the crystal bulk occurs via diffusion and also because the surface is covered with a monolayer of Si atoms.

We believe that the mechanism of the incorporation of *S*-vacancies migrating over the surface and penetrating the crystal bulk is an autocatalytic process. It provides the formation of vacancy complexes consisting of one *S*- and two *V*-vacancies located within a certain neighborhood of the *S*-vacancy. The *S*-vacancy that evolved into such complexes is smaller than the free *S*-vacancy. To form a monolayer of Si atoms, the *S*-vacancies of vacancy complexes migrate into the crystal bulk without capturing Si-atoms [6]. This results in the quadratically increasing dependence of the frequency of migration of *S*-vacancies into the crystal bulk on the concentration of *V*-vacancies.

The concentration of *V*-vacancies, which results in depletion of the surface of *S*-vacancies, continues unless the *S* concentration becomes lower than the critical value. This process is repeated again only upon a time sufficient for restoration of the critical concentration of the vacancy complexes. Diffusion of *S*-vacancies and impurity atoms over the crystal surface gives rise to an autocatalytic process of penetration of *S*-vacancies into the crystal bulk and the generation of the vacancy- and impurity-concentration waves.

Impurity atoms are captured by kinks and *S*-vacancies and also diffuse from the subsurface layer into the crystal bulk and are incorporated into the crystal. In this case, an important part is played by blocking of impurity atoms by mobile silicon adatoms and dimers in the kinks and subsurface layers. A nonuniform distribution of the vacancies in the bulk of a growing epitaxial layer gives rise to formation of inhomogeneous impurity structures.

KINETIC EQUATIONS AND THEIR SOLUTION

Consider doping of (110)Si layers with gallium or boron from molecular beams in vacuum such that no molecular complexes of the Ga_2-type can form on the crystal surface [7].

1063-7745/00/4506-1007$20.00 © 2000 MAIK "Nauka/Interperiodica"

The kinetic equations that describe growth, doping of epitaxial layer, and formation of vacancies are [2, 5, 6]

$$\begin{aligned}\partial\rho_1/\partial t &= W_0 - 2D(\rho_1, \rho_1)\rho_1^2 \\ &- [D(\rho_1, N)(N+h)(1-n_2/[N+h]) \\ &+ D(\rho_1, n_2)n_2 + D(\rho_1, \rho_2)\rho_2 \\ &+ D(\rho_1, N, N)N(N+h)(1-n_2/[N+h])^2]\rho_1,\end{aligned} \quad (1)$$

$$\begin{aligned}\partial\rho_2/\partial t &= D(\rho_1, \rho_1)\rho_1^2 \\ &- [D(\rho_2, N)(N+h)(1-n_2/[N+h]) \\ &+ D(\rho_2, n_2)n_2 + D(\rho_2, n_3)n_3 + D(\rho_1, \rho_2)\rho_1]\rho_2,\end{aligned} \quad (2)$$

$$\begin{aligned}\partial N/\partial t &= 2D(\rho_1, \rho_2)\rho_1\rho_2 \\ &- D(\rho_1, N, N)N(2N+h)(1-n_2/[N+h])^2\rho_1,\end{aligned} \quad (3)$$

$$\begin{aligned}\partial n_1/\partial t &= W - [K(n_1, 0) + D_{13}C_{se}X \\ &+ D(n_1, N)(N+h)(1-n_2/[N+h])]n_1 + K(n_2, n_1)n_2,\end{aligned} \quad (4)$$

$$\begin{aligned}\partial n_2/\partial t &= D(n_1, N)(N+h)(1-n_2/[N+h])n_1 \\ &- [K(n_2, n_1) + D(\rho_1, n_2)\rho_1 + D(\rho_2, n_2)\rho_2]n_2,\end{aligned} \quad (5)$$

$$\begin{aligned}\partial n_3/\partial t &= D_{13}C_{se}Xn_1 + [D(\rho_1, n_2)\rho_1 \\ &+ D(\rho_2, n_2)\rho_2]n_2 - [D(\rho_2, n_3)\rho_2 + D_{34}C_{ve}Y]n_3 \\ &+ D_{43}C_{se}Xn_4 + D_3(\partial^2 n_3/\partial x^2 + \partial^2 n_3/\partial y^2),\end{aligned} \quad (6)$$

$$\begin{aligned}\partial n_4/\partial t &= [D_{34}C_{ve}Y + D(\rho_2, n_3)\rho_2]n_3 \\ &- [W_0 + D_{43}C_{se}X]n_4,\end{aligned} \quad (7)$$

$$\begin{aligned}\partial X/\partial t &= D(\rho_1, N, N)\rho_1 N(N+h) \\ &\times (1-n_2/[N+h])^2/C_{se} + D(\rho_1, C_s)\rho_{1e} \\ &- [D(\rho_1, N)\rho_1(N+h)\gamma(1-n_2/[N+h]) \\ &+ D(\rho_1, C_s)(\rho_{1e}+\rho_1) + \omega^+ + D_{43}n_4 \\ &+ D_{13}n_1]X + [\omega^- + D_{43}n_3]Y \\ &- \delta C_{ve}^2 D(\rho_1, N)\rho_1(N+h)(1-n_2/[N+h])XY^2 \\ &+ D_s(\partial^2 X/\partial x^2 + \partial^2 X/\partial y^2),\end{aligned} \quad (8)$$

$$\begin{aligned}\partial Y/\partial t &= [D(\rho_1, N)\rho_1(N+h)\gamma(1-n_2/[N+h]) \\ &\times C_{se}/C_{ve} + \omega^+ C_{se}/C_{ve} + D_{43}n_4]X \\ &- [W_0 + \omega^- + D_{43}n_3]Y + \delta C_{ve}C_{se}D(\rho_1, N) \\ &\times \rho_1(N+h)(1-n_2/[N+h])XY^2.\end{aligned} \quad (9)$$

Here, t is the time of epitaxial-layer growth; x and y are the Cartesian coordinates of a point on the crystal surface; n_j (j = 1, 2, 3, 4) is the concentration of impurity atoms with valence j; ω^+ and ω^- are the frequencies of the diffusion transitions of *S*-vacancies into the bulk and the reverse transition of *V*-vacancies into the *S* state, such that $\omega^+ C_{se} = \omega^- C_{ve}$, where C_{se} and C_{ve} are the equilibrium concentrations of the *S*- and *V*-vacancies; N and h are the kink concentrations associated with growth processes and misorientation of the surface with respect to (110)Si; W_0 and W are the silicon and impurity-flux densities measured in the units of the frequency of a growing monolayer of silicon atoms; $X = C_s/C_{se}$ and $Y = C_v/C_{ve}$ are the relative concentrations of *S*- and *V*-vacancies; $K(n_1, 0)$ and $K(n_2, n_1)$ are the frequencies of impurity adatom desorption and the transitions of impurity from kinks to the desorbed state; D_{ij} is the frequency of the change of impurity valence from i to j; D_3 and D_s are the coefficients of surface diffusion for "triply coordinated" impurity atoms and *S*-vacancies; and $D(a, b)$ and $D(a, b, c)$ are the frequencies of interactions between the objects with the concentration a with the objects with the concentrations b and b, c.

The factor $(1 - n_2/[N + h])$ takes into account kink poisoning with impurity and determines the fraction of impurity-free kinks. The autocatalytically induced diffusion of *S*-vacancies forming the vacancy complexes into the crystal bulk is described by the terms $\delta C_{ve}^2 D(\rho_1, N)\rho_1(N + h)(1 - n_2/[N + h])XY^2$ and $\delta C_{ve}C_{se}D(\rho_1, N)\rho_1(N + h)(1 - n_2/[N + h])XY^2$ in Eqs. (8) and (9). Here, the frequency $D(\rho_1, N)\rho_1(N + h)$ determines the capture of a silicon adatom by a kink, whereas the factor $\delta C_{ve}^2 Y^2 = \delta C_v^2$ describes the probability of localization of two *V*-vacancies in the hemisphere $V_0 = 2\pi R_0^3/3$ of the radius R_0 in the vicinity of the *S*-vacancy. The quantity $\delta = \delta_0\Omega$, where $\delta_0 \approx 1$, is the probability that an *S*-vacancy would pass from the vacancy complex into the bulk during growth of a monolayer of Si-adatoms. $\Omega \approx N_0^2$ is the number of possible distribution of two *V*-vacancies over N_0 points of the crystal lattice within the volume V_0. In the numerical computations, we assumed that $R_0 \approx 7$ and $\delta = 5 \times 10^5$. The probability γ of migration of an *S*-vacancy not entering the vacancy complex into the crystal bulk during growth of a Si monolayer is assumed to be much less than the probability δ_0.

Equations (1)–(9) take into account the mobility of silicon dimers, which block impurity atoms in the kinks (with a frequency of $D(\rho_2, n_2)\rho_2 n_2$) and in the subsurface layer (with a frequency of $D(\rho_2, n_3)\rho_2 n_3$). The *S*-vacancies are generated mainly when the ends of the atomic chains at the (110)Si surface approach one another to a distance of one atomic diameter (with a frequency of $D(\rho_1, N, N)\rho_1 N(N + h)(1 - n_2/[N + h])^2$). The equilibrium mechanism of vacancy generation (at a frequency of G_e, which, in accordance with the principle of detailed equilibrium, equals the frequency $D(\rho_1, C_s)\rho_{1e}$ of the equilibrium annihilation of *S*-vacan-

cies) is less important. The kinetic equations describe only the processes of surface diffusion of *S*-vacancies and subsurface impurity atoms. These processes occur more intensely than diffusion of *V*-vacancies and impurity atoms in the first volume monolayer.

To solve the system of Eqs. (1)–(9) at the crystal surface, we have to introduce into consideration a discrete spatial square net with a step of h_s and substitute the second partial derivatives by their discrete analogues [8].

In the numerical computations of impurity, vacancy, kink, adatom, and silicon dimer concentrations (measured in the atomic fractions), the domain of integration for Eqs. (1)–(9) was chosen in the form of a square with a side equal to 0.38 μm. All the concentrations were assumed to be equal to 10^{-10} at all the boundaries of this domain except for the values $X = Y = 1$ and $n_4 = 2 \times 10^{-8}$. The initial concentration values were assumed to be equal to the corresponding values at the boundaries of the integration domain.

The computations were made at the parameter values characteristic of gallium-doped (110)Si layers [9]:

$$\rho_{1s} = C_{se} = \exp(-24/RT), \quad (10)$$

$$C_{ve} = \exp(-30/RT), \quad (11)$$

$$D(\rho_1, C_s) = 10^{13}\exp(-35/RT), \quad (12)$$

$$D_{13} = 10^{13}\exp(-36.5/RT - G), \quad (13)$$

$$\omega^{+} = 10^{13}\exp(-50/RT), \quad (14)$$

$$D(\rho_1, N, N) = 10^{13}\exp(-26/RT), \quad (15)$$

$$D(\rho_1, N) = D(\rho_1, \rho_2) = 10^{13}\exp(-24/RT), \quad (16)$$

$$\delta = 5 \times 10^5, \quad \gamma = 0.07, \quad (17)$$

$$D(n_1, N) = 10^{13}\exp(-20/RT)0.03, \quad (18)$$

$$D(\rho_1, \rho_1) = 10^{13}\exp(-30.64/RT), \quad (19)$$

$$D(\rho_2, n_2) = 10^{13}\exp(-50/RT), \quad (20)$$

$$D(\rho_2, N) = 10^{13}\exp(-30/RT), \quad (21)$$

$$D(\rho_1, n_2) = 10^{13}\exp(-24/RT)0.004, \quad (22)$$

$$K(n_1, 0) = 10^{13}\exp(-45/RT + G), \quad (23)$$

$$K(n_2, n_1) = 10^{13}\exp(-40/RT + G), \quad (24)$$

$$D(\rho_2, n_3) = 10^{13}\exp(-E/RT - G), \quad (25)$$

$$E = 24(1 + 0.3\ln(1 + \ln(1 + n_s/2 \times 10^{-7}))), \quad (26)$$

$$n_s = n_1 + n_2 + n_3 + n_4, \quad (27)$$

$$D_3 = 10^{13}\exp(-27.24/RT), \quad (28)$$

$$D_s = 10^{13}\exp(-27.24/RT), \quad (29)$$

$$D_{34} = D_{43} = 10^{13}\exp(-50/RT) \times (1 + [n_s/(n_i 2 \times 10^{-29})]^2), \quad (30)$$

$$\text{where} \quad n_i = 10^6\exp(47.195747 + 1.9932522 \times 10^{-3}T - 7422.7459/T). \quad (31)$$

In Eqs. (10)–(31), the activation energy is measured in kcal/mol; the impurity concentration (31), in m^{-3} [10].

Usually, the energy of a vacancy formation far from the silicon and germanium surface of these crystals is evaluated as 1.9 eV ≈ 43.8 kcal/mol [11]. The energy of vacancy formation in the first subsurface volume layer of the crystal was taken to be 30% lower than the above value, i.e., 1.3 eV ≈ 30 kcal/mol, whereas the energy of the surface-vacancy formation was taken to be 24 kcal/mol ≈ 1.04 eV. Such low energies of the formation of equilibrium point defects at the crystal surface are necessary to provide a nonuniform vacancy distribution.

If an epitaxial layer grows on the native semiconductor substrate, the *G* value (the increment in energy of an electric field of the crystal caused by the appearance at the surface of one impurity atom) expressed in the *kT* units, where *k* is the Boltzmann constant, is determined from the equation

$$G = \frac{F_a(\cosh\Psi_0 - 1)/|\sinh\Psi_0|}{1 + \dfrac{N_{ret}/2^{1/2}(\cosh\Psi_0 - 1)^{1/2}}{x_0 n_i|\sinh\Psi_0|}F_a(1 - F_a)}. \quad (32)$$

Here, $N_{ret} = 10^{19}$ m^{-2} is the reticular density of atoms at the (110)Si surface, n_i is the intrinsic carrier concentration in the semiconductor, x_0 is the Debye radius of point charge screening in a semiconductor with the relative dielectric constant ε (for silicon, ε = 12):

$$x_0^2 = kT\varepsilon\varepsilon_0/(2e^2 n_i). \quad (33)$$

Here, ε_0 is the electric constant, Ψ_0 is the potential of the electric field at the crystal surface in the *kT*/*e* units, and *e* is the absolute value of the electron charge determined by the equation

$$eN_{ret}n_s F_a/(2\varepsilon\varepsilon_0 n_i kT)^{1/2} = 2\sinh(\Psi_0/2). \quad (34)$$

We also assume that the ionization degrees of all the impurity atoms at the crystal surface are the same and equal

$$F_a = 1/[2\exp([E_a - F]/RT - \Psi_0) + 1], \quad (35)$$

with the effective energy being $E_a = E_v + 3$ kcal/mol, where E_v is the energy of the valence-band top of silicon and *F* is the Fermi level.

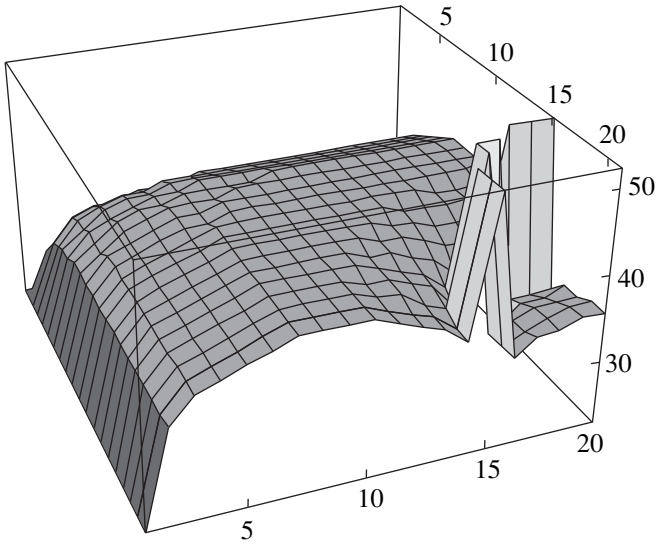

Fig. 1. Stationary distribution of volume vacancy concentrations in the plane of the gallium-doped epitaxial (110)Si layer at $h = 0$, $V = 25$ μm/h, $W = 7.155 \times 10^{-4}$ s^{-1}, and $T = 845$ K. Along the vertical axis, the points of a discrete net with a step of $h_s = 0.01$ μm represent the values of 10 log$Y$. One fourth part of the surface (0.19×0.19 μm^2) is shown.

RESULTS AND DISCUSSION

At the initial stage (prior to formation of the stationary vacancy–impurity structure), one observes the self-oscillations of the vacancy and impurity concentrations with the period usually not exceeding 20–30 atomic monolayers. The stationary vacancy and impurity distributions are formed within 1–2 s and have the form of cylinders with generatrices normal to the crystal surface.

Figures 1 and 2 show the stationary distributions of *V*-vacancies and gallium atoms substituting tetrahedrally coordinated silicon atoms in the subsurface region of the epitaxial (110)Si layer at the temperature $T = 845$ K, the growth rate $V = 25$ μm/h, and the density of the of adsorbed gallium-atom flux $W = 7.155 \times 10^{-4}$ s^{-1}. This W value corresponds to the impurity concentration in the sublimating silicon source equal to 10^{18} cm^{-3}.

The oscillations in vacancy concentrations result only in the change of n_3 and n_4 caused by diffusion of *S*- and *V*-vacancies; therefore, the *V*-vacancy and Ga concentration distributions in the crystal bulk n_4 on the whole, are similar.

The regions with vacancy and impurity concentrations one hundred times higher than their average concentrations have a diameter of about 0.01 μm and are located at distances of about 0.1 μm from one another and from the integration-domain boundaries. The characteristic size of inhomogeneity in the impurity distribution is about 0.02 μm.

Variations in the diffusion coefficients D_3 and D_s result in deformation of the spatial vacancy and impurity structures. In particular, a 20-fold decrease in D_s results in the reduction of the distances between the concentration maxima up to 0.03 μm. A decrease in D_3 increases the average impurity concentration but does not lead to "decomposition" of the vacancy–impurity structure into smaller fragments.

The time τ of diffusion spreading of the stationary cylindrical-vacancy and impurity structures is quite pronounced. At the substrate temperature $T = 845$ K

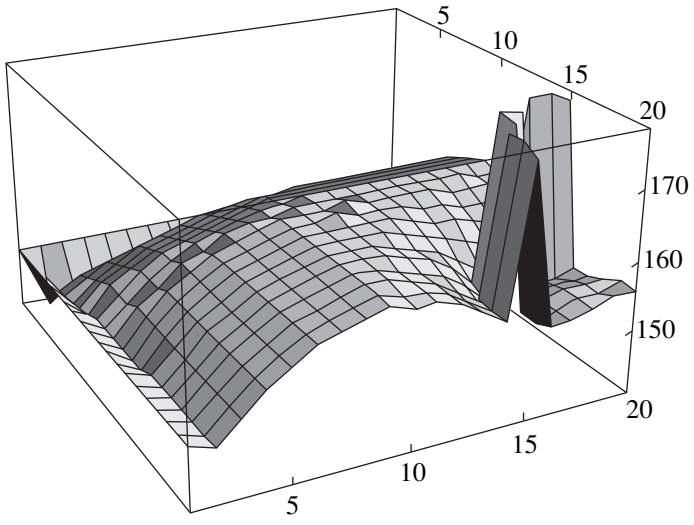

Fig. 2. Stationary distribution of gallium concentration $N_1 = n_4/2 \times 10^{-23}$ cm^{-3} with respect to the surface of the epitaxial (110)Si layer at $h = 0$, $V = 25$ μm/h, $W = 7.155 \times 10^{-4}$ s^{-1}, and $T = 845$ K. Along the vertical axis, the points of the discrete net with a step of $h_s = 0.01$ μm represent the values of 10 log N_1. One fourth part of the surface (0.19×0.19 μm^2) is shown.

and the volume diffusion coefficient of *V*-vacancies and impurities equal to $10^{13}\exp(-50/RT) \sim 1\ s^{-1}$, this time is $\tau \approx 0.7$ h at the diffusion length 0.01 μm.

The frequency of diffusion jumps in $D_{34} = D_{43}$ Eq. (30) and the impurity concentration n_s decrease with a decrease in *W*; the distribution of this concentration over the surface becomes uniform at $W < 10^{-5}\ s^{-1}$, whereas the self-organization and the inhomogeneity in the vacancy distribution are preserved.

At $W > 10^{-2}\ s^{-1}$, the phenomenon of vacancy self-organization and also inhomogeneity in impurity distribution do not take place. This is explained by an increase of the rate of the layer doping and is not associated with kink poisoning.

The vacancy self-organization can occur only within narrow ranges of the growth rate, temperature, the degree of surface misorientation of the substrate with respect to (110)Si and the impurity-flux density. Figure 3 shows the ranges of the growth-parameter variations for an epitaxial layer calculated by the methods of qualitative theory of differential equations [12] permitting self-oscillations of vacancy concentrations and the formation of stationary space vacancy–impurity structures.

With an increase in the misorientation *h* of the substrate with respect to the (110)Si, the temperature range of self-oscillations of the vacancy system over the epitaxial-layer thickness increases. Thus, at $V = 20$ μm/h, $h = 0$, and $W < 5 \times 10^{-6}\ s^{-1}$, the vacancy self-oscillations arise in the temperature range of 830–848 K; at $h = 5 \times 10^{-3}$, in the range of 800–830 K; and at $h = 10^{-2}$, in the range of 770–810 K.

With an increase in *h* at the given temperature, the range of epitaxial-layer growth rate providing the self-oscillations of the vacancy system broadens. Thus, at $h = 0$ and $T = 847$ K, this range equals 19.30 μm/h, whereas at $h = 0.005$ and the same temperature it is 26–49 μm/h.

Simulation of doping of the epitaxial (110)Si layers with boron was performed on the basis of Eqs. (1)–(9) with the substitution of the impurity-adatom desorption frequencies $K(n_1, 0)$ and the frequencies of impurity-adatom detachment from the kinks $K(n_2, n_1)$ by the values $K(n_1, 0) = 10^{13}\exp(-65/RT + G)$ and $K(n_2, n_1) = 10^{13}\exp(-60/RT + G)$. In this case, the period of vacancy–impurity self-oscillations increases by no more than 20%, and, on the whole, the main results obtained for doping with gallium remain valid for doping with boron. The experimentally observed period of self-oscillations of the boron-concentration equals 250 Si-monolayers [1], which is much higher than the period of the vacancy–impurity oscillations. Therefore, the cause of the impurity self-organization described in [1] is not associated with the self-organization of the vacancy system of the crystal.

In the case of growth of a semiconductor layer, the concentration self-oscillations along the specimen perimeter result in the formation of a 0.1-μm-thick wall with an inhomogeneous vacancy distribution at the moment 0.5 s after the beginning of the growth process. At the moment 1 s after the beginning of the growth process, the vacancy distribution within a half-area of the specimen surface in the vicinity of its boundaries becomes inhomogeneous. Then, a partial decomposition of the walls into individual fragments and cylindrical regions penetrating the crystal normally to its surface is observed far from the specimen boundaries.

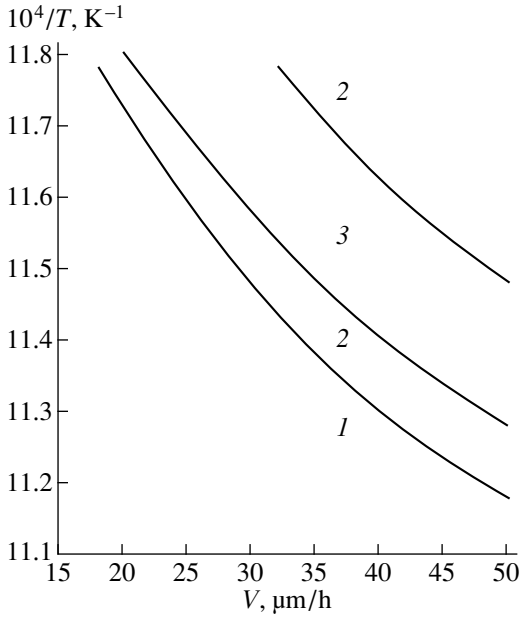

Fig. 3. The regions of vacancy distribution over the thickness of the grown epitaxial (110)Si layer at $h = 0$ and $W = 0$ as functions of the reciprocal temperature and growth rate: (*1*) monotonic, (*2*) oscillatory, and (*3*) attenuating oscillatory distributions.

CONCLUSIONS

The effect of space–time self-organization of the vacancy–impurity system of a gallium- and boron-doped homoepitaxial (110)Si layer has been predicted. The effect is caused by the formation of vacancy complexes consisting of one surface and two volume vacancies.

The growth rates, growth temperatures, and the degree of the epitaxial-layer misorientation with respect to the (110)Si layer, for which monotonic attenuating-oscillation and self-oscillation distributions of vacancies and impurities can be observed along the grown-layer thickness, have been determined. Depending on the conditions of the layer deposition and the quality of the substrate preparation, the period of self-oscillations can vary from 5 to 30 atomic monolayers.

If the mobility of surface vacancies is sufficiently high, the formation of a stationary space vacancy–impurity structure is possible. This structure usually

consists of a system of cylindrical tubes with a diameter of about 0.1 μm, which are located normally to the crystal surface. The vacancy concentration in tubes is 50–100 times higher than the average concentration, which, in turn, is higher by a factor of 10^3–10^4 than the equilibrium concentration. The time necessary for the formation of the stationary structure at the growth rate 25 μm/h and the temperature 845 K is not higher than 1–2 s. The characteristic dimension of elementary inhomogeneities in the vacancy and impurity distributions ranges within 0.01–0.02 μm. Cylindrical tubes with high vacancy and impurity concentrations are spaced by distances of about 0.1 μm.

REFERENCES

1. M. I. Ovsyannikov, A. S. Perov, V. I. Perova, and N. A. Alyabina, Kristallografiya **32** (6), 1499 (1987) [Sov. Phys. Crystallogr. **32**, 881 (1987)].
2. A. S. Perov and V. I. Perova, Poverkhnost', No. 5, 123 (1992).
3. O. P. Pchelyakov, Z. Sh. Yanovitskaya, I. P. Ryzhenkov, *et al.*, Poverkhnost', No. 5, 20 (1996).
4. Zh. I. Alferov, D. Bimberg, A. Yu. Egorov, *et al.*, Usp. Fiz. Nauk **165** (2), 224 (1995) [Phys. Usp. **38**, 215 (1995)].
5. A. S. Perov, Izv. Vyssh. Uchebn. Zaved., Fiz., No. 12, 92 (1981).
6. A. S. Perov and V. I. Perova, Kristallografiya **39** (3), 536 (1994) [Crystallogr. Rep. **39**, 477 (1994)].
7. V. A. Gugin, V. V. Postnikov, T. D. Komrakova, and R. A. Rubtsova, Izv. Akad. Nauk SSSR, Neorg. Mater. **18** (1), 5 (1982).
8. A. A. Samarskiĭ and A. V. Gulin, *Numerical Methods. Textbook for Higher Learning* (Nauka, Moscow, 1989).
9. A. S. Perov and V. V. Postnikov, Kristallografiya **29** (3), 546 (1984) [Sov. Phys. Crystallogr. **29**, 325 (1984)].
10. P. S. Kireev, *Physics of Semiconductors* (Vysshaya Shkola, Moscow, 1969).
11. P. I. Baranskiĭ, V. P. Klochkov, and I. V. Potykevich, *Electronics of Semiconductors. Properties of Materials. Reference Book* (Naukova Dumka, Kiev, 1975).
12. N. N. Bautin and E. A. Leontovich, *Methods and Techniques of Qualitative Study of Dynamical Systems on a Plane* (Nauka, Moscow, 1976).

Translated by L. Man

Crystallography Reports, Vol. 45, No. 6, 2000, pp. 1013–1017. Translated from Kristallografiya, Vol. 45, No. 6, 2000, pp. 1097–1101.

SURFACE

Effect of Duration of Thermal Diffusion of Boron on Silicon Structure Studied by Triple-Crystal X-ray Diffractometry

A. P. Petrakov, S. V. Shilov, and G. G. Zaĭnulin

Syktyvkar State University, Oktyabr'skiĭ pr. 55, Syktyvkar, 167001 Russia

E-mail: petrakov@ssu.edu.komi.ru

Received February 12, 1999; in final form, May 26, 1999

Abstract—The effect of thermal diffusion of boron on the structure of subsurface silicon layers has been studied by the method of triple-crystal X-ray diffractometry. The deformation and the static Debye–Waller factor profiles are determined. The dependence of the structure parameters on diffusion duration is discussed. © *2000 MAIK "Nauka/Interperiodica".*

INTRODUCTION

Diffusion of elements of groups III and V of the Periodic Table into the subsurface layer of silicon single crystals is widely used in technology of semiconductor materials [1, 2]. All the elements of groups III and V form covalent bonds with silicon atoms and occupy the crystal lattice positions. The presence in the lattice of impurity atoms with covalent radii different from those of the main elements gives rise to lattice deformation.

The changes in the lattice parameter can be determined from the diffraction reflection (or rocking) curves obtained in the double-crystal diffraction geometry [3–5]. Solving the inverse X-ray diffraction problem and using rocking curves, one can also study the deformation profile along the crystal depth [6–9].

However, this method cannot be used for studying crystals with defects, because a double-crystal diffraction experiment does not provide the separation of X-ray intensities scattered by defects and the ordered part of the crystal lattice. In order to separate these two types of scattering, one has to use the triple-crystal diffraction scheme [10].

We had the aim to study the structure of the subsurface layers of silicon single crystals as a function of thermal diffusion of boron atoms from the surface film by the method of triple-crystal X-ray diffractometry.

EXPERIMENTAL

The (111) surfaces of the single crystal silicon wafers were coated with 1000-Å-thick boron films. The angle of surface misorientation with respect to the (111) plane did not exceed 5″. Boron films were deposited onto the 0.5-mm-thick silicon wafers with the aid of a millisecond ruby laser with a free generation in vacuum. The film thicknesses were determined from the positions of the interference maxima on the integrated curves of the X-ray total external reflection [11].

Then, the specimens with deposited boron films were annealed for 20, 40, or 60 min in a helium (99.99%) atmosphere at 1000°C. The temperature was uniformly increased within 50 min from 22 up to 1000°C.

The diffusion-induced changes in the subsurface region of silicon single crystals were studied on a triple-crystal X-ray diffractometer (CuK_{α_1} radiation, the θ-2θ mode). The angular velocity of the analyzer was two times higher than that of the specimen. We also used scanning by an analyzer at the fixed angle of the specimen rotation. The diffractometer was supplied with a slit silicon monochromator with triple (111) reflection. The analyzer was also a silicon single crystal but with single (111) reflection.

EXPERIMENTAL RESULTS AND DISCUSSION

Figure 1 shows the calculated and experimental rocking curves obtained in the θ–2θ mode. The zeroth value of the angle corresponds to the exact Bragg position, large angles are positive, small angles are negative.

The curve obtained from the initial substrate has only one intense peak at $\theta = 0$. A 20-min-long thermal diffusion results in the formation of an additional weak maximum in the range of positive angles. A 40-min diffusion almost did not change the angular position of this peak, but a 60-min diffusion displaced this peak to zero.

The positions of additional peaks on the θ–2θ curves coincide with the positions of additional maxima on the reduced-intensity function $P(\alpha) = I_{mp}\alpha^2/k$, where I_{mp} is the intensity of the main peak on the triple-crystal curves and k is the normalization coefficient determined from the condition $P(\alpha) = 1$ for the crystal prior to diffusion [4]. This shows that the use of the θ–2θ

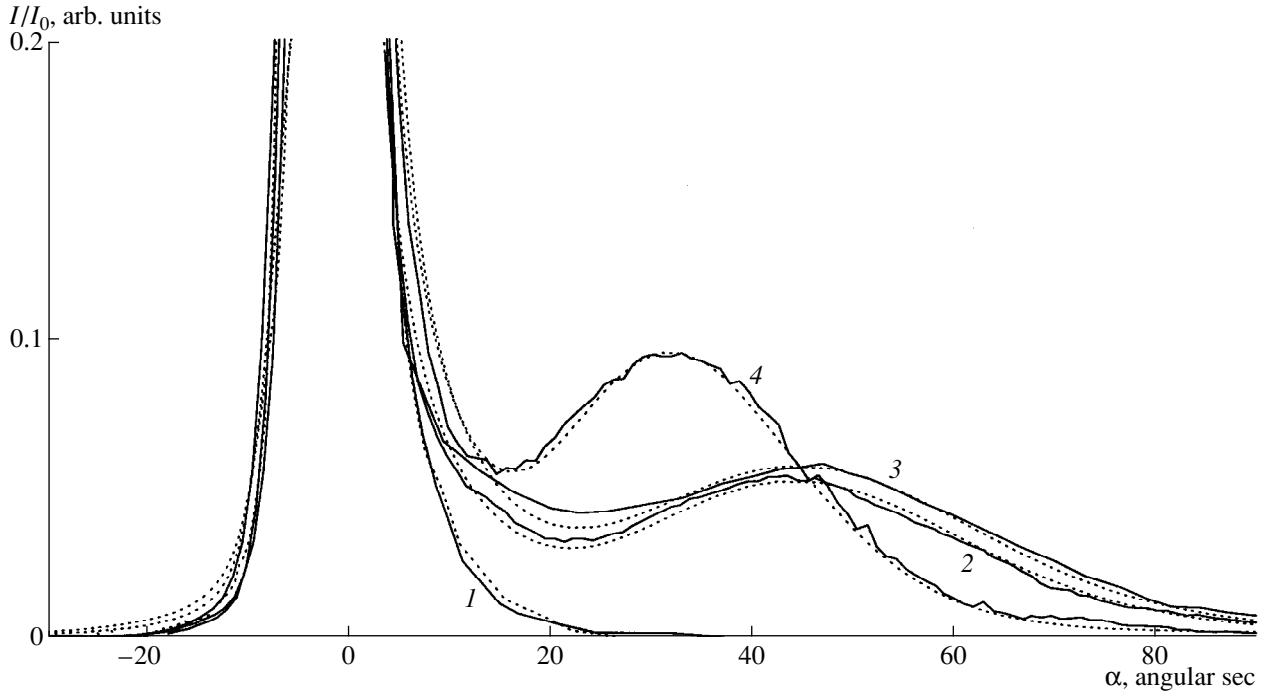

Fig. 1. Experimental (solid lines) and calculated (dash lines) θ–2θ curves (*1*) prior to diffusion and upon (*2*) 20-, (*3*) 40-, and (*4*) 60-min-diffusion.

mode does not allow recording of the radiation scattered by defects [12, 13].

Figure 2 shows the triple-crystal spectra from the specimens obtained in the scanning mode by an analyzer at the fixed angle of specimen rotation ($\alpha = -30''$). The spectrum of the initial silicon substrate is characterized by the presence of a pseudopeak in the angular position $\theta = -\alpha$ and the main peak in the position $\theta = -2\alpha$.

A 20-min diffusion gave rise to diffuse scattering in the vicinity of zero and several-fold reduction of the intensity of the main peak. A double increase of the diffusion duration was accompanied by an almost double reduction of the diffuse-scattering intensity with simultaneous double increase of the main-peak intensity. A further increase of the diffusion time to 60 min reduced diffuse scattering even more but increased the intensity of the main peak.

Figure 3 shows the deformation and the static Debye–Waller factor *f* profiles. A 20-min diffusion results in the deformed layer with the minimum depth *L*. The deformation, which is maximal in the vicinity of the surface, exponentially decreases with the crystal depth. The static Debye–Waller factor *f*, with the value considerably less than unity at the surface, decreases with the crystal depth down to ~38 μm and then starts increasing, approaching the unity.

An increase of diffusion duration up to 40 min results in an increase of the deformed-region depth and the *f* factor in the subsurface layer. A one-hour diffusion is characterized by a more pronounced deformation, an increase of *f* in the vicinity of the surface, and a further increase in *L*.

The appearance of an additional peak in the range of positive angle on the θ–2θ curves upon diffusion is explained by the presence of a layer with a negative deformation. Penetrating into the crystal depth, boron atoms occupy the positions at the lattice points. Since the tetrahedral covalent boron radius (r_B = 0.88 Å) is smaller than that of silicon (r_{Si} = 1.17 Å), the lattice "shrinks."

The angular position of an additional maximum is proportional to deformation ($\Delta d/d = -\alpha \cot\theta_B$, where θ_B is the Bragg angle). It should be emphasized that the θ-2θ curves provide the determination only of certain effective deformation, because the deformation profile is smooth and has no stepwise shape (Fig. 3).

Thus, a 20-min diffusion gives rise to the effective deformation $\Delta d/d = -1.1 \times 10^{-3}$. With an increase of diffusion duration up to 40 min, the deformation remains almost unchanged. According to Vegard's law, deformation is proportional to the concentration of impurity atoms occupying the lattice points, $\Delta d/d = 1.44\beta C$, where $\beta = (r_B r_{Si})/Nr_{Si} = -4.97 \times 10^{-24}$ cm^3 is the deformation coefficient (impurity-induced contraction) [4, 14] and $N = 4.99 \times 10^{22}$ cm^{-3} is the density of silicon atoms. Thus, to the maximum deformation in Fig. 4 ($\Delta d/d = 1.4 \times 10^{-3}$) there corresponds a boron concentration of $C \approx 2 \times 10^{20}$ cm^{-3}, which is considerably lower than the solubility limit (~10^{21} cm^{-3} at 1000°C [1, 15]).

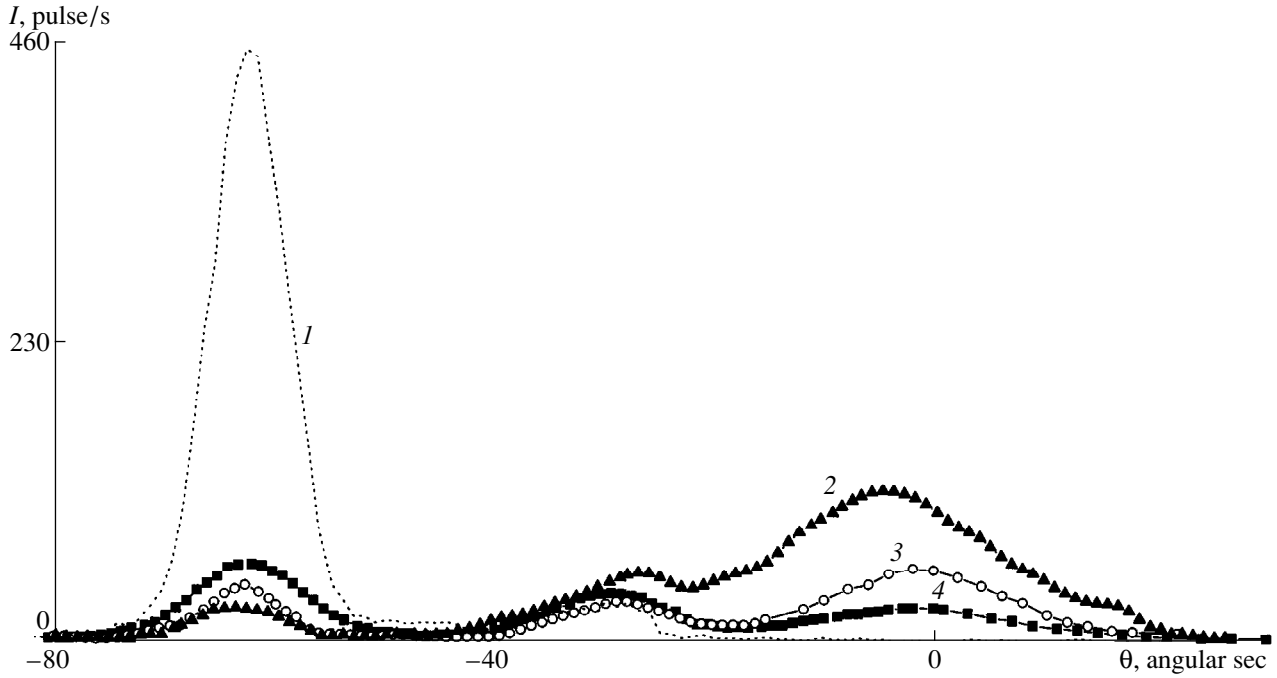

Fig. 2. Triple-crystal curves. Scanning with an analyzer at the fixed angle of specimen rotation $\alpha = -30''$. For notation see Fig. 1.

A further increase of diffusion time up to 60 min is accompanied by a considerable decrease of the absolute value of the effective deformation (to 0.73×10^{-3}) and, thus, the boron concentration. This is explained by the fact that for the time exceeding 40 min, the diffusion and evaporation of the film resulted in its disappearance. Thus, the condition of diffusion from a constantly refilled source is not fulfilled anymore. Some boron atoms, which diffused from the subsurface region into crystal bulk, reduced the effective deformation.

The thickness of the deformed layer can be determined from the width of the maxima of the reduced-intensity function [4]. During the 20-min diffusion, the thickness of the deformed layer attained a value of 0.60 μm; with an increase of the diffusion duration up to 40 and then 60 min, it increased up to 0.65 and 0.74 μm, respectively. Such a nonuniform change of the deformed-layer thickness indicates that the diffusion processes occurring at these stages are different. Indeed, an increase of the deformed-layer thickness with a simultaneous decrease of the effective deformation upon a 60-min thermal treatment indicates that the condition of a constantly refilled diffusion source is not fulfilled. Obviously, the film completely disappeared within ~40 min, and, therefore, the deformed-layer thickness could increase only due to diffusion from the subsurface layer, which was also confirmed by the deformation profiles in Fig. 3.

The deformation and the static Debye–Waller factor profiles, $\Delta d(z)/d$ and $f(z)$, were obtained by fitting the theoretically calculated θ-2θ curves to the experimental ones on the basis of the Taupin equations with due regard for two polarization states and the convolution [8, 16]. The unique solution of this problem can be obtained only with the invocation of some additional information. Therefore, we used as the initial approximation in numerical modeling the thickness of the deformed layer (calculated from the peak width on the reduced intensity curve), the maximum deformation (determined from the angular position of this peak under the assumption of a stepwise profile), and the profile $f(z)$ (obtained from the intensities of the main peaks on the triple-crystal curves [17]).

Upon a 20-min diffusion, the maximum deformation was observed near the surface. Then, deformation exponentially decreased with an increase of the crystal depth, which corresponded to the existence of diffusion layers [7].

An increase of the diffusion duration up to 40 min, almost does not change the maximum deformation. However, a decrease of deformation with the crystal depth becomes more smooth. The unchanged value of the maximum deformation indicates that under these conditions, the boron concentration attains its limiting value. The observed increase of the deformed-layer thickness and a smoother decrease of the deformation with the crystal depth indicates the occurrence of diffusion from a constantly refilled source.

With a still further increase of diffusion duration up to 60 min, the maximum deformation considerably decreases, whereas the thickness of the deformed layer increases.

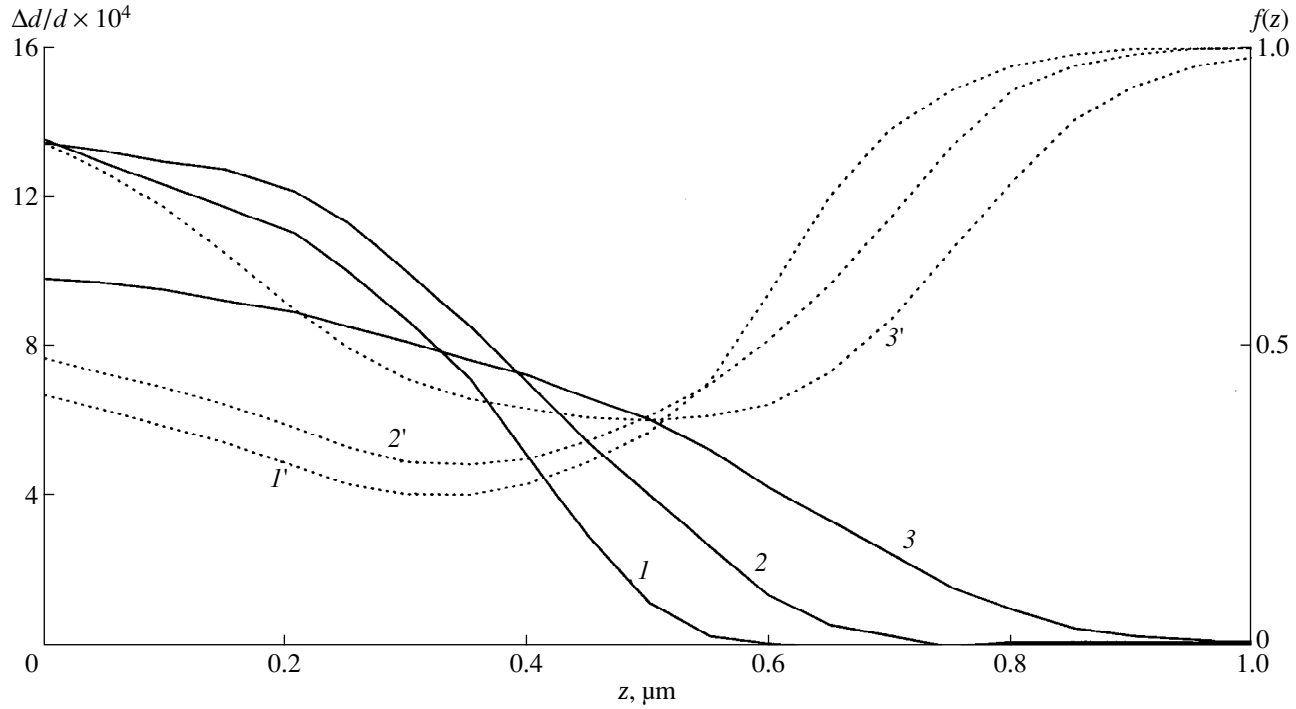

Fig. 3. Profiles of (*1–3*) the spatial deformation distribution $\Delta d(z)/d$ and (*1'–3'*) the static Debye–Waller factor $f(z)$. For notation see Fig. 1.

In the process of diffusion, some lattice defects are generated in the subsurface region, which is seen from the formation of a diffuse maximum on triple-crystal curves. The experimental points on the dependence of the diffuse-maximum intensity on the angle of specimen rotation (on a double logarithmic scale) are located along the lines with a slope close to 3–4, which is characteristic of the loops in the Stokes–Wilson region [4, 18, 19].

The considerable difference between the intensities of the diffuse maxima at the positive and negative rotation angles of the specimen indicates that these loops consist of interstitial atoms. Indeed, some boron atoms occupy interstitials between the lattice points. The estimate made by the Weisser formula [1] yields the value $B_i/B_s \sim 10^{-5}$, where B_i and B_s are the boron concentrations at interstitials and lattice points, respectively. The existence of the dislocation loops of the interstitial type in boron-doped silicon is confirmed by other independent studies [20].

The radii of the loops estimated by the formula $R \approx 1/h\Delta\alpha$, where h is the reciprocal-lattice vector and $\Delta\alpha$ is the angular width of the diffuse maximum, equal 0.34 μm. With an increase of diffusion duration, the diffuse-scattering intensity decreases, which indicates the reduced number of detects in the subsurface layer. This is also confirmed by an increase of the minimum value of the static Debye–Waller factor with an increase of diffusion duration in Fig. 3.

The "degree of defectness" can decrease because of smaller defect sizes and their lower concentration. The unchanged angular width of diffuse scattering indicates that the defects have stable dimensions [21]. A decrease of the degree of defectness can be explained by a faster increase of the diffusion region with time in comparison with the number of defects and the corresponding decrease in the defect concentration.

It should be noted that we mean a defect concentration averaged over the diffusion region. The formation of defects decreases the static Delye–Waller factor *f*, which slowly increased in the vicinity of the surface with an increase of the diffusion time up to 40 min. A further increase of diffusion time up to 60 min is accompanied by more intense increase of the static factor *f*.

The above studies lead to the following conclusion. In the process of thermal diffusion of boron from the deposited boron film into the silicon substrate, the substrate lattice is "contracted." During a 20- to 40-min diffusion, the thickness of the deformed layer increases almost without visible changes of the maximum deformation. A further increase of the diffusion duration results in an increase of the deformed-layer thickness with a simultaneous decrease of the effective deformation. The deformation is maximal in the vicinity of the surface and exponentially decreases with the crystal depth. The diffusion layer contains the loops of interstitial boron atoms. The maximum defect concentration is

observed in the layer located at a certain distance from the surface.

REFERENCES

1. *Atomic Diffusion in Semiconductors*, Ed. by D. Shaw (Plenum, London, 1973; Mir, Moscow, 1975).
2. V. E. Borisenko, *Solid-Phase Processes in Semiconductors Subjected to Pulsed Heating* (Nauka i Tekhnika, Minsk, 1992).
3. A. M. Afanas'ev, P. A. Aleksandrov, and R. M. Imamov, *X-ray Diffraction Characterization of Submicron Layers* (Nauka, Moscow, 1989).
4. V. A. Bushuev and A. P. Petrakov, Fiz. Tverd. Tela (St. Petersburg) **35** (2), 355 (1993) [Phys. Solid State **35**, 181 (1993)].
5. I. N. Smirnov, Dokl. Akad. Nauk SSSR **221** (2), 332 (1975) [Sov. Phys. Dokl. **20**, 224 (1975)].
6. A. Fukuhara and Y. Takano, Acta Crystallogr., Sect. A: Cryst. Phys., Diffr., Theor. Gen. Crystallogr. **A33** (1), 137 (1977).
7. V. Holy and J. Kubena, Czech. J. Phys. B **29** (10), 1161 (1982).
8. V. A. Bushuev and A. P. Petrakov, Kristallografiya **40** (6), 1043 (1995) [Crystallogr. Rep. **40**, 968 (1995)].
9. V. I. Punegov, A. P. Petrakov, and N. A. Tikhonov, Phys. Status Solidi A **122** (2), 449 (1990).
10. A. Iida, Phys. Status Solidi A **54** (2), 701 (1979).
11. M. A. Andreeva, S. F. Borisova, and S. A. Stepanov, Poverkhnost', No. 4, 5 (1985).
12. P. Zaumseil, Phys. Status Solidi A **91** (1), K31 (1985).
13. J. M. Vanderberg, B. A. Hamm, M. B. Panish, and H. Temkin, J. Appl. Phys. **62** (4), 1278 (1987).
14. M. Servidori, A. Zani, and G. Garulli, Phys. Status Solidi A **70** (2), 691 (1982).
15. V. S. Vavilov, V. F. Kiselev, and B. N. Mukashev, *Defects in Silicon Bulk and on Silicon Surface* (Nauka, Moscow, 1985).
16. A. P. Petrakov and E. A. Golubev, Fiz. Tverd. Tela (St. Petersburg) **40** (1), 156 (1998) [Phys. Solid State **40**, 140 (1998)].
17. A. P. Petrakov and V. A. Bushuev, Pis'ma Zh. Tekh. Fiz. **19** (19), 92 (1993) [Tech. Phys. Lett. **19**, 637 (1993)].
18. P. H. Dederichs, Phys. Rev. B **4** (4), 1041 (1971).
19. P. H. Dederichs, J. Phys. F: Met. Phys. **3**, 471 (1973).
20. B. I. Boltaks, *Diffusion in Semiconductors* (Fizmatgiz, Moscow, 1961; Academic, New York, 1963).
21. V. A. Bushuev, Fiz. Tverd. Tela (Leningrad) **31** (11), 70 (1989) [Sov. Phys. Solid State **31**, 1877 (1989)].

Translated by L. Man

Crystallography Reports, Vol. 45, No. 6, 2000, pp. 1018–1023. Translated from Kristallografiya, Vol. 45, No. 6, 2000, pp. 1102–1107.

SURFACE

Discharge Indentation of Silicon Carbide Crystals

V. A. Karachinov

Novgorod State University, Novgorod, 173003 Russia

Received December 29, 1998; in final form, July 19, 1999

Abstract—The morphology of fracture faces formed upon discharge indentation of 6*H*-polytype of silicon carbide single crystals has been studied by optical methods. The experiments performed provided the evaluation of face brittleness. © *2000 MAIK "Nauka/Interperiodica".*

INTRODUCTION

As is well known, all the mechanical tests of crystals can reveal a set of properties characterizing elasticity, plasticity, and strength of these crystals. Usually all the classical methods of evaluation of these properties are based on the study of indentations (made by a mechanical indenter on a crystal face) or traces in the form of rosettes (revealed by the subsequent etching of the crystal) [1]. It is also well known that an electric breakdown of a wide class of single crystal dielectrics can result in the formation of traces in the form of oriented discharge channels. In the process of discharge, the elements of plastic deformation can be formed and, in some organic crystals, the so-called Fröhlich breakdown can also occur, which gives rise to crystal cracking [2, 3].

An electric discharge in SiC crystals can result in the formation of surface patterns consistent with the crystal symmetry. Most often, the discharge provides SiC luminescence in the green spectrum range and is accompanied by various sonic effects. Two forms of discharge—surface and bulk—can cause complete crystal fracture. In this case, three main fracture modes are possible over a rather wide energy range of electric discharge, namely, the liquid-phase mode, explosion-like evaporation, and mode and shock-type fracture mode (the so-called Yutkin effect) [4–7, 8]. Despite the fact that the main element of the fracture patterns is an erosion pit, it is possible to create such discharge conditions that the change in the morphology of the fracture patterns would allow the evaluation of the strength properties of SiC crystals and, in particular, the crystal propensity to brittle fracture.

Below, we describe the experimental study of such processes in silicon carbide crystals.

EXPERIMENTAL

The discharge indentation of SiC crystals was performed on a laboratory setup consisting of a generator of single pulses and a system of sliding steel needlelike and cylindrical electrodes applied to crystal faces. The energy E_p of electric pulses ranged within 1.1×10^{-2}–0.9 J. The medium was a transformer oil at room temperature. The specimens were platelike and bulk single crystals of 6*H*-SiC polytype with natural and preliminarily polished and etched (KOH melt) falls. The specimen thickness varied within 450–4000 μm; the concentration of uncompensated donors was $N_d - N_a = 5 \times 10^{18}$ cm^{-3}. The average dislocation density evaluated from the hexagonal etch pits was $N_D = 1 \times 10^4$ cm^{-2} for the platelike crystals and $N_D = 5 \times 10^5$ cm^{-2} for the bulk crystals.

The morphological characteristics of indented regions were studied by optical and chemical methods (metallographic microscope, etching in the KOH melt) and by scanning-electron microscopy (a BS-340 microscope) in the mode of secondary ion emission.

EXPERIMENTAL RESULTS AND DISCUSSION

Our studies showed that a shock acoustic wave generated during partial discharge provides the formation of the fracture zone in the crystal, whose structure depends on the properties of the initial crystal and the experimental conditions. Consider the effect of such intense factors as the face orientation and the dislocation structure [1, 3].

The discharge indentation of the (0001) face can give rise either to the local crystal fracture (Fig. 1a) or the cleavage of the platelike crystal along the $(10\bar{1}0)$ plane (Fig. 1b).

The fracture region consists of the basic depression; a system of radial and circular cracks; and some stressed regions (Fig. 1a, *3*), whose boundaries can be visualized due to effects of light interference [9].

The shape of the basic depressions depends on the pulse energy. The use of the transient modes of face fracture including SiC evaporation provided the formation of depressions with the shape close to paraboloids of rotation with the axes coinciding with the [0001] direction. In the case of pure brittle fracture, the depres-

1063-7745/00/4506-1018$20.00

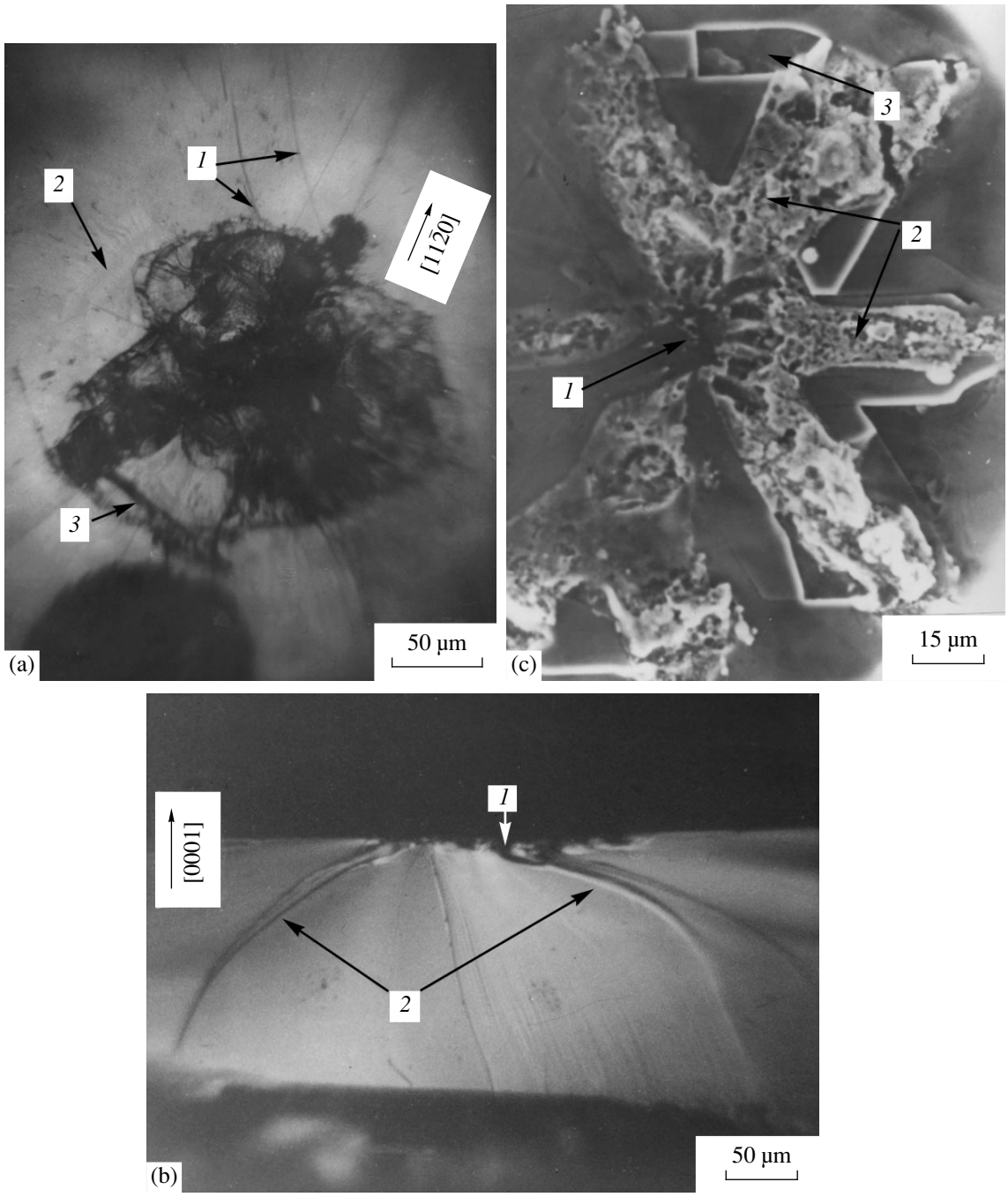

Fig. 1. The (0001) fracture face of a platelike SiC crystal: (a) local fracture [(0001)Si face, E_p = 0.7 J, cylindrical electrode], (*1*) radial cracks, (*2*) stressed region, (*3*) circular crack; (b) morphology of the SiC cleavage along the (1010) plane (cylindrical electrode) (*1*) discharge region from the side of the (0001)Si face, (*2*) cleavage steps caused by channels of partial volume breakdown; (c) snow-flake fracture pattern (scanning electron microscope, needlelike electrode, (0001)Si face), (*1*) the region of the needlelike electrode contact with the specimen, (*2*) elongated erosion pits, (*3*) cracks (cleavages).

sions had, in addition to hexagonal elements, the symmetry elements of the face. Moreover, clearly bounded fracture regions having no visible radial cracks were also observed on the crystal surface. These regions had arbitrarily shaped erosion pits limited by closed hexagonal cracks at a certain distance from the pit edges. The crack sides were parallel to the $(10\bar{1}0)$ cleavage plane.

The detailed study of the material fragments "cleaved out" from the crystal showed that they are associated with the so-called secondary cracks parallel to the (0001) face. Propagating upon a shock pulse in

Fig. 2. Crack of a complicated shape with a cleavage (scanning electron microscope, bulk SiC crystal, $(11\bar{2}0)$ face, $E_p = 0.5$ J).

the field of residual stresses, these cracks intersect the crystal surface and provide the detachment of some material fragments. In this case, the effect of the discharge indentation becomes similar to the effect produced by a sharp mechanical indenter [10].

The radial cracks emerging onto the crystal surface were usually rather long; were oriented along the $[11\bar{2}0]$ and $[10\bar{1}0]$ directions; and, according to their structure, could be related to "brittle cracks" [1]. The generation of radial cracks was mainly associated with the crystal fracture along the cleavage planes. The circular cracks often played the role of the elements "closing" the radial cracks. The front of these cracks or front fragments often emerge to the face surface and, thus, give rise to sectorial cleavage of the crystal.

Table 1. Brittleness of different faces of 6*H*-SiC crystals

6*H*-SiC single crystals	Brittleness index***			
	(0001) C	(0001) Si	$(11\bar{2}0)$	$(10\bar{1}0)$
Platelike crystals*	3	3	4	5
Bulk crystals**	4	4	4	5

* Grown by the Lely method.
** Grown by the method developed at the Leningrad Electrochemical Institute (LETI method).
*** Measured on the Ikornikova scale [12].

The fracture of SiC crystals along the cleavage planes resulted in the formation of an uneven surface with cleavage micro- and macrosteps originating from the basic depression (Fig. 1b). The formation of such steps is caused by channels of partial volume breakdown of the crystal within the basic depression and the propagation of a shock-wave-induced crack over the planes located at different levels.

We should like to mention here the experiments with a needlelike electrode applied to the (0001)Si face. In this case, snowflake patterns similar to dislocation rosettes were formed (Fig. 1c). However, etching of SiC crystals with such fracture patterns in the KOH melt revealed no traces of sliding. The etching pattern had individual groups of hexagonal etch pits seemingly associated with growth dislocations and etching grooves along the cracks.

The formation of snowflake patterns can also be caused by the orientation of electric discharges along the energetically favorable $[11\bar{2}0]$ directions and the formation of the corresponding shock waves. This mechanism is also confirmed by the formation of elongated erosion pits (Fig. 1c).

Comparing the crystallographic indices of the fracture traces forming a snowflake pattern (elongated erosion pits, cracks, and "cleaved-out" regions) with the well-known elements of brittle fracture in 6*H*-SiC crystals (with the wurtzite structure) [1, 10, 11], one can single out two main fracture systems—that along the $(10\bar{1}0)$ cleavage planes and that along the (0001) planes associated with parting. The latter phenomenon is also confirmed by the presence of smooth steps of "cleaved-out" material and cracks (Fig. 1c, *3*).

The brittle fracture of the $(11\bar{2}0)$ face began at the energy $E = 0.36$ J. One of the diagonals of the basic square depression was oriented parallel to the *c*-axis. The fracture region had characteristic cracks and cleaved-out regions of complicated shapes (Fig. 2), which often distorted the shape of the basic depression. In the experiments, the surface of this face had nets formed by cracks intersecting at right angles. These cracks corresponded to the fracture system formed along the $(10\bar{1}0)$ cleavage and the (0001) parting planes.

The traces of noticeable brittle fracture of the $(10\bar{1}0)$ face were observed even at low pulse energies ($E = 0.08$ J). The electric break-down was accompanied by pronounced cracking and crystal fracture via material being layered off along the cleavage planes (Fig. 3a). The ratio between the area of the basic depression and the visible fracture region amounted to 10. The fracture region usually had a well-developed structure around a rectangular depression (Fig. 3b),

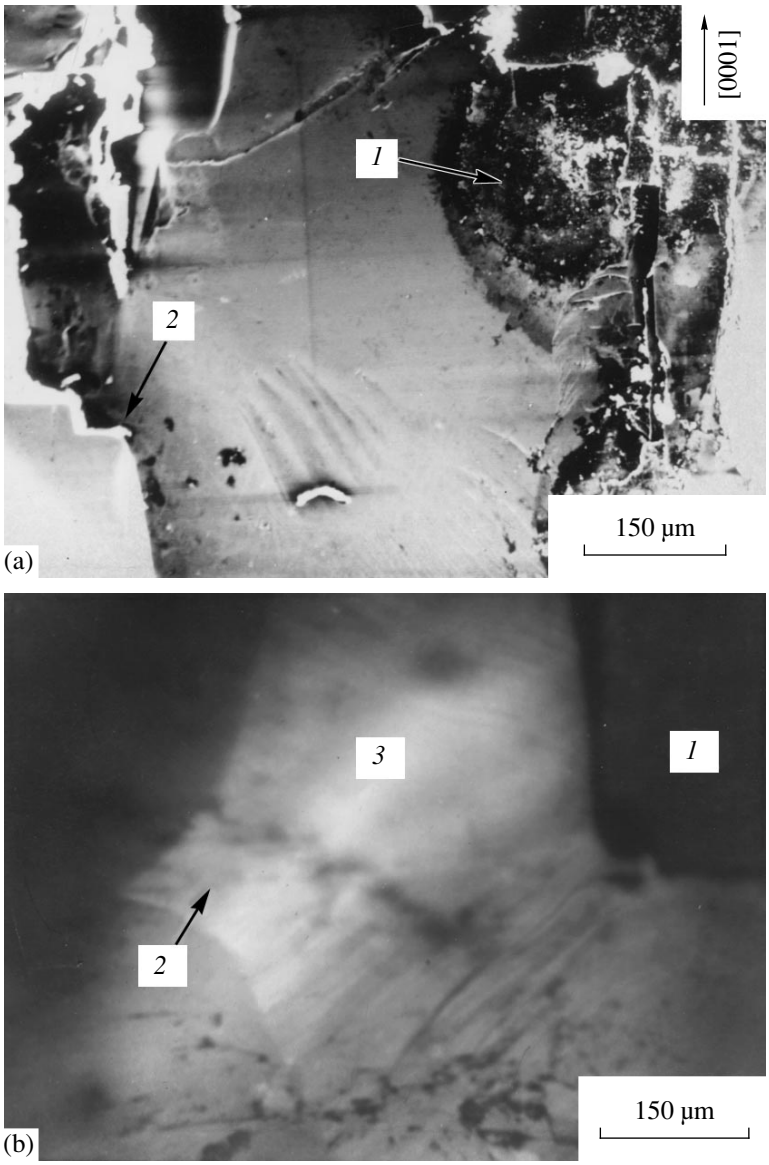

Fig. 3. The $(10\bar{1}0)$ fracture face of a bulk SiC crystal (a) layering-off of the material along the cleavage plane (scanning electron microscope, E_p = 0.5 J, cylindrical electrode); (*1*) discharge region, (*2*) fracture steps; (b) the structure of the fracture region (E_p = 0.1 J, cylindrical electrode) (*1*) basal depression, (*2*) rectilinear crack, (*3*) region of material layering-off (stressed zone) visualized due to light refraction.

whose angles served the origins of the rectilinear cracks (Fig. 3b, *2*) propagating in the [0001] directions. An increase of the pulse energy resulted in the formation of a multilevel fracture region along the $[10\bar{1}0]$ direction separated by regular steps and rather long cracks on the crystal surface.

Using the results of the above experiments, we evaluated the brittleness of the 6*H*-SiC-polytype faces (Table 1) according to the Ikornikova scale [12].

Table 1 shows that the SiC faces had various forms of brittleness. This reflects the fact that the specific characteristics of SiC deformation are determined by the existence of directed covalent bonds in the crystal. It is well known [7, 11] that SiC crystals experience brittle fracture at temperatures below 600–500°C, which is caused not by the change in the mechanism providing plastic deformation but rather by a high value of the Peierls barrier, which provides the occurrence of the competing fracture process. The experiments show that in the process of discharge indentation of SiC crystals, fracture proceeds not only along the cleavage and parting planes. Table 2 illustrates the location of the elements of plastic deformation and fracture with respect to the faces studied.

In terms of crystallography, Table 2 clarifies the formation of faces possessing different brittleness if one takes into the account that the corresponding brittleness

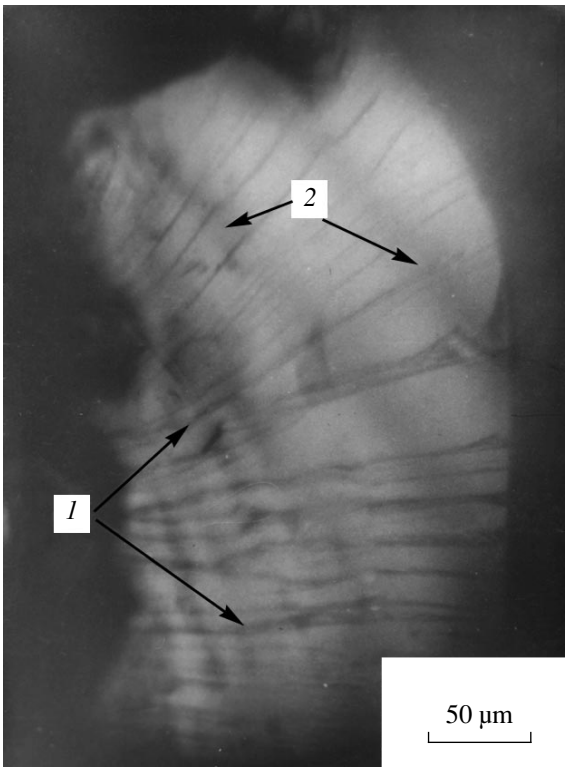

Fig. 4. Creek patterns [the (0001)C face, cylindrical electrode] (*1*) cleavage microsteps, (*2*) interference bands.

index is determined by the number of cracks formed owing to the above fracture and sliding systems. A higher value of the brittleness for the faces of bulk crystals seem to be explained by a higher density of dislocations and other defects in such crystals [1, 14].

The relation between the dislocation structure of the crystals and their brittle fracture is associated mainly with two experimentally observed phenomena—the formation of creek patterns and parting.

It is well known that the most widespread cause of the cleavage-step formation is the presence of screw dislocations intersecting the fracture plane [1, 3]. In bulk SiC crystals grown along the [0001] direction, the main contribution into the dislocation structure is given by threading dislocations parallel to the *c*-axis [5, 11]. At the same time, the density of dislocations emerging onto the (0001) face of the platelike crystals grown by the Lely method is insignificant. Therefore, the discharge indentation of the (0001) faces of bulk crystals is characterized by the formation of a boundary built by an ensemble of screw (threading) dislocations, which generates a series of cleavage steps forming, in turn, the creek patterns (Fig. 4). A similar situation is also observed in the indentation of the $(10\bar{1}0)$ face of faceted crystals with a high density of basal dislocations with screw components [14].

Table 2. Schematic location of the elements of plastic deformation and fracture with respect to the faces studied in 6*H*-SiC crystals with the wurtzite structure

Indented face	Possible sliding system [13]	Fracture system	
		cleavage	parting
(0001)	Pyramidal $(1\bar{2}12)$, 1/3 $[1\bar{2}1\bar{3}]$ $(12\bar{1}2)$, 1/3 $[\bar{1}2\bar{1}3]$	$\{10\bar{1}0\}$	(0001)
$(11\bar{2}0)$	Pyramidal $(\bar{1}101)$, 1/3 $[\bar{1}\ \bar{1}20]$ $(1\bar{1}01)$, 1/3 $[\bar{1}\ \bar{1}20]$ Basal (0001), $[\bar{1}\ \bar{1}20]$	$\{10\bar{1}0\}$	–
$(10\bar{1}0)$ (cleavage plane)	Pyramidal $(01\bar{1}1)$, 1/3 $[\bar{2}110]$ $(1\bar{1}01)$, 1/3 $[\bar{1}\ \bar{1}20]$ Prismatic $(1\bar{1}00)$, 1/3 $[\bar{1}\ \bar{1}20]$ $(01\bar{1}0)$, 1/3 $[\bar{2}110]$	$\{1\bar{1}20\}$	–

Platelike crystals with a pronounced defect-containing *D*-layer and a considerable density of basal dislocations during indentation of the (0001) faces showed not only the break along the cleavages but also the formation of even cleavages (steps) along the (0001) plane. It seems that parting in such crystals can be caused by the impurity mechanism of bond weakening (e.g., in the *D*-layer) and by the break along the cleavage planes [1].

Thus, the fracture pattern formed by a single discharge can be used for evaluating the face brittleness.

The morphology of the fracture faces along the cleavage and parting planes depends on the crystallographic orientation of the surface subjected to indentation, specific features of the dislocation structure, and the geometry of the traces of partial volume breakdown of the material.

REFERENCES

1. L. A. Shuvalov, A. A. Urusovskaya, I. S. Zheludev, *et al.*, *Modern Crystallography*, Vol. 4: *Physical Properties of Crystals*, Ed. by B. K. Vaĭnshteĭn, A. A. Chernov, and L. A. Shuvalov (Nauka, Moscow, 1981; Springer-Verlag, Berlin, 1988).
2. *Progress in Dielectrics*, Ed. by J. B. Borks and J. H. Schulman (Wiley, New York, 1959; Gos. Énerg. Inst., Moscow, 1962).
3. Yu. A. Tkhorik and L. S. Khazan, *Plastic Deformation and Misfit Dislocations in Heteroepitaxial Systems* (Naukova Dumka, Kiev, 1983).
4. O. G. Bazhenov and V. A. Karachinov, Pis'ma Zh. Tekh. Fiz. **22** (21), 26 (1996) [Tech. Phys. Lett. **22**, 875 (1996)].
5. V. A. Karachinov, in *Proceedings of the III International Conference "Crystals: Growth, Properties, Real Structure, Application," Aleksandrov, 1997*, Vol. 2, p. 223.
6. V. A. Karachinov, Zh. Tekh. Fiz. **68** (7), 133 (1998) [Tech. Phys. **43**, 868 (1998)].
7. D. S. Ivanov and V. A. Karachinov, in *Proceedings of the International Workshop "Silicon Carbide and Related Materials," State Univ., Novgorod, 1997*, p. 16.
8. L. A. Yutkin, *The Electrohydraulic Effect* (Mashinostroenie, Moscow, 1955).
9. M. M. Frocht, *Photoelasticity* (Wiley, New York, 1941; Gostekhizdat, Moscow, 1948).
10. Yu. S. Boyarskaya, D. Z. Grabko, and M. S. Kats, *Physics of Processes at Microindentation* (Shtiintsa, Chisinau, 1986).
11. *Silicon Carbide*, Ed. by H. K. Henisch and R. Roy (Pergamon, Oxford, 1968; Mir, Moscow, 1972).
12. N. Yu. Ikornikova, *Microhardness* (Akad. Nauk SSSR, Moscow, 1951), p. 100.
13. A. A. Predvoditelev, Kristallografiya **7** (6), 938 (1962) [Sov. Phys. Crystallogr. **7**, 759 (1962)].
14. V. A. Karachinov, in *Collection of Articles, from Various Institutes of Higher Learning* (Novgorod. Politekhn. Inst., Novgorod, 1989), p. 81.

Translated by L. Man

Crystallography Reports, Vol. 45, No. 6, 2000, pp. 1024–1028. Translated from Kristallografiya, Vol. 45, No. 6, 2000, pp. 1108–1113.

Sensitivity of Doped Semiconductor Melts to Microgravitation during Crystallization in Space

A. V. Kartavykh

Institute of Chemical Problems of Microelectronics,
Bol'shoĭ Tolmachevskiĭ per. 5, Moscow, 109017 Russia
E-mail: otdel3@mail.girmet.ru

Received April 13, 1999; in final form, March 1, 2000

Abstract—A new approach has been suggested for evaluating the sensitivity of doped crystallization systems to microgravitation. The approach is based on the differential analysis of the Burton–Prim–Slichter equation under the boundary conditions characteristic of the growth processes on board spacecrafts. A new quantity has been introduced into consideration—a sensitivity coefficient to microgravitation, K_s, proportional to the change of the dopant concentration C_s in a growing crystal under the constant dynamical conditions resulting in the diffusion of the boundary δ-layer in the melt. The K_s values are calculated for electrically active "small" dopants in Ge and Si crystals. It is shown that the degree of impurity and electrophysical inhomogeneity in crystals grown under the same microgravitation conditions on board a space vehicle is essentially dependent on the dopant type. The principles of choosing dopants, as well as some technological procedures for reducing noncontrollable factors affecting the impurity homogeneity of semiconductor single crystals grown onboard a spacecraft, are developed. *© 2000 MAIK "Nauka/Interperiodica".*

INTRODUCTION

The main trend of the space materials science of semiconductors is the purposeful use of various factors that can influence the material in a space flight (and, first and foremost, microgravitation playing the role of a technological medium) in order to develop new technologies of single crystal growth providing a highly homogeneous distribution of electrophysical properties over the crystal. The first successful steps along this path have already been made. In particular, we managed to grow Ge crystals from melts with the unique microinhomoheneity of dopant distributions over the crystal bulk (~1.0–1.5%) in an orbital flight [1, 2]. However, these results were obtained only in some of the space experiments.

On the whole, numerous growth experiments on board spacecrafts indicate the extreme sensitivity of the impurity-distribution parameters in the solid phase to the processes of heat and mass transfer (HMT) occurring in melts during their crystallization [2]. This phenomenon should be interpreted as the collective effect of a number of factors on the hydrodynamic situation in melts resulting in the specific stirring effects and the noncontrollable thickness variation of the boundary δ-layers (δ_{lr}) at the interfaces.

The dopant concentration in a solid phase is related to the diffusion-layer thickness by the general Burton–Prim–Slichter equation [3]

$$k = C_s/C_l = k_0/[k_0 + (1 - k_0)\exp(-v\delta_{lr}/D)], \qquad (1)$$

where k and k_0 are the effective and the equilibrium coefficients of impurity distribution, respectively; v is the crystallization rate; and D is the coefficient of impurity diffusion in the melt. It is seen that at the steady-state crystallization rate v, the inhomogeneity of the impurity distribution in a growing crystal is a function of the variation in the thickness δ_{lr} of the effective diffusion layer, which is determined by the intensity of melt stirring dependent, in turn, on the dynamics of the liquid flows in the vicinity of the crystallization front. Thus, the key problem in growth of homogeneously doped single crystals in space is the maintenance of the given δ_{lr} value in the local regions of the crystallization front at each given moment within the whole growth process. Thus, first of all, it was necessary to establish all the factors that can affect δ_{lr} on board spacecraft and then to find the methods for purposeful control of these factors on board spacecrafts by applying special external factors to the melt.

However, the optimization of external crystallization conditions is not a universal method. A higher homogeneity of crystals can also be achieved by the appropriate use of physical–chemical characteristics of the crystallization system. In many "terrestrial technological" processes, positive results can be achieved rather simply by the appropriate choice of dopant. An analogous approach is also justified for technologies of growth of semiconductor single crystals under the conditions of an orbital flight.

The present study is aimed at developing the principles of the theoretical analysis of the sensitivity of the

1063-7745/00/4506-1024$20.00

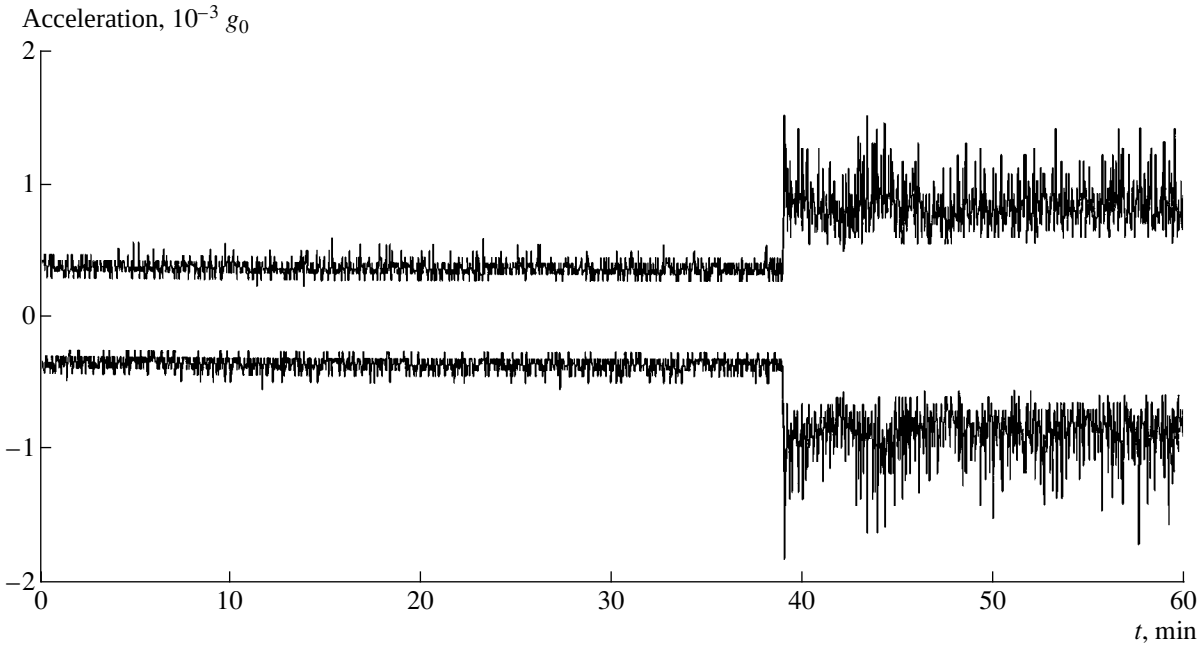

Fig. 1. Fragment of the record of technogenic microaccelerations along the axis of a crystal growing in a reactor of the zone-melting *Zona 4* setup on board a *Photon* spacecraft [5]. The servo drive for the melted-zone motion was switched on 40 minutes after the beginning of the experiment.

melts doped with various impurities to microgravitation during crystallization. The model objects were elemental semiconductors.

CHARACTERISTIC FEATURES OF CRYSTALLIZATION ON BOARD SPACECRAFTS

The analysis of the dopant distribution along the space-grown single crystals indicates that the intensity of melt stirring under microgravitation was rather poor, with the δ_{lr} value being much higher (of the order of 3–6 mm) than that in terrestrial crystallization (0.1–1.0 mm). The large thickness of δ_{lr} provides a high sensitivity of the crystallization process (and also the inhomogeneous incorporation of impurities into a crystal) to various fundamental and technogenic factors.

The sources of technogenic microaccelerations deteriorating the homogeneity of "space crystals" were discussed earlier [2, 4]. Here, we only consider a record of acceleration in the growth chamber of a *Zona-4* growth setup caused by functioning of servo drive electric motors [5] (Fig. 1). Earlier [4], we considered the dopant inhomogeneity in single crystals grown under the conditions of noncontrollable vibrations on board spacecrafts. The most hazardous vibrations on board unmanned spacecraft are low-frequency vibrations in the range <100 Hz.

The relation between the inhomogeneity and the fundamental heat and mass transfer in the molten zone is less studied. We should like to mention, first of all, the thermogravitation convection still taking place under residual quasistationary microaccelerations (of the order of 10^{-4}–$10^{-5}g_0$). In container-free (floating zone) crystallization processes, an important contribution to the formation of inhomogeneous electrophysical properties of a crystal growing in space is introduced by the capillary-type (Marangoni) convection [6, 7]. It was shown experimentally that the Marangoni convection can be considerably intensified in heavily doped semiconductor melts by introducing a surfactant [8, 9], which is localized in the regions adjacent to the free melt surface and, with an increase of the dopant concentration, gradually propagates into the melt bulk.

The detailed analysis of various nonstationary convection mechanisms in space-growth experiments is beyond the scope of our article. However, we should like to note that the simultaneous action of these mechanisms can give rise to the noncontrollable intensification of melt stirring; oscillations in the thermal and diffusion boundary layers at the crystallization front; and, as a consequence, to the oscillations of the *k*-values of the dopants present in the liquid phase.

ANALYSIS OF CRYSTALLIZING SYSTEM SENSITIVITY TO MICROGRAVITATION

Now, we show that inhomogeneous doping of a crystal growing from melt under the conditions of nonstationary stirring of the melt is essentially dependent on the dopant type. Differentiating Eq. (1) with respect to the hydrodynamically-dependent variable δ_{lr}, we

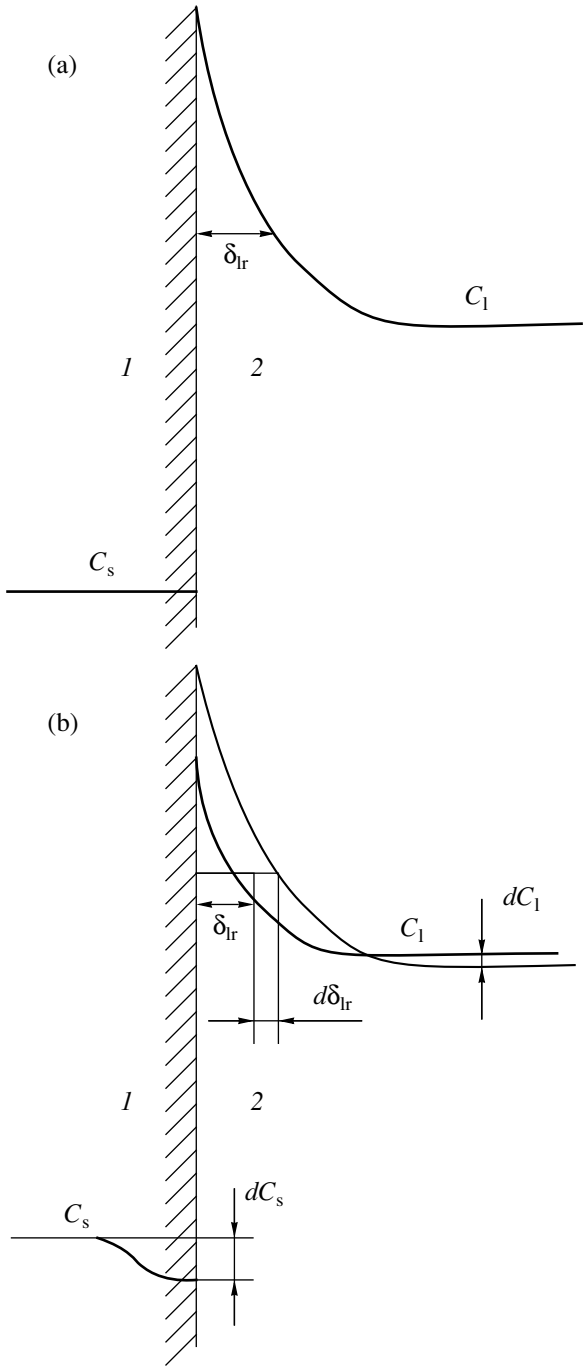

Fig. 2. Schematic distribution of the dopant concentration in the vicinity of the interface: (a) under the steady-state crystallization conditions and (b) under the effect of the elevated external microaccelerations giving rise to the boundary-layer diffusion; (*1*) crystal and (*2*) melt.

obtain

$$K_s = \frac{dk}{d\delta_{lr}} = \frac{v k_0(1-k_0)\exp\left(-\frac{v\delta_{lr}}{D}\right)}{D\left[k_0 + (1-k_0)\exp\left(-\frac{v\delta_{lr}}{D}\right)\right]^2}. \quad (2)$$

The physical sense of the derivative $dk/d\delta_{lr}$ reflects the sensitivity of k to the changes of the hydrodynamic situation in the vicinity of the crystallization front of the melt, e.g., as a result of drastic changes in the intensity of the nonstationary stirring process (Fig. 2). We should also note that, in this case, the variations in the $k = C_s/C_l$ lead, first of all, to inhomogeneity of doping of a growing crystal, because the average dopant concentration C_l far from the interface in a large melt volume only slightly changes due to diffusion of the doped δ-layer:

$$dk = d\left(\frac{C_s}{C_l}\right) \approx \frac{dC_s}{\text{const}}. \quad (3)$$

Equation (2) can be applied to space crystallization for comparative estimation of the sensitivities of various doped crystallization systems to the effect of the nonstationary microgravitation on the melt (the so-called *g*-jitter). It should be emphasized that differentiation of form (2) is appropriate if the crystallization rate is independent of the variations in the hydrodynamic conditions, v = const. In practice, this approximation signifies that one considers only relatively "weak" factors quickly acting onto the melt, which cannot considerably change the thickness of the thermal boundary layer δ_t. The rigorous estimation of the applicability range of this approximation should be the subject of a special study. Here, we should like to note that such an estimation has the sense only for semiconductor melts, where the ratios of the Prandtl and the Schmidt numbers have low values ($Pr/Sc \sim 10^{-3}$). This signifies that the thermal boundary layer is located inside the diffusion one, i.e., $\delta_t < \delta_{lr}$. Therefore, the thermal boundary layer is less sensitive to the changes in the liquid flow than the diffusion layer.

As seen from Eq. (2), the value of the sensitivity coefficient to microgravitation K_s depends on the dopant kind via its physical–chemical constants k_0 and D. Consider an example of dopants widely used for Ge and Si (see the table). We use the experimental data obtained earlier in our study of the terrestrial Ge crystallization and crystallization aboard an automatic Photon satellite. During horizontal growth of Ge by floating zone technique in a Zona-4 setup under the earth conditions, the stationary layer thickness was $\delta_{lr} \cong 1$ mm [8, 9]. In the space experiment by the floating zone technique, the corresponding value was $\delta_{lr} \cong 4$–6 [7–9]. The above values are characteristic of a rate of $v \cong 4$–5 mm/h used in these experiments. The estimates of v and δ_{lr} are used to construct the dependences $K_s = f(\delta_{lr})$ for dopants listed in the table. The dependences of the coefficients K_s of the crystallization systems on the stationary thickness δ_{lr} calculated by Eq. (2) are shown in Fig. 3 and have a number of practically important features.

For most of the dopants in Ge and Si melts, $K_s = f(\delta_{lr})$ are increasing functions (except for As, B, P, and Si). Thus, the sensitivity of most crystallization sys-

Physical and chemical parameters of the most important dopants for germanium and silicon single crystals [11–13]

Dopant		Equilibrium distribution coefficient k_0		*Diffusion coefficient in melt D, cm^2/s	
		in Ge	in Si	in Ge	in Si
Donors	P	8×10^{-2}	0.35	$\sim 1 \times 10^{-4}$	5.1×10^{-4}
	As	2×10^{-2}	0.3	1.26×10^{-4}	2.4×10^{-4}
	Sb	3×10^{-3}	2.3×10^{-2}	5.5×10^{-5}	1.5×10^{-4}
Acceptors	B	–	0.8	–	2.4×10^{-4}
	Al	–	3×10^{-3}	–	2.3×10^{-5}
	Ga	8.7×10^{-2}	8×10^{-3}	7.5×10^{-5}	4.8×10^{-4}
	In	1×10^{-3}	4×10^{-4}	1×10^{-4}	6.9×10^{-4}

* The data at temperatures close to the melting points of Ge and Si.

tems to the external dynamical factors (including the apparatus vibrations) is really higher under the space conditions than under the Earth's conditions. In each case, an increase of sensitivity (and deterioration of doping homogeneity of a growing crystal) is proportional to the slope of the corresponding curve.

The families of the calculated $K_s = f(\delta_{lr})$ curves for various dopants provide the choice of a concrete Ge- or Si-based system, which is the least sensitive to microaccelerations during crystal growth in space. Thus, inhomogeneity in the axial dopant distribution in the doped Ge single crystals grown decreases in the row Ge(Ga) ⟶ Ge(P) ⟶ Ge(As) ⟶ Ge(Sb) ⟶ Ge(In), with all the other conditions being the same (including the equal levels of microgravitation perturbations on board the spacecraft). For Si, a similar row of sensitivities to nonstationary microaccelerations is different: Si(Al) ⟶ Si(As) ⟶ Si(B) ≈ Si(P) ⟶ Si(Sb) ⟶ Si(Ga) ⟶ Si(In). Thus, it is possible to choose the optimum dopant and grow a single crystal

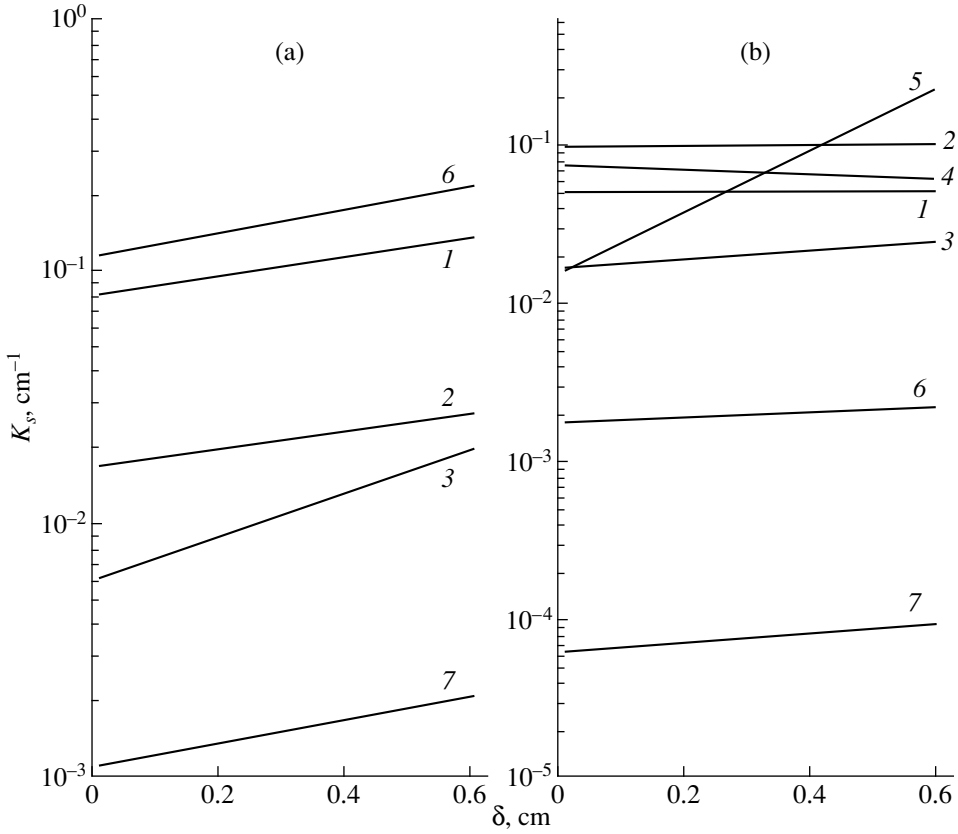

Fig. 3. Sensitivity coefficient of (a) doped Ge and (b) doped Si melts to microgravitation during crystallization versus the thickness δ_{lr}. The calculations were performed by Eq. (2) for the following dopants: (*1*) P, (*2*) As, (*3*) Sb, (*4*) B, (*5*) Al, (*6*) Ga, and (*7*) In.

with the preset conductivity type and the most homogeneous axial distribution of electrophysical properties such as carrier concentration and mobility.

The sensitivity of most of the doped melt–crystal systems to microgravitation changes with each new stationary value of δ_{lr} attained in the crystallization process. In real growth processes in space, the thickness of the boundary layer can be decreased by purposefully creating a stable controllable artificial "soft" stirring of the melt, which can also be optimized. Thus, for Sb-doped Ge crystals, the value of K_s can be reduced almost two times by decreasing δ_{lr} from 6 to 3 mm.

The latter fact can be used for development of new technologies for growing homogeneous semiconductor crystals in space under the influence of controllable weak factors. One such factor is the application of an external rotational low-induction magnetic fields to the melt, the so-called magnetohydrodynamical factor. In this case, the alternate field should necessarily be a high-frequency one, such that the mass inertia of the melt would suppress the development of oscillating hydrodynamic flows at the crystallization front, thus providing the formation of an averaged stable δ-layer with a controllable thickness. In some experiments, the rotary stirring fields with the induction of 0.1–0.2 mT and the frequency of 400 Hz were used. The results obtained confirm the strong effect of such fields on the heat and mass transfer under the conditions of a space flight [2, 6]. The programmed control of the boundary-layer thickness is based on the following empirical formula [10]:

$$\delta_{lr}/D = (\delta_{lr}/D)_0 \exp(-\gamma H^2), \qquad (4)$$

where $(\delta_{lr}/D)_0$ is the conjugated parameter of the diffusion δ-layer without an effect of the microhydrodynamic factor, H is the magnetic-field intensity, and γ is the empirical coefficient of sensitivity to the magnetohydrodynamic factor. For melts of metals in a 400-Hz field, this coefficient is of the order of 10^{-8} m^2 A^{-2} [10].

Increasing the magnetic field intensity H during crystallization, it is possible to attain the necessary value of δ_{lr}. On the one hand, in accordance with Eq. (1), this causes a certain decrease of the doping level in a growing crystal. On the other hand, in accordance with Eq. (2), it also results in a better homogeneity of the dopant distribution due to a reduced sensitivity to noncontrollable external vibrational accelerations.

CONCLUSIONS

A new approach is suggested for evaluating sensitivity of doped crystallization systems to microgravitation. It reduces to the differential analysis of the Burton–Prim–Slichter equation under the boundary conditions typical of the experimental growth of crystals on board spacecrafts.

The notion of the sensitivity coefficient to microgravitation $K_s = dk/d\delta_{lr}$ is introduced. This coefficient is proportional to the change in a dopant concentration C_s in a growing crystal under the action of equal dynamic factors onto the boundary δ-layer in the melt. Such an action can be provided by any (controllable or random) external forces resulting in the spreading of the diffusion layer in the liquid zone, in particular, the onboard accelerations (g-jitters) or alternate magnetic fields. The coefficients K_s are calculated for electrically active "small" dopants in germanium and silicon.

It is also shown that the degree of impurity and electrophysical inhomogeneity in crystals grown in space, with the microgravitation conditions being the same, is essentially dependent on the dopant type. The principles for choosing appropriate dopants and the technological procedures reducing the effect of noncontrollable factors of the orbital flight on the crystallization process and growth of semiconductor crystals with a highly uniform the distribution of electrophysical properties are also suggested.

REFERENCES

1. É. S. Kopeliovich, V. V. Rakov, and N. A. Verezub, Tsvetn. Met., No. 8, 52 (1991).
2. M. G. Mil'vidskiĭ, N. A. Verezub, A. V. Kartavykh, *et al.*, Kristallografiya **42** (5), 913 (1997) [Crystallogr. Rep. **42**, 843 (1997)].
3. J. Burton, R. Prim, and W. Slichter, J. Chem. Phys. **21** (11), 1987 (1953).
4. M. G. Mil'vidskii, A. V. Kartavykh, E. S. Kopeliovich, *et al.*, J. Journals (UNESCO) **2** (1), 6 (1998).
5. H. Hamacher, H. E. Richter, R. Jilg, and S. Drees, *QSAM Ergebnisse von FOTON-11* (DLR, Munich, 1998).
6. A. V. Kartavykh, É. S. Kopeliovich, M. G. Mil'vidskiĭ, *et al.*, Kristallografiya **42** (4), 755 (1997) [Crystallogr. Rep. **42**, 694 (1997)].
7. A. V. Kartavykh, É. S. Kopeliovich, M. G. Mil'vidskiĭ, and V. V. Rakov, Kristallografiya **43** (6), 1136 (1998) [Crystallogr. Rep. **43**, 1075 (1998)].
8. A. V. Kartavykh, E. S. Kopeliovich, M. G. Mil'vidskii, and V. V. Rakov, J. Cryst. Growth **205** (4), 497 (1999).
9. A. V. Kartavykh, E. S. Kopeliovich, M. G. Mil'vidskii, and V. V. Rakov, Microgravity Sci. Technol. **12** (1), 16 (1999).
10. W. C. Johnston and W. A. Tiller, Trans. AIME **221**, 331 (1961).
11. A. Ya. Nashel'skiĭ, *Technology of Semiconductor Materials* (Metallurgiya, Moscow, 1972).
12. A. Ya. Nashel'skiĭ, *Semiconductor Single Crystals* (Metallurgiya, Moscow, 1978).
13. Yu. M. Shashkov, *Growth of Single Crystals by Pulling* (Metallurgiya, Moscow, 1982).

Translated by L. Man

Crystallography Reports, Vol. 45, No. 6, 2000, pp. 1029–1034. Translated from Kristallografiya, Vol. 45, No. 6, 2000, pp. 1114–1119.

CRYSTAL GROWTH

Skeletal Growth Forms of Crystals in Terms of Variational Principles of Nonequilibrium Thermodynamics

E. B. Treĭvus

Institute of the Earth Crust, St. Petersburg State University, Universitetskaya nab. 7/9, St. Petersburg, 199164 Russia

Received January 19, 1999; in final form, August 25, 1999

Abstract—The analysis of skeletal growth forms leads to the conclusion that the universal Glansdorff–Prigogine principle of evolution and the principle of the minimum entropy production in self-organizing processes (the Klimontovich principle) are valid at some stages of skeleton evolution in NH_4Cl crystals. However, in all these cases, the principle of the maximum resistance of the system to the change in the value of the entropy production can be applied. *© 2000 MAIK "Nauka/Interperiodica".*

As far as we know, the morphology of skeletal crystals was interpreted in terms of the variational principles of thermodynamics of irreversible processes only in one article [1], despite the fact that such an analysis seems to be rather important for understanding the causes of formation and evolution of these crystal forms often encountered in the crystallization under both natural and laboratory conditions. In turn, such an analysis can promote the development of the variational principles of nonequilibrium thermodynamics on the basis of practical examples.

Skeletal crystals considered in numerous articles [2–5] can be divided into two main classes:

Crystals with unbranched skeletal forms divided, in turn, into the crystals with edge and vertex skeletons [2]. The former are characterized by depression of faces and preservation of edges, whereas the latter, by depression of both faces and edges. In other words, the latter crystals can grow only in the directions toward crystal vertices. The surfaces of these skeletons are either smoothly curved or stepped and are formed by faces with small indices (Figs. 1a, 1b).

Branched skeletal forms (Fig. 1c). It seems that the experiments on iodoform crystals performed by Dogiel remain the only studies of the process of the transformation of a faceted crystal into a branched skeleton. Experiments performed by Dogiel are also remarkable for being the first attempt at studying the process of skeleton formation made as far back as the 1870s [8, 9]. Unfortunately, the authors of the cited papers [8, 9] only described their experiments but drew no conclusions. Veĭnberg [7], who reproduced the corresponding figure, referred to [9]. However, it seems that the figure was taken from one of Dogiel's other publications, which I myself failed to find. Lehman [10] also reproduced the same figure and also without the reference to the original.

The causes of a large variety of skeletal crystals are still unclear. However, it is well known that the formation of a stepped nonbranched skeletal crystal is caused by morphological instability during layer growth of the crystal faces [3].

Usually, one makes no distinction between skeletal crystals and dendrites. In fact, only those skeletal crystals relate to dendrites whose development is accompanied by misorientation of various skeletal branches with respect to one another and the also of the crystal structure within each individual branch [11, 12]. It should be indicated that the morphology of such formations is referred to as *dense branching morphology.*

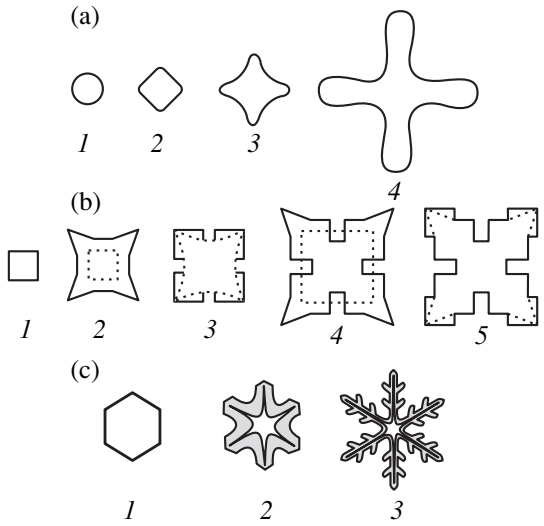

Fig. 1. Shape transformations of (a) a spherical NH_4Cl crystal into a smooth "vertex skeleton" in an aqueous solution [6], (b) a faceted KCl crystal into the stepwise vertex skeleton in an aqueous solution [6], and (c) a faceted iodoform crystal into a skeletal one in the alcohol solution [7] at room temperature.

1063-7745/00/4506-1029$20.00 © 2000 MAIK "Nauka/Interperiodica"

However, we believe that these formations are often mistakenly taken for branched unnsplit skeletons, despite the fact that misorientations caused by crystal split and skeleton formation are of a different nature. These processes do not necessarily occur simultaneously. Therefore, one has to distinguish between the terms skeleton and dendrite. The misoriented dendritic formations, i.e., the forms of dense branching morphology, were beyond the scope of the present study and therefore are not considered in this article.

In many instances, the transition to the skeletal growth is preceded by the periodic capture of solution inclusions into the crystal and can be considered as a precursor of the loss of faceting stability [13]. The skeleton formation begins with the appearance of a depression on the face. An unnbranched edge skeleton crystal can be considered as an nonovergrown inclusion in a face.

The moment of formation of a skeleton crystal may or may not be accompanied by an increase in the face growth rate [13]. Thus, an increase of the face growth rate is not a necessary factor accompanying the beginning of skeleton formation. A crystal that lost the faceting stability is gradually developed into a skeleton formation with a constantly developing surface (Fig. 1). In this case, the faces with rational indices have the tendency to be "substituted" by surfaces with irrational indices and higher surface energies. Stepped skeletons (similar to those shown in Fig. 1b) are observed rather rarely.

In addition to the transformation of convex forms into skeleton ones, there are also some examples of the jumpwise transition from one orientation of the skeleton trunks to another (see below).

Skeletal crystals should be considered as a specific class of dissipative structures studied in nonequilibrium thermodynamics [14]. Unbranched smooth skeletons can be treated as a random (turbulent) dissipative structure in distinction from the skeletal forms characterized by periodic structures.

Skeleton formation begins either with an increase of the supersaturation above a certain critical value or, at the given supersaturation, only with the attainment of a certain critical crystal dimension. This dimension decreases with an increase of supersaturation [3]. The formation of various dissipative structures is also associated with the attainment of certain threshold values of the parameters characterizing these structures [14], which makes the skeleton crystals even more similar to dissipative structures traditionally considered in nonequilibrium thermodynamics.

In what follows, we consider, for definiteness, crystal growth from solutions under constant supersaturation, temperature, and pressure. The variation of the isothermal–isobaric potential of such a system during crystal growth is described by the well-known expression

$$dG = -\Delta\mu dm + \gamma_{av} dS, \quad (1)$$

where $\Delta\mu$ is the difference between the chemical potentials of the substance crystallized in the solution and the crystal (for simplicity, we consider here a single-component crystal), m is the crystal mass, and γ_{av} is the specific free surface energy of the crystal averaged over the surface S. The entropy production P is determined by the derivative of G with respect to time τ at the given absolute temperature T as [15]

$$TP = -\frac{d}{d\tau}(G) = \dot{m}\Delta\mu - \gamma_{av}\dot{S}. \quad (2)$$

Here $\dot{m}$ is the rate of the change in the crystal mass and $\dot{S}$ is the rate of the change in the surface area ("surface flow"). Thus, the parameter γ_{av} can be considered as a driving force "conjugated" with this flow. It should be indicated that, in principle, the surface area at the given crystal mass can change arbitrarily; i.e., $\dot{S}$ can also vary irrespectively of $\dot{m}$. According to the Gibbs–Duhem equation, γ is only slightly dependent on the supersaturation of the solution on the crystal surface.

TRANSITION FROM THE CONVEX GROWTH FORM TO THE SKELETAL ONE

There are several approaches to the analysis of dissipative structure formations within the variational principles of the nonequilibrium thermodynamics. Hill [1] limited such consideration to the discussion of the principles of the minimum and the maximum entropy production; however, there exist some more general principles taking into account the variation of the entropy production with time.

Universal evolution principle (the so-called Glansdorff–Prigogine principle). In [14–17], the total differential of the entropy production dP is represented as a sum of two partial differentials d_JP and d_XP related to the flows J and forces X. According to the Glansdorff–Prigogine principle, the quantity d_JP can either increase or decrease during the time-dependent entropy production in the nonequilibrium process. No conclusions about the ratio between the quantities d_JP and d_XP were made. Therefore, no decisive conclusion can be made about the sign of the dP variation (its increase or decrease). At the same time, it is stated [14–17] that, in an irreversible process having the tendency to the stationary state, the following inequality is valid:

$$\frac{d_XP}{d\tau} \le 0. \quad (3)$$

In other words, in essence, the principle states that the rate of the change of the entropy production caused by

the change of the driving forces can only decrease or be equal to zero.

Since in accordance with the Glansdorff–Prigogine principle, the quantity γ is changed during skeleton formation, we can differentiate Eq. (2) with respect to γ_{av} and then also with respect to τ under the condition that $\Delta\mu$ is constant:

$$T\frac{d_X P}{d\tau} = -\left(\frac{\partial \dot{m}}{\partial \gamma_{av}}\Delta\mu + \dot{S} + \gamma_{av}\frac{\partial \dot{S}}{\partial \gamma_{av}}\right)\frac{d\gamma_{av}}{d\tau}. \quad (4)$$

Consider the evolution of the crystal shown in Fig. 1a. The above transformation of its shape results in the fact that the relative area of the regions with irrational orientations and elevated values of the surface energy γ increases, i.e., $d\gamma_{av}/d\tau > 0$. Since during the skeleton formation $\dot{m}$ continues to increase, then $\partial \dot{m}/\partial \gamma_{av} > 0$. It is obvious that the surface flow $\dot{S}$ and the free surface energy γ are always positive. Further on, if one takes a crystal even of a spherical shape, then, at the constant linear growth rate (which is usually the case at the constant supersaturation), the quantity $\dot{S}$ increases with time. Thus, the signs of the changes in γ_{av} and $\dot{S}$ are the same, and $\partial \dot{S}/\partial \gamma_{av} > 0$. Therefore, according to Eq. (4), the derivative $d_X P/d\tau$ is negative. Similar speculations can also be made for the transformation of a faceted crystal into a skeletal one. Therefore, the transition of a convex crystal into a smooth skeletal (unbranched) one and then into a branched one is quite consistent with the Glansdorff–Prigogine principle.

A specific example of the periodic transformation of a vertex ledge with a curved face into a step with rational indices (Fig. 1b) shows a decrease in the surface energy γ_{av} characterizing this ledge with time; i.e., the sign of the $d\gamma_{av}/d\tau$ derivative is negative. Simultaneously with a decrease of γ, the quantity $\dot{S}$ increases. Thus, $\partial \dot{S}/\partial \gamma_{av} < 0$. The sign of $\partial \dot{m}/\partial \gamma_{av}$ can hardly be predicted. In order to satisfy inequality (3), i.e., the Glansdorff–Prigogine principle, the expression in parentheses in Eq. (4) should be negative. However, it is still unclear whether it is negative in this case.

Principle of minimum entropy production in self-organizing processes (Klimontovich principle) [18, 19]. According to this principle, a nonequilibrium system with a dissipative (ordered) structure in the stationary state has a lower value of entropy production in comparison with its value for the structure unstable under the given conditions (the "comparison system"). Now consider the quantity P described by Eq. (2). The comparison system depends on the shape of the initial convex crystal, and it can be either a spherical or a faceted body formed under the same supersaturation and the same mass flow. The values characterizing the quantities $\dot{S}$ and γ_{av} for this crystal are less than the analogous values for the skeletal crystal. Thus, in accordance with this principle and Eq. (2), the value of P for a skeletal crystal is less than the corresponding value for a convex crystal growing at the same value of $\Delta\mu$. We should like to emphasize that this is a euristic principle, which, at present, can be illustrated by only one example (transformation of a laminar liquid flow into a turbulent one).

The principle of the maximum resistance of the system to the change in the entropy production with time. This principle is, in fact, the generalization of the Klimontovich principle, which corresponds only to the particular case where the entropy production increases during the process. The principle of the maximum resistance was formulated as the establishment of this fact on an example of the stationary faceted growth forms and stationary rounded forms of their dissolution [20–22]. A growing crystal with flat faceting has an increasing surface and therefore is characterized by an increase in the entropy production with time. The crystal "chooses" such a shape at which the entropy production at each given moment is minimal; i.e., it changes its shape at the minimum rate. On the contrary, during dissolution, the crystal surface reduces, and the entropy production also decreases with time. In this case, the crystal "prefers" to choose the form which provides the maximum entropy production at each given moment of time. Thus, in this case as well the rate of the change in the entropy production is minimal. Thus, the above principle provides the combination of the stationary growth and dissolution forms of crystals. In terms of this principle, the transformation of a convex crystal into a skeletal one is quite logical, because crystal growth is accompanied by an increase of entropy production, whereas skeleton formation hinders this process. Thus, the formation of skeletal crystals can be interpreted in terms of any of the above three variational principles.

ORIENTATIONAL TRANSITIONS OF BRANCHED SKELETAL CRYSTALS

The changes in the structure of a branched skeletal crystal reduce to the reorientation of the directions of skeleton branches under certain values of the relative supersaturation and are studied in detail for NH_4Cl crystals at 25°C [23]. At $\sigma \simeq 0.11$, the branches oriented along the $\langle 100\rangle$ directions change the orientation to that along the $\langle 110\rangle$ directions; at $\sigma \simeq 0.21$, the branch orientation along $\langle 110\rangle$ is changed to that along $\langle 111\rangle$. The former orientational transition is seen on the curve of the linear growth rate along the skeleton trunk as a decrease in the growth rate, whereas the latter orientational transition is accompanied by an increase of the linear growth rate by a factor of 7–8 along the branch axis (Fig. 2). The horizontal segment of the growth rate in Fig. 2 corresponds to the transient supersaturation region between two orientations, in which the vertex of the skeleton branch splits. It should be

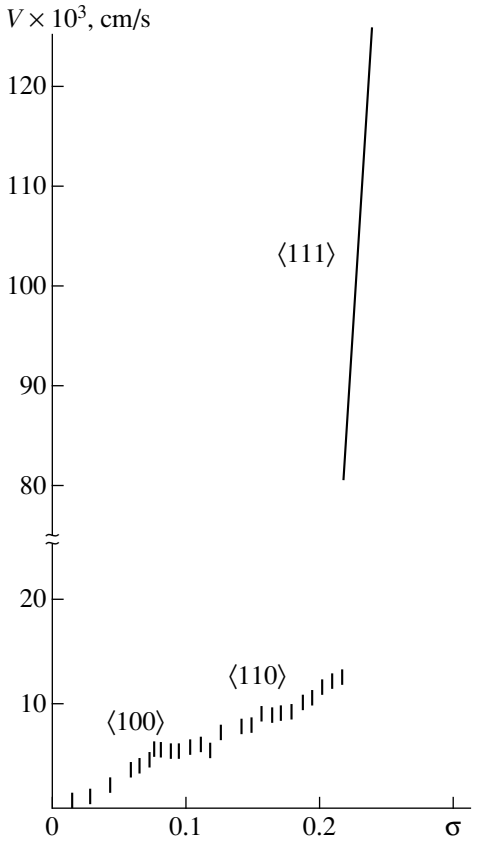

Fig. 2. Linear growth rate along the skeleton trunk of NH_4Cl crystals in aqueous solution as a function of relative supersaturation at 25°C [23]. Various trunk orientations corresponding to different σ values are shown.

noted that the existence of NH_4Cl crystal with the orientations of the skeleton branches along the ⟨100⟩ and ⟨111⟩ directions was described in [24, 25]. The orientational transitions in skeletal growth seem to be quite a common phenomenon. They were also observed in other halides with the same *P* lattice and also in halides with the *F* lattice [25]. The jump in the growth rate in the orientational transition mentioned above was also confirmed in [26].

The second orientational transition in skeletal NH_4Cl crystals was interpreted as an illustration of the principle of the maximum entropy production [1]. However, the first transition, occurring at a lower supersaturation σ and accompanied by a decrease of the entropy production (because of a tendency to a decrease of the growth rate), was not mentioned in [1]. Thus, no unique interpretation of both orientational transitions can be made on the basis of only one of the extremum principles of entropy production (i.e., either minimum or maximum), which makes these principles somewhat deficient.

Now, consider each of the above transitions in the skeletal NH_4Cl structure separately.

With this aim, first analyze the γ values for various faces of NH_4Cl crystals. According to the theory developed in [27, 28], the specific surface energy of these crystals should increase in the row of simple forms as follows: {110}, {100}, and {111}, with the {110} faces being the only faces of layer growth. However, the aforementioned relates only to crystals, which are in contact with their own vapors. Solvent adsorption can change the picture. Moreover, the computations are usually made for the total surface energy, whereas the above equations include the free surface energy. It is still unclear whether the face sequences for these two types of energy are the same or different.

It is well known that NH_4Cl crystals show quite good cleavage along the cube faces [29]. This indicates that (100) nets are the densest for these crystals, and therefore, the cube faces are really morphologically important. According to [29], the {211} form is the most typical for NH_4Cl crystals growing in aqueous solutions without any additives. A very slow growth of initially spherical NH_4Cl crystals (Fig. 1a) results in crystal faceting [6]. According to the photograph published in [6], the prevailing growth form in these crystals is tetragontrioctahedron, most probable, the {211} form. According to [27, 30], at low supersaturations, the CsCl-type crystals (including NH_4Cl) have the {110} form. With an increase of the supersaturation σ, the crystals of this group acquire the {100} and {111} faces (the latter appear rather rarely). Since the skeleton formation in NH_4Cl crystals begins at very law supersaturations σ, it is hardly probable that the author of the cited studies could follow the evolution of the crystal form of NH_4Cl in such a detail. It is more probable that he observed this evolution on some other crystals of this family.

Kliya [31] made an attempt to obtain the equilibrium form of NH_4Cl crystals in aqueous solutions by keeping the skeletal crystals under the isothermal conditions and observing their transformation into well-faceted crystals. She indicates the faces formed in the sequence {100}, {110}, {111}, and {211}; however, it is unclear whether it corresponds to the sequence of development of these faces in the crystal. Thus, it is unclear from her article which is the sequence of γ values and how important the differences in γ values are for formation of various simple forms. Still, it is remarkable that she found the most important simple forms of NH_4Cl crystals in aqueous solutions.

Generalizing the data considered above [6, 27–31], one can draw the conclusion that the minimum surface energy γ in aqueous solutions should be possessed by the {211} and {110} faces, the next value is possessed by the {100} faces, and, finally, and the lowest γ values are characteristic of the {111} faces. Thus, the most important morphological zones of NH_4Cl crystals are ⟨110⟩, ⟨100⟩, and ⟨111⟩. It is along these zones that the acute-bottom (singular) gullies should occur on the polar γ diagram. In this case, there are two (100) and

two (110) faces and four (211) and four (111) faces in the ⟨110⟩ zone; there are four (100) and four (110) faces in the ⟨100⟩ zone; and there are six (110) faces in the ⟨111⟩ zone.

Considering the "saturation" of the above three zones with the most important singular faces and the above relationships for these faces, one can draw the conclusion that the deepest gullies (having the minimum γ_{av} values) should characterize the first of the above zones, whereas the shallowest gullies (with the maximum γ_{av} values), the last zone.

The ⟨100⟩ ⟶ ⟨110⟩ *transition.* The tip of the branch is acutely angled, so that the surface energy of the end of the skeleton trunk has the zeroth value. Here, the decisive role is played by side surface of the branches. In accordance with the above consideration, in this transition, the γ_{av} value should decrease; i.e., the derivative $d\gamma_{av}/d\tau < 0$ should be less than zero. At the same time, the growth rate along the trunk axis also decreases and, therefore, the increment in the mass $\dot{m}$ and the change in the area of the side surface $\dot{S}$ of the skeleton trunk also decrease. Here, we ignored the fact that the rates of side growth of branches are different prior to and upon the transition because we believe that this difference has only insignificant effect on $\dot{S}$. Thus, in this transition, the changes in $\dot{m}$, $\dot{S}$, and γ_{av} are of the same sign. Therefore, $\partial\dot{m}/\partial\gamma_{av} > 0$ and $\partial\dot{S}/\partial\gamma_{av} > 0$, and the quantity in parentheses in Eq. (4) is positive. Thus, both multipliers in the right-hand side of Eq. (4) have different signs, and the Glansdorff–Prigogine principle is inapplicable in this case.

The comparison system here is a skeletal crystal with branches oriented along ⟨100⟩ and with the same rate of mass change, $\dot{m}$. Since in this transition, γ_{av} and $\dot{S}$ decrease, the value of P upon the transition increases with respect to the corresponding value for the comparison system in estimation of P by Eq. (2). Thus, in this case, the Klimontovich principle is also not applicable. At the same time, the entropy production decreases, and the transition to the skeletal crystal with new branch orientations smooths this decrease because of a lower value of the term $\gamma_{av}\dot{S}$. In other words, it hinders this decrease, in accord with the last of the three principles described above.

The ⟨110⟩ ⟶ ⟨111⟩ *transition.* As was indicated above, the ⟨111⟩ face zone should have higher γ_{av} values in comparison with analogous values for the ⟨110⟩ zone. Performing the analysis similar to that made above, one can readily see that this transition confirms both universal evolution ($d_X P/d\tau < 0$) and Klimontovich principles. At the same time, this transition can also be interpreted in terms of the latter of the three principles; i.e., in the ⟨110⟩ ⟶ ⟨111⟩ transition, the total entropy production increases. An increase of the numerical value of the term responsible to the "area flow" in Eq. (2) hinders an increase of the entropy production, i.e., again "smooths" this increase. Thus, unlike the previous transition, the ⟨110⟩ ⟶ ⟨111⟩ transition can be interpreted in terms of any of the above three variational principles.

It follows from the above that at all the stages of the shape evolution of NH_4Cl crystals (the transformation of a convex crystal into a skeletal one and two transitions in the skeleton morphology), only the principle of the maximum system resistance to the changes in the entropy production remains valid.

Thus, the difference between the chemical potentials is the key factor of the process, whereas the mass flow introduces the major contribution to the entropy production. On the contrary, the "surface flow" and its contribution to the entropy production hinder any changes in the entropy production.

REFERENCES

1. A. Hill, Nature **348** (300), 426 (1990).
2. I. I. Shafranovskiĭ, *Lectures on Crystal Morphology of Minerals* (Lviv. Univ., Lviv, 1960).
3. A. A. Chernov, E. I. Givargizov, K. S. Bagdasarov, V. A. Kuznetsov, L. N. Demianets, and A. N. Lobachev, in *Modern Crystallography*, Vol. 3: *Crystal Growth*, Ed. by B. K. Vaĭnsteĭn, A. A. Chernov, and L. A. Shuvalov (Springer-Verlag, Berlin, 1984; Nauka, Moscow, 1980).
4. J. S. Kirkaldy, Rep. Prog. Phys. **55** (6), 723 (1992).
5. C. N. Nanev, Bulg. Chem. Commun. **26** (1), 3 (1993).
6. A. Papapetrou, Z. Kristallogr. A **92** (1/2), 89 (1935).
7. G. P. Veĭnberg, *Ice. Properties, Formation, and Disappearance of Ice* (Gostekhizdat, Moscow, 1940).
8. J. Dogiel, Bulletin de l'Academie Imperiale des Sciences de St. Petersburg **20**, 337, 22–30 (1875).
9. J. Dogiel, Melanges physiques et chimiques tires du Bulletin de L'Academie Imperiale des Sciences de St. Petersburg **9**, 266 (1877).
10. O. Lehmann, *Molekularphysik* (Engelmann, Leipzig, 1888), Vol. I.
11. V. A. Mokievskiĭ and S. N. Semenyuk, Zap. Vses. Mineral. O–va **81** (2), 100 (1952).
12. T. G. Petrov, E. B. Treĭvus, Yu. O. Punin, and A. P. Kasatkin, *Crystal Growth from Solutions* (Nedra, Leningrad, 1983).
13. T. G. Petrov, in *Growth of Crystals*, Ed. by A. V. Shubnikov and N. N. Sheftal' (Akad. Nauk SSSR, Moscow, 1961), Vol. 3, p. 147.
14. W. Ebeling, *Strukturbildung bei Irreversiblen Prozessen* (Teubner, Leipzig, 1976; Mir, Moscow, 1979).
15. I. Prigogine and R. Defay, *Thermodynamique chimique conformément aux méthodes de Gibbs et al., De Donder* (Desoer, Liége, 1944; Nauka, Novosibirsk, 1966).
16. P. Glansdorff and I. Prigogine, *Thermodynamic Theory of Structure, Stability and Fluctuations* (Wiley, New York, 1971; Mir, Moscow, 1973).

17. G. Nicolis and I. Prigogine, *Self-Organization in Non-Equilibrium Systems* (Wiley, New York, 1977; Mir, Moscow, 1979).
18. Yu. D. Klimontovich, Usp. Fiz. Nauk **158** (1), 59 (1989) [Sov. Phys. Usp. **32**, 416 (1989)].
19. E. B. Pelyukhova and É. E. Fradkin, *Self-Organization of Physical Systems* (St. Peterburg. Univ., St. Petersburg, 1997).
20. E. B. Treĭvus, Kristallografiya **12** (3), 508 (1967) [Sov. Phys. Crystallogr. **12**, 432 (1967)].
21. E. B. Treĭvus, *Kinetics of Crystal Growth and Dissolution* (Leningrad. Gos. Univ., Leningrad, 1979).
22. E. B. Treĭvus, *Introduction in Thermodynamics of Crystal Genesis* (Leningrad. Gos. Univ., Leningrad, 1990).
23. S.-K. Chan, H. H. Reimer, and M. Kahlweit, J. Cryst. Growth **32** (3), 303 (1976).
24. D. D. Saratovkin, *Dendritic Crystallization* (Metallurgizdat, Moscow, 1957).
25. M. Hille, H. Rau, and J. Schlipf, in *Growth and Perfection of Crystals*, Ed. by R. H. Doremus *et al.* (Wiley, New York, 1958), p. 325.
26. K. A. Blackmore, K. M. Beatty, M. J. Hui, and K. A. Jackson, J. Cryst. Growth **174** (1–4), 76 (1997).
27. R. Kern, Bull. Soc. Fr. Mineral. Crystallogr. **78** (10–12), 497 (1955).
28. B. Honigmann, *Gleichgewichts- und Wachstumsformen von Kristallen* (D. Steinkopff, Darmstadt, 1958; Inostrannaya Literatura, Moscow, 1961).
29. P. Groth, *Chemische Kristallogfaphie* (W. Engelmann, Leipzig, 1906), Vol. 1.
30. R. Kern, Bull. Soc. Fr. Mineral. Crystallogr. **76** (7–9), 325 (1953).
31. M. O. Kliya, Dokl. Akad. Nauk SSSR **100** (2), 259 (1955).

Translated by L. Man

Crystallography Reports, Vol. 45, No. 6, 2000, pp. 1035–1040. Translated from Kristallografiya, Vol. 45, No. 6, 2000, pp. 1120–1125.

CRYSTAL GROWTH

Structural Mechanism of the Impurity Effect on Kinetics of Crystal Growth. Crystallochemical Aspect

A. B. Kuznetsov*, T. A. Eremina*, N. N. Eremin, T. M. Okhrimenko*, N. G. Furmanova*, and E. P. Efremova***

** Shubnikov Institute of Crystallography, Russian Academy of Sciences, Leninskiĭ pr. 59, Moscow, 117333 Russia*

*** Moscow State University, Vorob'evy gory, Moscow, 119899 Russia*

Received November 26, 1998

Abstract—It has been established that metal impurities M^{3+} (Fe^{3+}, Cr^{3+}) and M^{2+} (Co^{2+}, Ni^{2+}) have a different effect on the kinetics of face growth of potassium dihydrophosphate (KDP) and potassium acid phthalate (KAP) crystals, which can hardly be interpreted in terms of the existing concepts. The crystallochemical analysis and computer modeling of the KDP structure provided the establishment of different mechanisms of incorporation of M^{2+} and M^{3+} impurities into the crystal structure: the first impurities form impurity clusters, whereas the second impurities occupy isolated positions. This fact predetermines the different deformation of the crystal matrix caused by M^{2+} and M^{3+} ions. The allowance for this fact provided the interpretation of different distribution coefficients of M^{2+} and M^{3+} impurities and their specific effect on the growth kinetics and defect concentration in KDP and KAP crystals. © *2000 MAIK "Nauka/Interperiodica".*

INTRODUCTION

The effect of impurities on the growth kinetics of crystals is provided by numerous physical and chemical factors in the interactions of impurity molecules (ions, atoms, etc.) with a growing crystal [1–3]. In modern growth theory, the impurity effect is associated mainly with adsorption of impurities on crystal faces and the corresponding changes of the kinetic and thermodynamic parameters of crystallization [4]. The more pronounced influence of the first factor leads to the well-known inverse dependences of the growth rates on the impurity concentration, $R(C_i)$, whereas the variation of the thermodynamics parameter (a decrease in the free energy of growth steps) increases the growth rate. Thus, the combined action of both factors can lead to the dependence $R(C_i)$ possessing the maximum in the range of low-impurity concentrations [4] (the so-called catalytic effect of impurity). The experiments showed [5–7] that the catalytic effect is a phenomenon characteristic of numerous organic impurities that are not captured by a crystal during the growth process. At the same time, we also established that the catalytic effect of inorganic impurities (metal ions) incorporated into the crystal matrix can manifest itself in more specific ways—it took place under high supersaturations and was absent at low supersaturations, which was inconsistent with the known theoretical concepts [4].

It can be assumed that the "anomalous" effect of inorganic impurities is provided by local stresses arising in the crystal matrix due to incorporation of impurity ions. It is well known that various stresses, e.g., dislocation-induced ones, decrease the velocity of growth-step motion [8]. According to [9], an increase of the thermodynamic potential of the crystal due to incorporation of impurity ions and, correspondingly, a decrease of the driving force of crystallization can increase the inhibitory effect of impurities adsorbed on crystal surface. According to the assumption made in [10], this factor can be even more pronounced than the effect of impurity adsorption on the surface.

Below, we present the experimental data on the effect of impurities of tri- and bivalent metals on the kinetics of face growth of potassium dihydrophosphate (KDP) and potassium acid phthalate (KAP) crystals grown from aqueous solutions. We analyzed the mechanism of incorporation of tri- and bivalent cations into the KDP structure on the basis of the crystallochemical data and computer modeling of the KDP structure containing Fe^{3+} and Fe^{2+} impurity ions. The results of this analysis are compared with the data on the effect of these impurities on growth kinetics.

EXPERIMENTAL METHOD

KDP and KAP crystals were grown in the kinetic mode by the method described in [7, 11]. The impurities were introduced into a well-stirred (for 24 h) saturated KDP and KAP solutions at the saturation temperatures 50 and 40°C, respectively. The growth experiment was also performed within 24 h. The theoretical modeling of the KDP structure was made by minimizing the energy of atomic interactions with the use of partly covalent pair potentials [12] specially constructed for this compound.

1063-7745/00/4506-1035$20.00

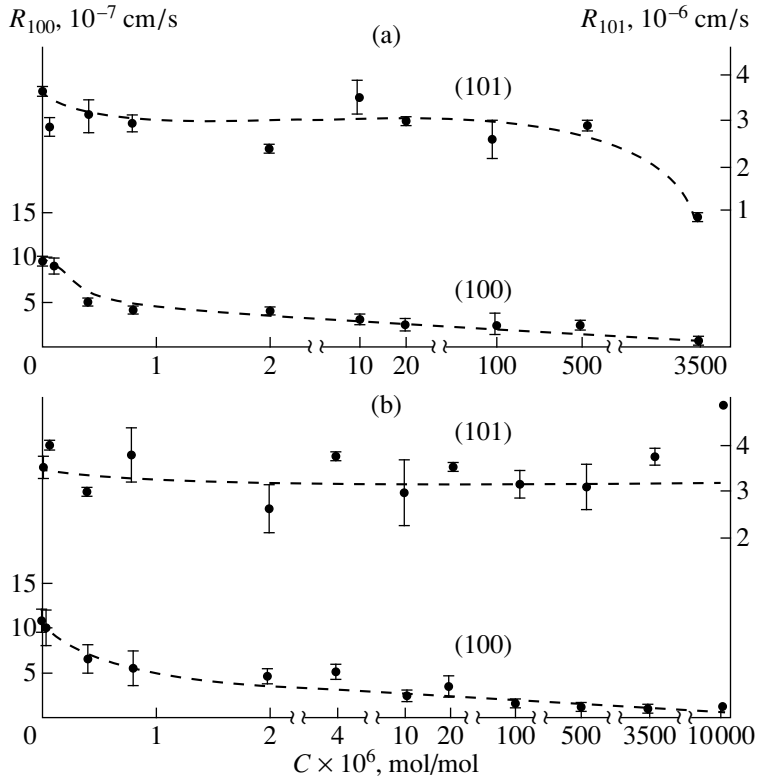

Fig. 1. Effect of (a) Ni^{2+} and (b) Co^{2+} impurities on the growth kinetics of KDP crystals; $\sigma = 0.021$.

EXPERIMENTAL RESULTS

The Effect of Bivalent and Trivalent Metal Impurities on Growth Kinetics of KDP and KAP Faces

Figure 1 illustrates the effect of Co^{2+} and Ni^{2+} impurities on growth kinetics of (101) and (100) faces of KDP crystals. A decrease of the growth rate of the faces with an increase of the impurity concentration is very common and is especially well seen on the (100) face.[1] For the (101) face, the scatter of the experimental points is more pronounced; nevertheless, the general character of the $R(C_i)$ dependence shows that the catalytic effect of impurities is absent even at the lowest impurity concentrations. Similar dependences were also obtained for KAP crystals (Fig. 2). An increase of growth rates for the faces of KAP crystals with an increase of the Co^{2+} content up to 0.4×10^{-7} mol Co^{2+}/mol in KAP is explained by the formation of macrodefects: gas–liquid inclusions, cracks along the cleavages, etc. Cracking can be associated with the probable incorporation of Co^{2+} cations into the interblock layer along cleavage planes and formation of hydrated complexes of the composition $[Co(H_2O)_6]^{2+}$ pushing away the anionic layers [13]. Similar cracking, although less marked, was observed in the presence of Ni^{2+} impurities at the concentrations exceeding 10^{-6} mol Ni^{2+}/mol in KAP. It should be indicated that the negative effect of M^{2+} impurities on KDP crystals at elevated concentrations manifested itself in the formation of blocks especially pronounced in the presence of the Ni^{2+} impurity.

Other types of $R(C_i)$ dependences are characteristic of the Cr^{3+} and Fe^{3+} impurities. Figure 3 shows that the growth rates of the (101) face of KDP crystals and the faces of KAP crystals first increase with an increase of the Cr^{3+} concentration (the catalytic effect of impurities) and then start decreasing. Visually, the KAP crystals remained homogeneous within the whole range of impurity concentrations. The most pronounced catalytic effect is observed for the Fe^{3+} impurity in KDP crystals [Fig. 4a, the (101) face]. However, the effect becomes steady-state only at high supersaturations, $\sigma \geq 0.06$. At lower supersaturations, the effect is absent (Fig. 4b), which, as has already been indicated, contradicts the theoretical model of crystal growth [4], where a decrease of the energy of the edge step caused by impurity adsorption is the major form of the manifestation of the catalytic effect of impurities.

Crystallochemical Analysis of Incorporation of the M^{2+} and M^{3+} Impurities into the KDP Structure

It was shown [14] that the impurity Fe^{3+} ion in a KDP crystal should occupy the interstitial position with the coordinates (0.25, 0.35, 0.125). The geometric con-

[1] Impurity concentration was determined as the ratio of the number of moles of impurity to the number of moles of the matrix material in the solution.

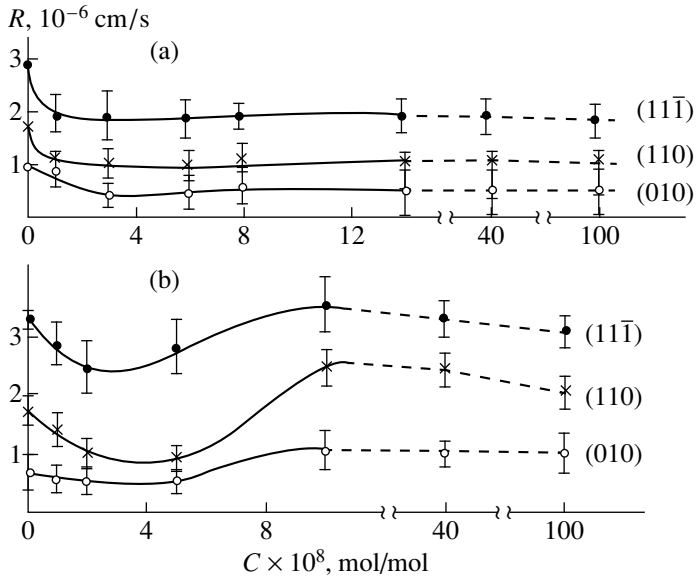

Fig. 2. Effect of (a) Ni^{2+} and (b) Co^{2+} impurities on the growth kinetics of KAP crystals, $\sigma = 0.031$.

ditions for incorporation of this ion require the removal of the two nearest K^+ ions and a hydrogen ion compensating the charge of Fe^{3+} cation. The subsequent consideration of the KDP structure containing Fe^{3+} impurity [12] was based on this model and revealed essential structural distortions in the nearest neighborhood of the impurity ion. These results allowed us to analyze the successive incorporation of Fe^{3+} cations into the KDP structure.

The structure distortions revealed that the structure has a "chain" of voids. The incorporation of a Fe^{3+} ion into one of the links of this chain promotes the favorable conditions for incorporation of another similar ion into the neighboring link of the chain (Fig. 5). However, the valence balance shows that certain portions of this chain periodically accumulate positive charges. In order to compensate these charges, some additional vacancies are required. Therefore, at low concentrations, Fe^{3+} ions would strive for isolated positions with empty neighboring positions. The results of the above analysis are also applicable to Cr^{3+} cations with the ionic radii close to that of Fe^{3+}: $r_{Fe^{3+}} = 0.67$ Å, $r_{Cr^{3+}} = 0.64$ Å.

The situation drastically changes for a bivalent cation, e.g., Fe^{2+}, Co^{2+}, or Ni^{2+}. Similar to the case of a trivalent ion, we used the method of the atom–atom potentials (the GULP program [15]) and constructed various models of a defect center for Fe^{2+} ions (the results will be considered in another publication). The calculations showed that for M^{2+} ions with the ionic radii close to those of Fe^{3+} (Fe^{2+}, Co^{2+}, Ni^{2+}), the position with the coordinates (0.25, 0.35, 0.125) in the KDP structure still remains the most favorable. Therefore, the results of the geometric analysis performed for Fe^{3+} are valid in this case as well. However, the geometric requirements and the valence balance show that the incorporation of a Fe^{3+} ion requires the removal from the lattice of two K^+ ions and one proton. At the incorporation of a Fe^{2+} ion, the crystal remains electrically neutral if only two K^+ ions are removed. To meet the geometric conditions, the remaining H atom should be displaced from its position by ~0.5 Å and thus be "transformed" into another point defect. In other words, bivalent cations distort the initial structure much more pronouncedly than trivalent ones. Therefore, the incorporation of a Fe^{2+} ion into the KDP structure is energetically less favorable than that of a Fe^{3+} ion, with the corresponding energies of defect formation being +1.44 and –4.79 eV, respectively. (All the values were obtained with the use of the refined set of pair potentials, with the energy of formation of a Fe^{3+} defect being different from the energy given in [12].)

The analysis of various types of incorporation of M^{2+} ions into the neighboring links of the chain described above showed that, contrary to the case of trivalent cations, the distribution of bivalent cations in geometrically favorable neighboring positions not only provides the electroneutrality of the defect region but is also somewhat more energetically favorable than the formation of an isolated M^{2+} defect. Thus, for a defect consisting, e.g., of three Fe^{2+} cations, the corresponding energy equals +4.23 eV (+1.41 eV per impurity ion in the chain in comparison with +1.44 eV in the isolated position).

Thus, in a KDP crystal, the trivalent impurity "prefers" to exist as an isolated ion, whereas the bivalent cation, obeying the requirements of electroneutrality,

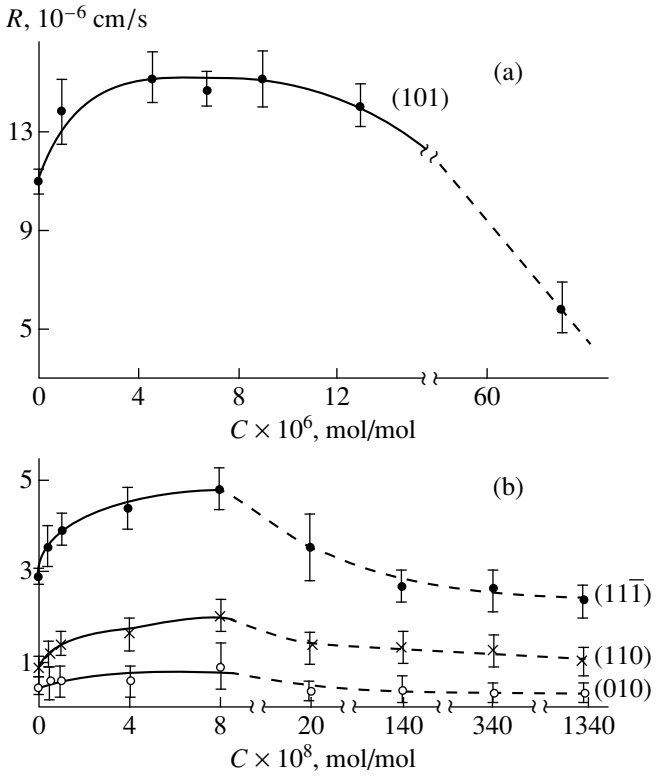

Fig. 3. Effect of Cr^{3+} impurity on the growth kinetics of (a) KDP crystals $\sigma = 0.063$ and (b) KAP crystals $\sigma = 0.031$.

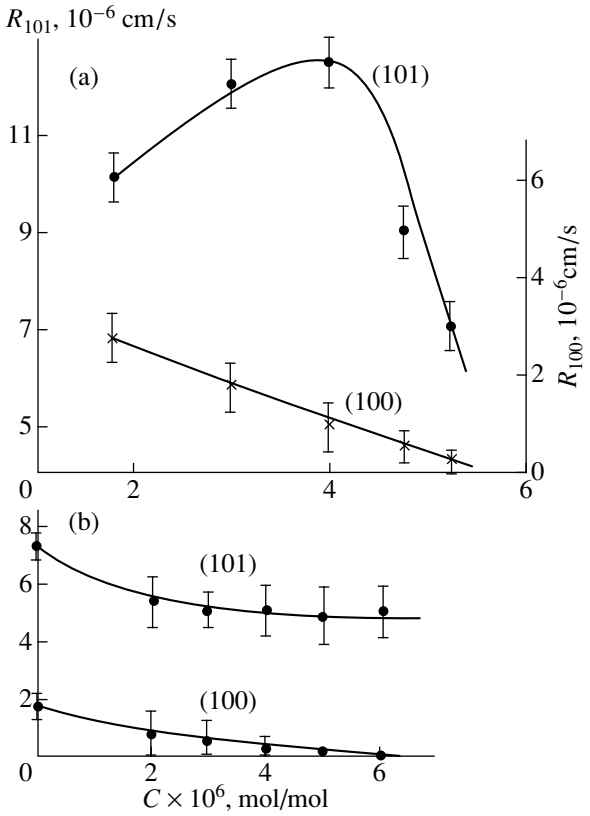

Fig. 4. Effect of Fe^{3+} impurities on the growth kinetics of KDP crystals: (a) $\sigma = 0.063$, (b) $\sigma = 0.03$.

"prefers" to form clusters. Such M^{2+} cluster formations deform the crystal structure even more pronouncedly. Therefore, they should provide a more pronounced inhibitory effect M^{2+} than M^{3+} impurities.

RESULTS AND DISCUSSION

It should be indicated that different structures of the defect centers caused by incorporation of M^{2+} and M^{3+} impurities revealed by computer modeling are consistent with the above fact of a stronger effect of impurity cations on the formation of macrodefects and with the characteristics of the coefficients k of M^{3+} and M^{2+} distribution in the crystal. It is well known [16, 17] that the coefficients k of bivalent cations in KDP and KAP crystals are much lower than those of trivalent ones. One of the reasons for such a situation in KDP crystals is a more pronounced deformation of the crystal lattice by M^{2+} clusters hindering the incorporation of these cations into the lattice and also by a much higher energy of formation of Fe^{2+} defects. On the other hand, the incorporation of Fe^{3+} and Cr^{3+} cations with an increase of their concentration in the starting solution and their incorporation into isolated positions in the KDP crystals show the necessity of filling the neighboring position with these cations as well. As was indicated above, this process, accompanied by the additional deformation of the crystal matrix, hinders the incorporation of impurity ions. This can be one possible cause for a decrease of $k_{Fe^{3+}}$ in KDP crystals experimentally confirmed in [18].

Now, analyze the experimental data on growth kinetics of KDP crystals in the presence of M^{2+} and M^{3+} impurities in terms of different deformability of the crystal matrix. With due regard for this factor, the effect of impurity on the growth kinetics should depend on three parameters—the changes in the kinetic and thermodynamic factors and the structure deformation caused by impurity incorporation. The first two factors depend on the adsorption on the surface (e.g., of organic molecules) and are analyzed in modern theory of crystal growth. If no impurities are incorporated into the crystal, only the first two factors are important, and the catalytic effect of impurities can take place also in the region of low impurity concentrations [7]. If the impurity ions are captured by the crystal, the stresses arising in the structure enhance the decelerating effect of the kinetic parameter and, thus, decrease the relative contribution of the thermodynamic factor. This, in turn, reduces the catalytic effect of impurities. If deformations of the crystal lattice are pronounced even at a low concentration of impurity ions, the catalytic effect does not necessarily manifest itself in the whole range of the impurity concentrations. This situation is implemented

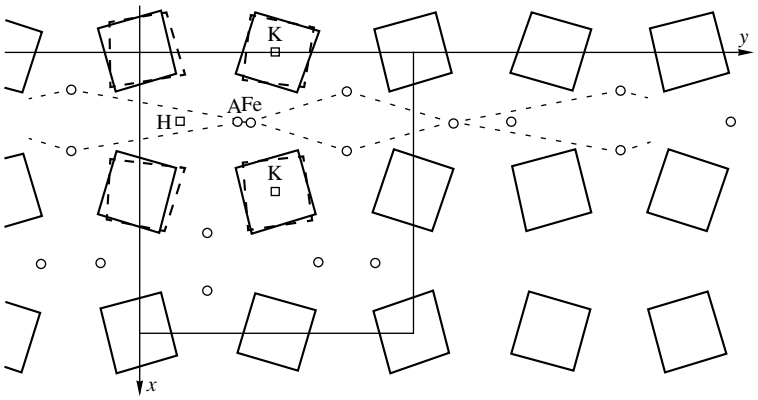

Fig. 5. Structure of a defect center formed by a Fe^{3+} ion in the KDP structure. Bold dashed lines show the rotation of PO_4-tetrahedra in the region of the primary defect A. For comparison, the corresponding tetrahedra in pure KDP crystals are shown by bold solid lines. Thin dashed lines show the geometrically favorable "chains of voids." Circles indicate the void centers, whereas squares indicate hydrogen and potassium vacancies.

for bivalent ions. Therefore, the Co^{2+} and Ni^{2+} ions can produce no catalytic effect on the growth kinetics of KDP crystals.

Unlike M^{2+}, the trivalent Fe^{3+} and Cr^{3+} ions forming isolated impurity centers at low concentrations deform the crystal matrix to a lesser degree. The contribution of this factor to the total inhibitory effect of impurities is much smaller, and the catalytic effect of impurities can also be experimentally observed for Fe^{3+} and Cr^{3+}. However, the effect manifests itself mainly at high supersaturations, which can be explained by a reduced value of the coefficient k for Fe^{3+} and Cr^{3+} decreasing with an increase of the supersaturation [19]. This predetermines the minimum Fe^{3+} and Cr^{3+} concentrations under high supersaturations. Therefore, the contribution of the structure factor to the total inhibitory effect of impurities on the growth kinetics at high supersaturations should be minimal, and the catalytic effect should take place. Nevertheless, for the (100) face of KDP crystals, this effect is not observed even at high supersaturations. This is explained by the fact that $k_{Fe^{3+}}$ for the (100) growth pyramid of the KDP crystal is higher than that for the (101) pyramid (which agrees with the crystallochemical characteristics of the structure of these faces [14]). Obviously, the Fe^{3+} concentration on the (100) plane does not decrease to the values necessary for the manifestation of the catalytic effect at high supersaturations.

Thus, different mechanisms of Co^{2+} and Ni^{2+} incorporation, on the one hand, and Fe^{3+} and Cr^{3+} incorporation, on the other hand, allow one to explain the specific features of the distribution of their coefficients, the growth kinetics, and the defect formation in crystals. Naturally, the scheme suggested above is of the qualitative nature because, at present, data on the coefficients of impurity capture in solutions at very low impurity concentrations are very scarce, whereas the program used in the calculations allows for the analysis of the "cluster" impurity center consisting of at least three impurity atoms. This hinders the quantitative estimation of stresses in the crystals at low impurity concentrations. Nevertheless, we believe that the above facts confirm once again an important role of local impurity-induced deformations in crystal growth.

ACKNOWLEDGMENTS

This study was supported by the Russian Foundation for Basic Research, project no. 96-03-34141.

REFERENCES

1. A. A. Chernov, E. I. Givargizov, Kh. S. Bagdasarov, *et al.*, in *Modern Crystallography*, Vol. 3: *Crystal Growth*, Ed. by B. K. Vaĭnshteĭn, A. A. Chernov, and L. A. Shuvalov (Nauka, Moscow, 1980; Springer-Verlag, Berlin, 1984).
2. K. Sangwal, Prog. Cryst. Growth Charact. Mater. **32**, 3 (1996).
3. S. Veintemillas-Verdaguer, Prog. Cryst. Growth Charact. Mater. **32**, 75 (1996).
4. R. J. Davey, in *Industrial Crystallization 78*, Ed. by E. J. de Jong and S. J. Jancic (North-Holland, Amsterdam, 1979), p. 169.
5. V. A. Kuznetsov, T. M. Okhrimenko, and Kh. S. Bagdasarov, Kristallografiya **41** (3), 557 (1996) [Crystallogr. Rep. **41**, 527 (1996)].
6. V. A. Kuznetsov, T. M. Okhrimenko, and E. P. Efremova, Kristallografiya **45** (2000) (in press) [Crystallogr. Rep. **45** (2000) (in press)].
7. V. A. Kuznetsov, T. M. Okhrimenko, and M. Rak, J. Cryst. Growth **193** (2), 164 (1998).
8. N. Cabrera and M. M. Levine, Philos. Mag. **1**, 450 (1956).
9. V. V. Voronkov, Kristallografiya **19** (3), 475 (1974).

10. N. T. Barret, G. M. Hamble, K. J. Roberts, and J. M. Sherwood, J. Cryst. Growth **94** (3), 689 (1989).
11. V. A. Kuznetsov, T. M. Okhrimenko, and M. Rak, Proc. SPIE **3178**, 100 (1997).
12. T. A. Eremina, V. A. Kuznetsov, T. M. Okhrimenko, *et al.*, Kristallografiya **43** (5), 906 (1998) [Crystallogr. Rep. **43**, 852 (1998)].
13. N. G. Furmanova, T. A. Eremina, T. M. Okhrimenko, and V. A. Kuznetsov, Kristallografiya **45** (2000) (in press) [Crystallogr. Rep. **45** (2000) (in press)].
14. T. A. Eremina, V. A. Kuznetsov, T. M. Okhrimenko, and N. G. Furmanova, Kristallografiya **41** (4), 717 (1996) [Crystallogr. Rep. **41**, 680 (1996)].
15. J. D. Gale, *JULP: User Manual* (Royal Institution and Imperial College, London, 1992–1994).
16. M. H. Hottenhuis and C. B. Lucasius, J. Cryst. Growth **91** (4), 623 (1988).
17. O. V. Demirskaya, A. N. Kislomed, Yu. N. Velikhov, *et al.*, Vysokochist. Veshchestva, No. 1, 14 (1989).
18. V. D. Franke and R. S. Bubnova, *Physics of Crystallization*, Kalinin St. Univ., Kalinin, 1979.
19. C. Belonet, E. Dunia, and J.E. Petroff, J. Cryst. Growth **23** (4), 243 (1974).

Translated by L. Man

Crystallography Reports, Vol. 45, No. 6, 2000, pp. 1041–1046. Translated from Kristallografiya, Vol. 45, No. 6, 2000, pp. 1126–1132.

Growth of Mixed Crystals under the Nonstationary Conditions. 1. Equilibria and Quasiequilibria[1]

S. V. Moshkin, M. A. Kuz'mina, O. M. Boldyreva, and T. I. Ivanova

St. Petersburg State University, Universitetskaya nab. 7/9, St. Petersburg, 199164 Russia

Received February 24, 1998; in final form, March 1, 2000

Abstract—A thermodynamic model of a quasiequilibrium between the solution and an elastically stressed layer formed during growth of a two-component mixed crystal under nonstationary conditions has been constructed. The derived equations are solved numerically for the system potassium biphtalate–rubidium biphtalate–water. It is shown that the inconsistency between the experimental and the calculated data are associated, first and foremost, with the relaxation processes at defects. *© 2000 MAIK "Nauka/Interperiodica".*

INTRODUCTION

Growth of mixed crystals is essentially dependent on formation of crystals with the fixed stoichiometry and is associated with possible changes in the growing-crystal composition caused by different crystallization conditions. Any nonstationarity in growth conditions for a mixed crystal results in the change of the crystal composition because, in the general case, the coefficients of component distribution depend on all the growth parameters. The nonstationary growth conditions are also characteristic of natural crystallization (which, in particular, results in the formation of zonal crystals). In commercial crystallization, nonstationary growth conditions are usually observed for crystals whose properties vary over the volume [1]. Growth of bizonal crystals [2] and heteroepitaxial films [3–5] in which a crystalline layer is grown onto a nonnative substrate can also be considered as nonstationary crystallization.

Numerous experimental data indicate that growth of crystalline layers onto nonnative substrates differs from growth of the films on native substrates under the same conditions. In particular, the coefficients of components distribution [1, 2], growth rates [1, 2], and the equilibrium conditions [3, 4] in these two cases are different; the specific defects formed in these cases are also different [2, 5]. It is shown [3, 4] that the differences are associated with internal stresses in a growing layer caused, in turn, by different unit-cell parameters of the layer and the substrate. The internal stresses affect both the thermodynamic properties of the material and the growth characteristics, in particular, the kinetic coefficients of elementary reactions at the growth point. On the other hand, the stresses themselves can vary and be redistributed during crystal growth because of the varying thickness and composition of the grown layer and formation of misfit dislocations and other defects. Moreover, if the distribution coefficients of the components differ from unity, the composition of the growing layer and, therefore, the stresses in this layer depend on the diffusion processes in the boundary layer of the solution. The theoretical model of the nonstationary growth of mixed crystals, which takes into account all the above processes, will be considered in a series of articles.

The present article, the first in this series, is devoted to the thermodynamic analysis of equilibria and quasiequilibria in the system substrate–stressed layer–solution for a defect-free crystal. The simplified model suggested here is the basic model for the further analysis of the kinetic factors and the processes of stress relaxation at defects, because the expressions obtained for this model enter the systems of equations that describe these more complicated processes.

CONDITIONS FOR EQUILIBRIUM IN THE SYSTEM LIQUID SOLUTION–SOLID SOLUTION

The equilibria in the system unstressed crystal–liquid crystallization medium for ideal solutions are described in detail in [6, 7]. Introduce the notation and give several well known relationships necessary for the further consideration. We assume that the crystal under consideration is an isomorphous mixture of two components, *A* and *B*, forming an ideal solid solution. Denote the component concentrations in the crystal (in molar fractions) as X_i ($i = A, B$), with $X_B = 1 - X_A$. The chemical potentials of the components are $\mu_i^s = M_i^s + RT\ln(X_i)$, where M_i^s is the chemical potential of pure *i*th component in the solid phase, *R* is the gas constant, and *T* is the absolute temperature. We assume that the crystallization medium is an ideal three-component solution of the components *A* and *B*. The third compo-

[1] Additional materials can be requested at the address html:\\www.freebee.techno.ru/s_moshkin/Paper 97.htm.

1063-7745/00/4506-1041$20.00 © 2000 MAIK "Nauka/Interperiodica"

nent C (solvent) does not enter the solid phase. Let C_i be the concentrations of the components in the liquid phase and C_i^0 be the concentrations of the solution which is in equilibrium with the crystal of the composition X_A, X_B. The chemical potentials of the components in the solution are $\mu_i^l = M_i^l + RT\ln(C_i)$. In ideal solutions, M_i^l are independent of the component concentrations, and the condition for equality of chemical potentials in the equilibrium $\mu_i^s = \mu_i^l$ yields

$$C_i^0 = X_i \exp(\Delta M_i/RT), \quad (1)$$

where $\Delta M_i = M_i^s - M_i^l$.

The compositions of the solution and the crystal can be conveniently described in dimensionless variables characterizing the component ratios in each phase, namely,

$$\gamma_s = X_B/(X_A + X_B) \equiv X_B, \quad \gamma_l = C_B/(C_A + C_B).$$

The solubility of the isomorphous mixture C^0 (the molar fraction of the total amount of salts in the equilibrium solution) can be represented as a function of the mixture composition γ_s:

$$C^0 = (1-\gamma_s)\exp(\Delta M_A/RT) + \gamma_s \exp(\Delta M_B/RT). \quad (2)$$

The equilibrium values of the distribution coefficients $r_i = X_i/C_i^0$ can be determined from (1) as $r_i = \exp(-\Delta\mu_i/RT)$. A more convenient form of the representation of the coefficient characterizing the component distribution is

$$k = r_A/r_B = X_A C_B^0/C_A^0 X_B = \exp((\Delta M_B - \Delta M_A)/RT). \quad (3)$$

THE ALLOWANCE FOR STRESSES IN THE SYSTEM SUBSTRATE–GROWN LAYER–SOLUTION

Consider the situation, where a substrate with the lattice parameters different from the parameters of the crystal, which is in equilibrium with the solution of isomorphous mixture, is placed into the solution with the component ratio γ_l. It should be mentioned that the difference in the substrate and crystal parameters is such that it allows epitaxial growth. Such a substrate can be a crystal of the same phase but its composition should be different from the solution composition (in terms of Eq. (1)). We assume that there is no mass transfer between the substrate and the solution, which, corresponds, e.g., to the case of complete coating of the substrate with a grown layer. We also assume that the rate of diffusion between the substrate and the growing phase is negligible in comparison with the rates of the exchange processes between the crystal and the liquid phase. For simplicity, consider the cubic substrate and the cubic growing phase, with the intergrowth plane (001).

Consider a thin layer of the "isomorphous mixture" with the parameter a grown onto the substrate with the parameter a_1. We assume that in the intergrowth plane, the substrate parameter acquires the value equal to that of the substrate and that all the strains in this layer remain elastic; in other words, no misfit dislocations can be formed. For thin layers, this assumption is justified even at considerable differences between the layer and substrate parameters [5]. Thus, the grown layer is in an elastically stressed state, and the energy of elastic stresses per unit volume is $U = c_{ijkl}\varepsilon_{ij}\varepsilon_{kl}/2$ [8], where ε_{ij} are the components of the strain tensor in the grown layer and c_{ijkl} are the components of the elastic stiffness tensor of the layer.

In our case, the stresses are parallel to the intergrowth plane, and the coordinate axes of the system coincide with the main axes of the strain and stress tensors; in other words, all the components of the stress tensor (except two) are zeroes. The corresponding components of the strain tensor are $\varepsilon_{11} = \varepsilon_{22} = \varepsilon = (a - a_1)/a$ or, taking into account that $a \approx a_1$, we have $-\varepsilon = (a - a_1)/a_1$. Since the parameter a in an ideal solid solution linearly depends on the crystal composition, $a = a_0 + \xi X_A$, where ξ is a constant coefficient. The stress energy of one mole of the substance in the grown layer can be written as $U = cNV(a_0 - a_1 + \xi X_A)^2/a_1^2 z$, where $c = c_{1111} + c_{1122}$, N is the Avogadro number, V is the unit-cell volume, and z is the number of formula units in the unit cell.

Now, we can write the specific total thermodynamic potential of a stressed layer grown onto the substrate, Z_S, for the particular case of a cubic crystal[2] in the form

$$Z_s = cNV(a_0 - a_1 + \xi X_A)^2/a_1^2 z + X_A(M_A^s + RT\ln(X_A)) + X_B(M_B^s + RT\ln(X_B)).$$

[2] The stress energy in a grown layer for a noncubic crystal is

$$U = \frac{NV}{2z}\left(\frac{(c_{11}^* + c_{12}^*)(a_{01}^* - a_{11}^* + \xi_1^* X_A)^2}{(a_{11}^*)^2} + \frac{(c_{22}^* + c_{21}^*)(a_{02}^* - a_{12}^* + \xi_2^* X_A)^2}{(a_{12}^*)^2}\right),$$

where a_{0i}^* and a_{1i}^* are the dimensions of the unit-cell projection onto the principal axes of the strain tensor for the grown layer in the intergrowth plane, ξ_i^* are the coefficients in the equations that describe the dependence of these dimensions on the concentration of the component A, c_{ij}^* are the components of the elastic-stiffness tensor rotated toward the same axes. For monoclinic and triclinic crystals, and for the intergrowth planes in general positions, the determination of the principal axes of the strain tensor for the grown layer is a nontrivial problem.

The additional term in the expression for Z_S related to stresses nonlinearly depends on the component concentrations in the crystal. As a result, the total thermodynamic potential for the crystal stops being additive with respect to the component masses and concentrations; in other words, the solid solution stops being ideal [9]. In particular, this manifests itself in the fact that the thermodynamic potentials are not uniform functions of concentrations, i.e., $Z_S \neq \sum_i X_i \partial Z_s/\partial X_i$.

One should not use the derivative of the thermodynamic potentials with respect to concentrations (i.e., the chemical potentials) in order to describe the equilibria in such systems. Instead, one has to use a more general principle of the total thermodynamic potential of the system (ΔZ_σ) in the equilibrium state [9], which is also valid for nonideal systems. The variation in ΔZ_σ during growth of one mole of isomorphous mixture of the composition X_A from an infinite volume of the solution of the composition C_A, C_B on the substrate with the unit-cell parameter a_1 is

$$\Delta Z_\sigma = cNV(a_0 - a_1 + \xi X_A)^2/a_1^2 z + X_A(RT\ln(X_A/C_A) + \Delta M_A) + (1 - X_A)(RT\ln((1 - X_A)(1 - \gamma_l)/\gamma_l C_A) + \Delta M_B).$$

Obviously, in both equilibrium and quasiequilibrium processes, only a layer with the composition corresponding to the minimum ΔZ_σ value can grow, i.e., a layer which satisfies the condition

$$\partial\Delta Z_\sigma/\partial X_A = RT\ln(\gamma_l X_A/(1 - \gamma_l)(1 - X_A)) + 2cNV\xi(a_0 - a_1 + \xi X_A)/a_1^2 z = 0. \quad (4)$$

Equation (4) determines only a possible composition of the stressed crystalline layer. The direction of the process occurring in the system depends on the sign of ΔZ_σ (the layer grows at $\Delta Z_\sigma < 0$); it is dissolved at $\Delta Z_\sigma > 0$ and both processes are in equilibrium at $\Delta Z_\sigma = 0$. Thus, the second condition for the equilibrium in the system is

$$cNV(a_0 - a_1 + \xi X_A)^2/a_1^2 z + X_A[RT\ln(X_A/C_A) + \Delta M_A] + (1 - X_A) \times [RT\ln((1 - X_A)(1 - \gamma_l)/\gamma_l C_A) + \Delta M_B] = 0. \quad (5)$$

One has necessarily to take into account that Eqs. (4) and (5) describe the true equilibrium in the systems substrate–stressed layer–solution only in there is no mass transfer between the substrate, on the one side, and the grown layer and the solution, on the other. If a substrate is the crystal of the same phase but of different composition, only a quasiequilibrium can be attained. In this case, the true equilibrium can be attained only if the substrate is completely substituted by the substance whose composition is determined by Eq. (1).

No analytical solution of the system (4), (5) of transcendental equations is possible. These equations can be solved numerically for a concrete set of parameters entering these equations.

EFFECT OF INTERNAL STRESSES ON EQUILIBRIA IN THE SYSTEM POTASSIUM BIPHTALATE–RUBIDIUM BIPHTALATE–WATER

The above equations were solved numerically for the system potassium biphtalate (KBP)–rubidium biphtalate (RBP)–water studied in detail experimentally [1, 2]. This system clearly demonstrates the phenomena provided by different chemical compositions of the solution and the crystal [2], which is explained by a considerable mismatch of the unit-cell parameters of KBP and RBP.

Of course, the solutions in this system are far from being ideal. However, all the above speculations remain valid upon the substitution of the concentrations by the activities under the condition that the activity coefficients are independent of the concentrations, i.e., for regular solutions. As far as we know, there is no published data on the activity coefficients for KBP and RBP, however a number of experiments indicate that it is possible to use the approximation of regular solutions for the system under consideration. In particular, the solubility isotherms for the system are not too far from the linear dependence (1), whereas the distribution coefficient is almost constant and close to the value calculated by Eqs. (3). Moreover, the calculated results given below, should be considered, first and foremost, as the illustration of the above theoretical model.

In our experiments, a seeding $(K,Rb)C_8H_5O_4$ crystal of the composition γ_s was placed into the solution with the component ratio, which is nonequilibrium with respect to this crystal, $\gamma_l = C_{RBP}/(C_{RBP} + C_{KBP})$. In the calculations, we used the values of the constants determined experimentally. The potassium and rubidium biphtalate crystals are orthorhombic; therefore, we introduced the corresponding corrections into Eqs. (4) and (5). We considered the {010} faces of the $(K,Rb)C_8H_5O_4$ crystals in which the main directions of deformation coincided with the crystallographic *a*- and *c*-axes. The values of the components c_{ijkl} of the elastic-stiffness tensors were determined from the coefficients s_{ijkl} of the elastic-compliance tensor [10].

Figure 1 illustrates the calculated data for the equilibrium coefficient of Rb distribution in the layers grown on a KBP substrate, and Fig. 2 shows the solubility of the layer material depending on the ratio of the component concentrations in the solution and in the substrate.

The quantitative characteristic of the quasiequilibrium conditions obtained for the system provided the calculation of the internal stress-induced changes in the chemical potentials of the components of the growing phase. Thus, in equilibrium, the chemical potentials of

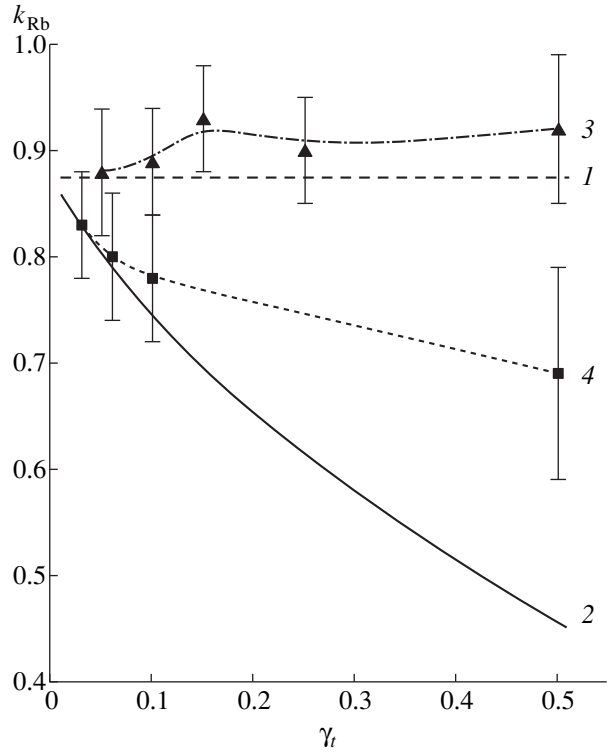

Fig. 1. (*1*, *2*) Theoretically calculated and (*3*, *4*) experimentally measured coefficients of Rb distribution (k_{Rb}) in a KBP crystal (*1*, *3*) and (*2*, *4*) unstressed layers grown on the (010) face as functions of the solution composition γ_l at $T = 50°C$.

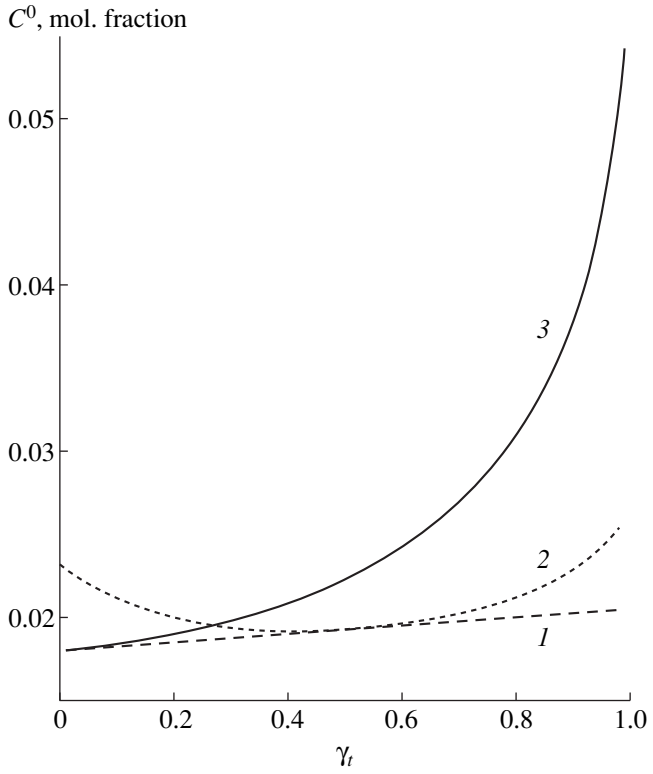

Fig. 2. (*1*) Solubility $C^0 = C^0_K + C^0_{Rb}$ of the native crystal calculated by Eq. (2) and (*2*) stressed layers grown onto the (010) face of (*1*) $K_{0.5}Rb_{0.5}C_8H_5O_4$ and (*3*) KBP crystals as functions of the component ratio in the solution, γ_l, at $T = 50°C$.

the components in the solid and the liquid phases are equal and one can write $\Delta\mu_i^s(\gamma_s) = RT\ln(C_i^0(\gamma_s, \sigma)/C_i^0(\gamma_s))$, where $\Delta\mu_i^s(\gamma_s)$ is the stress-induced change in the chemical potential of the component *i* in the layer of the composition γ_s; $C_i^0(\gamma_s)$ is the concentration of the component *i* in the solution, which is in equilibrium with an unstressed crystal of the compositions γ_s; and $C_i^0(\gamma_s, \sigma)$ is the concentration of the component *i* in the solution, which is in equilibrium with the stressed layer of the same composition. The examples of the stress contributions to the chemical potentials of the components are shown in Fig. 3 as functions of the composition of the grown layer. These dependences confirm our intuitive concept, according to which the component reducing the stress can easily be incorporated into a crystal. Figure 3 also shows the dependence of $\Delta Z_s = X_{KBP}\Delta\mu^s_{KBP} + X_{RBP}\Delta\mu^s_{RBP}$ (coinciding with the specific molar energy of stresses) as a function of the layer composition.

For the systems, in which the temperature dependences of the solubilities of pure components are close to linear, it is possible to calculate the variations in the saturation temperature of the solution for the stressed layer. Let $C_i^0(T) = C_i^* + \alpha_i T$, where $C_i^0(T)$ are the solubilities of pure components at the temperature *T* and C_i^* and α_i be the constant coefficients. Then, using Eq. (1), we can write $\Delta M_i = RT\ln(C_i^* + \alpha_i T)$. Substituting the latter expression into Eqs. (4) and (5) and solving the obtained system of equations, we can determine the change in the saturation temperature with respect to the stressed layer at the constant solution composition. Figure 4 shows an example of the dependence of this temperature for the (KBP + RBP) solution, which is in equilibrium with the native crystal at 50°C, as functions of the component ratio in the solution and the substrate composition.

The stresses in the growing layer depend on the crystallographic orientation of the intergrowth plane. Therefore, all the dependences shown in Figs. 1–4 should be different for different faces of various simple forms of the crystal. Since under real conditions growth of stressed layers is usually accompanied by formation of various defects and, therefore, the local stress relaxation, the different portions of the same layer can have different compositions and solubilities.

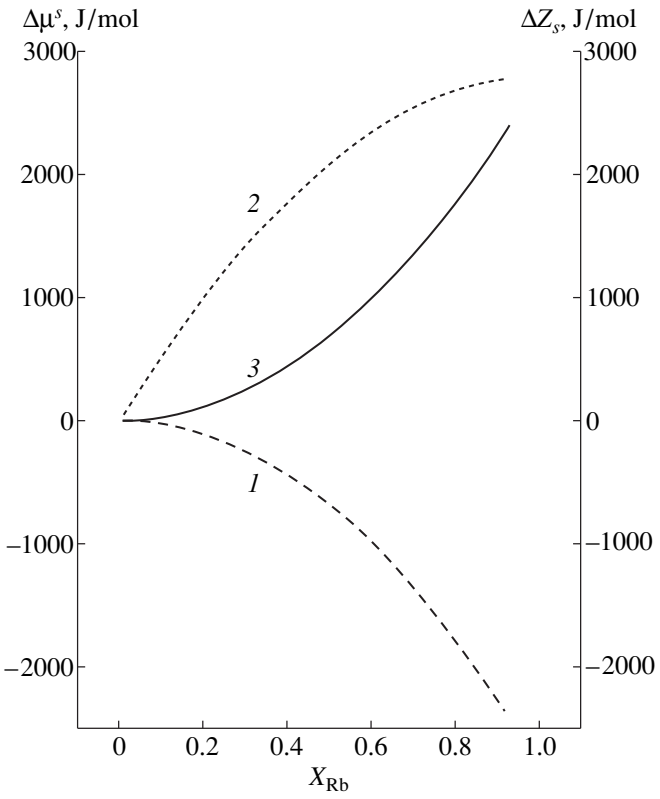

Fig. 3. Additional term describing the chemical potential $\Delta\mu_i^s$ of the components of (*1*) KBP and (*2*) RBP crystals and (*3*) the total thermodynamic potential ΔZ_s of the layer grown on the (010) face of a KBP crystal as a function of the layer composition X_{Rb} at $T = 50°C$.

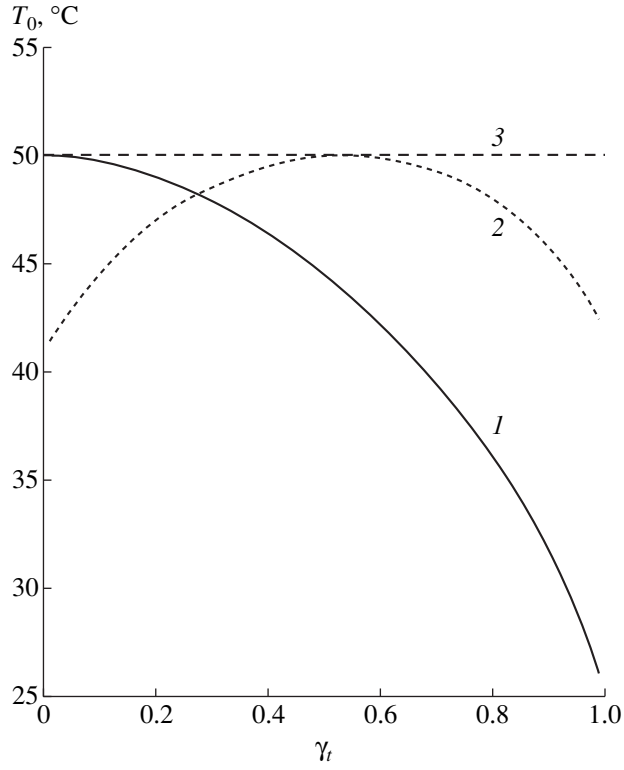

Fig. 4. Supersaturation temperatures of the solution, T_0, with respect to the stressed layers grown onto the (010) face of (*1*) KBP and (*2*) $K_{0.5}Rb_{0.5}C_8H_5O_4$ crystals as functions of the solution composition. (*3*) The solution saturated with respect to the crystal of the same composition at 50°C.

The calculation of the equilibrium composition of the solution provides the determination of the supersaturation of the solution nonequilibrium with respect to the stressed layer. The thermodynamic supersaturation is determined as the difference between the chemical potentials of any component of the given solution and of the solution having the same ratio of the components γ_l, which is in equilibrium with the stressed layer at the same temperature. For a constant γ_l, the above-indicated differences for both components are equal. However, because of different solubilities in different regions of the grown layer (characterized by different elastic stresses), only the local supersaturations of the solution with respect to certain regions of the growing surface should be considered.

COMPARISON WITH EXPERIMENT

The $(K,Rb)C_8H_5O_4$ crystals used for studying the composition and defects in the grown layers were synthesized by the dynamic method of growth at lowering of the temperature [11]. The mode of lowering of the temperature provided the constancy of the relative supersaturation ($\Delta C/C_0 \approx 0.06$) and the allowance for the dependence of solubility on temperature and γ_l and the change in the mass of growing crystals in each experiment. We grew crystals of three types: homogeneous (on a seed crystal obtained from the solution used in the experiment), bizonal (on KBP seeds for solutions with different γ_l), and gradient crystals (on KBP seed from the solution, whose composition was continuously varied during the experiment from $\gamma_l = 0$ to $\gamma_l = 0.3$). The methods used for growth of $(K,Rb)C_8H_5O_4$ crystals are described in detail elsewhere [1, 2].

It is seen from the above figures that the most stress-sensitive characteristic is the distribution coefficient *k*. Figure 1 shows the experimental dependences of k_{Rb} in unstressed $(K,Rb)C_8H_5O_4$ crystals and stressed layers of bizonal crystals grown on a KBP seed. The satisfactory correspondence of the experimental k_{Rb} values for the stressed layer with the theoretically calculated dependence is observed only at small differences in the compositions of the substrate and the layer ($\Delta\gamma \le 0.07$). At pronounced differences $\Delta\gamma$, the interzonal boundary has quite a large number of defects, mainly misfit dislocation forming at $\Delta\gamma \ge 0.04$. This results in a consid-

erable reduction of internal stresses at the growth front and decreases the change in k_{Rb}.

It is rather difficult to determine the exact value of the saturation temperature of the solution with respect to the stressed layer, because, in the static growth mode used for the determination of the saturation temperature [11], the composition of the subsurface layer of the solution changes with the seed dissolution. For less accurate measurements in the dynamic mode, the change in the saturation temperature of the solution with respect to the grown layer was established only for gradient crystals and it was shown that, at the end of the experiment (when the solution composition corresponds to $\gamma_l = 0.25$–0.30), the equilibrium between the gradient crystal and the solution is attained at the temperature by 1–1.5°C lower than the temperature of the solution saturation with respect to the unstressed crystal. The calculated stress (with due regard for the stress redistribution in the crystal bulk during its growth) [12] in the surface layer of a gradient crystal is lower by a factor of 2–2.5 than in the grown layer of the bizonal crystal with the same value of $\Delta\gamma$. With due regard of this fact, the experimental variation of the saturation temperature for a gradient crystal amounts up to 50–80% of its theoretical value. Such a good correspondence is explained by a relatively low number of defects in gradient crystals in comparison with their number in bizonal crystals. As a result, the real stresses at the growth front of gradient crystals are much closer to the calculated values. The lower number of defects in gradient crystals is explained, first of all, by the fact that seed regeneration occurs in the solution of the same composition, i.e., in the absence of any stresses. The dislocation density determined by selective etching of cleavages along the (010) planes [2] in the gradient crystals is several times lower than that in the intergrowth zone of bizonal crystals having the same calculated stresses.

Taking into account the limitations of the above theoretical model, the agreement of the data calculated on the basis of this model with the experimental data seems to be quite satisfactory. At the same time, it is obvious that the quantitative description of real growth processes occurring in mixed crystals under nonstationary conditions require the modification of this model—introduction into it of the processes of defect formation and internal-stress relaxation at defects.

ACKNOWLEDGMENTS

The study was supported by the Russian Foundation for Basic Research, project no. 97-05-64218. The authors are grateful to E.D. Prudnikov for analyzing the compositions of the solutions used.

REFERENCES

1. S. V. Moshkin, O. M. Boldyreva, T. I. Ivanova, *et al.*, J. Cryst. Growth **172** (1–2), 226 (1997).
2. M. A. Kuz'mina, S. V. Moshkin, O. M. Boldyreva, and I. P. Shakhverdova, in *Physics of Crystallization* (Tver. Gos. Univ., Tver, 1994), p. 103.
3. Yu. B. Bolkhovityanov, J. Cryst. Growth **55** (3), 591 (1981).
4. Yu. B. Bolkhovityanov, in *Crystal Growth* (Nauka, Moscow, 1990), Vol. 18, p. 158.
5. G. H. Olsen and M. Ettenberg, in *Crystal Growth. Theory and Techniques*, Ed. by C. Goodman (Plenum, London, 1974; Mir, Moscow, 1981), Vol. 2.
6. A. N. Kirgintsev, L. A. Isaenko, and V. A. Isaenko, *Impurity Distribution in Directional Crystallization* (Nauka, Novosibirsk, 1977).
7. G. I. Gorshteĭn, Doctoral Dissertation in Chemistry (Moscow, 1956).
8. L. D. Landau and E. M. Lifshitz, *Course of Theoretical Physics*, Vol. 7: *Theory of Elasticity* (Nauka, Moscow, 1982; Pergamon, New York, 1986).
9. K. A. Putilov, *Thermodynamics* (Nauka, Moscow, 1971).
10. L. M. Belyaev, G. S. Belikova, A. B. Gil'varg, and I. M. Sil'vestrova, Kristallografiya **14** (4), 645 (1969) [Sov. Phys. Crystallogr. **14**, 544 (1969)].
11. T. G. Petrov, E. B. Treĭvus, Yu. O. Punin, and A. P. Kasatkin, *Crystal Growth from Solutions* (Nedra, Leningrad, 1983).
12. M. A. Kuz'mina, S. V. Moshkin, I. P. Shakhverdova, and O. M. Boldyreva, in *Proceedings of II Ural Crystallographic Conference "Crystallography-98," 1998* (Institute of Geology, Comi Research Center, Ural Division, Russian Academy of Sciences, Syktyvkar, 1998), p. 19.

Translated by L. Man

Crystallography Reports, Vol. 45, No. 6, 2000, pp. 1047–1048. Translated from Kristallografiya, Vol. 45, No. 6, 2000, pp. 1133–1134.

The Mechanism of the Intergrowth Formation[1]

N. K. Tolochko, A. Z. Myal'dun, and V. A. Yanusov

Institute of Technical Acoustics, Belarussian Academy of Sciences, pr. Lyudnikova 13, Vitebsk, 210717 Belarus

Received January 25, 1999

As is well known [1], small crystals, which are deposited from a supersaturated solution onto the faces of a large crystal, can "stick" to these faces and form "intergrowths." The faces of such intergrowths, having the same crystallographic indices, can have different mutual orientations. A regular mutual orientation of the crystals can be promoted by both internal and external factors, in particular, the effect of vibrations [2, 3]. In this work, we studied the characteristics of intergrowth microcrystals and the crystalline substrate depending on their dimensions. The experiments were made on potassium aluminum alum and potassium dihydrogen phosphate (KDP) crystals by the techniques described elsewhere [2, 3]. The intergrowth along the {111} planes was studied for alum–alum pair and along the {100} planes for the KDP–KDP pair.

Small portions of alum crystals larger than 150 μm or KDP crystals larger than 50 μm were introduced into the native solution above the horizontal face of a 2- to 3-cm-large crystal of the same substance. Thus, small crystals were deposited onto the face of the large crystal and formed an intergrowth. Upon 5–10 min of deposition, the crystals were kept in the solution for 15–20 min to provide better intergrowth. The saturation temperature of all the solutions was 36.1°C. Deposition and intergrowth took place at the supersaturation of 3.6°C for alum and 1.1°C for KDP. The number of microcrystals intergrown with the substrate, their orientations, and dimensions were determined under a microscope with a rotating table. No less than a hundred intergrowths were examined in each experiment. The results were averaged over several experiments.

About 21% of all alum intergrowths were formed on faces other than {111} and were not considered. All the KDP intergrowths were attached to the substrate by the {100} faces.

Experiments with alum showed that the regular intergrowth along the {111} faces (with the misorientation angles $0° < \alpha < 5°$) was characterized by the epitaxy coefficient $K = 0.14$. The epitaxy coefficient was determined as $K = n(h - a)/Nh$, where n was the number of crystals under the epitaxial maximum on the histogram (crystal distribution in the angle α), N was the total crystal number, h was the maximum height, and a was the background level [4]. It was established that the average size of the microcrystals in regular intergrowths is 11% less than the size averaged over all the crystals intergrown with substrate. In other words, the trend to the regular intergrowth increases for smaller crystals.

The orientation of KDP microcrystals was determined for several ranges of their dimensions: D = 10–20, 20–30, and 30–40 μm. The epitaxy coefficient for the crystals from the range $10 < D < 20$ μm with the intergrowth faces {100} and the misorientation angle $0° < \alpha < 10°$ was determined as $K = 0.15$. The epitaxy coefficient for the ranges $20 < D < 30$ μm and $30 < D < 40$ μm was equal to $K = 0.10$ and $K = 0.07$, respectively.

Thus, both alum and KDP show the trend to the regular intergrowth with a decrease of their dimensions. The dimensions from 50 to 150 μm seem to be critical: the crystals exceeding these dimensions show no oriented intergrowth. Thus 10- to 20-cm-large crystals show a preferable orientation with respect to the substrate, whereas 30- to 40-cm-large crystals are characterized by statistically distributed orientations.

The preferable orientation of deposited crystals was observed earlier and was considered to be the result of their electrostatic interaction with the substrate [5]. A small crystal can rotate from its initial position to the position providing regular intergrowth under the condition that the time necessary for its complete "self-orientation" does not exceed the time necessary for intergrowth (i.e., the time necessary for crystallization of the solution layer between a microcrystal and the large crystal). It is obvious that the time of self-orientation is shorter for small crystals because they are less inert. Moreover, according to [6], the growth rate of microcrystals depends on their size [6], which should also affect the process of crystal orientation.

[1] The paper is deposited at VINITI, 1999, Vitebsk, no. 2611-V99.

1063-7745/00/4506-1047$20.00

REFERENCES

1. A. V. Shubnikov, *Selected Works on Crystallography* (Nauka, Moscow, 1975).
2. V. V. Azarov, V. V. Klubovich, N. V. Sobolenko, and N. K. Tolochko, Kristallografiya **34** (2), 519 (1989) [Sov. Phys. Crystallogr. **34**, 312 (1989)].
3. V. V. Klubovich, N. V. Sobolenko, and N. K. Tolochko, Vestsi Akad. Navuk Belarusi, Ser. Fiz.-Mat. Navuk, No. 1, 66 (1992).
4. Yu. V. Plotkina, Author's Abstract of Candidate's Dissertation in Geology–Mineralogy (St. Peterburg. Gos. Univ., St. Petersburg, 1998).
5. J. Plotkina and A. Glikin, in *Abstracts of XII Int. Conference on Crystal Growth, Jerusalem, Israel, July 26–31, 1998*, p. 364.
6. A. M. Askhabov, *Processes and Mechanisms of Crystal Genesis* (Nauka, Leningrad, 1984).

Translated by A. Mel'nikova

Crystallography Reports, Vol. 45, No. 6, 2000, pp. 1049–1058. Translated from Kristallografiya, Vol. 45, No. 6, 2000, pp. 1135–1145.

CRYSTAL GROWTH

Crystallographic Characteristics of Growth of Nepheline Single Crystals under Hydrothermal Conditions

T. B. Kosova and L. N. Demyanets

Shubnikov Institute of Crystallography, Russian Academy of Sciences, Leninskiĭ pr. 59, Moscow, 117333 Russia

Received February 1, 1999; in final form, September 8, 1999

Abstract—Crystallographic characteristics of growth of nepheline single crystals $Na_3K[AlSiO_4]_4$ on seeds parallel to the faces of the equilibrium and nonequilibrium forms of these crystals have been studied. Kinetics of crystallization of nepheline single crystals in hydrothermal alkali solutions is studied for various crystallographic directions at different temperatures and supersaturations. It is established that growth rates of the crystal faces decrease in the sequence $V_{\{10\bar{1}1\}} > V_{\{\bar{1}2\bar{1}0\}} > V_{(0001)} > V_{\{10\bar{1}0\}}$. The activation energy of the crystallization process for the (0001) monohedron and $\{10\bar{1}1\}$ pyramid faces are 38.5 ± 2.0 and 48.1 ± 2.0 kJ/mol, respectively. Specific features of regeneration of nepheline crystals are studied. Two types of regeneration pyramids are established, which differ by their crystallographic orientations with respect to the faces of the equilibrium forms. It is also established that the optimum regeneration surfaces are normal to the $\{0001\}$ and $\{10\bar{1}0\}$ faces of the equilibrium forms of the crystals (with the $\langle 0001\rangle$ and $\langle 1\bar{1}00\rangle$ zone axes, respectively). The morphology of the growth surface of nepheline single crystals is studied. The mechanisms of face growth are established for various substrate orientations. It is shown that the growth mechanisms are different in different regeneration directions. The optimum shapes and the crystallographic orientations of the substrates providing a decrease of the number of inherited defects and the maximum volume of the grown material are found. © *2000 MAIK "Nauka/Interperiodica".*

INTRODUCTION

Nepheline, a framework aluminosilicate of the complicated composition (described by the ideal formula $Na_3K[AlSiO_4]_4$), is characterized by the hexagonal symmetry with the noncentrosymmetric sp. gr. $P6_3$ determining its piezo- and pyroelectric properties [1]. The crystal structure of nepheline [2] can be considered as a derivative of a high-temperature hexagonal tridymite. Alumnum–oxygen and silicon–oxygen tetrahedra form the framework, whose small voids are occupied by sodium atoms, whereas larger voids are occupied by potassium and sodium atoms. These connected voids form channels providing ionic conductivity of the Na-nepheline [3]. The nepheline structure [2] is characteristic only of the middle members of the $NaAlSiO_4$–$KAlSiO_4$ series, whereas the end members of this series belong to other structure types [3–6]. In nature, nepheline single crystals are encountered very seldom and usually are of the volcanic origin. The natural nepheline crystals most often occur as aggregates textured along the *c*-axis.

Under laboratory conditions, small (300–500 μm, sometimes, 1–2 mm long) nepheline crystals have been grown by the method of spontaneous crystallization since the late nineties of the 19th century [7]. The method of their growth reduced to the reaction between NaOH and Na_2CO_3 with various natural aluminosilicates at high temperatures [8, 9].

We grew large crystals of the composition close to ideal ($Na_3K(AlSiO_4)_4$) from hydrothermal solutions in the temperature range of the thermodynamic stability ($T > 450$°C) and in the metastable range ($T < 450$°C) [10–13]. The hydrothermal media were alkali NaOH + KOH solutions; the charge was prepared from crushed natural nepheline or the mixture of SiO_2 and the excessive amount of Al_2O_3 oxide.

Below, we describe the further study of growth of nepheline single crystals from high-temperature aqueous solutions. We consider the crystallographic aspect of nepheline growth on seeds, the kinetics of seeded growth, the morphology of growth surfaces, and the real structure of the crystals grown.

1. EXPERIMENTAL

The preliminary study of sodium aluminosilicate stability as a function of the medium composition and temperature showed that the stability range of nepheline in alkali solutions lies at temperatures above ~450°C (the calculated data [10], Fig. 1a). With the temperature rise, the stability boundary between nepheline and cancrinite is shifted to higher NaOH concentrations (the experimental data [7], Fig. 1b). The introduction of potassium ions into the system provides

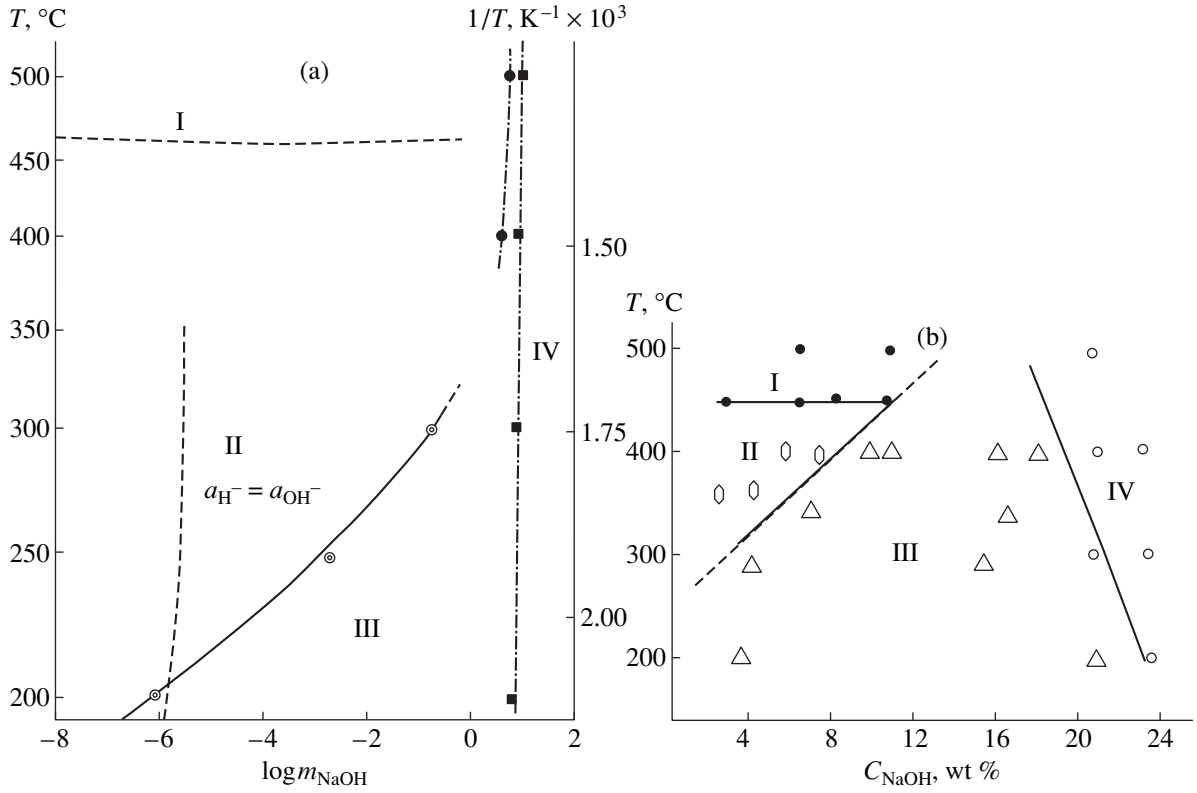

Fig. 1. Stability fields of aluminosilicates: (I) nepheline, (II) nepheline-hydrate, (III) cancrinite, (IV) sodalite in the Na_2O–Al_2O_3–SiO_2–H_2O system [10, 11]. (a) Calculated and (b) experimental data. Notation: a_{H^+} and a_{H^-} are ion activities in the solution, m is solution molality, ⊙ equilibrium between Na-cancrinite and Na-nepheline-hydrate I; ● equilibrium between Na-nepheline and Na-cancrinite; ■ equilibrium between Na-cancrinite and Na-sodalite.

no noticeable effect on the boundary shift. The experiments on nepheline growth performed over a wide temperature range led to the conclusion that seeded growth of nepheline single crystals is possible at considerably lower temperatures (of the order of 350°C) and also in the range of its thermodynamic instability. Under metastable conditions, nepheline can be grown only on seeds (which is explained by similar structures of nepheline and nepheline-hydrate (stable under these conditions), whereas the parasitic crystals formed in the growth zone have the structure either of the stable crystalline phase of nepheline-hydrate of the composition $NaAlSiO_4 \cdot nH_2O$ or of cancrinite $Na_8[AlSiO_4]_6\{CO_3(OH)_2\} \cdot nH_2O$ (depending on the concentration of the solvent used). Metastable growth of nepheline crystals on a seed is explained by the high activity of the crystal surface, which forms a subsurface layer with a structure similar to that of the substrate.

Nepheline single crystals were grown by the method of direct temperature gradient at the constant temperatures in the dissolution and the growth zones separated by a baffle. The experiments were performed in 0.2- and 1.0-l-autoclaves made of alkali-resistant steel. In some cases, the inner surface was additionally lined with Ag and Pt. For heating, two-zone furnaces were used. The temperature in the dissolution zone was varied within 350–500°C, the concentration of the NaOH solvent was 3–15 wt % at $T < 450$°C and 3–22 wt % at $T > 450$°C. The crystals for the studies of kinetics and morphology were grown under the optimum growth conditions (Table 1).

Nepheline crystals were grown onto the substrates of various shapes and crystallographic orientations and were cut out from natural or synthesized nepheline crystals. In the first experiments, the seeds were unfaceted fragments of textured intergrowths of natural nepheline (from Ural deposits). Seeded growth yielded large nepheline crystals with a hexagonal habit, which then were used to cut out the substrates of various crystallographic orientations for further growth of nepheline single crystals.

The kinetics of nepheline crystallization on oriented seeds was studied at various q-ratios (one to two) in the initial solution and at temperatures ranging within 350–500°C (i.e., the ranges of metastable and stable growth). Growth rates were measured on crystals grown from ~20 × 20 × 1.5-mm-large (0001), $\{10\bar{1}0\}$, $\{10\bar{1}1\}$, and $\{11\bar{2}0\}$ oriented plane-parallel plates.

Table 1. Growth parameters of nepheline single crystals grown under the optimum conditions [12]

Main characteristics	Variation ranges
Solvent	NaOH 10–15 wt % + KOH 10–15 wt %
	at the volume ratio q = (NaOH/KOH) = 1–2
Charge	Natural nepheline
Seed	Natural nepheline; synthesized nepheline
Seed orientation	(0001), $(10\bar{1}0)$ and $(10\bar{1}1)$ plates and bars elongated in $[h\bar{h}00]$ and $[h\bar{h}01]$ directions
Temperature in the growth zone	400–430°C
Temperature in the dissolution zone	420–470°C
Temperature difference	20–50°C
Fill coefficient	0.6–0.8
Open space of the baffle	3–10%

The crystals grown were studied by the X-ray diffraction (on DRON-4 and CAD-4F diffractometers) and DTA (on DTA-TG Thermoflex, Rigaku Denki setups) methods, by chemical analysis (silicate analysis, X-ray microanalysis, JXA-840 setup), and by chemical etching. Morphological studies were performed on NEOPHOT-32 and MIM-8 microscopes.

2. RESULTS AND DISCUSSION

2.1. Symmetry and Composition of Grown Crystals

A typical crystal is shown in Fig. 2. Usually, the crystals were faceted by the (0001) and (0001) monohedron faces, the $\{01\bar{1}0\}$ hexagonal prism faces, and, somewhat less often, by the $\{01\bar{1}1\}$ and $\{01\bar{1}2\}$ faces. The hydrodynamic characteristics resulted in the fact that the growth pyramids were represented by one or two neighboring real faces of the same simple form. The crystals had the dimensions up to $40 \times 40 \times 60$ mm (those grown in 1-l-large autoclaves) and $15 \times 15 \times 20$ mm (those grown in 0.2-l-large autoclaves). Regeneration of unfaceted fragments of natural or synthesized nepheline provided the formation of the $\{10\bar{1}1\}$ and $\{10\bar{1}2\}$ pyramid faces at the initial growth stages (with $\rho = 61.4°$ and 28.3°, respectively). During further growth, these faces disappeared and, finally, the crystals were faceted only with the prism and monohedron faces (or faces of several monohedra if the crystals had the twinning planes normal to the sixfold axis). Such an equilibrium shape for nepheline crystals is shown in Fig. 2b. The grown nepheline crystals are characterized by the macrosymmetry 6*mm* or 6/*mmm* and not 6 (indicated in the X-ray studies [2]). One of the causes of such a high macrosymmetry of the grown nepheline crystals is a high seed quality, preserving the texture of the natural material. Usually, the seeds were plane-parallel plates cut out normally to various crystallographic directions and consisting of several individual 1.5–2.0-mm-large blocks packed either parallel or antiparallel to the c-axis ($-c \| +c$) and misoriented in the (0001) monohedron plane. Growth of nepheline crystals on plane-parallel plates cut out normally to the $\langle 0001 \rangle$ direction provided the clear observation of the initial texture (macropolycrystallinity) upon crystal etching.

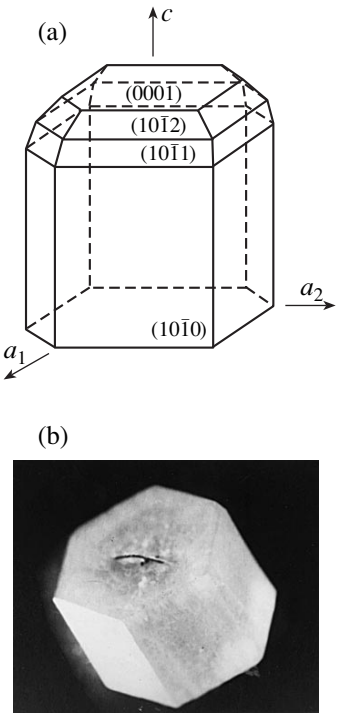

Fig. 2. Habit of nepheline crystals: (a) major simple forms; grown single crystal (magnification ×4); and (b) equilibrium form.

Table 2. Compositions of the starting charge and the crystals grown

Sample	Oxides, wt %								Formula
	Na_2O	K_2O	MgO	CaO	Al_2O_3	SiO_2	Fe_2O_3	FeO	
1	15.94	6.00	0.76	0.35	32.37	43.63	0.41	0.17	$Na_{2.96}K_{0.74}Al_{3.70}Si_{4.19}Fe_{0.04}O_{16}$
2	15.27	7.86	–	–	33.52	42.11	–	1.23	$Na_{2.88}K_{0.96}Al_{3.84}Si_{4.10}Fe_{0.10}O_{16}$
3	15.88	7.28	–	–	33.60	43.24	–	–	$Na_{2.96}K_{0.88}Al_{3.80}Si_{4.16}O_{16}$
4	16.43	7.08	–	–	32.32	43.39	–	0.78	$Na_{3.08}K_{0.88}Al_{3.68}Si_{4.20}Fe_{0.06}O_{16}$
5	17.21	5.67	–	–	33.98	42.50	–	0.64	$Na_{3.20}K_{0.68}Al_{3.88}Si_{4.08}Fe_{0.04}O_{16}$
6	16.81	6.31	–	–	33.29	42.35	–	1.23	$Na_{3.20}K_{0.73}Al_{3.80}Si_{4.12}Fe_{0.10}O_{16}$

Note: Sample 1 is natural nepheline (from Ural deposits), samples 2–6 are grown single crystals.

The second cause of a higher symmetry is crystal twinning during the growth process: the crystals acquire the twinning plane normal to the *c*-axis. The traces of this twinning plane are well seen on the prism face (the twinning plane is usually well seen by the naked eye in the vicinity of a wire on which the seed is hanged). Unlike [14], where the synthesized nepheline crystals were the polysynthetic albite-type twins, we never observed any polysynthetic twinning.

The structural studies show that nepheline single crystals grown without any substrates (spontaneous nucleation in the cold zone of the autoclave at the growth temperature of 430°C) possess the desirable polar symmetry (a sixfold axis) and are characterized by short-column or prismatic habit and the $\{01\bar{1}0\}$ prism faces and the (0001) monohedron face. Usually, the opposite end of the crystal (attaining the size of 5 mm) is fixed at the autoclave wall or on a mounting wire.

The results of the chemical analysis of the initial charge and the grown crystals are listed in Table 2. The typical composition of the crystals grown in the presence of excessive sodium ($q = 2$) is described by the formula $Na_{3.20}K_{0.68}Al_{3.88}Si_{4.08}Fe_{0.04}O_{16}$. Crystals grown in Pt inserts had no traces of iron. Crystal parameters were measured on crystals grown on seeds and on spontaneously grown crystals containing no twins. The lattice parameters were determined as $a = 10.013(3)$ and $c = 8.406(2)$ Å and are consistent with the data in [2].

The differential thermal analysis (DTA) of the grown nepheline crystals showed that they usually contained about 1% water, which evaporated during crystal heating to a temperature of 200°C. The DTA curves obtained during heating and cooling show a reversible phase transition at temperatures ranging within (940–980)°C ± 5°C (depending on the potassium content). This phase transition shows a weak hysteresis of ~10°C and, according to [14], indicates the formation of a high-temperature phase. At a temperature 160–200°C, no phase transition characteristic of the varieties with low potassium content was observed.

The major defects in the bulk of nepheline crystals are gas–liquid and solid inclusions. The latter had the form of needle- or platelike nepheline crystals with the dimensions of 0.01–0.03 mm. The *c*-axis of the platelike inclusions was usually parallel to the *c*-axis of the matrix crystal, whereas the needlelike crystals were arranged at random. The gas–liquid inclusions were located rather regularly and formed a subcellular structure clearly seen as a discontinuous subhexagonal net of gas–liquid inclusions on the monohedron faces in the transmitted light.

2.2. Growth Kinetics of Nepheline Crystals

Kinetics of nepheline crystals grown on seeds depends on the solvent composition, the growth temperature, the temperature difference ΔT, and the crystallographic orientation of the seed. Growth kinetics was studied on crystals with the composition $Na_{2.88}K_{0.96}Al_{3.84}Si_{4.08}Fe_{0.08}O_{16}$ close to ideal, $Na_3K(AlSiO_4)_4$.

An essential effect on nepheline growth is produced by the Na/K ratio in the initial solution. In the absence of potassium in the alkali solution, the growth rates of prism, monohedron, and pyramid faces were close to zero. The surfaces of such orientations (preliminarily etched in diluted HCl solutions) showed almost no material increment, so that the experiments resulted only in the appearance of growth morphology. This can be explained by the fact that the end Na-containing member of the $NaAlSiO_4$–$KAlSiO_4$ series has a structure different from that of the nepheline structure (monoclinic, sp. gr. $P2_1$ [1] or $P2_1/n$, the beryllonite structure type [1, 6, 14, 15]). The presence of nepheline seed did not initiate growth of aluminosilicate with the nepheline structure. Despite the presence of Na in the nepheline charge, growth from pure KOH solutions did not result in growth of crystals with the nepheline structure (sp. gr. $P6_3$); in fact, the crystals grown had the kalsilite structure $(K,Na)AlSiO_4$ (sp. gr. $P6_3$, the twice shorter lattice parameter $a = 5.149$, $c = 8.643$ Å [6, 15]). At the volume NaOH/KOH ratio ranging within 2.0–0.5 (2 : 1–1 : 2), only nepheline crystals with the char-

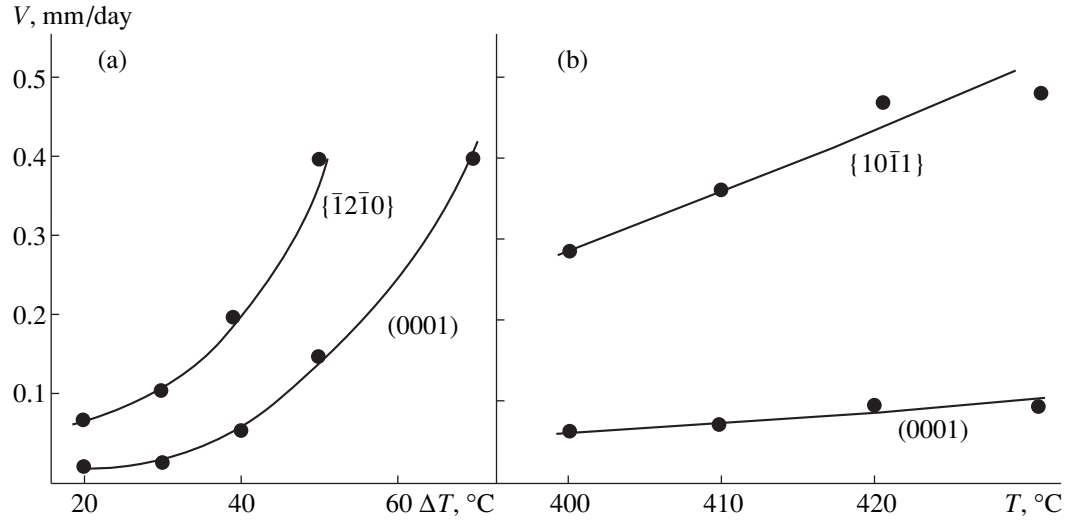

Fig. 3. Kinetics of seeded nepheline $Na_3K[AlSiO_4]_4$ crystallization in aqueous NaOH (15%) + KOH (15%) solutions. Dependence of the growth rate of the (0001) monohedron and the $\{\bar{1}2\bar{1}0\}$ prism faces on the temperature difference T_p at a constant growth temperature (400°C) for (a) the (0001) monohedron and (b) the $\{10\bar{1}1\}$ pyramid at ΔT = const = 40°C.

acteristic compositions grew (see Table 2). The growth rates of nepheline faces increased in the following sequence $V_{\{10\bar{1}1\}} > V_{\{\bar{1}2\bar{1}0\}} > V_{(0001)} > V_{\{10\bar{1}0\}}$. The minimum growth rates were observed for the monohedron and prism faces related to the equilibrium crystal form, which were preserved in the final crystal faceting. In the temperature range 350–500°C, growth rates varied within the limits 0.01–0.06 mm/day for the $\{10\bar{1}0\}$ prism, 0.02–0.40 mm/day for the monohedron, 0.07–0.40 mm/day for the $\{\bar{1}2\bar{1}0\}$, and 0.3–0.6 mm/day for the $\{10\bar{1}1\}$ pyramid faces. A higher potassium content in the solution results in an increase of the face growth rates. Thus, in growth from the solutions with 15 wt % NaOH + 15 wt % KOH at ΔT = 30°C at a temperature of 400°C, the growth rates along the $\langle 0001\rangle$ and $\langle\bar{1}2\bar{1}0\rangle$ directions were equal to 0.02 and 0.10 mm/day, respectively, at q = 2 and 0.03 and 0.16 mm/day at q = 1.

Dependence of the growth rates on the temperature drop ΔT and the growth temperature for some faces are shown in Fig. 3. It is seen that at constant temperature, the growth rate varies with "relative supersaturation" ΔT by the parabolic law (within 0.02–0.40 mm/day for the monohedron face at ΔT = 20–70°C and within 0.08–0.40 mm/day for the pyramid faces at ΔT = 20–45°C.

We also calculated the activation energies for the growth process of a monohedron and the $\{10\bar{1}1\}$ pyramid faces from the data on the growth rate depending on the inverse temperature (Fig. 4). These energies are equal to 38.5 ± 2 and 48.1 ± 2 kJ/mol (9.2 ± 0.5 and 11.5 ± 0.5 kcal/mol, respectively). The values of the activation energies show that, in our experiments, the growth rates are determined by the kinetics of the surface processes and are not limited by the diffusion processes occurring in the autoclave volume. Thus, it was assumed that growth proceeds in the steady-state mode.

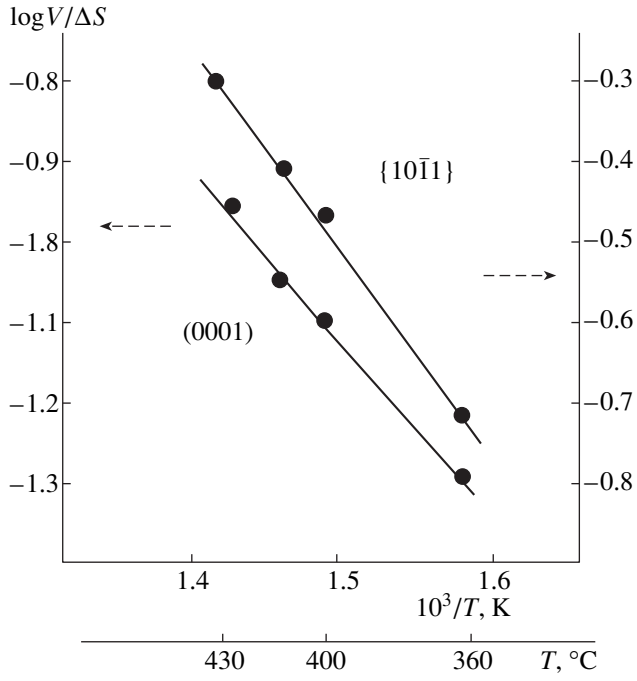

Fig. 4. Dependence of the growth-rate constant $\log V/\Delta S$ on the reciprocal temperature for the (0001) and $\{10\bar{1}1\}$ faces (the left- and right-hand scales, respectively) at ΔT = const = 40°C.

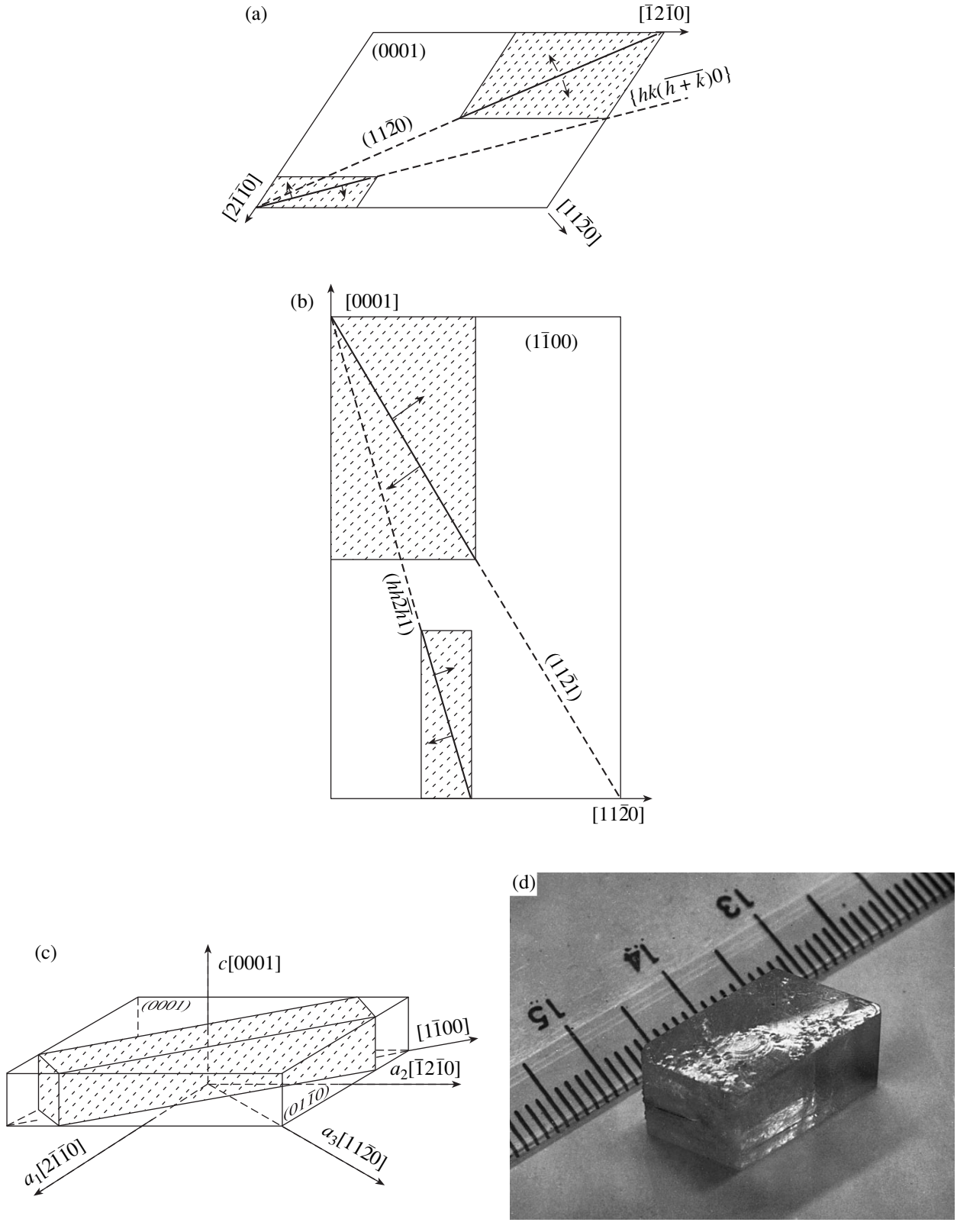

Fig. 5. Regeneration pyramids of nepheline crystals grown on seeds parallel to the {$hk(h+k)0$} and {$hh2hl$} faces. Solid lines show the seed, arrows indicate the regeneration direction. Projections onto (a) the (0001) and (b) (1 $\bar{1}$ 00) planes, (c) final crystal habit, and (d) a barlike seed.

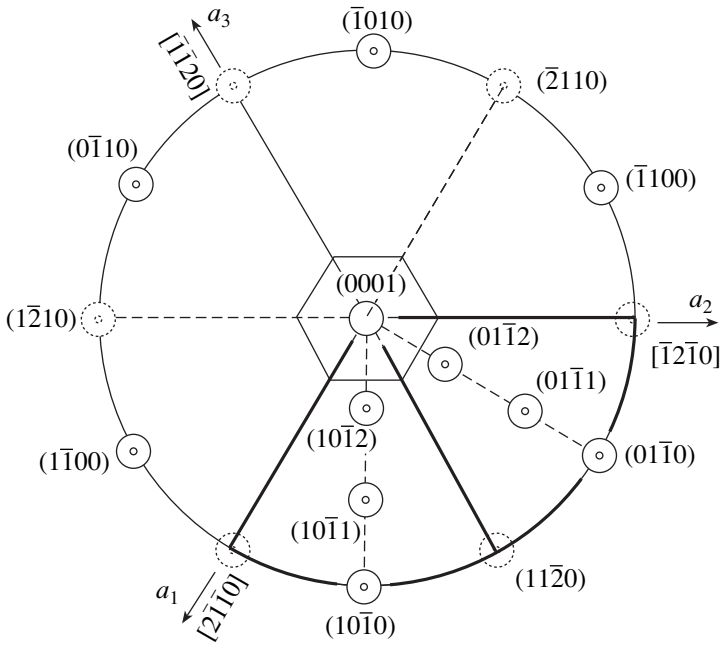

Fig. 6. Stereographic projection onto the (0001) plane showing the regeneration zones of the growth surface. Solid lines show the optimum $\{hk(\overline{h+k})l$ and $\{hh\overline{2h}\,l\}$ regeneration zones with the $\langle 0001\rangle$ and $\langle 10\bar{1}\,0\rangle$ zone axes normal to the equilibrium forms, respectively.

2.3. Regeneration of Nepheline Crystals

Regeneration of a crystal is the process of transformation of an initial arbitrary shape of the crystal into the "faceted" growth form stable under certain conditions [16]. Growth of single crystals on crystalline seeds is always the regeneration process occurring differently on different types of seed surfaces (singular, belonging to the equilibrium form, or artificially set oriented surface).

If a substrate is a plane-parallel plate with the developed (0001), $\{10\bar{1}0\}$, or $\{10\bar{1}1\}$ faces represented in faceting of the nepheline crystal and belonging to the faces of the equilibrium form, then growth proceeds normally to the substrate plane. The structural information is transferred from the surface with the maximum area present in the seed faceting to a growing crystal. During growth, such faces are translated in parallel and, thus, always remain in the final crystal faceting. In this case, growth pyramids are formed whose bases are the growing faces, and the vertices are located at the center of the crystals (if growth is performed from a point seed [17]). Nepheline crystals growing on such plane-parallel substrates normally to the $\langle 0001\rangle$ direction have the texture (macropolycrystallinity) of natural seeds inherited by the growing layer, which can clearly be revealed by the etching of the (0001) monohedron face of the grown crystal. As a result, crystal macrosymmetry increases up to 6*m* or 6/*mmm*. Substrate defects (grain boundaries, twins, and cracks) "pass" into the bulk of the growing crystal. During crack healing and overgrowth of solid inclusions, heterometry caused by different chemical and crystallochemical characteristics of the seed plate and the overgrown material can give rise to formation of some new defects (growth dislocations, stresses).

To reduce the negative influence of seed defects inherited by the overgrown material from a large area of the seed, we chose seeds with the such shapes and the crystallographic growth directions such that the maximum material mass would grow on the surfaces not present in the final equilibrium crystal faceting. These surfaces are the bases of regeneration pyramids [16], whose vertices coincide with one of the crystal vertices (the point of intersection of the real equilibrium faces of the crystal). Such a face should have the minimum possible area under the given experimental conditions. Hereafter, discussing hydrothermal crystallization of nepheline crystals, we use the term *regeneration* [16] only if the face area diminishes during the growth process and thus disappears from the final crystal faceting because of "junction" of the faces of the equilibrium forms. We studied nepheline growth on plane-parallel seeds parallel to the faces of the equilibrium forms and on the $\{10\bar{1}1\}$ and $\{10\bar{1}2\}$ pyramid faces (the so-called regenerative growth) and the artificially set $\{11\bar{2}\,0\}$ prism and $\{11\bar{2}\,l\}$ pyramid faces (l = 1–3). An example of the regeneration pyramid for nepheline crystals is shown in Fig. 5 with the preservation of the real a/c ratio.

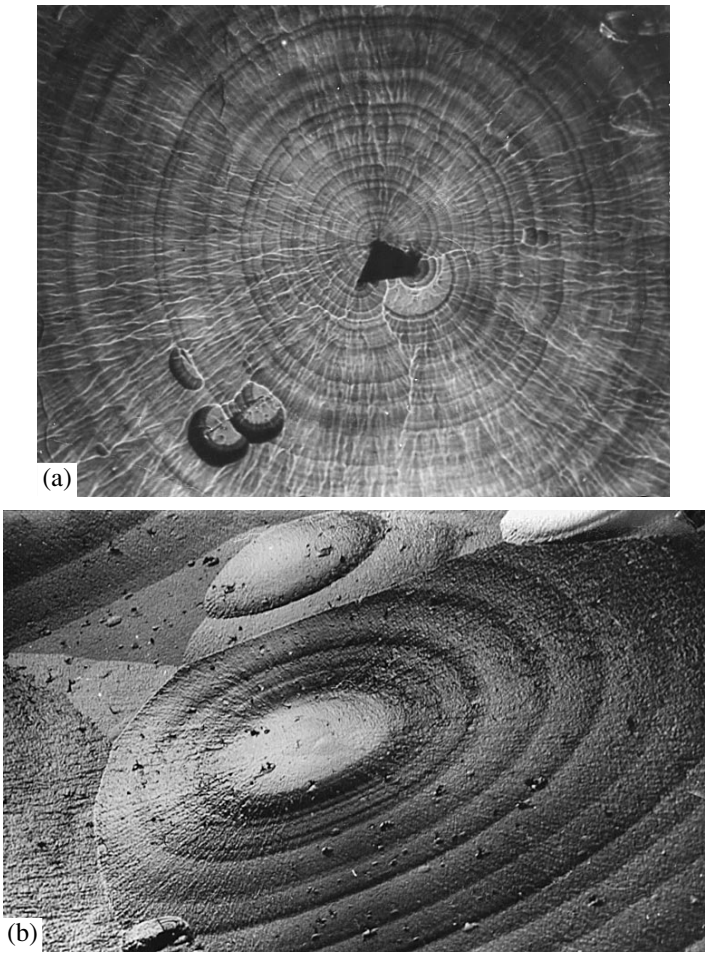

Fig. 7. Morphology of growth surfaces of nepheline single crystals: (a) the (0001) face (magnification ×350) and (b) the $(10\bar{1}1)$ face (magnification ×200).

The approach used allowed us to find the appropriately oriented substrate shape. For example, we used the seeds cut off in the shape of a thin rectangular rod with the (0001) and $(000\bar{1})$ monohedron faces, the $\{01\bar{1}0\}$ and the $\{11\bar{2}0\}$ prism faces 1–3 mm long in the direction of the *c*-axis. The substrate area from which defects are inherited by the crystal is rather small, and the minimum thickness of the seed is determined by the experimental conditions under which the seed would not be dissolved during the attainment of the required temperature mode. The rods with the faces parallel to the $\{1\bar{1}00\}$ and $\{11\bar{2}l\}$ faces provide regeneration along the $[11\bar{2}l]$ directions (Figs. 5a, 5b). The habit of the crystal grown on the seed of the former orientation is shown in Fig. 5c; its growth proceeds along the $[11\bar{2}0]$ direction.

The quality of the crystals depends on the crystallographic characteristics of seed regeneration and, thus, also on the mechanism of the regeneration-surface growth. The best nepheline crystals are obtained in the case, where the regeneration plane is normal to one of the equilibrium faces—(0001) monohedron face or the $(10\bar{1}0)$ prism face (Fig. 6). These conditions are met by the faces with both rational and irrational indices forming the $\{hk(\overline{h+k})0\}$ zones (with $k \neq 0$) with the $\langle 0001\rangle$ axis and $\{hh\overline{2h}\,l\}$ zones (with $h \neq 0$) with the $\langle 10\bar{1}0\rangle$ axis. The optimum growth directions in the zones corresponding to the maximum increment of the material during regeneration are $[11\bar{2}0]$ and $[11\bar{2}\,l]$. In the former case, the growing (regenerating) planes are normal to the (0001) equilibrium face, whereas in the latter case, they are normal to the equilibrium $(1\bar{1}00)$ face. The highest growth rate is observed along the $[11\bar{2}0]$ direction. In this case, regeneration pyramids are formed hereafter referred to as type-1 regeneration pyramids.

The regeneration pyramids of the 2nd type are formed by the growing $\{hkil\}$ faces in the general posi-

tions and the $\{h0\bar{h}l\}$ surfaces with the zone axis $\langle\bar{1}2\bar{1}0\rangle$. In both cases, the regenerating faces are not perpendicular to the faces of the equilibrium forms. The growth mechanism and the quality of the material overgrown onto these regeneration pyramids differ from those of the previous type. Thus, nepheline crystals grown on the substrates parallel to $\{10\bar{1}1\}$ and $\{10\bar{1}2\}$ have regeneration pyramids with a much larger number of gas–liquid inclusions in comparison with the number of inclusions in the material overgrown on the $(11\bar{2}0)$ and $(11\bar{2}l)$ surfaces.

The growth morphology of the surfaces of nepheline crystals is determined by the type and the growth mechanism of the corresponding face. Thus, the (0001) and $(000\bar{1})$ monohedron faces and $\{10\bar{1}0\}$ prism faces belonging to the equilibrium form (*F*-faces) grow by the spiral–layer mechanism, i.e., layer by layer, and are characterized by a macrorelief with one or several macrospirals often seen with a naked eye. The surface of the (0001) face is shown in Fig. 7. The macrostep heights (measured on an interference microscope) range within 700–1300 Å. Thin plateletlike nepheline crystals are usually formed at the top of the dislocation hillock at the site of dislocation emergence to the face surface (a black platelet seen in the center in Fig. 7a). A similar relief is also observed at the faces of another equilibrium form—the $\{10\bar{1}0\}$ prism. In this case, the growth hillocks are represented by polygonal spirals elongated in the direction of the [0001] axis.

Morphologically, the regenerating faces of the $\{10\bar{1}1\}$ and $\{10\bar{1}2\}$ pyramids are characterized by the so-called "multiheaded growth" with numerous vicinal cone-like hillocks on the faces (Fig. 7b) and clearly seen growth steps. The pyramid faces originate from numerous screw dislocations that emerge onto the surface at the vertices of the vicinal hillocks normally to the $\{10\bar{1}1\}$ and $\{10\bar{1}2\}$ pyramid faces [in the general case $\{hkil\}$ faces] according to the normal growth mechanism (which reminds growth of the basal face of quartz).

Morphology of regenerating planes normal to the faces of the equilibrium forms is essentially different from the above discussed. The layers propagate along the $[11\bar{2}0]$ direction normal to the regeneration surface (Fig. 8). In this case the surfaces of steps–islands are parallel to the (0001) face of the equilibrium form. On the $(11\bar{2}0)$ face, these steps are of the rounded or have a polygonal (hexagon-like) shape. If one prevents the contact between the (0001) face of the seed and the growth medium using a platinum platelet, then it is possible to observe the formation of regeneration islands with the subsequent layer propagation over the platelet surface. On the $(11\bar{2}1)$ surface, regeneration results in formation of faceted vicinal growth pyramids. The faces of these pyramids are parallel to the $(10\bar{1}0)$ faces of the equilibrium prism.

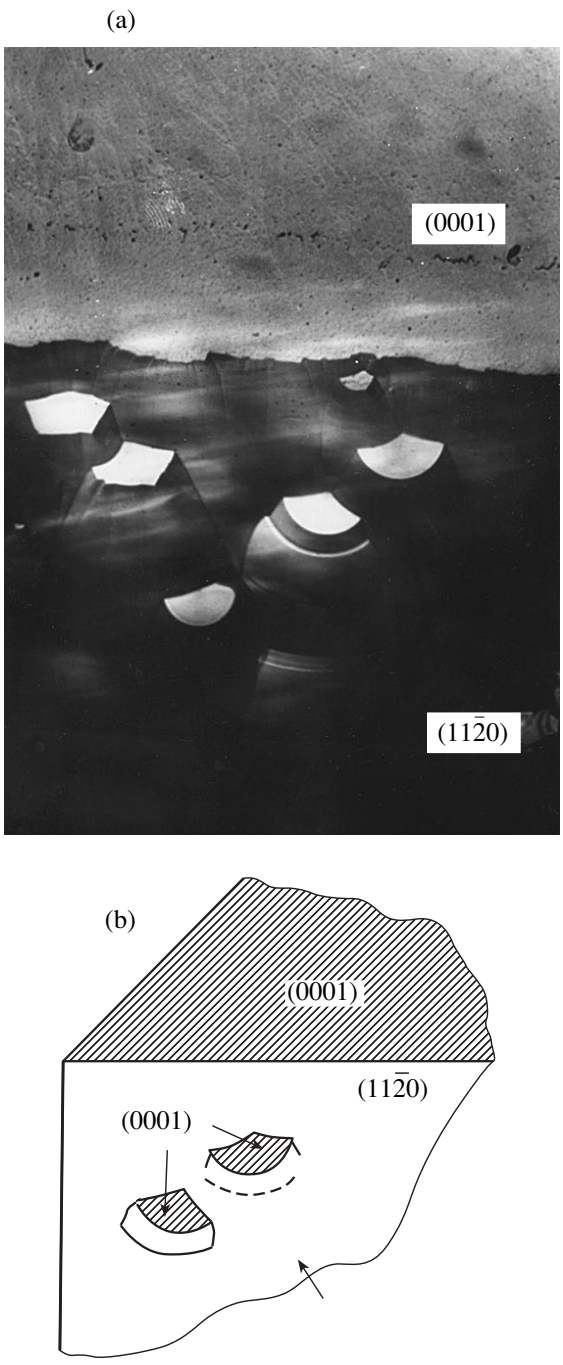

Fig. 8. (a) Growth accessories and (b) scheme of their formation on the $\{11\bar{2}0\}$ prism surface. The (0001) surfaces are hatched.

The above characteristics of growth morphology and regeneration surfaces show that the growth mechanisms along different crystallographic directions and in different types of regeneration pyramids are different.

CONCLUSIONS

Crystallographic characteristics of seeded growth of nepheline single crystals, $Na_3K[AlSiO_4]_4$, have been studied. The higher macrosymmetry of the grown crystals is explained by the inheritance of the initial-seed texture and crystal twinning during the growth process.

The kinetics of nepheline crystallization from hydrothermal alkali solutions was studied as a function of growth temperature and relative supersaturation. The growth rates along various crystallographic directions decrease in the sequence $V_{\{10\bar{1}1\}} > V_{\{\bar{1}2\bar{1}0\}} > V_{(0001)} > V_{\{10\bar{1}0\}}$. The activation energies of crystallization are determined for the (0001) monohedron face and the $\{10\bar{1}1\}$ pyramid faces as 38.5 ± 2.0 and 48.1 ± 2.0 kJ/mol, respectively.

The specific features of regenerative growth of nepheline single crystals are also studied. Two types of regeneration pyramids are established, which are differently oriented with respect to the faces of the equilibrium forms of the (0001) monohedron and the $\{10\bar{1}0\}$ prism. It is found that the optimum regeneration surfaces for nepheline growth are normal to the monohedron and a prism faces and form two zones of $\{hk(\overline{h+k})0\}$ surfaces (at $k \neq 0$) with the zone axis $\langle 0001\rangle$ and $\{hh\overline{2h}l\}$ surfaces (at $h \neq 0$) with the zone axis $\langle 10\bar{1}0\rangle$. Growth of nepheline crystals on seeds with such orientation provides the formation of the regeneration pyramids of the first type. The $\{h0\bar{h}l\}$ surfaces with the zone axis $\langle\bar{1}2\bar{1}0\rangle$ and the $\{hkil\}$ surfaces in the general position not perpendicular to the equilibrium faces form the regeneration pyramids of the second type. Growth mechanisms for the pyramids of the first and the second types are different.

The morphology of growth surfaces of nepheline single crystals is also studied.

ACKNOWLEDGMENTS

This study was supported by the Russian Foundation for basic Research, project no. 96-05-65220.

REFERENCES

1. L. J. Bonczar and G. R. Barsch, J. Appl. Phys. **46** (10), 4339 (1975).
2. Th. Hahn and M. J. Buerger, Z. Kristallogr. **106**, 308 (1955).
3. G. Roth and H. Bohm, Solid State Ionics **18/19**, 553 (1986).
4. C. M. B. Henderson, Am. Mineral. **65**, 970 (1980).
5. B. Hippler and H. Bohm, Z. Kristallogr. **187** (1/2), 39 (1989).
6. P. A. Sandomirskiĭ, N. V. Belov, and Yu. I. Sigalovskaya, Geokhimiya, No. 10, 1509 (1980).
7. P. N. Chirvinskiĭ, *Synthesis of Minerals in the 19th Century* (Univ. Izvestiya, Kiev, 1903–1906), p. 3.
8. L. B. Sand, R. Roy, and E. F. Osborn, Econ. Geol. **52** (2), 169 (1957).
9. R. Barrer and E. White, J. Chem. Soc., 1561 (1952).
10. T. B. Kosova and L. N. Dem'yanets, in *Crystal Growth from High-Temperature Aqueous Solutions* (Nauka, Moscow, 1977), p. 12.
11. T. B. Kosova and L. N. Dem'yanets, in *Crystal Growth from High-Temperature Aqueous Solutions* (Nauka, Moscow, 1977), p. 43.
12. T. B. Kosova and L. N. Dem'yanets, USSR Inventor's Certificate No. 1701756, Byull. Izobret., No. 48 (1991).
13. T. B. Kosova and L. N. Demianets, in *Proceedings of the Fourth International Symposium on Hydrothermal Reactions, Nancy, France, 1993*, p. 117.
14. C. M. B. Henderson and J. Roux, Contrib. Mineral. Petrol. **61**, 279 (1977).
15. K. H. Klaska, *Strukturuntersuchungen an Tridymitabkömmlingen (Beryllonitrejhe, Trinephelin): Dissertation* (Hamburg Univ., Hamburg, 1974).
16. A. M. Askhabov, *Regeneration of Crystals* (Nauka, Leningrad, 1979).
17. G. G. Lemmleĭn, *Morphology and Genesis of Crystals* (Nauka, Moscow, 1973).

Translated by L. Man

Crystallography Reports, Vol. 45, No. 6, 2000, pp. 1059–1061. Translated from Kristallografiya, Vol. 45, No. 6, 2000, pp. 1146–1148.

CRYSTAL GROWTH

Crystal Growth and Polymorphism of Li_2MgSiO_4

V. V. Dozmarov*, L. D. Iskhakova*, Yu. A. Velikodnyĭ, L. G. Makarevich*, A. V. Gaĭster***, and E. M. Dianov***

** Fiber Research Center, Institute of General Physics, Russian Academy of Sciences, ul. Vavilova 38, Moscow, 117942 Russia*

E-mail dozmarov@fo.gpi.ac.ru

*** Department of Chemistry, Moscow State University, Vorob'evy gory, Moscow, 119899 Russia*

**** Institute of General Physics, Russian Academy of Sciences, ul. Vavilova 38, Moscow, 117942 Russia*

Received April 26, 1999

Abstract—A method for growing Cr^{4+} : Li_2MgSiO_4 single crystals with the longest luminescence lifetime of all the *ortho*silicates and germanates is developed. The thermographic and X-ray diffraction analyses of the crystals grown showed that Li_2MgSiO_4 crystals undergo a reversible phase transition in the temperature range from 498 to 618°C. The low-temperature phase with the unit-cell parameters a = 6.2915(7), b = 10.688(1), c = 4.9946(5) Å, β = 90.479(9)°, Z = 4 is a monoclinically distorted high-temperature modification (isostructural) to orthorhombic Li_2MgGeO_4 crystals. Within the experimental error, the unit-cell parameters of the low-temperature phase linearly depend on temperature, but the angle β varies from 90.38° to 90°. The coefficients of linear thermal expansion along the crystallographic axes are equal to 1.76×10^{-5}, 1.26×10^{-5}, and 1.74×10^{-5} K^{-1}; the coefficient of volume expansion is equal to 4.91×10^{-5} K^{-1}. The phase transition is not accompanied by any essential transformation of the structural motif and causes no fracturing or defect formation. © *2000 MAIK "Nauka/Interperiodica".*

Single crystals of Cr^{4+} : Li_2MgSiO_4 from the group *ortho*silicates and germanates with the stoichiometric compositions $M_2^{2+}XO_4$ and $Li_2A^{2+}XO_4$ (X = Si or Ge) are of great interest as materials for solid-state lasers tunable in the IR range. They possess the longest luminescence lifetime of all the Cr^{4+}-doped materials. According to [1], their lifetime ranges from 100 to 400 μs at 300 and 50 K, respectively; the luminescence lifetime at room temperature is 60 μs [2]; the luminescence is observed within the range 1100–1400 nm.

No methods for growing laser-quality crystals of this rather promising material have been developed as yet. The luminescence [1] was studied on ceramic samples only. Growth of Li_2MgSiO_4 single crystals in the shape of small ~8-mm-long and 1-mm-thick platelets was reported in [3]. The crystals were grown from the melt with the use of the lithium molybdate, Li_2MoO_4, solvent. The lack of reliable data on structure and polymorphic transition for Li_2MgSiO_4 hinders growth of optical-quality crystals. According to [3], Li_2MgSiO_4 does not undergo any polymorphic transformation at heating to 1200°C; the corresponding X-ray diffraction patterns are similar to those of tetragonal Li_2MgSiO_4 obtained in [4]. The existence of the tetragonal phase reported in [4] has not been confirmed by the following studies. The polymorphism of Li_2MSiO_4 (M = Mg, Zn, Co) was described in [5], where it was also reported that Li_2MgSiO_4 undergoes a phase transition in the vicinity of 600°C [5]. Both phases have structures similar to that of the high-temperature phase of lithium phosphate, γ-Li_3PO_4. No X-ray study was made. According to [6], Li_2MgSiO_4 crystals are isostructural to the high-temperature Li_2MgGeO_4 phase (the γ-Li_3PO_4 structure type).

In this study, we report growth of Cr^{4+} : Li_2MgSiO_4 single crystals and the data on their polymorphism the thermal-expansion coefficient.

Single crystals of the composition Cr^{4+} : Li_2MgSiO_4 were grown from flux. We tried several solvents, namely, LiF and Li_2MoO_4 as well as lead, boron, vanadium, and sodium oxides. The study of phase formation and the determination of the crystallization fields for Li_2MgSiO_4 reduced to test crystallization in small volumes of the melt (about 1 cm^3) with the use of several molar ratios of Li_2MgSiO_4 and the solvent. The temperature of the crystallization onset was established from the appearance of spontaneously grown crystals on a platinum-wire probe. The cooling rate was 20–50°C/h. The phases formed were identified using the X-ray phase analysis.

The test experiments showed that the PbO–B_2O_3–LiF-solution based system (the activating ion was introduced in the form of K_2CrO_4) is the most appropriate for growing Cr^{4+} : Li_2MgSiO_4 crystals. The crystals were grown on seeds located in the subsurface flux layer and were grown to considerable dimensions in

Variation of the unit-cell parameters for Li_2MgSiO_4 at 20–1000°C

T, °C	Unit-cell parameters				*V*/z, Å^3
	a, Å	*b*, Å	*c*, Å	β, deg	
20	6.2915(7)	10.688(1)	4.9946(5)	90.479(9)	83.96(4)*
400	6.332(2)	10.733(6)	5.016(3)	90.44(3)	85.2(2)*
490	6.343(2)	10.740(3)	5.024(2)	90.34(3)	85.7(1)
540	6.347(1)	10.746(2)	5.048(2)	90.30(3)	86.0(2)
600	6.3555(9)	10.756(2)	5.043(1)	90.38(2)	86.18(8)*
700	6.366(2)	10.783(4)	5.048(2)		86.6(2)**
800	6.381(1)	10.798(2)	5.062(1)		87.2(1)**
850	6.393(4)	10.807(5)	5.068(2)		87.6(2)**
1000	6.400(5)	10.820(8)	5.080(4)		88.0(4)**

* Monoclinic phase, sp. gr. $P2_1/n$.

** Orthorhombic phase, sp. gr. *Pmna*, $Z = 4$.

combination of this method with the Czochralski pulling technique. The main defects in crystals were solution inclusions. The volume of the grown single crystals was about 1 cm^3. The luminescence studies showed the excited-state lifetime the longest of all the materials of this class—130 μs at the excitation by Na^{3+} : YAG laser at a wavelength of 1064 nm [7].

The phase transformations in Li_2MgSiO_4 were studied with the use of the Setaram derivatograph in the temperature range 20–1200°C. The experiments were performed in a platinum crucible filled with 122.8 mg of charge at a heating rate of 5°C/min; the standard was Al_2O_3.

The diffraction patterns from the initial sample at room temperature were obtained with a DRON-4-13 X-ray diffractometer and in an FR-552 camera. High-temperature measurements were performed using a Guiniet-type camera (CuK_α radiation with a semiconductor-grade germanium as an internal standard). The unit-cell parameters were refined by the least square procedure using the Powder-2 program complex written by P. N. Oleinikov.

The X-ray studies of Cr^{4+} : Li_2MgSiO_4 were performed in order to determine the crystallization fields (a DRON-4-13 diffractometer) and showed that the Li_2MgSiO_4 crystals were isostructural to Li_2MgGeO_4 (sp. gr. *Pmna*), which is consistent with the data from [6]. However, the shape of some reflections (e.g., *hkl* 121, 131, etc.) showed that, in fact, they are the superpositions of two reflections, which we managed to separate by obtaining diffraction patterns in an FR-552 camera providing a higher resolution and sensitivity. Thus, several additional weak reflections were recorded. These X-ray diffraction patterns were indexed within a lower symmetry—monoclinic, probable sp. gr. $P2_1/n$—and not in the orthorhombic sp. gr. *Pmna*.

The reversible phase transformation is observed in the temperature interval of 498–618°C (with a maximum at 598°C). A nonsymmetrical shape of the corresponding endothermal effect gradually decreasing within 498–589°C and several weak peaks with feebly marked endothermal effects seem to be associated with the fact that restructuring starts in individual blocks of the single crystal. Above the phase-transition temperature, the orthorhombic phase is stable, which is isostructural to germanate of the same composition [8]. The structure of Li_2MgXO_4 can be considered as the modified γ-Li_3PO_4 structure with lithium and magnesium cations distributed over the lithium sites of the phosphate structure. The structure of the low-temperature phase is, in fact, a monoclinically distorted structure of a high-temperature modification. The refined unit-cell parameters are listed in table. According to the X-ray data, the sample still contains a monoclinic phase at 600°C, then, the phase transition is completed at 630°C.

Within the experimental accuracy, the temperature dependences of the unit-cell parameters and *V*/*z* for Li_2MgSiO_4 are linear. The thermal expansion coefficients along the crystal axes *X*, *Y*, and *Z* are 1.76×10^{-5}, 1.26×10^{-5}, and 1.74×10^{-5} K^{-1}, respectively; the volume expansion coefficient equals 4.91×10^{-5} K^{-1}. A tendency to form a kink at about 600°C is characteristic only of the *b*- and *c*-parameters. In fact, changes essentially the phase transition changes only the angle β (by ~0.4°). Therefore, this phase transition cannot give rise to fracturing or defect formation and affect the lasing properties of this crystal. This was confirmed by the optical microscopy study of the all crystals grown. In [8], the relation between the Li_2MgGeO_4 and $M_2^{2+}XO_4$ structures (the olivine structure type) was established. The structures are formed by the hexagonal close packing of oxygen atoms with *X*(4+) cations being distributed over the tetrahedral sites. They differ only by location of lithium and *M*(2+) cations. The Li and Mg cations in the Li_2MgXO_4 (*X* = Si, Ge) are distributed over the tetrahedral positions; whereas in the olivine structure, the *M*(2+) cations are distributed over two positions and are surrounded with six oxygens forming an octahedron. We also calculated the thermal expansion coefficients for forsterite Mg_2SiO_4 (a = 5.982(1), b = 10.207(1), c = 4.756(1) Å, sp. gr. *Pnma*) using the data from [9]. These coefficients along the crystallographic axes are 1.50×10^{-5}, 1.65×10^{-5}, and 9.08×10^{-6} K^{-1}; the volume expansion coefficient equals 4.13×10^{-5} K^{-1}. The corresponding coefficients for Li_2MgSiO_4 only slightly differ from those for forsterite.

Thus, we developed the method for growing Cr^{4+} : Li_2MgSiO_4 single crystals—a promising material for tunable solid-state lasers with the longest excited-state lifetime. The high-temperature X-ray study revealed two polymorphic modifications: a low-temperature

monoclinic and a high-temperature orthorhombic ones. The orthorhombic–monoclinic phase transition occurring during crystallization does not affect the high quality of the crystals grown. The close thermal expansion coefficients of Li_2MgSiO_4 single crystals with these coefficients of forsterite (a widely used material for tunable solid-state lasers) allows one to hope that the mechanical strength Li_2MgSiO_4 single crystals can make them competitive with forsterite in their use as heated laser elements.

ACKNOWLEDGMENTS

This study was supported by the Russian Foundation for Basic Research, project no. 98-02-17340.

REFERENCES

1. C. Anino, J. Thery, and D. Vivien, Opt. Mater. **8**, 121 (1997).
2. V. Petričevič, A. B. Bykov, A. Seas, *et al.*, in *Proceedings of the Conference on Lasers and Electro-Optics, Baltimore, USA, May 18–23, 1997*, p. 489.
3. M. Setogouchi and C. Sakamoto, J. Cryst. Growth **24/25**, 674 (1974).
4. I. M. Stewart and G. J. P. Buchi, Trans. Br. Ceram. Soc. **62**, 615 (1962).
5. A. R. West and F. P. Glasser, J. Solid State Chem. **4**, 20 (1972).
6. Powder Diffraction File. Data Cards. Inorganic Section. Card No. 24-633. JCPDS, Swarthmore, Pensilvania.
7. V. V. Dozmarov, V. N. Protopopov, L. D. Iskhakova, and E. M. Dianov, in *Proceedings of the XVI International Conference on Coherent and Nonlinear Optics, June 29–July 3, 1998, Moscow*, ThV39.
8. B. Monnae, Rev. Chim. Miner. **13**, 588 (1976).
9. J. R. Smyth and R. M. Hazen, Am. Mineral. **58**, 588 (1973).

Translated by A. Zalesskiĭ

Crystallography Reports, Vol. 45, No. 6, 2000, p. 1062. Translated from Kristallografiya, Vol. 45, No. 6, 2000, p. 1150.

INFORMATION

Letter to the Editorial Board

Dear Sirs:

Recently, you have published the paper entitled *Crystal Structure of Strontium Hilgardite* by O. Ferro, D.Yu. Pushcharovskiĭ, S. Teat, S.A. Vinogradova, E.V. Lovskaya, and I.V. Pekov (Crystallogr. Rep., vol. 45, no. 3, p. 410). Soon after the publication, we received a letter from the Commission on New Minerals and Mineral Names of the International Mineralogical Association confirming that our proposal to revalidate *kurgantaite* had been approved on July 4, 2000. Therefore, we recommend to refer to the structure described in our article mentioned above as that of *kurgantaite*.

D.Yu. Pushcharovskiĭ

Translated by L. Man

1063-7745/00/4506-1062$20.00 © 2000 MAIK “Nauka/Interperiodica”

Crystallography Reports, Vol. 45, No. 6, 2000, pp. 1063–1064. Translated from Kristallografiya, Vol. 45, No. 6, 2000, pp. 1151–1152.

OBITUARY

Aida Aleksandrovna Urusovskaya (1929–2000)

On June 26, 2000, Aida Aleksandrovna Urusovskaya passed away.

All those who knew Aida Aleksandrovna or, at least, once had private or scientific contacts with her clearly realized what a great and irreplaceable this loss is. Each has his or her own memories, knows his or her own Urusovskaya, and recollects her as a very bright person possessing natural charm, modesty, a pure soul, and a rare liking for hard work, which manifested itself in various sides of her talent. She was a person who shared the same fate as the country in which she was born and worked.

Aida Aleksandrovna was born on January 18, 1929, in Nizhniĭ Novgorod. Even in her school years, she showed an inclination to natural sciences and found great pleasure in solving mathematical problems. Upon graduating from school with a Silver Medal in 1947, Urusovskaya entered the physics and mathematics faculty of Gorky (Nizhniĭ Novgorod) State University. As a postgraduate student of Academician Nikolai Vasil'evich Belov, she defended her diploma work devoted to the ramsaite structure. Professor Belov recommended that she enter the postgraduate course at the Institute of Crystallography of the USSR Academy of Sciences in Moscow under the guidance of Professor M.V. Klassen-Neklyudova. Upon proving that she could perform fine experiments, Klassen-Neklyudova agreed to guide Urusovskaya's research (1952). Until the very last days of her life, Urusovskaya was closely related to the Institute of Crystallography, to which she devoted more than half a century.

For experts in physics of plasticity in real crystals, both in this country and abroad, Urusovskaya was identified with the Institute of Crystallography. Behind the great authority enjoyed by Urusovskaya in the scientific community, there were decades of hard work, continuous scientific search, high demands to herself accompanied by the exceptional benevolence to all her colleagues, the readiness to help everybody with valuable advice, cordiality, attention, and goodwill to all her colleagues.

Urusovskaya started her scientific carrier in the period of the worldwide discussion between the adherents and adversaries of the concept of dislocations. In that time, the adherence to any idea developed in the West was always associated with the risk of being accused of political unreliability with all the following consequences. Despite this, Urusovskaya successfully performed experimental studies (undertaken by the initiative of Klassen-Neklyudova) to confirm the existence of dislocations in crystals.

In the period between the defenses of her Candidate (1955) and Doctoral (1981) Dissertations, Urusovskaya studied the characteristics of microplasticity

1063-7745/00/4506-1063$20.00 © 2000 MAIK "Nauka/Interperiodica"

and the nature of local barriers in ionic crystals using the data on macroscopic deformation. She suggested the method for treating the stress relaxation curves to determine the density and velocity of dislocations and to identify the nature of the hindrances limiting dislocation motion. For the first time, she managed to reveal the dislocation mechanism underlying the formation of indentation figures, irrational twinning, and kink formation. She showed that all these effects are caused by dislocation glide. She also developed the detailed methods for studying the "defect" structure of cesium iodide crystals (selective etching, volume decoration, and preparation of specimens for transmission electron microscopy study).

A new, remarkable page of her carrier had become the investigation of the effect of electric and magnetic fields on ionic crystals. For many years, Urusovskaya guided the pioneering experimental studies, which resulted in the discovery and the characterization of the macroscopic magnetoplastic effect in nonmagnetic crystals. She established that the application of low-intensity (less than 0.5 T) magnetic fields can reduce the yield stress of nonmagnetic materials by a considerable factor and change the character of their stress–strain curves.

Difficulties could not stop Urusovskaya in her scientific work; it looked like the difficulties only transformed her scientific work into everyday attempts of overcoming all the barriers during her research, including trying to overcome her illness. A deep interest in science and a highly developed sense of responsibility allowed her to continue her work until the very last days of her life.

For several decades, Urusovskaya had taught numerous graduate and postgraduate students and numerous researchers from many scientific centers of the ex-Soviet Union and present-day Russia who prepared their dissertations under her guidance. Urusovskaya is an expert in the field of mechanical properties of crystals and is well known in the Baltic countries, the Far East, Moldavia, Siberia, Georgia, and Ukraine. Foreign scientists who had passed through her school now successfully work in Poland and India. Urusovskaya, a doctor in physics and mathematics professor, had become the recognized authority in her field.

In addition to her scientific activity, her numerous coworkers and colleagues remember other sides of her creative nature. Her beautiful singing was always the highlight of the institute's parties and numerous conferences, scientific schools, and seminars in which she participated. She relaxed by singing Russian folk songs and the so-called city songs ("romances") as well as classical music.

Sometimes, she changed from singing to splashes of painting or making dresses for her concerts. No matter what activity she was engaged in at the moment, she made everything with devotedness, enthusiasm, inspiration, and professionalism. Such a lucky combination of harmony and balance in her mind, soul, and hands is a rare gift in itself. Of course, such generosity and wholeness of nature in our fractured and divided world are too rare to disappear unnoticed.

Translated by L. Man

Crystallography Reports, Vol. 45, No. 6, 2000, pp. 887–893. Translated from Kristallografiya, Vol. 45, No. 6, 2000, pp. 967–973.

CRYSTAL SYMMETRY

On the Rosette, Tablet, and Hypertablet Groups of *P*-Symmetries and Their Relation to the Groups of Multidimensional Symmetries

A. F. Palistrant

Moldova State University, ul. Matteevicha 60, Chisinau, 277009 Moldova

E-mail: alexandr@usm.md

Received November 23, 1998

Abstract—The rosette, tablet, and the first- and second-order hypertablet $G^P_{r...}$ groups of *P*-symmetries have been fully derived at $P \simeq G_{20}$, G_{320}, G_{4320}, and G_{54320}, respectively. The relation of these groups to the modeled multidimensional symmetry groups is established. The formulas are derived for the total numbers of the $G^P_{r...}$ groups in terms of the number of the initial symmetry groups of the category $G_{r...}$ and the number of junior groups generated by the groups of this category in their generalization with due regard for the above *P*-symmetries. *© 2000 MAIK "Nauka/Interperiodica".*

1. All the generalizations of the Shubnikov antisymmetry [1] and the Belov color symmetry [2], in which the law of variation in the properties attributed to the points of a figure is directly combined with an isometric transformation acting on the points alone and independent of their choice, are included into the unified scheme of the Zamorzaev *P*-symmetry [3]. The development of these ideas involving the generalization of various categories of classical crystallographic symmetry groups and their application to the physical crystallography, science, and art are presented in [4] and [5], respectively. The geometrical applications to the similarity symmetry and the conformal and the multidimensional symmetries are presented in [6–8]. The geometrical principle underlying the classification of *P*-symmetries is especially fruitful for multidimensional applications of the *P*-symmetry [8, 9, Sect. 1.2]. It allows one to describe the category of the six-dimensional point groups with the invariant three-dimensional plane G_{630} in terms of the point crystallographic groups G^P_{30} of these 32 *P*-symmetries [8, 10]; the categories of five- and six-dimensional plane point groups G_{520} and G_{6320}, in terms of the rosette and tablet groups G^P_{20} and G^P_{320} [8]; the categories of the five- and six-dimensional plane linear groups G_{521} and G_{6321}, in terms of the border and ribbon groups G^P_{21} and G^P_{321} [8, 11]; and the category of the five-dimensional plane groups G_{52}, in terms of the two-dimensional (parquet) groups G^P_2 [12]. Later, the geometrical principle was extended to hypercrystallographic *P*-symmetries [13] and to the rosette, tablet, and hypertablet *P*-symmetries [14–16].

Following the studies of simple and multiple antisymmetry [6], color symmetry (*p*-symmetry) [7], and color antisymmetry ((*p*')-symmetries and (*p*, 2)-symmetries) [7], the focus in deriving the groups $G^P_{r...}$ of the *P*-symmetry (generalizing the classical groups $G_{r...}$) was made on obtaining the junior (color) groups. These groups are of interest mainly for physical applications (e.g. for the magnetic, electric, and magnetoelectric symmetries). Moreover, multidimensional applications require the study of senior (grey) groups (whose derivation is trivial) and the so-called intermediate groups, completely absent in terms of simple antisymmetry. In multiple antisymmetry, the role of such groups is played by senior groups of certain kinds and junior groups of some other kinds (the type C^kM^m). These groups can be easily derived, provided the junior *m* groups of independent kinds of the type M^m are known [6]. However, it is by no means easy for *p*- and (*p*')-symmetries and even much more difficult for the *P*-symmetry. To facilitate the cumbersome calculation of intermediate groups of the *P*-symmetry, Zamorzaev [17] introduced the concept of strong isomorphism of the groups and the isomorphism of the *P*-symmetries and also proved the relation between the number of various junior groups of some *P*-symmetries and the number of different intermediate groups of other *P*-symmetries.

Along similar lines, all the symmetry groups, making up the categories $G_{(r+2)r...}$, $G_{(r+3)(r+2)r...}$, and $G_{(r+4)(r+3)(r+2)r...}$, respectively, are interpreted in terms

of the classified groups $G^P_{r\ldots}$ of the rosette, tablet, and hypertablet *P*-symmetries [14–16]. However, the cited publications reported only the calculation of the total number of the groups $G^P_{r\ldots}$ of the rosette, tablet, and hypertablet *P*-symmetries for certain selected categories of the symmetry groups. The ever increasing importance of the *n*-dimensional crystallography (see e.g. [18]) aroused the interest in the complete derivation and a more detailed description of all the groups of the rosette, tablet, and hypertablet *P*-symmetries of each subdivision (i.e., point, space, plane, layer, etc) and their application to the study of the corresponding multidimensional symmetry groups.

In the present paper, the attention is primarily focused on the classification of the rosette, tablet, and hypertablet *P*-symmetries into isomorphism classes with the aim to derive universal formulas for calculating the number of the groups $G^P_{r\ldots}$ generated by an arbitrary category $G_{r\ldots}$ generalized with due regard for the above *P*-symmetries and to consider their possible multidimensional applications.

2. One should remember the essence of *P*-symmetry and some related facts. Each point of a figure is attributed at least one subscript $i = 1, 2, \ldots, p$. Then, a certain group *P* of substitutions of these subscripts is fixed, so that the transformation of the *P*-symmetry of the figure is called an isomeric transformation, which would transform each point with the subscript *i* into a point with the subscript k_i, so that the substitution can be written as $\varepsilon = \begin{pmatrix} 1 & 2\ldots p \\ k_1 & k_2\ k_p \end{pmatrix} \in P$.

Any transformation of the *P*-symmetry *g* is a commutative product of the symmetry transformation *s* and the substitution ε. The transformations of the *P*-symmetry of the figure form the group *G*, whereas the symmetry transformations involved constitute the generating group *S*, and the substitutions of indices, the group P_1. If $P_1 = P$, then *G* is called a group of complete *P*-symmetry; if $e \subset P_1 \subset P$, it is called a group of incomplete *P*-symmetry. If *G* is a group of complete *P*-symmetry, then $H = G \cap S$ is its symmetry subgroup and $Q = G \cap P$ is the subgroup of substitutions of indices. The group *G* is called senior if $Q = P$, junior if $Q = e$, and intermediate (*Q*-intermediate) if $e \subset Q \subset P$. The basic Zamorzaev theorem [7, 8] on *P*-symmetry states the following. Any group *G* of the complete *P*-symmetry can be derived from its generating group *S* by (i) singling out the normal devisors *H* and *Q* in *S* and *P* such that there exists the isomorphism of the factor-group *S*/*H* on *P*/*Q*, (ii) pairwise multiplication of the cosets (matching in isomorphism), and (iii) the combination of the obtained products.

In the scheme of *P*-symmetry, the rosette *P*-symmetries, whose zero-dimensional groups G^P_0 model the rosettes symmetry groups G_{20}, are restricted to the *p*- and (*p*')-symmetries at $p = 1, 2, 3, 4, 5, 6$ [14, 15]. The groups of the substitutions, specifying the tablet *P*-symmetries at $P \simeq G_{320}$, are derived from the groups of substitutions specifying the rosette *P*-symmetries by their generalization with due regard for antisymmetry [14–16]. In other words, the substitutions characterizing the tablet *P*-symmetries are subdivided into generating (G), senior (C), and junior (M) groups [6], from which it follows that the number of the tablet *P*-symmetries equals 31. This follows from the fact that this number is equal to the number of the rosette antisymmetry groups G^1_{20} modeling the tablet groups G_{320} [6]. In turn, the hypertablet *P*-symmetries of the first order at $P \simeq G_{4320}$ are characterized [16] by such groups of substitutions which are derived from the groups of substitutions specifying the rosette *P*-symmetries via their generalization involving the twofold antisymmetry [6]. Consequently, there are 125 hypertablet *P*-symmetries of the first order because the number of the rosette groups of the twofold antisymmetry G^2_{20} modeling all the groups of the hypertablet symmetry G_{4320} is also 125 [6], whereas the groups of substitutions specifying these *P*-symmetries correspond to all types of fully classified groups of twofold antisymmetry. These are [6] G, C_i (senior of the kind $i = 1, 2$), C_{12} (senior of the kind (1, 2)), M_i (junior of the kinds $i = 1, 2$), M_{12}, C_1M_2 (senior of the kind 1, junior of the kind 2), C_2M_1, $C_{12}M_1$, and M_1M_2 (junior of the kinds 1 and 2).

Finally, at $P \simeq G_{54320}$, the hypertablet *P*-symmetries of the second order are restricted to such *P*-symmetries whose groups of substitutions are obtained from the groups of substitutions of the rosette *P*-symmetries via their generalization involving the threefold antisymmetry [6]. Therefore, there are 671 such *P*-symmetries, because the number of different rosette groups of the threefold antisymmetry G^3_{20} is also 671 [6]. As regards the groups of substitutions characterizing the above hypertablet *P*-symmetries of the second order and whose zero-dimensional groups G^P_0 model all the groups of the category G_{54320}, these groups of substitutions correspond to all the groups of the threefold antisymmetry obtained in their complete classification [6]: G, C_i ($i = 1, 2, 3$), C_{1j} ($j = 2, 3$), C_{23}, C_{123}, C_1C_j, C_2C_3, C_1C_{23}, C_2C_{13}, C_3C_{12}, $C_{12}C_{13}$, and C_3 (senior of all seven kinds); M_i, M_{1j}, M_{23}, M_{123}; C_1M_j, C_1M_{23}, C_2M_1, C_2M_3, C_3M_j, C_3M_{12}, $C_{12}M_j$, $C_{12}M_{13}$, $C_{13}M_j$, $C_{13}M_{12}$, $C_{23}M_k$ ($k = 1, 2$), $C_{23}M_{12}$, $C_{123}M_i$, C_1C_2M (senior of kinds 1 and 2, junior independently of the their kind), C_2C_3M, $C_2C_{13}M$, $C_3C_{12}M$, $C_{12}C_{23}M$, M_1M_j, M_2M_3, M_kM_{123}, M_3M_{12}, $M_{12}M_{13}$, C_jM_2 (senior of the *i*th kind, junior of other kinds), $C_{12}M_2$, $C_{13}M_2$, $C_{23}M_2$, $C_{123}M_2$, and M_3 (junior of all seven kinds).

Now, remember the concept of the strong isomorphism of the groups and the isomorphism of the *P*-symmetries [17]. Two elements of a group are equiv-

alently included into this group if there exists the group automorphism mapping one element onto the other one. The equivalent inclusion is preserved in group isomorphisms. Let G_1 and G_2 be the groups with set relationships of equivalence, which require the coincidence of their orders and possesses the property of equivalence. Then, the isomorphism of the group G_1 on G_2 is called strong if it provides the property that all the equivalent and equally included elements in G_1 have corresponding equivalent elements in G_2 and the nonequivalent elements equally included into G_1 have corresponding nonequivalent elements in G_2. Further, the *P*-symmetry is isomorphic to the *P*'-symmetry if the groups of substitutions *P* and *P*' specifying these groups are strongly isomorphic, i.e., $P \cong P'$.

3. Now, proceed to the groups $G^P_{r...}$ for $P \simeq G_{20}$, G_{320}, G_{4320}, and G_{54320}. As was mentioned above, these groups are classified into the senior, intermediate, and junior ones. The derivation of the senior groups is trivial: $G = S \times P$, where *S* is the generating (classical) group and *P* is the group of the substitutions of indices, which characterizes the *P*-symmetry. The junior groups of this *P*-symmetry are derived from certain generating group *S* (in accordance with the basic theorem) only if the latter possesses such a normal devisor *H* that $S/H \simeq P$. The same basic theorem also implies that the study of *Q*-intermediate groups of the *P*-symmetry involves the sorting of the nontrivial normal devisors *Q* of the group of substitutions *P*. Then, it is also possible to calculate the number of these groups if the junior groups are known, because the number of different *Q*-intermediate groups of the *P*-symmetry within the given family is equal to the number of different junior groups of the *P*-symmetry with the same generating group if $P/Q \cong P_0$ [17]. In this case, not only are the numbers of different junior groups (in this family equal to the number of various junior groups of the P_0-symmetry) the same, but the numbers of intermediate groups are also the same within the families of groups of the isomorphic *P*-symmetries. The calculation of the groups $G^P_{r...}$ of certain *P*-symmetries requires the detailed analysis of only one group of each class of isomorphism and not of all the *P*-symmetries; therefore, the calculation of the number of groups is essentially simplified. Below, we make use of such a possibility.

4. Let us derive the universal formula for calculating groups $G^P_{r...}$ of the rosette *P*-symmetries at $P \simeq G_{20}$. The groups of the substitutions characterizing these *P*-symmetries are subdivided into 9 classes of strong isomorphism: 1; 2, 1'; 3; 4; 6; 2'; 3'; 4'; 6'. Consequently, generalizing the category $G_{r...}$ containing *K* symmetry groups with 10 rosette *P*-symmetries, we distinguish *K* generating, $9 \cdot K$ senior, and $2M_2 + M_3 + M_4 + M_6 + M_{2'} + M_{3'} + M_{4'} + M_{6'}$ junior groups $G^P_{r...}$ (the subscript *P* of the symbols M_P denoting the number of junior groups indicates the specific *P*-symmetry associated with the number M_P, whereas the factor 2 indicates the number of the *P*-symmetries within the class of isomorphism of the symmetry 2).

To calculate the number of *Q*-intermediate groups $G^P_{r...}$ of these *P*-symmetries, one should first establish all the possible nontrivial normal devisors *Q* for one group of substitutions from each class of strong isomorphism and then construct the factor-group *P*/*Q*.

For the first four *P*-symmetries, the category $G_{r...}$ generates no intermediate groups. For the 4-symmetry, we have *Q* =2 and $4/2 \cong 2$; therefore, the number of the 2-intermediate groups $G^4_{r...}$ coincides with the number of M_2 junior groups generated by the category $G_{r...}$ for the symmetry 2. At the symmetry 6, we have *Q* = 2 and 3, while $6/2 \cong 3$ and $6/3 \cong 2$. Consequently, the number of the *Q*-intermediate groups $G^6_{r...}$ coincides with the number $M_2 + M_3$. For the (2')-symmetry, we have *Q* = 2 and 1', while $P/2 \cong P/1' \cong 2$; therefore, among the groups $G^{2'}_{r...}$, we have $2M_2$ *Q*-intermediate groups. For the (3')-symmetry *Q* = 3 and $P/3 \cong 2$; therefore, there are M_2 3-intermediate groups $G^{3'}_{r...}$. For the (4')-symmetry and *Q* = 4 and 2', the factor-groups are $P/4 \cong P/2' \cong 2$, while for *Q* = 2, the factor groups are $P/Q \cong 2'$, whence it follows that there are $2M_2 + M_{2'}$ *Q*-intermediate groups among $G^{4'}_{r...}$ groups. Finally, for the (6')-symmetry and *Q* = 2 the factor-group is $P/Q \cong 3'$; for *Q* = 3, the factor group is $P/Q \cong 2'$, while for *Q* = 6 and 3', the factor group is $P/6 \cong P/3' \cong 2$. Therefore, in this case, we obtain $2M_2 + M_{2'} + M_{3'}$ intermediate groups. Finally, we conclude that the generalization of the category $G_{r...}$ with due regard for 10 rosette *P*-symmetries yields $9M_2 + M_3 + 2M_{2'} + M_{3'}$ *Q*-intermediate groups $G^P_{r...}$ (here, the symbol M_P retains its meaning and the numerical factors specify the number of all the possible factor-groups *P*/*Q* strongly isomorphic to the groups of the substitutions *P* characterizing the above *P*-symmetries).

Thus, generalizing the *K* groups of the category $G_{r...}$ with due regard for 10 rosette *P*-symmetries, we arrive at the complete number of the groups $G^P_{r...}$, which is equal to $10 \times K + 11 \times M_2 + 2 \times M_3 + M_4 + M_6 + 3 \times M_{2'} + 2 \times M_{3'} + M_{4'} + M_{6'}$. These groups model the symmetry groups of the category $G_{(r+2)r...}$. Attributing the values corresponding to the given category to M_P, one can confirm the numerical factors G^P_{20}, G^P_2, G^P_{21}, G^P_{210}, and G^P_{320} for $P \simeq G_{20}$ obtained earlier in [7, 8].

5. Let us derive a formula for calculating the number of groups $G^P_{r...}$ of 31 tablet *P*-symmetries for $P \simeq G_{320}$. The groups of substitutions specifying these *P*-symme-

tries are now subdivided into 17 classes of isomorphism: (1) 1; (2) 2, $\underline{1}$, $\underline{2}$, 1', $\underline{1}$'; (3) 3; (4) 4, $\underline{4}$; (5) 6, 3$\underline{1}$, $\underline{6}$; (6) 2', 2'$_-$; (7) 2$\underline{1}$, $\underline{2}$', (1')$\underline{1}$; (8) 3', 3'$_-$; (9) 4', 4'$_-$; (10) $\underline{4}$'; (11) 6', 6'$_-$; (12) $\underline{6}$', (3')$\underline{1}$; (13) 4$\underline{1}$; (14) 6$\underline{1}$; (15) (2')$\underline{1}$; (16) (4')$\underline{1}$; and (17) (6')$\underline{1}$, where the bar under the symbol of the generating group element indicates the combination of the corresponding subscript substitution with the sign reversal.

Generalizing the category $G_{r\ldots}$ under consideration with the tablet *P*-symmetries, we obtain *K* generating $30 \times K$ senior and $5 \times M_2 + M_3 + 2 \times M_4 + 3 \times M_6 + 2 \times M_{2'} + 3 \times M_{2\underline{1}} + 2 \times M_{3'} + 2 \times M_{4'} + M_{\underline{4}'} + 2 \times M_{6'} + 2 \times M_{\underline{6}'} + M_{4\underline{1}} + M_{\underline{6}\underline{1}} + M_{(2')\underline{1}} + M_{(4')\underline{1}} + M_{(6')\underline{1}}$ junior groups. The symbols M_P and numerical factors have the same meaning as in the case of the rosette *P*-symmetries. The number of the lacking *Q*-intermediate groups $G^P_{r\ldots}$ of the tablet *P*-symmetries can be obtained upon the derivation of the corresponding general formula. This, in turn, requires (see Sect. 3) a detailed study of all the factor-groups *P*/*Q* for only the one group of the substitutions from each class of strong isomorphism. Then the number of the intermediate groups generated by the category $G_{r\ldots}$ at the given *P*-symmetry must be multiplied by the number of *P*-symmetries in its class of isomorphism.

The classes (1)–(6), (8), (9), and (11) of the tablet *P*-symmetries contain the rosette *P*-symmetries. Let us determine the number of the *Q*-intermediate groups in the category $G^P_{r\ldots}$ at *P*-symmetries of these classes. For the *P*-symmetries of the classes (1)–(3), the category $G_{r\ldots}$ generates no intermediate groups. For the 4-symmetry, this category, as is shown in Sect. 4, generates M_2 intermediate groups. Therefore, since class (4) contains two *P*-symmetries, the category in question generates $2M_2$ intermediate groups at the *P*-symmetries of this class. Considering the *P*-symmetries of classes (5), (6), (8), (9), and (11) in a similar way, one can find that at the *P*-symmetries of the above nine classes of isomorphism containing the rosette *P*-symmetries, there are $19M_2 + 3M_3 + 4M_{2'} + 2M_{3'}$ *Q*-intermediate groups in the category $G^P_{r\ldots}$.

For the remaining eight classes of the tablet *P*-symmetries containing no rosette symmetries, the calculation of the intermediate groups of the category $G^P_{r\ldots}$ should be considered in more detail. Thus, for the (2$\underline{1}$)-symmetry and $Q = \underline{1}$, 2, and $\underline{2}$, we obtain $P/Q \cong 2$. Consequently, for this *P*-symmetry, the category $G_{r\ldots}$ generates $3M_2$ intermediate groups, whereas for the *P*-symmetry of class (7), this category generates $9M_2$ intermediate groups, since the class mentioned above contains 3 *P*-symmetries. For the ($\underline{4}$')-symmetry and $Q = \underline{4}$, 2', and 2'$_-$, we obtain $P/Q \cong 2$. If $Q = 2$, then $P/Q \cong 2\underline{1}$. Therefore, for the *P*-symmetry of class (10), the category considered above generates $3M_2 + M_{2\underline{1}}$ intermediate groups. For the ($\underline{6}$')-symmetry and $Q = 2$, we have $P/Q \cong 3'$. If $Q = 3$, then $P/Q \cong 2\underline{1}$; for $Q = 3'$, $\underline{6}$, and 3'$_-$, the factor-groups $P/Q \cong 2$. As a consequence, for the (6')-symmetry, the category considered above generates $M_{3'} + M_{2\underline{1}} + 3M_2$ intermediate groups; for the *P*-symmetries of class (12), the same category generates $2M_{3'} + 2M_{2\underline{1}} + 6M_2$ such groups.

It is easy to verify that for the eight classes (7), (10), (12)–(17) of the tablet *P*-symmetries containing no rosette symmetries, the category $G_{r\ldots}$ generates $39M_2 + M_3 + 2M_4 + 3M_6 + 6M_{2'} + 3M_{3'} + 2M_{4'} + 2M_{6'} + 14M_{2\underline{1}} + 2M_{(2')\underline{1}}$ intermediate groups, whereas for all the tablet *P*-symmetries, there are $58 \times M_2 + 4 \times M_3 + 2 \times M_4 + 3 \times M_6 + 10 \times M_{2'} + 5 \times M_{3'} + 2 \times M_{4'} + 2 \times M_{6'} + 14 \times M_{2\underline{1}} + 2 \times M_{(2')\underline{1}}$ *Q*-intermediate groups in the category $G^P_{r\ldots}$.

Summing up, the generalization of the *K* symmetry groups of the category $G_{r\ldots}$ with due regard for 31 tablet *P*-symmetries yields the complete number of the groups $G^P_{r\ldots}$ equal to $31 \times K + 63 \times M_2 + 5 \times M_3 + 4 \times M_4 + 6 \times M_6 + 12 \times M_{2'} + 7 \times M_{3'} + 4 \times M_{4'} + M_{\underline{4}'} + 4 \times M_{6'} + 2 \times M_{\underline{6}'} + 17 \times M_{2\underline{1}} + M_{4\underline{1}} + M_{\underline{6}\underline{1}} + 3 \times M_{(2')\underline{1}} + M_{(4')\underline{1}} + M_{(6')\underline{1}}$. These groups model the symmetry groups of the category $G_{(r+3)(r+2)r\ldots}$.

Attributing the values corresponding to this category, to M_P, one can confirm the numerical data for G^P_{20}, G^P_{21}, and G^P_{320} for $P \simeq G_{320}$ obtained in [14–16].

6. Now, derive the formula for calculating the groups $G^P_{r\ldots}$ of 125 hypertablet *P*-symmetries of the first order for $P \simeq G_{4320}$. Following [19], we can abridge the list of the *P*-symmetries and the specific types of the *Q*-intermediate groups by using method *A*, which reduces the procedure to writing down only one representative of the symbols of three different groups *P* (or *Q*) of the same form. Thus, writing ($\underline{1} - A$), we mean the list $\underline{1}$-, *1-, and *$\underline{1}$-, whereas writing (*2$\underline{1}$ – *A*), we mean the list *2$\underline{1}$-, *$\underline{2}$*1-, and $\underline{2}$*$\underline{1}$-. A bar under the symbol of a group element indicates to the combination of the corresponding substitution of the indices with the interchange of only the first signs "+" or "–"; the asterisks on the upper left of the symbol indicate the interchange of only the second signs; the combination of a bar and an asterisk means simultaneous interchange of both the first and the second signs.

The groups of the substitutions, specifying the hypertablet *P*-symmetries of the first order, are distributed over 25 classes of strong isomorphism as follows: (1) 1; (2) 2, ($\underline{1} - A$), ($\underline{2} - A$), 1', and (1'$_-$ – *A*) (altogether 11 *P*-symmetries); (3) 3; (4) 4 and ($\underline{4} - A$) (altogether 4 *P*-symmetries); (5) 6, (3$\underline{1} - A$), and ($\underline{6} - A$) (altogether 7 *P*-symmetries); (6) 2' and (2'$_-$ – *A*) (altogether 4 *P*-symmetries); (7) (2$\underline{1} - A$), $\underline{1}$*1, (*2$\underline{1} - A$), ((1')$\underline{1} - A$),

($\underline{2}'-A$), (($1'_-$)*1 – A), and ($\underline{2}$*' – A) (altogether 19 P-symmetries); (8) 3' and ($3'_-$ – A) (altogether 4 P-symmetries); (9) 4' and ($4'_-A$) (altogether 4 P-symmetries); (10) ($\underline{4}'-A$) and ($\underline{4}$*' – A) (altogether 6 P-symmetries); (11) 6', ($6'_-$ – A) (altogether 4 P-symmetries); (12) ($\underline{6}'-A$), ((3')$\underline{1}-A$), ((3*')$\underline{1}-A$), and ($\underline{6}$*' – A) (altogether 12 P-symmetries); (13) ($4\underline{1}-A$) and ((*$4\underline{1}-A$) (altogether 6 P-symmetries); (14) ($6\underline{1}-A$), $3\underline{1}$*1, and (*$6\underline{1}-A$) (altogether 7 P-symmetries); (15) (($\overline{2}'$)$\underline{1}-A$) and ((2*')$\underline{1}$ – A) (altogether 6 P-symmetries); (16) $2\underline{1}$*1, (1')1*1, and (*2')$\underline{1}-A$) (altogether 5 P-symmetries); (17) ((4')$\underline{1}$ – A) and ((4*')$\underline{1}$ – A) (altogether 6 P-symmetries); (18) ((*4')$\underline{1}-A$) (altogether 3 P-symmetries); (19) ((6')$\underline{1}$ – A) and ((6*')$\underline{1}$ – A) (altogether 6 P-symmetries); (20) (3')$\underline{1}$*1 and ((*6'$\underline{1}$ – A) (altogether 4 P-symmetries); (21) $4\underline{1}$*1; (22) $6\underline{1}$*1; (23) (2')$\underline{1}$*1; (24) (4')$\underline{1}$*1; and (25) (6')$\underline{1}$*1. Taking into account that classes (6) and (7), (9) and (10), (11) and (12), (15) and (16), (17) and (18), and (19) and (20) contain junior groups of antisymmetry from the same family and thus are isomorphic to each other [6], we obtain 25 nonisomorphic symmetries among 125 hypertablet P-symmetries of the first order and also 25 strongly nonisomorphic and 19 nonisomorphic groups of the substitution groups characterizing 125 P-symmetries. This result confirms the statement made in [17] that the relationship of strong isomorphism divides any class of isomorphic groups into subclasses.

Using the statements made in Section 3, we conclude that generalization of the category $G_{r...}$ with due regard for 125 hypertablet P-symmetries of the first order yields K generating $K \times 124$ senior, $11 \times M_2 + M_3 + 4 \times M_4 + 7 \times M_6 + 4 \times M_2 + 19 \times M_{2\underline{1}} + 4 \times M_{3'} + 4 \times M_{4'} + 6 \times M_{\underline{4}'} + 4 \times M_{6'} + 12 \times M_{\underline{6}'} + 6 \times M_{4\underline{1}} + 7 \times M_{6\underline{1}} + 6 \times M_{(2')\underline{1}} + 5 \times M_{2\underline{1}*1} + 6 \times M_{(4')\underline{1}} + 3 \times M_{(*4')\underline{1}} + 6 \times M_{(6')\underline{1}} + 4 \times M(*6')_{\underline{1}} + M_{4\underline{1}*1} + M_{6\underline{1}*1} + M_{(2')\underline{1}*1} + 4 \times M_{(4')\underline{1}*1} + M_{(6')\underline{1}*1}$ junior (the symbols M_P and the numerical factors have the same meaning as earlier), and an unknown number of intermediate groups.

Before proceeding to the search for the absent Q-intermediate groups generated by the category $G_{r...}$ with due regard for the hypertablet P-symmetries of the first order, we should like to note that the tablet P-symmetries are contained in 17 classes of isomorphism, namely, (1)–(15), (17), and (19). Considering the P-symmetries of these 17 classes of isomorphism in the same way as 9 classes of isomorhism of the tablet P-symmetries containing the rosette symmetries, in Sect. 5, one can readily see that the category $G^P_{r...}$ contains $279M_2 + 14M_3 + 12M_4 + 21M_6 + 44M_{2'} + 22M_{3'} + 12M_{4'} + 12M_{6'} + 6M_{\underline{6}'} + 85M_{2\underline{1}} + 12M_{(2')\underline{1}}$ intermediate groups.

Consider in more detail the Q-intermediate groups $G^P_{r...}$ for the remaining 8 classes of isomorphism of the hypertablet P-symmetries of the first order.

For the ($2\underline{1}$*1)-symmetry, if $Q = (\underline{1}-A)$, 2, and ($\underline{2}-A$), we obtain $P/Q \cong 2\underline{1}$; if $Q = (2\underline{1}-A)$, (*$2\underline{1}-A$), and $\underline{1}$*1, we have $P/Q \cong 2$. In accordance with Section 3, it follows that for the P-symmetry, the category $G_{r...}$ generates $7M_2 + 7M_{2\underline{1}}$ Q-intermediate groups, whereas for the P-symmetries of class (16), the number of such groups is five times higher.

For the ((*4')$\underline{1}$)-symmetry, if Q = (2')$\underline{1}$, (2*')$\underline{1}$, *$4\underline{1}$, *4', *$\underline{4}'$, *4'$_-$, and *$\underline{4}'_-$, we obtain $P/Q \cong 2$; if Q = *4, *$\underline{4}$, $2\underline{1}$, 2', and ($2'_-$ – A), we have $P/Q \cong 2\underline{1}$. For the cases $Q = \underline{1}$ and $\underline{2}$, we have $P/Q \cong \underline{4}'$, whereas for Q = 2, we obtain $P/Q \cong 2\underline{1}$*1. Consequently, there are $7M_2 + 7M_{2\underline{1}} + 2M_{4'} + M_{2\underline{1}*1}$ Q-intermediate groups of this P-symmetry, while for the P-symmetries of class (18), the number of such groups is three times higher.

For the ((*6')$\underline{1}$)-symmetry and for Q = 3, we obtain $P/Q \cong 2\underline{1}$*1; for $Q = \underline{1}$, *2, and *$\underline{2}$, we have $P/Q \cong \underline{6}'$. For the cases $Q = 3\underline{1}$, 3', ($3'_-$ – A), *6, and *$\underline{6}$, we have $P/Q \cong 2\underline{1}$; for Q = (3')$\underline{1}$, (3*')$\underline{1}$, *$6\underline{1}$, *6', *$\underline{6}'$, *6'$_-$, and *$\underline{6}'_-$, we have $P/Q \cong 2$. Finally, if Q = *$2\underline{1}$, then $P/Q \cong 3'$. Thus, we conclude that for the ((*6')$\underline{1}$)-symmetry, the category $G^P_{r...}$ contains $7M_2 + 7M_{2\underline{1}} + M_3 + 3M_{\underline{6}'} + M_{2\underline{1}*1}$ Q-intermediate groups; for the P-symmetries of class (20), the number of such groups is four times higher.

For the ($4\underline{1}$*1)-symmetry, if $Q = (\underline{1}-A)$ and ($\underline{2}-A$), the factor groups $P/Q \cong 4\underline{1}$; if Q = 2, then $P/Q \cong 2\underline{1}$*1. For the cases Q = 4, ($\underline{4}$ – A), and ($2\underline{1}$ – A), we have $P/Q \cong 2\underline{1}$; for $Q = \underline{1}$*1 and (*$2\underline{1}$ – A), we have $P/Q \cong 4$; finally, for Q = ($4\underline{1}$ – A), (*$4\underline{1}$ – A), and $2\underline{1}$*1, we obtain $P/Q \cong 2$. Consequently, for the P-symmetry of class (21), the category $G_{r...}$ generates $7M_2 + 4M_4 + 7M_{2\underline{1}} + 6M_{4\underline{1}} + M_{2\underline{1}*1}$ intermediate groups. For the ($6\underline{1}$*1)-symmetry, if Q = 3, we obtain $P/Q \cong 2\underline{1}$*1, whereas if $Q = (\underline{1}-A)$, 2, and ($\underline{2}-A$) of the factor group is $P/Q \cong 6\underline{1}$. For $Q = \underline{1}$*1, ($2\underline{1}-A$) , and (*$2\underline{1}-A$), we have $P/Q \cong 6$; for $Q = (3\underline{1}-A)$, 6, and ($\underline{6}-A$), we have $P/Q \cong 2\underline{1}$; for $Q = 2\underline{1}$*1, we have $P/Q \cong 3$. Finally, if $Q = 3\underline{1}$*1, ($6\underline{1}$ – A), $\underline{6}$*1, and $\underline{6}$*$\underline{1}$ then $P/Q \cong 2$, from which it follows that for the P-symmetry of class (22), the category $G_{r...}$ generates $7M_2 + M_3 + 7M_{2\underline{1}} + 7M_6 + 7M_{6\underline{1}} + M_{2\underline{1}*1}$ intermediate groups.

For the (($2'\underline{1}$*1)-symmetry, if $Q = (\underline{1}-A)$ and ($\underline{2}$ – A), the factor groups are $P/Q \cong (2')\underline{1}$; if Q = 2, 1', and ($1'_-$ – A), the factor groups are $P/Q \cong 2\underline{1}$*1; whereas if $Q = \underline{1}$*1, (*$2\underline{1}$ – A), the factor-groups are $P/Q \cong 2'$;. Further, if Q = ($2\underline{1}$ – A), 2', ($2'_-$ – A), ((1')$\underline{1}$ – A), ((1*')$\underline{1}$ – A), ($\underline{2}'$ – A), and ($\underline{2}$*' – A) then $P/Q \cong 2\underline{1}$. Finally, if $Q = 2\underline{1}$*1, ((1')$\underline{1}$*1, (2*')$\underline{1}$, (*2')$\underline{1}$, ((2')$\underline{1}-A$), ($2'_-$)*1, ($\underline{2}'$)*1, ($2'_-$)*$\underline{1}$, and ($\underline{2}'$)*$\underline{1}$, then $P/Q \cong 2$. Hence, it follows that the total number of the Q-intermediate groups generated by the category $G_{r...}$ for the

P-symmetry of class (23) equals $11M_2 + 19M_{2\underline{1}} + 4M_{2'} + 6M_{(2')\underline{1}} + 5M_{2\underline{1}^*1}$.

For the $(4')\underline{1}^*1$-symmetry and $Q = (\underline{1} - A)$ and $(\underline{2} - A)$, the factor groups are $P/Q \cong (4')\underline{1}$, whereas for $Q = 2$, we have $P/Q \cong (2')\underline{1}^*1$. If $Q = \underline{1}^*1$ and $(^*2\underline{1} - A)$, then $P/Q \cong 4'$; if $Q = (\bar{2}\underline{1} - A)$ and $(\bar{\underline{4}} - A)$, then $P/Q \cong (2')\underline{1}$. Further, for $Q = 4$, $2'$, and $(2'_- - A)$, the factor-groups are $P/Q \cong 2\underline{1}^*1$; while for $Q = (4\underline{1} - A)$, $4'$, $(4'_- - A)$, $(\underline{4}^{*\prime} - A)$, $(\underline{4}^{*\prime} - A)$, $((2')\underline{1} - A)$, and $((2^{*\prime})\underline{1} - A)$, the factor groups are $P/Q \cong 2\underline{1}$. As a result, if $Q = (^*4\underline{1} - A)$ and $2\underline{1}^*1$, then $P/Q \cong 2'$, whereas if $Q = 4\underline{1}^*1$, $((4')\underline{1} - A)$, $((4'_-)\underline{1} - A)$, $((^*4')\underline{1} - A)$, and $(2')\underline{1}^*1$, the factor groups are $P/Q \cong 2$. Hence it follows that at the P-symmetry of class (24), there are $11M_2 + 4M_{2'} + 19M_{2\underline{1}} + 5M_{2\underline{1}^*1} + 6M_{(2')\underline{1}} + 4M_{4'} + M_{(2')\underline{1}^*1} + 6M_{(4')\underline{1}}$ Q-intermediate groups in $G^P_{r\ldots}$.

Finally, for the $((6')\underline{1}^*1)$-symmetry and for $Q = 3$, we obtain $P/Q \cong (2')\underline{1}^*1$; whereas for $Q = (\underline{1} - A)$ and $(\underline{2} - A)$, we have $P/Q \cong (6')\underline{1}$. If $Q = 2$, then $P/Q \cong (\underline{6}')^*1$. For the cases $Q = \underline{1}^*1$ and $(^*2\underline{1} - A)$, the factor-groups are $P/Q \cong 6'$. In turn, if $Q = \bar{2}\underline{1}^*1$, then $P/Q \cong 3'$; if $Q = (2\underline{1} - A)$, then $P/Q \cong \underline{6}'$; whereas for the cases $Q = (3\underline{1} - A)$ and $(\underline{6} - A)$, we have $P/Q \cong (2'_-)^*1$. Further, if $Q = 6$, $3'$, and $(3'_- - A)$, the factor groups are $P/Q \cong 2\underline{1}^*1$, while if $Q = (^*6\underline{1} - A)$ and $3\underline{1}^*1$, then $P/Q \cong 2'$. If $Q = ((3')\underline{1} - A)$, $((3^{*\prime})\underline{1} - A)$, $(6\underline{1} - A)$, $6'$, $(6'_- - A)$, $(\underline{6}' - A)$, and $(\underline{6}^{*\prime} - A)$, then $P/Q \cong 2\underline{1}$; and finally, if $Q = 6\underline{1}^*1$, $((6')\underline{1} - A)$, $((6^{*\prime})\underline{1} - A)$, $((^*6')\underline{1} - A)$, and $(3')\underline{1}^*1$, then $P/Q \cong 2$. Thus, at the P-symmetry of class (25), the category $G_{r\ldots}$ generates $11M_2 + 19M_{2\underline{1}} + 4M_{2'} + 5M_{2\underline{1}^*1} + 6M_{(2')\underline{1}} + 3M_{\underline{6}'} + M_{3'} + 4M_{\underline{6}'} + M_{(\underline{6}')^*1} + 6M_{(6')\underline{1}} + M_{(2')\underline{1}^*1}$ Q-intermediate groups.

It is easy to show that for the P-symmetries of the isomorphism classes (16), (18), and (20)–(25) containing no tablet P-symmetries, the category $G_{r\ldots}$ generates $131M_2 + M_3 + 4M_4 + 7M_6 + 12M_{2'} + 5M_{3'} + 4M_{4'} + 155M_{2\underline{1}} + 6M_{4\underline{1}} + 7M_{6\underline{1}} + 18M_{(2')\underline{1}} + 6M_{(6')\underline{1}} + 6M_{(4')\underline{1}} + 6M_{\underline{4}'} + 15M_{\underline{6}'} + 24M_{2\underline{1}^*1} + 2M_{(2')\underline{1}^*1} + M_{(\underline{6}')^*1}$ intermediate groups.

As a result, we conclude that the category $G^P_{r\ldots}$ of 125 hypertablet P-symmetries of the first order contains $410M_2 + 15M_3 + 16M_4 + 28M_6 + 56M_{2'} + 27M_{3'} + 16M_{4'} + 16M_{6'} + 240M_{2\underline{1}} + 7M_{6\underline{1}} + 30M_{(2')\underline{1}} + 6M_{(4')\underline{1}} + 6M_{(6')\underline{1}} + 6M_{\underline{4}'} + 24M_{2\underline{1}^*1} + 2M_{(2')\underline{1}^*1} + 21M_{\underline{6}'} + M_{(\underline{6}')^*1} + 6M_{4\underline{1}}$ intermediate groups in addition to the generating senior and junior groups listed above.

Thus, generalizing the K symmetry groups of the category $G_{r\ldots}$ with due regard for 125 hypertablet P-symmetries of the first order, we obtain the complete number of the groups $G^P_{r\ldots}$ equal to $125 \times K + 421 \times M_2 + 60 \times M_3 + 20 \times M_4 + 35 \times M_6 + 60 \times M_{2'} + 31 \times M_{3'} + 20 \times M_{4'} + 20 \times M_{6'} + 12 \times M_{\underline{4}'} + 33 \times M_{\underline{6}'} + 259 \times M_{2\underline{1}} + 12 \times M_{4\underline{1}} + 14 \times M_{6\underline{1}} + 36 \times M_{(2')\underline{1}} + 12 \times M_{(4')\underline{1}} + 12 \times M_{(6')\underline{1}} + 29 \times M_{2\underline{1}^*1} + 3 \times M_{(^*4')\underline{1}} + 5 \times M_{(^*6')\underline{1}} + M_{4\underline{1}^*1} + M_{6\underline{1}^*1} + 3 \times M_{(2')\underline{1}^*1} + 4 \times M_{(4')\underline{1}^*1} + M_{(6')\underline{1}^*1}$. These groups model the symmetry groups of the category $G_{(r+4)(r+3)(r+2)r\ldots}$ of the $(r + 4)$-dimensional Euclidian space.

Now, attributing the values, corresponding to the category G_{20} to M_P, one can confirm the numerical factor G^P_{20} for $P \simeq G_{4320}$ obtained in [16].

7. Without going into detail, we only indicate here that, at $P \simeq G_{54320}$, the generalization of the category $G_{r\ldots}$ containing K symmetry groups, with due regard for 671 hypertablet P-symmetries of the second order, yields K generating 670 K senior, $23M_2 + M_3 + 8M_4 + 15M_6 + 8M_{2'} + 91M_{2\underline{1}} + 8M_{3'} + 8M_{4'} + 28M_{\underline{4}'} + 8M_{6'} + 56M_{\underline{6}'} + 28M_{4\underline{1}} + 35M_{6\underline{1}} + 28M_{(2')\underline{1}} + 71M_{2\underline{1}^*1} + 28M_{(4')\underline{1}} + 42M_{(^*4')\underline{1}} + 28M_{(6')\underline{1}} + 56M_{(^*6')\underline{1}} + 14M_{4\underline{1}^*1} + 15M_{6\underline{1}^*1} + 14M_{(2')\underline{1}^*1} + 14M_{(4')\underline{1}^*1} + 7M_{(\hat{4}'\underline{1}^*1)} + 9M_{2\underline{1}^*1\hat{1}} + 14M_{(6')\underline{1}^*1} + 8M_{(\hat{6}')\underline{1}^*1} + M_{4\underline{1}^*1\hat{1}} + M_{6\underline{1}^*1\hat{1}} + M_{(2')\underline{1}^*1\hat{1}} + M_{(4')\underline{1}^*1\hat{1}} + M_{(6')\underline{1}^*1\hat{1}}$ junior groups (here, bars, asterisks, the symbols M_P, and the related numerical factors have the same meaning as above, a circumflex over the symbol of an element indicates the combination of the corresponding substitution of indices with the interchange only in the third signs "+" and "–" attributed to the points), and also $3520M_2 + 66M_3 + 120M_4 + 225M_6 + 376M_{2'} + 3766M_{2\underline{1}} + 171M_{3'} + 120M_{4'} + 112M_{\underline{4}'} + 120M_{6'} + 301M_{\underline{6}'} + 112M_{4\underline{1}} + 140M_{6\underline{1}} + 392M_{(2')\underline{1}} + 940M_{2\underline{1}^*1} + 112M_{(4')\underline{1}} + 42M_{(^*4')\underline{1}} + 112M_{(6')\underline{1}} + 77M_{(^*6')\underline{1}} + 14M_{4\underline{1}^*1} + 15M_{6\underline{1}^*1} + 70M_{(2')\underline{1}^*1} + 14M_{(4')\underline{1}^*1} + 44M_{2\underline{1}^*1\hat{1}} + 14M_{(6')\underline{1}^*1} + M_{(\hat{6}')\underline{1}^*1} + 2M_{(2')\underline{1}^*1\hat{1}}$ intermediate groups (here the symbols M_P have the same meaning as earlier, whereas the numerical factors specify the number of all the possible factor-groups P/Q strongly isomorphic to the group of the substitutions and characterizing the P-symmetry indicated in the symbol M_P).

Summing up, the generalization of the K symmetry groups of the category $G_{r\ldots}$ with due regard for 671 hypertablet P-symmetries of the second order yields the complete number of the $G^P_{r\ldots}$ groups equal to $671 \times K + 3543 \times M_2 + 67 \times M_3 + 128M_4 + 240 \times M_6 + 384 \times M_{2'} + 3857 \times M_{2\underline{1}} + 179 \times M_{3'} + 128 \times M_{4'} + 150 \times M_{\underline{4}'} + 128 \times M_{6'} + 357 \times M_{\underline{6}'} + 140 \times M_{4\underline{1}} + 175 \times M_{6\underline{1}} + 420 \times M_{(2')\underline{1}} + 1011 \times M_{2\underline{1}^*1} + 140 \times M_{(4')\underline{1}} + 84 \times M_{(^*4')\underline{1}} + 140 \times M_{(6')\underline{1}} + 133 \times M_{(^*6')\underline{1}} + 28 \times M_{4\underline{1}^*1} + 30 \times M_{6\underline{1}^*1} + 84 \times M_{(2')\underline{1}^*1} + 28 \times M_{(4')\underline{1}^*1} + 7 \times M_{(\hat{4}')\underline{1}^*1} + 53 \times M_{2\underline{1}^*1\hat{1}} + 28 \times M_{(6')\underline{1}^*1} + 9 \times M_{(\hat{6}')\underline{1}^*1} + M_{4\underline{1}^*1\hat{1}} + M_{6\underline{1}^*1\hat{1}} + 3 \times M_{(2')\underline{1}^*1\hat{1}} + M_{(4')\underline{1}^*1\hat{1}} + M_{(6')\underline{1}^*1\hat{1}}$. These

groups model the symmetry groups of the category $G_{(r+5)(r+4)(r+3)(r+2)r\ldots}$ of the $(r + 5)$-dimensional Euclidian space.

Thus, the formulas for calculating the groups $G^P_{r\ldots}$ of the complete P-symmetry for $P \simeq G_{20}$, G_{320}, G_{4320}, and G_{54320} are obtained.

8. In conclusion, we should like to emphasize that in the course of the solution of the formulated problem, the following subsidiary results are also obtained: (1) The rosette, tablet, and hypertablet (of the first and second orders) P-symmetries are distributed over the isomorphism classes (i.e., the classes containing the P-symmetries characterized by the groups of substitutions having the same structures). (2) The nontrivial normal devisors of the groups of substitutions corresponding to all the P-symmetries of each the type are derived. (3) The factor-groups of the groups mentioned above with respect to their normal devisors are constructed and the groups of substitutions, to which the former groups are strongly isomorphic, are indicated.

All these results provided the derivation of such an expression for calculating the complete number of the groups $G^P_{r\ldots}$ of the rosette, tablet, and hypertablet P-symmetries, in which in addition to the numerical factors, there are also the following multipliers: the number of the initial symmetry groups and the number of the junior groups generated by the category $G_{r\ldots}$ during its generalization with one P-symmetry from each class of isomorphism, into which all the P-symmetries of each type are divided.

REFERENCES

1. A. V. Shubnikov, *Symmetry and Antisymmetry of Finite Figures* (Akad. Nauk SSSR, Moscow, 1951).
2. N. V. Belov and T. N. Tarkhova, Kristallografiya **1** (1), 4 (1956) [Sov. Phys. Crystallogr. **1**, 5 (1956)].
3. A. M. Zamorzaev, Kristallografiya **12** (5), 819 (1967) [Sov. Phys. Crystallogr. **12**, 717 (1967)].
4. V. A. Koptsik, Kristallografiya **12** (5), 775 (1967) [Sov. Phys. Crystallogr. **12**, 684 (1967)].
5. A. V. Shubnikov and V. A. Koptsik, *Symmetry in Science and Art* (Nauka, Moscow, 1972; Plenum, New York, 1974).
6. A. M. Zamorzaev, *Theory of Simple and Multiple Antisymmetry* (Shtiintsa, Chisinau, 1976).
7. A. M. Zamorzaev, É. I. Galyarskiĭ, and A. F. Palistrant, *Color Symmetry, Its Generalizations and Applications* (Shtiintsa, Chisinau, 1978).
8. A. M. Zamorzaev, Yu. S. Karpova, A. P. Lungu, and A. F. Palistrant, *P-Symmetry and Its Further Development* (Shtiintsa, Chisinau, 1986).
9. A. M. Zamorzaev and A. F. Palistrant, Dokl. Akad. Nauk SSSR **256**, 856 (1981) [Sov. Phys. Dokl. **26**, 115 (1981)].
10. A. F. Palistrant, Dokl. Akad. Nauk SSSR **260**, 884 (1981) [Sov. Phys. Dokl. **26**, 908 (1981)].
11. A. F. Palistrant, *Studies in General Algebra and Geometry and Their Applications* (Shtiintsa, Chisinau, 1986), p. 124.
12. A. F. Palistrant and A. M. Zamorzaev, in *Space Groups. To Hundredth Anniversary of Their Denvation* (Nauka, Moscow, 1992), p. 112.
13. A. M. Zamorzaev and V. S. Pachi, in *Algebraic Structures and Geometry* (Shtiintsa, Chisinau, 1991), p. 54.
14. A. F. Palistrant, in *Algebraic Structures and Geometry* (Shtiintsa, Chisinau, 1991), p. 92.
15. A. F. Palistrant, Izv. Akad. Nauk Resp. Mold., Mat., No. 4, 35 (1992).
16. A. F. Palistrant, Izv. Akad. Nauk Resp. Mold., Mat., No. 1, 21 (1994).
17. A. M. Zamorzaev, Izv. Akad. Nauk Resp. Mold., Mat., No. 1, 75 (1994).
18. H. Innchyn, Acta Crystallogr., Sect. A: Found. Crystallogr. **A51**, 659 (1995).
19. A. M. Zamorzaev, Izv. Akad. Nauk Resp. Mold., Mat., No. 2, 22 (1995).

Translated by A. Zolot'ko

Crystallography Reports, Vol. 45, No. 6, 2000, pp. 894–895. Translated from Kristallografiya, Vol. 45, No. 6, 2000, pp. 974–975.

STRUCTURE OF INORGANIC COMPOUNDS

Reinvestigation of the NiP_2 Structure

S. V. Orishchin, V. S. Babizhetskiĭ, and Yu. B. Kuz'ma

Franko State University, ul. Kirilla i Mefodiya 6, Lviv, 290005 Ukraine

Received March 22, 1999; in final form, November 11, 1999

Abstract—Single crystals of the composition NiP_2 were synthesized from a tin-based flux. The crystal structure of the compound was determined by X-ray diffraction analysis; sp. gr. *C*2/*c*; PdP_2 structure type; the unit-cell parameters $a = 0.6352(1)$ nm, $b = 0.56042(9)$ nm, $c = 0.5621(1)$ nm, $\beta = 119.62(2)°$; $R_F = 0.047$ and $R_w = 0.042$ were calculated over 561 independent reflections with $F_{hkl} > 4\sigma(F_{nkl})$. © *2000 MAIK "Nauka/Interperiodica".*

Phosphide of the composition NiP_2 has been studied by X-ray powder diffraction analysis, which showed that the crystals were monoclinic with two possible space groups *C*2/*c* or *Cc*; the unit-cell parameters were determined as $a = 0.6366$ nm, $b = 0.5615$ nm, $c = 0.6072$ nm, $\beta = 126.22°$ [1]. Later, the atomic coordinates in the NiP_2 structure were also determined (sp. gr. *C*2/*c* at the same unit-cell parameters) by the X-ray diffraction study of the single crystals (the photographic method, $R = 0.096$). The structure was related to the PdP_2 structure type [2]. The fact that the NiP_2 structure was established with the use of the unit-cell parameters reported in [1] without any additional refinement and a high value of the *R* factor have cast doubt upon the validity of the structure determination of NiP_2, in particular, after the NiP_2 crystals were related to the PdP_2 structure type [3]. In this connection, we decided to reinvestigate the NiP_2 structure.

Single crystals of NiP_2 phosphide were prepared by crystallization from tin-based flux. The starting nickel and red phosphorus powders of the purity grade no worse than 99.7 wt % of the major component were taken in the molar ratio of 1 : 3. The thoroughly mixed components were pressed into a briquet. A part of the briquet (1 g) and tin (2 g) were placed into a corundum crucible then sealed into a quartz ampule, which was heated in a muffle furnace to 1370 K at a rate of 100 K/day, and kept for 50 h at this temperature. Then it was slowly cooled (150 K/day) to room temperature. The tin matrix was dissolved in a dilute (1 : 1) hydrochloric acid; the undissolved residue was dried in air at room temperature to yield gray plateletlike single crystals. The single crystals were studied by the Laue and rotation methods, and by obtaining the reciprocal lattice photographs (KFOR camera, Mo*K* radiation) and using the method of diffractometry (KM-4 diffractometer, λMo$K\alpha$ radiation, $2\theta_{max} = 80.17°$). The structure was solved by the direct methods with the use of the CSD program package [4].

The X-ray diffraction study confirmed that the NiP_2 structure is monoclinic; sp. gr. *C*2/*c*; unit-cell parameters $a = 0.6352(1)$ nm, $b = 0.56042(9)$ nm, $c = 0.5621(1)$ nm, $\beta = 119.62(2)°$. The unit-cell parameters determined in the present study substantially differ from those reported in [1, 2]. The atomic coordinates and thermal parameters ($nm^2 \times 10^{-2}$) in the NiP_2 structure are as follows: Ni in 4(*c*)—$x = y = 1/4$, $z = 0$, $B_{iso} = 0.56(2)$ ($B_{11} = 0.66(3)$, $B_{22} = 0.51(2)$, $B_{33} = 0.55(2)$, $B_{12} = -0.07(2)$, $B_{13} = 0.31(2)$, $B_{23} = 0.01(2)$); P in 8(*f*)—$x = 0.1995(2)$, $y = 0.1153(2)$, $z = 0.3361(2)$, $B_{iso} = 0.54(2)$ ($B_{11} = 0.45(4)$, $B_{22} = 0.60(3)$, $B_{33} = 0.52(3)$, $B_{12} = 0.02(3)$, $B_{13} = 0.22(3)$, $B_{23} = 0.00(2)$). The final values of the reliability factors, $R_F = 0.047$ and $R_w = 0.042$, were calculated over 561 independent reflections with $F_{hkl} > 4\sigma(F_{hkl})$.

The atomic arrangement in the NiP_2 structure (Fig. 1a) confirms the PdP_2 structure type [5]. Nikel atoms are located in the centers of almost regular squares of phosphorus atoms ($\delta_{Ni-P} = 0.2200(2)$ and 0.2202(1) nm), whereas phosphorus atoms are located in the centers of slightly distorted tetrahedra (Figs. 1b and 1c, respectively) and form zigzag chains (Fig. 1d) ($\delta_{P-P} = 0.2217(1)$ and 0.2222(2) nm). A characteristic feature of the NiP_2 structure is the minimum δ_{Ni-P} interatomic distance (0.2200 nm) shorter than the minimum δ_{P-P} interatomic distance (0.2217 nm), with the latter being close to the sum of the covalent radii of P atoms (0.220 nm). The δ_{Ni-P} distance (0.2200 nm) is substantially shorter than the sum of the corresponding atomic radii ($r_{Ni} = 0.126$ nm and $r_P = 0.110$ nm [4]), which is indicative of partial ionization of the atoms in the NiP_2 structure.

In order to determine the possible homogeneity range of NiP_2 phosphide, we examined crystallization of specimens containing 0.55 and 0.70 molar fractions of phosphorus, i.e., the specimens from two different composition ranges—$NiP_2 + Ni_5P_4$ and $NiP_2 + NiP_3$. The specimens were prepared by sintering the charge of

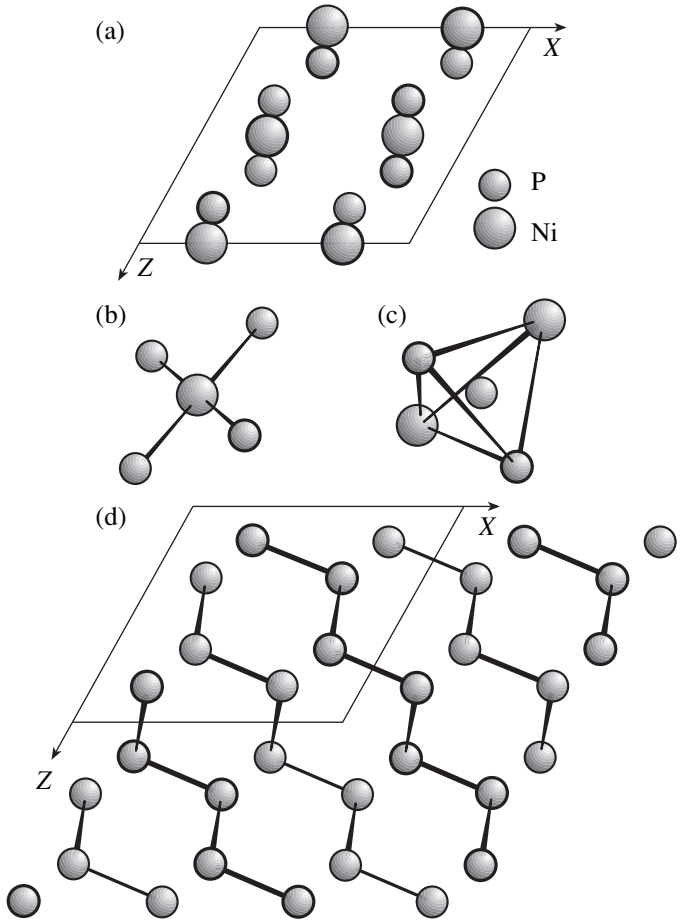

Fig. 1. (a) NiP_2 structure projected onto the *XZ* plane, (b) coordination polyhedron of $[NiP_4]$, (c) coordination polyhedron of $[P(Ni_2P_2)]$, and (d) zigzag chains of phosphorus atoms.

the preliminarily pressed powdered components in evacuated quartz ampules slowly (100 K/day) heated to 1070 K, kept at this temperature for 100 h, and then cooled in the furnace. The X-ray phase analysis (DRON-3M diffractometer, CuK_α radiation) confirmed that the specimens consisted of two phases. The unit-cell parameters of NiP_2 phosphide in the equilibrium with Ni_5P_4 are a = 0.63608(3), b = 0.56142(3), c = 0.56297(2) nm, β = 119.535(2)°, V = 0.17492(2) nm^3. The unit-cell parameters of NiP_2 phosphide in the equilibrium with NiP_3 are a = 0.63660(2), b = 0.56147(3), c = 0.56302(2) nm, β = 119.573(2)°, V = 0.17503(2) nm^3. This fact indicates that the NiP_2 phosphide has a narrow homogeneity range at 1070 K.

REFERENCES

1. S. Runqvist, Acta Chem. Scand. **15** (2), 451 (1961).
2. E. Larsson, Ark. Kemi **23** (32), 335 (1965).
3. W. B. Pearson, *Crystal Chemistry and Physics of Metals and Alloys* (Wiley, New York, 1972; Mir, Moscow, 1977), Vol. 2.
4. L. G. Akselrud, Yu. N. Grin, P. Yu. Zavalij, *et al.*, in *Collected Absracts of 12th Eurorean Crystallographic Meeting, Moscow, 1989*, Vol. 3, p. 156.
5. W. H. Zachariansen, Acta Crystallogr. **16**, 1252 (1963).

Translated by T. Safonova

Crystallography Reports, Vol. 45, No. 6, 2000, pp. 896–901. Translated from Kristallografiya, Vol. 45, No. 6, 2000, pp. 976–981.

STRUCTURE OF INORGANIC COMPOUNDS

Crystal Structures of Double Vanadates $Ca_9R(VO_4)_7$. IV. R = Er, Tm, Yb, and Lu

A. A. Belik*, S. V. Grechkin*, L. O. Dmitrienko*, V. A. Morozov*, S. S. Khasanov, and B. I. Lazoryak***

** Chemistry Department, Moscow State University, Vorob'evy gory, Moscow, 119899 Russia*

*** Institute of Solid-State Physics, Russian Academy of Sciences, Chernogolovka, Moscow oblast, 142432 Russia*

Received July 29, 1998; in final form, June 23, 1999

Abstract—Crystal structures of $Ca_9R(VO_4)_7$ compounds with R = Er (**I**), Tm (**II**), Yb (**III**), and Lu (**IV**) have been studied by the Rietveld method. All these compounds are isostructural to $Ca_3(VO_4)_2$ and crystallized in the trigonal system (sp. gr. $R3c$, $Z = 6$) with the following unit-cell parameters: (**I**) a = 10.8554(5), c = 37.967(1) Å; (**II**) a = 10.8550(5) and c = 37.950(1) Å; (**III**) a = 10.8564(5) and c = 37.924(1) Å; (**IV**) a = 10.8566(5) and c = 37.880(1) Å. In compounds **I**–**IV**, the rare-earth and calcium cations statistically occupy three positions—$M(1)$, $M(2)$, and $M(5)$. The number of R^{3+} cations in the $M(5)$ position increases from 1.3(1) for Er up to 3.0(1) for Lu. The occupancy of the $M(1)$ and $M(2)$ positions with R^{3+} cations decreases with a decrease of the radius of R^{3+}. The data on the distribution of R^{3+} cations for the whole series (R = RE and Y) are given and discussed in detail. © *2000 MAIK "Nauka/Interperiodica".*

INTRODUCTION

The present paper is the last part of the structural study of the $Ca_9R(VO_4)_7$ compounds (R = RE, Y). Below, we present the data on the structure of $Ca_9R(VO_4)_7$ compounds with R = Er (**I**), Tm (**II**), Yb (**III**), and Lu (**IV**) and summarize the data on the dependences of unit-cell parameters and the cation distributions over the $M(1)$–$M(5)$ positions of the initial $Ca_3(VO_4)_2$ structure [1] as functions of the radius of R^{3+} for the whole series of rare-earth cations.

EXPERIMENTAL

The synthesis of the samples, the conditions of obtaining X-ray diffraction patterns, and the methods used for the refinement of crystal structures are described in detail in the previous parts of this study [2, 3]. The structures of compositions **I**–**IV** were refined by the Rietveld method [4] using the RIETAN-94 program [5, 6]. According to the X-ray phase analysis, compounds **I**–**IV** consist of only one phase. Table 1 presents the main data on the diffraction experiment and the refinement of the structures of compounds **I**–**IV**.

At the first stage of the structure refinement of compounds **I**–**IV**, we used the f-curve for Ca^{2+} for all the cationic positions. The occupancies obtained (Table 2, $n_{f\text{-Ca}}$) showed that R^{3+} cations occupy the $M(1)$, $M(2)$, and $M(5)$ positions, with the $M(3)$ position being occupied by calcium cations alone and the $M(4)$ position being empty. Then, we refined the distribution of R^{3+} cations over the $M(1)$, $M(2)$, and $M(5)$ positions with due regard of their complete occupancy ($n_{Ca} + m_R = 1$). The $M(4)$ position was taken to be vacant. For the $M(3)$ position, the f-curve for Ca^{2+} cations was used and the occupancy was taken to be fixed and equal to unity: $n_{Ca} = 1$. Thus, we obtained the following numbers of R^{3+} cations per unit cell: 5.8 for **I**, 5.2 for **II**, 5.2 for **III**, and 6.0 for **IV**. Further refinement was performed at the fixed value of the R^{3+} cations in the unit cell (six). The obtained distributions of R^{3+} cations over the positions of the structure (n_{Ca}, m_R) are indicated in Table 2.

As an example, Fig. 1 shows the experimental, calculated, and the difference X-ray diffraction patterns for the specimen of compound **III**. The atomic coordinates and the parameters of atomic thermal vibrations for compounds **I**–**IV** are indicated in Table 3.

DISCUSSION OF RESULTS

The unit-cell parameters and the number of R^{3+} cations in the $M(1)$–$M(5)$ positions for the $Ca_9R(VO_4)_7$ structures (R = RE, Y) are listed in Table 4. Figure 2 shows the dependence of the unit-cell parameters and the number of R^{3+} cations on the radius of the R^{3+} cation at the coordination number c.n. = 8 [7]. As is seen from Fig. 2, each compound of the composition $Ca_9R(VO_4)_7$ (R = RE, Y) is characterized by its own distribution of R^{3+} cations over the structure positions. The occupancy of the positions with R^{3+} cations regularly changes with

Table 1. Conditions of X-ray experiment and the refinement of the $Ca_9R(VO_4)_7$ structures (R = Er (**I**), Tm (**II**), Yb (**III**), and Lu (**IV**))

Characteristic	Compound			
	I	**II**	**III**	**IV**
Sp. gr.	*R*3*c*	*R*3*c*	*R*3*c*	*R*3*c*
	$Z = 6$	$Z = 6$	$Z = 6$	$Z = 6$
Range of angles 2θ, deg	10–140	10–110	10–110	10–110
Scan step, deg	0.01	0.01	0.01	0.01
I_{max}, pulse	34410	26711	25697	26806
Unit-cell parameters				
a, Å	10.8554(5)	10.8550(5)	10.8564(5)	10.8566(5)
c, Å	37.967(1)	37.950(1)	37.924(1)	37.880(1)
V, Å^3	3874.6	3872.6	3870.9	3866.5
Number of Bragg reflections	826	546	546	545
Number of refined parameters*	17 + 62	17 + 61	17 + 62	17 + 60
Reliability factors**				
R_{WP}; R_P	4.24; 3.26	4.89; 3.77	4.02; 3.13	5.06; 3.76
R_I; R_F	3.95; 2.31	4.18; 1.91	3.05; 1.29	3.32; 1.66
S	1.46	1.85	1.53	1.89
(D–W) d	0.98	0.63	0.89	0.59

* The first number indicates the background and the profile parameters, the scale factor, the unit-cell parameters, and the zero shift; the second number indicates the positional and thermal atomic parameters and the occupancies.
** Calculated by formulas from [5].

Table 2. Occupancies of the $M(1)$, $M(2)$, and $M(5)$ positions in $Ca_9R(VO_4)_7$ (R = Er (**I**), Tm (**II**), Yb (**III**), and Lu (**IV**) and the number of R^{3+} cations in each position

Position		Compound			
		I	**II**	**III**	**IV**
$M(1)$	n_{Ca}	0.870(5)	0.893(5)	0.905(5)	0.909(6)
	m_R	0.130(5)	0.107(5)	0.095(5)	0.091(6)
	Number of R^{3+} cations	2.3(1)	1.9(1)	1.7(1)	1.6(1)
	$n_{f\text{–Ca}}$	1.25(1)	1.26(1)	1.20(1)	1.23(1)
$M(2)$	n_{Ca}	0.870(5)	0.873(5)	0.902(5)	0.925(5)
	m_R	0.130(5)	0.127(5)	0.098(5)	0.075(5)
	Number of R^{3+} cations	2.3(1)	2.3(1)	1.8(1)	1.4(1)
	$n_{f\text{–Ca}}$	1.28(1)	1.30(1)	1.21(1)	1.19(1)
$M(5)$	n_{Ca}	0.799(8)	0.702(8)	0.577(6)	0.499(7)
	m_R	0.221(8)	0.298(8)	0.423(6)	0.501(7)
	Number of R^{3+} cations	1.33(5)	1.79(5)	2.54(5)	3.01(5)
	$n_{f\text{–Ca}}$	1.51(1)	1.77(1)	2.05(1)	2.30(1)
$M(4)$	$n_{f\text{–Ca}}$	0.014(8)	–0.07(1)	0.04(1)	–0.09(1)
$M(3)$	$n_{f\text{–Ca}}$	1.022(6)	0.999(6)	1.025(7)	1.048(6)

Note: n_{Ca} and m_R are the occupancies of the position with calcium and R^{3+} cations, respectively, and $n_{f\text{–Ca}}$ is the occupancy of the position calculated with the use of the f-curves for Ca^{2+}.

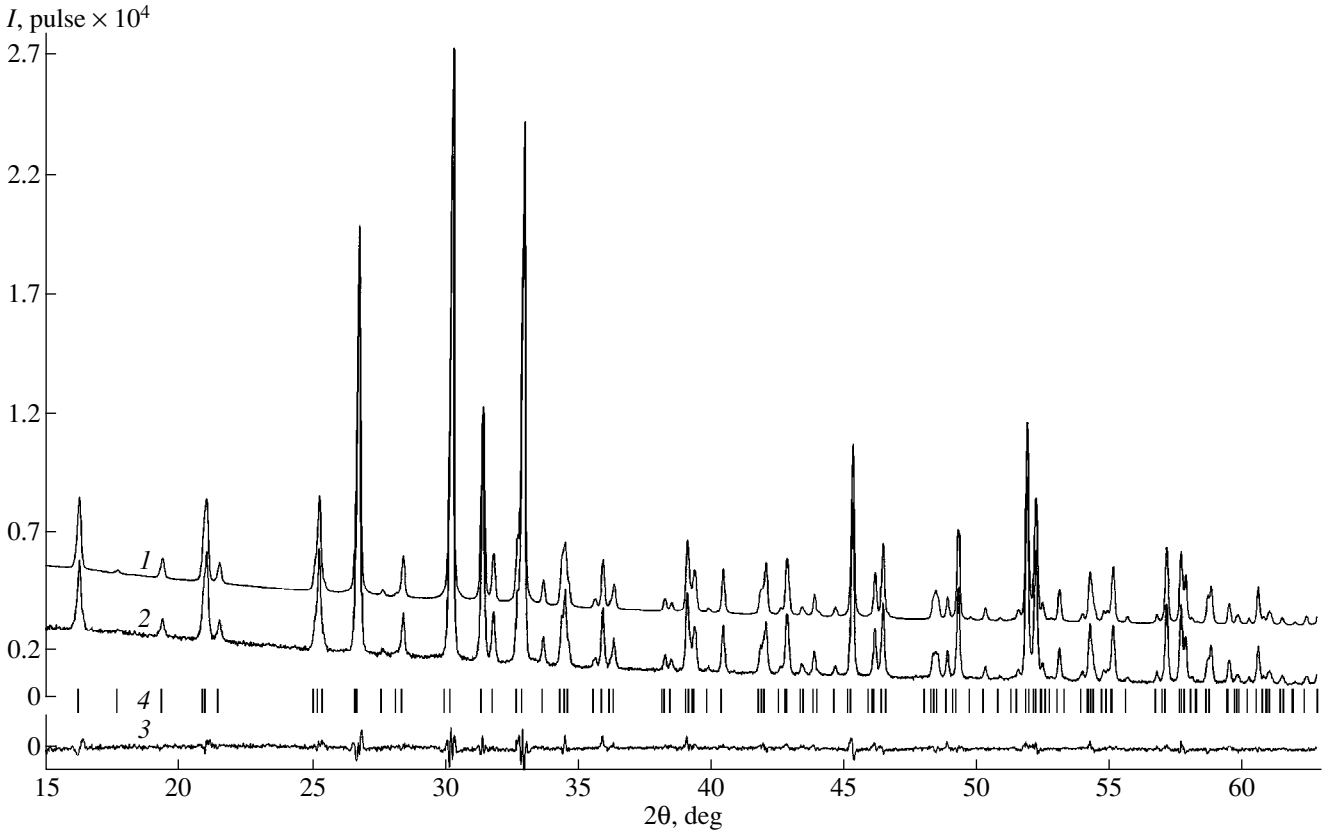

Fig. 1. A fragment of the (*1*) calculated, (*2*) experimental, (*3*) difference, and (*4*) graphical representation of diffraction patterns from $Ca_9Yb(VO_4)_7$. The calculated diffraction pattern is shifted with respect to the experimental one by 2500 pulses.

a decrease of the radius of the R^{3+} cation for the whole series of $Ca_9R(VO_4)_7$ structures with R = RE, Y. These compounds can be divided into two groups according to the character of distribution of R^{3+} cations over the structure positions. The first group is formed by compounds with R = La–Eu; the occupancy of the $M(3)$ position with R^{3+} cations in this group monotonically decreases—from 4.0 to 0.8 per unit cell; on the contrary, the occupancy of the $M(1)$ and $M(2)$ positions with R^{3+} cations monotonically increases. In these compounds, the $M(5)$ position is occupied by Ca^{2+} cations alone. The second group is formed by compounds with R = Tb–Lu and Y; the occupancy of the $M(5)$ position with R^{3+} cations monotonically increases from 0.6 to 3.0 per unit cell, whereas the occupancy of the $M(1)$ and $M(2)$ positions with R^{3+} cations monotonically decreases. The $M(3)$ position is filled with Ca^{2+} cations alone. The $Ca_9Gd(VO_4)_7$ compound separates these two groups. In this compound, Gd^{3+} cations and calcium statistically occupy the $M(1)$ and $M(2)$ positions, whereas the $M(3)$ and $M(5)$ positions are completely occupied by Ca^{2+} cations. The division of the $Ca_9R(VO_4)_7$ compounds into two groups is consistent with the division suggested in [8] and is based on the dependence of the unit-cell parameter on the size of an R^{3+} cation.

The calculation of the Madelung constants for the model whitlockite-like compounds [9] (the family to which the structures under consideration belong) showed that the most pronounced energy gain is obtained if trivalent cations occupy the $M(1)$, $M(2)$, and $M(5)$ positions, whereas the minimum energy gain is obtained if the $M(3)$ position is occupied. As is seen from Fig. 2, the R^{3+} cations occupy the $M(1)$ and $M(2)$ positions in the whole series of $Ca_9R(VO_4)_7$ compounds with R = RE and Y.

The analysis of the interatomic distances in the polyhedra of the $Ca_3(VO_4)_2$ compounds showed that rare earth cations can occupy the $M(1)$, $M(2)$, and $M(3)$ positions [10]. The largest polyhedron formed for the $M(3)$ positions in $Ca_3(VO_4)_2$ and $Ca_9R(VO_4)_7$ (R = RE and Y): $\langle M(3)\text{–}O\rangle$ = 2.57 Å (for $Ca_3(VO_4)_2$ and c.n. = 8 [1]). The M(2) position is surrounded with six oxygen atoms located at distances of ~2.40 Å and two oxygen atoms located at distances of ~2.85 Å. In $Ca_3(VO_4)_2$, $\langle M(2)\text{–}O\rangle$ equals 2.41 Å at c.n. = 6; this distance is 2.53 Å at c.n. = 8. In $Ca_3(VO_4)_2$, $\langle M(1)\text{–}O\rangle$ = 2.44 Å at c.n. = 7. The sum of the ionic radii of La^{3+} and O^{2-} ($r_{VIII}(La^{3+}) + r(O^{2-})$ = 2.58 Å [7]) is close to the aver-

Table 3. Structural parameters of the $Ca_9R(VO_4)_7$ compounds (R = Er (**I**), Tm (**II**), Yb (**III**), and Lu (**IV**))

Atom	R^{3+}	x	y	z	B_{iso}	Atom	R^{3+}	x	y	z	B_{iso}
M(1)**	**I**	0.7253(2)	0.8612(2)	0.4307(1)	0.87(4)	O(12)	**III**	0.015(1)	0.8615(8)	0.2584(3)	0.5*
	II	0.7291(4)	0.8637(4)	0.4322(4)	0.93(8)		**IV**	0.018(1)	0.8512(9)	0.2576(3)	1.04(7)
	III	0.7268(3)	0.8631(3)	0.4311(1)	0.83(7)	O(21)	**I**	0.6973(9)	0.8979(9)	0.1781(3)	2.0(2)
	IV	0.7283(4)	0.8641(4)	0.4308(1)	0.73(7)		**II**	0.738(1)	0.919(1)	0.1799(4)	2.7(3)
M(2)**	**I**	0.6134(2)	0.8235(2)	0.2338(1)	0.38(4)		**III**	0.713(1)	0.910(1)	0.1777(4)	4.2(3)
	II	0.6151(3)	0.8244(4)	0.2349(2)	0.47(7)		**IV**	0.716(1)	0.911(1)	0.1792(4)	1.04(7)
	III	0.6136(3)	0.8254(3)	0.2339(1)	0.43(6)	O(22)	**I**	0.760(1)	0.765(1)	0.1214(3)	1.0*
	IV	0.6164(4)	0.8252(4)	0.2338(1)	0.70(7)		**II**	0.765(2)	0.762(2)	0.1234(4)	2.5(4)
Ca(3)**	**I**	0.1251(3)	0.2692(2)	0.3244(1)	1.12(5)		**III**	0.762(1)	0.761(1)	0.1235(3)	1.4(3)
	II	0.1236(4)	0.2707(3)	0.3255(2)	0.76(7)		**IV**	0.763(1)	0.759(1)	0.1231(3)	1.04(7)
	III	0.1231(3)	0.2700(3)	0.3246(1)	1.12(6)	O(23)	**I**	0.7208(8)	0.0154(7)	0.1115(2)	0.1(1)
	IV	0.1207(4)	0.2664(3)	0.3233(1)	0.97(7)		**II**	0.721(1)	0.021(1)	0.1117(4)	0.4(3)
M(5)**	**I**	0	0	0	1.81(5)		**III**	0.718(1)	0.013(1)	0.1103(3)	0.7(2)
	II	0	0	0	1.92(8)		**IV**	0.719(1)	0.014(1)	0.1098(3)	1.04(7)
	III	0	0	0	1.60(5)	O(24)	**I**	0.5009(8)	0.7502(9)	0.1250(3)	0.9(1)
	IV	0	0	0	0.75(5)		**II**	0.498(1)	0.755(1)	0.1218(4)	0.3(3)
V(1)	**I**	0	0	0.2669(1)	0.82(7)		**III**	0.499(1)	0.752(1)	0.1243(4)	1.3(3)
	II	0	0	0.2663(2)	0.8(1)		**IV**	0.496(1)	0.751(1)	0.1235(3)	1.04(7)
	III	0	0	0.2666(1)	1.1(1)	O(31)	**I**	0.5896(8)	0.9551(8)	0.0448(3)	0.5*
	IV	0	0	0.2680(1)	1.3(1)		**II**	0.600(1)	0.955(1)	0.0460(4)	0.5*
V(2)	**I**	0.6836(2)	0.8575(2)	0.1338(1)	0.36(5)		**III**	0.591(1)	0.955(1)	0.0463(3)	0.5*
	II	0.6796(3)	0.8537(4)	0.1335(2)	0.52(8)		**IV**	0.593(1)	0.954(1)	0.0460(3)	1.04(7)
	III	0.6839(3)	0.8564(4)	0.1339(1)	0.18(7)	O(32)	**I**	0.567(1)	0.675(1)	0.0505(3)	1.3(2)
	IV	0.6855(3)	0.8578(4)	0.1345(1)	0.30(7)		**II**	0.557(1)	0.670(2)	0.0484(5)	1.5(3)
V(3)	**I**	0.6550(2)	0.8472(3)	0.0321(1)	0.31(5)		**III**	0.568(1)	0.680(1)	0.0507(3)	0.4(2)
	II	0.6508(4)	0.8483(4)	0.0323(2)	0.39(8)		**IV**	0.563(1)	0.685(1)	0.0523(3)	1.04(7)
	III	0.6541(4)	0.8498(4)	0.0325(1)	0.81(8)	O(33)	**I**	0.8315(7)	0.926(1)	0.0464(3)	0.5*
	IV	0.6546(4)	0.8535(4)	0.0325(1)	0.23(7)		**II**	0.828(1)	0.923(2)	0.0379(3)	0.5*
O(11)	**I**	0	0	0.3155(3)	1.0*		**III**	0.830(1)	0.924(1)	0.0431(4)	0.5(2)
	II	0	0	0.3086(6)	4.0(6)		**IV**	0.8292(9)	0.920(1)	0.0400(3)	1.04(7)
	III	0	0	0.3149(4)	0.5*	O(34)	**I**	0.6337(7)	0.8244(9)	0.9887(2)	1.4(1)
	IV	0	0	0.3152(4)	1.04(7)		**II**	0.637(1)	0.836(1)	0.9900(3)	0.5*
O(12)	**I**	0.0107(8)	0.8543(6)	0.2582(2)	0.5*		**III**	0.6291(8)	0.830(1)	0.9888(3)	0.2(2)
	II	0.011(1)	0.8593(9)	0.2599(3)	0.6(3)		**IV**	0.6219(9)	0.824(1)	0.9919(2)	1.04(7)

* The fixed value of B_{iso}.

** The M(1), M(2), and M(5) positions are filled with Ca^{2+} and R^{3+} in the ratios given in Table 2; the occupancy of the Ca(3) position equals unity. Notation for oxygen atoms: the first number is the ordinal number of the vanadium atom, the second number is the ordinal number of the oxygen atom in a tetrahedron.

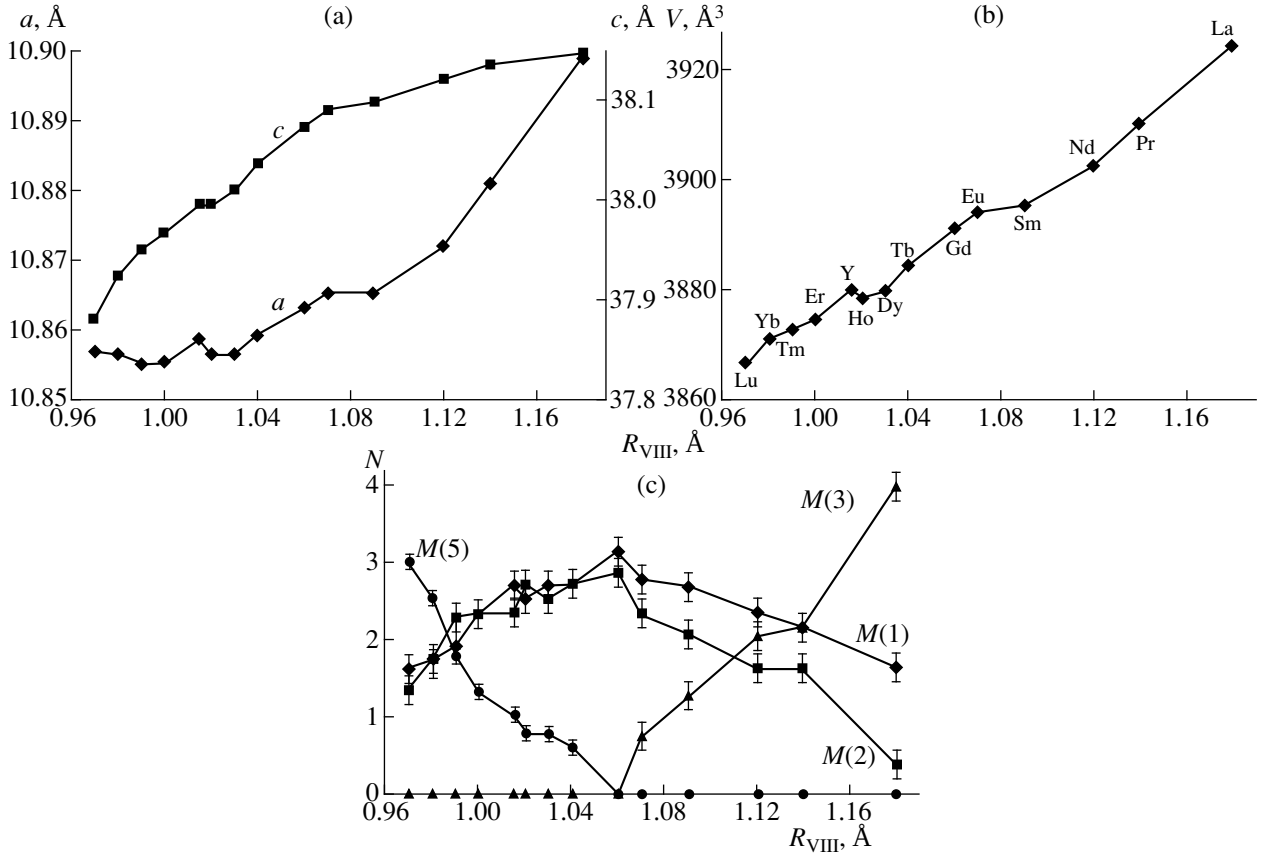

Fig. 2. (a, b) The change in the unit-cell parameters and (c) the number of R^{3+} cations in the $M(1)$–$M(5)$ positions depending on the radius of the R^{3+} cations (at c.n. = 8 [7]) for the $Ca_9R(VO_4)_7$ compounds (R = RE and Y).

aged interatomic distance in the position $M(3)$ and considerably exceeds the average distances for the $M(1)$ and $M(2)$ positions. Therefore, the $M(3)$ position is occupied mainly by large cations, e.g., La^{3+}. With a decrease of the R^{3+} radius, the geometric mismatch of the $M(1)$ and $M(2)$ positions decreases, and the main part is played by the energy factor. Therefore, the occupancy of the $M(3)$ position with R^{3+} cations decreases, whereas the occupancies of the $M(1)$ and $M(2)$ positions increase. The dimensions of the polyhedra for the $M(1)$ and $M(2)$ positions are best satisfied by R cations, R = Gd, Tb, Dy, Ho, and Y, with the radii varying within 1.04–1.01 Å (at c.n. = 8) [7]. As is seen from Fig. 2, these cations occupy mainly the $M(1)$ and $M(2)$ positions almost in the same way.

In the initial $Ca_3(VO_4)_2$ structure, the $M(5)$ position is somewhat sterically hindered, because the sum of the ionic radii $r_{VI}(Ca^{2+}) + r(O^{2-}) = 2.40$ Å [7] exceeds the average ⟨Ca(5)–O⟩ distance equal to 2.30 Å [1]. The cations with a radius less than that of calcium ($r_{VI}(Ca^{2+}) = 1.00$ Å) should remove the stresses by occupying the position $M(5)$. The $M(5)$ position in the compounds $Ca_9R(VO_4)_7$ (R = RE and Y) is occupied first with Tb^{3+} ($r_{VI} = 0.923$ Å). The process is more intense the smaller the radius R^{3+}. The occupancies of positions $M(1)$ and $M(2)$ with R^{3+} cations decrease (a bell-shaped dependence in Fig. 2). It seems that the energy gain due to stress removal in the $M(5)$ position is higher than that in the case where the R^{3+} cations (R = Tb–Lu) are located in the $M(1)$ and $M(2)$ positions. However, even for Lu^{3+} ($r_{VI} = 0.848$ Å), some Lu^{3+} cations are located in the $M(1)$ and $M(2)$ positions.

It should also be emphasized that in the $Ca_9R(VO_4)_7$ compounds (R = La–Eu), the occupancy of the $M(2)$ position with R^{3+} cations is lower than the occupancy of the $M(1)$ position. This agrees with the geometric dimensions of these positions [a polyhedron for the $M(2)$ position is smaller than the polyhedron of the $M(1)$ position]. As was to be expected, the maximum difference in the occupancy of the $M(1)$ and $M(2)$ positions with R^{3+} cations is observed for the largest La^{3+} cation. For the compounds with R = Gd–Lu and Y, the $M(1)$ and $M(2)$ positions are equally (with due regard for the experimental error) occupied with R^{3+} cations.

Using the data obtained, one can choose cations–diluents for reducing the concentration quenching in the $Ca_3(VO_4)_2$-based luminescent materials [11–14]. Thus, the use of Gd^{3+} cations as diluents for Nd^{3+}

Table 4. Unit-cell parameters of the $Ca_9R(VO_4)_7$ compounds (R = RE and Y) and the number of R^{3+} cations in the structure positions

R	r_{VIII}, Å [7]	Unit-cell parameters			Number of R^{3+} cations in the position			
		a, Å	c, Å	V, Å^3	M(1)	M(2)	M(3)	M(5)
La	1.18	10.8987(5)	38.147(1)	3924.1(3)	1.6(3)	0.4(2)	4.0(2)	
Ce	1.14	10.8552(5)	38.037(1)	3881.6(3)	1.1(1)	0.3(1)	1.1(1)	
Pr	1.14	10.8808(7)	38.135(1)	3910.0(3)	2.1(2)	1.7(2)	2.2(2)	
Nd	1.12	10.8720(5)	38.121(1)	3902.2(3)	2.3(2)	1.6(2)	2.0(2)	
Sm	1.09	10.8652(5)	38.098(1)	3894.9(3)	2.7(1)	2.0(1)	1.3(2)	
Eu	1.07	10.8651(5)	38.089(1)	3894.0(3)	2.8(3)	2.3(2)	0.8(2)	
Gd	1.06	10.8631(5)	38.072(1)	3890.8(3)	3.1(1)	2.9(1)		
Tb	1.04	10.8592(5)	38.035(1)	3884.2(3)	2.7(2)	2.7(2)		0.6(1)
Dy	1.03	10.8564(5)	38.009(1)	3879.6(3)	2.7(2)	2.6(2)		0.8(1)
Ho	1.02	10.8565(5)	37.995(1)	3878.3(3)	2.6(2)	2.6(2)		0.8(1)
Y	1.015	10.8588(5)	37.995(1)	3879.9(3)	2.6(2)	2.3(2)		1.0(1)
Er	1.00	10.8554(5)	37.967(1)	3874.6(3)	2.3(1)	2.3(1)		1.33(5)
Tm	0.99	10.8550(5)	37.950(1)	3872.6(3)	1.9(1)	2.3(1)		1.79(5)
Yb	0.98	10.8564(5)	37.924(1)	3870.9(3)	1.7(1)	1.8(1)		2.54(5)
Lu	0.97	10.8566(5)	37.880(1)	3866.5(3)	1.6(1)	1.4(1)		3.01(5)

reduces the Nd^{3+} concentration mainly in the M(1) and M(2) positions but does not change the concentration in the M(3) position. The use of La^{3+} cations as diluents reduces the Nd^{3+} concentration mainly in the M(3) position.

ACKNOWLEDGMENTS

The study was supported by the Russian Foundation for Basic Research, project no. 97-03-33224a.

REFERENCES

1. R. Gopal and C. Calvo, Z. Kristallogr. **137**, 67 (1973).
2. A. A. Belik, V. A. Morozov, S. S. Khasanov, and B. I. Lazoryak, Kristallografiya **42** (5), 818 (1997) [Crystallogr. Rep. **42**, 751 (1997)].
3. V. A. Morozov, A. A. Belik, R. N. Kotov, *et al.*, Kristallografiya **45** (1), 19 (2000) [Crystallogr. Rep. **45**, 13 (2000)].
4. H. M. Reitveld, Acta Crystallogr. **22**, 151 (1967).
5. F. Izumi, in *The Rietveld Method*, Ed. by R. A. Young (Oxford Univ. Press, Oxford, 1993), Chap. 13.
6. Y.-I. Kim and F. Izumi, J. Ceram. Soc. Jpn. **102**, 401 (1994).
7. R. D. Shannon, Acta Crystallogr., Sect. B: Struct. Crystallogr. Cryst. Chem. **B32**, 751 (1976).
8. B. I. Lazoryak, L. O. Dmitrienko, and S. V. Grechkin, Zh. Neorg. Khim. **35** (5), 1095 (1990).
9. B. N. Viting, Candidate's Dissertation in Chemistry (Mosk. Gos. Univ., Moscow, 1990).
10. B. I. Lazoryak, Usp. Khim. **65** (4), 307 (1996).
11. L. H. Brixner and P. A. Flournoy, J. Electrochem. Soc. **112**, 303 (1965).
12. C.-Z. Li, W.-H. Yang, and Y.-C. Chang, Ferroelectrics **142**, 131 (1993).
13. A. A. Fotiev, V. K. Trunov, and V. D. Zhuravlev, *Vanadates of Bivalent Metals* (Nauka, Moscow, 1985), p. 269.
14. M. Ya. Khodos, I. A. Leonidov, and A. A. Fotiev, Zh. Neorg. Khim. **29** (9), 2383 (1984).

Translated by L. Man

Crystallography Reports, Vol. 45, No. 6, 2000, pp. 902–906. Translated from Kristallografiya, Vol. 45, No. 6, 2000, pp. 982–986.

STRUCTURE OF INORGANIC COMPOUNDS

Structure and Electric Conductivity of Na_3PO_4 Single Crystals

A. A. Belik*, A. B. Bykov, I. A. Verin**, A. M. Golubev***, A. K. Ivanov-Shitz*, and A. V. Nistyuk******

** Chemistry Department, Moscow State University, Vorob'evy gory, Moscow, 119899 Moscow*

*** Shubnikov Institute of Crystallography, Russian Academy of Sciences, Leninskiĭ pr. 59, Moscow, 117333 Russia*

**** Moscow State Academy of Fine Chemical Technology, Moscow, Russia*

***** Bauman State Technical University, Moscow, Russia*

Received February 17, 1999

Abstract—Single crystals of the composition Na_3PO_4 have been grown from flux. The unit-cell parameter of the cubic crystals at room temperature was refined to a value of $a = 7.424(1)$ Å; the atomic coordinates were refined within the sp. gr. *Fm*3*m*. Electric conductivity of single crystals equals $(2–4) \times 10^{-3}\ \Omega^{-1}\ cm^{-1}$ at 300°C. The electron component of conductivity is less than the ionic one by three orders of magnitude. © *2000 MAIK "Nauka/Interperiodica".*

INTRODUCTION

Sodium orthophosphate of the composition Na_3PO_4 has two polymorphic modifications: the tetragonal α-phase (sp. gr. *P*42*c* [1, 2]) existing at room temperature and the one transforming into the cubic γ-phase (sp. gr. *F*432 [3] or *Fm*3*m* [4]) at 320–330°C. The structure of the γ-modification has a simple motif; however, it is in fact rather complicated for the detailed analysis of the mutual arrangement of the structural fragments. Both types of the γ-phase structure are described in literature and characterized by considerable disorder of oxygen atoms, which seems to be associated with the rotation of tetrahedral PO_4-groups. Sodium atoms in the modification described by the sp. gr. *F*432 and phosphorus atoms in the modification described by the sp. gr. *Fm*3*m* are also disordered. All the structural models of the γ-phase were suggested on the basis of the data for polycrystal samples and are similar. They differ only by the choice of the fixed cation occupying a special position. In [3], the phosphorus atom is located at the origin, whereas in [4], a sodium cation is placed into the special position with the coordinates (1/4 1/4 1/4).

The high-temperature modification is stabilized by heterovalent substitutions, which results in a decease of the number of cations per formula unit [5] and provides the appearance of high ionic conductivity due to disorder in the Na^+ subsystem. Thus, a solid electrolyte of the composition $Na_{2.5}Zr_{0.125}PO_4$ has the conductivity $\sigma = 0.025\ \Omega^{-1}\ cm^{-1}$ at 300°C [6]. For the $Na_{3-x}(P_{1-x}S_x)O_4$ solid solutions, the conductivity increases with x and attains the value of $\sigma = 0.013\ \Omega^{-1}\ cm^{-1}$ at $x = 0.5–0.6$ and the temperature of 300°C [7].

The conductivity of pure Na_3PO_4 studied on polycrystal samples [1, 7–9] varies from 5×10^{-3} to $\sim 10^{-5}\ \Omega^{-1}\ cm^{-1}$ at 300°C. In the temperature range 300–320°C, a jump in conductivity is observed, which is associated with the $\alpha \longrightarrow \gamma$ phase transition accompanied by the change of the activation energy [1, 7, 8].

There are no data on ionic conductivity of Na_3PO_4 single crystals; therefore, at present, no sufficiently justified conclusions on the structural models of ionic transport can be made.

EXPERIMENTAL

Single crystals of the composition Na_3PO_4 were grown from flux in the $Na_2O–P_2O_5–NaF–V_2O_5$ system. Crystallization was performed in a platinum crucible at 950–750°C. X-ray spectral analysis on a JEOL JXA 8600S spectrometer showed the presence of 0.1–0.15% of V-impurity.

The samples chosen for the X-ray diffraction analysis were rolled into spheres with a diameter of 0.3–0.4 mm. The sample quality was checked by the Laue diffraction patterns and also the widths and the intensities of diffraction maxima. The experimental sets of diffraction–reflection intensities were obtained on an automatic Enraf–Nonius diffractometer (MoK_α radiation, $\theta/2\theta$ scan). The structure parameters were refined in the full matrix approximation with the use of the SHELX complex of programs [10].

Ionic conductivity was measured by the method of impedance spectroscopy in the frequency range from 5 to 5×10^5 Hz (a TESLA BM-507 impedancemeter). Prior to measurements, silver and graphite electrodes were applied to the parallel surfaces of the samples.

1063-7745/00/4506-0902$20.00 © 2000 MAIK "Nauka/Interperiodica"

The measurements were performed both on oriented and nonoriented samples on a setup described in detail elsewhere [11] in a ~10 Pa vacuum and in air in the temperature range 80–530°C. The data obtained were processes using the EQUIVCRT package of programs kindly provided by Dr. Boukamp [12].

Electron conductivity was determined by the Wagner method of blocking electrodes at 250 and 400°C. Applying the constant potential difference (0.025–0.500 V) to the electrodes, we recorded the steady-state current in the circuit for 10–30 min. The obtained current–voltage characteristics were linear at the potentials not exceeding 0.4 V; therefore, the conductivity was calculated by the Ohm formula with due regard for geometric dimensions of the single crystals studied.

RESULTS AND DISCUSSION

The Na_3PO_4 single crystals had a low stability and, being stored for several days in air, disintegrated (acquired the polycrystalline state). However, the storage life in dry atmosphere increased several dozens times. The X-ray phase analysis indicates that the single crystals grown belong to the high-temperature cubic modification.

The best single-crystal samples of Na_3PO_4 crystals were used to measure the reflection intensities with $I > 3\sigma_I$ collected within a half-sphere of the reciprocal space up to the maximum value of $\sin\theta/\lambda = 0.89$ (altogether 947 reflections). Upon averaging the crystallographically equivalent reflections ($R_{av} = 0.016$), the set contained 81 crystallographically independent reflections. The refined value of the lattice parameter is a = 7.424(1) Å, which is consistent with the lattice parameter of the modification described by the sp. gr. $Fm3m$ [7]. For the modification described by the sp. gr. $F432$, the unit cell parameter equals a = 7.512 Å.

Atomic coordinates and parameters of atomic thermal vibrations in the γ-Na_3PO_4 structure

Atom	x/a	y/b	z/c	B_{iso}/B_{eq}
P	0.000(0)	0.000(0)	0.000(0)	2.65(8)
O(1)	0.171(7)	0.113(7)	0.040(7)	8.2(8)
O(2)	0.019(6)	−0.189(6)	0.094(6)	7.3(7)
O(3)	−0.173(7)	0.096(7)	0.069(6)	8.8(8)
O(4)	−0.016(7)	−0.030(5)	−0.206(4)	4.1(5)
Na(1)	0.453(5)	0.476(7)	0.487(6)	5.5(6)
Na(2)	0.254(5)	0.262(7)	0.282(4)	2.6(4)

The systematic extinctions indicated the face-centered unit cell. Since no indications to dissymmetrization were revealed, the structure parameters were refined within the most symmetric sp. gr. $Fm3m$. In the initial model, the cations occupied the special positions, whereas two different variants of the arrangement of oxygen anions were considered. The first variant was based on the minimum crystal-lattice energy calculated by the PMC program [13]. The second variant corresponded to the known data [3, 4]. Both initial models yielded almost the same results. The final value

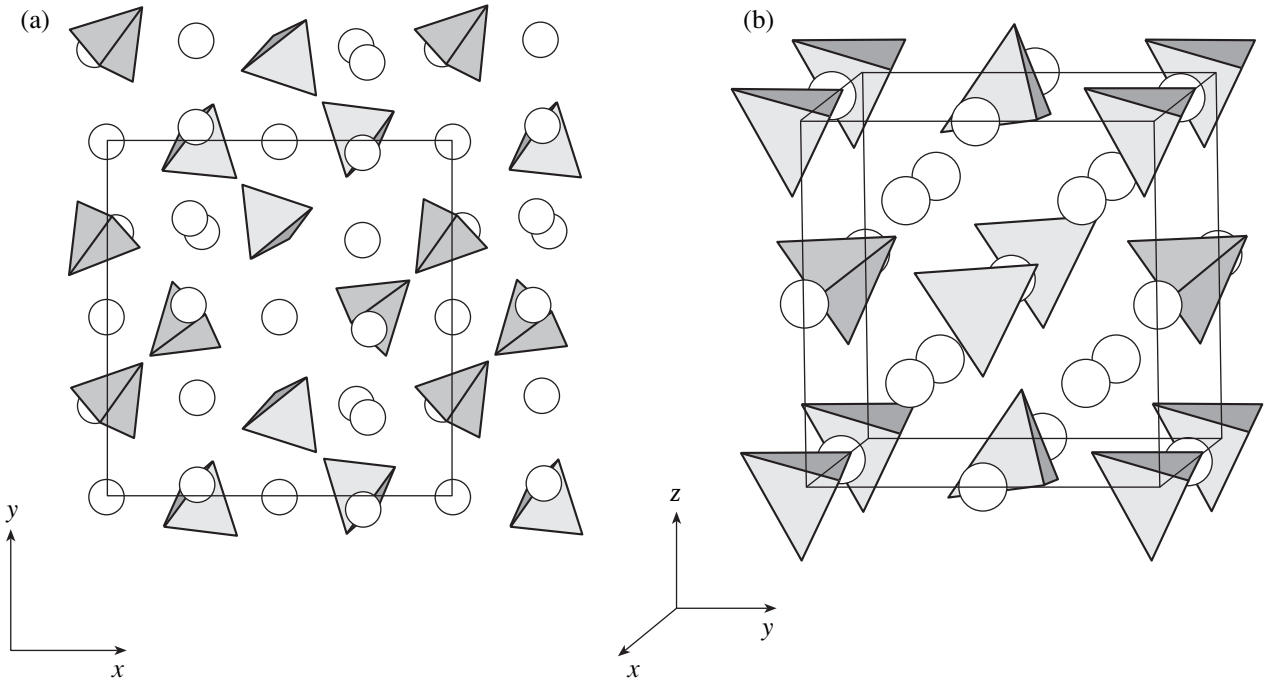

Fig. 1. (a) Arrangement of $(PO_4)^{3-}$-tetrahedra in the Na_3PO_4 structure projected onto the XY plane (sodium cations are depicted by circles) and (b) one of possible motifs of the γ-modification structure.

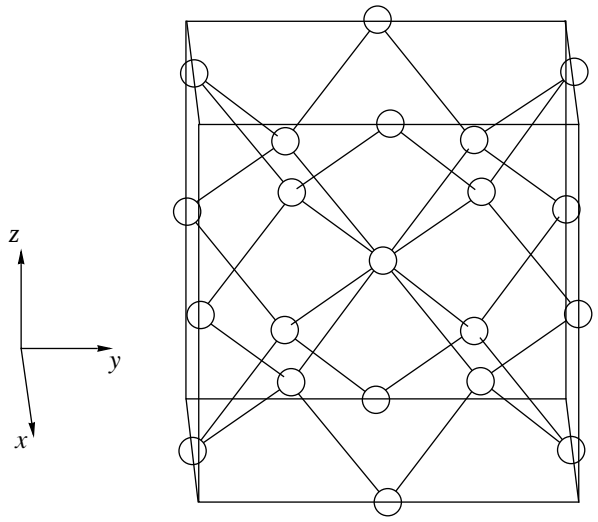

Fig. 2. Three-dimensional framework formed by sodium cations in the structure of the γ-modification Na_3PO_4.

of the *R*-factor with due regard for anisotropy of atomic thermal vibrations was 0.062. The atomic coordinates obtained are listed in table. The main interatomic distances are P–O = 1.55–1.57 Å and Na–O = 2.20–2.98 Å. The valence angles in PO_4-tetrahedra range within 108°–111°.

Thus, the structure of the γ-Na_3PO_4 crystals can be described as a cubic close packing of PO_4 anions with all the tetrahedral and octahedral voids being occupied by Na cations. Because of a high structure symmetry, the symmetry of a PO-tetrahedron is somewhat inconsistent with the octahedral symmetry of the central atom of this tetrahedron, which gives rise to disorder in the structure caused by statistical rotations of tetrahedra and an increase of their averaged symmetry to octahedral. Moreover, in order to saturate the valence strengths of oxygen anions, the tetrahedron rotations should provide necessary Na–O distances. This results in the displacements of sodium cations from their fixed

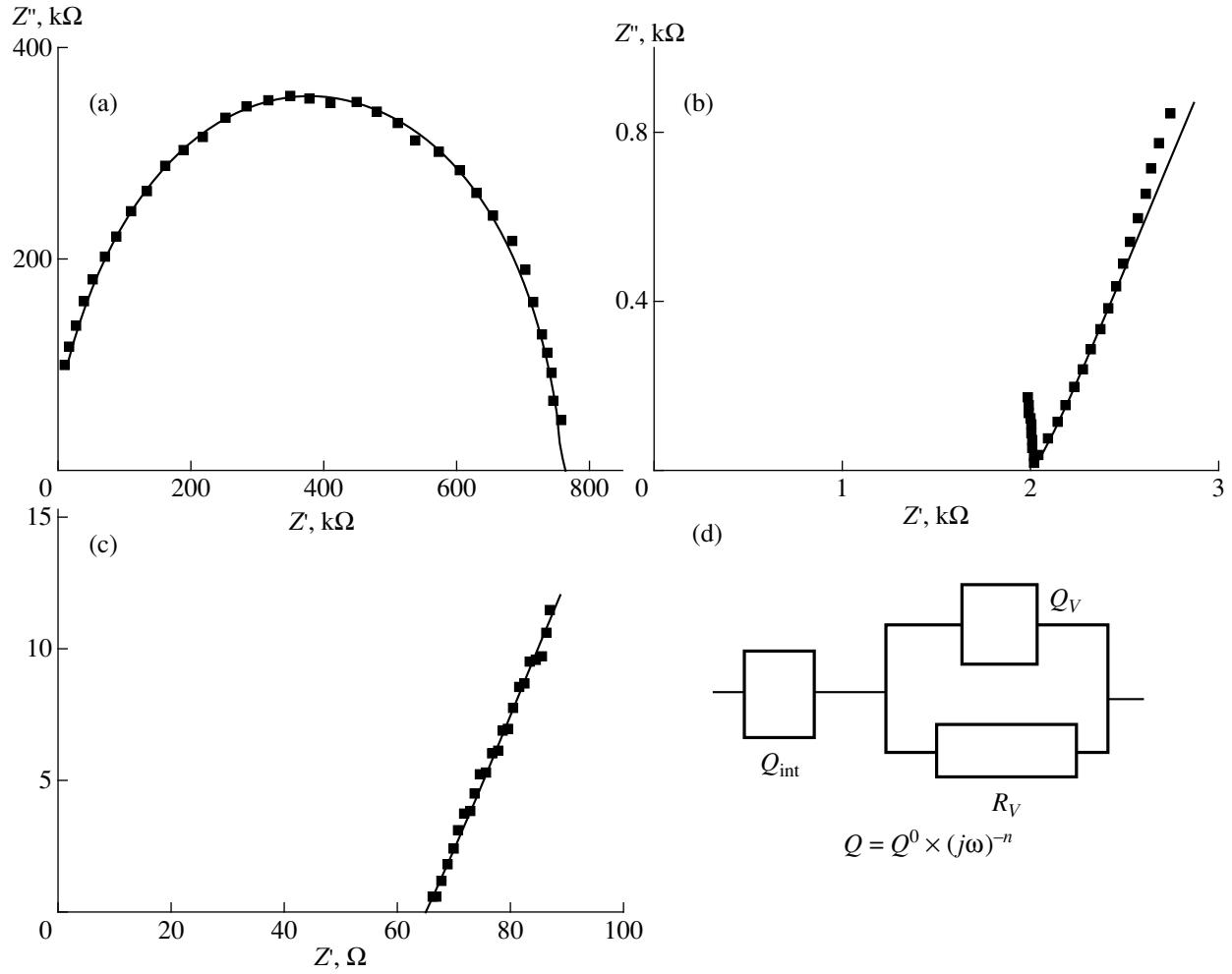

Fig. 3. Characteristic hodographs of Na_3PO_4 single crystals at three temperatures (a) 140, (b) 240, and (c) 500°C and (d) the equivalent circuit describing these hodographs. The circuit parameters: (a) $R_V = 759$ kΩ, $Q_V^0 = 6.6 \times 10^{-12}$ F, $n = 0.957$; (b) $R_V = 2.04$ kΩ, $Q_V^0 = 1.2 \times 10^{-10}$ F, $n_V = 0.958$, $Q_{int}^0 = 1.4 \times 10^{-4}$ F, $n_{int} = 0.511$; (c) $R_V = 66.4$ Ω, $Q_{int}^0 = 1.5 \times 10^{-2}$ F, $n_{int} = 0.329$.

special positions and, thus, also in additional disordering. The structure of the completely ordered low-temperature α-modification can also be described as a close packing of phosphate anions. However, in this case, the structure is "compressed" along one of the orthogonal axes, which results in the lattice distortion, which lowers the symmetry to tetragonal. The orientation of PO_4-tetrahedra is such that one of the threefold pseudoaxes is located in the *XY* plane but is not directed toward Na cations (Fig. 1a). In the γ-modification, the threefold axes of PO_4 tetrahedra are directed toward sodium cations occupying the octahedral voids. In the model suggested in [3], this axis coincides with the coordinate axis, whereas, according to [4], the tetrahedron axis should deviate from the coordinate axis. The structure refinement performed in this study also shows that the tetrahedron axis directed toward sodium cations deviates from the coordinate axis.

In the case of static disordering, the tetrahedra in the structure can be differently oriented. Figure 1b shows one of the possible variants, with the sodium cations being located in the special positions.

The crystallographic positions occupied by sodium cations form a three-dimensional lattice (Fig. 2). If this lattice has some vacancies, thermal vibrations of atoms or their heterovalent substitutions can give rise to cation hoppings, which can be facilitated by rotations of the anionic PO_4 tetrahedra according to the well-known "paddle-wheel" mechanism [14]. Thus, the Na_3PO_4 crystals have all the possibilities for transport of Na^+ ions.

To confirm the above assumptions, we measured conductivity of grown Na_3PO_4 single crystals. The characteristic experimental impedance hodographs ($Z^* = Z' + jZ''$) are shown in Figs. 3a–3c. The measurements performed with the use of various electrodes both in air and in vacuum showed no essential differences in the hodograph shape. At high temperatures, the hodographs are straight lines forming an angle with the abscissa. With a decrease of the temperature, a slightly distorted semicircumference is formed, with the center being located below the abscissa. At low temperatures, only this circumference is left. These hodographs are well described by the equivalent circuit shown in Fig. 3d. The resistor R_V relates to the bulk resistivity of the crystals associated with the ionic transport; the frequency-dependent elements $Q_V(\omega)$ and $Q_{int}(\omega)$ model the processes of electric relaxation in the crystal bulk and at the electrode/electrolyte interface. Conductivity along different directions in oriented and nonoriented samples coincided within the measurement errors.

Figure 4 shows the temperature dependences of conductivity in Na_3PO_4 crystals. It is seen that σ-values in single crystals ($2–4 \times 10^{-3}$ at 300°C) are higher than conductivity in ceramic Na_3PO_4 samples [1, 7, 8] but almost coincide with the results indicated in [9] for

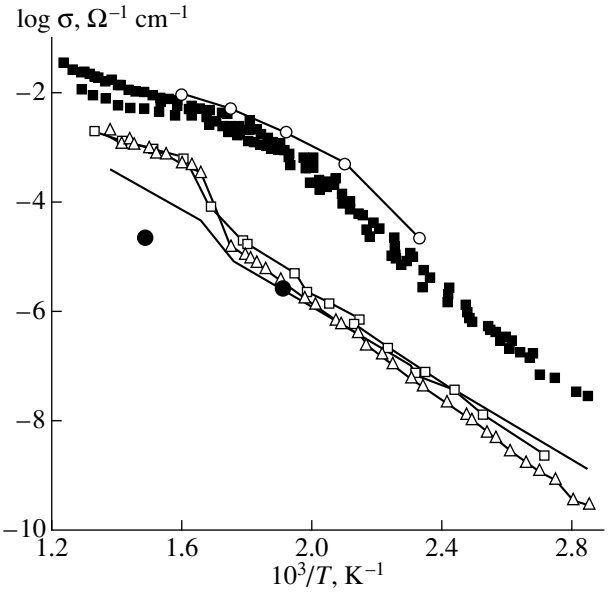

Fig. 4. Conductivity data for Na_3PO_4. Ionic conductivity (filled squares) and electronic conductivity (filled circled) are compared. Data [1] are shown by straight line; data [7], by squares; data [8], by triangles; and data [9], by circles.

doped Na_3PO_4 crystals. Despite the indication to a jump in conductivity at 300–320°C [1, 7, 8] we observed only the change in the conductivity-activation energy at ~270°C. The values of E_{act} were slightly different for different single crystal samples (which seems to be associated with crystal aging) and ranged within 0.99–1.09 and 0.33–0.41 eV at $T < 270$ and $T > 270$°C, respectively.

Electron conductivity of Na_3PO_4 single crystals is considerably lower than ionic conductivity (Fig. 4). The electron-transport number ($t_{el} = \sigma_{el}/\sigma_{tot}$) at the temperatures of 250 and 400°C amounts to 0.0016. Electron conductivity of pure Na_3PO_4 crystals can even be lower, because the value of t_{el} obtained in our study can be determined by the presence of V impurity (about 0.15%) in single crystals.

ACKNOWLEDGMENTS

This study was supported by the State Committee of the Russian Federation on Higher Education, project no. 95-0-9.3-316 and the Program in the Field of Fundamental Natural Sciences, project no. 97-9.2-33.

REFERENCES

1. J. F. Brice, B. Majidi, and H. Kessler, Mater. Res. Bull. **17**, 143 (1982).
2. E. Lissel, M. Jansen, E. Jansen, and G. Will, Z. Kristallogr. **192** (2), 233 (1990).
3. D. M. Wiench and M. Jansen, Z. Anorg. Allg. Chem. **461**, 101 (1980).

4. J. M. Newsam, A. K. Cheetham, and B. C. Tofield, Solid State Ionics **1**, 377 (1980).
5. M. Palazzi and F. Remy, Bull. Soc. Chim. Fr. **8**, 2795 (1971).
6. S. J. Milne and A. R. West, Mater. Res. Bull. **19**, 705 (1984).
7. J. T. S. Irvine and A. R. West, J. Solid State Chem. **69**, 126 (1987).
8. J. T. S. Irvine and A. R. West, Solid State Ionics **28–30**, 214 (1988).
9. A. Hooper, P. McGeehin, K. T. Harrison, and B. C. Tofield, J. Solid State Chem. **24**, 265 (1978).
10. G. M. Sheldrick, *SHELX76: Program for Crystal Structure Determination* (Cambridge Univ., Cambridge, 1976).
11. A. K. Ivanov-Shitz, N. I. Sorokin, P. P. Fedorov, and B. P. Sobolev, Fiz. Tverd. Tela (Leningrad) **25** (6), 1748 (1983) [Sov. Phys. Solid State **25**, 1007 (1983)].
12. B. A. Boukamp, Solid State Ionics **20**, 31 (1986).
13. A. V. Dzyabchenko, V. K. Bel'skiĭ, and P. M. Zorky, Kristallografiya **24** (2), 221 (1979) [Sov. Phys. Crystallogr. **24**, 127 (1979)].
14. A. Lunden, Solid State Commun. **65**, 1237 (1988).

Translated by L. Man

Crystallography Reports, Vol. 45, No. 6, 2000, pp. 907–909. Translated from Kristallografiya, Vol. 45, No. 6, 2000, pp. 987–989.

STRUCTURE OF INORGANIC COMPOUNDS

Synthesis and Crystal Structure of Rubidium Oxovanadium(V) Diphosphate

E. V. Murashova and N. N. Chudinova

Kurnakov Institute of General and Inorganic Chemistry, Russian Academy of Sciences, Leninskiĭ pr. 31, Moscow, 117907 Russia

Received June 4, 1999

Abstract—Rubidium oxovanadium(V) double diphosphate, $RbV^{V}OP_2O_7$, was synthesized and characterized for the first time by the methods of X-ray diffraction analysis. The compound was crystallized from a phosphoric acid-, Rb_2CO_3-, V_2O_5-, and ZnO- or CuO-containing melt at 290°C. The unit-cell parameters are a = 4.6820(3), b = 9.003(1), c = 16.333(2) Å, β = 94.17(1)°; sp. gr. $P2_1/c$, Z = 2. The crystal structure consists of corrugated layers of diphosphate groups and sharing-vertices vanadium(V) octahedra. One of the oxygen atoms of the oxo group belonging to the VO_6-octahedron forms no contact with the phosphorus atom and participates only the coordination of the rubidium atom. The V–O distance with the participation of the oxo atom is somewhat shortened whereas that with the participation of oxygen in the *trans* position, somewhat elongated. Rubidium atoms are located between the layers. *© 2000 MAIK "Nauka/Interperiodica".*

Vanadium(V) is readily reduced to V(IV) and then to V(III) in polyphosphoric acid melts at 200–400°C. In this temperature range, V(III)-containing compounds are formed mainly in the M_2O–V_2O_5–$P_2O_5(H_2O)$ systems, where M = Na, K, or Cs, i.e., in MVP_2O_7 (M = Na [1], K [2, 3], or Cs [4]), $Na_3VP_8O_{23}$ [5], $MVHP_3O_{10}$ (M = K [2] or Cs [6]), $K_2V_2P_8O_{24}$ [2], and $Cs_3V_3P_{12}O_{36}$ [7]. In this study, we made an attempt to prepare a double phosphate of vanadium and rubidium in the abovementioned temperature range. A mixture of Rb_2CO_3, V_2O_5, and an 85%-H_3PO_4 solution taken in the atomic ratio Rb : V : P = 7.5 : 2 : 15 was heated in a Teflon crucible for 7 days at 290°C. Under these conditions, a fine-crystalline phase was formed in the melt. To separate the crystals from the melt, the mixture was washed with water. However, this resulted not only in the dissolution of the melt but of the solid phase as well. The synthesis in the presence of Zn or Cu oxides yielded larger yellow needlelike crystals also soluble in hot water. Nevertheless they were separated from the melt by rapid washing with a large amount of cold water. Then the crystals were dried between the sheets of filter paper under a lamp. The crystals thus obtained were not hydroscopic.

The composition of the synthesized $RbVOP_2O_7$ was established from the X-ray diffraction data (Table 1). The structure was solved using the Patterson function. The atomic coordinates and thermal parameters were refined by the least squares method in the anisotropic approximation (Table 2) with the use of the SHELX97 program package [8]. Vanadium atoms are in oxidation state V, which is not characteristic of vanadium phosphates formed in this temperature range.

A $RbVOP_2O_7$ crystal has a layer structure. The diphosphate groups (two PO_4 tetrahedra share an oxygen vertex) and VO_6 octahedra form corrugated layers. Each octahedron shares five oxygen vertices with four diphosphate groups, one group sharing two vertices with the octahedron (Fig. 1). The sixth vertex of the octahedron [the O(8) atom of the oxo group] is "free" and participates only in the coordination sphere about the Rb atom. The V–O distances within octahedra vary over a wide range. The minimum V–O distance in the oxo group is 1.583(3) Å, whereas the maximum distance (to the oxygen atom in the *trans* position with

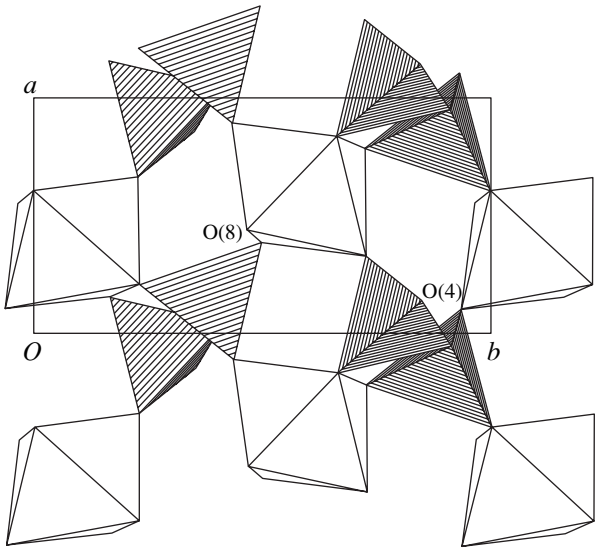

Fig. 1. A $[VOP_2O_7]^-_{2\infty}$ layer projected along the [001] direction.

1063-7745/00/4506-0907$20.00 © 2000 MAIK "Nauka/Interperiodica"

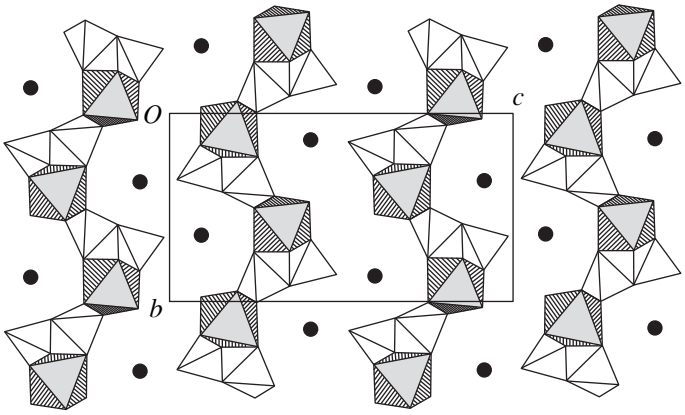

Fig. 2. $RbVOP_2O_7$ structure projected along the [100] direction.

respect to the former atom) is 2.237(3) Å. The remaining distances range from 1.866(3) to 1.938(3) Å. In the diphosphate group, the O(4) atom remains "free" and, thus, is coordinated with three Rb atoms.

The rubidium atoms are located between the layers (Fig. 2). The nearest environment of a rubidium atom consists of seven oxygen atoms. The Rb–O distances range from 2.828 to 3.166 Å. The shortest Rb–Rb distance in the layer is 4.001 Å.

In the series of compounds with the analogous formulas ($KNbOP_2O_7$ [9] and $CsNbOP_2O_7$ [10]) studied earlier and $RbVOP_2O_7$, the $RbVOP_2O_7$ and $KNbOP_2O_7$ compounds have substantially different structures. The latter compound is not a layer structure, because the oxygen atom (located in the *trans* position with respect to the niobyl oxygen atom) of the NbO_6 octahedron of one layer is shared by the diphosphate group of another layer. The $RbVOP_2O_7$ and $CsNbOP_2O_7$ structures differ mainly in the interatomic V–O and Rb–O distances, which are shorter than the Nb–O and Cs–O distances. This, in general, results in a 2-Å decrease of the parameter *c* in the $RbVOP_2O_7$ structure.

In conclusion, it should be mentioned that condensed vanadium(V) phosphates are studied insufficiently. The data were obtained mainly for vanadium(V) monophosphates of the following types: V(V)- and P(V)-containing monophosphates statistically distributed over the anionic part of the compound (for example, $NaP_{0.34}V_{0.66}O_3$ [11]), heteropolycompounds of composition $[CN_3H_6]_8HPV_{14}O_{42} \cdot 7H_2O$ [12], and vanadium(V) monophosphates (for example, $Na_2(VO_2)PO_4$ and $K_2(VO_2)PO_4$ [13]). Some phos-

Table 1. Main crystallographic parameters, details of the X-ray data collection and the refinement of the $RbVOP_2O_7$ structure

System	Monoclinic	System	Monoclinic
a, Å	4.6820(3)	Diffractometer*	IPDS (Stoe)
b, Å	9.003(1)	Scanning mode	ω/2θ
c, Å	16.333(2)	N_a^{**}	5959
β, deg	94.17(1)	N_i^{**}	1533
Sp. gr.	$P2_1/c$	N_o^{**}	1186
Z	2	N_p^{**}	109
V, Å^3	686.6(1)	R_{int}	0.043
ρ_{calc}, g/cm^3	3.157	*wR2*	0.083
μ, mm^{-1}	8.96	*R*1	0.035
$2\theta_{max}$, deg	56	*Gof*	0.94
Crystal dimensions, mm	$0.05 \times 0.05 \times 0.2$		

* λMoK_α; graphite monochromator; ψ-scan, absorption correction was applied to the X-ray data set.

** N_a is the number of measured reflections, N_i is the number of independent reflections, N_o is the number of independent reflections with $I > 2\sigma(I)$, and N_p is the number of the parameters to be refined.

Table 2. Atomic coordinates and thermal parameters in the $RbVOP_2O_7$ structure

Atom	*x/a*	*y/b*	*z/c*	B_{eq}, Å^2	Atom	*x/a*	*y/b*	*z/c*	B_{eq}, Å^2
Rb	0.4041(1)	0.64103(6)	0.08860(3)	2.06(1)	O(3)	0.3347(8)	0.2268(3)	0.1498(2)	1.42(5)
V	0.4076(2)	0.5688(1)	0.33873(5)	0.95(1)	O(4)	0.1436(8)	0.3490(3)	0.0170(2)	1.65(6)
P(1)	0.0740(3)	0.2817(1)	0.0957(1)	0.91(2)	O(5)	0.1062(8)	0.4354(3)	0.3047(2)	1.47(5)
P(2)	−0.1402(3)	0.3884(1)	0.2442(1)	0.90(2)	O(6)	−0.3914(8)	0.4966(3)	0.2471(2)	1.33(5)
O(1)	−0.1603(7)	0.1637(3)	0.0877(2)	1.26(5)	O(7)	−0.2099(7)	0.2274(3)	0.2544(2)	1.09(5)
O(2)	−0.0464(8)	0.4138(3)	0.1520(2)	1.17(5)	O(8)	0.5582(8)	0.4651(3)	0.4073(2)	1.63(6)

phates containing both V(V) and V(IV) (for example, $Na_2(P_2V_3O_{13})$ [14]) were also described in the literature. A diphosphate of the composition $K(V_3P_4O_{17})$ was prepared from condensed vanadium phosphates [15]; however, this compound also includes V(V) and V(IV). Therefore, rubidium oxovanadium(V) diphosphate of the composition $RbVOP_2O_7$ synthesized and described above is the first representative of condensed vanadium phosphates containing vanadium in oxidation state V.

ACKNOWLEDGMENTS

We are grateful to Prof. R. Glaum (Justus-Liebig University of Giessen, Germany) for providing us with an IPDS (Stoe) diffractometer for collecting X-ray diffraction data for a $RbVOP_2O_7$ single crystal and N.Yu. Anisimova for useful discussion.

This study was supported by the Russian Foundation for Basic Research, project no. 98-03-32695.

REFERENCES

1. Y. P. Wang, K. H. Lii, and S. L. Wang, Acta Crystallogr., Sect. C: Cryst. Struct. Commun. **C45**, 1417 (1989).
2. A. V. Lavrov, M. Ya. Voĭtenkov, and E. G. Tselebrovskaya, Izv. Akad. Nauk SSSR, Neorg. Mater. **17** (1), 99 (1981).
3. L. Benhamada, A. Grandin, M. M. Borel, *et al.*, Acta Crystallogr., Sect. C: Cryst. Struct. Commun. **C47**, 424 (1991).
4. Y. P. Wang and K. H. Lii, Acta Crystallogr., Sect. C: Cryst. Struct. Commun. **C45**, 1210 (1989).
5. N. N. Chudinova, E. V. Murashova, and N. B. Karmanovskaya, Zh. Neorg. Khim. **39** (11), 1769 (1994).
6. B. Klinkert and M. Jansen, Z. Anorg. Allg. Chem. **567**, 77 (1988).
7. A. V. Lavrov, V. P. Nikolaev, G. G. Sadikov, and M. Ya. Voĭtenkov, Dokl. Akad. Nauk SSSR **259** (1), 103 (1981) [Sov. Phys. Dokl. **26**, 631 (1981)].
8. G. M. Sheldrick, *SHELX97: Program for the Solution and Refinement of Crystal Structures* (Univ. of Göttingen, Germany, 1997).
9. S. A. Linde, Yu. E. Gorbunova, A. V. Lavrov, and I. V. Tananaev, Dokl. Akad. Nauk SSSR **250** (1), 96 (1980) [Sov. Phys. Dokl. **25**, 4 (1980)].
10. V. P. Nikolaev, G. G. Sadikov, A. V. Lavrov, and M. A. Poraĭ-Koshits, Dokl. Akad. Nauk SSSR **264** (4), 859 (1982) [Sov. Phys. Dokl. **27**, 428 (1982)].
11. K. C. Idler, C. Calvo, and H. N. Ng, J. Solid State Chem. **25**, 285 (1978).
12. M. S. Pope, *Heteropoly and Isopoly Oxometalates* (Springer-Verlag, Berlin, 1983; Nauka, Novosibirsk, 1990).
13. V. C. Korthuis, R. D. Hoffmann, J. F. Huang, and A. W. Sleight, Chem. Mater. **5**, 206 (1993).
14. A. Haddad and T. Jouini, J. Solid State Chem. **112**, 218 (1994).
15. L. Benhamada, A. Grandin, M. M. Borel, *et al.*, J. Solid State Chem. **97**, 131 (1992).

Translated by T. Safonova

Crystallography Reports, Vol. 45, No. 6, 2000, pp. 910–915. Translated from Kristallografiya, Vol. 45, No. 6, 2000, pp. 990–995.

STRUCTURE OF INORGANIC COMPOUNDS

Morphotropic Series of $Ln Sc_3(BO_3)_4$ Compounds

G. M. Kuz'micheva*, V. B. Rybakov, S. A. Kutovoĭ***, O. V. Kuz'min***, and V. L. Panyutin*****

** Lomonosov State Academy of Fine Chemical Technology, pr. Vernadskogo 86, Moscow, 117571 Russia*

E-mail: galkuz@orc.ru

*** Department of Chemistry, Moscow State University, Moscow, 119899 Russia*

**** Firn Research and Production Association, Krasnodar, Russia*

Received April 6, 1999

Abstract—Czochralski-grown $LnSc_3(BO_3)_4$ single crystals (*Ln* = La, Ce, Pr, Nd, or Tb) were studied by the methods of X-ray diffraction analysis. All the crystals, except for *Ln* = Tb, belong to the huntite family. The crystals with *Ln* = La, Ce are monoclinic, sp. gr. *C*2/*c*, $a = 7.727(1)$ Å, $b = 9.840(1)$ Å, $c = 12.046(3)$ Å, $\beta = 105.42(2)°$ and $a = 7.721(3)$ Å, $b = 9.834(3)$ Å, $c = 12.041(3)$ Å, $\beta = 105.39(3)°$, respectively. The $PrSc_3(BO_3)_4$ crystals were grown from the melt of the composition $(Pr_{1.1}Sc_{2.9})(BO_3)_4$. They are also monoclinic, sp. gr. *C*2, $a = 7.7138(6)$ Å, $b = 9.8347(5)$ Å, $c = 12.032(2)$ Å, $\beta = 105.387(7)°$. Crystals grown from the charge of the composition $(Pr_{0.99}Nd_{0.11}Sc_{2.9})(BO_3)_4$ are isostructural to $NdSc_3(BO_3)_4$ (sp. gr. *P*321 or *P*3). The unit-cell parameters of the latter crystals are twice as large ($a = 9.779(2) \times 2$ Å, $c = 7.943(1) \times 2$ Å) as those of huntite (sp. gr. *R*32), unlike the crystals grown from the melt of the composition $(Pr_{1.25}Sc_{2.75})(BO_3)_4$ (sp. gr. *P*321, $a = 9.7829(5)$ Å, $c = 7.9428(5)$ Å). The structure of the $(Tb_{0.25}Sc_{0.75})BO_3$ crystal ($a = 4.773(5)$ Å, $c = 15.48(1)$ Å) can be derived from the calcite-type structure ($CaCO_3$) with the statistical distribution of Tb and Sc atoms over two crystallographically independent positions in the space group $R\bar{3}$. © *2000 MAIK "Nauka/Interperiodica".*

INTRODUCTION

A sharp change in the crystal structure in the regular series of chemical compounds with retention of the quantitative ratios between the structural units is called morphotropy. In this work, we studied a morphotropic series of the Czochralski-grown $LnSc_3(BO_3)_4$ compounds of the huntite family.

In the structure of huntite ($CaMg_3(CO_3)_4$, sp. gr. *R*32; a_{hex} and c_{hex}), Ca atoms are located in the centers of distorted trigonal prisms, whose upper and lower bases are somewhat misoriented (not quite parallel); Mg atoms are located in the centers of distorted octahedra; and B atoms are surrounded with oxygen atoms occupying the vertices of equilateral [B(1)] and isosceles [B(2)] triangles (Fig. 1). In the structures of the huntite family, a huntite-type sublattice with the sp. gr. *R*32 and the parameters a_{hex} and c_{hex} can be singled out [1].

The data on the crystal structures of rare-earth scandium borates are scarce, and the information on their symmetry is sometimes contradictory. According to the results of the X-ray diffraction analysis, Czochralski-grown $LaSc_3(BO_3)_4$ single crystals belong to the monoclinic system, sp. gr. *C*2/*c* [2], which is in agreement with the data reported in [3]. The comparison of the X-ray goniometric data for rare-earth scandium and aluminum borates [4], a huntite-like structure (sp. gr. *R*32), was proposed for the polycrystalline $LnSc_3(BO_3)_4$ compounds (*Ln* = Ce, Pr, Nd, or Sm). However, X-ray diffraction study of the crystal structure of Czochralski-grown $NdSc_3(BO_3)_4$ crystals showed that these crystals possess a superstructure with respect to the huntite structure (the sp. gr. *P*321 or *P*3 with the doubled unit-cell parameters) [5]. The single-crystal $(La_{0.5}Nd_{0.5})Sc_3(BO_3)_4$ solid solution, also grown by the Czochralski method, can crystallize in the space groups *R*32 or *C*2/*c* depending on the seed type [6]. It was suggested [7–9] that the $LnSc_3(BO_3)_4$ single crystals (*Ln* = Gd or Y), grown from flux belong to the sp. gr. *R*32. X-ray diffraction study of the Czochralski-grown single crystals $(Ce_{1-x}Gd_x)Sc_3(BO_3)_4$ solid solutions ($x = 0.2$ or 0.3), provided the establishment of the space group and the unit-cell parameters (*P*321, $a = a_{hex}$, $c = c_{hex}$) [10].

The determination of the symmetry and structures of rare-earth scandium borates of the huntite family has acquired a great importance, because rare-earth scandium borates are promising materials for laser matrices and nonlinear optics. Different symmetries of these crystals and their possibility to change the space group with the loss (or acquisition) of a center of symmetry is directly associated with the loss (or acquisition) of nonlinear-optical properties by a laser crystal. Thus, the creation of efficient actively nonlinear media based on these compounds is impossible without the establishment of structural transitions in these compounds.

1063-7745/00/4506-0910$20.00 © 2000 MAIK "Nauka/Interperiodica"

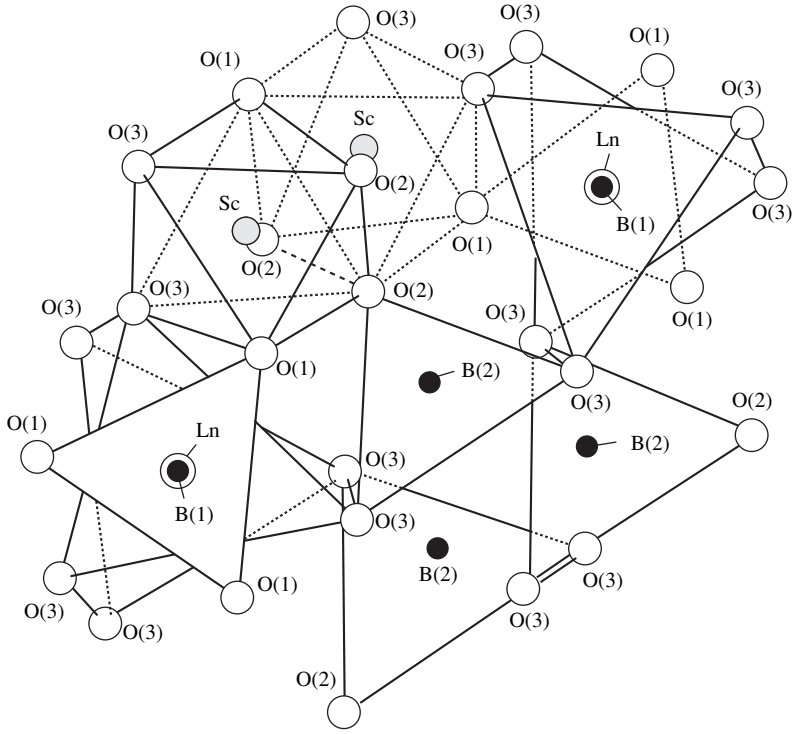

Fig. 1. Connection of the polyhedra in the structure of the huntite type (sp. gr. *R*32).

All the aforesaid motivated our study of these compounds.

EXPERIMENTAL

Rare-earth scandium borates were grown from melts on a Kristall-3 apparatus according to a procedure reported in [11]. X-ray diffraction studies of powdered specimens were carried out on a DRON-2.0 diffractometer ($\lambda Cu K_\alpha$ radiation, planar graphite monochromator, angular range $2° < 2\theta < 75°$, scan rate 1 °/min, diagram-tape velocity 60 mm/h) and on an HZG-4A diffractometer ($\lambda Cu K_\alpha$ radiation). The qualitative phase analysis of the specimens was performed with the use of the automated PDF-2 data base. No admixture phases were found within the accuracy of X-ray phase analysis (< 2 wt %). The unit-cell parameters of the powdered single crystals were refined by the least squares method.

The X-ray diffraction data were collected from single crystals ground to spheres (0.5 mm in diameter) on an automated four-circle CAD-4 diffractometer ($Mo K_\alpha$ radiation, graphite monochromator, ω–θ scanning technique, scanning range for diffraction reflections $1.0 + 0.34\tan\theta$, scan rate was 1–7 °/min) at room temperature. The unit-cell parameters were determined with the aid of automated indexing of 20–25 reflections with the interplanar spacings $d > 0.874$ Å.

The experimental data were corrected for the Lorentz and polarization factors and anomalous scattering, the absorption corrections were introduced by the North–Phillips method, and the correction for isotropic extinction was introduced by the Zachariasen method.

The crystal structures were refined by the full-matrix least squares method with the use of anisotropic thermal parameters for almost all the atoms. All the computations were carried out by the SHELXL97 program package. For all single crystal specimens, we collected X-ray data and performed the computations using the same procedures. In the computations, we used the atomic scattering curves for neutral atoms.

Both single crystals and polycrystalline specimens were tested for possible asynchronous generation of the second harmonic. The characteristics of the laser used were as follows: the lasing wavelength 1.064 μm, the pulse repetition frequency 10 Hz, the pulse duration 18 ns, and the radiation power density in the pulse 20 MW/cm^2.

RESULTS AND DISCUSSION

Indexing of the X-ray diffraction patterns obtained from a powdered specimen of blend obtained from the charge of the composition $TbSc_3(BO_3)_4$ showed that the crystal under study had a hexagonal unit cell similar to that of $ScBO_3$ [2] and, consequently, the $(Tb,Sc)BO_3$

Table 1. Crystallographic data and details of X-ray diffraction study

Characteristic	$(Tb,Sc)BO_3$	$PrSc_3(BO_3)_4$	$(Pr,Nd)Sc_3(BO_3)_4$
Sp. gr.	$R\bar{3}$	$C2$	$P321$ or $P3$
a, Å	4.773(5)	7.7138(6)	$9.779(2) \times 2$
b, Å		9.8347(5)	
c, Å	15.48(1)	12.032(2)	$7.943(1) \times 2$
β, deg		105.387(7)	
V, Å^3	305.4(8)	880.1(1)	$657.9(2) \times 8$
d_{calc}, g/cm^3	4.32	3.86	3.87
$\mu(MoK_\alpha)$, cm^{-1}	110.5	77.25	77.5
$\sin\theta/\lambda_{max}$, Å^{-1}	1.078	0.903	0.804
Total number of reflections	721	2720*	1937**
Number of reflections with $I > 2\sigma(I)$	581	2571*	1546**
R_{hkl}/R_w, %	5.15/6.09	3.06/7.56*	7.7/10.3**

* Computations were made within the sp. gr. $C2/c$.

** Computations were made for the sublattice of the sp. gr. $P321$.

composition. X-ray diffraction study of a single crystal on an automated diffractometer revealed some additional $h\bar{h}0l$-type reflections with $l \neq 2n$. These reflections are allowed in the sp. gr. $R\bar{3}$ and $R3$ but are forbidden in the sp. gr. $R\bar{3}c$, in which $ScBO_3$ (the calcite type $CaCO_3$) crystallizes. No generation of the second harmonic was observed in the crystals under study, which indicates the centrosymmetric sp. gr. $R\bar{3}$.

The details of the X-ray diffraction study are given in Table 1. The atomic coordinates and thermal parameters are listed in Table 2.

By varying the mixed f curves for Tb and Sc, the lowest R factor was obtained for the composition $(Tb_{0.25}Sc_{0.75})BO_3$, which is close to the initial charge composition. In the transition from the $ScBO_3$ (r_{Sc} = 0.75 Å structure, r is the ionic radius of Sc at the coordination number of 6 [13]) to the $(Tb_{0.25}Sc_{0.75})BO_3$ structure (r_{Tb} = 0.92 Å), the Sc position is split into two positions with the lower symmetry and larger unit-cell parameters: a = 4.748(1) Å, c = 15.262(2) Å for $ScBO_3$ and a = 4.773(5) Å, c = 15.48(1) Å for $(Tb,Sc)BO_3$ (Fig. 2). In the latter structure, (Tb,Sc)(1) and (Tb,Sc)(2) "atoms" occupy the centers of regular octahedra (the (Tb,Sc)–O distances equal to 2.141(2) and 2.139(2) Å, respectively), whereas B atoms occupy the centers of regular planar triangles (the B–O equals 1.377(2) Å).

Table 2. Coordinates of the basis atoms and thermal parameters (Å$^2 \times 10^3$) for the $(Tb,Sc)BO_3$ structure

Atom	x/a	y/b	z/c	U_{eq}
(Tb,Sc)(1)	0	0	0	7.9(2)
(Tb,Sc)(2)	0	0	0.5	7.9(2)
B(1)	0	0	0.2497(8)	4.2(6)
O(1)	0.7116(2)	0.0001(1)	0.2498(3)	6.2(2)

Unfortunately, the refinement of the position occupancies provided no determination of the differences in the compositions of various crystallographic positions, because the R factor remained almost the same irrespective of the types of the f curves used. In other words, the structure is well described within the sp. gr. $R\bar{3}c$. It can be assumed that the observed symmetry violation is caused by partial cation ordering over the crystallographic positions of the structure. A similar situation was also observed for the $LaSc_3(BO_3)_4$: Cr crystals [2]. Thus, for the chromium-activated crystals, the monoclinic symmetry of the nominally pure crystal is changed to the triclinic system because of partial ordering of chromium ions over the octahedral positions in the structure.

An increase in the radius of a rare-earth element or its concentration should lead to splitting of the oxygen positions and complete ordering of the *Ln* and Sc atoms in the positions accompanied by a change of the coordination-polyhedron symmetries and, consequently, the symmetry of the crystal. In this case, the coordination environment of the Sc atoms should remain octahedral (the angle of the mutual rotation of the triangular bases is $\varphi = 60°$) or distorted octahedral ($\varphi \neq 60°$), which is most typical of Sc atoms, whereas the changes in the coordination polyhedra should be observed, first and foremost, for the *Ln* atoms ($r_{Ln} > r_{Sc}$). The distortion of an octahedron is most probably associated with a decrease in the φ angle ($0° < \varphi \ll 60°$), i.e., with its transformation into a trigonal prism with a larger volume; moreover, it is well known that the rare-earth ele-

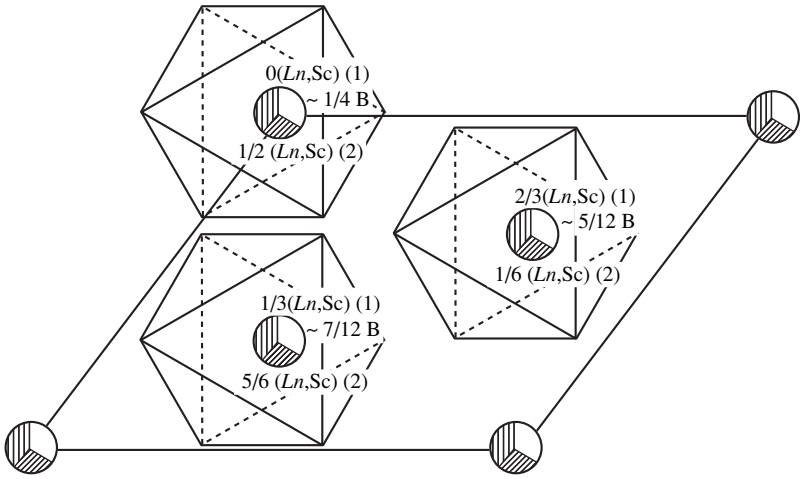

Fig. 2. Coordination polyhedra in the (Tb,Sc)BO_3 structure (sp. gr. $R\bar{3}$).

ments of the first half of the series tend to be located in the trigonal-prism-based coordination polyhedra [14]. A combination of a trigonal prism and an octahedron is characteristic of borates of the huntite family.

Actually, the single-crystal solid solutions of the composition (Ce,Gd)$Sc_3(BO_3)_4$ (r_{Gd} = 0.94 Å, r_{Ce} = 1.01 Å) crystallize in the sp. gr. *P*321 and have the structures derived from the huntite structure [11]. Compared to the latter (the sp. gr. *R*32), the structure of (Ce,Gd)$Sc_3(BO_3)_4$ has twice the number of the crystallographic positions occupied by atoms with the retention of the same unit-cell parameters ($a = a_{hex}$, $c = c_{hex}$). The (Ce,Gd)(1) and (Ce,Gd)(2) "atoms" occupy the centers of distorted trigonal prisms ($\varphi \approx 15°$), whereas Sc(1) and Sc(2) atoms occupy the centers of distorted octahedra, B(1) and B(2) atoms occupy the centers of equilateral triangles, and B(3) and B(4) atoms occupy the centers of isosceles and scalene triangles, respectively. In the cases of the ratios Ce : Gd = 0.8 : 0.2 or 0.7 : 0.3, a superstructure is formed ($a = c_{hex}$, $b = b_{hex}$, $c = 2a_{hex}\cos 30°$, $\beta \sim 90°$, sp. gr. *A*2), which is not observed in the case of Ce : Gd ≈ 0.68 : 0.32 [1].

The $NdSc_3(BO_3)_4$ compound (r_{Nd} = 0.98 Å) has a superstructure with respect to the huntite-type structure with the doubled unit-cell parameters $a = 9.775(1) \times 2$ Å, $c = 7.930(2) \times 2$ Å [1], sp. gr. *P*321 or *P*3 [5]. In the disordered $NdSc_3(BO_3)_4$ structure, the atomic positions (primarily, the positions occupied by the oxygen atoms) are weakly displaced with respect to the positions in the $NdGa_3(BO_3)_4$ huntite-type structure (sp. gr. *R*32) with a smaller unit-cell volume and a higher symmetry.

The $PrSc_3(BO_3)_4$ single crystal (r_{Pr} = 0.99 Å), grown from a charge of the composition $(Pr_{1.1}Sc_{2.9})(BO_3)_4$, belongs to the monoclinic system (Table 1). The systematic-absence conditions for the overwhelming majority of reflections indicated the space group *C*2/*c* or *Cc* ($h + k = 2n$ for *hkl*; $h = 2n$, $l = 2n$ for *h*0*l*; $h = 2n$ for *h*00). However, a small number of additional *h*0*l* reflections with $l = 2n - 1$ and $I \geq 3\sigma(I)$, characteristic of the sp. gr. *C*2/*m*, *C*2, or *Cm*, were found. For these crystals, the asynchronous generation of the second harmonic indicated a noncentrosymmetric structure (most probably described by the space group *C*2, a subgroup of *C*2/*c*). Since the number of additional reflections was small, we refined the crystal structure within the sp. gr. *C*2/*c*. The positional and the thermal parameters of the structure are listed in Table 3.

In the $PrSc_3(BO_3)_4$ structure, Pr atoms occupy the centers of distorted trigonal prisms ($\varphi \approx 10°$; Pr–O, 2.434–2.456(2) Å); Sc(1) and Sc(2) atoms are located in distorted octahedra (Sc(1)–O, 2.062–2.139(2) Å; Sc(2)–O, 2.047–2.132(2) Å); and B(1) and B(2) atoms are surrounded with oxygen atoms located at the vertices of scalene triangles (Fig. 3) (B–O, 1.368–1.380(3) Å; O–B–O, 117.2–123.1(2)°).

Table 3. Coordinates of the basis atoms and thermal parameters ($Å^2 \times 10^3$) for the $PrSc_3(BO_3)_4$ structure (sp. gr. *C*2/*c*)

Atom	*x/a*	*y/b*	*z/c*	U_{eq}
Pr	0	0.0343(1)	0.250	7.1(1)
Sc(1)	0	0.5733(1)	0.250	4.1(1)
Sc(2)	0.0476(1)	0.2500(1)	0.5251(1)	4.3(1)
B(1)	0.2025(3)	0.3034(2)	0.2261(2)	5.3(6)
B(2)	0.2457(3)	0.0247(2)	–0.0004(2)	6.2(6)
O(1)	0.2035(2)	0.5581(2)	0.7398(1)	9.5(5)
O(2)	0.2472(2)	0.1155(2)	0.4951(2)	6.8(5)
O(3)	0.0688(2)	0.2354(2)	0.1484(1)	8.6(5)
O(4)	0.3880(2)	0.0951(2)	0.0682(1)	6.7(5)
O(5)	0.3391(2)	0.2282(2)	0.2947(1)	11.3(3)
O(6)	0.4025(2)	0.4107(2)	0.0686(1)	7.2(5)

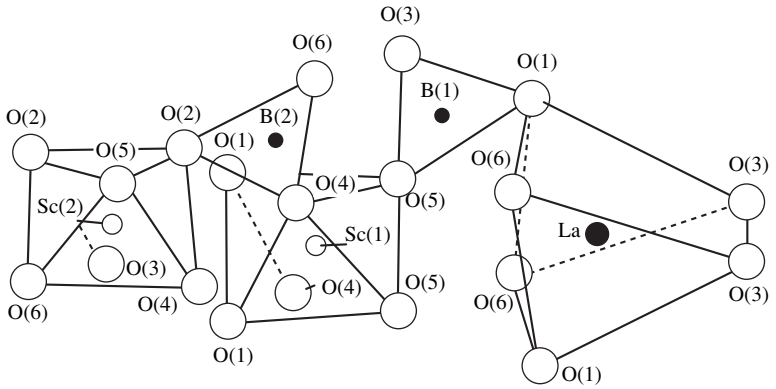

Fig. 3. Connection of the polyhedra in the $LaSc_3(BO_3)_4$ structure (sp. gr. *C*2/*c*).

However, single crystals grown from the charge of composition $(Pr_{1.25}Sc_{2.75})(BO_3)_4$ are isostructural to $(Ce,Gd)Sc_3(BO_3)_4$ (a = 9.7829(5) Å, c = 7.9428(5) Å, the sp. gr. *P*321), which may be caused by redistribution of the Pr and Sc cations over the crystallographic positions of the structure accompanied by the change of the crystal symmetry. Some more detailed studies are necessary to prove the existence of the monoclinic and triclinic polymorphous modifications of $PrSc_3(BO_3)_4$ crystals.

The addition of a small amount of Nd to $PrSc_3(BO_3)_4$ yielded the charge of the composition $(Pr_{0.99}Nd_{0.11}Sc_{2.9})(BO_3)_4$, provided the formation of the $(Pr,Nd)Sc_3(BO_3)_4$ solid solution. This solid solution belongs to the trigonal system (sp. gr. *P*321) with a superstructure of the $NdSc_3(BO_3)_4$ type and the doubled unit-cell parameters (Table 1). Unfortunately, we failed to determine the Pr : Nd ratio in the crystal by the X-ray diffraction analysis.

Similar to the isostructural $LaSc_3(BO_3)_4$ crystals (r_{Ce} = 1.03 Å) with the parameters of the monoclinic unit cell a = 7.727(1) Å, b = 9.840(1) Å, c = 12.046(3) Å, β = 105.42(2)° [2], the $CeSc_3(BO_3)_4$ crystals (r_{Ce} = 1.01 Å) belong to the centrosymmetric monoclinic (space group *C*2/*c*) with the unit-cell parameters a = 7.721(3) Å, b = 9.834(3) Å, c = 12.041(3) Å, β = 105.39(3)°.

In contrast to the crystals of $LaSc_3(BO_3)_4$ and $CeSc_3(BO_3)_4$, the loss of the center of symmetry observed in $PrSc_3(BO_3)_4$ crystals is caused by small displacements of oxygen atoms in comparison with their positions in the centrosymmetric $LaSc_3(BO_3)_4$ structure (Fig. 3). These displacements may be caused by the vacancies in the boron positions and the easy gliding of the oxygen planes with respect to each other [1]. The above behavior of the $PrSc_3(BO_3)_4$ crystal structure indicates that it is on the verge of instability—the partial replacement of Pr or Sc atoms by smaller or larger size atoms should lead to the formation of structures of the $LaSc_3(BO_3)_4$ (sp. gr. *C*2/*c*), $(Ce,Gd)Sc_3(BO_3)_4$ (sp. gr. *P*321), or $NdSc_3(BO_3)_4$ (a superstructure, sp. gr. *P*321 or *P*3) types. This assumption is indirectly supported by the fact that, depending on the growth conditions, the $(La_{0.5}Nd_{0.5})Sc_3(BO_3)_4$ solid solution, in which the weighted average radius of the cation in the *Ln* position ($r_{La,\,Nd}$ ~ 1.00 Å) is close to the Pr radius, can crystallize in both trigonal and monoclinic systems [6].

Our study shows that the Czochralski-grown rare-earth scandium borate crystals in the series of rare-earth elements are transformed with an increase of the radius of the rare-earth element: $Sc_4(BO_3)_4$ (sp. gr. $R\bar{3}c$) → $(Tb,Sc)_2(Sc,Tb)_2(BO_3)_4$ (sp. gr. $R\bar{3}$) → $LnSc_3(BO_3)_4$ (sp. gr. *P*321) → $NdSc_3(BO_3)_4$ (superstructure, sp. gr. *P*321 or *P*3) → $PrSc_3(BO_3)_4$ (sp. gr. *C*2) → $CeSc_3(BO_3)_4$ (sp. gr. *C*2/*c*) → $LaSc_3(BO_3)_4$ (sp. gr. *C*2/*c*).

The $LnM_3(BO_3)_4$ crystal structures (*M* = Al, Ga, Cr, or Fe) also belong to the huntite family (the structure classification can be found in reviews [15–18]). The $LnGa_3(BO_3)_4$ and $LnFe_3(BO_3)_4$ compounds crystallize in the huntite structure type (sp. gr. *R*32). The $LnCr_3(BO_3)_4$ compounds form a morphotropic series. Thus, the compound with *Ln* = Nd belongs to the monoclinic system (sp. gr. *C*2/*c*), whereas the compounds with *Ln* = Sm or Gd belong to the trigonal system (sp. gr. *R*32). The structures of the $LnAl_3(BO_3)_4$ compounds are more diversified, although they differ from $LnSc_3(BO_3)_4$, structures with characteristic disorder [1]. The $LnAl_3(BO_3)_4$ compounds with *Ln* = Pr–Lu are isostructural to huntite (sp. gr. *R*32). In addition, the polymorphs or the polytypes described by the space group *C*2/*c* are known for the compounds with *Ln* = Pr–Eu, whereas polymorphs or polytypes described by the space groups *C*2/*c* and *C*2 are known for the compounds with *Ln* = Pr and Gd (the structures of aluminum and scandium borates described by the space group *C*2 are different). Probably, such structural behavior of rare-earth borates depends on the size ratio of *Ln* and *M* atoms and the growth conditions.

CONCLUSIONS

It was found that the Czochralski-grown $LnSc_3(BO_3)_4$ compounds with *Ln* = La, Ce, Pr, Nd, or Tb form a morphotropic series. The $LaSc_3(BO_3)_4$ and $CeSc_3(BO_3)_4$ compounds are isostructural and have centrosymmetric monoclinic structures, unlike the noncentrosymmetric monoclinic $PrSc_3(BO_3)_4$ crystal, whose structure is almost unstable. The partial replacement of the praseodymium by the neodymium and an increase in the praseodymium concentration in the melt change the monoclinic symmetry to trigonal either with the doubling of the unit-cell parameters in comparison with the huntite structure (the structure of the $NdSc_3(BO_3)_4$ type) or without parameter doubling (the structure of the $(Ce,Gd)Sc_3(BO_3)_4$ type). The $(Tb,Sc)BO_3$ structure has no trigonal prisms typical of *Ln* atoms in the structures of the huntite family. This fact may be attributed to the tendency of the rare-earth elements of the second half of the series to be located in octahedra.

Apparently, the morphotropic series is formed due to the "rigidity" of the B-polyhedra, which control the stability of the crystal structure. With the change of the compositions of prismatic or octahedral positions and the formation of vacancies in the boron position because boron volatility in the course of growth, the symmetry of the B-polyhedra changes, which, in turn, results in the change of the symmetry group.

The general tendency observed for the $LnM_3(BO_3)_4$ compounds with *M* = Al, Sc, or Cr is the change of the symmetry from monoclinic to trigonal with a decrease of the radius of the rare-earth element and the formation of individual the scandium borate structures.

ACKNOWLEDGMENTS

This study was supported by the International Center for Diffraction Data (ICDD), project no. 97-08.

REFERENCES

1. G. M. Kuz'micheva, V. B. Rybakov, S. G. Novikov, *et al.*, Zh. Neorg. Khim. **44** (3), 352 (1999).
2. A. V. Goryunov, G. M. Kuz'micheva, B. V. Mukhin, *et al.*, Zh. Neorg. Khim. **41** (10), 1605 (1996).
3. V. A. Lebedev, V. F. Pisarenko, Y. M. Chuev, *et al.*, Adv. Solid-State Lasers **1**, 460 (1996).
4. I. R. Magunov, S. V. Voevudskaya, A. P. Zhirnova, *et al.*, Izv. Akad. Nauk SSSR, Neorg. Mater. **21** (9), 1532 (1985).
5. V. B. Rybakov, G. M. Kuz'micheva, E. V. Zharikov, *et al.*, Zh. Neorg. Khim. **42** (10), 1594 (1997).
6. J.-P. Mean, T. Jensen, and G. Huber, IEEE J. Quantum Electron. **21**, 131 (1991).
7. Guofu Wang, H. G. Gallagher, T. P. J. Han, and B. Henderson, in *Abstracts of the XI International Conference on Crystal Growth, ICCG XI, The Hague, 1995*, p. 818.
8. Guofu Wang, H. G. Gallagher, T. P. J. Han, and B. Henderson, Appl. Phys. Lett. **67** (26), 3906 (1995).
9. Guofu Wang, H. G. Gallagher, T.P. J. Han, and B. Henderson, J. Cryst. Growth **163**, 272 (1996).
10. V. B. Rybakov, G. M. Kuz'micheva, B. V. Mukhin, *et al.*, Zh. Neorg. Khim. **42** (1), 9 (1997).
11. S. A. Kutovoĭ, V. V. Laptev, and S. Yu. Matsnev, Kvantovaya Élektron. (Moscow) **18** (2), 149 (1991).
12. D. A. Keszler and H. Sun, Acta Crystallogr., Sect. C: Cryst. Struct. Commun. **C39**, 1505 (1988).
13. R. Shannon, Acta Crystallogr. **32**, 751 (1976).
14. G. M. Kuz'micheva, in *Problems of Crystal Chemistry* (Nauka, Moscow, 1989), p. 15.
15. B. F. Dzhurinskiĭ, in *Rare-Earth Compounds. Systems with Oxides of Elements of Groups I–III. Chemitry of Rare-Earth Elements* (Nauka, Moscow, 1983), p. 137.
16. H. H. Bartsch, Dissertazion zur Erlandung des Doktorgrades (Naturwissenschaften der Universität, Hamburg, 1984), p. 101.
17. N. I. Leonyuk and L. I. Leonyuk, Prog. Cryst. Growth Charact. Mater. **31**, 179 (1995).
18. N. I. Leonyuk, Prog. Cryst. Growth Charact. Mater. **31**, 279 (1995).

Translated by T. Safonova

Crystallography Reports, Vol. 45, No. 6, 2000, pp. 916–918. Translated from Kristallografiya, Vol. 45, No. 6, 2000, pp. 996–998.

STRUCTURE OF INORGANIC COMPOUNDS

Crystal Structure of Crystal Hydrate $NaCs_5Mo_7O_{24} \cdot 5H_2O$

Z. I. Khazheeva*, E. G. Khaĭkina*, K. M. Khal'baeva*, T. A. Shibanova, V. N. Molchanov**, and V. I. Simonov****

** Baĭkal'sk Institute of Utilization of Natural Resources, Siberian Division, Russian Academy of Sciences, Ulan-Ude, Russia*

*** Shubnikov Institute of Crystallography, Russian Academy of Sciences, Leninskiĭ pr. 59, Moscow, 117333 Russia*

Received October 27, 1998; in final form, October 27, 1999

Abstract—The structure of $NaCs_5Mo_7O_{24} \cdot 5H_2O$ was established by X-ray diffraction analysis (λMo, 7279 reflections, R_{aniso} = 5.3%). The parameters of the triclinic unit-cell are as follows: a = 10.517 Å, b = 10.824 Å, c = 16.916 Å, α = 66.94°, β = 67.14°, γ = 72.40°; Z = 2; $P\bar{1}$. The compact groups consisting of seven MoO_6-octahedra are linked into a three-dimensional framework via a system of hydrogen bonds. Five independent Cs atoms are located in large cavities of the framework. The coordination environment of a Na atom is an octahedron formed by oxygen atoms of water molecules. © *2000 MAIK "Nauka/Interperiodica".*

The studied crystals were grown by evaporation of an aqueous solution of the mixture of Na_2MoO_4 and Cs_2MoO_4 in the 1 : 3 ratio. The transparent colorless plateletlike crystals are unstable at room temperature. The X-ray diffraction data were collected on an automated CAD-4F Enraf-Nonius diffractometer (MoK_α radiation, graphite monochromator, ω/2θ scan, variable scan rate, $\sin\theta/\lambda \le 0.7$ Å^{-1}) from a 0.25 × 0.125 × 0.125-mm-large crystal in a silicone oil. The triclinic unit-cell parameters were refined over 25 strong reflections as a = 10.517(2) Å, b = 10.824(4) Å, c = 16.916(15) Å, α = 66.94(5)°, β = 67.14(4)°, γ = 72.40(5)°, V = 1606 Å^3. The total of 7279 reflections with the integrated intensities $I_{hkl} > 3\sigma(I)$ were measured. The drift of intensities of the control reflections was no higher than 5% throughout the X-ray data set. The experimental absorption curve was not measured. All the calculations associated with the structure solu-

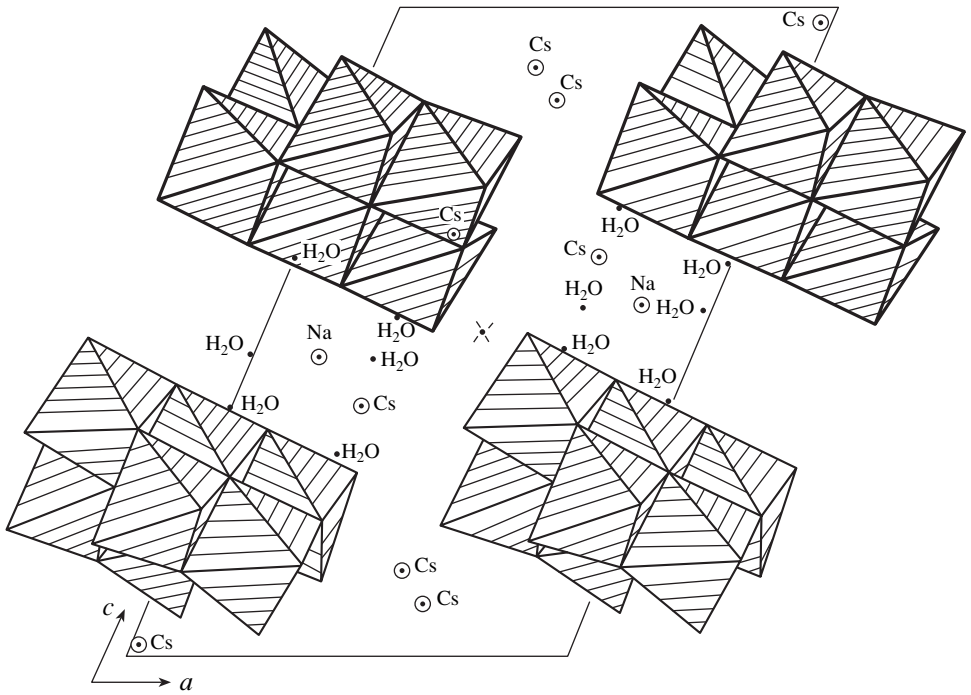

The $NaCs_5Mo_7O_{24} \cdot 5H_2O$ structure projected onto the *ac*-plane.

1063-7745/00/4506-0916$20.00 © 2000 MAIK "Nauka/Interperiodica"

Atomic coordinates and isotropic thermal parameters for $NsCs_5Mo_7O_{24} \cdot 5H_2O$

Atom	*x*/*a*	*y*/*b*	*z*/*c*	B_{eq}, Å^2
Mo(1)	0.21813(10)	0.20577(11)	0.14031(7)	1.35
Mo(2)	−0.02547(9)	0.05238(9)	0.32845(6)	0.87
Mo(3)	0.26953(9)	−0.12221(10)	0.21755(7)	1.25
Mo(4)	−0.32962(10)	0.27097(11)	0.38768(7)	1.48
Mo(5)	−0.01503(9)	−0.07529(10)	0.17180(7)	1.10
Mo(6)	−0.30269(9)	0.11684(10)	0.25387(7)	1.10
Mo(7)	−0.06749(10)	0.39287(10)	0.22874(7)	1.31
Cs(1)	0.35648(9)	0.33498(8)	0.64844(6)	2.28
Cs(2)	0.30562(8)	0.06002(10)	0.38348(6)	2.15
Cs(3)	0.98632(11)	0.28703(10)	0.98000(6)	2.68
Cs(4)	0.62754(9)	0.02669(15)	0.07814(7)	3.35
Cs(5)	0.44646(12)	0.42575(12)	0.86566(11)	4.16
Na	−0.1557(6)	−0.3961(5)	−0.4630(4)	3.03
O(1)	0.3127(10)	0.3082(10)	0.1413(8)	3.02
O(2)	0.0389(10)	0.4808(9)	0.2316(7)	2.93
O(3)	−0.1164(8)	−0.1920(8)	0.1955(6)	1.98
O(4)	−0.3851(7)	−0.0131(8)	0.2768(6)	1.37
O(5)	0.2900(9)	0.1947(9)	0.0317(6)	2.39
O(6)	−0.1826(8)	0.5178(8)	0.1763(6)	2.26
O(7)	0.0867(8)	−0.0566(9)	0.0622(6)	1.83
O(8)	−0.3997(9)	0.2584(9)	0.1993(7)	2.88
O(9)	0.3747(8)	−0.1379(9)	0.1142(5)	2.22
O(10)	−0.4435(9)	0.4093(8)	0.3432(7)	2.63
O(11)	0.3546(8)	−0.2423(9)	0.2890(6)	2.23
O(12)	−0.3942(10)	0.2370(10)	0.5029(6)	2.18
O(13)	0.3247(7)	0.0391(8)	0.2052(5)	1.32
O(14)	−0.1815(8)	0.3681(8)	0.3553(6)	1.58
O(15)	0.1195(7)	−0.2054(7)	0.2340(5)	1.58
O(16)	−0.3881(7)	0.1276(8)	0.3773(5)	1.58
O(17)	0.1054(7)	−0.0834(7)	0.3595(5)	1.22
O(18)	−0.1403(8)	0.0790(8)	0.4280(5)	1.67
O(19)	0.0517(7)	0.3366(7)	0.1249(5)	1.51
O(20)	−0.1510(7)	0.0901(7)	0.1478(5)	1.34
O(21)	0.0718(7)	0.1999(7)	0.2797(5)	1.22
O(22)	−0.1309(6)	−0.0363(6)	0.3050(4)	1.13
O(23)	0.0993(6)	0.0445(6)	0.1889(5)	0.99
O(24)	−0.1769(6)	0.2275(7)	0.2685(5)	1.39
O(25)*	0.2977(10)	0.1944(9)	0.5294(7)	3.19
O(26)*	0.0065(12)	0.2669(12)	0.4678(7)	4.04
O(27)*	0.0009(12)	0.4127(10)	0.6160(7)	3.90
O(28)*	0.7147(15)	0.4620(14)	0.5373(9)	5.11
O(29)*	0.3022(16)	0.3832(16)	0.3081(12)	6.99

* H_2O molecules.

tion and refinement were made by the SHELXS86 [1] and AREN [2] program packages. The arrangement of the Mo atoms was determined by the SHELXS86 program package. Then the Cs, Na, and O atoms were localized by the method of successive approximations by the AREN program package with due regard for crystallo chemical considerations. In the course of the refinement, the absorption correction ($\mu r_{max} = 1.4$) for an arbitrarily shaped sample was applied [3]. The distribution of the R factor in $\sin\theta/\lambda$ is indicative of substantial extinction in the crystals. The anisotropic refinement of the model by the full-matrix least squares method with allowance for the secondary-extinction coefficient resulted in $R_w = 6.4\%$ and $R = 5.3\%$. The final coordinates of the basis atoms and their individual isotropic temperature factors (the anisotropic temperature factors can be obtained from the authors) are given in the table. The $NaCs_5Mo_7O_{24} \cdot 5H_2O$ structure projected onto the (010) plane is shown in the figure.

In this type of the coordination, polyhedra of Mo atoms and the mode of their mutual arrangement indicate that the compound under study belongs to block structures. The coordination octahedron of a Mo atom is formed by oxygen atoms. The $[MoO_6]$-octahedra share the edges and the vertices to form a block of seven octahedra. This block corresponds to the heptanuclear anion of the composition $[Mo_7O_{24}]^{6-}$. The Mo(2) octahedron with bridging vertices is located in the center of this block. The oxygen vertices of the remaining six octahedra are either terminal or bridging.

The structure under study exhibits the features typical of many oxygen-containing compounds of Mo [4]. The Mo–O distances in the octahedra vary over a wide range. The following characteristic features inherent in all the Mo-octahedra can be followed on a Mo(1) octahedron containing two shortest bonds [Mo(1)–O(1) (1.707 Å) and Mo(1)–O(5) (1.732 Å)] in the *cis* positions with respect to one another; the long Mo(1)–O(23) (2.164 Å) bond in the *trans* position with respect to the shortest Mo(1)–O(1) bond (1.707 Å); two equal Mo(1)–O(13) and Mo(1)–O(19) bonds of the intermediate lengths (1.974 and 1.927 Å, respectively) in the *trans* positions with respect to one another. The sums of the bond lengths belonging to the *trans* partners are 3.871, 3.980, and 3.901 Å. The average Mo–Mo distance in the octahedra linked via sharing the edge is 3.294 Å. The lengths of the O–O edges in the octahedra vary within a narrow range (the average value 2.75 ± 0.1 Å).

The water molecules form the hydrogen bonds with the oxygen atoms of the anionic $[Mo_7O_{24}]^{6-}$ blocks. The O–O distances range within 2.800–3.154 Å; the corresponding oxygen atoms are located at small distances from molybdenum (1.706–1.936 Å). As a result, the anionic $[Mo_7O_{24}]^{6-}$ blocks are linked by via a system of hydrogen bonds and form infinite corrugated chains along the *c*-axis (figure).

The nearest environment of the Na atom is formed by six water molecules located at the vertices of a distorted octahedron.

The alkaline Cs atoms occupy the cavities of the framework and are surrounded by oxygen atoms of the anionic $[Mo_7O_{24}]^{6-}$ block. The Cs–O bond lengths range within 2.7–3.0 Å.

REFERENCES

1. G. M. Sheldrick, *SHELXS86: Program for the Solution of Structures* (Univ. of Göttingen, 1986).
2. V. I. Andrianov, Kristallografiya **32** (1), 228 (1987) [Sov. Phys. Crystallogr. **32**, 130 (1987)].
3. N. Walker and D. Stuart, Acta Crystallogr., Sect. A: Found. Crystallogr. **A39**, 158 (1983).
4. M. A. Poraĭ-Koshits and L. O. Atovmyan, *Crystal Chemistry and Stereochemistry of Coordination Compounds of Molybdenum* (Nauka, Moscow, 1974).

Translated by T. Safonova

Crystallography Reports, Vol. 45, No. 6, 2000, pp. 919–925. Translated from Kristallografiya, Vol. 45, No. 6, 2000, pp. 999–1005.

STRUCTURE OF INORGANIC COMPOUNDS

Dissymmetrization of Crystal Structures of Alum with Anomalous Birefringence

A. G. Shtukenberg, I. V. Rozhdestvenskaya, O. V. Frank-Kamenetskaya, I. I. Bannova, S. V. Kulakova, T. I. Ivanova, and Yu. O. Punin

St. Petersburg State University, Universitetskaya nab. 7/9, St. Petersburg, 199164 Russia

Received September 8, 1997; in final form, January 18, 2000

Abstract—Dissymmetrization of α-alum crystals of two isomorphous series, $(NH_4,K)Al(SO_4)_2 \cdot 12H_2O$ and $K(Al,Cr)(SO_4)_2 \cdot 12H_2O$, with different values of anomalous birefringence has been studied by X-ray diffraction methods. Dissymmetrization is revealed mainly from the comparison of the intensities of crystallographically equivalent reflections in the space group $Pa\bar{3}$ characteristic of alum. The degree of dissymmetrization depends on the position in which the isomorphous replacements occurs, as well as on the growth sector of the crystal, and shows a good correlation with birefringence. © *2000 MAIK "Nauka/Interperiodica".*

INTRODUCTION

Although anomalous birefringence in the crystals of solid solutions of alum has been known since the late nineteenth century [1], its origin is still unclear. Numerous indirect data [2] confirm the assumption that optical anomalies of alum crystals are associated with the mechanism of growth dissymmetrization [3]. In essence, the mechanism reduces to the following: the sites of one regular system of points, which are crystallographically equivalent in the crystal bulk, become nonequivalent on its surface or at the end of a growth step and can orderly be occupied by the ions of the solid solution in the process of crystal growth. During crystal growth, this ordered surface-layer structure is "buried" in the crystal bulk and thus becomes "frozen" [4]. However, one cannot directly relate this phenomenon to the observed optical anomalies without preliminary experimental analysis of dissymmetrization of the crystal structure. The present study is devoted to the analysis of specific features of dissymmetrization of the crystal structure of α-alum depending on the type of substituting cations and birefringence by the method of X-ray diffraction analysis.

As is well known, α-alum (sp. gr. $Pa\bar{3}$) has the composition $A^+M^{3+}(SO_4)_2 \cdot 12H_2O$, where $A^+ = K^+$, NH_4^+, Rb^+, Tl^+, etc., and $M^{3+} = Al^{3+}$, Cr^{3+}, Fe^{3+}, etc. The end members of the isomorphous series are isotropic, whereas all the other members possess anomalous birefringence described in detail in our earlier study [5]. Maximum birefringence is observed in the growth sectors of the (111) octahedron faces and is much lower (by an order of magnitude) in the growth sectors of weakly developed (100) cube faces and (110) rhombododecahedron faces. The birefringence is an order of magnitude less. The birefringence strength $\Delta = n_g - n_p$ depends on the molar fraction x of one of the components of a binary isomorphous mixture according to the parabolic law $\Delta = 4\Delta_{max}x(1 - x)$ and attains its maximum value $\Delta_{max} \approx n \times 10^{-5}$ in the middle of the series. In the growth sector ⟨111⟩, the optical indicatrix is a biaxial ellipsoid, close to a uniaxial one, whose major axes (essentially different from two other axes) is almost normal to the growth front. For isomorphous series in which the substitution occurs in the position A^+, this axis is n_p; if substitution occurs in the position $M^{3+} - n_g$, this axis is n_p. In the growth sectors ⟨100⟩ and ⟨110⟩, the indicatrix orientation is less regular and cannot be described in such a simple way.

CHECKING OF CRYSTAL HOMOGENEITY AND PREPARATION OF SPECIMENS

We studied crystals of two isomorphous series, $(NH_4,K)Al(SO_4)_2 \cdot 12H_2O$ (the first series) and $K(Al,Cr)(SO_4)_2 \cdot 12H_2O$ (the second series), i.e., the crystals with substitution in the positions A^+ and M^{3+}, respectively. Alum crystals were grown from aqueous solutions by the method of isothermal decrease of supersaturation at 30°C; the initial supersaturation $\Delta C/C$ was varied from 0.05 to 0.3. The composition of the grown crystals was determined by the methods of flame photometry (for the first series) and calorimetry (for the second series).

To reveal possible heterogeneity of alum crystals, we analyzed the diffraction-maximum profiles of single crystals [6]. Proceeding from the nature of the optical indicatrix, an inhomogeneous chemical layer most probably formed along the direction normal to the growth front (e.g., along the [111] growth direction in the ⟨111⟩ growth sector). Therefore, we obtained diffraction reflections from the crystals of the composition

Table 1. Characteristics of specimens of alum crystals $A^{+}M^{3+}(SO_4)_2 \cdot 12H_2O$

Specimens	*KV*1	*KV*2	*KV*3
Composition	$A = K_{0.49}(NH_4)_{0.51}$ M = Al	$A = K_{0.49}(NH_4)_{0.51}$ M = Al	A = K $M = Al_{0.95}Cr_{0.05}$
Growth sector	⟨111⟩	⟨100⟩	⟨111⟩
$\Delta = n_g - n_p$, 10^{-5}	6.0	1.0	1.6
a, Å	12.212(2)	12.212(2)	12.170(2)
b, Å	12.211(3)	12.211(2)	12.172(2)
c, Å	12.214(1)	12.211(2)	12.171(2)
a_{av}, Å	12.213(2)	12.211(2)	12.171(2)
α, deg	90.01(1)	89.99(1)	90.01(1)
β, deg	90.02(1)	90.01(1)	90.00(1)
γ, deg	89.99(2)	90.01(1)	90.01(1)

Table 2. Crystallographically equivalent reflections in the diffraction class $m\bar{3}$ and its subgroups

Diffraction group	Group multiplicity	Equivalent reflections
$m\bar{3}$	24	hkl lhk klh $hk\bar{l}$ $lh\bar{k}$ $kl\bar{h}$ $h\bar{k}l$ $l\bar{h}k$ $k\bar{l}h$ $h\bar{k}\bar{l}$ $l\bar{h}\bar{k}$ $k\bar{l}\bar{h}$ $\bar{h}\bar{k}l$ $\bar{l}\bar{h}k$ $\bar{k}\bar{l}h$ $\bar{h}\bar{k}\bar{l}$ $\bar{l}\bar{h}\bar{k}$ $\bar{k}\bar{l}\bar{h}$ $\bar{h}kl$ $\bar{l}hk$ $\bar{k}lh$ $\bar{h}k\bar{l}$ $\bar{l}h\bar{k}$ $\bar{k}l\bar{h}$
$\bar{3}$	6	$L_3 \parallel [111]$ $L_3 \parallel [\bar{1}11]$ $L_3 \parallel [1\bar{1}1]$ $L_3 \parallel [\bar{1}\bar{1}1]$ hkl $\bar{h}kl$ $h\bar{k}l$ $\bar{h}\bar{k}l$ $h\bar{k}\bar{l}$ $hk\bar{l}$ $\bar{h}k\bar{l}$ $hk\dot{l}$ lhk $\bar{l}hk$ $l\bar{h}k$ $\bar{l}\bar{h}k$ $l\bar{h}\bar{k}$ $l\bar{h}\bar{k}$ $\bar{l}h\bar{k}$ $lh\bar{k}$ klh $\bar{k}lh$ $k\bar{l}h$ $\bar{k}\bar{l}h$ $k\bar{l}\bar{h}$ $k\bar{l}\bar{h}$ $\bar{k}l\bar{h}$ $kl\bar{h}$
mmm	8	hkl $h\bar{k}l$ $\bar{h}\bar{k}l$ $\bar{h}kl$ $hk\bar{l}$ $h\bar{k}\bar{l}$ $\bar{h}\bar{k}\bar{l}$ $\bar{h}k\bar{l}$
$2/m$	4	$L_2 \parallel [100]$ $L_2 \parallel [010]$ $L_2 \parallel [001]$ hkl hkl hkl $\bar{h}kl$ $h\bar{k}l$ $\bar{h}\bar{k}l$ $h\bar{k}\bar{l}$ $h\bar{k}\bar{l}$ $\bar{h}\bar{k}\bar{l}$ $h\bar{k}\bar{l}$ $\bar{h}k\bar{l}$ $hk\bar{l}$
$\bar{1}$	2	hkl $\bar{h}\bar{k}\bar{l}$

$(K_{0.49}(NH_4)_{0.51})Al(SO_4)_2 \cdot 12H_2O$ (with the maximum birefringence strength), from the (111) growth planes in the ⟨111⟩ growth sector, and from the (110) growth planes in the ⟨110⟩ growth sector. For comparison, similar experiments were also performed for "nongrowth" (111) and (110) planes of the corresponding growth sectors. The standard was an isotropic $KAl(SO_4)_2 \cdot 12H_2O$ crystal.

The profiles of the 555, 666, 777 and 440, 660, 880 diffraction maxima were obtained from the growth faces and from the oriented sawn surfaces of the 5- to 15-mm-large crystals on a DRON-2.0 diffractometer (point-by-point record, 2θ-θ scan, CoK_α-radiation, graphite monochromator, scan step 0.02°, time constant 5 s). The Co-radiation was chosen due to its high resolution power at far 2θ angles. The theoretical diffraction patterns calculated for various models showed that the use of this radiation would allow the establishment of the pronounced distortions of reflection profiles even in the case of large concentration differences (up to 5 : 1) and slight (about 10%) composition differences of alternating layers.

All the reflections from both the standard crystal and the crystal under study were symmetric and, thus, indicated the absence of the noticeable chemical inhomogeneity in the layers along the growth directions and in the directions inclined to these directions. Computer simulation showed a good correspondence between the reflection profiles calculated for one-component models and the corresponding experimental profiles for these models. The dimensions of the coherent-scattering regions varied within 1100–1300 Å. Thus, if the crystals were chemically heterogeneous, this heterogeneity was insignificant and could hardly be the source of the optical anomalies observed in alum.

For the further study, we chose three specimens with different birefringence strengths (Table 1). The *KV*1 and *KV*2 specimens from various growth sectors of the same single crystal possessed the maximum birefringence strength within the first isomorphous series [5]. In the *KV*3 specimen from the second isomorphous series, the chromium concentration and, therefore, birefringence were quite low, because alum with high chromium content is instable and is decomposed in the air atmosphere.

Spherical specimens with diameters ranging within 0.2–0.4 mm were obtained by slight dissolution of specially prepared specimens cut out from the corresponding growth sectors with dimensions exceeding 0.5 mm in water.

ANALYSIS OF SYMMETRY

The study of the specimens by the Weissenberg method showed no violations of the cubic symmetry (sp. gr. $Pa\bar{3}$).

The further study of the symmetry of alum single crystals was performed on a Syntex $P2_1$ single-crystal four-circle X-ray diffractometer (θ/2θ scan for the *KV*1 specimen and the ω scan for the *KV*2 and the *KV*3 specimens; MoK_α-radiation, graphite monochromator). The unit-cell parameters were determined using the least squares procedure over 25 reflections (10.0.0, 880, and 12.0.4 reflections and all the crystallographically equivalent reflections within the cubic diffraction class $m\bar{3}$). They showed no deviations from the cubic symmetry (Table 1). Moreover, neither the satellite nor the odd *h*00-, 0*h*0-, or 00*h*-type reflections forbidden in sp. gr. $Pa\bar{3}$ were revealed.

The preliminary analysis of the symmetry was based on the comparison of the reflection intensities equivalent in the diffraction class $m\bar{3}$ and its sub-

Table 3. Values of the parameter χ for coordinate reflections

Reflections \ Specimens	*KV*1	*KV*2	*KV*3
200, 020, 002	1	3	1
400, 040, 004	57	7	28
600, 060, 006	32	2	25
800, 080, 008	–	–	2
10.0.0, 0.10.0, 0.0.10	3	2	13
12.0.0, 0.12.0, 0.0.12	2	1	2
14.0.0, 0.14.0 0.0.14	1	1	1

Table 4. Values of the parameter χ for intensities of general-type reflections for the cubic and the orthorhombic symmetries

Specimens	Reflections	Cubic symmetry	Orthorhombic symmetry			
		$\chi = \chi_{av}$	$\chi 1$	$\chi 2$	$\chi 3$	χ_{av}
*KV*1	332	5	4	3	5	1
	132	15	6	5	3	10
	421	6	4	3	3	2
	251	4	2	4	2	1
*KV*2	332	4	3	4	3	1
	132	4	4	3	2	1
	421	7	7	5	3	1
	251	3	3	3	2	1
*KV*3	332	9	4	not determined	6	2
	132	22	21		20	5
	421	17	10		15	3
	251	5	3		3	1

Note: The comparison of the intensities of the equivalent reflections for the trigonal and the monoclinic models did not confirm the above data and therefore are omitted here. For notation see the text.

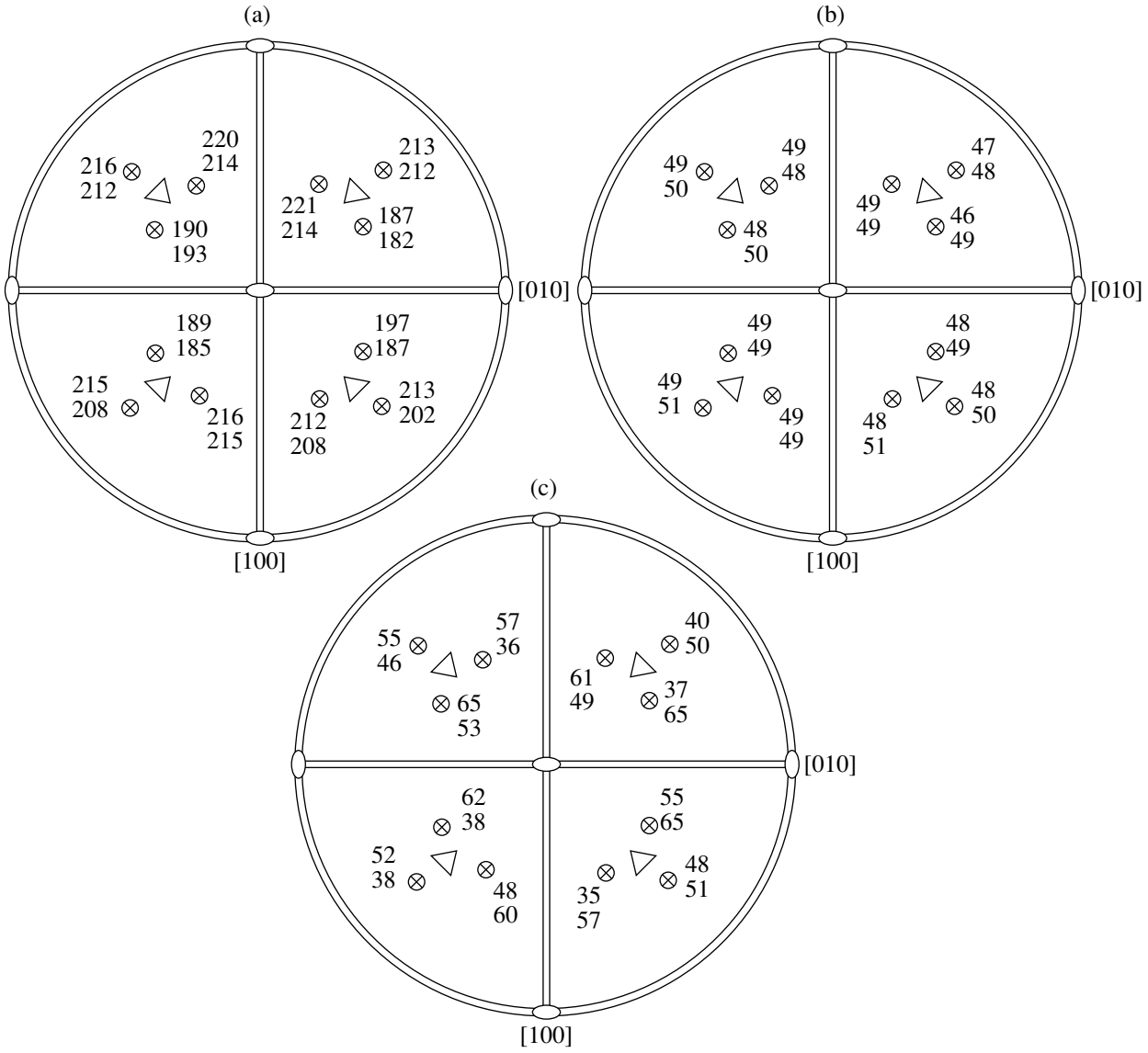

Fig. 1. Relative integrated intensities of reflections equivalent to the 132 reflection in the diffraction class $m\bar{3}$ for specimens (a) *KV*1 ($\sigma_I = \pm(0.5–1.5)$ arb. units), (b) *KV*2 ($\sigma_I = \pm(0.9–1.1)$ arb. units), and (c) *KV*3 ($\sigma_I = \pm(2.3–2.7)$ arb.units). The upper number shows the intensity for the *hkl*-type reflections, the lower number, the intensity of the $hk\bar{l}$-type reflections.

groups. The division of all the reflections into groups of equivalent reflections was made under the assumption of trigonal (four variants), orthorhombic, monoclinic (three variants), and triclinic symmetries (Table 2).

To compare the intensities of the corresponding groups of reflections, we used the parameter $\chi = \frac{I_{max} - I_{min}}{\sigma_{max}}$, where I_{max} and I_{min} are the maximum and the minimum reflection intensities and σ_{max} is the maximum experimental error of their determination, which was evaluated by scanning along the ψ-axis and comparing the intensities of centrosymmetric reflections. The parameter χ was calculated in two variants: inside each group of reflections, which were assumed to be equivalent ($\chi 1$, $\chi 2$, …), and between different groups, which were characterized by the average intensities in the corresponding groups of reflections (χ_{av}). Obviously, if $\chi 1$, $\chi 2$, … $< \chi_{av}$, the differences between the reflection intensities within the group are less than the differences in the intensities of various groups (at $\chi_{av} > 3$) and the assumption about the lower symmetry (dissymmetrization) is justified; otherwise, it is not.

Scanning along the ψ-axis with a step of 10° confirmed that the differences in the intensities are not associated with the specimen shape and multiple reflection.

Table 5. Values of the parameter χ for the intensities of general-type reflections for the specimen *KV*3 of the trigonal symmetry

hkl	$\chi 1$	$\chi 2$	$\chi 3$	$\chi 4$	$\chi 5$	$\chi 6$	$\chi 7$	$\chi 8$	$\chi 9$	$\chi 10$	$\chi 11$	$\chi 12$	χ_{av}
332	2	1	1	1	1	2	3	1	1	0.2	2	3	7
132	2	2	0.2	2	2	2	4	2	2	1	0.4	1	20
421	2	2	3	1	1	1	4	2	2	0.4	1	2	15
251	3	1	3	0.3	1	0.4	1	0.6	0.2	0.4	0.4	2	4

Note: For notation see the text.

Table 6. Violation of the symmetry elements in the diffraction class $m\bar{3}$ of the specimen *KV*3

Symmetry element	Equivalent reflections	Total number of equivalent reflections	Number of groups of reflections not obeying the symmetry element under the conditions that			
			$\chi = \frac{I_{max} - I_{min}}{\sigma_{max}} > 3$		$\varepsilon = \frac{I_{max} - I_{min}}{I_{min}} > 1$	
			number of groups of reflections	percentage of the total number of groups	number of groups of reflections	percentage of the total number of groups
m_y	hkl $h\bar{k}l$	1308	138	10.55	6	0.46
m_z	hkl $hk\bar{l}$	1187	187	15.75	8	0.67
3_1	hkl lhk klh	458	170	37.12	7	1.53
3_2	$h\bar{k}\bar{l}$ $l\bar{h}\bar{k}$ $k\bar{l}\bar{h}$	867	339	39.10	27	3.11
3_3	$h\bar{k}l$ $l\bar{h}k$ $k\bar{l}h$	1356	514	37.91	14	1.03
3_4	$hk\bar{l}$ $lh\bar{k}$ $kl\bar{h}$	849	270	31.80	27	3.18

Comparing the intensities of coordinate reflections (Table 3), we established that the parameter was $\chi > 3$, at least for one group of reflections; in other words, the intensities of two reflections in the group were essentially different and the symmetries of all the three alum specimens were lower than cubic. For the specimens *KV*1 and *KV*3, the intensities were considerably different. For the specimen *KV*2, the intensities were different only for the 400 reflections, which indicated a lower degree of dissymmetrization in this specimen.

For the specimen *KV*2, the real symmetry was lower than the cubic symmetry, but the structural distortions were insignificant (Fig. 1; Tables 3 and 4), so that no justified conclusions about the crystal symmetry could be made. The intensity analysis of reflections of the general type allowed us to exclude the assumptions about the trigonal and monoclinic symmetries for the specimens *KV*1 and *KV*3 (Fig. 1). The intensities of the corresponding reflections for the *KV*1 specimen differed much more than for the specimen *KV*2 (Figs. 1a, 1b;

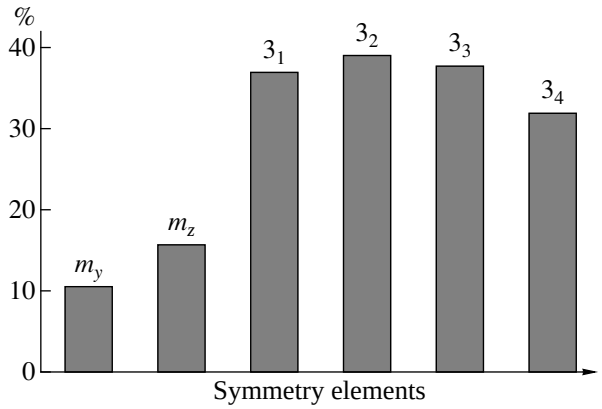

Fig. 2. Percentage of groups of reflections violating the symmetry elements of the diffraction class $m\bar{3}$ in the *KV*3 specimen.

Table 4) from the same isomorphous series (Table 1). The *KV*1 specimen also possessed a much more pronounced birefringence strength. These results and the data obtained from the intensity analysis of the coordinate reflections (Table 3) indicate a more pronounced (in comparison with the specimen *KV*2 from the ⟨100⟩ growth sector) dissymmetrization of the specimen *KV*1 from ⟨111⟩ growth sector despite the fact that both specimens have the same composition. The intensity ratio of the specimen *KV*1 obeys the orthorhombic symmetry sufficiently well (the diffraction class *mmm*) (Table 4). Nevertheless, the $\chi 1$, $\chi 2$, and $\chi 3$ values considerably exceed the value 3, which indicates the violation of the orthorhombic symmetry.

The *KV*3 specimen from the second isomorphous series possessing a low birefringence strength (comparable with that of the *KV*2 specimen) is characterized by the most pronounced differences in the intensities of the corresponding reflections. The intensity ratios (Fig. 1c, Tables 3–5) indicate the triclinic symmetry, whence it follows that the substitution in the position M^{3+} (specimen *KV*3) gives rise to a more pronounced dissymmetrization than the substitution in the position A^+ (specimen *KV*1). Using the analogy with a ruby crystal [7], one can assume that the substitution of Al^{3+} by Cr^{3+} results in the displacement of the orderly distributed impurity cation Cr^{3+} from the Al^{3+} position, which promotes the further dissymmetrization.

Thus, the analysis of the intensities of selected X-ray diffraction reflections showed that the symmetry of all the alum crystals studied is lower than cubic. The degree of their dissymmetrization depends not only on the impurity concentration but also on the position occupied by these impurities and, if the crystal composition is constant, also on the growth sector, which agrees quite well with the data on the birefringence strength (Table 1).

For a more detailed checking of possible triclinic symmetry of the *KV*3 specimen, a three-dimensional set of intensities was collected within half of the reciprocal space ($2\theta = 0°$–$80°$, $0 \le h \le 19$, $-19 \le k \le 19$, $-19 \le l \le 19$) on the same diffractometer (ω-method, MoK_α-radiation, graphite monochromator, 5929 reflections with $I > 3\sigma(I)$). All the experimental intensities were corrected for the *LP*-factor and absorption for spherical specimens ($\mu_r = 0.085$).

Studying dissymmetrization in garnets, Takéuchi [8] suggested to evaluate the degree of invalidity of individual symmetry elements in a crystal with the aid of a histogram showing the fraction of reflections not obeying the symmetry operation under consideration. In the construction of the histogram for the *KV*3 specimen (Fig. 2, Table 6), the intensities were taken to be different if they differed by more than 3σ. The analysis of this histogram showed that the symmetry planes and the threefold symmetry axes in the crystal under study were considerably invalid. It should be emphasized that the symmetry axes were "violated" to a considerably larger degree than the symmetry planes, with the fractions of reflections not obeying various threefold axes or symmetry planes being rather close.

With due regard of all possible subgroups of the space group of alum ($Pa\bar{3}$, Fig. 3), the analysis of the histogram in Fig. 2 led to the conclusion that the sym-

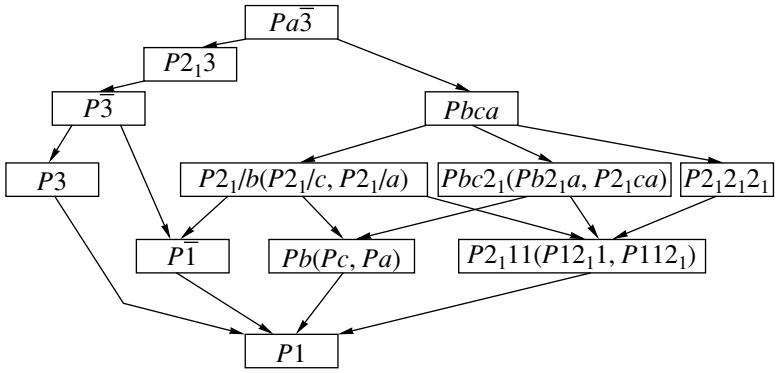

Fig. 3. Possible space groups of birefringent alum crystals (subgroups of the group $Pa\bar{3}$).

metry of the specimen *KV*3 considerably differs from the symmetries of the cubic space groups $Pa\bar{3}$ and $P2_13$ and the trigonal groups $P\bar{3}$ and $P3$. The deviation from the symmetries of the orthorhombic and the monoclinic groups were also quite pronounced, although somewhat less marked.

Even if the studied alum crystals were really chemically heterogeneous, this heterogeneity was insignificant and could hardly give rise to any optical anomalies.

The different intensities of X-ray reflections equivalent in the diffraction class $m\bar{3}$ allow for the interpretation of birefringence of alum crystals—it is caused by lowering of their symmetry to triclinic, which seems to be associated with partial ordering of cations that can substitute one another. In particular, such ordering was revealed in birefringent garnet crystals [8]. However, one should not exclude that the established differences in the reflection intensities are caused not only by dissymmetrization, but also by some additional factors, e.g., anisotropic extinction.

The results obtained at this stage of the study indicate that the degree of the assumed dissymmetrization of the crystals depends on the position in which the isomorphous substitution occurs and, at the constant crystal composition, also on the growth sector of the crystal, which is consistent with the birefringence data. In the alum crystals $K(Al_{0.95}Cr_{0.05})(SO_4)_2 \cdot 12H_2O$ (the $\langle 111 \rangle$ growth sector), the "violation" of both threefold symmetry axes and the symmetry planes is observed, with the violation of the threefold axis being more pronounced than the violation of the symmetry planes. At the same time, all the observed violations of various symmetry planes were close, as were all the violations of various threefold symmetry axes.

ACKNOWLEDGMENTS

This study was supported by the Russian Foundation for Basic Research, projects nos. 96-05-65577, 96-05-65579, and 00-05-65181.

REFERENCES

1. G. Chermak, *Handbook of Mineralogy* (Tip. Imper. Akad. Nauk, St. Petersburg, 1870).
2. A. G. Shtukenberg, Yu. O. Punin, and O. G. Kovalev, Kristallografiya **43** (3), 505 (1998) [Crystallogr. Rep. **43**, 465 (1998)].
3. A. V. Shubnikov, *Selected Works on Crystallography* (Nauka, Moscow, 1975).
4. A. M. Anufriev, G. R. Bulka, V. M. Vinokurov, *et al.*, in *Inhomogeneity of Minerals and Crystal Growth* (Nauka, Moscow, 1980), p. 10.
5. A. G. Shtukenberg, V. N. Solov'ev, and Yu. O. Punin, in *Physics of Crystallization* (Tverskoĭ Gos. Univ., Tver, 1994), p. 76.
6. O. V. Frank-Kamenetskaya and T. I. Ivanova, Cryst. Res. Technol. **32** (1), 195 (1997).
7. V. G. Tsirel'son, Itogi Nauki Tekh., Ser. Kristallokhim. **27** (1993).
8. Y. Takéuchi, N. Haga, S. Umizu, and G. Sato, Z. Kristallogr. **158**, 53 (1982).

Translated by L. Man

Crystallography Reports, Vol. 45, No. 6, 2000, pp. 926–929. Translated from Kristallografiya, Vol. 45, No. 6, 2000, pp. 1006–1009.

STRUCTURE OF INORGANIC COMPOUNDS

Defect Structure of $Na_{0.5-x}R_{0.5+x}F_{2+2x}$ (R = Ho,Yb) Solid Solutions (Fluorite Type)

L. P. Otroshchenko*, L. E. Fykina, A. A. Bystrova***, and B. P. Sobolev***

** Shubnikov Institute of Crystallography, Russian Academy of Sciences, Leninskiĭ pr. 59, Moscow, 117333 Russia*

*** Karpov Research Institute of Physical Chemistry, Obninsk Branch, Obninsk, Moscow oblast, Russia*

**** Research Center of Fiber Optics, Institute of General Physics, Russian Academy of Sciences, ul. Vavilova 38, Moscow, 117942 Russia*

Received January 21, 1999; in final form, February 1, 2000

Abstract—The structure of $Na_{0.395}Ho_{0.605}F_{2.210}$ (**I**) and $Na_{0.446}Yb_{0.554}F_{2.108}$ (**II**) crystals has been studied by the neutron diffraction method. A low occupancy of the main positions of fluorine atoms (F_c) is established. Interstitial fluorine atoms in crystal (**I**) occupy two positions, 48*i* and 32*f*, with the parameter $w = 0.293$ (the so-called relaxed fluorine atoms). In crystal (**II**), interstitial fluorine atoms occupy four positions, general 48*i*, 32*f* ($w = 0.322$), 32*f* ($v = 0.414$) positions and the special 4*b* position (1/2, 1/2, 1/2) in the center of the large cubic void (the so-called Goldschmidt position). © *2000 MAIK "Nauka/Interperiodica".*

Among the nonstoichiometric phases with the fluorite structure formed in the fluorine-containing systems, the $Na_{0.5-x}R_{0.5+x}F_{2+2x}$ solid solutions show the maximum difference in the valences of substituted Na^+ and R^{3+} cations (R = Pr–Lu, Y). In comparison with well-known fluorite phases of the composition $M_{1-x}R_xF_{2+x}$, the content of rare-earth trifluorides in the $Na_{0.5-x}R_{0.5+x}F_{2+2x}$ phases is substantially higher, whereas M^{2+} ions are absent (M = Ca, Sr, Ba, Cd, Pb). The defect structure (where some positions are not fully occupied) of $Na_{0.5-x}R_{0.5+x}F_{2+2x}$ phases is still not clearly understood.

The first X-ray diffraction study of $Na_{0.39}Y_{0.61}F_{2.22}$ was undertaken in 1983 [1], whereas the crystals of the $M_{1-x}R_xF_{2+x}$ type have been intensely studied since 1969. The second X-ray and neutron-diffraction studies of this phase were made in 1997 [2] and showed that additional fluorine atoms occupy the 48*i* and 32f_c positions with the parameter $w = 0.293$ (the so-called "relaxed" F atoms).

The study of a phase with one rare-earth element (yttrium) cannot yield a complete picture of the defect structure of $Na_{0.5-x}R_{0.5+x}F_{2+2x}$ solid solutions for the whole series of rare-earth elements. Different thermal behavior and different types of the atomic ordering observed in nonstoichiometric phases with lowering of the temperature [3] provide indirect evidence on different structures of the phases containing rare-earth elements from the beginning and the end of the RE series.

To observe the evolution of the defect $Na_{0.5-x}R_{0.5+x}F_{2+2x}$ structure with different rare-earth elements, we studied the phases with R = Ho (**I**) and Yb (**II**). We expected that phase (**I**) would be analogous to the yttrium-containing phase, because yttrium is located between Ho and Er in the rare-earth system and is located two elements apart from ytterbium.

Single crystals of compositions **I** ($Na_{0.395}Ho_{0.605}F_{2.210}$) and **II** ($Na_{0.446}Yb_{0.554}F_{2.108}$) have been grown by Stockbarger method at the Institute of Crystallography of the Russian Academy of Sciences under the conditions minimizing the oxygen content in the grown crystals. The rare-earth content has been refined using the compositional dependences of the unit-cell parameters [4].

The diffraction data were collected on a Syntex diffractometer at the source of the VVRTs reactor of the Karpov Research Institute of Physical Chemistry (λ = 1.167, Cu-monochromator). Both crystals studied showed no deviations from the fluorite symmetry (sp. gr. $Fm3m$). The experimental data were collected for the complete sphere of the reciprocal space.

For compound **I**: a = 5.520(1) Å; 740 reflections with $I_{hkl} > 3\sigma$; R_{av} = 5.54%; 34 crystallographically independent reflections; the specimen diameter 5.23 mm.

For compound **II**: a = 5.452(1) Å; 687 reflections with $I_{hkl} > 3\sigma$; R_{av} = 5.73%; 28 crystallographically independent reflections; the specimen diameter 5.05 mm.

The Fourier synthesis, the refinement by the full-matrix least squares method with the use of the Gram–Charlier expansion to account for the anharmonicity of atomic thermal vibrations up to the 3rd order of F_c (in compound **I**), and the introduction of the extinction correction (Becker–Coppens type-1) have been made with the use of the PROMETHEUS program [5].

1063-7745/00/4506-0926$20.00 © 2000 MAIK "Nauka/Interperiodica"

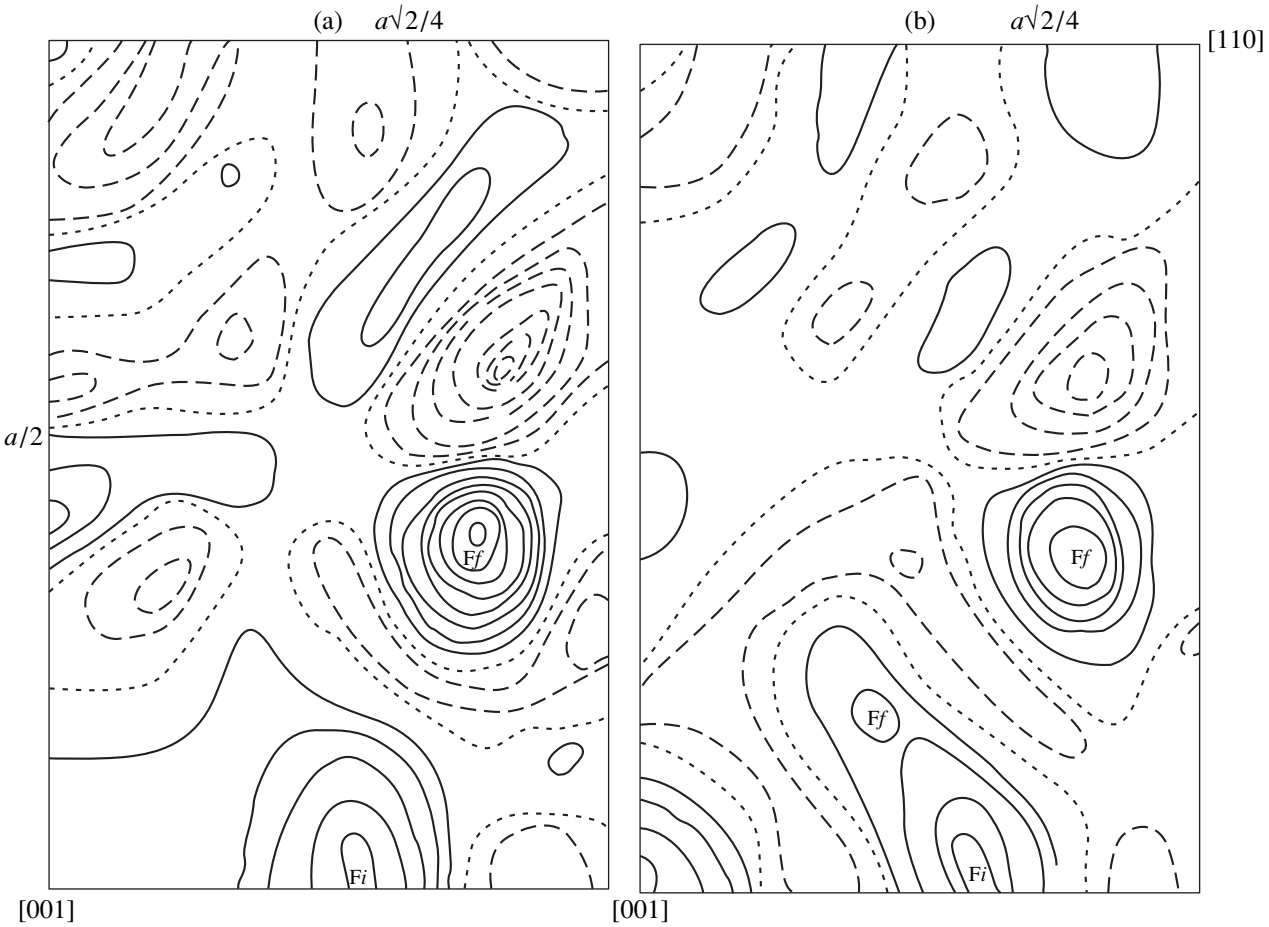

Fig. 1. Maps of the difference nuclear density obtained by subtracting the isotropic defect model of the fluorite structure for (a) $Na_{0.395}Ho_{0.605}F_{2.210}$ and (b) $Na_{0.446}Yb_{0.554}F_{2.108}$ solid solutions, section by $x - y = 0$ plane. Solid isolines represent the positive nuclear density; dashed lines, the negative neutron density; dot and dash lines indicate the zeroth nuclear density. The isolines are spaced by 0.02×10^{-12} cm/Å^3. The coordinate grid is drawn in unit-cell fractions.

The refinement of structures **I** and **II** under the assumption of the 100% occupancy of the cationic position involved the refinement of position occupancies, atomic positional, and thermal vibration parameters by the least squares method.

The analysis of the (110) Fourier sections obtained after the subtraction of the isotropic defect fluorite model (R_w = 16.9%, R = 11.2% for **I** and R_w = 12.1%, R = 7.5% for **II**) shows the residual nuclear density for crystal **I** in two positions, 48*i* and 32*f*: with the parameter w = 0.293 (the relaxed fluorine atom). The peak height is 0.10×10^{-12} cm/Å^3 for fluorine in the 48*i* position and 0.16×10^{-12} cm/Å^3 for fluorine in the 32*f* position (Fig. 1a).

For crystal **II**, the residual nuclear density is observed in the following four positions: (1) 48*i* with the maximum height 0.08×10^{-12}; (2) 32*f* with the parameter w = 0.322 (the relaxed fluorine atom) with the maximum height 0.10×10^{-12} cm/Å^3; (3) 32*f* with the parameter v = 0.414 and the maximum height 0.04×10^{-12} cm/Å^3; and (4) in 4*b* with the maximum height 0.08×10^{-12} cm/Å^3 (Fig. 1b).

The parameters in these compounds were refined for several models (which had different thermal parameters and additional positions for fluorine atoms). Table 1 gives the data for only the final model for compound **I**, because it seems to be most reliable (34 independent structure factors, 13 parameters to be refined). Table 2 lists the data for five structure models of compound **II** in the isotropic approximation. As was indicated [6], the nuclear density at the point (1/2, 1/2, 1/2) of the difference synthesis depends on the strategy of refinement of all the atoms in the structure. For four models (1–4, Table 2), we assumed that no atom was located at this point. However, the difference Fourier maps for all these models showed the nuclear density at (1/2, 1/2, 1/2). Table 2 shows that model 5 [*R*-factors, the quality of difference syntheses, and the sum of position occupancies by F atoms (partial occupancy of 48*i*, 32*f* with w = 0.32, the so-called relaxed F atoms, 32*f* with w = 0.41, and 4*b*)] is more advantageous than models 1–4.

Table 1. The data for refined structures $Na_{0.395}Ho_{0.605}F_{2.21}$ (**I**) and $Na_{0.446}Yb_{0.554}F_{2.108}$ (**II**)

Atoms, position	Parameters*	**I**	**II**
(Na, *R*); 4*a* (000)	$B \times 10^2$	1.367 (27)	1.904 (37)
F; 8*c* (1/4, 1/4, 1/4)	*g*	1.001 (6)	1.498 (18)
	$B \times 10^2$	B_{iso} = 1.776 (39)	B_{eq} = 3.204 (87)
	$B_{11} = B_{22} = B_{33} \times 10^2$	–	0.0270 (4)
	$C_{123} \times 10^3$	–	0.0288 (30)
F; 48*i* (1/2, *u*, *u*)	*g*	0.626 (17)	0.238 (19)
	u	0.125 (1)	0.135 (6)
	$B_{11} \times 10^2$	0.0498 (40)	0.0182 (57)
	$B_{22} = B_{33} \times 10^2$	0.0219 (19)	0.0081 (28)
	$B_{23} \times 10^2$	0.0181 (18)	0.0154 (33)
	$B_{eq} \times 10^2$	3.804 (39)	1.36 (40)
F; 32*f* (*w*, *w*, *w*)	*g*	0.583 (10)	0.192 (31)
	w	0.293 (1)	0.322 (6)
	$B_{iso} \times 10^2$	1.600 (77)	2.8 (6)
F; 32*f* (*v*, *v*, *v*)	*g*	–	0.150 (64)
	w	–	0.414 (15)
	$B_{iso} \times 10^2$	–	5.120 (1.68)
F; 4*b* (1/2, 1/2, 1/2)	*g*	–	0.030 (12)
	B_{iso}	–	1.99 (77)
	R_w	2.1%	2.4%
	R	1.6%	1.9%

* The values of atomic thermal parameters are measured in Å^2; *g* is the total occupancy of the corresponding position.

Table 2. Isotropic thermal parameters *B* (Å^2), heights of the residual maxima ρ (10^{-12} cm/Å^2) on difference nuclear-density maps, and the reliability factor *R* (%) for five models of structure **II**

Characteristics	Models				
	1	2	3	4	5
R_w	12.1	8.8	7.3	5.8	5.1
R	7.5	5.9	4.9	4.3	3.7
B_{Fc}	3.31	3.28	3.26	3.12	3.06
B_{Fi}		2.32	2.76	1.89	1.62
$B_{Ff(www)}$			1.20	0.90	0.70
$B_{F'f(vvv)}$				1.55	1.44
B_{Fb}					1.04
ρ_{Fi}	4				
$\rho_{Ff(www)}$	5	5	2	2	
$\rho_{Ff(vvv)}$	2	2	1		
ρ_{Fb}	4	2	3	3	
The total occupancy *g* of the positions of fluorine atoms	1.50	1.91	1.99	2.11	2.108

The refinement of models 4 and 5 in the anharmonic approximation of thermal vibrations of F atoms in the 4*c* positions (up to the 3rd order of magnitude) and anisotropic approximation for F atoms in the position 48*i* improved the quality of the difference map and reduced the *R*-factors. However, the difference synthesis of the nuclear density for model 4 still showed the residual density in the (1/2, 1/2, 1/2) position, with the reliability factors being R_w = 2.7% and *R* = 2.4%. The refinement of model 5 has significantly improved the difference synthesis and reduced the *R*-factors down to R_w = 2.4% and *R* = 1.9%. The quality of the difference nuclear-density map, the reliability factors, and the sum of the occupancies of fluorine atoms favor model 5 refined in the anharmonic anisotropic approximation (Table 2), with the following four additional positions of F atoms being simultaneously occupied: 48*i*, 32*f* with *w* = 0.322, 32*f* with *v* = 0.414, and 4*b*. Table 1 summarizes the final data of the refinement for both compounds.

It was established that the main anionic positions are not fully occupied with fluorine atoms. Crystal **I** has four vacancies per unit cell, i.e., a half of the main positions of fluorine atoms by 50%. Crystal **II** has two vacancies per unit cell, i.e., the main fluorine position is occupied by 25%.

As was to be expected, the location of additional fluorine atoms in **I** is similar to that in $Na_{0.5-x}Y_{0.5+x}F_{2+2x}$. Two interstitial positions, 48*i* and 32*f* with $w = 0.293$ (relaxed fluorine atoms), are occupied [1, 2]. In crystals **II**, four positions are partially occupied—48*i*, 32*f* with $w = 0.322$ (relaxed F), 32*f* with $v = 0.414$, and 4*b* (1/2, 1/2, 1/2) (the Goldshmit position) in the center of large empty cubes.

Thus, for the first time the evolution of the defect structure of nonstoichiometric fluorite phases of the composition $Na_{0.5-x}R_{0.5+x}F_{2+2x}$ with rare-earth elements from holmium to ytterbium has been established.

ACKNOWLEDGMENTS

The neutron-diffraction part of the work was supported by State Scientific–Technical Program *Current Trends in Physics of Condensed Matter* (the topic *Neutron Diffraction Studies of Matter*, project no. 045). The study was supported by the Russian Foundation for Basic Research, project no. 96-03-32250.

REFERENCES

1. L. Pontonnier, G. Patrat, G. Leonard, *et al.*, Solid State Ionics **9/10**, 549 (1983).
2. E. A. Zhurova, B. A. Maksimov, S. Hull, *et al.*, Kristallografiya **42** (2), 277 (1997) [Crystallogr. Rep. **42**, 238 (1997)].
3. P. P. Fedorov, I. I. Buchinskaya, O. S. Bondareva, *et al.*, Zh. Neorg. Khim. **41** (11), 1920 (1996).
4. P. P. Fedorov, V. B. Aleksandrov, O. S. Bondareva, *et al.*, Kristallografiya (in press).
5. U. H. Zucker, E. Perenthaler, W. F. Kuhs, *et al.*, J. Appl. Crystallogr. **16**, 358 (1983).
6. L. A. Muradyan, B. A. Maksimov, V. B. Aleksandrov, *et al.*, Kristallografiya **31** (4), 661 (1986) [Sov. Phys. Crystallogr. **31**, 390 (1986)].

Translated by A. Darinskiĭ

Crystallography Reports, Vol. 45, No. 6, 2000, pp. 930–933. Translated from Kristallografiya, Vol. 45, No. 6, 2000, pp. 1010–1013.

STRUCTURE OF INORGANIC COMPOUNDS

Refinement of the Crystal Structure of a Fe,Sr-Analogue of Kentbrooksite

I. A. Ekimenkova*, R. K. Rastsvetaeva*, and A. P. Khomyakov**

** Shubnikov Institute of Crystallography, Russian Academy of Sciences, Leninskiĭ pr. 59, Moscow, 117333 Russia*

E-mail: rast@rsa.crystal.msk.ru

*** Institute of Mineralogy, Geochemistry, and Crystal Chemistry of Rare Elements, ul. Veresaeva 15, Moscow, 121327 Russia*

Received December 30, 1999

Abstract—The crystal structure of a new high-strontium representative of the eudialyte family has been refined. The mineral is isostructural to kentbrooksite and differs from the latter mainly by isomorphously replaced Mn (by Sr) in the *M*(3)-polyhedron "conjugated" with a polyhedral $NbFe_3$ cluster. © *2000 MAIK "Nauka/Interperiodica".*

The mineral barsanovite [1, 2] (an analogue of kentbrooksite [3]) differs from the other representatives of the eudialyte family by the different combination of the elements which prevail in the key positions for isomorphic replacements; by a pronounced acentric arrangement of the structural fragments; and, as a consequence, by the stable piezoelectric effect in the crystals [1, 2]. In this article, we report the structure determination of a barsanovite-like mineral somewhat loosely called Fe,Sr-kentbrooksite. This mineral was discovered by one of the authors in volatile alkaline- and rare-element-enriched ultraagpaitic pegmatites at the Alluaiv Mountain of the Lovozero alkaline massif (the Kola Peninsula). This mineral occurs as unfaceted greenish yellow grains up to 0.5–1 mm in diameter and, similar to barsanovite, is one of the optically negative uniaxial representatives of the eudialyte family.

The composition of the Fe,Sr-kentbrooksite, which was determined by electron-microprobe analysis, corresponds to the empirical formula (with respect to the sum of the cations equal to 53; $Z = 3$)

$$Na_{13.34}K_{0.23}Ca_{4.86}Sr_{1.53}Fe_{2.01}$$
$$\times Mn_{1.44}REE_{0.29}Zr_{3.11}Ti_{0.19}Hf_{0.04}Nb_{0.67}Si_{25.39}O_{75.76}Cl_{0.87}.$$

The structural data for the mineral and the details of the X-ray diffraction study are given in Table 1.

Assuming that the crystal structure of this mineral is similar to that of barsanovite, we used the atomic coordinates reported in [2] as a starting model. The atomic coordinates, the equivalent atomic thermal parameters, and the occupancies of the positions for Fe,Sr-kentbrooksite are given in Tables 2 and 3. The notation of the atomic positions corresponds to [2] except for some Na positions and a number of anions. Since the interatomic distances between the framework atoms are typical of this mineral, Table 4 lists only the distances in the polyhedra of the extraframework atoms.

The X-ray diffraction study demonstrated that the new mineral is structurally similar to kentbrooksite. Similar to the structures of other representatives of this family, the structure of the mineral is based on the framework of three- and nine-membered rings of SiO_4-tetrahedra and Zr- and Ca-octahedra. Because of the deficiency of Ca atoms in the mineral, the octahedra

Table 1. Structural data for the new mineral and details of the X-ray diffraction study

	Values
Unit-cell parameters, Å	$a = 14.245(2)$, $c = 29.959(10)$
Unit-cell volume, Å^3	$V = 5264.8$
Sp. gr., Z	$R3m$; 3
Radiation, λ, Å	MoK_α
Crystal dimensions, mm	0.35
Diffractometer	CAD-4
Scanning mode	ω/2θ
$\sin\theta/\lambda$, Å^{-1}	<0.703
Ranges of the indices of measured reflections	$-16 < h < 20$, $-20 < k < 20$, $-26 < l < 42$
R_{int} for equivalent reflections	0.024
Total number of reflections	4366 $I > 3\sigma(I)$
Number of independent reflections	1439 $\|F\| > 4\sigma(F)$
Program	AREN [4]
Absorption correction	DIFABS [5]
Number of independent positions	47
R factor upon anisotropic refinement	0.033

1063-7745/00/4506-0930$20.00

Table 2. Coordinates and equivalent thermal parameters (B_{eq}) of the framework atoms

Atom	*x/a*	*y/b*	*z/c*	B_{eq}, Å^2	Atom	*x/a*	*y/b*	*z/c*	B_{eq}, Å^2
Zr	0.3280(1)	0.1640(1)	0.1667(1)	1.15(3)	O(6)	0.5714(3)	0.6104(3)	0.2260(1)	1.2(2)
Ca	0.4052(1)	0.3314(1)	0.3331(1)	0.99(3)	O(7)	0.2528(3)	0.2259(3)	0.2066(1)	1.3(2)
Si(1)	0.6092(1)	0.6044(1)	0.0970(1)	0.64(8)	O(8)	0.4420(5)	0.2210(4)	0.2905(2)	1.8(3)
Si(2)	0.1400(1)	0.0700(1)	0.0800(1)	1.0(1)	O(9)	0.1800(2)	0.360(3)	0.2201(2)	1.0(3)
Si(3)	0.2693(1)	0.3253(1)	0.2367(1)	0.59(8)	O(10)	0.1840(6)	0.0920(4)	0.1307(2)	1.8(3)
Si(4)	0.2097(1)	0.4194(1)	0.0744(1)	0.8(1)	O(11)	0.1787(2)	0.3574(4)	0.0282(2)	1.2(3)
Si(5)	0.5262(1)	0.2631(1)	0.2505(1)	0.8(1)	O(12)	0.6051(2)	0.3952(2)	0.2532(2)	1.3(3)
Si(6)	0.4602(1)	0.5398(1)	0.2559(1)	0.7(1)	O(13)	0.2330(6)	0.1165(4)	0.0433(2)	1.7(3)
O(1*a*)*	0.2076(5)	0.6038(4)	0.2496(2)	1.1(1)	O(14)	0.4845(2)	0.5154(2)	0.3047(1)	1.2(3)
O(1*b*)*	0.212(3)	0.606(2)	0.269(1)	1.8(9)	O(15)	0.0146(5)	0.5073(3)	0.1153(2)	1.2(3)
O(2)	0.4000(4)	0.2979(4)	0.1251(1)	1.7(2)	O(16)	0.0612(2)	0.1224(3)	0.0732(2)	1.4(3)
O(3)	0.6246(3)	0.0348(3)	0.0448(1)	1.1(2)	O(17)	0.2742(3)	0.5484(4)	0.0659(3)	3.9(3)
O(4)	0.0429(3)	0.2989(3)	0.2891(1)	1.2(2)	O(18)	0.4718(6)	0.2359(4)	0.2020(2)	1.8(3)
O(5)	0.1065(4)	0.3877(5)	0.1069(1)	2.0(2)					

* The occupancies of the O(1*a*) and O(1*b*) positions are 0.8 and 0.2, respectively.

Table 3. Coordinates, equivalent thermal parameters (B_{eq}), multiplicities (Q), and occupancies of the positions (q) of the extraframework atoms

Atom	*x/a*	*y/b*	*z/c*	B_{eq}, Å^2	*Q*	*q*
Fe	0.4980(2)	0.5020(2)	0.0008(2)	1.16(8)	9	0.29(1)
Si(7)	0.3333	0.6667	0.0871(1)	1.01(8)	3	1.00
M(1)	0.3333	0.6667	0.2951(1)	1.48(4)	3	1.00
M(2)	0.1820(1)	0.3640(1)	0.3304(1)	1.04(3)	9	0.71(2)
M(3)	0.4672(2)	0.2336(1)	0.0486(1)	1.30(2)	9	1.00
Na(1*a*)	0.198(1)	0.099(1)	0.2869(3)	3.6(2)	9	0.50(3)
Na(1*b*)	0.210(1)	0.105(1)	0.2854(3)	3.3(2)	9	0.50(2)
Na(2*a*)	0.1089(3)	0.2178(5)	0.1540(2)	2.1(3)	9	0.53(3)
Na(2*b*)	0.127(4)	0.254(5)	0.148(2)	7(1)	9	0.10(4)
Na(2*c*)	0.0788(7)	0.1576(9)	0.1721(5)	3.6(5)	9	0.37(3)
Na(3*a*)	0.5682(4)	0.1364(5)	0.1725(2)	2.7(3)	9	0.55(4)
Na(3*b*)	0.5557(4)	0.1114(5)	0.1806(3)	2.4(4)	9	0.45(3)
Na(4*a*)	0.497(2)	0.775(2)	0.1732(5)	2.6(5)	18	0.15(3)
Na(4*b*)	0.4742(6)	0.7371(4)	0.1876(2)	3.5(2)	9	0.70(6)
OH(1)	0.3333	0.6667	0.1403(4)	1.3(5)	3	0.92(4)
OH(2)	0.6024(3)	0.3976(3)	−0.0032(2)	2.1(2)	9	1.00
H_2O(1)	0.619(4)	0.381(4)	0.095(3)	9.5(9)	9	0.20(2)
H_2O(2)	0.0	0.0	0.282(3)	10.9(6)	3	0.50(9)
Cl(1)	0.6667	0.3333	0.1018(2)	2.4(2)	3	0.60(4)
Cl(2)	0.0	0.0	0.2513(3)	2.2(2)	3	0.50(4)

Table 4. Characteristics of the coordination polyhedra of the extraframework atoms

Position	Composition ($Z = 1$)	Coordination number	M–O distance	
			range	average
Fe	$2.62Fe^{2+}$	4	2.066(6)–2.073(6)	2.070
Si(7)	3.0Si	4	1.591(5)–1.59(1)	1.59
M(1)	2.1Nb + 0.9Si*	6	1.900(6)–2.065(7)	1.983
M(2)	$3.34Fe^{2+}$ + 2.02Mn + 0.58Ti + 0.31Zr + 0.13Hf	5	2.092(5)–2.151(1)	2.114
M(3)	5.40Sr + 2.88Na + 0.72K	11	2.528(5)–2.930(4)	2.683
Na(1*a*)	4.5Na	8	2.50(1)–2.86(1)	2.68
Na(1*b*)	4.5Na	8	2.44(1)–3.01(1)	2.69
Na(2*a*)	4.77Na	8	2.540(8)–2.817(6)	2.655
Na(2*b*)	0.9Na	8	2.41(8)–2.84(8)	2.64
Na(2*c*)	3.33Na	7	2.39(1)–3.06(1)	2.66
Na(3*a*)	4.95Na	9	2.53(1)–2.988(9)	2.68
Na(3*b*)	4.05Na	9	2.49(1)–3.01(7)	2.67
Na(4*a*)	2.7Na	6	2.27(1)–2.93(2)	2.61
Na(4*b*)	6.3Na	8	2.24(1)–3.000(6)	2.66

* The coordination number of Si is 4.

forming the six-membered rings are isomorphically occupied by Ca and other elements; thus, the composition of this position is described as $(Ca_{4.85}Mn_{0.85}REE_{0.30})_{\Sigma 6}$.

It is a common practice to single out the so-called "key" microregions in the compounds of the eudialyte structural type. Similar to barsanovite [1, 2], one of these microregions is characterized by the statistical

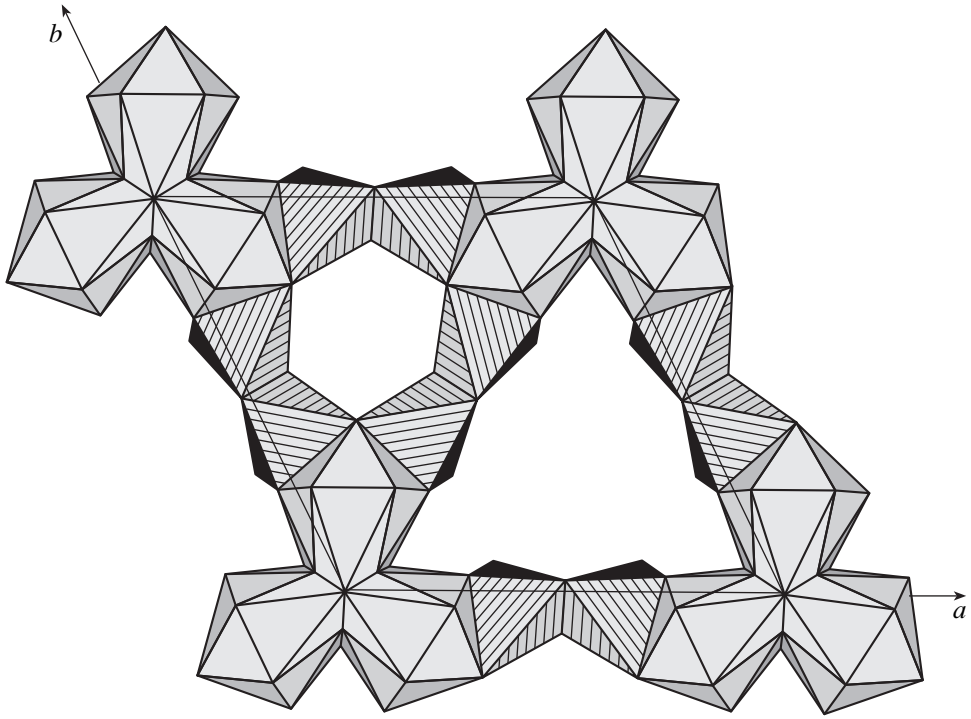

Fragment of the Fe,Sr-analogue of kentbrooksite projected onto the (001) plane. The rings of Ca octahedra are hatched with solid lines. The *M*(3) polyhedra are filled with dots.

distribution of Fe^{2+} ions over two alternative positions. In fact, these ions are located in a planar "square" at the junction of the six-membered rings of Ca octahedra and in the *M*(2) position based on the same "square" but are completed with an additional OH group (a five-vertex polyhedron). Two positions occupied by Fe atoms are spaced by a distance of 0.441(2) Å.

The second key microregion is, in fact, the central region of the pair of the nine-membered silicon–oxygen rings. A Si-tetrahedron is located in the center of one of these rings. The *M*(1) octahedral position is located in the center of the second nine-membered ring. The *M*(1) position is occupied by Nb (70%) and Si atoms. In the specimen studied, no splitting of this position into two new positions (octahedral and tetrahedral) typical of such structures was observed. An additional OH group "closing" the Si-tetrahedron was not localized either. Apparently, this is explained by low (compared to Nb) occupancy of the position by "lighter" Si atoms. Three five-vertex iron polyhedra are linked via a Nb octahedron, thus forming a polyhedral $NbFe_3$ cluster characteristic of barsanovite.

In the structure of the mineral, the *M*(3) position (see figure) close to the cluster should also be considered as a key microregion. In most of the representatives of the eudialyte family, this position is occupied by Na atoms, whereas in kentbrooksite, this position is occupied along with Na also by Mn (prevailing element), an Mn, *REE*, and Sr. In the new mineral, this position is occupied mainly by Sr, which distinguishes the new mineral from kentbrooksite.

The new mineral contains a small number of H_2O molecules and OH groups, whereas Cl atoms are located on a threefold axis.

The crystallochemical formula of the new mineral based on the X-ray diffraction data agrees with the results of the chemical analysis and can be written according to the {framework}–{zeolite portion} scheme ($Z = 3$) as follows: $\{(Ca_{4.85}Mn_{0.85}REE_{0.30})_{\Sigma 6} \times Zr_3[Si_3O_9]_2[Si_9O_{24}(OH,O)_3]_2\}\{Si_{1.0}(Si_{0.3}Nb_{0.7}) \times [Fe_{1.99}Mn_{0.67}Ti_{0.20}Zr_{0.10}Hf_{0.04}]_{\Sigma 3}(Sr_{1.80}Na_{0.96}K_{0.24})_{\Sigma 3} \times Na_{12}(OH)_{3.92}Cl_{1.1} \cdot 11H_2O\}$.

ACKNOWLEDGMENTS

This study was supported by the Russian Foundation for Basic Research, project nos. 99-05-65035 and 00-15-96633.

REFERENCES

1. R. K. Rastsvetaeva, Z. P. Razmanova, B. E. Borutskiĭ, and M. D. Dorfman, Zap. Vses. Mineral. O–va **3**, 65 (1990).
2. I. A. Ekimenkova, R. K. Rastsvetaeva, and A. P. Khomyakov, Dokl. Akad. Nauk **370** (4), 477 (2000).
3. O. Johnsen, Y. D. Grice, and R. A. Gault, Eur. J. Mineral. **10**, 207 (1998).
4. V. I. Andrianov, Kristallografiya **32** (1), 228 (1987) [Sov. Phys. Crystallogr. **32**, 130 (1987)].
5. N. Walker and D. Stuart, Acta Crystallogr., Sect. A: Found. Crystallogr. **A39** (2), 158 (1983).

Translated by T. Safonova

Crystallography Reports, Vol. 45, No. 6, 2000, pp. 934–938. Translated from Kristallografiya, Vol. 45, No. 6, 2000, pp. 1014–1018.

STRUCTURE OF INORGANIC COMPOUNDS

Refinement of the Crystal Structures of Two Marialites from the Kukurt Deposit of the East Pamirs

E. V. Sokolova*, E. R. Gobechiya*, A. A. Zolotarev, and Yu. K. Kabalov***

** Faculty of Geology, Moscow State University, Vorob'evy gory, Moscow, 119899 Russia*

*** Faculty of Geology, St. Petersburg State University, Universitetskaya nab. 7/9, St. Petersburg, 199034 Russia*

Received March 4, 1999; in final form, October 28, 1999

Abstract—The crystal structures of two marialite samples (*S*-1 and *S*-2) with the meionite component (9.6 and 17.0%, respectively) and the compositions $(Na_{3.35}Ca_{0.38}K_{0.24})_{\Sigma 3.97}(Si_{8.78}Al_{3.22}F^{3+}_{0.01})_{\Sigma 1.01}O_{24}Cl_{0.92}$ and $(Na_{3.21}Ca_{0.68}K_{0.11})_{\Sigma 3.90}(Si_{8.56}Al_{3.44}F^{3+}_{0.01})_{\Sigma 1.01}O_{24}Cl_{0.90}$, respectively, from the Kukurt deposit (the Pamirs, Tadzhikistan) were refined using the X-ray powder diffraction data by the Rietveld method. The chemical compositions of the samples *S*-1 and *S*-2 correspond to the discontinuity in the existence region of the marialite–meionite solid solution. The structures of *S*-1 and *S*-2 marialites were refined in the anisotropic/isotropic approximation (the Pearson function) to the reliability factors R_p = 4.80 and 5.00, R_{wp} = 6.10 and 6.50, R_B = 3.70 and 3.50, R_F = 4.70 and 4.90; s = 1.39 and 1.28, respectively. The unit-cell parameters were determined as a = 12.049(1) Å, c = 7.5670(8) Å, V = 1098.49(2) Å^3 for *S*-1 and a = 12.037(1) Å, c = 7.5535(1) Å, V = 1097.18(1) Å^3 for *S*-2, the sp. gr. $I4/m$, Z = 2. The analysis of the X-ray diffraction data allowed the refinement of the trend in the behavior of the unit-cell parameters depending on the composition of the Si–Al–O framework of scapolite. © *2000 MAIK "Nauka/Interperiodica".*

INTRODUCTION

Scapolite is extensively studied as a widespread rock-forming mineral. This study was undertaken as a part of the systematic structure studies of the minerals of the scapolite group performed at the Department of Crystallography and Crystal Chemistry at the Faculty of Geology of the Moscow State University [1–7]. The results presented below are of interest, because the samples of two marialites studied belong to the discontinuity in the existence range of the series of the marialite–meionite solid solutions suggested in our earlier studies [4, 6]. The data on the refined structures of nine scapolite samples containing 0.02–7.6 and 21.2–56.3% of the meionite component are complemented with the results of the structural studies of marialites with 9.6 and 17.0% of the meionite component. For minerals of the scapolite group described by the general formula $M_4T_{12}O_{24}A$ [where the major components are *M* (Na and Ca), *T* (Si and Al), and *A* (Cl, CO_3, and SO_4)], the meionite component is determined as *Me* = 100[Ca/(Na + Ca + K)] (%). Scapolites form a series of marialite–meionite solid solutions. The ideal formulas of the end members of the solid-solution series are $Na_4Al_3Si_9O_{24}Cl$(*Ma*) and $Ca_4Al_6Si_6O_{24}CO_3$(*Me*). In 1998, the S-dominant scapolite, which received the name of silvialite and having the ideal formula $Ca_4Al_6Si_6O_{24}(SO_4)$, was recognized as the third mineral type of the scapolite group [8]. However, many problems of the crystal chemistry of scapolites have not been solved as yet.

One of the problems constantly discussed is the number of fragments in the series of the marialite–meionite solid solutions. According to [9, 10], the series of the marialite–meionite solid solutions consists of three fragments (*A*, *B*, and *C*)—$Na_4Al_3Si_9O_{24}Cl$ (marialite)–$CaNa_3Al_4Si_8O_{24}Cl$, $CaNa_3Al_4Si_8O_{24}Cl$–$NaCa_3Al_5Si_7O_{24}CO_3$, and $NaCa_3Al_5Si_7O_{24}CO_3$–$Ca_4Al_6O_{24}CO_3$ (meionite)—and two discontinuity regions at 20–25% of *Me* (between the *A* and *B* fragments) and 60–67% of *Me* (between the *B* and *C* fragments). In [11, 12], the total series of the marialite–meionite solid solutions was divided into three isomorphous series with 9.0 > Si > 8.4, 8.4 > Si > 7.3, and 7.3 > Si > 6.0 and two regions of discontinuity corresponding to changes in the unit-cell-parameters. Since the numbers of silicon atoms per formula unit Si (apfu) equal to 7.3 and 8.4 correspond to $(Al_{4.7}Si_{7.3}O_{24})$ and $(Al_{3.6}Si_{8.4}O_{24})$, respectively, one can think that the studies [9, 10] and [11, 12] lead to the same conclusions. However, these conclusions are not supported by the sufficient number of X-ray of diffraction data.

The Rietveld method is the optimal approach to solving the problems of stereochemistry and crystal chemistry of scapolites. The refinement of the scapolite structures based on X-ray powder diffraction data obtained over a wide composition range allows one not

1063-7745/00/4506-0934$20.00 © 2000 MAIK "Nauka/Interperiodica"

only to update the structural data and to measure the unit-cell parameters with a high degree of accuracy (which is very important for constructing parameter–composition diagrams for solid solutions) but also to obtain systematic information for the whole series of samples. In this article, we report the results of the crystal structure refinement for two scapolite samples from the Kukurt deposit (the Pamirs, Tadzhikistan), *S*-1 and *S*-2, with 9.6 and 17.0% of meionite and the compositions $(Na_{3.35}Ca_{0.38}K_{0.24})_{\Sigma 3.97}(Si_{8.78}Al_{3.22}F^{3+}_{0.01})_{\Sigma 1.01}O_{24}Cl_{0.92}$ and $(Na_{3.21}Ca_{0.68}K_{0.11})_{\Sigma 3.90}(Si_{8.56}Al_{3.44}F^{3+}_{0.01})_{\Sigma 1.01}O_{24}Cl_{0.90}$, respectively, which correspond to the discontinuity in the existence region of the marialite–meionite solid solutions, which was assumed earlier.

EXPERIMENTAL

The scapolite samples, including the microprobe-analysis data (which were used to obtain the above-given chemical formulas for the minerals studied), were mineralogically described in [9].

The X-ray diffraction data for *S*-1 and *S*-2 marialites were collected on an automated ADP-2 diffractometer ($\lambda Cu K_\alpha$ radiation, Ni filter, the step in 2θ equal to 0.02°, the exposure time at a point 5 s). All the computations were performed using the WYRIET program (version 3.3) [13]. No reflections with $h + k + l \neq 2n$ exceeding the background, which would be inconsistent with a body-centered lattice, were observed. Hence, the structure was refined within the sp. gr. *I*4/*m*. The starting atomic coordinates were those reported in [1]. The peak profiles were approximated by the Pearson function with 6FWHM, where FWHM is the average peak width at a half-height. The asymmetry was refined for $2\theta < 40°$. The ionic scattering curves were used. The refinement was made by adding parameters and the continuous graphical modeling of the background. Using the chemical-analysis data [9], we placed Na and Ca atoms into the *M* positions at the constant composition of the K position (*A* are Cl atoms). The occupancies of the *T* positions were refined using the *f* curve for silicon.

RESULTS AND DISCUSSION

The details of X-ray data collection and structure refinement for two marialite samples are given in Table 1. The atomic coordinates and thermal parameters are listed in Table 2.

Stoichiometry. Apparently, the deficiency of negative charges in the chemical formulas of the scapolite samples should be compensated with the introduction into the formulas the calculated amounts of $(CO_3)^{2-}$ anions. Then, *S*-1 and *S*-2 marialites can be described by the crystallochemical formulas $(Na_{3.35}Ca_{0.38}K_{0.24})_{\Sigma 3.97}(Si_{8.78}Al_{3.22})_{\Sigma 12.0}O_{24}[Cl_{0.96}(SO_4)_{0.02}(CO_3)_{0.07}]_{\Sigma 2.05}$ and $(Na_{3.21}Ca_{0.68}K_{0.11})_{\Sigma 4.00} \times (Si_{8.56}Al_{3.44})_{\Sigma 12.0}O_{24}[Cl_{0.93}(SO_4)_{0.02}(CO_3)_{0.14}]_{\Sigma 2.09}$, respectively, $Z = 2$, sp. gr. *I*4/*m*, $\rho_{calc} = 2.54$ and 2.49 g/cm^3, respectively. The refined occupancies of the *M* positions agree well with the chemical-analysis data. In our previous studies [3, 6], we reported the data for scapolites with the compositions ranging within $Me_{0.2}$–$Me_{7.6}$ and $Me_{21.2}$–$Me_{56.3}$. It was assumed that the region of existence of the series of solid solutions has the discontinuity in the range $Me_{7.6}$–$Me_{21.2}$. The compositions of the samples *S*-1 (9.6% of *Me*, Si/Al = 2.73, Si(apfu) = 8.78) and *S*-2 (17.0% of *Me*, Si/Al = 2.49, Si(apfu) = 8.56) correspond to the discontinuity range assumed earlier. The stoichiometry of the series of marialite–meionite solid solutions is determined depending on type of isomorphous replacement [11]—the change in the Si/Al ratio in the tetrahedral *T* positions in the framework; the $2M^+ \longleftrightarrow M^{2+}$ replacement in the *M* positions in the framework cavities (usually, Na^+ and K^+ are replaced by Ca^{2+}), and the $2A^- \longleftrightarrow A^{2-}$ anionic replacements in the *A* positions in the framework cavities (mainly, Cl^- ions are replaced by CO_3^{2-} and *S*-containing anions). Evidently, there is no simple quantitative correlation between all the three types of isomorphous replacements. Thus, scapolites with the same Si/Al ratio can have different amount of the meionite component (*Me*) irrespective of the composition of the *A* position. For example, *S*-1 marialite differs from PAM-2 (7.5% of *Me*, Si/Al = 2.73, Si(apfu) = 8.78) [3]

Table 1. Details of X-ray data collection and structure refinement for *S*-1 and *S*-2 marialites containing 9.6 and 17.0% of *Me*, respectively

Characteristic	*S*-1	*S*-2
a, Å	12.049(1)	12.037(1)
c, Å	7.5670(8)	7.5720(1)
V_0, Å^3	1098.49(2)	1097.18(1)
Sp. gr.	*I*4/*m*	*I*4/*m*
Number of Bragg reflections	1257	1257
Number of parameters in the refinement	72	72
R_p	0.048	0.050
R_{wp}	0.061	0.065
R_{exp}	0.044	0.051
R_B	0.037	0.035
R_F	0.047	0.049
*s**	1.39	1.28
DWD**	1.14	1.41
σ_x***	1.910	1.666

* $s = R_{wp}/R_{exp}$ where R_{exp} is the expected value of R_{wp}.
** DWD is the Durbin–Watson *d* statistics [14].
*** σ_x is the factor used in the calculations of standard deviations [15].

Table 2. Atomic coordinates and thermal parameters in the structures of *S*-1 and *S*-2 marialites containing 9.6 and 17.0% of *Me*, respectively

S-1				*S*-2			
x	*y*	*z*	B_{iso} (Å^2)	*x*	*y*	*z*	B_{iso} (Å^2)
			M				
0.3744(7)	0.2964(7)	0.5	3.4(2)	0.3727(5)	0.2973(8)	0.5	5.0(2)
			T(1)				
0.3381(5)	0.4109(5)	0	1.3(1)	0.3375(5)	0.4130(4)	0	1.4(1)
			T(2)				
0.6615(3)	0.9145(3)	0.7938(3)	1.70(2)	0.6618(3)	0.9161(3)	0.7937(4)	1.43(7)
			O(1)				
0.4524(8)	0.353(1)	0	1.3(3)	0.4566(8)	0.3527(8)	0	2.8(3)
			O(2)				
0.695(1)	0.8790(8)	0	1.9(3)	0.6911(9)	0.8846(8)	0	2.3(2)
			O(3)				
0.3507(7)	0.9480(7)	0.785(1)	2.9(3)	0.3479(5)	0.9480(7)	0.781(1)	3.0(2)
			O(4)				
0.2719(7)	0.3731(5)	0.822(1)	1.8(2)	0.2706(7)	0.3748(4)	0.8278(9)	3.1(2)
			Cl				
0.5	0.5	0.5	5.5(4)	0.5	0.5	0.5	6.0(3)

by the amount of the meionite component but has the same amounts of silicon and aluminum.

Unit-cell parameters. The dependences of the unit-cell parameters *a*, *c*, and *V* on the number of Si atoms per formula unit for two scapolite samples with due regard of the data from [3, 6] are graphically presented in Figs. 1a–1c. The characteristic dependence of the parameter *a* on the composition is shown in Fig. 1a. Our results and the structural data [3, 5] show that there is no obvious dependence of the parameter *a* on Si(apfu) in the composition range 9 > Si > 8.34. In the range 8.17 > Si > 7.47, the parameter *a* linearly increases with the Si(apfu) content. The dependence of the parameter *c* on the composition is shown in Fig. 1b. In the composition range 9 > Si > 8.34, the parameter *c* increases from 7.5427 to 7.5809 Å. In the range 8.17 > Si > 7.47, the parameter *c* gradually decreases. An analogous dependence of the parameter *c* on the composition was described in [9] on the basis of the known X-ray diffraction data and the unit-cell parameters measured for scapolites from the Pamirs. The unit-cell volume *V* as a function the Si-content is shown in Fig. 1c. In the composition range 9 > Si > 8.34, no correlation between the silicon content and the unit-cell volume is observed, whereas in the range 8.17 > Si > 7.47, the unit-cell volume gradually increases.

Thus, there is no direct correlation between the change in the parameter *a* (V_0) and the Si-content in the range 9 > Si > 8.34 corresponding to sodium-enriched marialites. Our data confirm the conclusions [16] on the specific behavior of Na-enriched scapolites in the composition range 9 > Si > 8.34. Thus, irrespectively of the Ca^{2+} and Al^{3+} contents, no regular changes in the parameter *a* (V_0) were observed.

The *T*, *M*, and *A* positions in the crystal structure of scapolite. The Si–Al framework of scapolites is composed of two types of four-membered rings of SiO_4 and AlO_4 tetrahedra. The rings of the first type consist only of *T*(1) tetrahedra with the vertices aligned in the same direction. The rings of the second type consist of *T*(2) tetrahedra. The rings of both types are linked and form a framework such that five-membered rings are formed along the *c*-axis of the unit cell. The Na^+ and Ca^{2+} cations are located in the channels of this framework (the *M* position). In the samples studied, the average ⟨*T*–O⟩ distances indicate that the *T*(1) position is completely occupied by Si atoms (⟨*T*(1)–O⟩ = 1.598–1.615 Å), whereas the *T*(2) position is statistically occupied with Si and Al atoms (⟨ *T*(2)–O⟩ = 1.656–1.660 Å). A *T*(1) tetrahedron, in which the O–*T*(1)–O angles range within 108.1°–111.4°, is more regular than the *T*(2) tetrahedron, in which the O–*T*(2)–O angles range over a wider range (from 102.9° to 114.4°). It is commonly agreed that the *T*–O distances in the framework tetrahedra increase due to a higher Al content and, to a lesser degree, a higher content of more electropositive Ca atoms and not Na atoms. However, our data did not confirm this assumption, because no such correlations were observed in the composition range 9 > Si > 8.34.

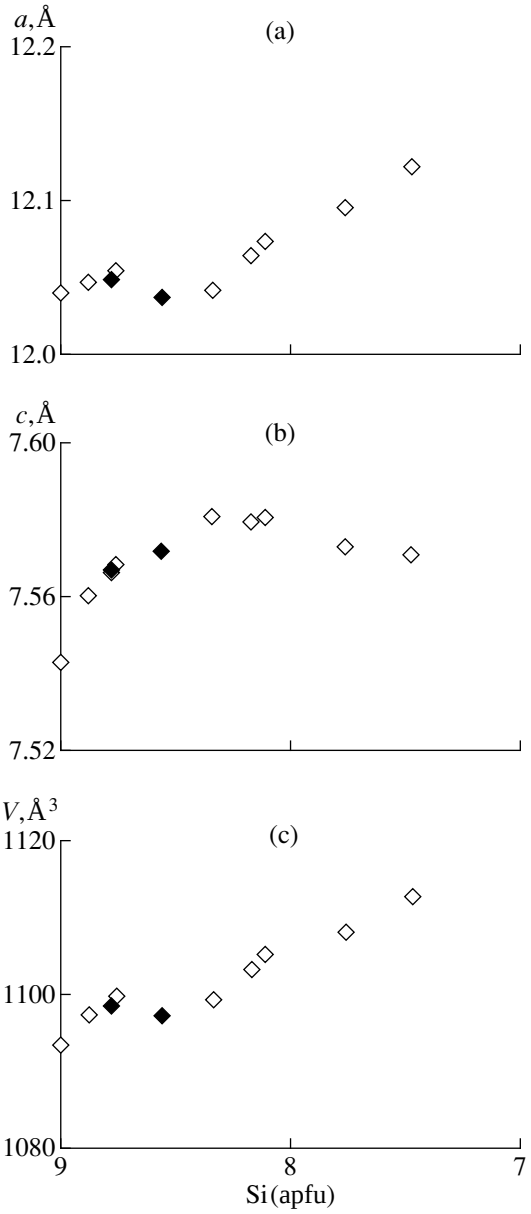

Fig. 1. Unit-cell parameters of scapolite as functions of Si content (the number of Si atoms per formula unit, apfu): (a) *a*, (b) *c*, and (c) *V*; ◆ correspond to the data obtained in the present study and ◇ indicates the data of our earlier studies [3, 6].

The refinement of the occupancy of the *M* position by the Ca^{2+}, Na^{+}, and K^{+} ions demonstrated that this position is occupied only partly. Although the chemical analysis indicated that this position was completely occupied, the refinement performed in our study revealed the presence of some vacancies in the *S*-1 and *S*-2 structures (7 and 10%, respectively). In the *S*-1 and *S*-2 samples, the ⟨*M*–O⟩ distances are equal (within the experimental error, 2.77 and 2.79 Å, respectively), although the content of "smaller" Ca atoms is higher in the *S*-2 sample. At coordination number 8, the effective ionic radii of Ca^{2+} and Na^{+} are 1.12 and 1.16 Å, respectively [17]. The potassium content (rK^{+} = 1.31 Å) produces no effect on the "size" of the *M* position. The results of the X-ray diffraction study of scapolite allows one to state that the *M* position is much less sensitive to the variations in the composition (namely, to the variation in the cation–ligand distances) than the *T* positions in the framework. In the crystal structures of our samples, the *A* position was occupied by Cl^{-} ions. This position had the maximum isotropic thermal parameters.

Bond angles in the framework. In the Si–Al framework of scapolites, the *T*–O–*T* angles along the *c*-axis of the unit cell are close to 139°. This value is energetically more favorable for an unstrained Si–O–Si fragment [18]. The ⟨*T*(2)–O(2)–*T*(2)⟩ angles vary from 138.8° to 142.8°, and the ⟨*T*(1)–O(4)–*T*(2)⟩ angles vary from 137.7° to 138.9°. The *T*(2)–O–*T*(2)' bond is virtually aligned along the *c* axis, whereas the *T*(1)–O–*T*(2) bond is inclined to it. Apparently the stability of the scapolite framework is higher at the maximum number of the Si–O–Si fragments with angles close to 139°. The *T*–O–*T* fragments along the *a* (*b*) axis are strained (the bond angles are close to 160°). Here, two types of angles can be distinguished, namely, the *T*(1)–O(1)–*T*(1)' angles between *T*(1) tetrahedra and the *T*(1)–O(4)–*T*(2) angles between tetrahedra of different types. All three atoms forming the *T*(1)–O(1)–*T*(1)' angle are located exactly in the (001) plane, whereas the plane of the *T*(1)–O(4)–*T*(2) angle is inclined to the (001) plane, but the inclination angle is substantially smaller than the angle between the *T*(1)–O–*T*(2) plane and the *c*-axis. For the scapolite sample under study, the ⟨*T*(1)–O(1)–*T*(1)'⟩ and ⟨*T*(1)–O(4)–*T*(2)⟩ angles range from 159.4° to 159.8° and from 149.0° to 148.4°, respectively.

CONCLUSIONS

The structures of two marialite samples were refined by the Rietveld method. Analyzing the X-ray diffraction data for the minerals of the scapolite group, one can draw the conclusion that the marialite–meionite series are continuous series of solid solutions existing in the range of Si content 9 > Si > 8.34. The samples have the space group *I*4/*m*, with Si(Al) atoms being statistically distributed over the *T* positions of the framework.

For the first time, an increase in the parameter *c* with a decrease of the silicon content in the marialite structure was observed in the range of the Si content 9 > Si > 8.34.

The topological analysis of the *T*–O–*T* bond angles in the framework of scapolite demonstrated that different "response" of the parameters *a* and *c* on the composition variation is associated with the degree of strain of the Si–O–Si bonds along the [100], [010], and [001] directions.

ACKNOWLEDGMENTS

The study was supported by the Russian Foundation for Basic Research, project no. 97-05-64000a.

REFERENCES

1. Yu. K. Kabalov, E. V. Sokolova, and V. S. Urusov, Kristallografiya **40** (5), 829 (1995) [Crystallogr. Rep. **40**, 766 (1995)].
2. Yu. K. Kabalov and E. V. Sokolova, Kristallografiya **41** (3), 461 (1996) [Crystallogr. Rep. **41**, 436 (1996)].
3. E. V. Sokolova, Yu. K. Kabalov, B. L. Sherriff, *et al.*, Can. Mineral. **34** (5), 1039 (1996).
4. E. V. Sokolova, Author's Abstract of Doctoral Dissertation (Moscow State University, Moscow, 1996).
5. Yu. K. Kabalov, E. V. Sokolova, B. Sherriff, and D. Jenkins, Kristallografiya **43** (4), 626 (1998) [Crystallogr. Rep. **43**, 578 (1998)].
6. B. L. Sherriff, E. V. Sokolova, Yu. K. Kabalov, *et al.*, Can. Mineral. **36** (5), 1261 (1998).
7. Yu. K. Kabalov, E. V. Sokolova, N. V. Kalygina, and J. Schneider, Kristallografiya **44** (6), 1049 (1999).
8. D. K. Teertstra, M. Schindler, B. L. Sherriff, and F. C. Hawthorne, Miner. Mag. **63**, 321 (1999).
9. A. A. Zolotarev, Zap. Vseross. Mineral. O–va **122** (2), 90 (1993).
10. A. A. Zolotarev, Zap. Vseross. Mineral. O–va **125** (1), 169 (1996).
11. D. K. Teertstra and B. L. Sherriff, Am. Mineral. **81**, 169 (1996).
12. D. K. Teertstra and B. L. Sherriff, Chem. Geol. **136**, 233 (1997).
13. J. Schneider, in *Proceedings of the IUCr International Workshop on the Rietveld Method "Profile Refinement on IBM-PC's," Petten, 1989*, p. 71.
14. R. G. Hill and H. D. Flack, J. Appl. Crystallogr. **20**, 356 (1987).
15. J.-F. Bérar and P. Lelann, J. Appl. Crystallogr. **24**, 1 (1991).
16. B. L. Sherriff and D. K. Teertstra, in *Abstracts of the 16th General Meeting IMA'94, Pisa, 1994*, p. 372.
17. R. D. Shannon and C. T. Prewitt, Acta Crystallogr., Sect. B: Struct. Crystallogr. Cryst. Chem. **B25**, 925 (1969).
18. F. Liebau, *Structural Chemistry of Silicates: Structure, Bonding, and Classification* (Springer-Verlag, New York, 1985; Mir, Moscow, 1988).

Translated by T. Safonova

Crystallography Reports, Vol. 45, No. 6, 2000, pp. 939–944. Translated from Kristallografiya, Vol. 45, No. 6, 2000, pp. 1019–1024.

STRUCTURE OF COORDINATION COMPOUNDS

Crystal and Molecular Structures of Nickel(II) Complex with Hetarylazo Ligand 2-(2'-*N*-Phenylaminonaphthylazo)-1-Octylbenzimidazole

A. S. Antsyshkina*, G. G. Sadikov*, A. S. Burlov, L. N. Divaeva**, and A. D. Garnovskiĭ****

** Kurnakov Institute of General and Inorganic Chemistry, Russian Academy of Sciences, Leninskiĭ pr. 31, Moscow, 117907 Russia*

E-mail: asants@ionchran.rinet.ru

*** Research Institute of Physical and Organic Chemistry, Rostov State University, pr. Stachki 194/3, Rostov-on-Don, 344104 Russia*

Received April 5, 1999

Abstract—The crystal structure of the nickel(II) complex NiL_2, in which the ligand is the 2-(2'-*N*-phenylaminonaphthylazo)-1-octylbenzimidazole derivative, is determined by X-ray diffraction analysis. The crystals are triclinic, a = 10.938(5) Å, b = 12.628(7) Å, c = 20.180(9) Å, α = 81.68(5)°, β = 80.70(4)°, γ = 82.03(4)°, Z = 2, and space group $P\bar{1}$ [the heavy-atom method, full-matrix anisotropic–isotropic least-squares refinement, R_1 = 0.0713 for 1910 reflections with $F \geq 4\sigma(F)$]. The structural units are octahedral molecular complexes with five-membered chelate metallocycles. The vertices of the coordination octahedron of the Ni atom are occupied by the N atoms of two planar ligands. The Ni–N bond lengths are 2.05–2.11(5) Å. Some molecular fragments are disordered. *© 2000 MAIK "Nauka/Interperiodica".*

INTRODUCTION

Determination of the crystal structure of the nickel(II) complex NiL_2 (**I**) with 2-(2'-*N*-phenylaminonaphthylazo)-1-octylbenzimidazole (H*L*) is a part of our investigation into the problem of the chelate isomerism (formation of five- or six-membered chelate rings) in metallochelate complexes of *o*-amino(hydroxy, mercapto)azo compounds (see [1, 2] and references therein).

Schemes 1 and 2 represent the possible structures of the complexes considered in [2]:

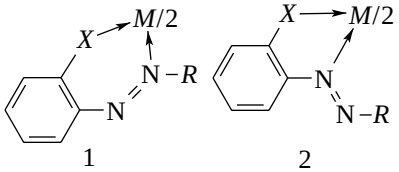

1

2

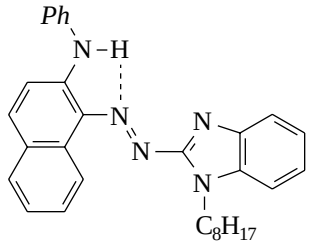

3

Here, X = O, S, N, or *Ts* (*Ts* = $SO_2C_6H_4$-*Me-p*); M = Ni, Cu, or Pd; and R is an aromatic heterocyclic substituent.

Metallochelate complexes with the ligands in which hetaryl substituents contain the donor N atom capable of coordinating the metal atom are of particular interest.

Such compounds were assigned the structures with four- and six-membered metallocycles (involving the hetaryl N atom) [3–6]. However, the formation of two five-membered metallocycles (with the hetaryl N atom not involved in metal coordination) seemed more favorable [4, 7]. This structure was found by X-ray diffraction analysis in the palladium(II) hetarylamine complex [1] (**II**). The formation of five-membered metallocycles appeared to be possible in the case when both N atoms of the azo group were involved in the metal coordination; an example of this coordination mode is provided by the binuclear tetrahedral copper(I) complex with an azoheteroaromatic radical as a ligand [2, 8].

In this paper, we report the results of the X-ray structure analysis of complex **I** with a highly branched ligand H*L* (scheme 3).

EXPERIMENTAL

The synthesis of crystals **I** was described in [2].

Crystals **I** are dark blue and have a prismatic habit. The unit cell is triclinic, a = 10.938(5) Å, b = 12.628(7) Å, c = 20.180(9) Å, α = 81.68(5)°, β = 80.70(4)°, γ = 82.03(4)°, V = 2702.8 Å^3, M = 2015.9, F(000) = 1068,

Coordinates and thermal parameters U_{eq} and U_{iso} of non-hydrogen atoms in compound **I**

Atom	*x*	*y*	*z*	U_{eq}/U_{iso}, Å^2	Atom	*x*	*y*	*z*	U_{eq}/U_{iso}, Å^2
Ni	0.1617(2)	0.4572(2)	0.2535(1)	0.0486(7)	N(1*b*)	0.067(1)	0.5593(9)	0.1841(5)	0.057(3)
N(1*a*)	0.342(1)	0.4716(9)	0.1992(6)	0.063(3)	N(2*b*)	0.0862(9)	0.348(1)	0.2109(5)	0.052(3)
N(2*a*)	0.227(1)	0.5560(8)	0.3093(6)	0.053(3)	N(3*b*)	0.226(1)	0.3104(9)	0.3029(5)	0.050(3)
N(3*a*)	0.011(1)	0.4895(9)	0.3283(6)	0.054(3)	N(4*b*)	0.113(1)	0.246(1)	0.2298(5)	0.059(3)
N(4*a*)	0.155(1)	0.5903(8)	0.3607(6)	0.060(3)	N(5*b*)	0.229(1)	0.131(1)	0.3118(6)	0.065(4)
N(5*a*)	0.051(1)	0.5788(9)	0.4181(7)	0.066(4)	C(1*b*)	0.008(1)	0.508(1)	0.1494(7)	0.055(4)
C(1*a*)	0.404(2)	0.534(1)	0.2250(7)	0.050(4)	C(2*b*)	0.020(1)	0.391(1)	0.1613(7)	0.056(4)
C(3*a*)	0.344(2)	0.582(1)	0.2850(8)	0.055(4)	C(3*b*)	−0.052(1)	0.3328(9)	0.1253(6)	0.077(5)
C(3*a*)	0.410(1)	0.6498(8)	0.3192(6)	0.062(4)	C(4*b*)	−0.043(1)	0.2209(9)	0.1352(6)	0.11(1)
C(4*a*)	0.3599(9)	0.6978(9)	0.3770(6)	0.071(5)	C(5*b*)	−0.104(2)	0.1672(7)	0.0977(8)	0.17(1)
C(5*a*)	0.431(1)	0.7591(9)	0.4042(5)	0.086(6)	C(6*b*)	−0.175(2)	0.225(1)	0.0503(9)	0.24(2)
C(6*a*)	0.552(1)	0.7725(9)	0.3736(7)	0.083(5)	C(7*b*)	−0.184(2)	0.337(1)	0.0403(8)	0.20(2)
C(7*a*)	0.6021(9)	0.725(1)	0.3158(6)	0.086(6)	C(8*b*)	−0.122(1)	0.3909(7)	0.0778(7)	0.11(1)
C(8*a*)	0.531(1)	0.6632(9)	0.2886(5)	0.074(5)	C(9*b*)	−0.130(2)	0.506(2)	0.067(1)	0.104(7)
C(9*a*)	0.594(1)	0.614(1)	0.2296(9)	0.073(5)	C(10*b*)	−0.074(2)	0.562(1)	0.1011(8)	0.075(5)
C(10*a*)	0.532(2)	0.552(1)	0.1986(7)	0.065(4)	C(11*b*)	0.060(1)	0.6686(7)	0.1785(6)	0.069(5)
C(11*a*)	0.381(2)	0.434(2)	0.134(1)	0.07(1)	C(12*b*)	−0.038(1)	0.720(1)	0.2192(7)	0.121(8)
C(12*a*)	0.402(2)	0.503(1)	0.075(1)	0.07(1)	C(13*b*)	−0.048(2)	0.831(1)	0.2188(9)	0.15(1)
C(13*a*)	0.436(2)	0.462(2)	0.013(1)	0.09(1)	C(14*b*)	0.039(2)	0.8907(7)	0.178(1)	0.15(1)
C(14*a*)	0.449(2)	0.352(2)	0.0114(9)	0.09(1)	C(15*b*)	0.138(2)	0.839(1)	0.137(1)	0.18(1)
C(15*a*)	0.428(3)	0.282(1)	0.071(1)	0.12(2)	C(16*b*)	0.148(1)	0.728(1)	0.1374(7)	0.136(9)
C(16*a*)	0.394(3)	0.323(2)	0.1326(9)	0.11(1)	C(17*b*)	0.188(1)	0.227(1)	0.2796(7)	0.063(4)
C(11*c*)	0.392(2)	0.400(2)	0.156(1)	0.06(1)	C(18*b*)	0.2959(7)	0.2637(7)	0.3510(4)	0.050(4)
C(12*c*)	0.339(2)	0.397(2)	0.098(1)	0.06(1)	C(19*b*)	0.3589(9)	0.3089(7)	0.3924(5)	0.068(5)
C(13*c*)	0.391(2)	0.323(2)	0.054(1)	0.08(1)	C(20*b*)	0.4233(9)	0.243(1)	0.4399(4)	0.084(5)
C(14*c*)	0.496(2)	0.252(2)	0.067(1)	0.11(1)	C(21*b*)	0.425(1)	0.1318(9)	0.4460(5)	0.098(6)
C(15*c*)	0.549(2)	0.255(2)	0.125(1)	0.12(1)	C(22*b*)	0.362(1)	0.0865(6)	0.4046(5)	0.092(6)
C(16*c*)	0.497(2)	0.329(2)	0.169(1)	0.07(1)	C(23*b*)	0.2973(7)	0.1525(8)	0.3571(4)	0.059(4)
C(17*a*)	0.043(2)	0.552(1)	0.3674(9)	0.059(4)	C(24*b*)	0.201(2)	0.028(1)	0.296(1)	0.090(6)
C(18*a*)	−0.1099(8)	0.4740(7)	0.3537(5)	0.052(4)	C(25*b*)	0.310(3)	−0.034(2)	0.259(2)	0.15(1)
C(19*a*)	−0.191(1)	0.4147(7)	0.3323(5)	0.067(5)	C(26*b*)	0.361(4)	0.013(3)	0.201(2)	0.20(2)
C(20*a*)	−0.311(1)	0.4100(8)	0.3672(6)	0.083(5)	C(27*b*)	0.478(6)	−0.070(4)	0.161(2)	0.24(2)
C(21*a*)	−0.3498(8)	0.4645(9)	0.4235(6)	0.090(5)	C(28*b*)	0.590(6)	−0.061(4)	0.133(4)	0.33(3)
C(22*a*)	−0.269(1)	0.5238(8)	0.4448(5)	0.081(5)	C(29*b*)	0.671(7)	−0.126(6)	0.095(4)	0.24(4)
C(23*a*)	−0.1488(9)	0.5285(6)	0.4099(5)	0.064(4)	C(30*b*)	0.735(7)	−0.082(4)	0.036(4)	0.29(3)
C(24*a*)	−0.038(2)	0.640(1)	0.4738(9)	0.081(5)	C(31*b*)	0.828(4)	−0.138(4)	0.003(3)	0.27(2)
C(25*a*)	−0.064(2)	0.761(1)	0.452(1)	0.097(6)					
C(26*a*)	−0.048(2)	0.819(2)	0.513(1)	0.105(7)					
C(27*a*)	0.087(2)	0.824(2)	0.520(1)	0.093(6)					
C(28*a*)	0.096(2)	0.878(2)	0.584(1)	0.112(7)					
C(29*a*)	0.222(3)	0.894(2)	0.595(2)	0.16(1)					
C(30*a*)	0.226(3)	0.948(3)	0.657(2)	0.22(2)					
C(31*a*)	0.283(5)	0.906(4)	0.703(2)	0.28(2)					

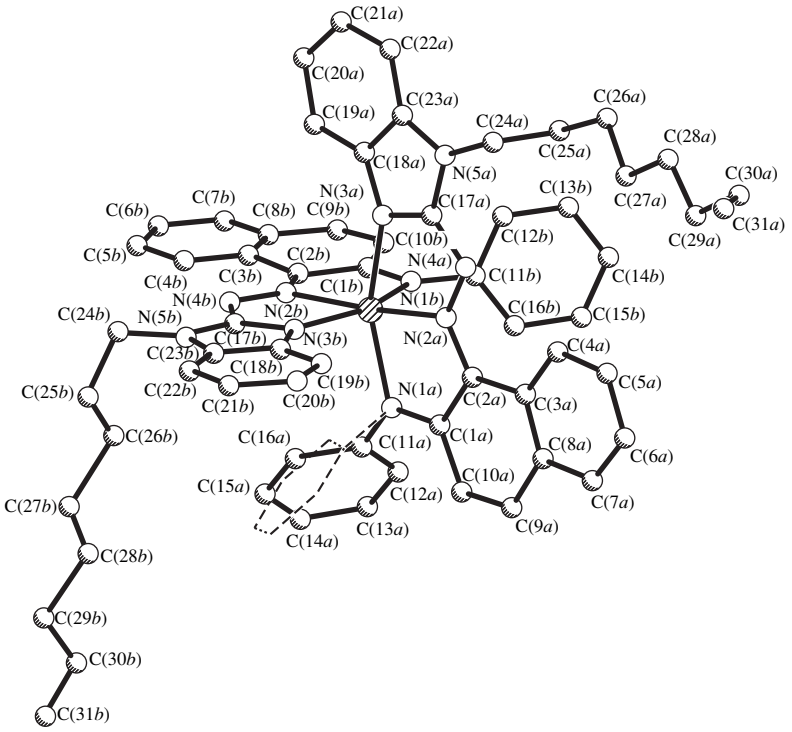

Fig. 1. Structure of complex **I**. The disordered fragment of ligand *A* is shown by dashed lines.

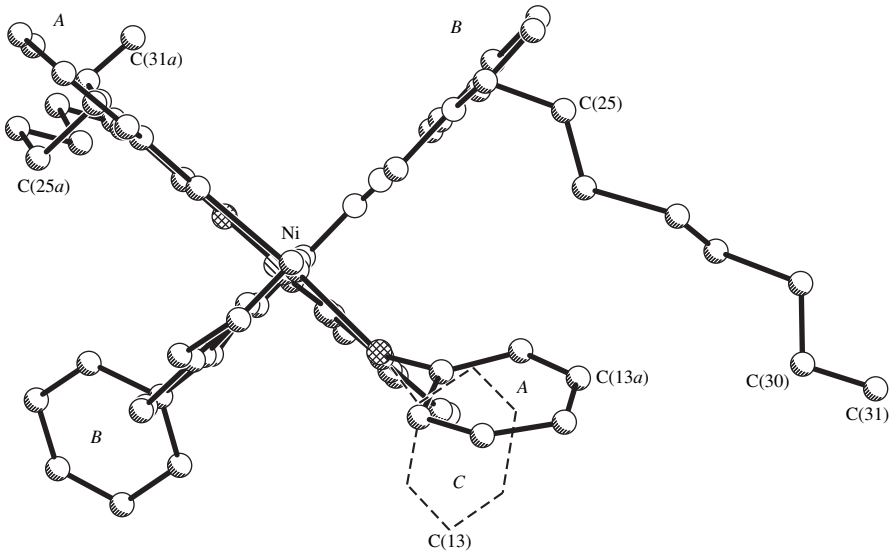

Fig. 2. Projection of complex **I** onto the plane of the main part of both independent ligands. The internal symmetry axis of the complex (C_2) lies in the plane of the figure. Labels *A* and *B* denote the corresponding ligands.

μ_{Mo} = 0.41 mm^{-1}, ρ_{calcd} = 1.239 g/cm^3, Z = 2, and space group $P\bar{1}$.

The experimental data were obtained on a Syntex $P2_1$ diffractometer (λMoK_α, graphite monochromator, $\theta/2\theta$ scan mode, $2\theta_{max} = 48°$).

The structure was determined by the heavy-atom method using the SHELXL93 program [9]. A part of the hydrogen atoms was located from the difference F maps. The full-matrix least-squares anisotropic (isotropic for H and disordered C atoms) refinement resulted in $wR2$ = 0.2301 and $GOOF$ = 0.73 for 3874 averaged reflections and the final value R_1 = 0.0713 for 1910 observed reflections [$F \geq 4\sigma F$].

In the course of the refinement, the cyclic fragments of the structure were restrained to be planar and the

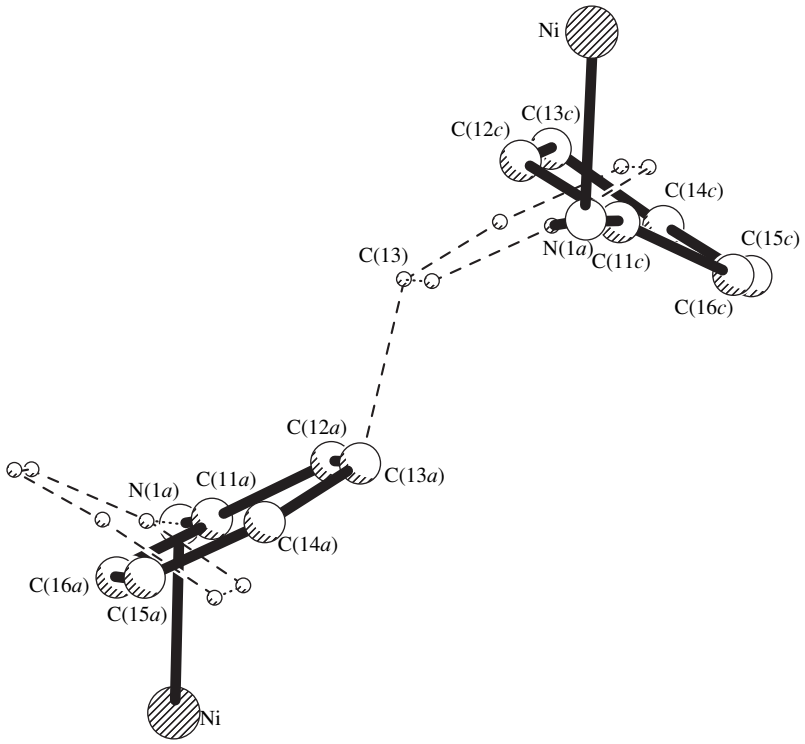

Fig. 3. Statistical disordering of the phenyl rings of ligand *A* in the region of interlayer contacts. The layers are parallel to the plane of the figure.

C–C bonds of the phenyl rings, other than those involved in the metallocycles, were restrained to be equal in length (1.395 Å).

In the structure solution, we found that one of the phenyl rings is disordered over two positions [C(11*a*)–C(16*a*) and C(11*c*)–C(16*c*)]. They were taken into account at the last stages of the refinement.

The coordinates of the non-hydrogen atoms in the structure are listed in the table.

Analysis of the anisotropic thermal parameters revealed that the positions of some atoms tend to split. This is especially true for the atoms of the six-membered C(3*b*)–C(8*b*) fragment of the more "rigid" ligand *B*. To a lesser degree, this trend is exhibited by the atoms of the hydrocarbon "tails" and, to the smallest degree, by an analogue of the disordered phenyl ring; that is, the C(11*b*)–C(16*b*) ring in which the position of the C(14*b*) atom is only slightly split.

RESULTS AND DISCUSSION

Based on the data of magnetochemical measurements (μ_{eff} = 3.68 μB at 297 K) and UV spectra (absorption in the 8000–10 200 range and at 12 400 cm^{-1}), complex **I** was assigned a tetrahedral structure with six-membered metallocycles [5].

According to the data of our X-ray diffraction study, crystal structure **I** is formed by octahedral molecular complexes with five-membered chelate metallocycles. These complexes are shown in Fig. 1. All vertices of the coordination octahedron of the Ni atom are occupied by the nitrogen atoms of two chemically equivalent ligands, namely, 2-(2'-*N*-phenylaminonaphthylazo)-1-octylbenzimidazole anions. The Ni–N bond lengths are 2.05–2.08(1) Å; the only exception is provided by the Ni–N(1*a*) bond, which is slightly elongated [2.11(1) Å]. This elongation is probably due to the statistical disordering of the C(11*a*)–C(16*a*) phenyl ring attached to N(1*a*). The angular distortions of the coordination polyhedron are more significant: the N(1*a*)NiN(3*a*) and N(1*b*)NiN(3*b*) angles between the bonds to the opposite vertices are 155.6(5)° in both cases. The deviations of the above atoms from their mean plane, which is arbitrarily considered an equatorial plane of the octahedron, indicate its tetrahedral distortion [the dihedral angle between planes N(1*a*)NiN(1*b*) and N(3*a*)NiN(3*b*) is 33°]. The angle between the bonds to the axial vertices N(2*a*) and N(2*b*) is close to the linear angle and equal to 171.9(4)°.

In other words, complex **I** is formed by two planar (within 3σ) tridentate ligands (*A* and *B*), which tend to be mutually perpendicular (the dihedral angle is 88°) and are bonded to the Ni atom through three active coordination nitrogen centers each. This structure corresponds to the meridional isomer of the octahedron with the twofold rotation axis. Thus, the internal sym-

metry of the coordination center of the central Ni atom is close to C_2 (Fig. 2).

Although the ligands are chemically equivalent, they differ in crystal-chemical behavior. Figure 2 shows that two halves of molecular complex **I** are geometrically different. The largest difference is observed in the orientation of the phenyl substituents. In one of the ligands (*B*), the phenyl ring is perpendicular to the main plane of the molecule (87°). In the other ligand (*A*), the corresponding ring is disordered over two positions that deviate from the main plane of the ligand almost symmetrically in opposite directions (66° and 58°); the dihedral angle between these two positions is 57° (Fig. 3). In complex **II**, which contains a similar ligand, the angle between the plane of the phenyl substituent and the main plane of the ligand is 65°.

The orientations of the octyl chains provide one more geometric difference between the ligands in **I**. The chain labelled *b* is stretched and aligned perpendicular to the planar fragment to which it is attached (Figs. 1, 2), whereas its analogue in the other half of the molecule is bent. In both ligands, the atoms close to the terminal atoms of the chain, specifically the C(30*a*) and C(31*a*) atoms, can be disordered over closely spaced positions.

The position of the C(3*b*)–C(8*b*) phenyl ring of ligand *B* is split. The degree of splitting increases with an increase in the distance of the atom from the center of the complex and reaches the maximum value for the most distant atom C(6*b*) [C(6*b*)··C(6*b*') 0.7 Å]. The position of the C(3*b*) atom only tends to split. A similar splitting, even though less pronounced, is observed for the C(11*b*)–C(16*b*') ring. This splitting is resolved only for the most distant atom C(14*b*), the two positions of which are spaced at 0.15 Å.

Let us consider the reasons for the statistical disordering of some components of the structure. Note that all disturbances of the equivalence and symmetry (disordering of the phenyl rings of ligand *A*, six-membered fragments of ligand *B* and, to some extent, hydrocarbon chains) are observed along the directions parallel to the *x*-axis, which is the shortest crystal axis. All the regions of disordering are concentrated at the boundaries of the layers, which are distinguished in the structure and aligned parallel to the coordinate plane (001) (Fig. 4). Each layer has a rather dense structure, and the layers are the regions of a relatively stable structure. The planar parts of the complexes form virtually the closest packing within the layer. Ligands *A* that are related by the inversion centers and translations along the *x*- and *y*-axes form a dense system of structural fragments parallel to one another. A similar system is formed by the *B* ligands in the perpendicular direction. Both systems mutually strengthen each other. The hydrocarbon "tails" and the phenyl rings of ligand *B* fill small cavities in the packing of the main parts of the complexes.

We can assume that the (001) plane is the growth surface in the course of the crystal formation. At the free surface of a separate layer, the phenyl rings of ligand *A* assume random orientations. Possibly, their initial orientation is the same as in ligand *B*, that is, perpendicular to the main part of the molecule. The packing of each next layer should result in a "conflict" situation (Fig. 3), which is avoided by the rotation of the phenyl rings of the "conflicting" ligands. The compromise orientation is reached spontaneously. It has no effect on similar neighboring regions; therefore, structure **I** is statistically disordered. It is important that, in the process of packing the layers, the phenyl ring achieves one of the two possible equilibrium positions (ring *A* or *C*, Fig. 3). Note that the *A* position is identical to that observed in **II**. One of the four combinations of ring contacts cannot occur, since it corresponds to the C(13*a*)··C(13*a*') distance equal to 1.84 Å. This means that the *C* orientation can occur twice as often as *A*. However, the least-squares refinement resulted in identical site-occupation factors 0.48 ± 0.02 for the atoms of both variants. Moreover, the isotropic thermal parameters of the corresponding atoms in two ligands were found to be almost equal. It follows that the actual mutual arrangement of the rings is the same in two variants: the rings are rotated by a considerable angle (57°).

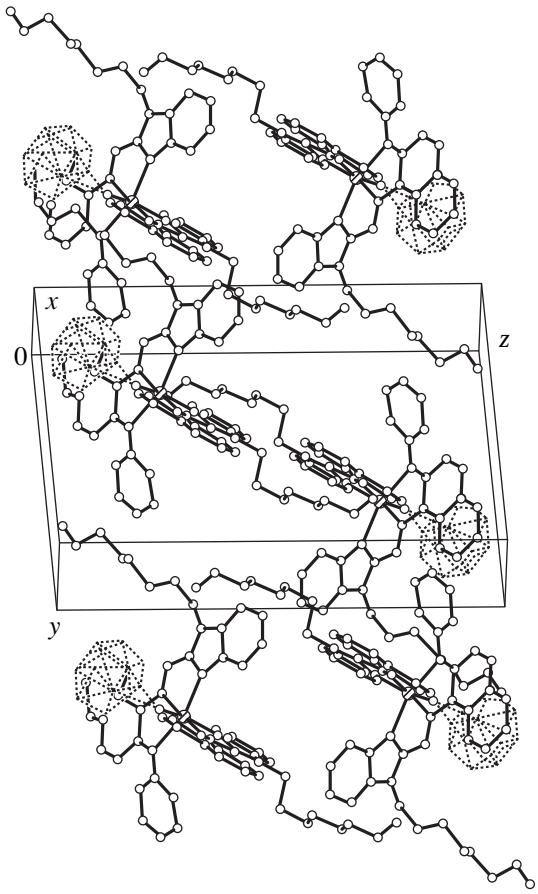

Fig. 4. Structure of a layered fragment in **I**. The disordered phenyl rings are shown by dotted lines. The layers are perpendicular to the plane of the figure and to the *z*-axis.

The combination of parallel rings, which is most convenient for steric reasons, is not formed at all.

REFERENCES

1. A. D. Karnovskiĭ, A. S. Burlov, A. S. Antsyshkina, and L. N. Divaeva, Zh. Neorg. Khim. **41** (1), 90 (1996).
2. A. S. Burlov, L. N. Divaeva, A. S. Antsyshkina, *et al.*, Koord. Khim. (2000) (in press).
3. A. T. Pilipenko and L. I. Savranskiĭ, Dokl. Akad. Nauk SSSR **195** (3), 614 (1970).
4. V. M. Ivanov, *Heterocyclic Nitrogen-Containing Azo Compounds* (Nauka, Moscow, 1982).
5. V. A. Alekseenko, V. A. Kogan, A. S. Burlov, *et al.*, Zh. Neorg. Khim. **30** (1), 252 (1985).
6. V. A. Alekseenko, A. S. Burlov, L. N. Divaeva, *et al.*, Zh. Neorg. Khim. **33** (9), 2307 (1988).
7. A. T. Pilipenko, E. A. Karetnikova, and V. V. Trachevskiĭ, Zh. Anal. Khim., No. 10, 1787 (1983).
8. N. Doslik, T. Sixt, and W. Kaim, Angew. Chem. **110** (17), 2521 (1998).
9. G. M. Sheldrick, *SHELXL93: Program for the Refinement of Crystal Structures* (Univ. of Göttingen, Göttingen, 1993).

Translated by I. Polyakova

Crystallography Reports, Vol. 45, No. 6, 2000, pp. 945–950. Translated from Kristallografiya, Vol. 45, No. 6, 2000, pp. 1025–1030.

STRUCTURE OF ORGANIC COMPOUNDS

Crystal Structures of *N*-(Salicylidene)-Tris(hydroxymethyl)methylamine and *N*-(5-Chlorosalicylidene)-Tris(hydroxymethyl)methylamine

Yu. M. Chumakov*, B. Ya. Antosyak*, M. D. Mazus*, V. I. Tsapkov, and N. M. Samus'****

** Institute of Applied Physics, Academy of Sciences of Moldova, Chisinau, 20-28 Moldova*

E-mail: chumakov.xray@phys.asm.md

*** Moldova State University, ul. Matteevicha 60, Chisinau, 277009 Moldova*

Received December 7, 1998; in final form, May 26, 1999

Abstract—The crystal structures of *N*-(salicylidene)-tris(hydroxymethyl)methylamine (**I**) and *N*-(5-chlorosalicylidene)-tris(hydroxymethyl)methylamine (**II**) have been determined. Crystals **I** are monoclinic, a = 10.518(2) Å, b = 8.691(2) Å, c = 12.513(2) Å, β = 101.54(2)°, space group $P2_1$, Z = 4, and R = 0.046. Crystals **II** are triclinic, a = 7.196(1) Å, b = 10.248(2) Å, c = 16.835(3) Å, α = 100.57(3)°, β = 90.42(3)°, γ = 94.68(3)°, space group $P\bar{1}$, Z = 4, and R = 0.072. The asymmetric cells in both crystals contain two independent molecules. In structure **I**, the molecules occur in two tautomeric forms: benzenoid and quinoid. In structure **II**, both molecules are in the quinoid form. *© 2000 MAIK "Nauka/Interperiodica".*

INTRODUCTION

It is known that salicylaldimines in solutions can occur in two tautomeric forms [1–3]:

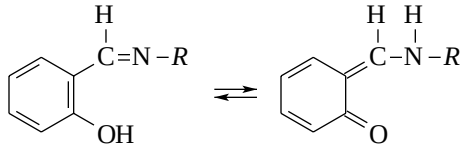

Benzenoid Quinoid

For the most part, the crystallization of these compounds results in the benzenoid form of aldimines. However, the equilibrium can be shifted toward the formation of the quinoid form with a change in the nature of both the solvent and substituents in the benzene ring and at the nitrogen atom.

In this respect, it was of interest to determine the structure of *N*-(salicylidene)-tris(hydroxymethyl)methylamine (**I**) and *N*-(5-chlorosalicylidene)-tris(hydroxymethyl)methylamine (**II**) prepared from a methanol–dimethylformamide (3 : 1) solution and to elucidate how the nature of the substituent in the benzene ring of azomethine affects the formation of its particular form.

EXPERIMENTAL

Salicylaldimine **I** was prepared according to the following procedure. A solution of salicylaldehyde (10 mmol) in dimethylformamide (10 ml) was added to a solution of tris(hydroxymethyl)aminomethane (10 mmol) in methanol (30 ml) with stirring and heating in a water bath (50°C). A slow evaporation of the resulting dark-orange solution for 2 days led to the precipitation of a yellowish-orange finely crystalline compound (the yield was 63%). The compound was filtered off with a glass filter, washed in a small amount of methanol, and dried in air. The composition of the compound obtained was determined by elemental analysis.

For $C_{11}H_{15}NO_4$ anal. calcd. (%): C, 58.67; H, 6.67; N, 6.22.

Found (%): C, 58.51; H, 6.60; N, 6.01.

Compound **II** was synthesized using a similar procedure by the interaction of a methanol solution of tris(hydroxymethyl)aminomethane with a dimethylformamide solution of 5-chlorosalicylaldehyde (the molar ratio of reactants was 1 : 1). The yield was 65% of the theoretically calculated value.

For $C_{11}H_{14}NO_4Cl$ anal. calcd. (%): C, 50.87; H, 5.39; Cl, 13.68; N, 5.39.

Found (%): C, 50.80; H, 5.21; Cl, 13.56; N, 5.27.

Azomethines **I** and **II** were readily soluble in dimethylformamide and dimethylsulfoxide and, upon heating, in water and alcohols. Single crystals **I** and **II** suitable for the X-ray diffraction analysis were obtained by the recrystallization of the studied compounds from a methanol–dimethylformamide solution (3 : 1).

The main crystal data and the refinement parameters for compounds **I** and **II** are given in Table 1. The X-ray diffraction analysis was carried out on a DAR-UMB

1063-7745/00/4506-0945$20.00 © 2000 MAIK "Nauka/Interperiodica"

Table 1. Crystal data, data collection, and refinement parameters for structures **I** and **II**

Empirical formula	$C_{11}H_{15}NO_4$	$C_{11}H_{14}NO_4Cl$
M	225.24	519.36
T, K	293(2)	293(2)
λ, Å	0.71073	0.71073
Crystal system	Monoclinic	Triclinic
Space group	$P2_1$	$P\bar{1}$
a, Å	10.518(2)	7.196(1)
b, Å	8.691(2)	10.248(2)
c, Å	12.513(3)	16.835(3)
α, deg	90	100.57(3)
β, deg	101.54(2)	90.42(3)
γ, deg	90	94.68(3)
V, Å^3	1120.7(4)	1216.0(4)
Z	4	4
ρ_{calcd}, Mg/m^3	1.335	1.418
μ, mm^{-1}	0.102	0.317
Crystal size, mm	$0.2 \times 0.2 \times 0.3$	$0.15 \times 0.2 \times 0.4$
No. of measured reflections	1757	2236
No. of unique reflections	1589 [$R_{(int)} = 0.0177$]	2020 [$R_{(int)} = 0.0224$]
No. of reflections/no. of parameters	1576/299	1960/344
Goodness-of-fit on F^2	0.962	1.098
R [$I > 2\sigma(I)$]	$R1 = 0.0464$, $wR2 = 0.1175$	$R1 = 0.0720$, $wR2 = 0.1820$
R (for all reflections)	$R1 = 0.0479$, $wR2 = 0.1338$	$R1 = 0.0823$, $wR2 = 0.2338$
Residual (maximum and minimum) densities in difference Fourier synthesis (e Å^{-3})	0.423 and −0.331	0.856 and −0.307

diffractometer (CuK_α radiation, graphite monochromator, ω–θ/2θ scan mode) at room temperature. No correction for absorption was applied to the intensity data. Both structures were solved by the direct methods using the SHELXS86 program package [4]. The refinement was performed by the least-square method in the anisotropic approximation for the non-hydrogen atoms and in the isotropic approximation for the hydrogen atoms with the use of the SHELXL93 program package [5]. The positions of the hydrogen atoms were obtained from geometric considerations, and the most probable orientations of the hydrogen atoms in the carboxyl OH groups were determined from the difference Fourier synthesis. These data were refined by the least-squares procedure. The coordinates of the non-hydrogen atoms in structures **I** and **II** are listed in Tables 2 and 3, respectively.

DESCRIPTION OF STRUCTURES

The asymmetric cells in both crystals contain two independent molecules *A* and *B* (Figs. 1, 2). In molecule *A* (**II**), the alcohol oxygen atoms are disordered in the $C(CH_2OH)_3$ fragment. For each of the C(9*A*), C(10*A*), and C(11*A*) carbon atoms, two peaks were located from the difference Fourier synthesis and were then refined as oxygen atoms with a multiplicity of 0.5. The bond lengths and angles in the planar salicylaldi-

Table 2. Coordinates of the non-hydrogen atoms ($\times 10^4$) and their equivalent isotropic thermal parameters U_{eq} ($Å^2 \times 10^3$) in structure **I**

Atom	*x*	*y*	*z*	U_{eq}
O(1*A*)	−2225(5)	−1275(5)	9040(4)	34(1)
O(2*A*)	−1093(6)	3414(6)	6100(5)	45(1)
O(3*A*)	336(5)	679(6)	8202(4)	42(1)
O(4*A*)	−2684(5)	320(6)	4690(4)	42(1)
N(1*A*)	−1989(5)	−291(6)	7098(4)	25(1)
C(1*A*)	−3471(7)	−2336(7)	7386(6)	29(2)
C(2*A*)	−4378(7)	−3396(7)	6901(6)	32(2)
C(3*A*)	−4868(6)	−4431(9)	7496(6)	35(2)
C(4*A*)	−4431(8)	−4484(9)	8581(7)	47(2)
C(5*A*)	−3575(8)	−3381(9)	9154(6)	44(2)
C(6*A*)	−3026(7)	−2247(7)	8535(6)	31(2)
C(7*A*)	−2866(7)	−1274(8)	6727(5)	29(2)
C(8*A*)	−1288(6)	718(8)	6501(6)	30(2)
C(9*A*)	−1794(7)	2364(7)	6614(6)	36(2)
C(10*A*)	197(7)	568(9)	7046(6)	40(2)
C(11*A*)	−1415(7)	182(7)	5352(6)	39(2)
O(1*B*)	−2240(5)	3197(6)	14027(4)	39(1)
O(2*B*)	−2651(6)	1656(7)	9704(5)	57(2)
O(3*B*)	−1073(5)	−1453(5)	11089(4)	37(1)
O(4*B*)	326(5)	1327(6)	13204(4)	45(1)
N(1*B*)	−2023(6)	2268(6)	12125(5)	33(2)
C(1*B*)	−3440(6)	4244(7)	12409(6)	28(2)
C(2*B*)	−4380(6)	5358(8)	11906(5)	36(2)
C(3*B*)	−4921(7)	6432(11)	12493(7)	47(2)
C(4*B*)	−4517(8)	6370(11)	13649(7)	49(2)
C(5*B*)	−3620(8)	5359(10)	14106(6)	49(2)
C(6*B*)	−3098(6)	4263(7)	13568(5)	31(2)
C(7*B*)	−2912(6)	3291(8)	11754(5)	31(2)
C(8*B*)	−1267(7)	1280(7)	11502(5)	27(2)
C(9*B*)	−1379(6)	1822(8)	10321(5)	35(2)
C(10*B*)	−1768(6)	−345(8)	11570(5)	33(2)
C(11*B*)	127(6)	1398(7)	12076(5)	32(2)

Table 3. Coordinates of the non-hydrogen atoms ($\times 10^4$) and their equivalent isotropic thermal parameters ($Å \times 10^3$) in structure **II**

Atom	*x*	*y*	*z*	U_{eq}
Cl(1*A*)	2491(4)	8282(2)	5620(1)	80(1)
O(1*A*)	467(7)	7599(5)	2184(3)	51(1)
N(1*A*)	547(7)	5042(5)	2094(3)	35(1)
C(1*A*)	1111(8)	6612(6)	3323(4)	36(2)
C(2*A*)	1563(10)	6793(7)	4149(4)	45(2)
C(3*A*)	1838(10)	8036(7)	4601(4)	48(2)
C(4*A*)	1617(11)	9142(8)	4248(5)	59(2)
C(5*A*)	1170(11)	8998(7)	3443(5)	52(2)
C(6*A*)	885(9)	7739(6)	2941(4)	38(2)
C(7*A*)	928(9)	5294(6)	2853(4)	40(2)
C(8*A*)	435(9)	3744(6)	1527(4)	35(2)
C(9*A*)	1683(13)	3966(7)	829(5)	60(2)
C(10*A*)	−1559(10)	3388(8)	1221(5)	56(2)
C(11*A*)	1142(11)	2656(6)	1931(4)	53(2)
Cl(1*B*)	2551(4)	2844(2)	4408(1)	81(1)
O(1*B*)	4565(7)	4572(4)	7839(3)	48(1)
O(2*B*)	1122(8)	431(5)	8267(4)	66(2)
O(3*B*)	5203(8)	−960(6)	8743(4)	76(2)
O(4*B*)	5441(8)	3190(5)	9500(3)	63(2)
N(1*B*)	4432(7)	2090(5)	7966(3)	35(1)
C(1*B*)	3879(9)	2785(6)	6722(4)	36(2)
C(2*B*)	3436(9)	2402(7)	5899(4)	48(2)
C(3*B*)	3195(10)	3324(8)	5424(5)	54(2)
C(4*B*)	3447(11)	4675(8)	5750(5)	60(2)
C(5*B*)	3896(10)	5105(7)	6556(5)	52(2)
C(6*B*)	4150(9)	4191(6)	7089(5)	39(2)
C(7*B*)	4020(8)	1805(6)	7206(4)	36(2)
C(8*B*)	4442(9)	1176(6)	8549(4)	34(2)
C(9*B*)	2430(9)	1028(7)	8873(4)	43(2)
C(10*B*)	5083(10)	−177(7)	8161(4)	45(2)
C(11*B*)	5793(10)	1847(7)	9240(4)	47(2)
O(2*A*)	1428(10)	5157(7)	550(4)	54(3)
O(2*AA*)	3513(16)	3801(16)	826(10)	62(6)
O(3*A*)	−2895(11)	3207(7)	1767(5)	54(3)
O(3*AA*)	−2542(17)	4247(12)	911(7)	52(5)
O(4*A*)	1115(10)	1509(6)	1354(5)	47(3)
O(4*AA*)	197(19)	2209(13)	2544(7)	59(5)

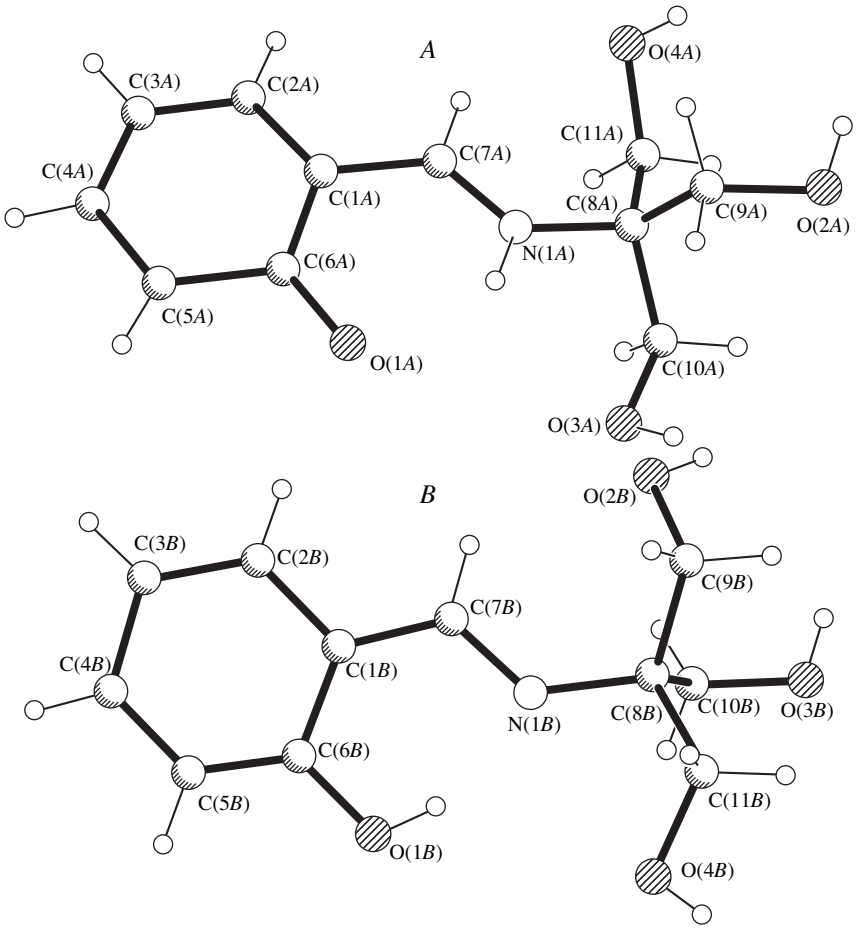

Fig. 1. Structure of molecule **I**.

mine fragments and in the $C(CH_2OH)_3$ groups of the studied compounds are in agreement with the data available in the literature [6–12]. The superposition of independent molecules in compounds **I** and **II** is displayed in Fig. 3. The molecules are the rotamers in which the $C(CH_2OH)_3$ groups are rotated about the N(1)–C(8) bonds. In compound **I**, the C(7)N(1)C(8)C(9), C(7)N(1)C(8)C(10), and C(7)N(1)C(8)C(11) torsion angles are equal to 108.1(7)°, 132.2(7)°, and 17.0(9)° in molecule *A* and 14(1)°, 109.3(8)°, and 132.8(7)° in molecule *B*. In compound **II**, these angles are 126.6(7)°, 114.0(7)°, and 171.4(9)° in molecule *A* and 87.9(7)°, 34.5(8)°, and 154.7(6)° in molecule *B*. Two tautomeric forms are observed in crystal **I** (Fig. 1): the proton is localized at the N(1*A*) nitrogen atom in molecule *A* and at the O(1*B*) oxygen atom in molecule *B* (the latter being in a benzenoid form). According to the Cambridge Structural Database (Version 5.14) [6], the majority of the structures containing the salicylaldimine fragment have a benzenoid form. Note that the shortest O–C distance (1.334 Å) in this fragment is observed in 2-(4,6-dimethyl-2-pyridyliminomethyl)phenol [7]. In molecule *B* (**I**), this distance is equal to 1.340(8) Å and virtually coincides with that in *N*-salicylidene-*p*-dimethylaminoaniline (1.343 Å) [8] and 2-(4-methyl-2-pyridyliminomethyl)phenol (1.336 Å) [9]. In *N*-phenylsalicylaldimine-5-sulfamate [10], in which the proton is localized at the azomethine nitrogen atoms, the O–C distance in the salicylaldimine fragment is equal to 1.298 Å. In compound **I**, the O–C distance in molecule *A* is equal

Table 4. Parameters of intramolecular hydrogen bonds in structures I and II

D–H···*A*	(H···*A*), Å	*D*–H···*A*, deg	*D*···*A*, Å
		I	
N(1*A*)–H(1*A*)···O(1*A*)	1.94(1)	137(1)	2.634(8)
O(1*B*)–H(1*B*)···N(1*B*)	1.82(1)	150(1)	2.566(8)
		II	
N(1*A*)–H(1*A*)···O(1*A*)	1.89(1)	139(1)	2.601(7)
N(1*B*)–H(1*B*)···O(1*B*)	1.89(1)	138(1)	2.585(7)

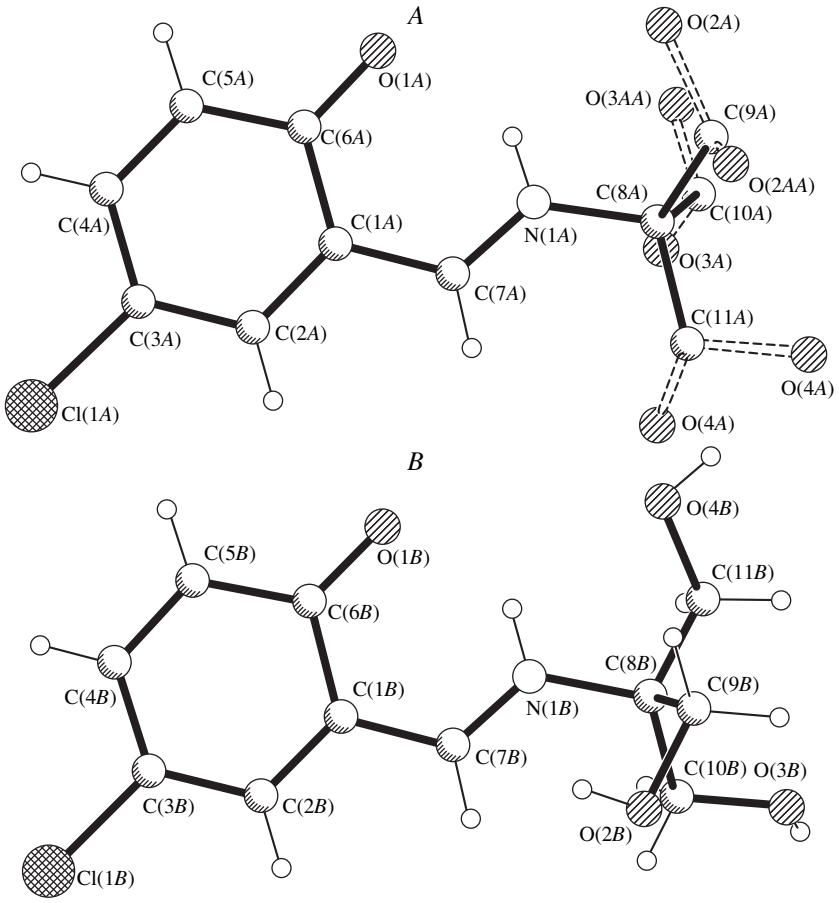

Fig. 2. Structure of molecule **II**.

to 1.268 Å, which virtually coincides with those in molecules *A* [1.287(8) Å] and *B* [1.277(8) Å] in compound **II**.

Therefore, the presence of chlorine atom in the 5-position of the benzene ring of compound **II** leads to the transfer of the proton to the azomethine nitrogen atom. At the same time, salicylaldimine in crystal **I** is characterized by two tautomeric forms. It should be noted that, in aldimine [10], in which the proton is localized at the nitrogen atom, the SO_3 group occupies the 5-position of the benzene ring.

In molecules *A* and *B* of both compounds, the O(1) and N(1) atoms form the intramolecular hydrogen bonds. The parameters of hydrogen bonds are presented in Table 4. Moreover, in structure **I**, molecules *A* and *B* are linked by the hydrogen bonds O(1*A*)··O(2*B*) and O(1*A*)··O(3*B*) and form chains running along the twofold screw axis due to the hydrogen bonds O(3*A*)–H(3*A*)··O(3*B*) (–*x*, *y* + 1/2, –*z* + 2) and O(4*B*)–H(4*B*)··O(2*A*) (–*x*, *y* – 1/2, –*z* + 2). These chains related by a translation along the *c* axis are joined by the hydrogen bonds O(2*A*)–H(2*A*)··O(1*B*) (*x*, *y*, *z* – 1) and O(4*A*)–H(4*A*)··O(1*B*) (*x*, *y*, *z* – 1).

In structure **II**, the molecules are linked into a three-dimensional framework by the hydrogen-bond system.

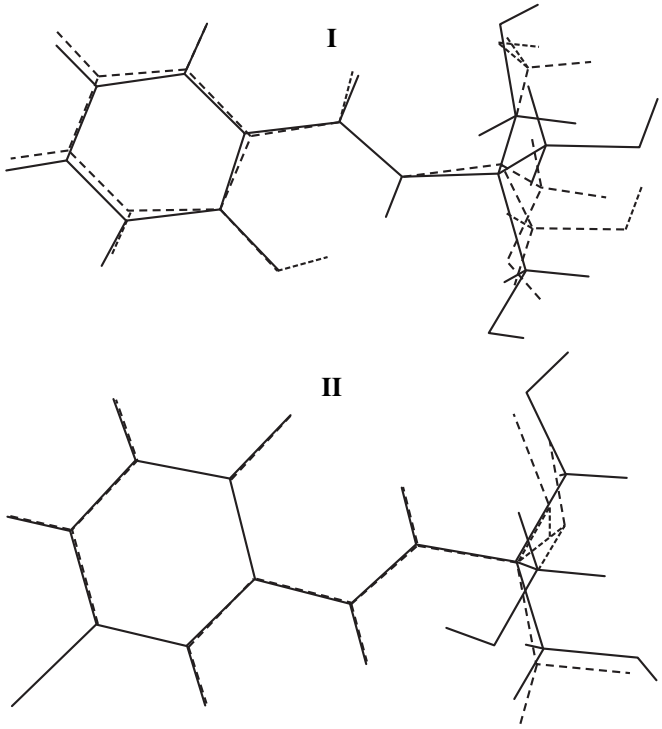

Fig. 3. Superposition of independent molecules **I** and **II**.

However, their analysis is made difficult by the disordering of the alcohol oxygen atoms in molecule *A*.

REFERENCES

1. D. H. Busch, in *Proceedings of the 9th International Conference on Coordination Chemistry, St. Moritz, Switzerland, 1966*, Ed. by W. Schneider (Verlag Helvetica Chimica Acta, Basle, 1966) [Usp. Khim. **38** (5), 822 (1969)].
2. A. Éshenmozer, Usp. Khim. **44** (8), 1524 (1973).
3. N. V. Gérbéléu, *Reactions on Matrices* (Shtiintsa, Chisinau, 1980).
4. G. M. Sheldrick, *SHELXS86: Program for the Solution of Crystal Structures* (Univ. of Göttingen, Göttingen, 1986).
5. G. M. Sheldrick, *SHELXL93: Program for the Refinement of Crystal Structures* (Univ. of Göttingen, Göttingen, 1993).
6. F. N. Allen and O. Kennard, Chem. Design Automat. News, No. 8, 131 (1992).
7. C. Escobar and M. T. Garland, Acta Crystallogr., Sect. C: Cryst. Struct. Commun. **C40**, 889 (1984).
8. S. M. Aldoshin, L. O. Atovmyan, and V. I. Ponomarev, Khim. Fiz. **3**, 787 (1984).
9. C. Escobar and M. T. Garland, Acta Crystallogr., Sect. C: Cryst. Struct. Commun. **C39**, 1463 (1983).
10. B. M. Gatehouse, Cryst. Struct. Commun. **11**, 1793 (1982).
11. Lin Xianti, Su Genbo, Li Zhengong, and Huang Gonfan, Jiegou Huaxue **6**, 214 (1987).
12. Y. Oddon, J.-P. Reboul, G. Pepe, *et al.*, Acta Crystallogr., Sect. C: Cryst. Struct. Commun. **C51**, 974 (1995).

Translated by O. Borovik-Romanova

Crystallography Reports, Vol. 45, No. 6, 2000, pp. 951–952. Translated from Kristallografiya, Vol. 45, No. 6, 2000, pp. 1031–1033.

STRUCTURE OF ORGANIC COMPOUNDS

Crystal and Molecular Structures of Pyruvic Acid Methyldithiocarbomethoxyhydrazone

B. Ya. Antosyak*, L. A. Nezhel'skaya, and T. I. Malinovskiĭ*†**

** Institute of Chemistry, Academy of Sciences of Moldova, Academiei 3, Chisinau, 20-28 Moldova*

*** Institute of Applied Physics, Academy of Sciences of Moldova, Academiei 5, Chisinau, 20-28 Moldova*

Received November 25, 1997; in final form, July 10, 2000

Abstract—The crystal structure of pyruvic acid methyldithiocarbomethoxyhydrazone $C_5H_8N_2O_2S_2$ is determined by X-ray diffraction. The crystals are orthorhombic, $a = 6.510(5)$, $b = 19.124(4)$, $c = 6.855(6)$ Å, and space group $P2_12_12_1$. The structure is solved by direct methods and refined to $R = 0.057$ for 923 reflections. The interatomic distances in the molecule agree with the data for noncoordinated thiosemicarbazones. In the structure, the double S=C bond [1.634(7) Å] is shorter than that in noncoordinated carbohydrazones containing a fragment of pyruvic acid. © *2000 MAIK "Nauka/Interperiodica".*

INTRODUCTION

The discovery of antibacterial, antiviral, and antitumor activities in hydrazones stimulated their synthesis and studies of structure and biological activity with the purpose to find more efficient and less toxic compounds. The main factors responsible for the biological activity of this class of compounds are the sulfur atom and the mobile hydrogen atom of the hydrazine residue. Replacement of these atoms or groups as a whole in a hydrazone by other organic radicals may result in a profound change in their biological activity. In this work, we determined the X-ray crystal structure of pyruvic acid methyldithiocarbomethoxyhydrazone and calculated the geometric parameters of the molecule.

EXPERIMENTAL

The composition of the compound is $C_5H_8N_2O_2S_2$ (**I**). Yellow prismatic crystals are orthorhombic, $a = 6.510(5)$, $b = 19.124(4)$, $c = 6.855(6)$ Å, $Z = 4$, space group $P2_12_12_1$, $\mu = 1.22$ cm^{-1}, and $d_{calcd} = 1.50$ g/cm^3. A crystal, $0.2 \times 0.3 \times 0.5$ mm, was chosen for the X-ray study. The intensities of 923 unique reflections with $I > 2\sigma$ were obtained on a DAR-UMB diffractometer with CuK_α radiation (graphite monochromator). The structure was solved by direct methods with the SHELXS86 program [1] using the default parameters. The non-hydrogen atoms were refined in the anisotropic approximation by a least-squares procedure with the SHELX76 program package [2] to $R = 0.070$. The H atoms were found from a difference synthesis of electron density (except for the hydrogen atom of the hydroxyl group). The refinement of the structure with consideration for individual thermal parameters of hydrogen atoms lowered the R factor to 0.057. No absorption correction was applied.

The final atomic coordinates in the structure are listed in the table. A fragment of the structure is shown in the figure.

RESULTS AND DISCUSSION

Molecule **I** (figure) is nearly planar. The O(1) atom of the carboxyl group shows the largest deviation from the rms plane through the non-hydrogen atoms (0.054 Å). The azomethine atom C(2) is coplanar with the dithiocarbamide fragment of the molecule. The torsion angle C(1)N(1)N(2)C(2) is actually 180°. A similar planar

Atomic coordinates ($\times 10^4$) and U_{eq} ($\times 10^3$) in pyruvic acid methyldithiocarbomethoxyhydrazone

Atom	x	y	z	U_{eq}
S(1)	8090(3)	5939(1)	4543(5)	45
S(2)	3487(3)	6149(1)	4380(4)	36
O(1)	–479(9)	4340(3)	4437(15)	46
O(2)	350(9)	3221(3)	4367(15)	53
N(1)	5321(10)	4948(3)	4502(16)	37
N(2)	3359(9)	4710(3)	4446(13)	31
C(1)	5733(12)	5645(3)	4496(14)	30
C(2)	3083(11)	4035(3)	4469(14)	29
C(3)	919(12)	3825(4)	4436(15)	36
C(4)	4686(14)	3482(4)	4541(23)	47
C(5)	4539(18)	7028(4)	4314(23)	53

† Deceased.

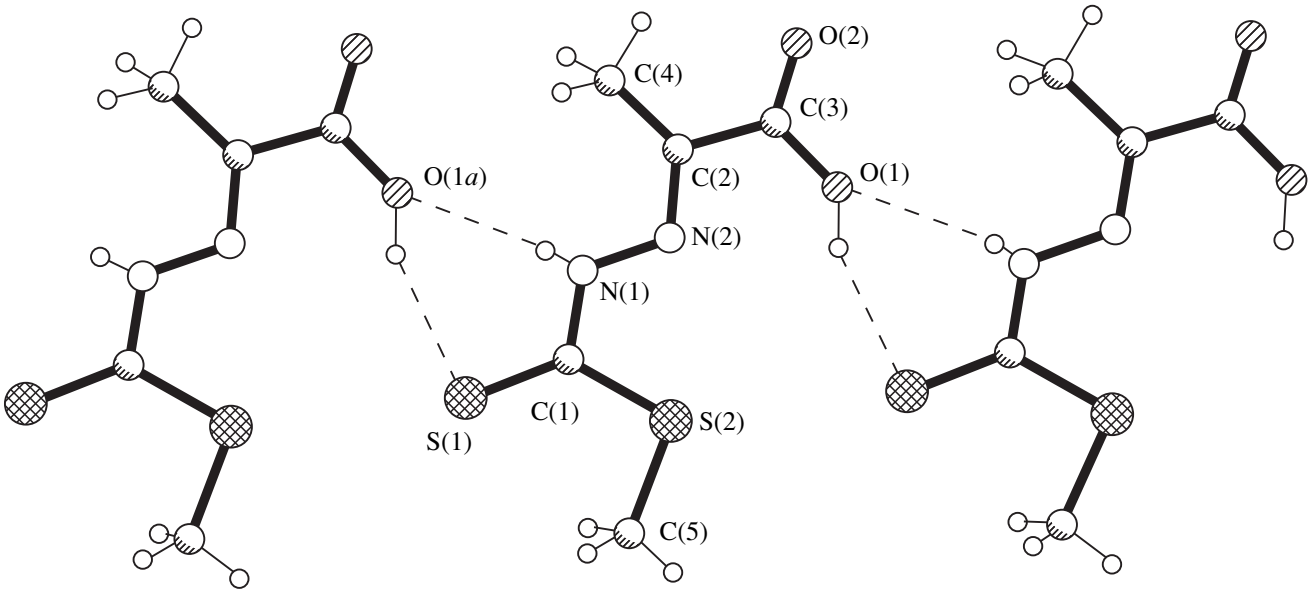

A fragment of the structure of pyruvic acid methyldithiocarbomethoxyhydrazone.

structure is observed in molecules of pyruvic acid thiosemicarbazone (**II**) [3].

The interatomic distances in the molecule are common for noncoordinated thiosemicarbazones [3–14] and are close to the corresponding distances in molecule **II**. A significant difference is observed only between the lengths of the S(1)=C(1) double bonds. In molecule **II**, these bonds are 1.675(3), 1.689(3), and 1.692(3) Å, whereas the corresponding distance in **I** shortens to 1.634(7) Å.

The orientation of the S(1)=C(1) and N(1)–N(2) bonds relative to the pair of atoms C(1) and N(1) is *trans*, which is characteristic of this class of compounds.

Thus, the substitution of the *S*-methyl fragment for the NH_2 group in the molecule of pyruvic acid thiosemicarbazone results in the only change in the molecular structure, namely, the shortening of the S=C double bond that exceeds the triple standard deviation.

Hydrogen bonds involving S(1), N(1) imine nitrogen, and O(1) carboxyl oxygen atoms are formed between the molecules related by the *a* translation (figure). The hydrogen bonds are characterized by the following parameters: N(1)…O'(1) bond is 2.971 Å, H(1)…O'(1) bond is 2.38 Å, and the N(1)–H(1)…O'(1) angle is 146°; and O'(1)…S(1) bond is 3.379 Å, H'(2)…S(1) bond is 2.38 Å, and the O'(1)–H'(2)…S(1) angle is 151°. These hydrogen bonds link the molecules in the crystal into infinite chains running along the *a*-axis. The chains are held together by van der Waals interactions.

REFERENCES

1. G. M. Sheldrick, Acta Crystallogr., Sect. A: Found. Crystallogr. **A46**, 467 (1990).
2. G. M. Sheldrick, *SHELX76: A Computer Program for Crystal Structure Determination* (Univ. of Cambridge, Cambridge, 1976).
3. B. Ya. Antosyak, V. N. Biyushkin, L. F. Chapurina, and T. I. Malinovskiĭ, Dokl. Akad. Nauk **327** (2), 219 (1992).
4. G. I. Palenik, D. F. Rendle, and W. S. Carter, Acta Crystallogr., Sect. B: Struct. Crystallogr. Cryst. Chem. **B30** (10), 2390 (1974).
5. B. Ya. Antosyak, V. N. Biyushkin, and N. I. Belichuk, Kristallografiya **29** (4), 722 (1984).
6. B. Ya. Antosyak, V. N. Biyushkin, L. A. Nezhel'skaya, *et al.*, Dokl. Akad. Nauk SSSR **304** (1), 103 (1989).
7. V. Kh. Kravtsov, V. N. Biyushkin, N. I. Belichuk, *et al.*, Kristallografiya **27** (1), 74 (1982).
8. Yu. M. Chumakov, V. N. Biyushkin, and V. G. Bodyu, Zh. Strukt. Khim. **26** (6), 114 (1985).
9. O. N. Rebrova, V. N. Biyushkin, T. I. Malinovskiĭ, *et al.*, Dokl. Akad. Nauk SSSR **260** (3), 633 (1981).
10. B. Ya. Antosyak, V. N. Biyushkin, N. I. Belichuk, and T. I. Malinovskiĭ, Dokl. Akad. Nauk SSSR **273** (6), 1375 (1983).
11. B. Ya. Antosyak, V. N. Biyushkin, T. I. Malinovskiĭ, and N. I. Belichuk, Dokl. Akad. Nauk SSSR **276** (2), 382 (1982).
12. O. N. Rebrova, V. N. Biyushkin, T. I. Malinovskiĭ, *et al.*, Dokl. Akad. Nauk SSSR **273** (6), 1386 (1983).
13. O. N. Rebrova, V. N. Biyushkin, L. A. Nezhel'skaya, *et al.*, Izv. Akad. Nauk Mold. SSR, No. 2, 23 (1987).
14. E. V. Slavyanov, V. N. Biyushkin, T. I. Malinovskiĭ, *et al.*, Dokl. Akad. Nauk SSSR **260** (5), 1131 (1981).

Translated by I. Polyakova

Crystallography Reports, Vol. 45, No. 6, 2000, pp. 953–960. Translated from Kristallografiya, Vol. 45, No. 6, 2000, pp. 1034–1042.

Role of Molecular Association in Formation of Polysystem Crystals of Some Hydroxyl-Containing Compounds

L. N. Kuleshova, V. N. Khrustalev, and M. Yu. Antipin

Nesmeyanov Institute of Organoelement Compounds, Russian Academy of Sciences, ul. Vavilova 28, Moscow, 117813 Russia

Received January 26, 1999; in final form, May 26, 1999

Abstract—A convenient simple method is proposed for the crystallochemical analysis of polysystem pseudosymmetric structures. The basic statistical data on the structures of polysystem crystals available in the Cambridge Structural Database are discussed. The role of molecular association in formation of the pseudosymmetry in organic crystals is discussed. *© 2000 MAIK "Nauka/Interperiodica".*

INTRODUCTION

Molecular-crystal engineering is a new vigorously developing field of materials science and crystal chemistry. Within the framework of this approach, molecular interactions play a decisive role in the formation of crystal structures, with the hydrogen bonds being of primary importance [1–3]. Therefore, the studies of molecular association in crystals via intermolecular hydrogen bonding is the most important line of investigations in this field. Earlier, we have considered the role of hydrogen bonding in the formation of crystal structures of hydroxyl-containing derivatives of hydropyridine [4, 5]. In the cited works, it was also indicated that crystal structures built by molecules occupying more than one ($Z' > 1$) system of crystallographically independent positions are the most widespread for hydroxyl-containing compounds forming strong hydrogen-bonded associates and received the name of polysystem crystals. According to the data available in the Cambridge Structural Database (CSD), polysystem crystals amount up to 8% of the total number of all the studied crystals. Polysystem structures constitute 21% of all the crystal structures of 3- and 4-hydroxyl-containing hydropyridine derivatives found in CSD (from a total of 120 compounds). It was also shown [6, 7] that polysystem crystals are often observed in other classes of hydroxyl-containing compounds (40% of alcohols and 45% of cholesterol derivatives). Apparently, it is possible to state that compounds capable of strong intermolecular hydrogen bonding should, most probably, have the unit cells with $Z' > 1$.

The aim of this work is to clarify the role of hydrogen bonding in the formation of polysystem structures in some hydroxyl-containing compounds. We restrict our consideration to the crystallostructural aspect ignoring the thermodynamic and kinetic factors, despite the fact that they also play an important part in the formation of crystal structures.

BASIC PRINCIPLES OF CRYSTALLOCHEMICAL ANALYSIS OF POLYSYSTEM CRYSTALS

First, consider some necessary statistical information on polysystem crystal structures based on the CSD data. Polysystem structures are most often observed in low-symmetry crystal systems especially in those described by the sp. gr. $P1$ [8]. Also, the percentage of structures with $Z' > 1$ is noticeably higher in chiral groups than in the corresponding centrosymmetric ones [9] (Table 1). The statistical studies [10] demonstrated that the geometric characteristics of the crystallographically independent molecules in polysystem crystals are usually similar. In some cases, it was possible to establish approximate symmetry transformations (pseudosymmetry elements) relating crystallographically independent molecules. Davies and Willer believe that approximate symmetry elements are present in about 27% of polysystem structures.[1]

The established transformations most often correspond to the crystallographic symmetry elements—center of inversion, rotation and screw axes, mirror and glide planes, translations, etc. The only difference from conventional symmetry consists in that these transformations, unlike the crystallographic operations, are obeyed only approximately. This is associated, first of all, with the facts that the structures of crystallographically independent molecules are not quite equivalent (and, sometimes, are even substantially different) and also because the position of the pseudosymmetry element in the unit cell does not coincide with any of the special crystallographic positions in a particular space group. At the same time, the position of the pseudosymmetry element is not arbitrary. Usually, a pseudosymmetry element is located in the vicinity of one of the special positions in the unit cell. Displacing this pseudoelement by a certain value Δr and placing it to the corresponding "special" point, we arrive at the more

[1] Private communication [8].

1063-7745/00/4506-0953$20.00 © 2000 MAIK "Nauka/Interperiodica"

Table 1. Occurrence of polysystem crystals

Space group	*N**	Space group	*N**
$P1$	45%	$P\bar{1}$	11.3%
$P2_1$	14%	$P2_1/c$	5.7%
$C2$	12.2%	$C2/c$	3%
$P2_12_12_1$	4.5%	$Pbca$	3%

* *N* percentage of polysystem crystals from the total number of crystals described by this space group.

symmetric space group (supergroup) than that of a real crystal (Fig. 1). Thus, the space group of a real crystal containing a pseudosymmetry element is a subgroup of the space group (supergroup) of a certain hypothetical crystal. The displacement of the pseudoelement (Δr) can be considered as a criterion for pseudosymmetry of the crystal structure [11]. Abrahams [12] assumed that at $\Delta r < 0.1$ Å, the probability of the wrong determination of the space group is rather high.

In the general case, if H is the real space group of the crystal containing a pseudosymmetry element, its supergroup G can be obtained as follows: $G = H + (g/t)H$, where $g(\bar{1}, m, 2, 2_1)$ and t are the rotational and the translational components, respectively. There are two major types of supergroups. Supergroup of type 1 possesses a higher symmetry class, with the unit-cell parameters and the volume being preserved. Supergroup of type 2 possesses the same symmetry class, but the translational parameters and the unit-cell volume are reduced by an integer factor.

Now, consider the typical instances of pseudosymmetry in a number of polysystem crystals of hydroxyl-containing compounds forming stable local associates due to intermolecular hydrogen bonding.

Crystal Structure of the 1 : 1 Adduct of Nitrosalicylic Aldehyde with Piperidine (sp. gr. $Pna2_1$, $Z' = 2$) [13]

Intermolecular hydrogen bonding gives rise to formation of crystallographically independent pairs of molecules—strong tetramers (Fig. 2). Within these tetramers, the proton is transferred from the hydroxyl

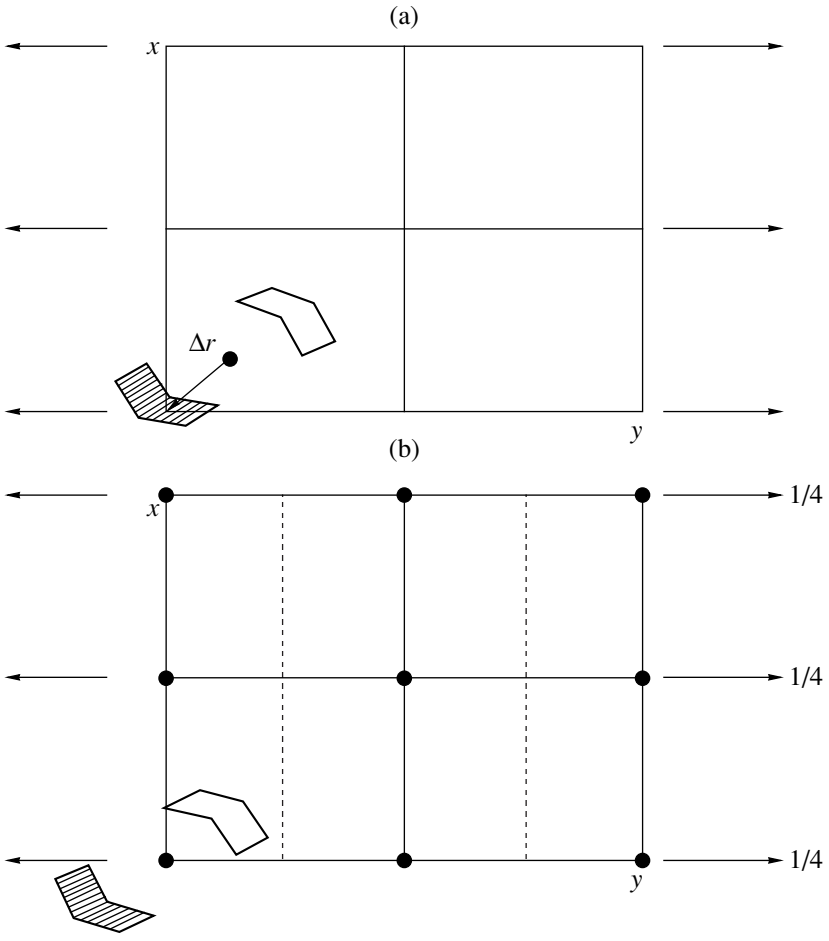

Fig. 1. Schematic representation of the molecule arrangement in (a) the polysystem crystal of the sp. gr. $P2_1$, $Z' = 2$ possessing a pseudocenter and (b) the supergroup $P2_1/c$, $Z' = 1$.

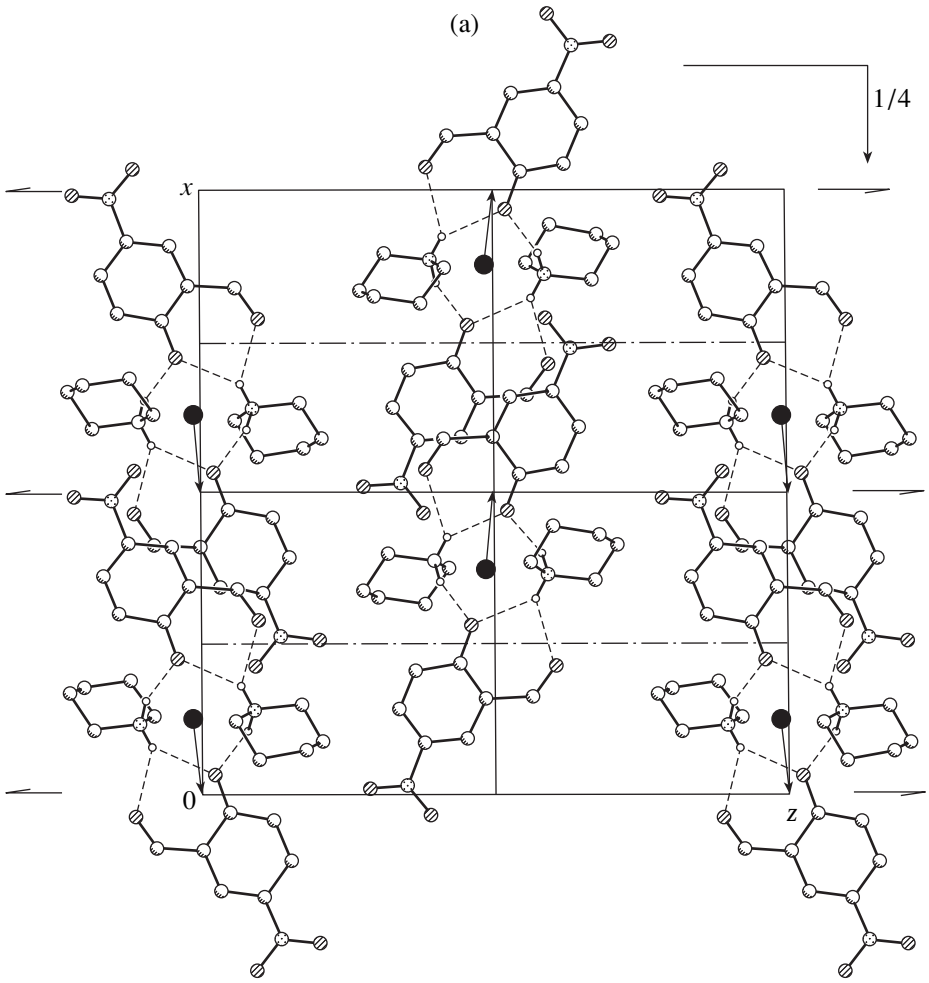

Fig. 2. Molecular packing of the adduct of nitrosalicylic aldehyde with piperidine in (a) the real crystal structure with $Pna2_1$, $Z' = 2$ and (b) the hypothetical supergroup $Pnma$, $Z' = 1$.

group of salicylic aldehyde to the nitrogen atom of piperidine. The independent pairs of the molecules in tetramers are related to one another by an approximate center of inversion (center of pseudoinversion) with the coordinates ($x = 0.375$, $y = 0.484$, $z = 0.491$). The crystallographically independent molecules have similar geometries: the average deviation of the atomic coordinates obtained upon bringing into coincidence of the centers of gravity of the molecules using the least squares method equals 0.21 Å. The molecular packing is shown in Fig. 2a. Small tetramer displacements with respect to one another ($\Delta r = 2.1$ Å) hinder the appearance of the crystallographic center of inversion and give rise to the formation of a polysystem pseudosymmetric crystal. The displacement of the base associate and a pseudocenter to a special crystallographic point with the coordinates [$x = 0.5$, $y = 0.5$, $z = 0.5$] would lead to the formation of the packing shown in Fig. 2b and, correspondingly, to the corresponding supergroup $Pnma$ with $Z' = 1$. In a real crystal, no such packing with the preservation of the unit-cell parameters is possible because of overlapping piperidine fragments (the distance between the nearest carbon atoms is 1.386 Å). On the other hand, an increase of the unit-cell parameters would make the packing rather loose.

The relation between the supergroup and the symmetry group of the real crystal may be written as follows: $(Pnma, Z' = 1) = (Pna2_1, Z' = 2) + \bar{1}\,[0.5, 0.5, 0.5]$.

Crystal Structure of 3,4-dihydroxy-2-oxo-1-methyl-4-phenylpiperidine (sp. gr. $Pca2_1$, $Z' = 2$) [4]

The crystallographically independent molecules in this compound have similar geometric characteristics. The average deviation of the atomic coordinates from the average value is 0.017 Å. Hydrogen bonding gives rise to formation of pseudocentrosymmetric dimers forming, in turn, infinite chains. The crystal structure as a whole consists of superimposed chains displaced relative each other to form optimum packing, which prevents the appearance of the crystallographic center of inversion in the real crystal. The displacement of the

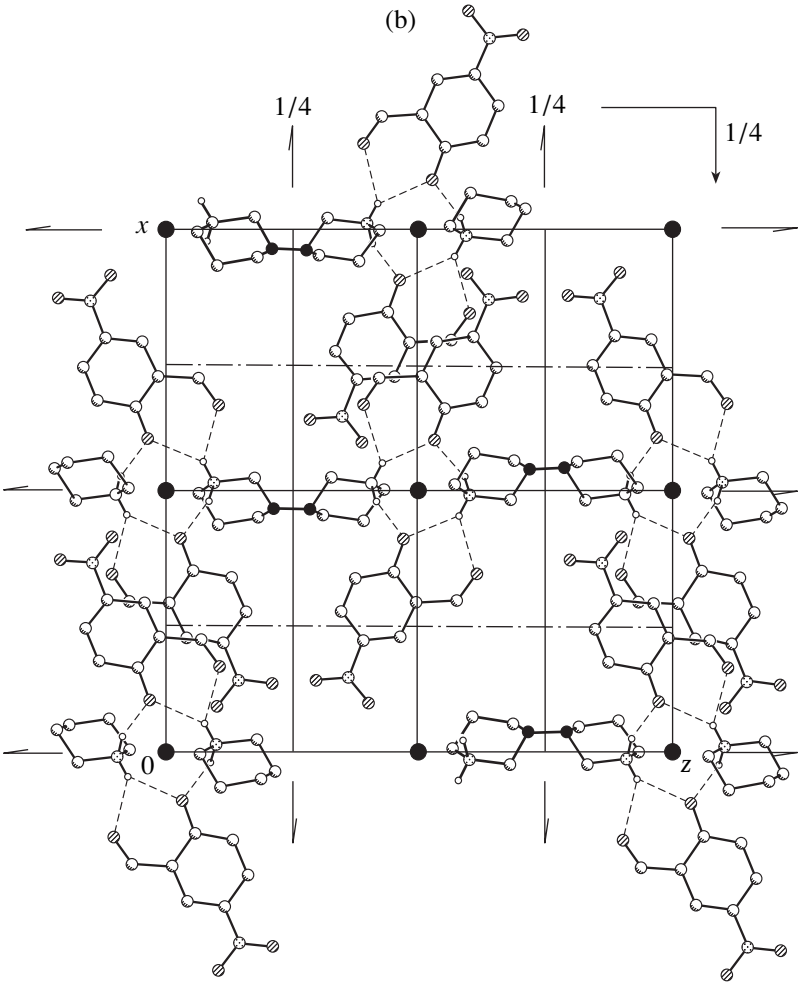

Fig. 2. (Contd.)

base associate together with the pseudocenter by $\Delta r = 1.5$ Å to the "special" point with the coordinates [$x = 0.0$, $y = 0.25$, $z = 0.0$] would have led to the centrosymmetric structure with the symmetry supergroup *Pbcn* and $Z' = 1$. The relation between the supergroup and the symmetry group may be written as follows:

$$(Pbcn, Z' = 1) = (Pca2_1, Z' = 2) + \bar{1}[0, 0.25, 0].$$

4-Hydroxybiphenyl (sp. gr. $P2_12_12_1$, $Z' = 2$) [14]

The compound has two polymorphs—monoclinic ($P2_1/c$) and orthorhombic ($P2_12_12_1$). In both modifications, the molecules are linked by OH···O hydrogen bonds into infinite chains parallel to the *y*-axis. In the orthorhombic modification, there are two molecules per asymmetric unit. Both molecules are planar and have similar geometric parameters. The deviations in the atomic coordinates do not exceed 0.04 Å. The crystallographically independent molecules are related by the local twofold rotation pseudoaxis intersecting the *yz* plane at the point [$y = 0.25$, $z = 0.03$] (Fig. 3a). The displacement of the base pair of the molecules together with the twofold rotation pseudoaxis by the small distance $\Delta r = 0.5$ Å to the position with the coordinates [$y = 0.25$, $z = 0$] would lead to the appearance of the crystallographic twofold axis, a double decrease in the *c*-parameter, and, thus, to the supergroup $P22_12_1$ with $Z' = 1$ (Fig. 3b). This case is an example of the supergroups of the second type (the same symmetry class, but twice smaller unit-cell). The relation between the supergroup and the symmetry group may be written as follows: $(P2_12_12, Z' = 1) = (P22_12_1, Z' = 2) + c/2$.

In this case, the formation of pseudosymmetry is obviously associated with the asymmetry (directionality) of the hydrogen bonding rather than with the associate displacement with respect to one another. In this connection, the localization of the hydrogen atom of the hydroxyl group is of considerable importance. In [15], both modifications were studied at different temperatures ranging from 295 to 80 K. Using the analogy with the biphenyl modifications [16], the authors hoped

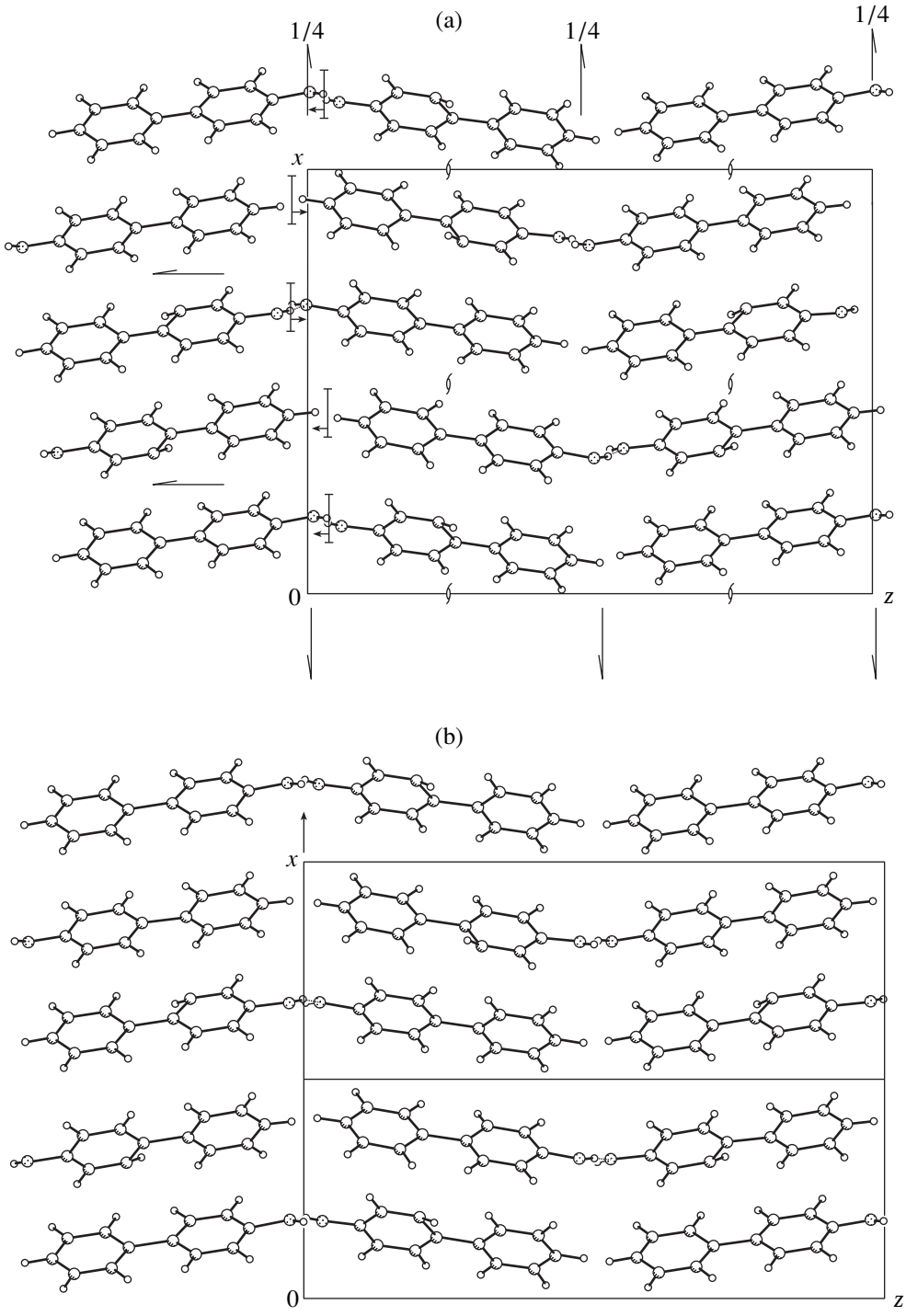

Fig. 3. Molecular packing of 4-hydroxybiphenyl in (a) the real ($P2_12_12_1$, $Z' = 2$) and (b) the hypothetical ($P2_12_12$, $Z' = 1$) space groups.

to prove the existence of the phase transformation from the monoclinic 4-hydroxybiphenyl to the orthorhombic modification. However, no signs of this transformation were revealed. At the same time, the authors believed that they found the indication to a possible phase transformation of the orthorhombic modification in the temperature range from 295 to 242 K. Unfortunately, no details to the effect are given [15].

RESULTS AND DISCUSSION

The above data raise the natural question whether the supergroup obtained upon the analysis of the pack-

Table 2. Crystallographic parameters of three polymorphic modifications of 8-(2-hydroxyethyl)adenine

Space group	$P2_12_12_1$	$P2_12_12_1$	$P2_1/c$
Modification	**I**	**II**	**III**
Z'	1	2	3
a	13.556	13.572	13.543
b	8.271	8.248	8.290
c	7.340	14.508	22.591
β	90	90	104.97
ρ_{calcd}, g/cm^3	1.445	1.466	1.457
Crystallization conditions	Evaporation of an unsaturated aqueous solution	Slow evaporation of a dilute aqueous solution	Rapid cooling of a saturated aqueous solution

ing is only a mere hypothetical abstraction or it can really exist in crystals under some particular conditions. Based on the CSD data, it may be concluded that supergroups can really be formed in crystals (at least in some instances). As examples, we refer to the following polymorphic modifications of the compounds available in CSD. These are: *o*-aminobenzoic acid AMBACO, ($Pbca$, $Z' = 1$) = ($P2_1cn$, $Z' = 2$) + $\bar{1}$ (0, 0, 0.25); 1,1-diethyl-3-thiobenzoylthiourea FAJTIT, ($P2_1/n$, $Z' = 1$) = (Pn, $Z' = 2$) + $\bar{1}$ (0.5, 0.5, 0.5); 2,5-dihydroxybenzoic acid BESKAL, ($P2_1/c$, $Z' = 1$) = (Pn, $Z' = 2$) + $\bar{1}$ (0, 0, 0); bis(4-ethoxycarbonylphenyl) biphenyl-4,4'-dicarboxylate SILXUG, ($P2_1/c$, $Z' = 1$) = (Pn, $Z' = 2$) + $\bar{1}$ (0, 0.5, 0); and 8-(2-hydroxyethyl)adenine FABFUJ, ($P2_12_12_1$, $Z' = 1$) = ($P2_12_12_1$, $Z' = 2$) + $c/2$. Moreover, the phase transformations were also established between various modifications of SILXUG and AMBACO.

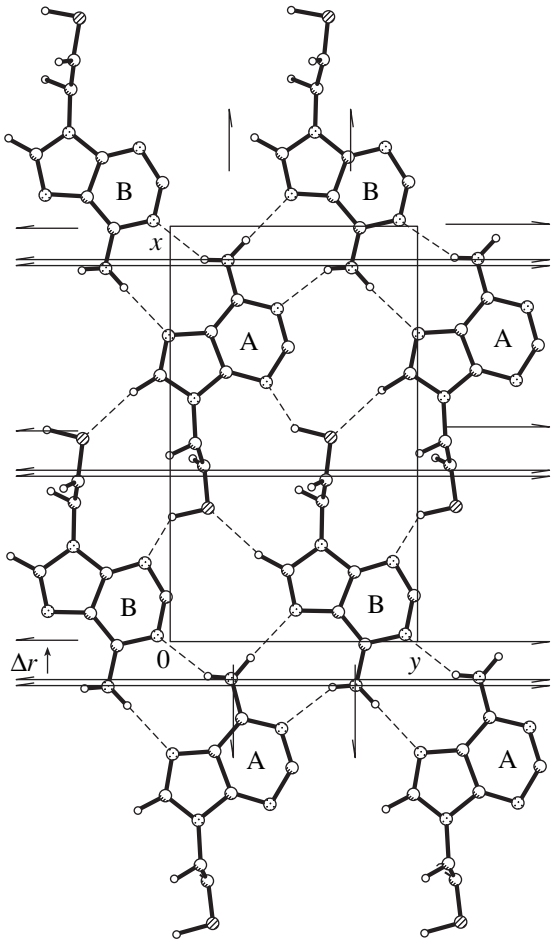

Fig. 4. Layer formed by hydrogen bonding in the polymorphic modifications of 8-(2-hydroxyethyl)adenine (the twofold screw pseudoaxes in modification **II** are indicated by double lines).

Now, consider three known modifications of 8-(2-hydroxyethyl)adenine FABFUJ [17] in more detail (Table 2). In all the modifications, the molecules are linked to form similar planar layers by the systems of intermolecular hydrogen bonds (Fig. 4). Different modes of layer packing are obtained by using crystallization under different conditions (Table 2). This gives rise to the formation of various crystal structures. Apparently, modification **I** can be considered as a supergroup of the second type with respect to modification **II** (Fig. 5). By displacing the twofold screw pseudoaxis in modification **II** by $\Delta r = 1.28$ Å, we arrive at the unit cell of twice smaller volume. This unit cell is analogous to that of modification **I**, i.e., ($P2_12_12_1$, $Z' = 1$) = ($P2_12_12_1$, $Z' = 2$) + $c/2$. The pseudosymmetry of modification **II** appears because the layers connected by hydrogen bonds are displaced with respect to each other. Apparently, this fact is also responsible for pseudosymmetry of polymorphic modification **III** of 8-(2-hydroxyethyl)adenine. In the latter structure, the superunit described by the same symmetry class and with the three-times smaller unit-cell volume can be singled out. Its parameters are $c' = 1/3c$, i.e., ($P2_1/c$, $Z' = 1$) = ($P2_1/c$, $Z' = 3$) + $c/3$. The pseudosymmetry of this modification was described in detail elsewhere [17].

Noteworthy is the fact that modification **II** grown under conditions the closest to equilibrium has the highest density and is completely ordered, whereas

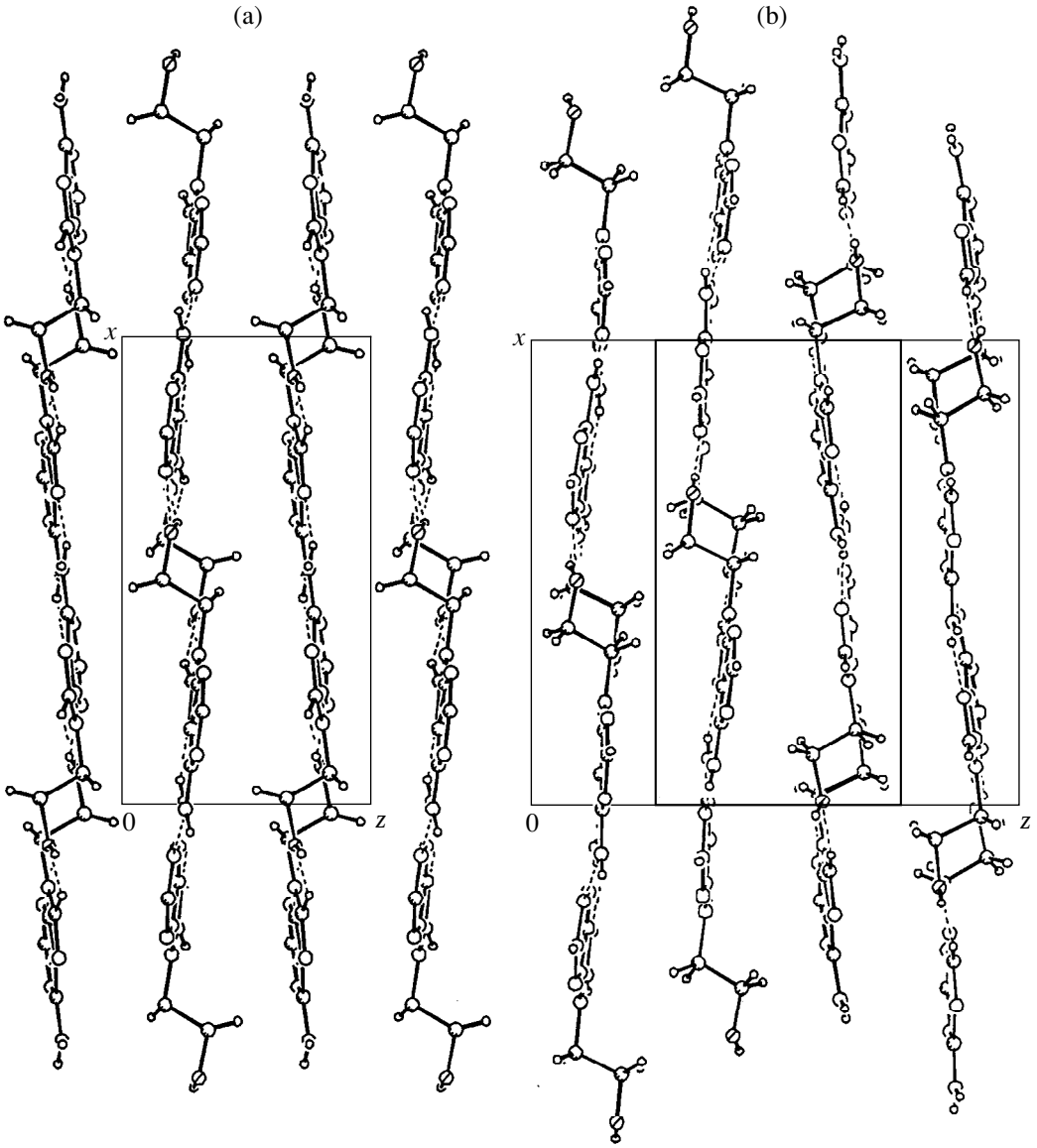

Fig. 5. Packing of layers of 8-(2-hydroxyethyl)adenine in modifications (a) **I** and (b) **II**.

modifications **I** and **III** are partly disordered along the *c*-axis. Unfortunately, no possible phase transformations in these crystals were examined in [17].

However, as was mentioned above, polymorphic transformations of the second type (the group with the pseudosymmetry ⟶ the supergroup) have been observed. For example, such phase transformation was observed in the modifications of *o*-aminobenzoic acid AMBACO [18, 19]: **I** ($P2_1cn$, $Z' = 2$) ⟶ 81°C ⟶ **II** (*Pbca*, $Z' = 1$). Modification **I** consists of crystallographically independent neutral molecules and zwitterions related by a pseudocenter of inversion with the coordinates [$x = -0.0053$, $y = -0.0095$, $z = -0.2595$]. The phase transformation to supergroup **II** takes place at 81°C and is accompanied by the proton migration, the displacement of the pseudocenter by $\Delta r = 0.2$ Å, and the rotation of the molecules with respect to one another by about 30°C (Fig. 6).

Emphasize once again that strong molecular associates are observed in all the crystal structures considered above. It can be suggested that these associates and their fragments can be present (at least partly) also in the initial mother liquor used for crystallization. In such a situation, the crystal is formed from more or less stable fragments rather than from isolated molecules, which apparently leads to the loss of the maximum symmetry because of small displacements of the fragments with respect to one another in order to form a closer packing. Such displacements provide the appearance of pseudosymmetry in crystals containing strong molecular associates.

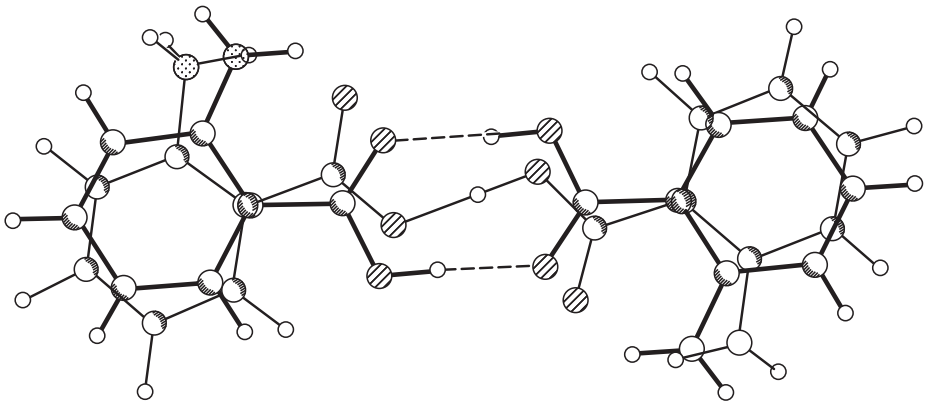

Fig. 6. Transformation of the *o*-aminobenzoic acid dimer upon the phase transformation **I** ⟶ **II** (thin and solid lines, respectively).

We believe that the systematic studies of the pseudosymmetry in polysystem crystals are rather promising for prediction of new polymorphic modifications of various compounds and the search for materials that can undergo phase transformations. Note that similar considerations have been quite successful in the search for inorganic crystals among the known inorganic structures with a pseudosymmetry [20] that may undergo ferroelectric–paraelectric phase transformations.

ACKNOWLEDGMENTS

This work was supported by the Russian Foundation for Basic Research, project nos. 00-03-32840a and 99-07-90133.

REFERENCES

1. G. R. Desiraju, *Crystal Engineering: The Design of Organic Solids* (Elsevier, Amsterdam, 1989).
2. G. R. Desiraju, Acc. Chem. Res. **29**, 441 (1996).
3. G. R. Desiraju, *The Crystal as a Supramolecular Entity* (Wiley, Chichester, 1996).
4. L. N. Kuleshova, V. N. Khrustalev, Yu. T. Struchkov, *et al.*, Kristallografiya **41** (4), 673 (1996) [Crystallogr. Rep. **41**, 636 (1996)].
5. L. N. Kuleshova and V. N. Khrustalev, Kristallografiya **45** (1), 84 (2000) [Crystallogr. Rep. **45**, 78 (2000)].
6. A. Gavezzotti, Acc. Chem. Res. **27**, 309 (1994).
7. B. M. Craven, Acta Crystallogr., Sect. B: Struct. Crystallogr. Cryst. Chem. **B35**, 1123 (1979).
8. C. P. Brock and J. D. Dunitz, Chem. Mater. **6**, 1118 (1994).
9. N. Padmaja, S. Ramakumar, and M. A. Vismamitra, Acta Crystallogr., Sect. A: Found. Crystallogr. **A46**, 725 (1990).
10. V. Sona and W. Gautham, Acta Crystallogr., Sect. B: Struct. Sci. **B48**, 111 (1992).
11. J. M. Igartua, M. I. Aroyo, and J. M. Pérez-Mato, Phys. Rev. B: Condens. Matter **54**, 12744 (1996).
12. S. C. Abrahams, Acta Crystallogr., Sect. B: Struct. Sci. **B45**, 228 (1989).
13. L. Yu. Ukhin, Zh. I. Orlova, S. V. Lindeman, and V. N. Khrustalev, Izv. Akad. Nauk, Ser. Khim. **5**, 940 (1995).
14. C. P. Brok and K. L. Haller, J. Phys. Chem. **88**, 3570 (1984).
15. C. P. Brok and G. L. Morelan, J. Phys. Chem. **90**, 5631 (1986).
16. W. R. Busing, Acta Crystallogr., Sect. A: Found. Crystallogr. **A39**, 340 (1983).
17. A. Takenaka, M. Shibata, and Y. Sasada, Acta Crystallogr., Sect. C: Cryst. Struct. Commun. **C42**, 1336 (1986).
18. G. E. Hardy, W. C. Kaska, B. P. Chandra, and J. I. Zink, J. Am. Chem. Soc. **103**, 1074 (1981).
19. C. J. Brown and M. Ehrenberg, Acta Crystallogr., Sect. C: Cryst. Struct. Commun. **C41**, 441 (1985).
20. S. C. Abrahams, Ferroelectrics **104**, 35 (1990).

Translated by T. Safonova

Crystallography Reports, Vol. 45, No. 6, 2000, pp. 961–967. Translated from Kristallografiya, Vol. 45, No. 6, 2000, pp. 1043–1049.

PHASE TRANSITIONS

Structural Transformations in $Pb(Mg_{1/3}Nb_{2/3})_{0.8}Ti_{0.2}O_3$ Single Crystals in Electric Field

I. N. Zakharchenko, O. A. Bunina, P. N. Timonin, and V. P. Sakhnenko

Research Institute of Physics, Rostov State University, pr. Stachki, Rostov-on-Don, 344090 Russia

Received November 23, 1998

Abstract—Phase transitions in single crystals of a ferroelectric–relaxor of the composition $Pb(Mg_{1/3}Nb_{2/3})_{0.8}Ti_{0.2}O_3$ in applied electric fields E ranging from 0 to 5 kV/cm have been studied by X-ray diffraction method. The evolution of the shape of the 224 reflection and the integrated intensity of the 005 reflections were studied in the field-cooled mode in the temperature range 290–430 K. Four temperature anomalies were established in the range of the fields used. It is concluded that, prior to the formation of the rhombohedral ferroelectric phase, the crystals exist in three inhomogeneous phases—ergodic and nonergodic dipole glasses and a mixed phase with the coexisting ferroelectric and glassy regions. The mechanism of the effect of Ti^{+4} ions on the phase transition in the crystal are also discussed. © *2000 MAIK "Nauka/Interperiodica".*

The phase transitions in the single crystals of the $Pb(Mg_{1/3}Nb_{2/3})_{1-x}Ti_xO_3$ solid solutions ($(1 - x)$PMN–xPT), ($x = 0.2$) in an applied electric field have been studied by X-ray diffraction methods. At $x < 0.4$, the crystals were identified with ferroelectrics–relaxors with a diffuse maximum of the temperature dependence of the dielectric constant ε. The position of this maximum depends on the frequency, anomalous dispersion in ε at low frequencies, and the hysteresis loop formed below the maximum of ε [1–3]. Thus, the dielectric properties of the crystals are similar to those of a pure $Pb(Mg_{1/3}Nb_{2/3})TiO_3$ (PMN) crystal, a classical representative of relaxors [4]. However, it is well known that a pure PMN crystal remains cubic up to the temperature of $T = 5$ K [5, 6], whereas, as the X-ray diffraction data show, the crystals of the composition $(1 - x)$PMN–xPT with $0.06 < x < 0.3$ undergo the phase transition to the rhombohedral phase occurring via intermediate dipole-glass and mixed phases [2, 7, 8]. At the same time, the study of the PMN structure in external electric fields showed that cooling below $T \approx 210$ K provides the polarization of a PMN crystal in an electric field E above a certain threshold value (~2 kV/cm) applied along the [111] direction [9–12].

A "field-induced ferroelectric phase" also exists in PMN–PT crystals [13–15]; however, the phase diagram of these crystals constructed in the coordinates "electric field (E)–temperature (T)" should differ from all the similar diagrams for pure PMN [9–11] undergoing the ferroelectric transition at $E = 0$. The present study is aimed to establish the characteristic features of the phase diagram E–T of a crystal with the composition 0.8PMN–0.2PT.

According to the electrophysical measurements [2], the crystals of the composition 0.8PMN–0.2PT undergo the dipole–glass transition at the temperature $T_{DG} = 352$ K and the ferroelectric transition at $T_F = 324$ K. At the temperature $T_M = 333$ K, a mixed phase is formed in which the regions of glassy and ferroelectric phases coexist. Somewhat different phase-transition temperatures were obtained in the X-ray diffraction studies [8]: $T_{DG} = 375$, $T_M = 336$, and $T_F = 323$ K. It was shown that the ferroelectric phase consists of domains with rhombohedrally distorted unit cells [7, 8].

In this connection, we undertook an X-ray diffraction study of phase transitions in 0.8PMN–0.2PT in constant fields ranging within $E = 0$–5 kV/cm and applied along the [100] direction in the temperature range of 290–430 K. The field orientation results in the formation of a polydomain structure in the ferroelectric phase and, similar to the case of $E = 0$, splitting of some reflections, which provides the establishment of the phase transition by studying the neighborhood of a single reflection of the cubic phase.

EXPERIMENTAL

The experiments were performed on a DRON 3.0 diffractometer (CuK_{α_1} monochromatic radiation). Platinum electrodes transparent for X-ray radiation were applied onto the (001) surface of the crystals. Similar to our previous studies [13–15], we used a device which provided the switching-on of an electric field with the simultaneous variation of the specimen temperature. The reflection profiles were recorded using θ–2θ and 1θ scan with the use of a wide counter aperture for measuring the integrated intensities. The detailed description of the intensity-data collection and further processing of these data are considered elsewhere [13–15].

1063-7745/00/4506-0961$20.00

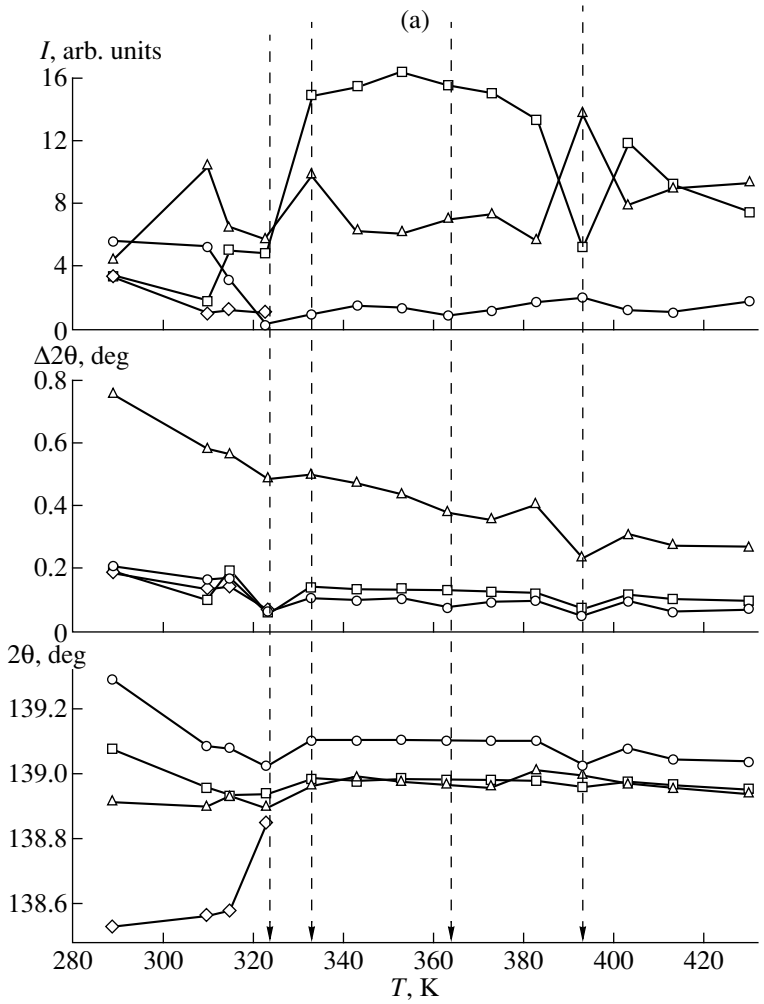

Fig. 1. Temperature dependences of the Gaussian parameters (intensity I, width $\Delta 2\theta$ and position 2θ) of the maximum approximating the 224 reflection at the field intensities E equal to (a) 0, (b) 3, and (c) 4 kV/cm. Dashed vertical lines indicate the points of anomalies in the profile shape.

The measurements were made in the so-called field-cooled mode; i.e., the field was switched on at T = 450 K, the crystal was kept for 15 min at this temperature, and then was cooled in a constant field. The time intensity of one reflection was recorded for about 10 min.

The temperatures of the phase transformations were determined from the changes of the profile parameters of the 224 reflection sensitive to rhombohedral distortions of the unit cell. Moreover, we also analyzed the integrated intensity of the 005 refection, whose structure factor noticeably varied upon the disappearance of the center of inversion in the perovskite-like unit cell [13].

RESULTS

The shapes of the 224-reflection profiles obtained in the field-cooled mode were analyzed using their approximation by a sum of several Gaussians. It was established that the best approximation was attained for three Gaussians at $T > T_F$ and four Gaussians at $T < T_F$ (the only exception are the data obtained in the field E = 4 kV/cm; in this case, three Gaussians provided a quite satisfactory approximation irrespectively of the temperature). Figure 1 shows the temperature dependences of the Gaussians parameters for some field intensities. At $T > T_F$, the maximum intensity I was usually possessed by a Gaussian with the average width of $\Delta(2\theta) \approx 0.2°$, which corresponded to scattering from the randomly-deformed cubic crystalline matrix. A wider Gaussian ($\Delta(2\theta) \approx 0.4°$) can be interpreted as a result of scattering by mesoscopic (of the order of 500 Å) polar (rhombohedral) clusters [8]. It is more difficult to explain the origin of a weak narrow line ($\Delta(2\theta) < 0.1°$). This line can be caused by scattering from clusters with the Nb : Mg order [16] or by the rather large (>2000 Å) deformed clusters of pure $PbTiO_3$.

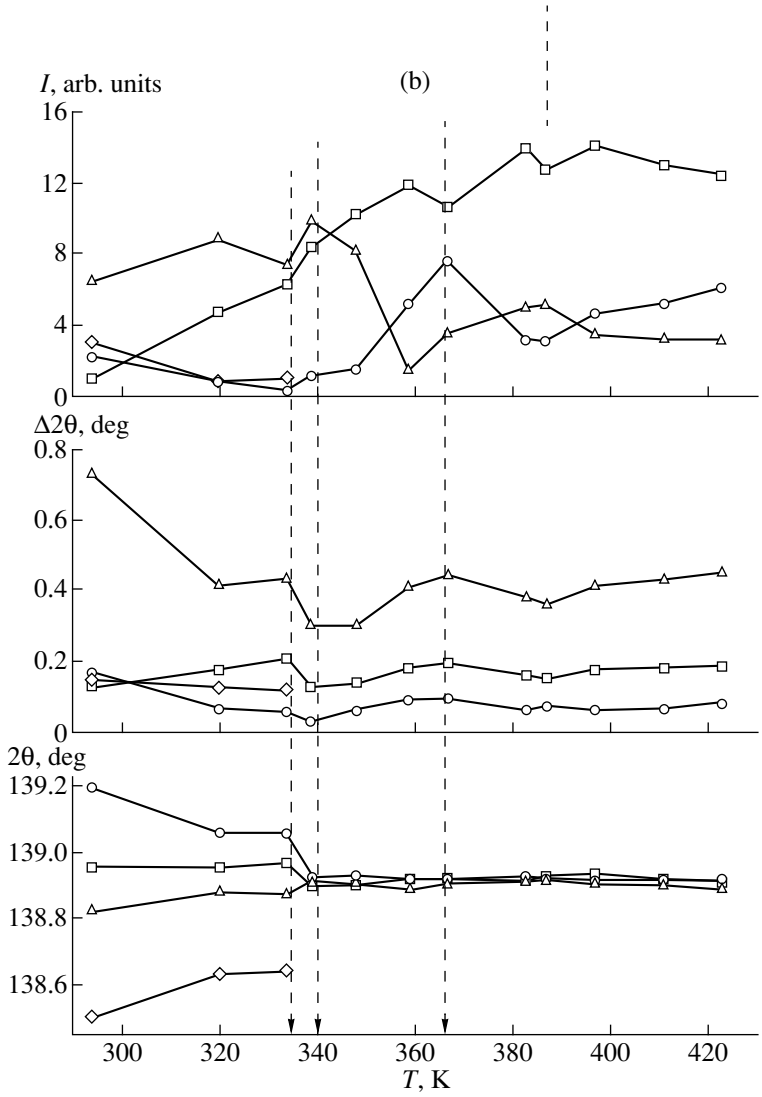

Fig. 1. (Contd.)

Irrespectively of the intensity of an applied electric field, the temperature dependences of the parameters of these lines show pronounced anomalies at four different temperatures, which are only slightly dependent on the intensity of the applied field (Fig. 1): $T_{DG1} \approx 390$–400, $T_{DG2} \approx 360$–370, $T_M \approx 333$–345, and $T_F \approx 324$–335 K. The temperature T_F corresponds to splitting of the 224 reflection into three lines having approximately equal widths and is, in fact, the temperature of transition to the ferroelectric rhombohedral phase [8], whereas all the remaining temperatures correspond to the kinks on the temperature dependences of the widths and intensities of the reflection components. Being the signs of the changes in both the dimensions and number of polar clusters and appearance of additional inhomogeneous deformations in the crystal caused by atomic displacements, these anomalies also provide evidence for the considerable restructuring occurring in the crystal.

At the same time, the above-indicated kinks can also be caused by the use of inadequate procedure of reflection-profile decomposition into Gaussian components (an extremely large number of fitting parameter) used in Eq. (9). In order to exclude this error and independently confirm that the anomalies in the 224 refection profile really correspond to the structural changes occurring in the crystal, we studied the temperature dependence of the integrated intensity of the 005 refection in various electric fields. The rhombohedral distortions do not cause splitting of this reflection; however, its structure factor can considerably increase with the loss of the unit-cell center of inversion. This effect can also be accompanied by other factors affecting the reflection intensity such as variations in the effective Debye–Waller factor (i.e. root-mean square atomic deviations) and extinction associated with both the changes in the global atomic structure (the primary

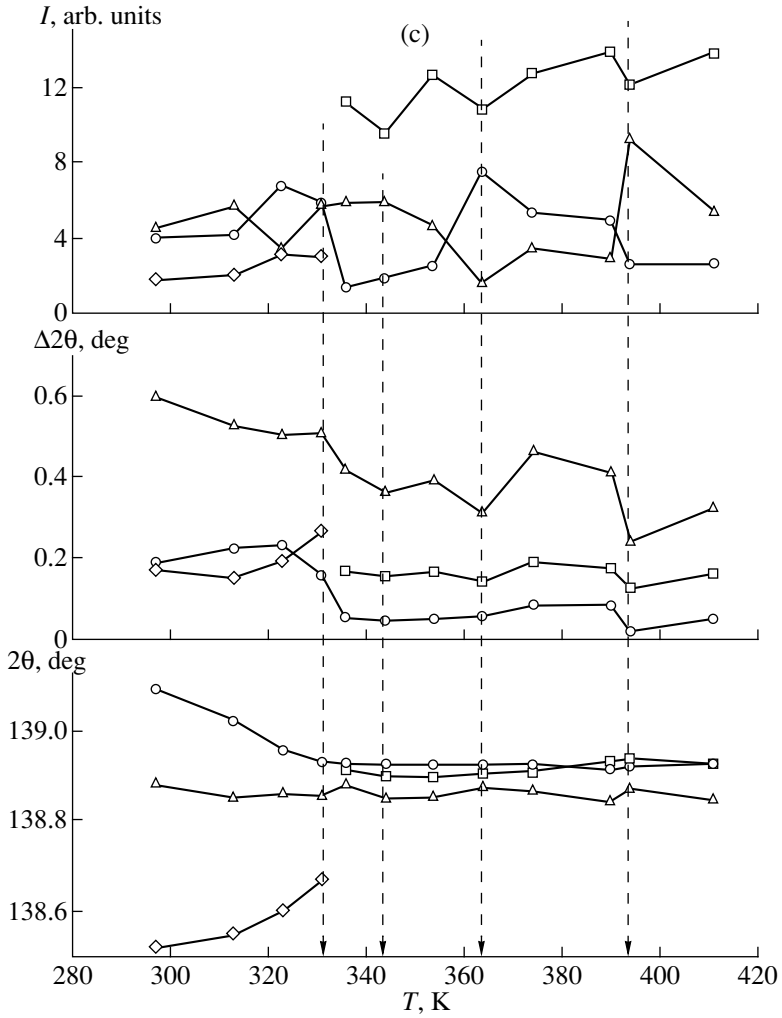

Fig. 1. (Contd.)

extinction) and the smaller dimensions of the coherency regions (the secondary extinction) [17].

The temperature dependence of the integrated intensity of the 005 refection at various electric-field intensities is shown in Fig. 2. At $T > T_{DG1}$, the intensity of this reflection is almost constant but starts increasing below this temperature, which seems to be associated with the change of the structure factor caused by additional atomic displacements "violating" the centrosymmetricity of cubic unit cells. At still lower temperatures, the intensity continues increasing and shows noticeable kinks at the temperatures corresponding to the anomalies in the shape of the 224 refection. These kinks seem to be associated with switching-on of the extinction mechanisms of increasing scattered intensity. Thus, these data confirm the structural changes occurring in the crystal at the above-indicated temperatures.

The most pronounced intensity increase is observed in the ferroelectric phase. Of the above three factors affecting the intensities of this phase, only the changes in the extinction conditions can explain this effect. A decrease of extinction due to the formation of smaller blocks observed in the phase-transition in $BaTiO_3$ crystals was explained by coexistence of various phases [18]. In the phase transition region, the reflection intensities first increased and then decreased approaching the initial values. In our case, no increase of block dimensions was observed.

CONCLUSIONS

The data obtained lead to the conclusion that the 0.8PMN–0.2PT crystals in the fields $E < 5$ kV/cm undergo the same set of phase transitions as in the absence of an electric field, with the transition temperatures being only slightly dependent on the intensity of the applied field. The phase diagram constructed by the points corresponding to the anomalies in the shape of the 224 reflection is shown in Fig. 3. The ferroelectric phase transition is also observed in an electric field, which indicates that it is a first-order phase transition.

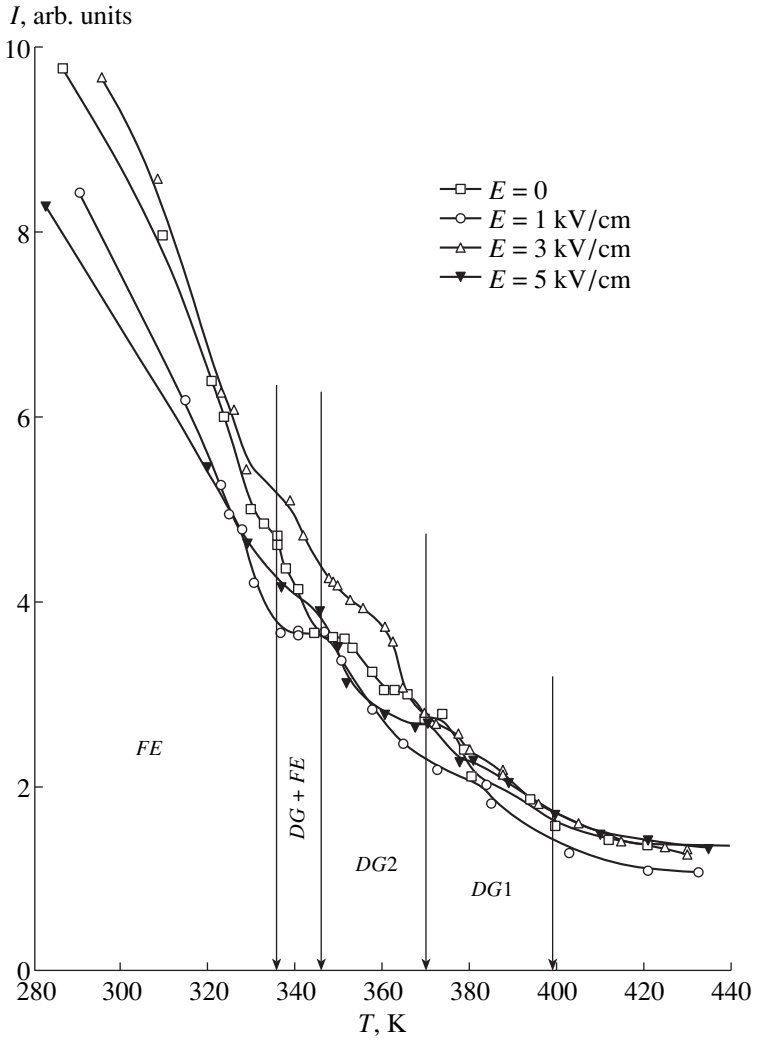

Fig. 2. Temperature dependence of the integrated intensity of the 005 reflection. Vertical lines correspond to anomalies in the shape of the 224 reflection. The probable existence ranges of the phases (denoted by letters) are indicated (see text).

The absence of characteristic jumps in the dielectric parameters [1, 2] in the field-cooled mode is explained by very large relaxation times inherent in the inhomogeneous phases preceding the ferroelectric phase. This hinders the determination of the equilibrium dielectric parameters of the crystal during the time of the experiment. However, such jumps can be observed during heating of the ferroelectric phase, as is the case for pure PMN in the fields with $E > 2$ kV/cm [9].

A new result obtained in this study is the existence of structural anomalies at $T_{DG1} \approx 390$–400 K which lead to the assumption about the existence of one more phase—the dipole glass type (*DG*1) at $T_{DG2} < T < T_{DG1}$. The latter phase is characterized by additional random atomic displacements violating the unit-cell centrosymmetricity. However, in distinction from the nonergodic glassy phase *DG*2, the atomic displacements in the *DG*1 phase should be uncorrelated on a macroscopic scale, because this phase is not ergodic. Indeed, the curve of the threshold field necessary for the transition to the polar phase upon zero field-cooling [14] (the curve with signs "+") (Fig. 3) does not go outside the boundaries of the *DG*1 phase. This signifies that only this phase and the mixed phase *DG* + *FE* are not ergodic; in other words, the crystal state in this phase depends on the path on the *T*–*E* diagram.

It should also be emphasized that the above *T*–*E* phase diagram differs from the phase diagram of pure PMN by the shape of the threshold-field curve. For PMN, this curve, determining the range of existence of the induced ferroelectric phase, lies at $E > 2$ kV/cm [9–11], whereas for 0.8PMN–0.2PT crystals, the threshold-field curve approaches the axis $E = 0$, so that the spontaneous ferroelectric transition can also take place in the absence of an electric field. Thus, the addition of Ti ions to PMN reduces the energy barrier between the glassy and the ferroelectric phases in the range of their coexistence.

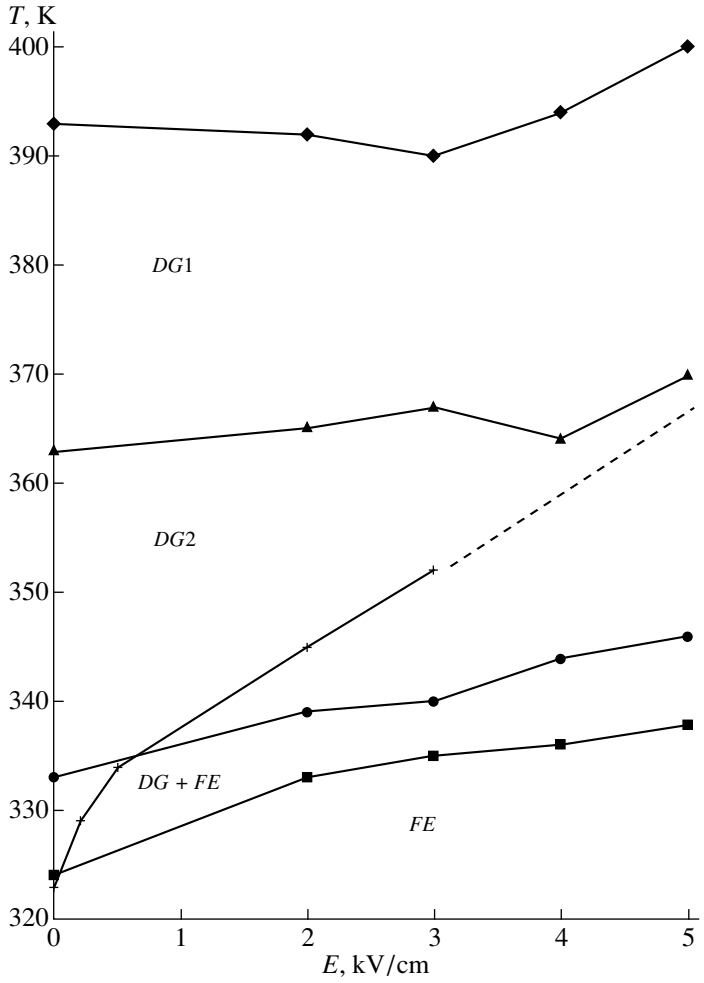

Fig. 3. Phase diagram of a 0.8PMN–0.2PT crystal corresponding to the shape anomalies for the 224 refection. The line with the signs "+" represents the dependence of the threshold field for the transition to the polar phase upon cooling in the zero-field-cooled mode [14].

At the same time, similar to the case of pure PMN, the field $E \approx 2$ kV/cm is critical for the 0.8PMN–0.2PT structure even at high temperatures. The field dependences of the parameters determined from the 224 profile at $T = 410$ K (we mean the "pseudocubic" unit-cell parameters corresponding to the centers of the Gaussians and the widths and the relative intensities of these Gaussians at $E > 2$ kV/cm) show considerable changes, indicating a drastic decrease of the fraction of mesoscopic polar clusters in the total volume of the crystal. It seems that such clusters merge together because of polarization switching under the effect of an applied field, whose intensity becomes higher than the average coercive field of a cluster (~2kV/cm). As a result, the enlarged polar regions become the elements of a pseudocubic matrix in which the ferroelectric phase is energetically more favorable than the dipole-glass phase at rather low temperatures. Obviously, the threshold field, providing the formation of the ferroelectric phase in the zero-field-cooled mode for pure PMN, remains equal to the coercive field of polar clusters also at $T < 210$ K [9–11]. This signifies that, with a decrease of the temperature, the polarization orientations in this crystal are still random, whereas a decrease of the threshold field to zero at $T = T_F$ in 0.8PMN–0.2PT crystals indicates their spontaneous switching and also a gradual increase of the dimensions of the energy polarized regions. This conclusion is confirmed by the noticeable narrowing of the broadest component of the 224 reflection at $T < T_{DG2}$ and $E > 0$ (Figs. 1b, 1c).

The most probable cause of spontaneous switching of polar clusters in PMN–PT crystals is the reduction of the intensity of the random electric field "fixing" the direction of the local polarization. This reduction is explained by the fact that the cells with Ti^{+4} ions are neutral, whereas the cells containing the Mg^{+2} and Nb^{+5} are not. A more detailed study of the mechanism of spontaneous ferroelectric transition and preceding transitions to glassy phases in the crystal under question requires a much larger volume of information. Thus, the determination of the temperature evolution of the

profile parameters of a large number of reflections (similar to that described above for the 224 refection) would allow the construction of the temperature dependences of the cluster dimensions, their average deformations, and the deformations of the pseudocubic crystal matrix [19]. These data would help to clarify the nature of phase transitions taking place in PMN and the related crystals.

ACKNOWLEDGMENTS

This study was supported by the Russian Foundation for Basic Research, project no. 96-02-16219.

REFERENCES

1. S. W. Choi, T. R. Shrout, S. J. Jang, and A. S. Bhalla, Ferroelectrics **100**, 29 (1989).
2. S. M. Emelyanov, F. I. Savenko, Yu. A. Trusov, *et al.*, Phase Transit. **45**, 251 (1993).
3. O. Bidault, M. Licheron, E. Husson, *et al.*, Solid State Commun. **98**, 765 (1996).
4. L. E. Cross, Ferroelectrics **76**, 241 (1987).
5. P. Bonneau, P. Garnier, G. Calvarin, *et al.*, Solid State Chem. **91**, 350 (1991).
6. N. de Mathan, E. Husson, G. Calvarin, *et al.*, J. Phys.: Condens. Matter **3**, 8159 (1991).
7. O. A. Bunina, I. N. Zakharchenko, and S. M. Emel'yanov, Izv. Akad. Nauk, Ser. Fiz. **57**, 160 (1993).
8. O. A. Bunina, I. N. Zakharchenko, P. N. Timonin, and V. P. Sakhnenko, Kristallografiya **40** (4), 708 (1995) [Crystallogr. Rep. **40**, 655 (1995)].
9. Z.-G. Ye and H. Schmid, Ferroelectrics **145**, 83 (1993).
10. R. Sommer, N. K. Yushin, and J. J. van der Klink, Phys. Rev. B **48**, 13230 (1993).
11. E. V. Colla, S. B. Vakhrushev, E. Yu. Koroleva, and N. M. Okuneva, Fiz. Tverd. Tela (St. Petersburg) **38**, 205 (1996) [Phys. Solid State **38**, 1202 (1996)].
12. O. Bidault, M. Licheron, E. Husson, *et al.*, J. Phys.: Condens. Matter **8**, 8017 (1996).
13. I. N. Zakharchenko, O. A. Bunina, P. N. Timonin, *et al.*, Kristallografiya **40** (4), 684 (1995).
14. I. N. Zakharchenko, O. A. Bunina, P. N. Timonin, *et al.*, Ferroelectrics **199**, 187 (1997).
15. I. N. Zakharchenko, O. A. Bunina, P. N. Timonin, *et al.*, Kristallografiya **43** (1), 71 (1998) [Crystallogr. Rep. **43**, 64 (1998)].
16. C. Boulesteix, F. Varnier, A. Llebaria, and E. Husson, J. Solid State Chem. **108**, 141 (1994).
17. D. E. Ovsienko and E. I. Sosnin, Fiz. Met. Metalloved. **3**, 516 (1956).
18. W. Kanzig, Helv. Phys. Acta **24**, 175 (1951).
19. P. N. Timonin, I. N. Zakharchenko, O. A. Bunina, and V. P. Sakhnenko, Phys. Rev. B **58**, 3015 (1998).

Translated by L. Man

Crystallography Reports, Vol. 45, No. 6, 2000, pp. 968–970. Translated from Kristallografiya, Vol. 45, No. 6, 2000, pp. 1050–1052.

PHASE TRANSITIONS

Effect of Uniaxial Pressures on the Phase Transitions in $(NH_4)BeF_4$ Crystals

V. I. Stadnik

Franko University, ul. Kirila i Mefodiya, Lviv, 290005 Ukraine

Received January 26, 1998; in final form, December 14, 1999

Abstract—The effect of uniaxial mechanical pressure along the principal crystallophysical directions on the phase transitions paraelectric–incommensurate–commensurate ferroelectric phases in $(NH_4)_2BeF_4$ crystals is studied by the optical method. It is established that the G_x and G_y pressures applied along the *x*- and *y*-axes shift the phase transitions towards lower temperatures, whereas the G_z pressure applied along the *z*-axis, towards higher temperatures. The possible existence of a triple point on the phase diagram is indicated. © *2000 MAIK "Nauka/Interperiodica".*

Two phase transitions are established in $(NH_4)_2BeF_4$ crystals: a second-order transition from the paraelectric phase to the incommensurate phase at T_i = 183 K and a first-order transition from the incommensurate phase to the ferroelectric commensurate phase at T_C = 177 K [1, 2]. Both high-temperature and low-temperature (ferroelectric) phases are orthorhombic and described by the sp.gr. *Pnam*-D_{2h}^{16} and $Pn2_1a$-C_{2v}^{9}, respectively [3]. The incommensurate phase is characterized by the wave vector $q_I = (1 - \delta)a_c$, where $\delta \approx 0.02$.

Earlier, the effect of a hydrostatic pressure *p* on the phase transitions in $(NH_4)_2BeF_4$ crystals was studied by various methods. The dielectric-constant measurements [4] showed that the pressures up to 10 kbar shift the phase transitions towards lower temperatures, with the coefficients being $dT_i/dp = -1.7$ and $dT_C/dp = -2.2$ K/kbar. The same coefficients obtained from the studies of the temperature dependences of velocities of sound propagation [5] were found to be $dT_i/dp \sim 2.39$ and $dT_C/dp \sim 2.93$ K/kbar. The dielectric-constant measurements performed in [6] under pressures up to 6 kbar yielded $dT_C/dp = -6.7$ K/kbar; the values of the dielectric constants obtained in [4] and [6] were almost equal.

We had the aim to study the effect of the uniaxial mechanical pressure along the principal crystallophysical directions on the position of phase-transition points in the $(NH_4)_2BeF_4$ crystal by the optical method. Within the temperature range studied, the crystals remained biaxial, optically negative, with the axis orientations $X \parallel N_g$ and $Y \parallel N_p$ (N_g and N_p are the bisectors of the obtuse and the acute angles between the optical axes, respectively).

The effect of the uniaxial pressure on the temperature and spectral behavior of birefringence was determined from the changes in the interference pattern recorded on a DFS-8 spectrograph. The sample in the diagonal position between the crossed nicols was placed into a cryostat. The interference spectrum in the focal plane of the spectrograph formed by a transmitted light beam consisted of a set of alternating vertical dark and light fringes. The condition for the formation of the interference fringes in the spectrum is the fulfillment of the equality

$$d(n_i - n_j) = k\lambda, \quad (1)$$

where *k* is the order of the interference fringe, *d* is the width of a sample along the direction of beam propagation, *i* and *j* are the crystallophysical directions, and n_i and n_j are the corresponding refractive indices.

With the temperature variation, the interference fringes are shifted and birefringence is determined as

$$\Delta n_i(\lambda, T) = k\lambda/d(T). \quad (2)$$

The compression of a sample results in a spectral shift of the interference fringes in the focal plane of the spectrograph. The temperature- and pressure-induced changes in birefringence Δn_i are then determined as

$$\Delta n_i(T, G_i) = k\lambda/d(T, G). \quad (3)$$

The measurements were made at pressures up to $G_i \approx 200$ bar. An accuracy of birefringence determination was $\delta\Delta n_i = \pm 2 \times 10^{-5}$.

The temperature dependences of birefringence Δn_z and Δn_x in the range of phase transitions for various directions of pressure application are shown in Figs. 1a and 1b.

The application of the pressure G_X increases, while the application of the pressures G_Y and G_Z decreases birefringence by about 1.2×10^{-4}, 1.7×10^{-4}, and 0.6×10^{-4}, respectively. The phase transitions are accompanied by the abrupt changes in the slopes of the curves $\Delta n_z(T)$ and $\Delta n_x(T)$. For example, $d\Delta n_z/dT \approx -7.20 \times 10^{-5}$

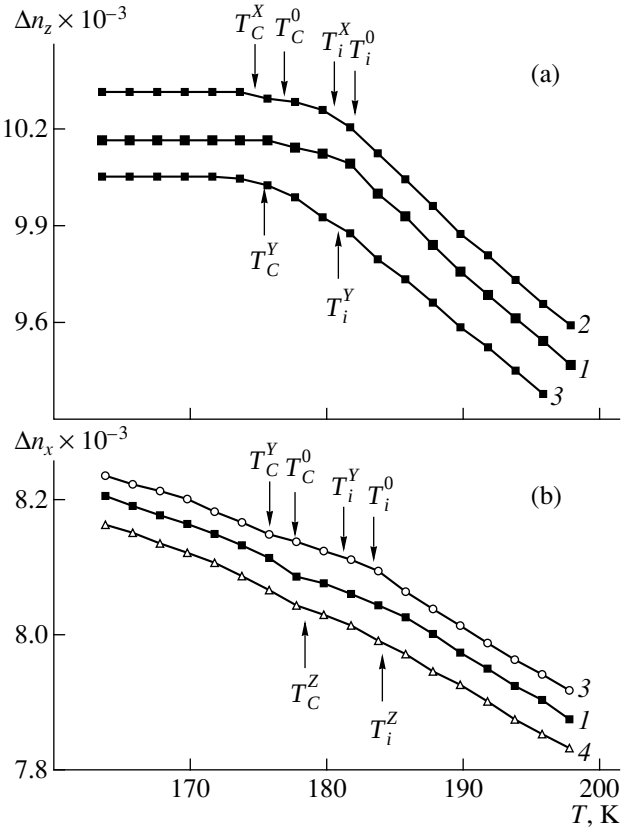

Fig. 1. Temperature dependence of birefringence (a) Δn_z and (b) Δn_x of the $(NH_4)_2BeF_4$ crystal (λ = 500 nm) under various pressures: (*1*) G_i = 0; (*2*) G_X = 200; (*3*) G_Y = 200; (*4*) G_Z = 200 bar. T_i^X, T_i^Y, T_i^Z are the points of the paraelectric–incommensurate phase transition under the pressures G_X, G_Y, and G_Z, respectively. T_C^X, T_C^Y, T_C^Z are points of the incommensurate–ferroelectric phase transition under the pressures G_X, G_Y, and G_Z, respectively.

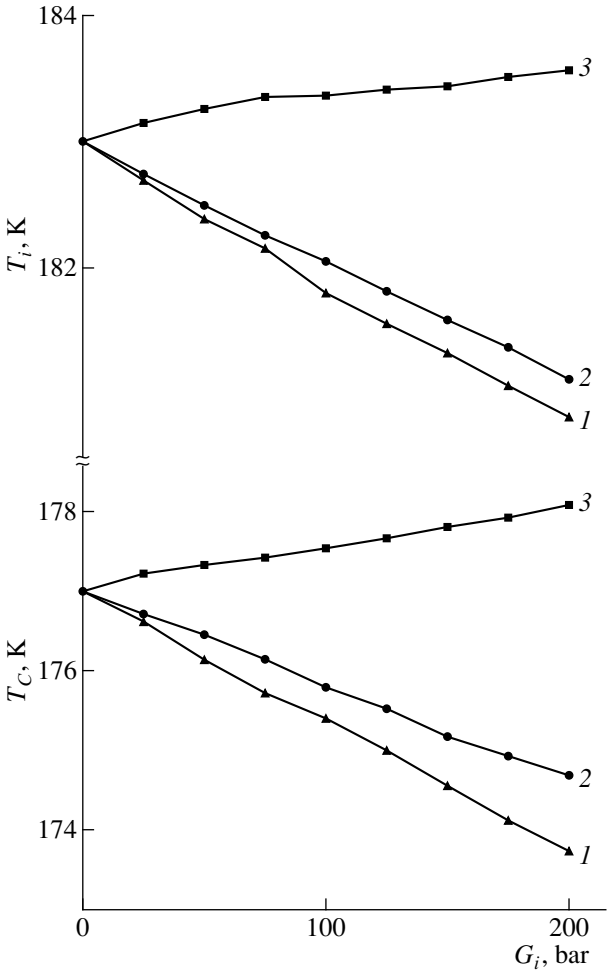

Fig. 2. Temperature–baric dependences for the phase transition points T_i and T_C of $(NH_4)_2BeF_4$ crystals. Pressures: (*1*) G_X; (*2*) G_Y; (*3*) G_Z.

and -1.80×10^{-5} K^{-1} at $G_X \neq 0$; $d\Delta n_x/dT \approx -0.80 \times 10^{-5}$ and -0.45×10^{-5} K^{-1} at $G_Z \neq 0$ at 190 and 180 K, respectively. At $G_X \neq 0$ and $G_Y \neq 0$, both phase transitions are shifted towards lower temperatures (T_i = 180.8 and T_C = 173.8, T_i = 181.2 and T_C = 174.6 K, respectively), whereas at $G_Z \neq 0$, to higher temperatures (T_i = 183.6 and T_C = –178.80 K).

Figure 2 shows the pressure dependences of the phase-transition points, which allow more accurate evaluation of the shifts of phase transitions: $dT_i/dG_X = -0.011$, $dT_C/dG_X = -0.016$, $dT_i/dG_Y = -0.009$ and $dT_C/dG_Y = -0.012$, $dT_i/dG_Z = 0.003$, and $dT_C/dG_Z = 0.005$ K/bar. The simultaneous effect of all the uniaxial pressures leads to the shift of the phase transitions towards lower temperatures: $dT_i/dG = dT_i/dG_X + dT_i/dG_Y + dT_i/dG_Z = -0.017$ K/bar, $dT_C/dG = dT_C/dG_X + dT_C/dG_Y + dT_C/dG_Z = -0.023$ K/bar. This qualitatively agrees with the effect of a hydrostatic pressure on phase transitions. However, the temperature coefficients characterizing the displacements of the phase transitions under the effect of hydrostatic pressure are considerably lower than those for the uniaxial pressures. This evidences a more pronounced effect of uniaxial pressures on the crystal structure. The uniaxial pressures G_X and G_Y increase and shift the temperature range of the existence of the incommensurate phase towards lower temperatures, while the pressure G_Z narrows this interval. Extrapolation of the $G_Z(T)$ dependences (see Fig. 3) shows that the incommensurate phase in $(NH_4)_2BeF_4$ crystals can disappear under the pressure $G_Z \approx 2.3$ kbar and the temperature $T \approx 190$ K, and the crystal can undergo a paraelecric–ferroelectric phase transition.

Consider the changes in the physical properties of the crystals observed under the effect of uniaxial stresses in terms of possible structural changes. As is

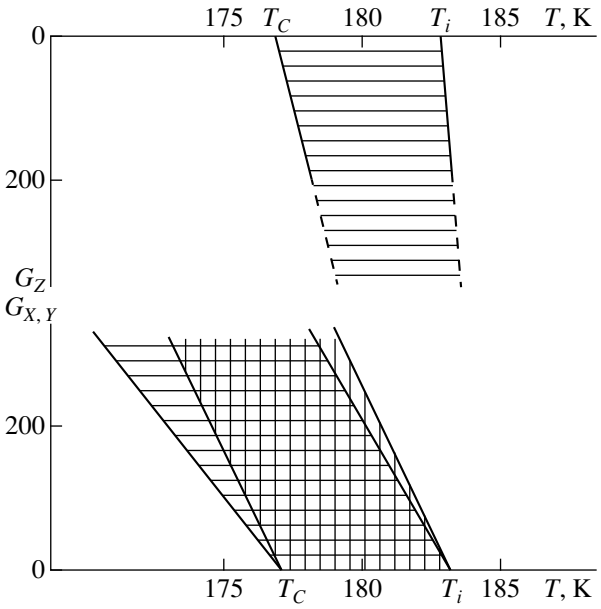

Fig. 3. The G–T phase diagrams for a $(NH_4)_2BeF_4$ crystal. The temperature range of existence of the incommensurate phase (at $T_C < T < T_i$) under the pressure G_X is limited by the horizontal lines; then under the pressure G_Y, by the vertical lines.

well known [7], the structure of this crystal at room temperature is described by the sp.gr. *Pnma*. In this case, tetrahedral BeF_4-groups are slightly distorted, while two nonequivalent ammonium ions are characterized by different distortions. For example, an NH_4 (1) ion, surrounded with five BeF_4-ions (1), is distorted only slightly, whereas an NH_4-ion (2) surrounded with six BeF_4-groups is distorted much more. The structure of the crystal in the paraelectric phase can be considered as a partly disordered state with respect to small rotations of BeF_4-groups preferably around the pseudo-sixfold axis X [8, 9].

The phase transition into a ferroelectric phase is accompanied by more pronounced rotations of BeF_4-tetrahedra about all the three axes of the structure (without essential changes in the configuration), but preferably around the X-axis. In this process, a tetrahedron is "frozen" in one of the positions of the paraelectric phase. If the effects of the applied field and the temperature decrease affect the crystal structure in the same way, the condition for a thermodynamic equilibrium in the phase transition is satisfied also at higher temperatures. Otherwise, the phase-transition temperature is shifted towards lower temperatures.

Since the phase transition to the ferroelectric phase is accompanied by a more pronounced rotation of the BeF_4-tetrahedra around the X-axis, the uniaxial pressure applied along the X-axis "compresses" the tetrahedra, i.e., hinders their rotation, and thus does not allow the crystal to transit to a new phase. Correspondingly, lower temperatures are required to provide a phase transition under the pressure G_x.

The rotation of the BeF_4-tetrahedra during a phase transition occurs in the YZ-plane. The shift of the phase-transition point towards lower temperatures under the pressure G_Y may be associated with the fact that G_Y hinders the rotation of the BeF_4-tetrahedra around the X-axis, and thus results in the fulfillment of the corresponding condition for the thermodynamic equilibrium at somewhat lower temperatures. The pressure G_Z facilitates the rotation of BeF_4-tetrahedra during the incommensurate–commensurate ferroelectric phase transition and, thus, facilitates the transition into a ferroelectric phase, which can now occur at higher temperatures.

The main cause of the higher temperature sensitivity of birefringence of crystals under the uniaxial pressure appears to be the character of the interactions between the modulated structure and the uniaxial deformation. It is well-known that soliton pinning at defects or at the crystal lattice gives rise to metastable states. The uniaxial pressure in the vicinity of the incommensurate phase affects the spatial ordering of a soliton structure. An increase of the temperature sensitivity of the incommensurate phase under the uniaxial pressure is explained by the pressure-induced changes in the soliton structure.

ACKNOWLEDGMENTS

The author is grateful to N. A. Romanyuk for valuable discussions.

REFERENCES

1. B. A. Strukov, T. A. Skomorokhova, V. A. Koptsik, and A. A. Boĭko, Kristallografiya **18** (1), 143 (1973) [Sov. Phys. Crystallogr. **18**, 86 (1973)].
2. A. Onodera and Y. Shiozaki, J. Phys. Soc. Jpn. **46**, 157 (1979).
3. I. Okaya, K. Vedam, and R. Pepinsky, Acta Crystallogr. **11**, 307 (1958).
4. K. Gesi and K. Ozawa, J. Phys. Soc. Jpn. **36**, 1496 (1974).
5. T. Hikita, T. Tsukahara, and T. Ikeda, J. Phys. Soc. Jpn. **51**, 2900 (1982).
6. A. M. Shirokov and T. A. Skomorokhova, Kristallografiya **19** (3), 580 (1974) [Sov. Phys. Crystallogr. **19**, 360 (1974)].
7. A. Onodera and Y. Shiozaki, Ferroelectrics **19** (1), 23 (1978).
8. S. V. Misyul', A. I. Kruglik, K. S. Aleksandrov, *et al.*, Kristallografiya **24** (5), 932 (1979) [Sov. Phys. Crystallogr. **24**, 533 (1979)].
9. S. V. Misyul', A. I. Kruglik, and V. I. Simonov, Kristallografiya **25** (3), 473 (1980) [Sov. Phys. Crystallogr. **25**, 273 (1980)].

Translated by A. Zalesskiĭ

Crystallography Reports, Vol. 45, No. 6, 2000, pp. 971–975. Translated from Kristallografiya, Vol. 45, No. 6, 2000, pp. 1053–1057.

Evaluation of the Point-Defect Concentration in $Y_3Fe_5O_{12}$ and Other Rare-Earth Iron Garnets

Yu. P. Vorob'ev*, O. Yu. Goncharov*, and V. B. Fetisov**

** Physicotechnical Institute, Ural Division, Russian Academy of Sciences, ul. Kirova 132, Izhevsk, 426000 Russia*

E-mail: gon@fti.udmurtia.su

*** Ural State University of Economics, ul. Vos'mogo Marta 62, Yekaterinburg, 620219 Russia*

Received April 8, 1998; in final form, January 20, 2000

Abstract—The nonstoichiometry of the yttrium–iron garnet has been analyzed. The predominant types of point defects and their concentrations in $Y_3Fe_5O_{12}$ and other rare-earth iron garnets are established. © *2000 MAIK "Nauka/Interperiodica".*

INTRODUCTION

Materials based on rare-earth iron garnets are widely used in various magnetic and magnetooptical devices [1, 2] in technology. The technology of synthesis and treatment of oxide crystals is associated with the formation of various defects affecting the physicochemical properties of the resulting materials. Below, we consider only point defects very important for garnets and, in particular, oxides and which are dictated by the necessity of elaborating the theory of nonstoichiometric compounds and the simple methods for identifying the type of defects and evaluating their concentrations.

The studies of the nonstoichiometry δ in the $Y_3Fe_5O_{12-\delta}$ garnets [3–12] yielded contradictory information on the nature of cation defects in yttrium–iron garnet (YIG). Unfortunately, the interpretation of these results leads to umbiquous conclusions not only about the concentration but also about the nature of cation defects in YIG. Hence, the lack of rigorous analytical relationships between the physical characteristics of yttrium–iron garnet and δ hinders the efficient fast quantitative analysis of nonstoichiometry.

The main purpose of this was to determine the predominant types of intrinsic defects giving rise to nonstoichiometry of yttrium–iron garnet and to evaluate their concentrations.

PROCEDURE FOR THE QUANTITATIVE EVALUATION OF DEFECT CONCENTRATIONS

The garnet unit cell contains eight formula units, $\{C_3\}[A_2](D_3)O_{12}$. Brackets in the formula indicate that the *C*, *A*, and *D* ions occupy crystallographically nonequivalent positions in the garnet structure. These positions differ in the coordination environment formed by oxygen atoms; namely, the $\{C\}$, $[A]$, and (D) ions are in dodecahedra, octahedra, and tetrahedra of oxygen atoms, respectively. The valences of the ions and their distribution over the nonequivalent $\{C\}$, $[A]$, and (D) positions in the garnet unit cell and the analysis of the most probable type of structural defects were performed [11, 13] with the use of the algorithm presented in Fig. 1. This algorithm is based on the comparison of the experimental unit-cell parameter a with the reference parameter $a_r = f(r_c, r_a, r_d)$ defined by the functional dependence [14]:

$$a_r = b_1 + b_2 r_c + b_3 r_a + b_4 r_d + b_5 r_c r_a + b_6 r_c r_d, \quad (1)$$

where $b_1 = 7.02954$; $b_2 = 3.31277$; $b_3 = 2.49398$; $b_4 = 3.34124$; $b_5 = -0.87758$; $b_6 = -1.38777$; and r_c, r_a, and r_d are weighted average radii of the ions [15] occupying the $\{C\}$, $[A]$, and (D) positions, respectively. The yttrium–iron garnet was synthesized by the solid-phase technology, and the samples were studied by X-ray phase analysis on a DRON diffractometer (FeK_α radiation, a manganese β-filter).

NONSTOICHIOMETRY OF $Y_3Fe_5O_{12}$

The variation in the unit-cell parameter of the yttrium–iron garnet was studied as a function of Y^{3+} content on crystals grown by the solid-phase technology in air at $T = 1400$–1500 K. The nonstoichiometry of YIG was specified by the ratio of the sintered oxides (the $Y_2O_3 : Fe_2O_3$ ratio ranged from 3 : 4.8 to 3 : 5.2). The dependence of the unit-cell parameter of $Y_xFe_{8-x}O_{12}$ crystals on the concentration of the Y^{3+} ions is shown in Fig. 2a. It is seen that the unit-cell parameter increases with an increase of nonstoichiometry. The estimation of the probability of intrinsic-defect formation in yttrium–iron garnet demonstrated

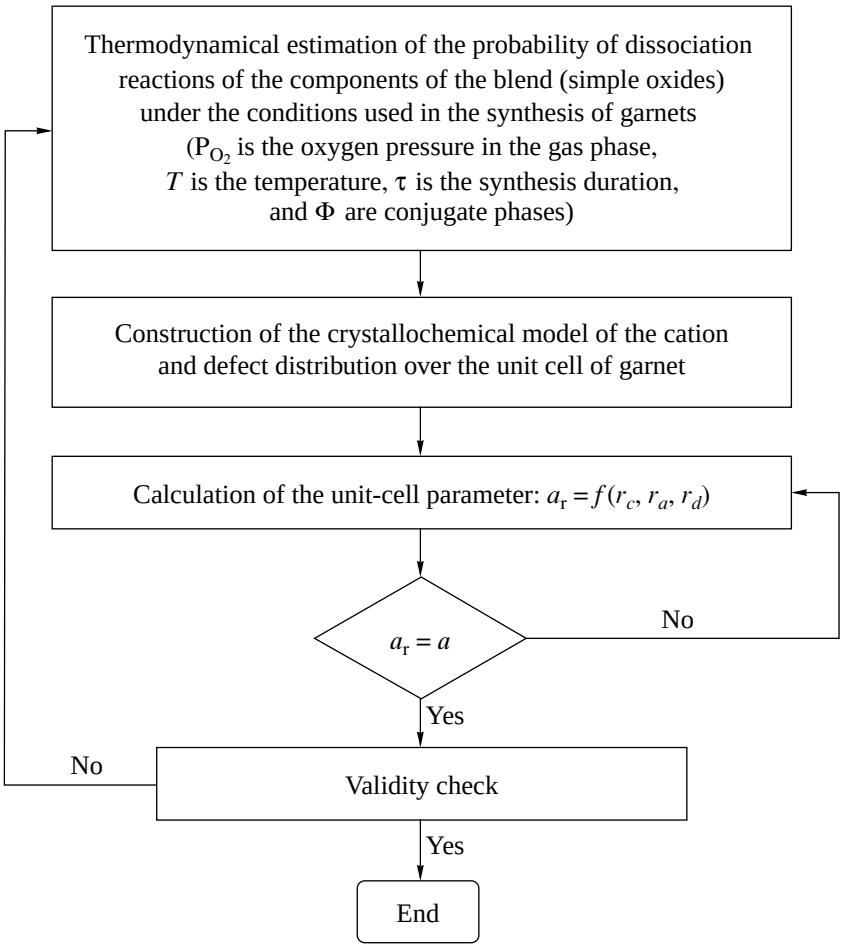

Fig. 1. Algorithm for constructing and calculating crystallochemical models of garnets.

[16] that the energetically most favorable anionic vacancies are those formed with the change in the charge of some Fe ions occupying octahedral positions. This conclusion is consistent with the experimental results [6, 8]. In addition, the experimental [12] and theoretical [16] studies demonstrated that at $x > 3$, excessive Y^{3+} ions occupy the octahedral positions, whereas at $x < 3$, the empty dodecahedral positions are filled with Fe ions. In the latter case, the probability of a change in the valence of the iron ions increases due to the larger size of the $\{Fe^{2+}\}$ ion compared to that of the $\{Fe^{3+}\}$ ion. Consequently, the crystallographic model of the nonstoichiometric yttrium–iron garnet can be represented as follows:

$$\{Y^{3+}_{3-\lambda_0}Fe^{2+}_{\lambda_0}\}[Y^{3+}_{\lambda_1}Fe^{3+}_{5-x-\lambda_0-\lambda}Fe^{2+}_{\lambda}](Fe^{3+}_3)O_{12-\delta}, \quad (2)$$

where

$$x \geq 3: \lambda_0 = 0, \quad \delta = \lambda/2 \quad (2a)$$

and

$$x < 3: \lambda_0 = 3 - x, \quad \delta = (\lambda + \lambda_0)/2. \quad (2b)$$

For the nonstoichiometric compositions of model (2), the following analytical equation for the calculation of the λ values was obtained according to the above-mentioned algorithm (Fig. 1):

$$\lambda = \frac{6(a - \alpha_1) - 3x\alpha_2 + 2\lambda_0^2\alpha_3 + \lambda_0\alpha_4}{[3\beta_1 - \beta_2\lambda_0]\beta_3}, \quad (3)$$

where

$$\alpha_1 = b_1 + b_2 r_{\{Y\}} + (b_4 + b_6 r_{\{Y\}}) r_{(Fe)} - \beta_1(r_{[Fe]} + 1.5\Delta r_{[Fe, Y]}), \quad \alpha_2 = \beta_1 \Delta r_{[Fe, Y]},$$

$$\alpha_3 = (b_2 + b_6 r_{(Fe)})\Delta r_{\{Y, Fe^*\}} - b_2 r_{[Fe]},$$

$$\alpha_4 = \beta_2 \Delta r_{[Fe, Y]},$$

$$\beta_1 = b_3 + b_5 r_{\{Y\}}, \quad \beta_2 = b_5 \Delta r_{\{Y, Fe^*\}}, \quad \beta_3 = \Delta r_{[Fe^*, Fe]}.$$

Here, $\Delta r_{\{ij\}} = r_{\{i\}} - r_{\{j\}}$, $Y = Y^{3+}$, $Fe = Fe^{3+}$, and $Fe^* = Fe^{2+}$.

The analysis of the results of calculations (Fig. 2b) showed that "dissolution" of an excessive amount of Fe_2O_3 in the yttrium–iron garnet led to an increase in the total concentration of the Fe^{2+} ions in the garnet due

to the appearance of the $\{Fe^{2+}\}$ ions in the dodecahedral positions and an increase in the concentration of the $[Fe^{2+}]$ ions in the octahedral positions. Fe ions probably also fill interstices in accordance with the following reaction [7]: $Fe_2O_3 \leftrightarrows 2Fe_i^{3+} + 3/2O_2 + 6e'$. An increase in the conductivity observed in [10] explains an increase in the number of electrons in the conduction band with an increase of the concentration of $[Fe^{2+}]$ (and Fe_i^{3+}) ions. However, we failed to separate the contributions of the $[Fe^{2+}]$ and Fe_i^{3+} ions to an increase of the unit-cell parameter observed at $x < 3$ and to take them into consideration in the calculation of the composition of the crystallochemical model (2).

For the samples of the yttrium–iron garnet (Table 1) sintered from oxides taken in the ratio $Y_2O_3 : Fe_2O_3 = 3 : 5$ at $T = 1400$–1500 K, the crystallochemical formula can be represented as $\{Y_3\}[Fe_{2-\lambda}^{3+}Fe_{\lambda}^{2+}](Fe_3)O_{12-\delta}$, where the λ and δ values were calculated according to Eq. (3). The calculated values given in Table 1 are close to the δ values (0.005–0.015 formula units) determined for polycrystalline YIG samples [3]. For single crystals, the δ values obtained from the thermogravimetric data [6] are somewhat less than those obtained in our calculations. The inconsistency can be explained by the following facts:

(1) The thermogravimetric method [6] is based on measurements of the changes in the sample weight, and, consequently, it allows one to estimate only a change in δ but not the initial nonstoichiometry, which can be substantial.

(2) Single-crystal samples can contain excessive yttrium ions [12, 17], which can lead to underestimation of δ (Fig. 2).

The nonstoichiometry of the garnet may depend not only on the conditions of its synthesis but also on the conditions of its subsequent treatment. After storage of the crystals (which were synthesized in an oxygen atmosphere) in air ($P_{O_2} \approx 0.21 \times 10^5$ Pa) at $T = 1273$ K, the unit-cell parameter a of YIG increased from 12.3744 ± 0.0003 to 12.3753 ± 0.0003 Å. Assuming that this increase is caused by the change in the charge of iron ions in the garnet to Fe^{2+} upon the formation of anionic vacancies as a result of the reaction

$$Y_3Fe_5O_{12} \leftrightarrows \{Y_3\}[Fe_{2-\lambda}^{3+}Fe_{\lambda}^{2+}](Fe_3)O_{12-\delta} + \delta/2O_2, \quad (4)$$

the change in the concentration of the Fe^{2+} ions was calculated from Eq. (3). It was found that the initial (after synthesis) λ value and the λ value after crystal storage in air are 0.012 and 0.02 formula units, respectively. In other words, the change in the partial pressure of oxygen led to the change in the concentration of the Fe^{2+} ions by 0.008 formula units ($\Delta\delta = 0.004$ formula units). After irradiation with neutrons, the unit-cell parameter of the yttrium–iron garnet was increased by 0.063 Å [18]. Assuming that the formation of anionic vacancies and $[Fe^{2+}]$ defects is responsible for the change in the parameter a, the composition described by formula (2) can be calculated from Eq. (3). We obtained $\lambda = 0.58$, which exceeds the maximum λ value (0.07) calculated

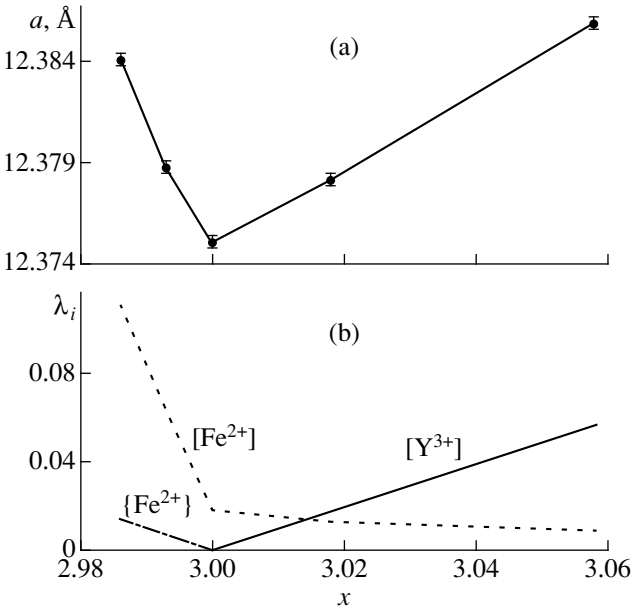

Fig. 2. Concentration dependences of (a) the unit-cell parameter of $Y_xFe_{8-x}O_{12}$ and (b) the concentration of iron ($[Fe^{2+}]$) and yttrium ($[Y^{3+}]$) ions in the octahedral positions and $\{Fe^{2+}\}$ ions in the dodecahedral positions in the yttrium–iron garnet.

Table 1. Unit-cell parameters a of the $\{Y_3\}[Fe_{2-\lambda}^{3+}Fe_{\lambda}^{2+}](Fe_3)O_{12-\delta}$ garnets determined from the $(12\,2\,2)_\alpha$ X-ray diffraction line

a, Å	B, deg	B, mm	λ	δ
12.3743	0.542	52	0.011	0.006
12.3769	0.25	24	0.035	0.018
12.3776	0.375	36	0.042	0.021
12.3779	0.396	38	0.044	0.022
12.3783	0.177	17	0.048	0.024
12.3791	0.208	20	0.056	0.028
12.3794	0.166	16	0.058	0.029
12.3803	0.292	28	0.066	0.033
12.3805	0.25	24	0.068	0.034
12.3806	0.208	20	0.069	0.035
12.3806	0.218	21	0.069	0.035

Note: B is the half-width of the $(12\,2\,2)_\alpha$ X-ray diffraction line; λ is the concentration (formula units) of the $[Fe^{2+}]$ ions calculated by Eq. (3); $\delta = 0.5\lambda$ characterizes the deficiency in the anionic sublattice; the accuracy: $\Delta a = \pm 0.0003$ Å and $\Delta B = \pm 0.5$ mm.

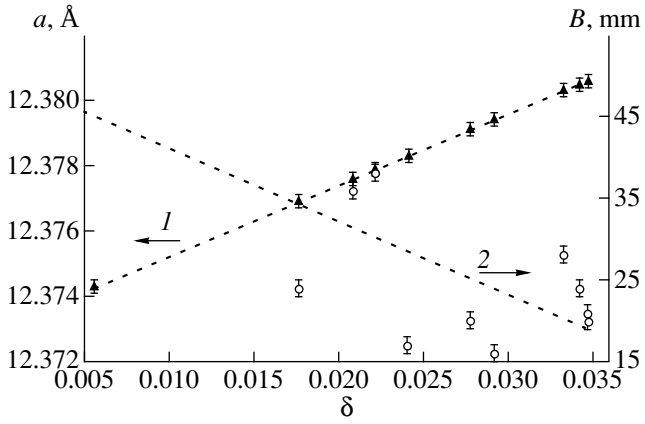

Fig. 3. (*1*) Unit-cell parameter *a* and (*2*) the half-width *B* of the $(12\ 2\ 2)_\alpha$ X-ray diffraction line as functions of nonstoichiometry (δ) of yttrium–iron garnet.

by us for YIG (Table 1) by more than eight orders of magnitude.

The results of the calculations (Table 1) were used to construct the dependences of the unit-cell parameter *a* of YIG and the half-width *B* of the X-ray diffraction line $(12\ 2\ 2)_\alpha$ on the nonstoichiometry of yttrium–iron garnet (Fig. 3):

$$a = 12.373 + 0.216\delta, \quad B = 47.1 - 791.7\delta. \qquad (5)$$

The linear correlation for the linear correlation between the *B* and δ values is characterized by the coefficient $r^2 = 0.47$, which is obviously inadequate to perform quantitative nonstoichiometry determination with the use of the *B* value. However, this coefficient allows the qualitative estimate of nonstoichiometry.

NONSTOICHIOMETRY OF RARE-EARTH IRON GARNETS

The experimental unit-cell parameters *a* of rare-earth iron garnets are larger than the reference values a_r (Table 2) calculated according to Eq. (1). In the first approximation, similar to the case of yttrium–iron garnet, this fact may be related to the change in the garnet composition due to formation of the $[Fe^{2+}]$ ions and anionic vacancies. Hence, the crystallochemical formula of rare-earth iron garnets can be written as

$$\{R_3\}[Fe^{3+}_{2-\lambda}Fe^{2+}_{\lambda}](Fe_3)O_{12-\delta}, \qquad (6)$$

where $\delta = 0.5\lambda$ and R^{3+} is a rare-earth ion. The λ-values for iron garnets of the rare-earth RFeG series described by formula (6) were evaluated with the use of the maximum values a_{max} (Table 2) calculated for a particular garnet [19, 20]. The maximum values λ_{max} (corresponding to a_{max}) calculated according to Eq. (3) are given in Table 2. Apparently, the concentration of the $[Fe^{2+}]$ ions in rare-earth iron garnets is not higher than 0.15 formula units.

The distribution of ions and defects in the yttrium–iron garnet can be represented by the following crystallochemical model:

$$\{Y^{3+}_{3-\lambda_0}Fe^{2+}_{\lambda_0}\}[Y^{3+}_{\lambda_1}Fe^{3+}_{5-x-\lambda_0-\lambda}Fe^{2+}_{\lambda}](Fe^{3+}_3)O_{12-\delta},$$

where $\lambda_0 = 0$ and $\delta = \lambda/2$ at $x \geq 3$ and $\lambda_0 = 3 - x$ and $\delta = (\lambda + \lambda_0)/2$ at $x < 3$.

The anion deficiency in YIG polycrystals from 0.005 to 0.035 formula units. The dependence of the unit-cell parameter on the δ value at $Y^{3+}/Fe^{3+} = 3:5$ is determined by the formula $a = 12.373 + 0.216\delta + 10^{-6}$ Å.

In rare-earth iron garnets

$$\{R_3\}[Fe^{3+}_{2-\lambda}Fe^{2+}_{\lambda}](Fe_3)O_{12-\delta}$$

with $\delta = 0.5\lambda$ (R^{3+} is a rare-earth ion), the concentration of the $[Fe^{2+}]$ ions is not higher than 0.15 formula units. One would expect that the characteristics of defect formation established in this work would also be valid for isomorphous solid solutions of rare-earth iron garnets.

Table 2. Unit-cell parameters of the $\{R_3\}[Fe^{3+}_{2-\lambda}Fe^{2+}_{\lambda}](Fe_3)O_{12-\delta}$ [19] iron garnets

R^{3+}	$Pr^{(s)}$	$Nd^{(s)}$	Sm	Eu	Gd	Dy	Tb
a_{max}	12.646	12.596	12.535	12.498	12.47	12.414	12.435
a_r	12.6314	12.5901	12.5281	12.4868	12.4661	12.4248	12.4041
λ_{max}	0.145	0.058	0.08	0.107	0.037	0.092	0.096

R^{3+}	Ho	Er	Tm	Yb	Lu	Y
a_{max}	12.384	12.349	12.325	12.302	12.29	12.378
a_r	12.3834	12.3421	12.3214	12.3008	12.2801	12.3731
λ_{max}	0.005	0.063	0.033	0.011	0.089	0.046

Note: The a_{max} values (Å) were determined experimentally; the a_r values were calculated by Eq. (1) at $\lambda = 0$; single crystals [20] are marked with the letter s.

REFERENCES

1. S. F. Akhmetov, *Garnet Faces* (Nauka, Moscow, 1990).
2. A. M. Balbashov and A. Ya. Chervonenkis, *Magnetic Materials for Microelectronics* (Énergiya, Moscow, 1979).
3. P. K. Larsen and R. Metselaar, J. Solid State Chem. **12**, 253 (1975).
4. R. Metselaar and P. K. Larsen, J. Phys. Chem. Solids **37**, 599 (1976).
5. P. K. Larsen and R. Metselaar, Phys. Rev. B **14**, 2520 (1976).
6. R. Metselaar and N. Huyberts, J. Solid State Chem. **22**, 309 (1977).
7. A. Ya. Neĭman, V. M. Zhukovskiĭ, I. P. Pazdnikov, *et al.*, in *Chemical Thermodynamics and Technology* (Nauka, Moscow, 1979), p. 145.
8. V. B. Fetisov, M. A. Dvinina, and Yu. P. Vorob'ev, Neorg. Mater. **19**, 1871 (1983).
9. Yu. P. Vorob'ev, T. I. Dragoshanskaya, S. L. Matskevich, *et al.*, Neorg. Mater. **16**, 1083 (1980).
10. G. V. Denisov, Author's Abstract of Candidate's Dissertation in Chemistry (Ural State Univ., Yekaterinburg, 1986).
11. Yu. P. Vorob'ev, Kristallografiya **34** (6), 1461 (1989) [Sov. Phys. Crystallogr. **34** (6), 876 (1989)].
12. P. Novák, J. Englich, H. Štepánková, *et al.*, Phys. Rev. Lett. **75**, 545 (1995).
13. O. Yu. Goncharov, Author's Abstract of Candidate's Dissertation in Chemistry (Ural State Univ., Yekaterinburg, 1997).
14. B. Strocka, P. Holst, and W. Tolksdorf, Philips J. Res. **33** (3–4), 186 (1978).
15. R. D. Shannon and C. R. A. Prewitt, Acta Crystallogr. **25**, 925 (1969).
16. H. Donnerberg and C. R. A. Catlow, J. Phys.: Condens. Matter **5**, 2947 (1993).
17. J. Dong and L. Kunquan, Phys. Rev. B **43**, 8808 (1991).
18. V. A. Sarin, N. N. Bydanov, A. K. Podsekin, and S. P. Solov'ev, in *Proceedings of the VII All-Russia Conference "Current State and Perspectives of Development of Methods for Synthesis and Analysis of Ferrite and Ferro- and Piezoelectric Materials," Ivano-Frankovsk, 1983*, p. 107.
19. A. N. Men', M. P. Bogdanovich, Yu. P. Vorob'ev, *et al.*, *Composition–Defects–Property of Solids. Method of Cluster Components* (Nauka, Moscow, 1977).
20. V. J. Fratello, C. D. Brandle, S. E. G. Slusky, *et al.*, Phys. Rev. B **34**, 7918 (1986).

Translated by T. Safonova

Crystallography Reports, Vol. 45, No. 6, 2000, pp. 976–978. Translated from Kristallografiya, Vol. 45, No. 6, 2000, pp. 1058–1060.

PHYSICAL PROPERTIES OF CRYSTALS

Polarizability of Fluoride Ions in Fluorides with Fluorite-Type Structure

N. I. Sorokin

Shubnikov Institute of Crystallography, Russian Academy of Sciences, Leninskiĭ pr. 59, Moscow, 117333 Russia

Received June 7, 1999

Abstract—The Wilson–Curtis equation $\ln(\alpha_{an}) = \ln(\alpha_{an}^0) - b/d^2$ relating the anion polarizability α_{an} to the anion–cation distances d in cubic NaCl-type alkali halides of the composition MX (M = Li, Na, K, Rb, Cs; X = F, Cl, Br, I) is found to be valid for the family MF_2 and $M_{1-x}R_xF_{2+x}$ crystals (M = Ca, Sr, Ba, Cd and R is a rare-earth metal) with the fluorite-type structure. © *2000 MAIK "Nauka/Interperiodica".*

Today, the "defect" crystals of the composition $M_{1-x}R_xF_{2+x}$ (M = Ca, Sr, Ba, Cd and R is a rare-earth metal) with the fluorite (CaF_2) structure and almost ionic bonding are extensively studied by various physicochemical methods as model solid-state materials for optics [1, 2]. Recently, it was shown that, within the framework of ionic bonding, the concepts of ionic radii [3, 4] and optical ionic refractions [2, 5] are also applicable to fluorite-type $M_{1-x}R_xF_{2+x}$ and $Na_{0.5-x}R_{0.5+x}F_{2+2x}$ crystals. It was also shown that the refractive index can be used for determining the chemical composition of the $M_{1-x}R_xF_{2+x}$ solid solutions with unit-cell parameters (commonly used in the determination of the composition) only slightly depending on the RF_3 concentration, e.g., for $Sr_{1-x}Nd_xF_{2+x}$. As was shown in [2], the change in the refractive index of $M_{1-x}R_xF_{2+x}$ crystals by a value of $\Delta n = 0.002$ corresponds to the change in the concentration of the rare-earth component by $\Delta x = 0.01$ (1 mol % RF_3).

Fedorov [2] used the constant ionic refraction of fluorine equal to $R_F = 2$ cm^3/mol to create a system of ionic refractions of rare-earth elements in $M_{1-x}R_xF_{2+x}$ crystals. However, it is well known [6, 7] that the crystal field reduces the electronic polarizability of anions α_{an} or refraction $R_F = 4\pi\alpha_F/3$ in ionic crystals in comparison with the polarizability of free anions and that the value of α_{an} depends mainly of the distances between anions and cations. Thus, fluoride anions in the MF_2 and $M_{1-x}R_xF_{2+x}$ crystals should be characterized by different polarizabilities α_F or refractions R_F.

Wilson and Curtis [8] suggested the following equation taking into account the effect of environment on the polarizability α_{an} of anions for a number of cubic alkali halide crystals MX (M = Li, Na, K, Rb, Cs; X = F, Cl, Br, I) with a sodium chloride structure:

$$\ln(\alpha_{an}) = \ln(\alpha_{an}^0) - b/d^2, \quad (1)$$

where b is the parameter characterizing the interaction of ions (the binding energy of ions in the crystal) and d is the shortest distance between an anion and a cation. We undertook this study to verify the validity of Eq. (1) for the family of MF_2 crystals (M = Ca, Sr, Ba, Cd) and anion-excessive $M_{1-x}R_xF_{2+x}$ solid solutions on their basis (cubic system CaF_2 structure type, sp. gr. $Fm\bar{3}m$, $Z = 4$).

Unit-cell parameters, refractive indices, and cation polarizabilities for MF_2 and $M_{1-x}R_xF_{2+x}$ crystals

Crystal	a, Å [1, 4]	n [2, 6]	α_M, Å^3 [9]	α_R, Å^3 [9]
BaF_2	6.200	1.475	1.564	
SrF_2	5.800	1.438	0.865	
CaF_2	5.463	1.434	0.472	
CdF_2	5.390	1.562	1.088	
$Ba_{0.72}La_{0.28}F_{2.28}$	6.115	1.525	1.564	1.048
$Ca_{0.72}La_{0.28}F_{2.28}$	5.620	1.505	0.472	1.048
$Ca_{0.77}Y_{0.23}F_{2.23}$	5.593	1.490	0.472	1.048
$Ca_{0.77}La_{0.23}F_{2.23}$	5.507	1.475	0.472	0.56
$Ca_{0.9}La_{0.1}F_{2.1}$	5.521	1.455	0.472	1.048
$Ca_{0.9}Y_{0.1}F_{2.1}$	5.482	1.450	0.472	0.56

1063-7745/00/4506-0976$20.00

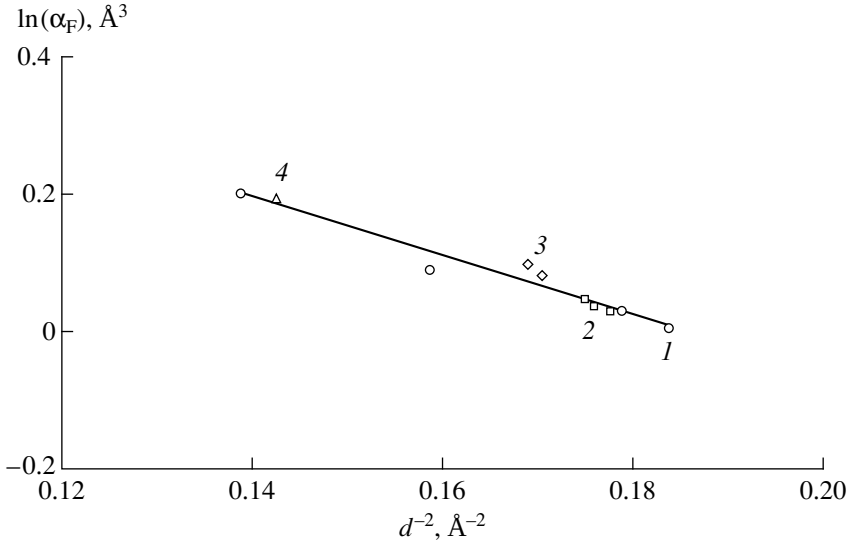

Polarizabilities of fluoride anions in the fluorite-type crystals of the compositions (*1*) MF_2 (M = Ba, Sr, Ca, Cd), (*2*) $Ca_{1-x}La_xF_{2+x}$ (x = 0.1, 0.23, 0.28), (*3*) $Ca_{1-x}Y_xF_{2+x}$ (x = 0.1, 0.23), and (*4*) $Ba_{1-x}La_xF_{2+x}$ (x = 0.28).

In the range of optic frequencies for cubic MF_2 and $M_{1-x}R_xF_{2+x}$ crystals, the Clausius–Mossotti equation is valid, i.e.,

$$(n^2 - 1)/(n^2 + 2) = (4\pi/3)\Sigma N_j\alpha_j, \qquad (2)$$

where n is the refractive index and N_j is the concentration of ions of the jth kind characterized by the electron polarizability α_j. In the visible spectral range, the electron polarizability provided by the shift of the electron shell of ions with respect to the core gives the main contribution to the total polarizability of the crystal, whereas the ionic and dipole components can be ignored. The sum of the products $N_j\alpha_j$ in Eq. (2) is related to the molecular polarizability α as follows:

$$\alpha = \Sigma p_j\alpha_j \qquad (3)$$

(the additivity principle), where $p_j = V_{mol}N_j$ are the molar fractions of the jth species (the number of ions of the jth kind per molecule) and V_{mol} is the molecular volume.

With regard for the fact that $V_{mol} = a^3/4$, the molar polarizabilities for fluorite-type crystals are found from Eqs. (2) and (3) in the form

$$\alpha = 3a^3(n^2 - 1)/16\pi(n^2 + 2), \qquad (4)$$

where a is the unit-cell parameter and $\alpha = \alpha_M + 2\alpha_F$ for MF_2 and $\alpha = (1 - x)\alpha_M + x\alpha_R + (2 + x)\alpha_F$ for $M_{1-x}R_xF_{2+x}$.

According to [7, 8], the electronic polarizability α_{cat} of cations for cubic alkali halide MX crystals only slightly differs from the electronic polarizability α^0_{cat} of free cations. Taking as the first approximation that $\alpha_{cat} \approx \alpha^0_{cat}$ and using the cation polarizabilities given by Pauling [9], it is possible to determine the polarizabilities α_F of fluoride anions in MF_2 and $M_{1-x}R_xF_{2+x}$ crystals from Eqs. (2)–(4). The experimental data used for calculating polarizabilities of fluoride anions in the MF_2 crystals (M = Ba, Sr, Ca, Cd) and $Ca_{1-x}La_xF_{2+x}$, $Ca_{1-x}Y_xF_{2+x}$, and $Ba_{1-x}La_xF_{2+x}$ solid solutions are given in table. The unit-cell parameters and the refractive indices of solid solutions are obtained from the $a = a(x)$ and $n = n(x)$ plots [1, 2, 4]. The α_F values are averaged over the polarizabilities of fluoride ions from various crystallographic positions. The shortest distances between the anions and cations in fluorite-type structures are $d = \sqrt{3}\,a/4$.

The figure shows the polarizabilities of fluoride ions in the $\ln(\alpha_F)$, d^{-2} coordinates. The processing of the data by the least squares procedure show that experimental dots fit the straight line with the slope b = 4.27 Å^{-2} (the linear-correlation coefficient R_{cor} = 0.98). The polarizability of free fluoride anions is α^0_F = 2.2 Å^3.

Thus, the variation of the polarizability of fluoride anions in the family of fluorite-type MF_2 and $M_{1-x}R_xF_{2+x}$ crystals (M = Ca, Sr, Ba, Cd, and R is a rare-earth metal) is satisfactorily described by Eq. (1). The latter equation provides the calculation of the refractive indices n of the nonstoichiometric $M_{1-x}R_xF_{2+x}$ phases from the known cation polarizabilities α_j.

ACKNOWLEDGMENTS

The author is grateful to B.P. Sobolev and P.P. Fedorov for a valuable discussion and the interest in his study.

REFERENCES

1. *Multicomponent Crystals Based on Heavy Metal Fluorides for Radiation Detectors*, Ed. by B. P. Sobolev (Inst. d'Estudis Catalans, Barcelona, 1994).
2. P. P. Fedorov, Doctoral Dissertation in Chemistry (Moscow, 1991).
3. N. I. Sorokin, Kristallografiya **35** (3), 791 (1990) [Sov. Phys. Crystallogr. **35**, 453 (1990)].
4. P. P. Fedorov and B. P. Sobolev, Kristallografiya **37** (5), 1210 (1992) [Sov. Phys. Crystallogr. **37**, 651 (1992)].
5. E. A. Krivandina, A. A. Bystrova, B. P. Sobolev, *et al.*, Kristallografiya **37** (6), 1523 (1992) [Sov. Phys. Crystallogr. **37**, 825 (1992)].
6. S. S. Batsanov, *Structural Refractometry* (Vysshaya Shkola, Moscow, 1976).
7. P. W. Fowler and P. Tole, Rev. Solid State Sci. **5** (2–3), 149 (1991).
8. J. N. Wilson and R. M. Curtis, J. Phys. Chem. **74** (1), 187 (1970).
9. C. Kittel, *Introduction to Solid State Physics*, 5th ed. (Wiley, New York, 1976; Nauka, Moscow, 1978).

Translated by A. Mel'nikova

Crystallography Reports, Vol. 45, No. 6, 2000, pp. 979–984. Translated from Kristallografiya, Vol. 45, No. 6, 2000, pp. 1061–1067.

Characterization of Ferroelectric Pyroelectric Materials Based on Their Switching in a Quasi-Static-Regime

N. R. Ivanov, S. P. Chumakova, A. V. Ginzberg, and V. V. Dolbinina

Shubnikov Institute of Crystallography, Russian Academy of Sciences, Leninskiĭ pr. 59, Moscow, 117333 Russia

Received June 28, 1999

Abstract—A method for studying ferroelectric domains in the crystals of the triglycine sulfate group is developed. It can be used, in particular, to dope crystals for pyroelectric applications. The method combines the use of the electrooptic effect and the surface decoration with nematic liquid crystals. It also provides an opportunity to characterize the degree of bulk and surface homogeneity of polar plates from the topographs of their switching in a uniform quasistatic electric field. *© 2000 MAIK "Nauka/Interperiodica".*

INTRODUCTION

The crystals of triglycine sulfate (TGS) group, such as undoped TGS proper, deuterated TGS (DTGS), and the same crystals doped with *L*-α alanine (LATGS and LADTGS), are used as pyroelectric materials. The crystals are monoclinic, show a large number of growth pyramids, and can be grown from the solutions as both ferroelectric and paraelectric phases. During the layer growth, crystallographically nonequivalent pyramid faces incorporate different amounts of dopants from the solution varying from layer to layer. This results in sectorial and zonal inhomogeneity of the dopant distributions in the crystal [1, 2]. In turn, this promotes the formation of internal domain structure with charged boundaries and the stable inhomogeneity of their ferroelectric, switching, and, thus, pyroelectric characteristics. Unfortunately, the growth conditions and the local processes of dopant incorporation into the crystal cannot always be stabilized. That is why the problem of the control of platelets cut out from the single crystals grown, which are intended for pyroelectric applications, is very important.

EXPERIMENTAL TECHNIQUES

Among a number of techniques used for a nondestructive quality control of ferroelectrics, an efficient method is the visualization of ferroelectric domains and the switching process with the use of nematic liquid crystals (NLC)—the so-called static and dynamic NLC methods [3–7]. Usually, the platelet surfaces are subjected to preliminary mechanical treatment (grinding and polishing), which strongly affects the static orientation of the liquid-crystal director. Therefore, the dynamic method is preferable [5], whose essence reduces to optical imaging of inhomogeneities arising in the NLC layer deposited onto the polar surface of a ferroelectric in the course of switching in an electric dc- or ac-field. Under specially chosen regimes, both the individual moving domain walls and the global topographic patterns of switched platelets can be revealed. Similar to most of the other high- and medium-resolution techniques, the NLC method is sensitive only to the surface effects. However, the domain structures and densities at the surface and in the bulk can considerably differ. That is why the NLC method is supplemented by the electrooptical method sensitive to the bulk processes. The latter was developed at the Shubnikov Institute of Crystallography (Moscow) and was first applied to non-linear-optics and electrooptics materials [8, 9]. Because of a high phase sensitivity ($2\pi \times 10^{-6}$), accuracy (1%), and resolution (0.1 mm) appropriate for topography (although it is somewhat lower than for the NLC method), this method of domain study is also applicable to other optically transparent ferroelectric materials, in particular, to pyroelectric crystals of the TGS group. The electrooptical method for the control of domains uses the hysteresis behavior of the effective electrooptical coefficient in ferroelectrics and its insensitivity to the leakage of the surface charge and, thus, provides recording either local hysteresis loops from a small fixed area (or, more exactly, from volumes of the order of $\sim(0.1\ \text{mm})^2 l$, where l is the platelet thickness) or the functions of depending on the domain density during polar-plate scanning at the given value of the electric field. The electrooptical and NLC methods are complementary. For thin platelets, the results obtained by both methods are consistent as far as the field-switching characteristics and topographs are concerned. These data show different types of growth inhomogeneities in crystals—sectorial, zonal, block, and granular inhomogeneities. In addition, the electrooptical method allows the observation of small-scale internal inhomogeneities with the characteristic size of the order of 0.1–1 mm. For a platelet completely covered by electrodes, the local static electrooptical loops are multicomponent (double, triple, etc.) even in the case of

1063-7745/00/4506-0979$20.00

usual symmetric integral hysteresis loop measured, for example, by the Soyer–Tower method. The local loops correspond to the dependence of the electrooptical coefficient at a given point in an applied field. In some cases, they can also reveal a partial or unipolar switching (especially at a slowly varying switching field) and do not exhibit any definite "coercive" or "bias" field. Therefore, it is more expedient to characterize the switching-process stages by certain threshold voltages dependent on the location of the area under study on the sample history. These features of local switching in an applied uniform electric field are associated with the presence of more or less fixed charged growth defects and, hence, with the domain nuclei and the pinned boundaries. The advantages of the methods of testing of the local quality in comparison with the characteristics of the integral ones become quite obvious at low values of the average domain densities; in other words, they are seen well on most of the uniform polarized platelets. In addition, the local methods are especially convenient for the studying the domain structure.

EXPERIMENTAL RESULTS

Below, we give several examples of inhomogeneity characterization of some pyroelectric materials of the TGS group, in particular, conventional and deuterated TGS doped by *L*-α alanine grown from the solution during lowering of the temperature and at fixed supersaturation and temperature in the ferroelectric and paraelectric phases. The *L*-α alanine concentration in the growth solution ranged within 10–40 wt % (hereafter, this content is indicated in parentheses after the abbreviation of the corresponding crystal). Earlier, it was shown that *L*-α alanine dopant was nonuniformly distributed over different growth pyramids and, on average, is lower than that in the growth solution by about a factor of 90–100 [10]. Other dopants also produce a pronounced effect on the rate of face growth and the single crystal morphology [11]. The sectorial inhomogeneity of such crystals is well revealed by the NLC method [2] from the topographs of switching [6, 7]. In the present study, the additional quantitative data on the domain density distribution and on the local hysteresis loops provided by the electrooptical method are considered for the first time, and the results obtained by the both methods are compared. As usual, the platelets were cut out from large (110)-type growth sectors. The samples were selected upon characterization of inhomogeneity of the polished ferroelectric platelets by visualizing the switching process by the dynamic NLC method. We used nematic liquid crystals with both positive and negative dielectric anisotropy, i.e., the mixtures of cyanobiphenyls ($\Delta\varepsilon > 0$), MBBA, and C-40 ($\Delta\varepsilon < 0$).

Figures 1a and 1b show two photographs of a set of four successive (from the outer edge to the seed) polished 3-mm-thick cuts of the *L*-α-alanine-doped TGS crystal. The pictures were taken in the course of switching in nematic liquid crystals (cyanobiphenyl mixtures). Figure 1a corresponds to the switching at dc voltage $V_{=} = 200$ V and ac voltage $V_{\sim}^{\text{eff}} = 120$ V at the frequency of $f = 70$ Hz and Fig. 1b, to $V_{=} = 500$ V. The pronounced switching inhomogeneity revealed in the platelets at fixed applied fields is related to different local concentration of *L*-α alanine and its distribution over the pyramids, layers, and blocks during crystal growth. In the case under study, the LATGS(10) crystal was grown by the method of temperature lowering.

Combining the NLC method with the method of polarization microscopy, we managed to reveal even smaller details of the switching process at the surface. Thus, Figs. 2a–2d illustrate the large-scale (layer) and small-scale (granular) macroscopic structural inhomogeneities as well as the coexistence of the "hard" and "soft" switching modes. In polar platelets, we usually observed the boundary between the unswitched and switched regions. We also managed to establish the general crystallographic orientation of the boundary, its small fluctuations, and its small displacements at a slow variation of the applied uniform electric field. In this case, the polished $25 \times 25 \times 1.1$-mm^3-large platelet was cut out from the LADTGS(30) crystal grown by the method of supersaturation at a fixed temperature (the paraelectric phase) and was studied at bias voltages (a) 300, (b) 350, (c) 450, and (d) 550 V. The details were visualized by the dynamic NLC method with $\Delta\varepsilon < 0$ (LC-440); $V_{\sim}^{\text{eff}} = 80$ V and $f = 100$ Hz.

To reveal the characteristic points at the surfaces of the ferroelectric platelets, the optical-switching patterns observed in a polarization microscope with the use of the NLC method can be represented as schematic "topographs" by taking a number of successive photographs. The electrooptical method also provides the "construction" of the topographic patterns but, in contrast to the NLC method, for both the switching field and the domain density. The latter ranges from zero to 1 (or to –1, depending on the matrix sign). The topographs of the domain density can be constructed at different levels of the gray scale; however, the process is rather cumbersome. Therefore, we limited ourselves to the demonstration of only some selected profiles of the domain density (scans) and of some local hysteresis loops (with the comparison with the corresponding data obtained by the NLC method).

A simplified schematic "topograph" of the inhomogeneous LADTGS(20) sample is shown in Fig. 3a. The $25 \times 25 \times 0.81$-mm-large sample was cut from a large crystal grown by the method of temperature lowering. Using a nematic liquid crystal (MBBA) in the low-frequency (about 100 Hz) ac-electric field with a high (more than 50 V) amplitude, we managed to obtain the dynamic contrast from the regions with different switching parameters colored in correspondence with the levels of the gray scale; the voltages at which they were revealed are given in parentheses. The light gray region denoted as "60 V" is switched via nucleation and

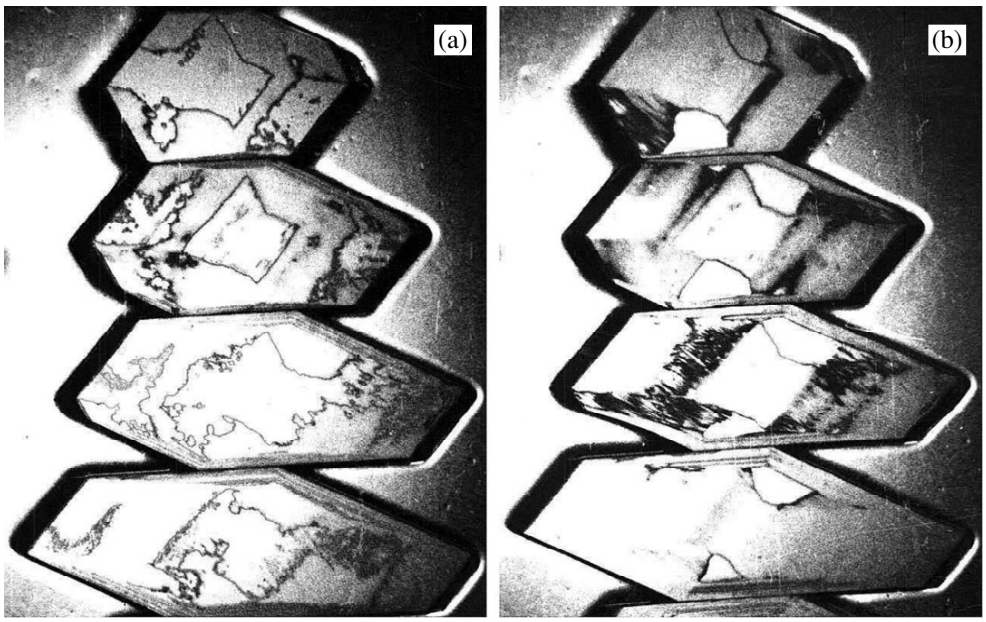

Fig. 1. Optical patterns of inhomogeneous switching for four successive polar cuts of the LADTGS(10) crystal obtained by the dynamic NLC method at different values of the switching voltage: (a) 200 and (b) 500 V. The platelets were 3 mm thick.

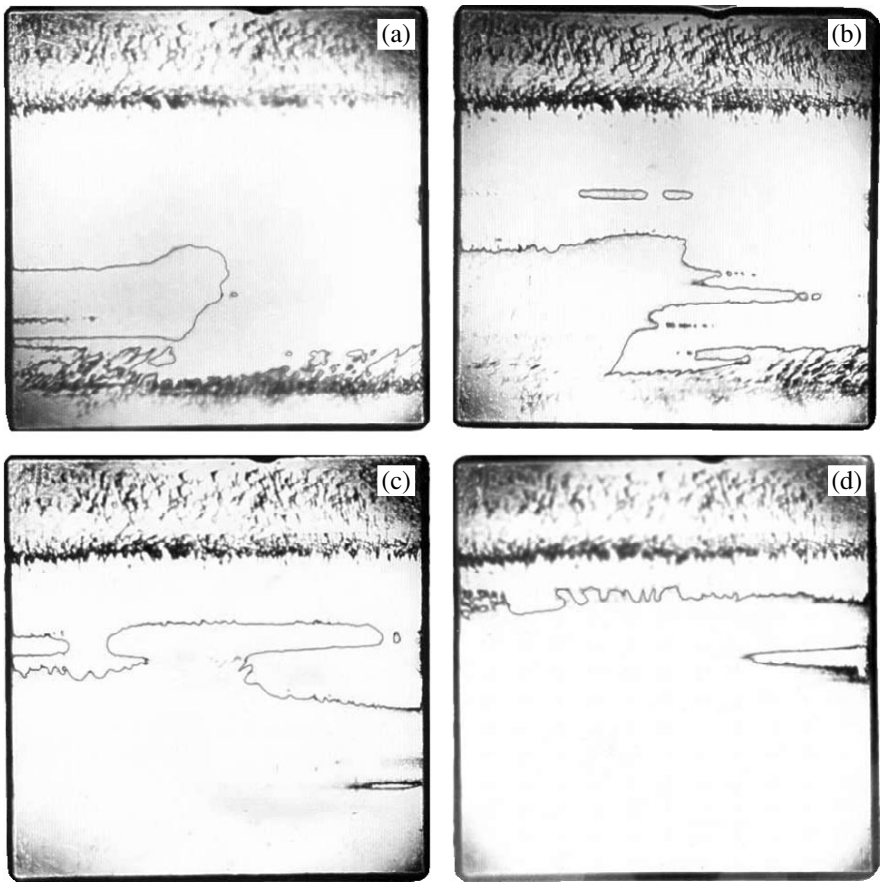

Fig. 2. Visualized switching region and large- and small-scale (granular) macrostructural inhomogeneity in the polar LADTGS(30) platelet made by the dynamic NLC method with $\Delta\varepsilon < 0$; $V_{\sim}^{\text{eff}} = 80$ V, and $f = 100$ Hz at different bias voltages: (a) 300, (b) 350, (c) 450, and (d) 550 V. The platelet dimensions: $25 \times 25 \times 1.1$ mm.

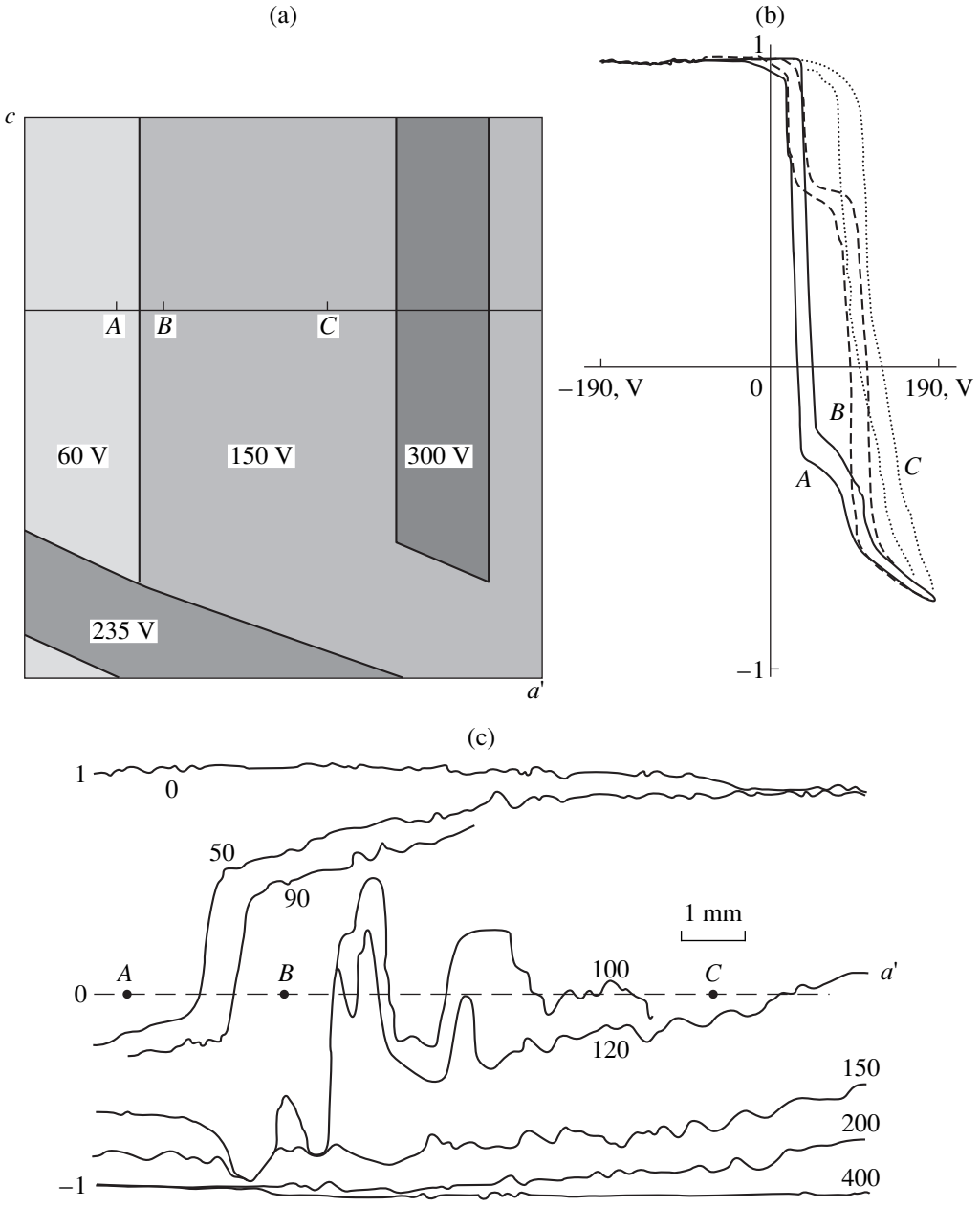

Fig. 3. (a) Topograph of the inhomogeneous $25 \times 25 \times 0.81$-mm-large LADTGS(20) platelet obtained by the NLC visualization of ferroelectric switching; (b) normalized local electrooptical hysteresis loops at the points *A*, *B*, and *C* of the platelet; (c) the results of the electrooptical scanning along the *a*' direction through the points *A*, *B*, and *C* of the same platelet at bias voltages ranging within 0–400 V.

intergrowth of the rows of one-dimensional domain nuclei elongated in the crystallographic direction $a' = a\sin\beta$. In the topograph, we also see the pyramid and growth level boundaries revealed by the NLC method in the course of the switching process (indicated by bold black lines). A thin horizontal line indicated the direction of electrooptical scanning. At the points *A*, *B*, and *C* of this scan, we measured the local loops of the electrooptical hysteresis considered below.

Figure 3b shows the local hysteresis loops LADTGS(20) plate obtained by the electrooptical method at the points *A*, *B*, and *C*. The multicomponent character of the hysteresis loops illustrates the inhomogeneity of the switching associated with the growth (dopant) inhomogeneity. Figure 3b agrees with the data obtained by the NLC and electrooptical methods. In addition, electrooptical scanning of the LADTGS(20) platelets allowed the construction of the domain-density curves along the *a*' axis at different values of the bias voltage at room temperature (Fig. 3c). One can clearly see the growth-induced inhomogeneity and a pronounced scatter in switching voltages. According to

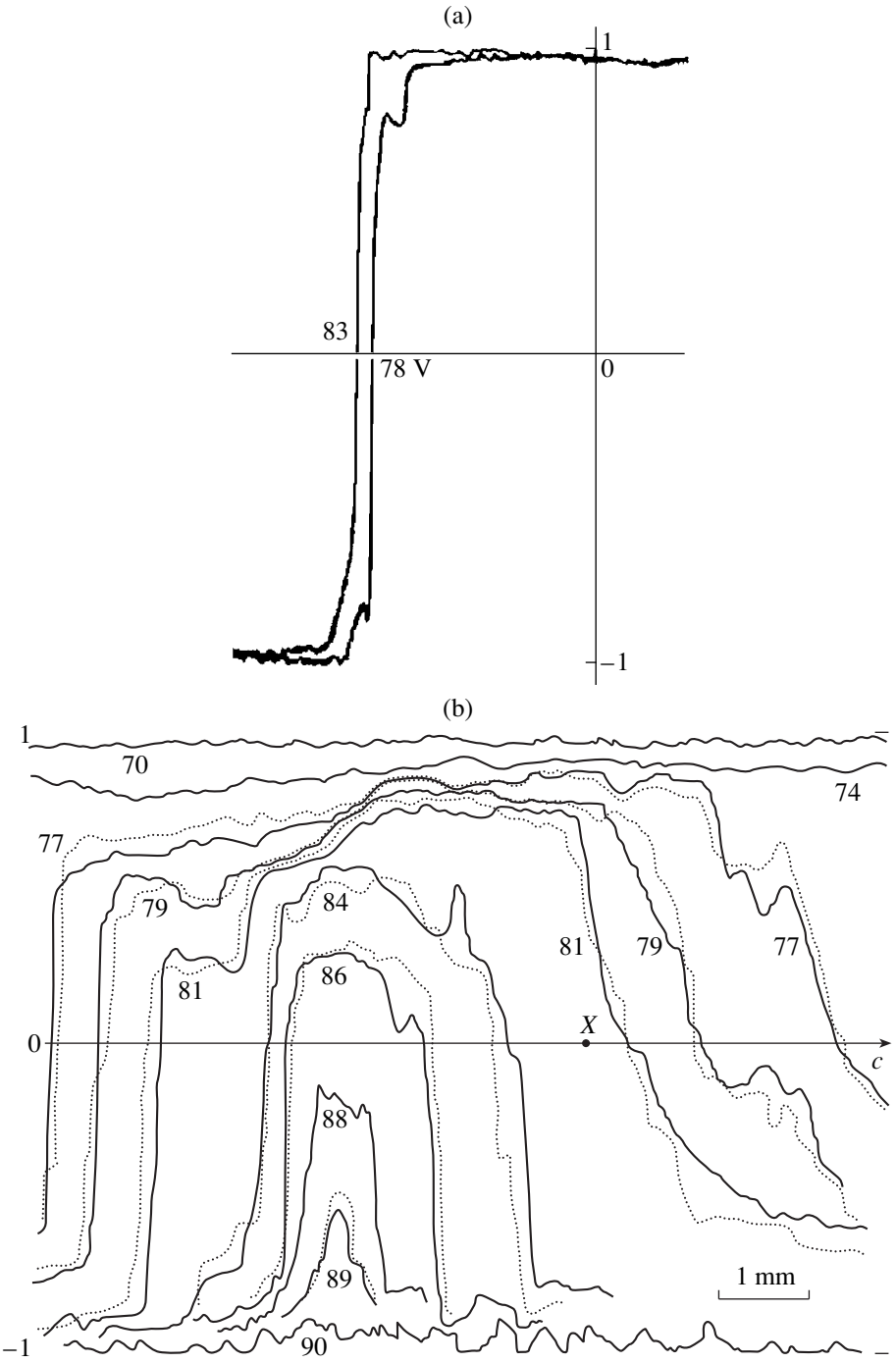

Fig. 4. (a) Normalized local electrooptical hysteresis loop at the point *X* of the *c* scan obtained at the fixed rate of voltage variation (0.33 V/s) for 0.99-mm-thick almost homogeneous polar LATGS(10) platelet, (b) the results of electrooptical scanning along the direction *c* through the point *X* of the same platelet at bias voltages ranging from 70 to 90 V (solid and dashed lines correspond to the increasing and the decreasing voltages, respectively).

the data obtained by the electrooptical method, a jump in the domain density at the boundary between the points *A* and *B* equals 0.28. At the boundary between the regions denoted as 150 and 300 V to the right of the point *C* and not covered by Fig. 3c (see also Fig. 3a), this jump is about 0.14. The gray-scale levels in Fig. 3a are chosen arbitrarily and do not correspond to the domain density. Using the electrooptical method, we revealed an additional fine layered structure between the points *B* and *C* (see scans 100 and 102 V). This structure seems to be "internal" since it was not revealed by the NLC method. The homogeneity or inhomogeneity of the polar plates in the *ac* planes is reflected by both the general switching pattern and the

scatter in the switching voltages and the local hysteresis loops. The (internal) inhomogeneity of polar cuts along the polar *b*-axis can be successfully revealed by electrooptics. It is discussed in more detail below in connection with the possibility (discovered recently) to extend the NLC method to nonpolar crystal cuts. In general, this inhomogeneity is associated with a significant difference in the switching characteristics of domains located in the near-surface layers and in the platelet bulk.

In Fig. 4a, we show the local hysteresis loop obtained by the electrooptical method at the point *X* of the *c* scan for "almost homogeneous" 0.99-mm-thick polished polar LATGS(10) platelet. The LATGS(10) crystal, from which the platelet was cut, was grown in the paraelectic phase by the supersaturation technique at room temperature. The shape of this loop is close to a rectangular single-component one (in fact, the loop is formed by three components, but under the similar conditions we sometimes observed the single-component loops). It is also saturated and symmetric with respect to its displaced center. All these features characterize the homogeneity degree of the sample under study. The distributions of the domain density for this platelet (determined from the data on electrooptical scanning at $T = 16.5°C$, $V_{\sim}^{\text{eff}} = 16$ V, $f = 6$ kHz) at different bias voltages are shown in Fig. 4b, from which it is seen that the insignificant scatter of switching voltages, the smooth coinciding curves obtained at the direct (solid lines) and reverse (dashed lines) runs, and the existence of only one switching center show the "growth" homogeneity of the ferroelectric platelets under study. Such a homogeneity is also confirmed by the shape of the local hysteresis loops (see the loop at the point *X* of the given scan, Fig. 4a). Here, the inhomogeneity observed is on a larger scale than in crystals without *L*-α-alanine dopant, which manifests itself only during switching in the bias fields and is characterized by one macroscopic defect per 1 cm^2 of the surface or per the surface as a whole for the homogeneous platelet. This leads to the switching and insignificant scatter in the switching fields (see Fig. 4b). Note that in the *ac* plane, the (010) pyramids are the most homogeneous—their domain density (at the fixed field) is constant and the layered structure manifests itself in a more pronounced scatter of the switching field and deviations of the loops from the rectangular shape.

Therefore, the inhomogeneity of TGS group of ferroelectrics revealed by our method reflects the distribution of defects in real crystals. This distribution is characterized by the aggregation of domains into macroscopic structures in accordance with their switching voltage and the contribution to the domain-density variation. The typical macroscopic structures are growth pyramids, layers, blocks, and grains. The transition to the homogeneous state corresponds to the simultaneous increase of the macroscopic-structure scale and a decrease in the switching-voltage scatter.

CONCLUSIONS

This method is suggested for characterization of inhomogeneities in pyroelectric materials such as crystals of the triglycine sulfate group. It is based on the simultaneous use of the decoration with nematic liquid crystals and the electrooptical scanning. We compared and analyzed the switching and domain-density inhomogeneities in polar platelets cut out from ferroelectric LATGS and LADTGS crystals grown by different methods from the solutions with different contents of *L*-α alanine. In particular, it was confirmed that the crystals grown by the fixed supersaturation method are more homogeneous than the crystals grown by the method of temperature lowering. This concerns both growth pyramids (in sectors) and internal pyramids in growth layers (in zones). Thin ferroelectric and pyroelectric platelets with the most homogeneous distribution of the *L*-α alanine dopant in the *ac* plane are obtained by growing a single (010) pyramid and controlling its internal layer growth inhomogeneity by the electrooptical method.

ACKNOWLEDGMENTS

We are grateful to N.A. Tikhomirova for fruitful collaboration.

REFERENCES

1. A. A. Chernov, in *Modern Crystallography*, Vol. 3: *Crystal Growth*, Ed. by B. K. Vaĭnshteĭn, A. A. Chernov, and L. A. Shuvalov (Nauka, Moscow, 1980; Springer-Verlag, Berlin, 1984).
2. B. Brezina and M. Havrankova, Cryst. Res. Technol. **22**, 753 (1987).
3. Y. Furuhata and K. Toriyama, Appl. Phys. Lett. **23** (7), 361 (1973).
4. V. P. Konstantinova, N. A. Tikhomirova, and M. Glogarova, Ferroelectrics **20**, 259 (1978).
5. N. A. Tikhomirova, L. I. Dontsova, S. A. Pikin, and L. A. Shuvalov, Pis'ma Zh. Éksp. Teor. Fiz. **29** (1), 37 (1979) [JETP Lett. **29**, 34 (1979)].
6. N. A. Tikhomirova, A. V. Ginzberg, L. I. Dontsova, *et al.*, Fiz. Tverd. Tela (Leningrad) **28** (10), 3055 (1986) [Sov. Phys. Solid State **28**, 1718 (1986)].
7. L. I. Dontzova, N. A. Tikhomirova, and L. A. Shuvalov, Ferroelectrics **97**, 87 (1989).
8. N. R. Ivanov, N. A. Tikhomirova, A. V. Ginzberg, *et al.*, Kristallografiya **39** (4), 659 (1994) [Crystallogr. Rep. **39**, 593 (1994)].
9. N. R. Ivanov, in *Proceedings of XIV All-Russia Conference on Physics of Ferroelectrics, Ivanovo, 1995*, p. 174.
10. M. Koralewski, J. Stankowska, and T. Jasinski, in *Abstracts of the 6th International Meeting on Ferroelectricity, Kobe, Japan, 1985*, p. 140.
11. M. Banan, A. K. Batra, and R. B. Lal, J. Mater. Sci. Lett. **8**, 1348 (1989).

Translated by K. Kugel

Crystallography Reports, Vol. 45, No. 6, 2000, pp. 985–990. Translated from Kristallografiya, Vol. 45, No. 6, 2000, pp. 1068–1074.

Electromagnetic-Wave Surfaces in Absorptive Uniaxial Crystals. I. Cones of Zero Birefringence and Cones of Equal Absorption for Isonormal Waves

V. I. Alshits*, V. N. Lyubimov*, W. Gierulski, and A. Radowicz****

** Shubnikov Institute of Crystallography, Russian Academy of Sciences, Leninskiĭ pr. 59, Moscow, 117333 Russia*

*** Kielce University of Technology, Al. 1000-lecia Pánstwa Polskiego, Kielce, 25314 Poland*

Received May 13, 1999

Abstract—The existence conditions of the circular cones of propagation directions for isonormal electromagnetic waves of two independent branches for weakly absorptive optically uniaxial crystals with the same phase velocities (which corresponds to the zero birefringence) have been studied, and the opening angles of these cones have been determined. It is shown that these cones are formed solely due to absorption. The circular cones of directions, which correspond to the equal absorption coefficients of two independent isonormal waves, were also studied in a similar way. The regions of existence of these cones are described in the explicit analytical form. The dependence of the opening angles of these cones on the components of the complex tensor of the inverse electric permittivity of crystals is also analyzed. It is shown that these two types of cones cannot coexist for one crystal. © *2000 MAIK "Nauka/Interperiodica".*

INTRODUCTION

The fundamental characteristics of the optical properties of crystals are the dependences of refractive indices and absorption coefficients of electromagnetic waves on the directions of their propagation. These dependences are represented by the corresponding wave surfaces, which have two sheets because, along an arbitrary direction of an anisotropic medium, two independent isonormal waves can propagate, the velocities and degrees of absorption of which in the general case are different. In transparent crystals of any symmetry, the geometry of the refractive-index surface is well known [1–3]. However, for absorptive crystals, it is rather difficult to describe the refractive-index surfaces. The complicated form of the corresponding equations makes it necessary to limit the consider consideration to particular numerical examples [2, 4]. Alternatively, we deal with highly symmetric anisotropic absorptive media here, providing the simplification of the general equations, which allows the exhaustive analytical examination of these surfaces. Such media are represented by hexagonal, tetragonal, and trigonal crystals with one highest order symmetry axis coinciding with the optical axis of the crystals. The optical properties of these crystals are analogous to the properties of transversely isotropic media. According to the definition of the optical axis [1, 2, 5], the velocities and the absorption coefficients of both independent branches of electromagnetic waves along the optical axis coincide. However, in absorptive crystals, the phase velocities and, therefore, also the refractive indices of two independent isonormal waves with different absorption coefficients can coincide along the direction different from the optical axis. This direction can be related as an optical pseudoaxis. Obviously, the same velocities of the isonormal waves correspond to the zero birefringence. The equal absorption coefficients of isonormal waves (but at different refractive indices) can also exist for the waves propagating along the directions not parallel to the optical axis. The specific directions of both types form cones, and, since the media studied are transversely isotropic, all these cones are circular.

Below, we describe our study of the characteristics of the surfaces of electromagnetic waves propagating in absorptive optically uniaxial crystals. The first of the two articles of this cycle is devoted to the establishment of the conditions for existence of the above-indicated cones and the dependence of their opening angle on the material characteristics. In fact, we deal with intersection of sheets in two-sheet wave surfaces for the crystals studied.

We restrict ourselves to the case of weakly absorptive crystals with due regard for the electromagnetic fields, which preserve their wave structure at distances considerably exceeding the wavelength (cf. [5, 6]).

1063-7745/00/4506-0985$20.00

INITIAL RELATIONSHIPS

Thus, we consider the propagation of plane electromagnetic waves with the frequency ω, which are harmonic in space and time (t), along the direction $\mathbf{m}$ ($\mathbf{m}^2 = 1$) in absorptive crystals

$$\begin{bmatrix}\mathbf{E}\\ \mathbf{H}\end{bmatrix} \equiv \begin{bmatrix}\mathbf{E}(\mathbf{r}, t)\\ \mathbf{H}(\mathbf{r}, t)\end{bmatrix} = \begin{bmatrix}\mathbf{E}^{(0)}(\mathbf{r})\\ \mathbf{H}^{(0)}(\mathbf{r})\end{bmatrix} e^{i\omega(n\mathbf{mr}/c - t)}. \quad (1)$$

Here, n is the refractive index, which is a function of the direction $\mathbf{m}$, and c is the velocity of light in vacuum. The amplitudes of the electric and magnetic fields, $\mathbf{E}$ and $\mathbf{H}$, respectively, depend on the coordinate $\mathbf{r}$ as

$$\begin{bmatrix}\mathbf{E}^{(0)}(\mathbf{r})\\ \mathbf{H}^{(0)}(\mathbf{r})\end{bmatrix} = \begin{bmatrix}\mathbf{E}^{(0)}\\ \mathbf{H}^{(0)}\end{bmatrix} e^{-\omega n'\mathbf{mr}/c}, \quad (2)$$

where $\mathbf{E}^{(0)}$ and $\mathbf{H}^{(0)}$ are the vectors characterizing the wave polarization and n' is its absorption coefficient also dependent on $\mathbf{m}$. By definition, the phase velocity of such a wave is

$$v = c/n. \quad (3)$$

The concrete form of the dependences $n(\mathbf{m})$ and $n'(\mathbf{m})$ is determined by the dielectric characteristics of the crystal, namely, by the permittivity tensor or the reciprocal permittivity tensor $\hat{B}$. The tensor $\hat{B}$ relates the electric field $\mathbf{E}$ to the induction $\mathbf{D}$ in an electromagnetic wave:

$$\mathbf{E} = \hat{B}\mathbf{D}. \quad (4)$$

In absorbtive crystals, the tensor $\hat{B}$ is complex:

$$\hat{B} = \hat{\beta} - i\hat{\beta}'. \quad (5)$$

The imaginary part of tensor (5) describes absorption of an electromagnetic wave.

Being a material characteristic of the transversely isotropic media, the tensor $\hat{B}$ in the standard crystallophysical reference system (where the axis x_3 is parallel to the highest-order symmetry axis [3]) is diagonal with two of the three components being equal

$$B_1 = B_2 = \beta_1 - i\beta_1', \quad B_3 = \beta_3 - i\beta_3'. \quad (6)$$

The components β_1, β_3, β_1', and β_3' determine all the characteristics of the media under consideration.

For optically uniaxial crystals, the Maxwell equations, satisfied by electromagnetic fields (1) and (2), are decomposed into two independent systems [1, 2]. One of these systems describes the ordinary waves, whereas the other, the extraordinary ones. In the case of weak absorption, these systems of equations yield the following refractive indices and absorption coefficients of ordinary (o) and extraordinary (e) waves:

$$n_o = \frac{1}{\sqrt{\beta_1}}\left(1 - \frac{3}{8}\xi^2\right), \quad (7)$$

$$n_e = \frac{1}{\sqrt{\beta_1(\gamma\sin^2\theta + \cos^2\theta)}} \times \left[1 - \frac{3}{8}\xi^2\frac{(\gamma'\sin^2\theta + \cos^2\theta)^2}{(\gamma\sin^2\theta + \cos^2\theta)^2}\right], \quad (8)$$

$$n_o' = \frac{1}{2\sqrt{\beta_1}}\xi, \quad (9)$$

$$n_e' = \frac{1}{2\sqrt{\beta_1(\gamma\sin^2\theta + \cos^2\theta)^3}}\xi(\gamma'\sin^2\theta + \cos^2\theta). \quad (10)$$

In the above equations, the angle θ is formed by the wave normal $\mathbf{m}$ and the axis x_3. We used the following notation:

$$\gamma = \beta_3/\beta_1 = \frac{1}{\bar{n}_e^2} \times \{n_o^2 + 3[(n_o')^2 - (\bar{n}_e' n_0/\bar{n}_e)^2]\}, \quad (11)$$

$$\gamma' = \beta_3'/\beta_1' = (\bar{n}_e'/n_o')\sqrt{\gamma^3}, \quad (12)$$

$$\xi = \beta_1'/\beta_1 = 2n_o'/n_o. \quad (13)$$

In these equations, we used not only the components of tensor $\hat{B}$ (6) but also the refractive indices and the absorption coefficients measured directly in the experiment. We also used the following notation in Eqs. (11) and (12):

$$\bar{n}_e \equiv n_e(\theta = \pi/2), \quad \bar{n}_e' \equiv n_e'(\theta = \pi/2). \quad (14)$$

Taking into account that phase velocity (3) is real and the intensity of electromagnetic waves decreases during their propagation, we arrive at the following inequalities:

$$\gamma > 0; \quad \gamma', \xi \geq 0. \quad (15)$$

In fact, quantity ξ (13) in expressions (7)–(10) is a small parameter ($\xi^2 \ll 1$) determining the effect of absorption.

CONES OF ZERO BIREFRINGENCE

Equating the refractive indices of two independent branches (7) and (8) upon singling out the root $\theta = 0$,

we arrive at the equation

$$4(1-\gamma)q^2/3 = \xi^2\{(1-\gamma')[(1-\gamma')\sin^2\theta - 2] + (1-\gamma)[3q + (1-\gamma)^2\sin^4\theta]\}, \quad (16)$$

where

$$q = 1 + (\gamma - 1)\sin^2\theta. \quad (17)$$

Since the parameter ξ is small, Eq. (16) can be satisfied only if the difference $(1-\gamma)$ is also small (which signifies weak dielectric anisotropy of the crystal). Under these conditions, $q \longrightarrow 1$ and the second term in the curly brackets can be ignored. Equation (16) is then considerably simplified and yields

$$\theta \equiv \psi = \arctan\sqrt{\frac{\gamma_{\max} - \gamma}{\gamma - \gamma_{\min}}} = \arctan\sqrt{\frac{\kappa}{\Delta n} - 1}. \quad (18)$$

Above, the following notation is used:

$$\gamma_{\max} = 1 + 3\xi^2(1-\gamma')/2, \quad (19)$$

$$\gamma_{\min} = \gamma_{\max} - 3\xi^2(1-\gamma')^2/4 = 1 + 3\xi^2[1-(\gamma')^2]/4, \quad (20)$$

$$\kappa = 3(\Delta n')^2/2n_o, \quad (21)$$

$$\Delta n \equiv n_o - \bar{n}_e, \quad \Delta n' \equiv n_o' - \bar{n}_e'. \quad (22)$$

In fact, Eqs. (18) represent two equivalent solutions of Eq. (16). The cones of zero birefringence with the opening angle 2ψ exist if the material characteristics of the crystal satisfy the following inequalities, written below in two following equivalent forms (Fig. 1):

$$\gamma_{\min} \le \gamma < \gamma_{\max}, \quad 0 \le \Delta n < \kappa. \quad (23)$$

These cones exist in the three-dimensional region of variation of the parameters γ, γ', and ξ. This region is determined by relationships (19), (20), and (23) (Fig. 2). At the boundaries of this region, the opening angle of the cone takes its minimum and maximum values:

$$\gamma \longrightarrow \gamma_{\max}, \quad \psi \longrightarrow 0, \quad (24)$$

$$\gamma \longrightarrow \gamma_{\min}, \quad \psi \longrightarrow \pi/2. \quad (25)$$

In the middle of this region, we have

$$\gamma_0 = \gamma_{\max} - (\gamma_{\max} - \gamma_{\min})/2, \quad \psi = \pi/4. \quad (26)$$

At the ψ angles set by Eq. (18), the refractive indices of the ordinary and the extraordinary waves are given by Eq. (7), with the absorption coefficients being different and determined by the Eqs. (9) and (10).

The results obtained can easily be interpreted. If there is no absorption and the dielectric anisotropy is weak [i.e., the parameter γ Eq. (11) is close to unity], the refractive indices n_o and n_e are close to one another (Fig. 1). Under these conditions, even a low absorption can essentially change the difference between the refractive indices. Indeed, if the absorption is such that the parameters γ, γ', and ξ satisfy the relationships (19), (20), and (23), the refractive indices of two isonormal waves are equal along the propagation directions characterized by the angles ψ set by formula (18).

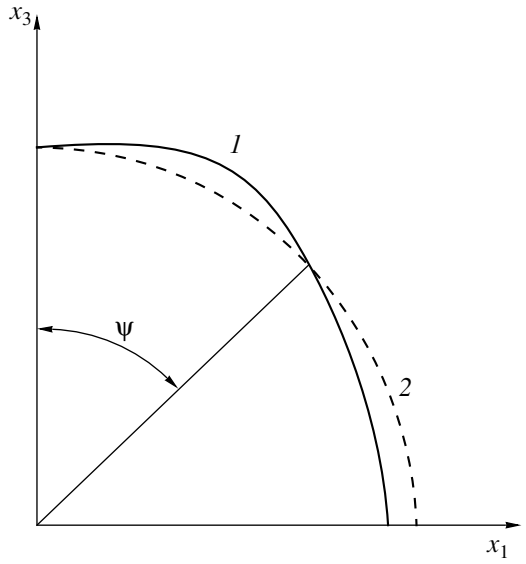

Fig. 1. The section of the refractive-index surface under the condition of the fulfillment of Eqs. (22): (*1*) n_e, (*2*) n_o.

The conditions for the existence of the above cones seem to be rather severe: the width of the existence region is of the order of ξ^2 {where $\xi \sim n_o'$, Eq. (13)} (Fig. 2). This region is extremely narrow in the vicinity of the point $\gamma = \gamma' = 1$ corresponding to the isotropy of the medium. However, one should take into account that the material characteristics of the crystal are frequency-dependent; therefore, varying ω, it is possible to satisfy conditions Eq. (23). Indeed, at the frequencies close to resonance (in the vicinity of the poles of the complex permittivity tensor), the components of tensor $\hat{B}$ Eq. (8) can be represented as [7]

$$B_j = \frac{(\omega - \omega_j)/\omega_j + i\delta_j}{-A_j} \quad (j = 1, 3). \quad (27)$$

For low dielectric anisotropy, the resonance frequencies ω_1 and ω_3 and the coefficients A_1 and A_3 are considered to be close to one another. In Eq. (27), the absorption parameters δ_j are assumed to be small, with both δ_j and A_j being frequency-independent.

For simplicity, we also assume that the parameters in Eq. (27) satisfy the following inequalities:

$$0 < \delta_1 - \delta_3 \ll (\omega_3 - \omega_1)/\omega_1 \ll 1, \quad \omega \longrightarrow \omega_1. \quad (28)$$

In this case, the cones exist only in a very narrow

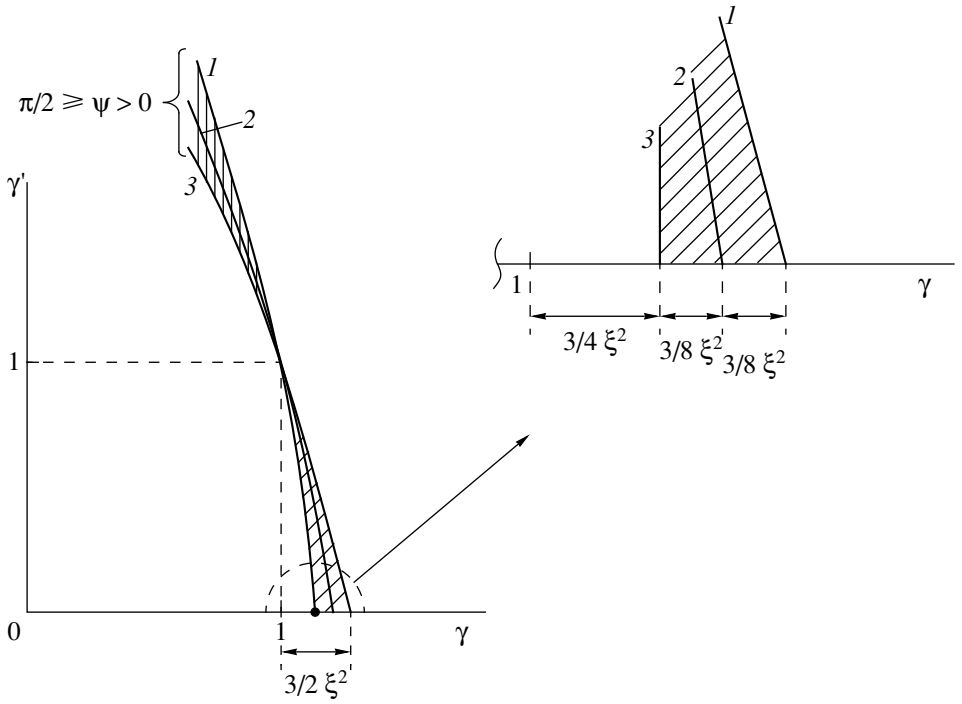

Fig. 2. The existence region of cones of zero birefringence (*1*) $\psi \longrightarrow 0$, $\gamma = \gamma_{max}$; (*2*) $\psi = \pi/4$, $\gamma = \gamma_0$, and (*3*) $\psi = \pi/2$, $\gamma = \gamma_{min}$.

frequency range (Fig. 3):

$$\tilde{\omega} < \omega \le \tilde{\tilde{\omega}}, \tag{29}$$

where

$$\tilde{\omega} = \omega_1 - \frac{3(\delta_1 - \delta_3)\delta_1\omega_1^2}{2(\omega_3 - \omega_1)A_1}, \tag{30}$$

$$\tilde{\tilde{\omega}} = \tilde{\omega} + \frac{3(\delta_1 - \delta_3)^2\omega_1^2}{4(\omega_3 - \omega_1)A_1} < \omega_1. \tag{31}$$

Thus, despite the severe condition (23), the existence of the cones of zero birefringence is not limited to "exotic crystals" alone, which have very specific parameters. These cones can exist in the vicinity of the resonance frequency of the dielectric-constant tensor in various media.

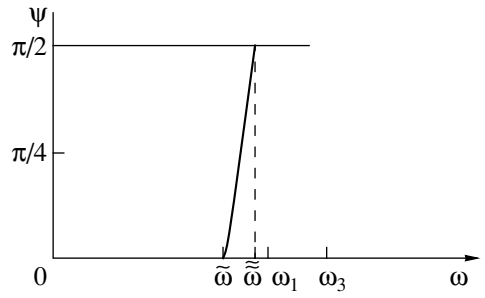

Fig. 3. Angle ψ as a function of frequency ω in the vicinity of the resonance frequencies ω_1 and ω_3.

CONES OF EQUAL ABSORPTION COEFFICIENTS

Equating Eqs. (9) and (10) for n_o' and n_e', respectively, we arrive at the expressions describing the cones of equal absorption of isonormal waves. Upon singling out the root $\theta = 0$, this equation can be represented in the form

$$\begin{aligned}&[\gamma^3 - (\gamma')^2]\tan^4\theta \\ &+ [3\gamma^2 - (\gamma')^2 - \gamma']\tan^2\theta + 3\gamma - 2\gamma' - 1 = 0,\end{aligned} \tag{32}$$

which is a square equation with an unknown $\tan^2\theta$, whereas its coefficients are the functions of two material characteristics, γ and γ', of the crystals. Unlike the previous case, the value of γ should not be close to unity.

The solution of Eq. (32) has the form

$$\theta \equiv \tilde{\psi} = \arctan\sqrt{\frac{-3\gamma^2 + (\gamma')^2 + 2\gamma' + \rho}{2[\gamma^3 - (\gamma')^2]}}, \tag{33}$$

where

$$\rho = \sqrt{(\gamma - \gamma')^3(4 - 3\gamma - \gamma')}. \tag{34}$$

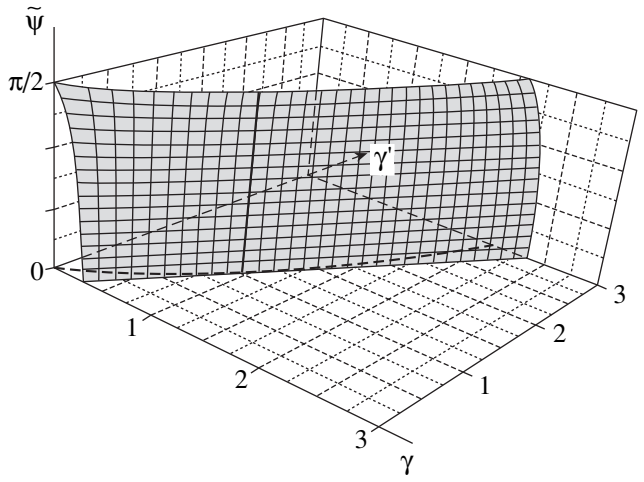

Fig. 4. The surface $\tilde{\psi}(\gamma, \gamma')$.

The cones of equal absorption of isonormal waves exist in the two-dimensional region of the variation of the γ and γ' parameters (Figs. 4, 5). One can see that, similar to the previous case of the cones of equal velocities, this region is described by inequalities (23), where the interval limits, γ_{max} and γ_{min}, are substituted by the functions

$$\tilde{\gamma}_{max} = (2\gamma' + 1)/3, \quad \tilde{\gamma}_{min} = \sqrt[3]{(\gamma')^2}, \qquad (35)$$

respectively.

Similar to the previous case, the angle $\tilde{\psi}$ attains its minimum and maximum values at the boundaries of the existence region; expressions (23) and (24) become valid upon the following substitutions: $\psi \longrightarrow \tilde{\psi}$, $\gamma_{max} \longrightarrow \tilde{\gamma}_{max}$, and $\gamma_{min} \longrightarrow \tilde{\gamma}_{min}$. In the middle of the existence range (Fig. 5, *2*), we have

$$\tilde{\gamma}_0 = \sqrt[3]{2(\gamma' + 1)^2} - 1, \quad \tilde{\psi} = \pi/4. \qquad (36)$$

For angles $\tilde{\psi}$ satisfying Eq. (33), the absorption coefficients for the ordinary and the extraordinary waves are described by Eq. (9). The refractive indices of these waves are described by Eqs. (7) and (8).

It is seen from the results obtained (Figs. 4–6) that the existence range in the vicinity of the isotropy point ($\gamma = \gamma' = 1$) is very narrow. Thus, if $\gamma' = 1.1$, the boundaries of the variation range of the parameter γ are set by the values

$$\tilde{\gamma}_{max} \approx 1.0666, \ \tilde{\gamma}_{min} \approx 1.0656, \ \tilde{\gamma}_{max} - \tilde{\gamma}_{min} \approx 0.0010.$$

With a further increase in the distance from the isotropy point, this interval increases, and, at $\gamma' = 2$, we obtain

$$\tilde{\gamma}_{max} \approx 1.67, \quad \tilde{\gamma}_{min} \approx 1.59, \quad \tilde{\gamma}_{max} - \tilde{\gamma}_{min} \approx 0.08.$$

However, even if the anisotropy is not too strongly pronounced (the existence region of the equal-absorption cones is rather narrow), it is possible to "enter" this region because of the frequency dispersion of the dielectric constant. Thus, in the vicinity of the close resonance frequencies ω_1 and ω_3 [see Eq. (27)], a narrow frequency range can arise in which the angle $\tilde{\psi}$ can vary over the whole range of its values: $0 < \tilde{\psi} \leq \pi/2$.

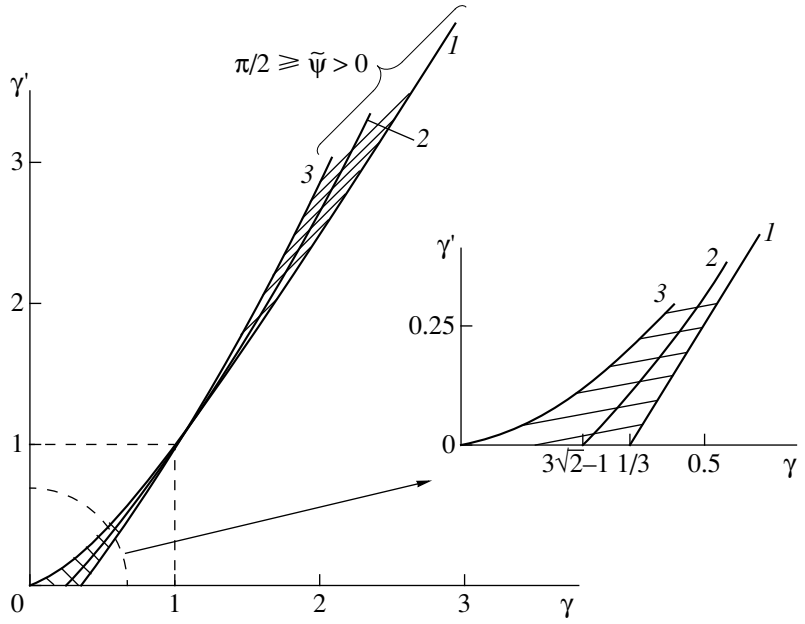

Fig. 5. The existence region of cones of equal absorption coefficients. (*1*) $\tilde{\psi} \longrightarrow 0$, $\gamma = \tilde{\gamma}_{max}$; (*2*) $\tilde{\psi} = \pi/4$, $\gamma = \tilde{\gamma}_0$; (*3*) $\tilde{\psi} = \pi/2$, $\gamma = \tilde{\gamma}_{min}$.

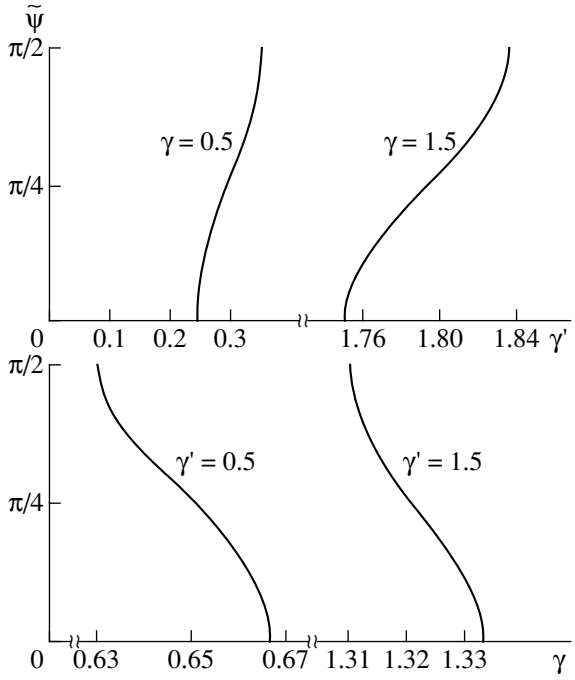

Fig. 6. The sections of the surface $\tilde{\psi}(\gamma, \gamma')$ by the planes γ = const and γ' = const.

This situation is analogous to that considered for the cones of equal velocities (Fig. 3).

RESULTS AND DISCUSSION

Traditionally, the transparent nonabsorptive optically uniaxial crystals are divided into two groups—positive and negative—depending on the mutual location of the sheets in the two-sheet surface of the refractive indices $n_{o,e}(\mathbf{m})$ [2, 3]. This terminology uniquely determines the sign of the birefringence in these crystals. If the sheet $n_o(\mathbf{m})$ is located inside the sheet $n_e(\mathbf{m})$, then the crystal is optically positive; if the sheet $n_o(\mathbf{m})$ is located outside the sheet $n_e(\mathbf{m})$, the crystal is optically negative. However, if optically uniaxial crystals are absorptive, this classification cannot be regarded as universal anymore because, as we have seen, the sheets can intersect one another (Fig. 1).

The comparison the existence regions of the cones of the equal velocities and cones of the equal absorption coefficients shows that these regions do not overlap (Figs. 2, 5). In other words, in an absorptive optically uniaxial crystal, these two types of cones cannot coexist. In particular, this signifies that no cones of optical axes can exist in the crystals under study. Only a cone of one of the two above types can exist, or no cones exist at all.

It should be indicated that the directions along which the absorption coefficients of two independent sheets coincide can be of practical interest. Indeed, if the waves propagate along an arbitrary direction of the absorptive crystal, then, generally speaking, they are absorbed differently. At a sufficiently large distance from the source, only one wave can "survive," namely, the one which is less absorbed by the crystal. However, if the propagation direction of the wave is chosen in such a way that the waves are absorbed, then the amplitude ratio of these waves is constant during their propagation. This may be important for designing and constructing various optical devices based on the interference of the waves with various polarizations.

ACKNOWLEDGMENTS

The authors are grateful to A.F. Konstantinova for her valuable discussion of the results. Two of us (V. Alshits and V. Lyubimov) are grateful to the University of Technology, Kielce, Poland, and the Russian Foundation for Basic Research, project no. 98-02-16069, for their support.

REFERENCES

1. F. I. Fedorov, *Theory of Gyrotropy* (Nauka i Tekhnika, Minsk, 1976).
2. A. F. Konstantinova, B. N. Grechushnikov, B. V. Bokut', and E. G. Valyashko, *Optical Properties of Crystals* (Nauka i Tekhnika, Minsk, 1995).
3. Yu. I. Sirotin and M. P. Shaskol'skaya, *Fundamentals of Crystal Physics* (Nauka, Moscow, 1975; Mir, Moscow, 1982).
4. A. M. Goncharenko, Kristallografiya **4** (5), 727 (1959) [Sov. Phys. Crystallogr. **4**, 670 (1959)].
5. V. I. Alshits and V. N. Lyubimov, Kristallografiya **45** (5), 731 (2000) [Crystallogr. Rep. **45**, 670 (2000)].
6. A. M. Goncharenko and F. I. Fedorov, Kristallografiya **3** (5), 587 (1958) [Sov. Phys. Crystallogr. **3**, 592 (1958)].
7. V. M. Agranovich and V. L. Ginzburg, *Crystal Optics with Spatial Dispersion and Excitons* (Nauka, Moscow, 1965; Springer-Verlag, New York, 1984, 2nd ed.).

Translated by L. Man

Crystallography Reports, Vol. 45, No. 6, 2000, pp. 991–994. Translated from Kristallografiya, Vol. 45, No. 6, 2000, pp. 1075–1078.

Electromagnetic-Wave Surfaces in Absorptive Uniaxial Crystals. II. Cones of Specific Ordinary Waves and Cones of Extreme Absorption

V. I. Alshits and V. N. Lyubimov

Shubnikov Institute of Crystallography, Russian Academy of Sciences, Leninskiĭ pr. 59, Moscow, 117333 Russia

Received June 30, 1999

Abstract—The conditions are established under which extraordinary electromagnetic waves in absorptive optically uniaxial crystals have a group velocity parallel to the wave normal (which corresponds to the definition of ordinary waves). It is shown that absorption can result in the formation of a circular cone of propagation directions of such specific ordinary waves, which can be formed only in nontransparent crystals. If the directions of wave propagation corresponding to the extreme directions of the refractive-index surface are symmetric (i.e., located along the optical axis or normally to it), absorption can cause the transformation of the refractive-index maximum into the minimum. The circular cones of the directions of wave propagation, for which the absorption coefficients of electromagnetic waves have extreme values, are also studied. *© 2000 MAIK "Nauka/Interperiodica".*

INTRODUCTION

As is well known, both ordinary and extraordinary waves can propagate in transparent optically uniaxial crystals. Ordinary waves can propagate along an arbitrary direction in a crystal and, in accordance with the definition given elsewhere [1], have a group velocity parallel to the wave normal (the propagation direction). This property is also inherent in extraordinary waves, but only if these waves propagate along two symmetric directions (along the optical axis and normally to it). This becomes quite clear if one takes into account that the direction of the group velocity is parallel to the geometric normal to the refractive-index surface [2]. It should also be indicated that the refractive-index surface of ordinary waves is a sphere, whereas that of extraordinary waves, an ellipsoid of rotation.

Below, we show that because of absorption, the group velocity of an extraordinary wave can be parallel to the wave normal also for the nonsymmetric directions of propagation (for the symmetric directions of propagation, this property takes place at any degree of absorption). The establishment of the propagation directions of such "specific ordinary waves" is closely related to the characteristic features of the refractive-index surfaces of absorptive optically uniaxial crystals begun in [3].

In essence, our approach reduces to the consideration of only weakly absorptive crystals, where the electromagnetic fields preserve their wavelike structure within the distances much longer than the wavelength [4, 5].

All the initial relationships necessary for the further consideration can be found in [3].

ORDINARY WAVES CAUSED BY ABSORPTION

Consider the geometric characteristics of refractive-index surfaces of absorptive optically uniaxial crystals (Figs. 1a–1d).

In a nonabsorptive isotropic medium, the tensor of the reciprocal dielectric constant is real; its diagonal components are equal; and the difference $\gamma - 1$, which characterizes the dielectric anisotropy goes to zero. Under such conditions, the refractive-index surface of extraordinary waves $n_e(\mathbf{m})$ degenerates into a sphere. If $\gamma - 1 \neq 0$, this surface is an ellipsoid of rotation and, if this ellipsoid is substantially different from a sphere, the weak absorption cannot qualitatively change its geometry.[1] However, if the difference $\gamma - 1$ is small and the ellipsoid only slightly differs from a sphere, then weak absorption can give rise to the formation of a new extremum on the surface, and the derivative $dn_e/d\theta$ goes to zero at angles $\vartheta = \chi$ satisfying the equation

$$\chi = \arctan\sqrt{\frac{\gamma_{\max} - \gamma}{\gamma - \bar{\gamma}_{\min}}}. \quad (1)$$

Here,

$$\gamma_{\max} = 1 + 3\xi^2(1 - \gamma')/2, \quad (2)$$

$$\bar{\gamma}_{\min} = \gamma_{\min} - 3\xi^2(1 - \gamma')^2/4, \quad (3)$$

$$\gamma_{\min} = \gamma_{\max} - 3\xi^2(1 - \gamma')^2/4. \quad (4)$$

[1] The refractive-index surface of ordinary waves remains a sphere irrespective of the degree of absorption.

1063-7745/00/4506-0991$20.00 © 2000 MAIK "Nauka/Interperiodica"

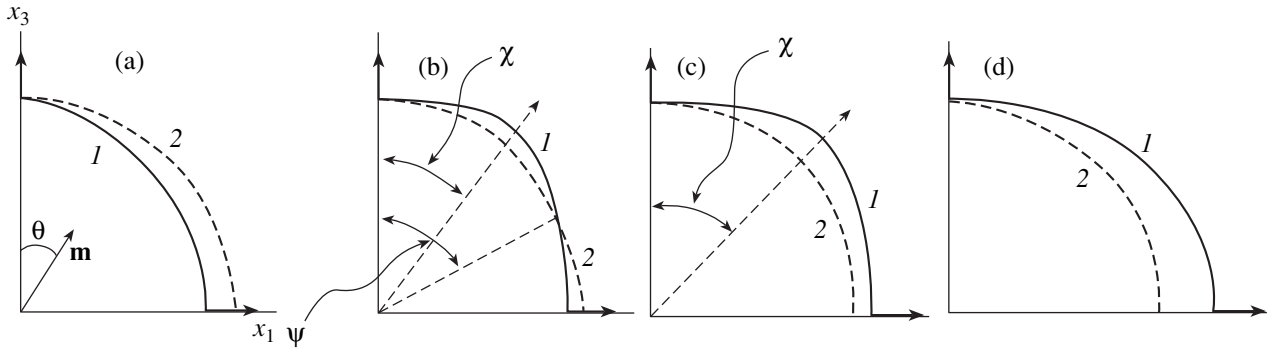

Fig. 1. Refractive-index surfaces for absorptive optically uniaxial crystals at different ratios of the anisotropy parameters: (a) $\gamma \geq \gamma_{max}$, (*1*) n_e, (*2*) n_0; (b) conditions Eq. (6) are met, i.e., the cone of specific ordinary waves and the cone of zero birefringence coexist (here, χ is the angle determining the cone of specific ordinary waves, and angle ψ determines the cone of the zero birefringence). (c) Conditions Eq. (7) are fulfilled (i.e., there exists only the cone of specific ordinary waves); (d) $\gamma \leq \bar{\gamma}_{min}$. Arrows indicate the normals to the refractive-index surface and correspond to specific ordinary waves.

We should like to emphasize that Eq. (1) and the analogous equation determining the cones of zero birefringence are similar [3]. These equations differ only by the substitution $\gamma_{min} \longrightarrow \bar{\gamma}_{min}$. Thus, the upper boundary of the existence of these cones γ_{max} considered here corresponds to the upper limit of the existence of cones of zero birefringence. However, the lower limits are different: $\bar{\gamma}_{min} < \gamma_{min}$ (here, γ_{min} is the lower limit of the region of existence of the cones of zero birefringence [3], whereas $\bar{\gamma}_{min}$ is the lower limit of the existence region of the cones of specific ordinary waves). The region of existence of extrema is somewhat wider (Fig. 2).

One can readily see that the extremum points considered here are the maxima. For angles χ satisfying Eq. (1), we have

$$n_e(\chi) = (n_e)_{max} = n_0 + \frac{(\gamma_{max} - \gamma)^2}{8\sqrt{\beta_1}(\gamma_{max} - \gamma_{min})}. \quad (5)$$

The existence of these extrema and, therefore, the specific ordinary waves due to absorption, correlates with the existence of cones of zero birefringence. Indeed, both exist simultaneously if the following condition is fulfilled (Fig.1b):

$$\gamma_{min} \leq \gamma < \gamma_{max}. \quad (6)$$

At the same time, under the condition

$$\bar{\gamma}_{min} < \gamma < \gamma_{min}, \quad (7)$$

only specific ordinary waves can exist (Fig. 1c). Outside ranges (6) and (7), neither specific ordinary waves nor the cones of zero birefringence can exist (Figs. 1a, 1d).

The cones studied here can exist solely due to dielectric anisotropy. In the transition to an isotropic absorbing medium, where $\gamma = \gamma' = 1$ and $\gamma_{max} = \bar{\gamma}_{min} = 1$, the region of existence of these cones disappears.

Now consider the symmetric extrema of the function $n_e(\vartheta)$ at $\vartheta = 0$ ($n_e(\vartheta = 0) \equiv n_0$) and at $\vartheta = \pi/2$ ($n_e(\vartheta = \pi/2) \equiv \bar{n}_e$) located on the surface $n_e(\mathbf{m})$. One can easily see that at $\gamma \geq \gamma_{max}$, the value of n_0 corresponds to the maximum, whereas the value of $\bar{n}_e$, to the minimum (Fig. 1a). On the other hand, at $\gamma \leq \bar{\gamma}_{min}$, the situation is reversed; i.e., n_0 corresponds to the minimum and $\bar{n}_e$ to the maximum (Fig. 1d). If the surface $n_e(\mathbf{m})$ has a nonsymmetrically located maximum [i.e., conditions Eqs. (6) or (7) are fulfilled], both n_0 and $\bar{n}_e$ necessarily correspond to the minima (Figs. 1b, 1c). It should also be indicated that, in transparent optically uniaxial crystals, the extrema of n_0 and $\bar{n}_e$ have opposite signs, whence it follows that absorption can give rise to the change of the extremum sign; i.e., it can transform the maximum into the minimum.

EXTREMA OF THE $n'_e(\mathbf{m})$ SURFACE

In this case, no special constraints are imposed on the parameter γ. In addition to the extrema corresponding to the wave propagation along the optical axis and normally to it, the function $n'_e(\vartheta)$ can also have an extremum at an angle $\vartheta = \tilde{\chi}$ satisfying the following equation:

$$\tilde{\chi} = \operatorname{arccot}\sqrt{\frac{\tilde{\gamma}_{max} - \gamma}{\gamma - \bar{\tilde{\gamma}}_{min}}\left(\frac{3}{\gamma' + 2}\right)}, \quad (8)$$

where

$$\tilde{\gamma}_{max} = (2\gamma' + 1)/3, \quad (9)$$

$$\bar{\tilde{\gamma}}_{min} = 3\gamma'/(\gamma' + 2). \quad (10)$$

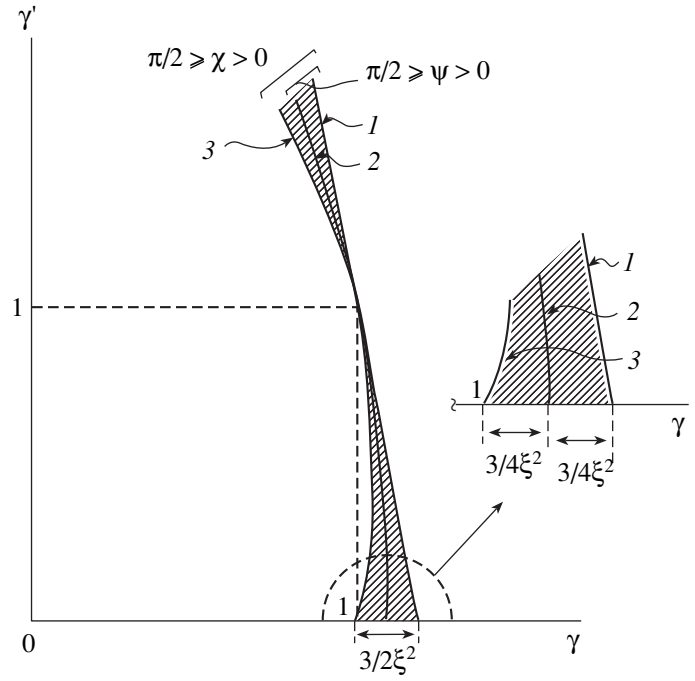

Fig. 2. Existence region of cones of specific ordinary waves (with the opening angle 2χ and cones of zero birefringence (with the opening angle 2ψ). (*1*) $\chi, \psi \longrightarrow 0$ ($\gamma = \gamma_{max}$), (*2*) $\psi = \pi/2$ ($\gamma = \gamma_{min}$), (*3*) $\chi = \pi/2$ ($\bar{\gamma} = \gamma_{min}$).

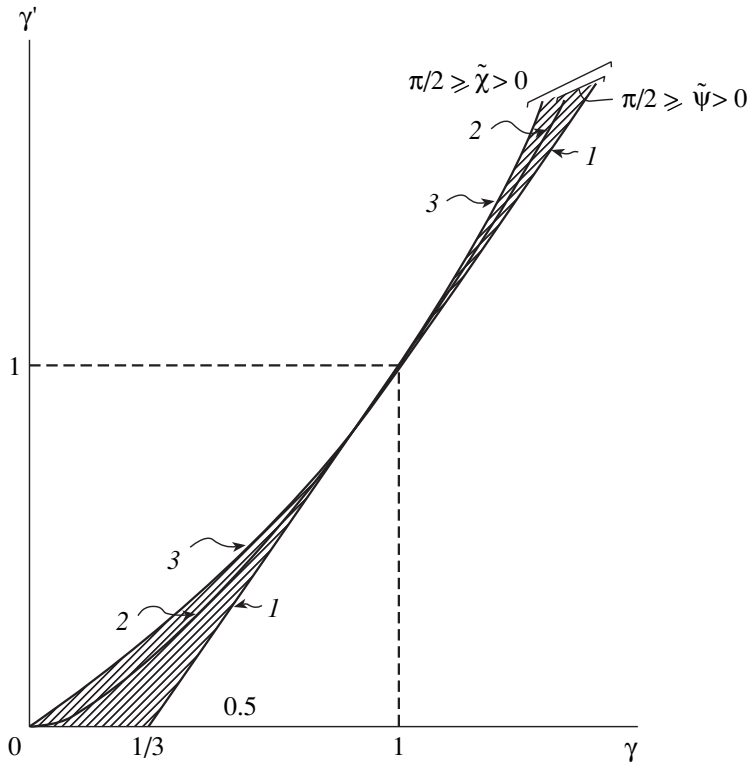

Fig. 3. Existence region of cones of extreme absorption (with the opening angle $2\tilde{\chi}$) and cones of equal absorption coefficients (with the opening angle $2\tilde{\psi}$): (*1*) $\tilde{\chi}, \tilde{\psi} \longrightarrow 0$ ($\gamma = \tilde{\gamma}_{max}$), (*2*) $\tilde{\psi} = \pi/2$ ($\gamma = \tilde{\gamma}_{min}$), (*3*) $\tilde{\chi} = \pi/2$ ($\gamma = \bar{\tilde{\gamma}}_{min}$).

The absorption coefficient for this extremum (the maximum) is determined by the formula

$$n'_e(\tilde{\chi}) = (n'_e)_{\max} = n'_0 \frac{2}{3\sqrt{3}} \sqrt{\frac{(\gamma' - 1)^3}{(\gamma - 1)^2(\gamma' - \gamma)}}. \quad (11)$$

The existence of extrema (8) correlates with the existence of the cones of equal absorption of isonormal waves [3]. This correlation can be described by inequalities (6) and (7) upon the substitutions $\gamma_{\max} \longrightarrow \tilde{\gamma}_{\max}$, $\gamma_{\min} \longrightarrow \tilde{\gamma}_{\min}$, and $\bar{\gamma}_{\min} \longrightarrow \bar{\tilde{\gamma}}_{\min}$. Then, conditions (6) describe the region in which the cones of the extreme absorption and the cones of equal absorption coefficients coexist, whereas conditions (7) describe the region in which only the cones of extreme absorption exist (Fig. 3). The upper limit $\tilde{\gamma}_{\max}$ of the existence region of extrema (8) coincides with the upper limit of the existence region of cones of equal absorption coefficients. However, the lower limits are different: the region of existence of extrema (8) is wider, because

$$\bar{\tilde{\gamma}}_{\min} \le \tilde{\gamma}_{\min} \equiv \sqrt[3]{(\gamma')^2}. \quad (12)$$

Here, $\tilde{\gamma}_{\min}$ is the lower limit of the existence region of cones of equal absorption coefficients [3], whereas $\bar{\tilde{\gamma}}_{\min}$ is the lower limit of the existence region of the cones of extreme absorption. These maxima of absorption coefficients exist solely because of dielectric anisotropy; in the transition to an absorptive isotropic medium, where $\tilde{\gamma}_{\max} = \bar{\tilde{\gamma}}_{\min} = 1$, the region of existence of these maxima disappears.

Qualitatively, the geometry of the surface $n'_e(\mathbf{m})$ is analogous to the geometry of the surface $n_e(\mathbf{m})$ described above (Figs. 1a–1d).

CONCLUSIONS

The comparison of the existence regions of the cones of specific ordinary waves and the cones of the extreme absorption shows that the regions of their existence do not overlap (Figs. 2, 3). A similar situation also takes place for the cones of zero birefringence and cones of equal absorption coefficients [3].

Under certain conditions, the cones considered above can exist in the vicinity of the resonance frequencies of the permittivity tensor of the crystal [3].

All the phenomena discussed are caused by the crystal anisotropy and disappear at the anisotropy parameter tending to zero.

Thus, we managed to establish the characteristic features of the effect of absorption on the optical properties of uniaxial crystals. It is shown that the absorption effect is not reduced to a mere decrease of electromagnetic-wave intensities during their propagation in the crystal. It can lead to qualitatively new phenomena not taking place in transparent crystals.

ACKNOWLEDGMENTS

The authors are grateful to A.F. Konstantinova for useful discussions. The study was supported by the Russian Foundation for Basic Research, project no. 98-02-16069.

REFERENCES

1. Yu. I. Sirotin and M. P. Shaskol'skaya, *Fundamentals of Crystal Physics* (Nauka, Moscow, 1979; Mir, Moscow, 1982).
2. F. I. Fedorov, *Optics of Anisotropic Media* (Akad. Nauk BSSR, Minsk, 1958).
3. V. I. Alshits, V. N. Lyubimov, W. Gierulski, and A. Radowicz, Kristallografiya **45** (6), 1068 (2000) [Crystallogr. Rep. **45**, 985 (2000)].
4. A. M. Goncharenko and F. I. Fedorov, Kristallografiya **3** (5), 587 (1958) [Sov. Phys. Crystallogr. **3**, 592 (1958)].
5. A. M. Goncharenko, Kristallografiya **4** (5), 727 (1959) [Sov. Phys. Crystallogr. **4**, 688 (1959)].

Translated by L. Man

Crystallography Reports, Vol. 45, No. 6, 2000, pp. 995–1000. Translated from Kristallografiya, Vol. 45, No. 6, 2000, pp. 1079–1084.

PHYSICAL PROPERTIES OF CRYSTALS

Diffraction of Light from Stripe Domain Structure with Inclined Domain Boundaries

D. I. Sementsov and I. F. Gismyatov

Ul'yanovsk State University, Ul'yanovsk, Russia

Received January 25, 1999; in final form, April 2, 1999

Abstract—It is shown that a stripe domain structure with inclined domain boundaries provides the characteristic trapezoidal distribution of the Faraday component of magnetization responsible for the magnetooptical diffraction. The distribution of the light field diffracted from the domain structure is obtained, and the dependences of the intensity and polarization characteristics of this field on the structure parameters are determined. © *2000 MAIK "Nauka/Interperiodica".*

INTRODUCTION

The theoretical aspects of magnetooptical diffraction from domain structures of single crystal ferrite garnets films and thin plates of rare-earth orthoferrites have been considered in numerous studied [1–7]. Most of the theoretical studies of magnetooptical diffraction were performed in the approximation of the binary distribution of magnetization in the magnetic lattice. In real stripe domain structures, the thickness of domain walls is much less than the width of the stripe domains, which justifies the use of the above approximation for describing magnetooptical diffraction from domain structures with vertical domain boundaries. However, the binary distribution of magnetization cannot explain some anomalies of the magnetooptic diffraction observed in the experiments with the films characterized by inclined domain boundaries [8, 9]. This is associated, first and foremost, with the fact that the real distribution of the Faraday component of magnetization responsible for light diffraction from stripe domain structures with inclined domain boundaries is more complicated than a binary distribution.

Domain boundaries in garnet films are vertical only if one of the crystallographic planes, e.g., (111), coincides with the film plane. However, the technology of film treatment is such that the plane normal to the film always slightly deviates from the exact crystallographic direction [10]. The deviation of the easy-magnetization plane and the domain boundary from the surface normal can exceed the corresponding deviation of the [111] axis.

The general form of a stripe domain structure with inclined domain boundaries is shown in Fig. 1a. For typical Bi-containing ferrite-garnet films, the exchange constant is $A \approx 3 \times 10^{-7}$ erg/cm, the constant of uniaxial anisotropy is $K \approx 5 \times 10^4$ erg/cm^3, and the saturation magnetization is $4\pi M_0 \approx 10^3$ G. The thickness of domain walls equals $\Delta \cong \pi\sqrt{A/K} \approx 0.1$ μm, and the domain width equals $S \cong (2\pi L\sqrt{AK}/M_0^2)^{1/2} \approx 5$ μm (at the film thickness $L \approx 10$ μm). Since $\Delta \ll S$, the transition over the domain boundary results in the stepwise spin rotation by an angle of 180°.

The distribution of the Faraday magnetization component along the direction of light propagation in stripe domain structure and, therefore, the effective magnetooptic parameter $Q(y)$ are proportional to this magnetization component and are essentially dependent on the inclination angle β of domain boundaries. Thus, under the normal light incidence onto the specimen (Fig. 1a), the magnetooptical parameter distribution is of the trapezoidal type if the width of the transition region $\delta = L\tan\beta < S$. If $\delta = S$, the trapezoidal distribution acquires a sawtooth shape (Fig. 1c). If $\delta > S$, the $Q(y)$ distribution changes into trapezoidal again, with the maximum value of the effective magnetooptic parameter $Q_0' = Q_0(1 - 2\Delta/\delta)$, half-period $S' = \delta - \Delta$, and the width of the transitions region $\delta' = \delta - 2\Delta$ (Fig. 1d). Below, we describe our study of the effect of domain-boundary inclination on the intensity and polarization characteristics of the light field diffracted from the magnetic-domain lattices with the above types of the magnetization distribution and the effective magnetooptical parameter.

BASIC RELATIONSHIPS

Let a laser beam be normally incident onto a single crystal layer with a stripe domain structure and inclined domain boundaries. In this case, M_z is the component of the magnetization vector **M** in the film, which is distributed in the film according to the trapezoidal law along the 0*Y*-axis. In the approximation of thin layers ($L \ll D^2/\lambda$, where D is the period of the domain structure and λ is the wavelength of the light wave), the distribution

1063-7745/00/4506-0995$20.00

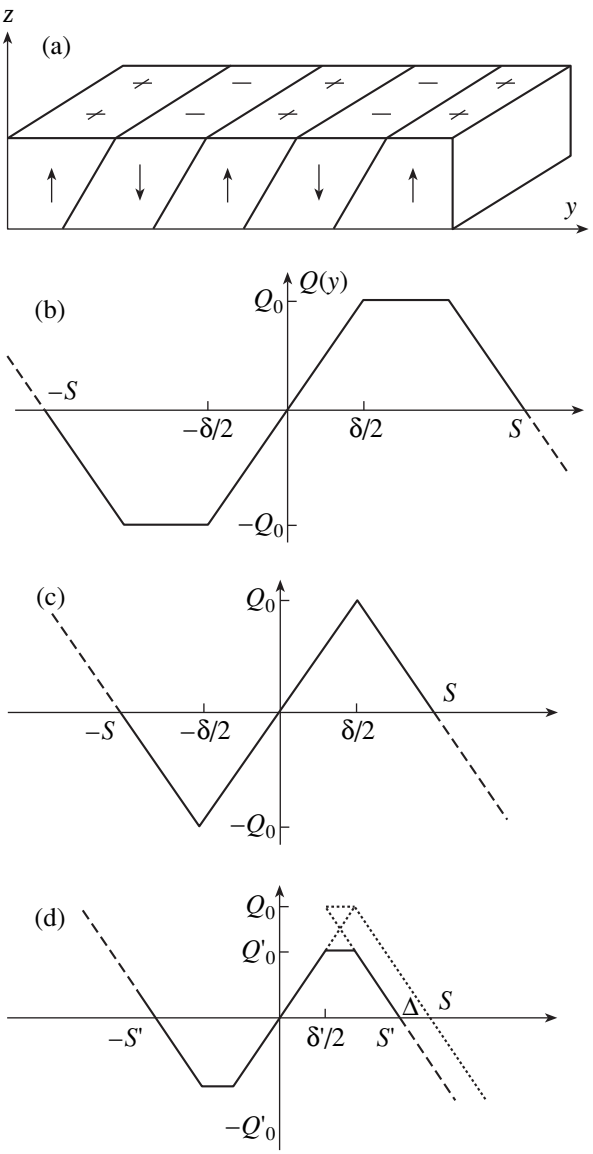

Fig. 1. (a) Stripe domain structure with inclined boundaries and (b–d) various types of the distribution of the effective magnetooptic parameter.

of the light transmitted by the layer in the far zone is determined as

$$\mathbf{E}(y_0, z) = C\int \mathbf{E}(y, L)\exp(-2\pi i f y)dy, \qquad (1)$$

where the factor $C = (1/\sqrt{\lambda z})\exp[ik_0(z + y_0^2/2z)]$, $k_0 = 2\pi/\lambda$, $f = y_0/\lambda z$, y_0 is the coordinate in the plane of the diffraction pattern (i.e., on the screen), and y is the current coordinate of the exit surface of the film. The integration limits in Eq. (1) are determined by the area of the illuminated region equal to $a = (2N + 1)D$, where N is a large integer ($N \approx 50$ at the laser-beam diameter $a \approx 1$ mm and $D \approx 10$ μm). If the light propagates in the longitudinal direction in the medium (**k** || **M**, where **k** is the wave vector of the light wave), the eigenwaves of the system are circularly polarized waves and the field in the medium is described by the expression

$$E^{\pm} = E_0^{\pm}\exp[ik_{\pm}(y)z],\ k_{\pm}(y) = k(1 \mp Q(y)/2). \quad (2)$$

Here, $E_0^{\pm}$ is the field at the entrance surface of the film and the wave number is $k = k_0\sqrt{\varepsilon}$, where ε is the dielectric constant of the medium (in the general case, it is a complex quantity, whose imaginary part determines light attenuation in the film). The dependence of the magnetooptical parameter on the coordinate y is determined in accordance with the trapezoidal law (Fig. 1b) with the widths of the oppositely magnetized domains being different:

$$Q(y) = \begin{cases} 2Q_0(S_1 - y)/\delta, & S_1 - \delta/2 \le y \le S_1 \\ Q_0, & \delta/2 \le y \le S_1 - \delta/2 \\ 2Q_0 y/\delta, & -\delta/2 \le y \le \delta/2 \\ -Q_0, & -S_2 + \delta/2 \le y \le -\delta/2 \\ -2Q_0(y + S_2)/\delta, & -S_2 \le y \le -S_2 + \delta/2, \end{cases} \qquad (3)$$

where $S_1 + S_2 = D$. With due regard for Eq. (2), the field at the exit surface of the film is determined as

$$E^{\pm}(y) = E_0^{\pm}\exp(ikL)\exp[\mp ikLQ(y)/2]. \qquad (4)$$

Substituting the above expression into Eq. (1) and integrating the result, we arrive at the distribution of the circular components of the diffracted field in the observation plane:

$$E^{\pm}(y_0) = \frac{i}{2}CE_0^{\pm}\frac{\sin\pi f a}{\sin\pi f D}\exp(ikL)J_{\pm}, \qquad (5)$$

where $J_{\pm}$ is the sum of five integrals corresponding to the domains of setting the function $Q(y)$. Upon calculations, we obtain

$$J_{\pm} = 2i\left(\frac{1}{\pi f} - \frac{\delta}{\alpha_{\pm}}\right)\sin\alpha_{\pm}$$
$$-\frac{\delta}{\alpha_{\mp}}[\exp(2\pi i f S_2) - \exp(-2\pi i f S_1)]$$
$$+\left(\frac{\delta}{\alpha_{\mp}} - \frac{1}{\pi f}\right)\{\exp[i(\alpha_{\pm} + 2\pi f b_2)]$$
$$-\exp[-i(\alpha_{\pm} + 2\pi f b_1)]\}.$$

Here, $b_i = S_i - \delta$, $\alpha_{\pm} = \pi f\delta \pm FL$, and $F = \pi Q_0/\lambda$ is the specific Faraday rotation of the polarization plane. The analysis of Eq. (5) shows that, in the general case, the diffraction maxima of the magnetooptic diffraction spectrum are located at the points $f = n/D$, where $n = 0, \pm1, \pm2, \ldots$, whereas their angular positions and widths are determined by the relationships $\sin\varphi_n = n\lambda/D$ and $\Delta\varphi_n = \lambda/a$, respectively. The further analysis of Eq. (5) is performed for various particular cases of the stripe

domain structure. In the case of linearly polarized incident radiation, the polarization state of the diffracted light field can be most conveniently analyzed not in terms of the circular components $E^{\pm}$ but rather in the Cartesian components $E_x = (E^+ + E^-)/2$ and $E_y = (E^+ - E^-)/2i$. In what follows, it is assumed that the field is $\mathbf{E}_0 = \boldsymbol{\tau}_x E_0$, i.e., that the field is *x*-polarized.

Now determine the field in the zeroth diffraction maximum of the nonsymmetric stripe domain structure with due regard for inclination of domain boundaries. Assuming that $f = 0$ in Eq. (5) and passing to the Cartesian field components, we obtain

$$E^{(0)} = \frac{A}{D} e^{ikL} \left\{ \boldsymbol{\tau}_x \left[\frac{2\delta}{FL} \sin FL + (b_1 + b_2) \cos FL \right] - i\boldsymbol{\tau}_y (b_1 - b_2) \sin FL \right\}, \quad (6)$$

where the constant $A = CE_0 a$. It follows from Eq. (6) that the polarization plane in the zeroth maximum is rotated with respect to the polarization plane of the incident radiation by an angle of

$$\theta_0 = \arctan\left[\frac{(b_2 - b_1)FL}{2\delta + (b_1 + b_2)FL \cot FL} \right]. \quad (7)$$

For rather thin films, the condition $FL \ll 1$ should be fulfilled, and expression (7) is transformed into the relationship

$$\theta_0 = \arctan[(\Delta S/D)FL], \quad (8)$$

whence it follows that, in this case, the contribution of transition regions to the formation of the light-field polarization in the zeroth order of diffraction is unessential. For thick films with considerable specific Faraday rotation, the rotation of the polarization plane in the zeroth maximum should essentially be determined by the width of the transitional region. Thus, for a thick film with $FL \approx \pi/2$, the following relationship should be fulfilled:

$$\theta_0 \cong \arctan[\pi(b_2 - b_1)/4\delta]. \quad (9)$$

For vertical domain boundaries ($\delta = 0$, $b_i = S_i$), the rotation of the polarization plane in the zeroth maximum is determined by the well-known relationship

$$\theta_0 = \arctan[(\Delta S/D)\tan FL], \quad (10)$$

whence it follows that for a symmetric stripe domain structure with both inclined and vertical domain boundaries, $\theta_0 = 0$; in other words, the field in the zeroth diffraction maximum is polarized in the same way as the incident radiation.

Figure 2 shows the rotation angle of the polarization plane of the light field in the zeroth diffraction maximum θ_0 as a function of the asymmetry parameter $\Delta S/D$ of the stripe domain structure (Fig. 2a) for two values of the effective thickness of the film ($FL = \pi/2$ and $\pi/12$) and (Fig. 2b) for the effective thickness at the fixed value of the asymmetry parameter ($\Delta S/D = 0.5$). The above dependences are given for several values of the transition-region widths (curves *1–7*): $\delta/D = 0$, 0.1, …, 0.6. It is seen that for thin films ($FL \ll 1$), the effect of the domain boundary inclination is unessential, whereas in the films with $FL = \pi/2$ and with vertical grain boundaries the angle θ_0 is independent of the domain-structure asymmetry.

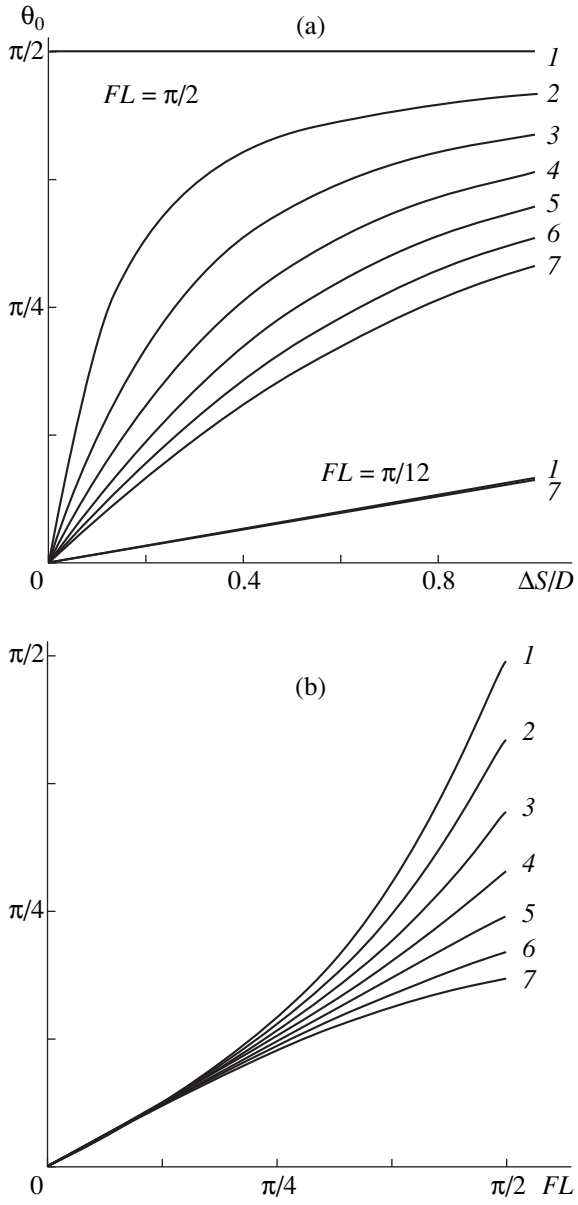

Fig. 2. Dependences of (a) the rotation angle of the polarization plane θ_0 in the zeroth diffraction maximum on the asymmetry parameter $\Delta S/D$ of the stripe domain structure and (b) the effective thickness of the film, *FL*, at $\Delta S/D = 0.5$ (curves *1–7*) for several values of the parameter δ/D: 0, 0.1, …, 0.6 (curves *1–7*).

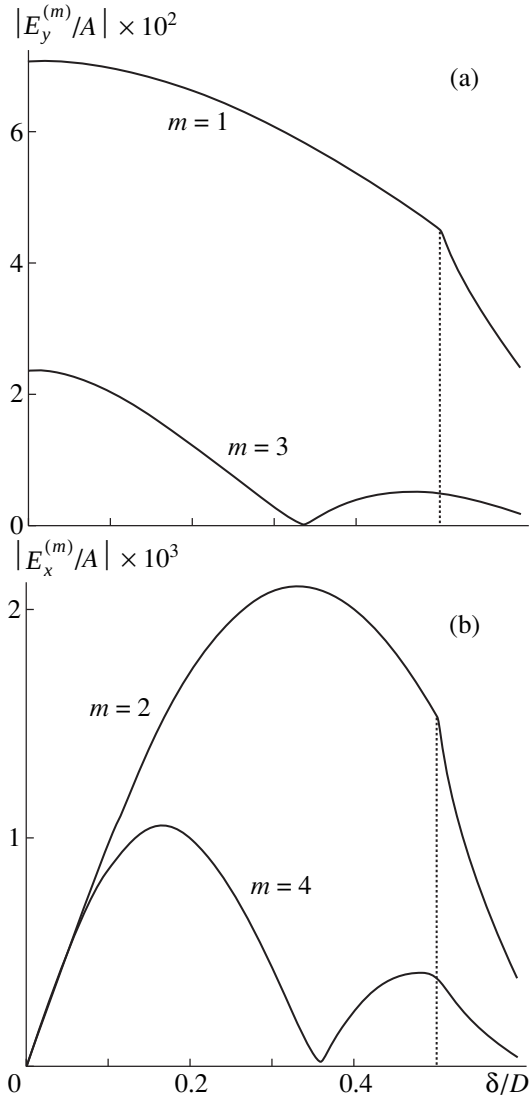

Fig. 3. Dependence of the field amplitude in the first four diffraction maxima on the transition-region width δ/D for the symmetric stripe domain structure.

SPECTRUM OF MAGNETOOPTIC DIFFRACTION FROM SYMMETRIC STRIPE DOMAIN STRUCTURES

The further analysis is performed for a symmetric stripe domain structure ($b_1 = b_2 = b$). In this case, the distribution of the diffracted light field has the form

$$\mathbf{E} = A\exp(ikL)\frac{\sin\pi fa}{a}\left\{\frac{\tau_x}{\sin\pi fS}\left[\cos FL\frac{\sin\pi fb}{\pi f}\right.\right.$$
$$+\frac{\delta}{\alpha_+}\sin\frac{\alpha_+}{2}\cos\frac{\pi fD-\alpha_+}{2}+\frac{\delta}{\alpha_-}\sin\frac{\alpha_-}{2}\cos\frac{\pi fD-\alpha_-}{2}\left.\right] \quad (11)$$
$$+\frac{i\tau_y}{\cos\pi fS}\left[\cos FL\frac{\sin\pi fb}{\pi f}-\frac{\delta}{\alpha_+}\sin\frac{\alpha_+}{2}\sin\frac{\pi fD-\alpha_+}{2}\right.$$
$$\left.\left.+\frac{\delta}{\alpha_-}\sin\frac{\alpha_-}{2}\sin\frac{\pi fD-\alpha_-}{2}\right]\right\}.$$

One can readily determine the changes in the diffraction spectrum caused by inclination of the domain boundaries. Unlike a symmetric stripe domain structure with vertical domain walls, the diffraction spectrum from the stripe domain structure with inclined domain boundaries has, along with the odd maxima of the *y*-polarization ($fD = 2n - 1$), the even maxima ($fD = 2n$) with the *x*-polarization:

$$E_x^{(2n)} = Ae^{ikL}\frac{\delta}{D}\left(\frac{\sin\alpha_-}{\alpha_-}+\frac{\sin\alpha_+}{\alpha_+}\right.$$
$$\left.-\frac{D}{\pi n\delta}\cos FL\sin\frac{2\pi n\delta}{D}\right),$$
$$E_y^{(2n-1)} = iAe^{ikL}\frac{\delta}{D}\left(\frac{\sin\alpha_-}{\alpha_-}-\frac{\sin\alpha_+}{\alpha_+}\right. \quad (12)$$
$$\left.+\frac{D}{\pi(n-1/2)\delta}\sin FL\cos\frac{(2n-1)\pi\delta}{D}\right).$$

As was to be expected [5], at $\delta = 0$, the diffraction spectrum has only odd orders of diffraction with the *y*-polarization:

$$E_x^{(2n)} = 0,\ E_y^{(2n-1)} = \frac{iA}{\pi(n-1/2)}\sin FL\exp(ikL). \quad (13)$$

Consider the particular case of a stripe domain structure with the sawtooth distribution of the M_z-component. In this case, $\delta = D/2$ and the magnetooptic diffraction spectrum is provided by the transitional regions with the linear law of the distribution of the effective magnetooptic parameter $Q(y)$:

$$E_x^{(2n)} = (-1)^{n+1}A\frac{FL\sin FL}{(\pi n)^2-(FL)^2}\exp(ikL),$$
$$E_y^{(2n-1)} = (-1)^{n+1}iA\frac{FL\cos FL}{\pi^2(n-1/2)^2-(FL)^2}\exp(ikL). \quad (14)$$

Figures 3a and 3b show the dependences of the field amplitudes in the first two odd and the first two even diffraction maxima on the width δ/D of the transition region for the film with the symmetric stripe domain structure of the thickness $L = 8$ μm and the parameters $F = 1$ °/μm and $\alpha = 500$ cm^{-1}. It is seen that the field amplitude is maximal in the even orders at $\delta \neq 0$, whereas in the odd orders, the film amplitude is maximal only in the case of the vertical domain boundaries. The formation of a kink at $\delta/D = 0.5$ is characteristic of the above dependences and is associated with a decrease of the maximum magnetooptic parameter observed with a further increase of the angle of domain-boundary inclination.

Figure 4 shows the field amplitude in the first two diffraction orders as a function of the effective film thickness for various values of the δ/D parameter. In the first order of diffraction, the $E_y^{(1)}$ field (which was polarized orthogonally with respect to the polarization of the incident wave, Fig. 4a) has the maximum value of the parameter $\delta \le D/2$ at the film thicknesses

$$L_m^{(1)} \cong F^{-1}\arctan(2F/\alpha). \quad (15)$$

At $\delta > D/2$, the maximum of the diffracted field shifts to the lower thickness values determined by the expression

$$L_m^{(1)} \cong \frac{\delta}{F(D-\delta)}\arctan\left[\frac{2F}{\alpha}\left(\frac{D}{\delta}-1\right)\right]. \quad (16)$$

The maxima of the diffracted field with the incident-wave polarization $E_x^{(2)}$ (Fig. 4b) correspond to the thickness $L_m^{(2)}$, which is the first positive root of the equation

$$1 + x\cot x - \frac{\alpha}{2F}x = 0, \quad (17)$$

where $x = FL$. The above dependences show that $L_m^{(2)} > L_m^{(1)}$ and the maximum amplitudes attained in the indicated orders of diffraction are essentially dependent on the width δ of the transition region, i.e., the inclination angle of domain boundaries.

ADDITIONAL ORDERS OF MAGNETOOPTIC DIFFRACTION

Along with the maxima of even and odd diffraction orders, the spectra of magnetooptic diffraction have two symmetric maxima formed due to diffraction from the transitional regions characterized by the linear distribution law $Q(y)$ not observed in the spectra from stripe domain structure with vertical domain walls. These maxima are located at the points $\pi f = \pm\gamma$, where $\gamma = FL/\delta$. The angular positions of these maxima are set by the angles $\varphi_\delta = \pm\lambda FL/\pi\delta$. The corresponding field components are determined as follows:

$$E_x^{(\delta)} = \frac{A}{2a\gamma}\exp(ikL) \times \frac{\sin\gamma a}{\sin\gamma S}(\gamma\delta\cos\gamma S + \cos\gamma\delta\sin\gamma b + \sin\gamma S), \quad (18)$$

$$E_y^{(\delta)} = \pm\frac{iA}{2a\gamma}\exp(ikL)\frac{\sin\gamma a}{\cos\gamma S}(\gamma\delta\sin\gamma S + \sin\gamma\delta\sin\gamma b).$$

In the case of a sawtooth pattern from the stripe domain structure ($S = \delta$), we have

$$E_x^{(\delta)} = \frac{AS}{2aFL}\exp(ikL) \times \sin(FLa/S)(FL\cot FL + 1), \quad (19)$$

$$E_y^{(\delta)} = \pm\frac{iAS}{2a}\exp(ikL)\sin(FLa/S)\tan FL,$$

whence it follows that at $FL \ll 1$, the field in the diffraction maxima of the orders under study is polarized almost along the x-axis and $E_y^\delta/E_x^\delta = \pm iF^2L^2/2$. Comparing the field amplitudes in the indicated additional

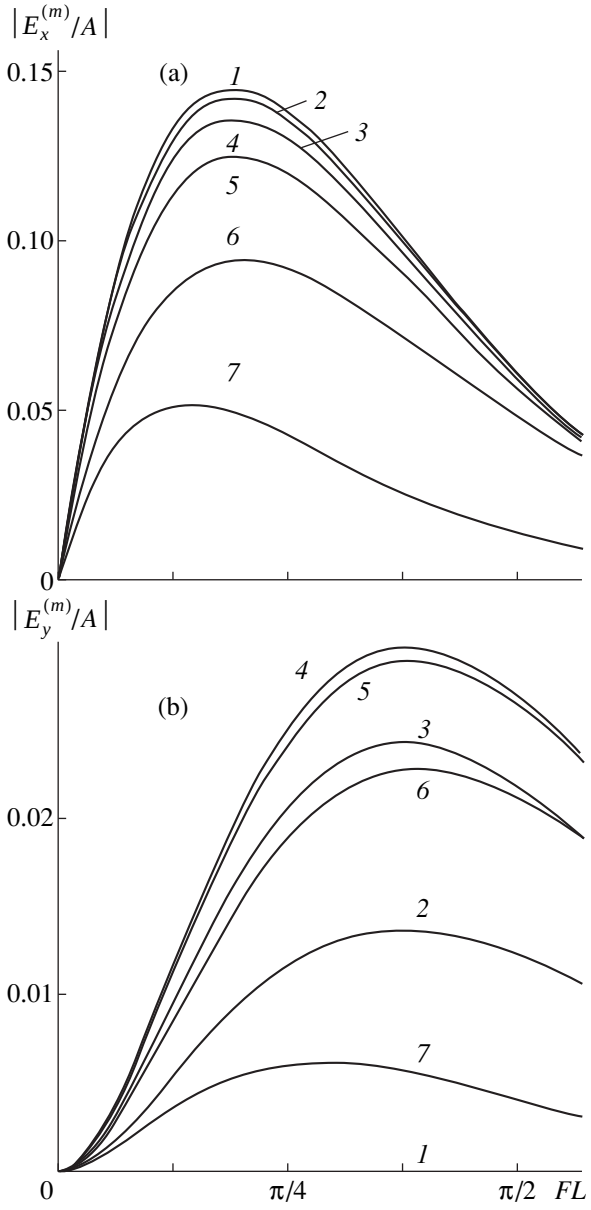

Fig. 4. Dependence of the field amplitude in (a) the first and (b) the second diffraction maxima on the effective thickness of the film for various values [curves (*1–7*)] of the parameter δ/D = 0, 0.1, …, 0.6.

and main (plus and minus first) orders of diffraction show that, for the films with $FL \ll 1$ and $a/S \gg 1$, we have

$$\left|\frac{E_y^{\pm 1}}{E_x^{\delta}}\right| \cong \frac{2aF^2L^2}{\pi S} \gg 1. \quad (20)$$

The distinguishing feature of these additional diffraction orders is the dependence of the orientation of the polarization plane of the field in the diffraction maximum $\theta_\delta = \arctan\left|E_y^\delta/E_x^\delta\right|$ on the width δ of the transition region. For the film with the parameters $F \cong 1\ °/\mu m$, $L \cong 8$, $D \cong 8$, $\delta \cong 2\ \mu m$, and the light wavelength $\lambda = 0.63\ \mu m$, the angular position of the above orders of diffraction is set by the angles $\varphi^{(1)} \cong 4.5°$ and $\varphi^{(\delta)} \cong 1°$.

MAGNETOOPTIC DIFFRACTION SPECTRUM FROM AN ISOLATED DOMAIN BOUNDARY

Consider the diffraction spectrum formed by a laser beam focused on the inclined domain boundary and transmitted by the transition region with the linear dependence $Q(y)$. Assuming that the beam width equals the width δ of the transition region, we obtain from Eq. (11)

$$E_x \propto \delta\left(\frac{\sin\alpha_+}{\alpha_+} + \frac{\sin\alpha_-}{\alpha_-}\right),$$
$$E_y \propto \pm i\delta\left(\frac{\sin\alpha_+}{\alpha_+} - \frac{\sin\alpha_-}{\alpha_-}\right), \quad (21)$$

where the upper and the lower signs in the expression for the component E_y relate to the regions with a decreasing and an increasing dependences $Q(y)$, respectively. For the regions of both types, the spectrum of magnetooptic diffraction should have the zeroth maximum ($f = 0$) and two side maxima ($f = \pm FL/\pi\delta$). In this case, the field in the zeroth and side maxima in the region with the decreasing dependence $Q(y)$ has the form

$$E_x^{(0)} \propto 2\delta\frac{\sin FL}{FL}, \quad E_y^{(0)} = 0,$$
$$E_x^{(\pm\delta)} \propto \delta\left(1 + \frac{\sin 2FL}{2FL}\right), \quad E_y^{(\pm\delta)} \propto \pm i\delta\left(1 - \frac{\sin 2FL}{2FL}\right). \quad (22)$$

With the change of the increasing type of the transition region to a decreasing one, the signs before $E_y^{(\pm\delta)}$ change to the opposite ones; i.e., the light field in these two cases is polarized in different ways. The angular position of the diffraction orders of the side reflections for the film with the above parameters is determined by the angle $\varphi_\delta \approx 1°$.

The above analysis of the specific features of magnetooptic diffraction can be performed in more detail by changing the trapezoidal distribution of the magnetooptic parameter by another, more adequate (to the real magnetization) distribution in the stripe domain structure with inclined domain boundaries. However, it is the comparison of the results obtained in such analysis with the corresponding experimental data that can provide the establishment of the real distribution.

REFERENCES

1. D. I. Sementsov and A. P. Gubarev, Opt. Spektrosk. **53** (3), 501 (1982) [Opt. Spectrosc. **53**, 295 (1982)].
2. G. Tielian and H. Yuchuan, J. Magn. Magn. Mater. **35**, 161 (1983).
3. V. V. Katal'nikov, A. V. Kovalev, and V. N. Pavlov, Zh. Tekh. Fiz. **55** (2), 394 (1985) [Sov. Phys. Tech. Phys. **30**, 231 (1985)].
4. G. S. Kandaurova and V. Kh. Osadchenko, Opt. Spektrosk. **62** (3), 703 (1987) [Opt. Spectrosc. **62**, 417 (1987)].
5. D. I. Sementsov and R. M. Grechishkin, Phys. Status Solidi A **118**, 271 (1988).
6. Yu. N. Zubkov, R. M. Grechishkin, and D. I. Sementsov, Kristallografiya **36** (6), 1484 (1991) [Sov. Phys. Crystallogr. **36**, 842 (1991)].
7. E. N. Il'icheva, A. V. Dubova, V. K. Peterson, *et al.*, Fiz. Tverd. Tela (St. Petersburg) **35** (5), 1167 (1993) [Phys. Solid State **35**, 594 (1993)].
8. G. S. Kandaurova, V. N. Mal'tsev, and V. Kh. Osadchenko, Opt. Spektrosk. **67** (2), 413 (1989) [Opt. Spectrosc. **67**, 241 (1989)].
9. Yu. N. Zubkov, I. M. Kozhemyakin, and T. M. Sementsova, Izv. Vyssh. Uchebn. Zaved., Fiz., No. 9, 68 (1997).
10. A. M. Balbashov and A. Ya. Chervonenkis, *Magnetic Materials for Microelectronics* (Énergiya, Moscow, 1979).

Translated by L. Man